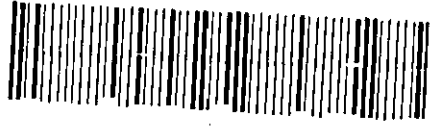

WALL COOLING BY GASEOUS INJECTION FOR A HIGH PERFORMANCE COMBUSTION SYSTEM.

by

Geoffrey John Sturgess.

D.L.C.(Eng.), D.I.C., A.F.R.Ae.S., C. Eng.

Thesis Submitted for the degree of

Doctor of Philosophy

in the Faculty of Engineering

Loughborough University of Technology

July, 1970.

INDEX

ACKNOWLEDGEMENTS

Grateful thanks for financial support of the experimental programme to the Ministry of Aviation under Agreement No. PD/170/06/ADM, and to the technician staff of the University who helped produce the test facility.

Particular acknowledgement is made to the kindness of Bristol Engine Division, Rolls Royce Ltd., and, Aircraft Engine Group, General Electric Co., both of whom made available certain experimental data: Also, to the continued encouragement of my former collegues of Rolls Royce with whom I have had many helpful discussions.

Finally, to my wife who typed the manuscript, and my long-suffering family who have patiently borne all the very real hardships associated with the production of this work.

The views presented in this thesis are my own and should not be attributed to any of the authorities mentioned above.

.....

ABSTRACT

The literature is reviewed and the effects of certain aerothermodynamic and geometric parameters on film effectiveness and local heat transfer coefficient are assessed. A difference in form and performance is recognised between the slots commonly used in research work and these used in practice. The developing film is modelled as a transition region preceeding a potential core and followed by an asymptotic, main region. For practical slots, it is shown that a transition region always exists in the film regardless of the injection velocity ratio; also, that the range of interest consists of the potential core and transition regions alone. A boundary layer theory for effectiveness is developed by taking account of the potential core and the jet-like nature of the real film. The resulting blowing group is tested against eleven very different practical geometry slots and excellent correlation of data is achieved. A universal equation is obtained for practical geometries of this general class. A theory is derived for film local heat transfer coefficient, in which potential core is accounted for: Comparison with experimental data is satisfactory. The key to film cooling theory is thus established as the potential core. A semi-empirical theory for potential core length is developed, in which slot lip thickness and boundary layers are accounted for. Measurements of hydrodynamic film development were made and the reality of the potential core established. The assumptions of the theory were substantiated by these measurements. Good predictions were obtained for most conditions. The theory is also tested against potential cores measured from the experimental

data of several research workers, covering wide ranges of injection conditions, slot height and, lip thickness. Excellent agreement is obtained. The degree of accuracy required of prediction for potential core is assessed by comparing measurements of film hydrodynamic development with predictions made using predicted potential core lengths as a starting point. Excellent agreement is again obtained. A final test is made by making predictions of film effectiveness and comparing against measured data from several additional practical slots over wide ranges of injection conditions. Once again, remarkable agreement is obtained. It is concluded that satisfactory predictions of potential core length and film effectiveness for practical slot geometries can be made.

.....

CHAPTER AND APPENDIX CONTENTS.

LIST OF TABLES AND FIGURES

.....

CHAPTER 1.

INTRODUCTION

1.1. Historical Background.

There are two ways in which the life of a high temperature component can be increased to an acceptable level by keeping the experienced temperatures within the limits imposed by material properties:

a). cooling,

b). preventive methods such as coatings, linings etc.

For many applications the weight and bulk penalties associated with preventive methods are unacceptable and active cooling must be adopted.

Film - cooling was first described by German rocket scientists in 1939 and has since found application under various guises in a wide variety of engineering situations. The aerospace industry can offer many examples of practical systems of film-cooling and its thermal inverse, film heating: Rocket motor combustion chambers, gas-turbine combustion chambers and jet-pipes, aircraft anti-icing systems, rain deflectors, windscreen heaters - all are examples of the basic film-cooling/ heating process. These applications however, offer such extremely diverse environmental and geometric situations that the common features involved in the process become submerged under dominating local influences peculiar to the particular problem under study. For this reason the present study is confined to just one such problem, that of film-cooling the aircraft gas-turbine combustion chamber.

Air appears as the logical coolant for gas-turbines because there is always an excess of it available over the amount required to burn the fuel in the combustion chamber primary zone, and it is available at a suitable pressure for injection. With air as a coolant it is not necessary to go to the expense of carrying a specialised coolant and associated tankage, pumps and delivery lines. The main advantage of air however, is that no heat is lost from the working cycle of the engine. The air cooling technique commonly in use for flametube is film-cooling; it consists of introducing through a series of discrete 'span-wise' slots, on and tangentially to the surface to be protected, a thin film of relatively cool air which acts as both coolant and shield between the hot gas-stream and the wall.

In the early years of the aircraft gas-turbines, combustion chambers were uncooled and with peak metal temperatures of the order of 900^{0}C, flametube life was correspondingly short. However, since the sole users at this time were the military to whom the short-life philosophy is no stranger, this was for the time being, acceptable although undesirable. Communist sources report that in 1955, 50 - 60 percent of aircraft engine troubles in the United States Air Force occured in flametubes due to excessive wall temperatures. With the advent of wall cooling by discrete injection of an air coolant on and along the heated wall surface, peak wall temperatures were reduced to the order of 600^{0}C with a very satisfactory improvement in flametube life. The Rolls Royce Dart turboprop engine entered service with uncooled flametubes which operated at a temperature of 850^{0}C and had a service life of some 300 hours only. The addition of film cooling in later Marks of engine reduced wall temperatures to 500^{0}C and service life in-

creased by an order of magnitude. The effect on flametube wall temperatures is shown in detail by figure 1.0, part a) which shows measured temperatures and, part b) the layout of the flametube together with the thermocouple positions. The particular chamber is a tubular configuration of early Soviet design typical of engines, model M and B, which powered MIG-15 and early MIG-17, aircraft (1A). The gas-turbine became an airborne power-plant of wide application in aeronautical engineering.

Engines must have more thrust, less weight and consume less fuel; these are the classic demands of the aircraft designer. Such apparently insatiable demands require first, an ever increasing thrust to weight ratio from the engine. The spectacular improvements in thrust to weight ratios achieved to date are shown in figure 1.1, which is constructed from data given by Lloyd (1.). Improvements in the techniques of lightweight construction and compressor design have contributed greatly to these improvements, initially in fact more so than increases in peak working temperatures. However, improvements in conventional construction techniques became less and less with passing time and in order to maintain progress, high temperature operation was dictated. It is worthwhile noting that the introduction of composite materials such as Hyfil, offers a step-change in light weight construction and, hand in hand with high temperature operation, possibilities of still further increases in thrust-weight ratios.

1.2. Benefits of High Temperature Operation.

In figure 1.2 the increase in specific thrust with increasing turbine entry temperature (T.E.T.), is shown for a simple turbo-jet. It may be seen that an increase in operating temperature always results in more thrust per pound mass of air entering the engine. This gives a reduction in engine weight, frontal area and hence installed drag, for a given thrust. However, if really high temperatures are contemplated the improved specific thrust is obtained at the expense of increased fuel consumption, particularly at subsonic flight speeds and low pressure ratios. This adverse effect is mitigated by having the design point for subsonic application at sea level static, the take -off condition. Really high temperatures are encountered only for short periods at take-off and the engine is throttled in the cruise to temperatures where fuel consumption is more economical.

Effects on thrust / weight ratio are shown in figure 1.3 for a twin spool by-pass engine for various T.E.T's. The additional advantages with this type of engine cycle over that of the straight turbojet are that increasing the operating temperature for the same installed thrust and size low-pressure compressor, enables the entire high pressure section to be smaller and lighter. The smaller high-pressure section results in a higher by-pass ratio which gives a lower specific fuel consumption, (S.F.C.). This is illustrated in figure 1.4.

Note that for the particular engine considered in figures 1.3 and 1.4, there is little point in increasing T.E.T. beyond about 1,600°K. Halls (2.) illustrates that for the by-pass engine it is advantageous in

specific fuel consumption to operate at cruise with temperatures almost as high as those at take-off. For both types of engine at a given T.E.T., increasing the pressure ratio decreases the S.F.C. and also the specific thrust, but only slightly.

The technical break-through which enabled high temperature operation to become possible was the introduction of turbine blade cooling. Figure 1.5 is reproduced from Hall's paper and shows the increasing T.E.T's of some Rolls Royce engines with time. Also shown on figures 1.2, 1.3 and 1.4 are the temperature limits for uncooled turbine blades together with the probable limit for conventional cooled blades(2), and, the stoichiometric mixture temperature for kerosine fuel.

It may be seen by reference to figure 1.4 that from about 1960 onwards, large increases in operating temperature have been achieved due to the development of cooled turbine blades, together with some improvements in material properties, These elevations in temperature are discernable in figure 1.1 as a firm and steady improvement in thrust / weight ratio from 1960. Reductions in specific fuel consumption have also been demonstrated. It is clear that both pressure ratios and turbine entry temperatures will in the future increase over todays already high values, (3.).

1.3. Consequences of High Temperature Operation.

As a result of the improvements in engine performance from increased pressure ratios and turbine entry temperatures as described above, together with the appearance of a supersonic cruise design-point, cooling the combustion chamber flametube to acceptable material levels has become a major problem. Despite film-cooling, wall temperatures have again risen to around

850°C and a considerable proportion of the gas-generator airflow is required as coolant. This is because the flametube environment, always adverse is now an extremely severe one and the "cooling potential" available has been rapidly reduced. The difficulties of increasing severity of environmental conditions have been highlighted by Roudebush (3A). Trends in combustion chamber operating conditions have been described by Jackson and Odgers (4) and figure 1.6 which shows the increase with time of combustion chamber inlet temperature, is reproduced from their paper. Flametube material for many years has been sheet Nimonic 75 alloy for which a desirable maximum temperature is about 800°C. For this material then it is possible to work out the available "cooling potential" - the difference in temperature between the coolant and the wall - and this is shown in figure 1.7 for predominantly British engines. The net result is an increase in the amount of air required as a coolant, which is illustrated in figure 1.8, again taken from Jackson and Odgers.

The amount of air required for combustion chamber cooling purposes is shown to be increasing with the more demanding conditions of operation now becoming standard. Does this constitute a problem and if so, what is the nature of the problem?

The flametube for the present purpose may be crudely divided into two main regions - the primary zone (P.Z.) where the flame is stabilized, and, the dilution zone (D.Z.) where turbine entry temperature is determined. The overall fuel / air ratio of the chamber will be determined by the basic engine specification at design point and is fixed therefore. The primary zone fuel / air ratio is chosen, depending on the exact application of the

engine, to satisfy all or some of the following main requirements:

(i) relight at altitude,

(ii) wide range of stability limits,

(iii) low smoke production.

For an ideal, well-designed film-cooling system the coolant should remain on the wall as virtually a discrete layer and the air so used therefore should not be counted in the P.Z. effective fuel / air ratio. Any increase in fuel / air ratio as a result of satisfying a film-cooling demand with air initially assigned to the primary zone will adversely affect to a greater or lesser degree all three of the main design requirements of this zone and would not in general, be possible. Primary zone fuel / air ratio must thus be regarded as fixed and air for cooling purposes debited to the dilution zone.

To avoid mechanical failures in the flametube the film cooling system must be made to work regardless of all other considerations outside those outlined above. Thus, with the premises above, success of the chamber as a whole is seen to depend upon the design of the dilution zone. The dilution zone problem is to design a high-rate mixing system to yield the temperature profiles required by the turbine in as short an axial length as possible under the lowest possible pressure loss. If this cannot be done in a given length and pressure drop because most of the dilution air is taken for cooling purposes, the whole performance of the chamber has to be compromised in various ways according to the severity of the problem:

(iv) pressure loss increased, and / or,

(v) dilution zone length increased, and / or,

(vi) some primary zone air used for cooling purposes, or,

(v) reduced flametube life.

Consideration of figures 1.2 - 1.4 showing the effects of turbine entry temperature on various aspects of engine performance, suggests that these temperatures will become very high, approaching values appropriate to stoichiometric overall fuel / air ratios. When this occurs it might be concluded that the film cooling problem will cease to be a problem as there will then be plenty of air available for cooling purposes. Figure 1.5 shows that this situation will almost certainly be encountered within the next 5-7 years, in research and development work at least. It does not mean however, the end of the film cooling problem but merely a change in its nature. The problem then will be the heavily loaded (thermally) turbine which will preclude the addition of any large amounts of air necessary to cool the turbine entry duct regions.

It has been argued that the overall film cooling system can adversely affect the whole performance of a combustion chamber if the coolant flow becomes too large a proportion of the total chamber airflow. However, even if the system is so designed as not to upset the dilution zone, and hence the rest of the chamber, problems of a local nature can still arise. If the performance of the individual injection device used is poor it may be necessary to inject locally, very large amounts of coolant so that:

(vii) in the primary zone, chilling of combustion reactions occurs causing blue smoke and also contributing to the presence of obnoxious substances in the exhaust,

(viii) in the turbine entry duct, bad radial temperature profiles

at the chamber exit are produced with deliterious effects upon turbine life.

Small gas turbine engines have their own special difficulties and the problems of small size combustors have been considered by Bell (5) who showed that wall cooling problems can become extremely difficult as advanced V/STOL aircraft demand higher specific shaft-horse power with reduced weight, volume and specific fuel consumption.

1.4. The Purposes of the Present Study.

The broad outlines of the problem to be studied have been given in section 1.3 above. The precise steps required to be taken in the study may be stated as follows: (1) To survey the available film-cooling literature and in particular, to ascertain gaps in knowledge where additional experimental work is necessary. (2). To use the information collected to bring order into the experimental data obtained from practical cooling devices. (3). To use this collated information to study practical systems in combustion chambers. (4). To establish design and prediction procedures for practical systems of film cooling.

In any study of this applied nature it is difficult to decide precisely how far situations should be idealised to render them amenable to theorectical treatment. To lean too much to either side is unsatisfactory. In view of the topicality of the subject, the approach in the present case is a reasonable balance between practical engineering and mathmatical development. This at any rate, was the aim. In this manner, it was hoped that the study would provide directly useful information for those engineers concerned with combustion chamber film cooling systems.

CHAPTER 2

LITERATURE SURVEY

(unless otherwise stated, the following remarks apply for zero pressure gradient, incompressible, two-dimensional, turbulent flows).

2.1. Introduction.

A considerable number of studies of the film cooling process have been made and often the mode of injection has varied widely. It is therefore useful to classify film cooling flow systems and this is done in figure 2.1: From this figure the position of practical systems in common useage may be seen. The majority of the published literature describes devices which fall into the two-dimensional, discrete slot category of film cooling. This should be borne in mind when considering the recommendations made throughout this chapter.

Early in film cooling research it was found by Scesa (6) that the standard impermeable wall, turbulent heat transfer relations could be used for the estimation of heat fluxes provided the heat transfer coefficient was based on the difference between actual wall temperature and the adiabatic wall temperature which would prevail under flow conditions identical to those under study,

$$\text{i.e.} \qquad h_{Eff} = \frac{\dot{q}_c}{T_{s,ad} - T_s} \qquad 2.1.$$

This proposition was subsequently confirmed by Seban, Chan and Scesa (7) and, Hartnett, Birkebak and Eckert (8) for both normal and tangential injection in regions remote from the injection plane and for mass velocity ratios M, where $M \equiv \frac{\rho_c u_c}{\rho_m u_m}$, less than unity.

If the blown wall is made adiabatic, the effects of injection are completely described by the ratio between the excess of mainstream over wall temperature to the excess of mainstream over injected-air temperature, provided the fluid property variations between the two streams are not significant and, the mass flow rate of coolant is small compared with that of the mainstream. This ratio, the normalised adiabatic-wall temperature distribution, is termed the film effectiveness,

$$\text{i.e.} \quad \eta \equiv \frac{T_m - T_{s,ad}}{T_m - T_c} \qquad 2.2.$$

Useful relationships between temperature, concentration and, enthalpy based definitions of effectiveness have been derived by Stollery and El-Ehwany (9),(10). Equality of these definitions for effectiveness depends on the equality of Schmidt, Lewis and Prendtl numbers with unity.

For low flow stagnation enthalpies and constant fluid properties, film cooling can be considered as equivalent to film heating, provided there is no radiation heat source to account for. For convenience, most film cooling studies have dealt with this thermal inverse problem of film heating; the definitions given above are not affected.

When the variation of effectiveness over a film-cooled surface is known the wall temperature distribution may apparently be calculated for a prescribed heat flux using equations 2.1 and 2.2 , together with a suitable known relationship for heat transfer coefficient.

2.2. Heat Transfer Coefficient

Investigation of heat transfer coefficients over a wide range of mass velocity ratio, $0.17 \leqslant M \leqslant 20.5$, was made by Seban (11)

who found a situation rather more complex than was suggested by the earlier work. For $M<1.0$, measured heat transfer coefficients, defined by equation 2.1, were compared with values calculated for the appropriate conditions from the usual Colburn equation

$$\frac{h_s}{\rho u_m c_p} = 0.037 \left(\frac{u_m x}{\nu}\right)^{-0.2} \qquad 2.3$$

Values of h_{Eff}/h_s equal to unity were only encountered at distances greater than about 70 slot heights downstream from the injection plane. Exactly how the local heat transfer coefficients approached those predicted by the Colburn equation was found to depend on the magnitude of the injection velocity and also, the nature of the flow within the slot. The earlier work had not detected these variations because minimum x- length Reynolds numbers had been rather large, being for Hartnett et al (8), about 10^6, representing a closest approach to injection of something over 8 inches or about 65 slot heights.

For $M > 1.0$, Seban obtained empirical correlations which can be arranged in the convenient forms,

$$St.Re_s^{0.3} = 0.1354 \left(\frac{x}{s}\right)^{-0.3} \qquad 2.4$$

for $\frac{x}{s} < 40$ and,

$$St.Re_s^{0.3} = 0.41 \left(\frac{x}{s}\right)^{-0.6} \qquad 2.5$$

for $\frac{x}{s} \geq 40$

The constant given in equation 2.4 is that obtained by fitting equation 2.5, which agrees well with other data to be presented, with Seban's data at the point $\frac{x}{s} = 40$; the constant given in the original paper would seem to be incorrectly reproduced. The existance of two equations suggests the heat transfer is controlled by the slot flow

and is almost independent of mainstream conditions - i.e. wall jet-like.

In a later paper by Seban and Back (12) these results of Seban's were reconsidered. The existance of the two equations was suggested to be perhaps due to an uncertainty in the measurement of the x- distance from injection. It was suggested it would be better to measure from an effective origin of the film from upstream of the actual injection point. A correction was therefore incorporated for the positive distance between the injection point and the effective origin of the film to account for its finite thickness at injection and equations 2.4 and 2.5 were thus represented by the single expression.

$$St.Re_s^{0.3} = 0.41\left(\frac{\xi}{s}\right)^{-0.6} \qquad 2.6$$

for $\frac{\xi}{s} \geq 30$ where, $\xi = x + x_o$

and, $x_o/s = 12$, was taken from the data of Seban (11), being the distance upstream of the effective origin of the film.

Seban (11) also quoted an empirical correlation due to Jakob for $M > 1.0$, which has been arranged as,

$$St.Re_s^{0.3} = 0.15\,Re_s^{0.1}\left(\frac{x}{s}\right)^{-0.6} \qquad 2.7$$

The above three sets of equations, 2.4, 2.5, 2.6, 2.7, are compared in figure 2.2, together with some impervious wall predictions from the Colburn equation for four of Seban's test runs. For equation 2.7 the slot Reynolds number was taken as 1,000 - 7,000, which range is appropriate for Seban's data. It may be observed from this figure that for distances greater than about 50 slot heights downstream, the data indicate Stanton number is considerably reduced over impervious wall values and normal turbulent boundary layer relationships are not applicable.

As unity mass velocity ratio was reached Seban (11) recorded an immediate transition to heat transfer values typical of impervious flat-plate flow.

Taking the Colburn analogy,

$$\frac{h}{\rho u_{max} c_p} \cdot P_r^{2/3} = \frac{\tau_s}{\rho u_{max}^2}$$

as a suitable relationship between the heat transfer and friction coefficients, and using empirical values for velocity decay and shear stress coefficient,

$$\frac{u_{max}}{u_c} = 3{\cdot}6 \left(\frac{\xi}{\xi_s} \right)^{-0{\cdot}45}$$

and,

$$\frac{\tau_s}{\rho u_{max}^2} = \frac{0{\cdot}054}{Re_s^{0{\cdot}25}}$$

derived from Seban's earlier data, Seban and Back (12) derive for $M > 1.0$, a prediction equation which may be written,

$$St.Re_s^{0{\cdot}3} = 0{\cdot}25\, Re_s^{0{\cdot}05} \left(\frac{\xi}{\xi_s} \right)^{-0{\cdot}6} \qquad 2.8.$$

This semi- empirical prediction is compared with the empirical correlations in figure 2.2.

A more general analysis was carried out by Myers, Shauer and Eustis (13) for the pure wall-jet ($M = \infty$), with an unheated starting length. The analysis was applied initially to the step-wall temperature case and later extended to arbitrary heating conditions through the use of superpositions. The hydrodynamic solution (14) was linked to the thermodynamic through the ratio of eddy diffusivities for heat and momentum. The chief difficulty comes in designating a suitable value to this ratio, λ. Lambda is not uniform across the film and although the arguments advanced for combining the distribution of λ for the free-jet together with that for the flat-plate to give the wall-jet case are not unconvincing, this problem should be investigated further before λ may be dealt with confidently.

The assumption was made that velocity and temperature profiles obeyed the usual 1/7th. power laws throughout the film and this is clearly unsupportable. However, using their theorectical result as a basis for correlation of data, they obtained the semi-empirical relationship for the wall-jet which may be arranged as,

$$St.Re_s^{0.3} = 0.118\,Re_s^{0.1}\left(\frac{x}{s}\right)^{-9/16}\left[1-\left(\frac{L}{x}\right)^{9/20}\right]^{-1/16} \qquad 2.9$$

for $45 \leqslant \frac{x}{s} \leqslant 186$ to $\pm 10\%$ where,

L = unheated starting length.

Equation 2.9 is compared in fig.2.2 with the other relationships for the case of zero unheated starting length and a Reynolds number range $16.6 \times 10^3 \leqslant Re_s \leqslant 37.8 \times 10^3$, appropriate to the tests of Myers et al. To extend the results to gases other than air, it was recommended that the calculated Stanton numbers be multiplied by the ratio $\left[Pr_{Air}/Pr_{Gas}\right]^{0.4}$

A further correlation for the two-dimensional wall-jet was obtained by Akfirat (15) as,

$$Nu = 0.097\,Re_s^{0.8}\left(\frac{x}{s}\right)^{-0.6} \qquad 2.10$$

which may be rearranged in the same form as the others as,

$$St.Re_s^{0.3} = 0.1386\,Re_s^{0.1}\left(\frac{x}{s}\right)^{-0.6} \qquad 2.11$$

if Prandtl number has the value of 0.7. Equation 2.11 is also shown in figure 2.2.

It may be seen from a consideration of the comparisons made in this figure that the agreement between experimental data is good at large distances from the injection plane and that Seban and Back's predictions are reasonable. Nearer the slot Stanton numbers become reduced and it would appear normal boundary layer values might be appropriate. Seban and Back's method does predict the form of this but underestimates the heat transfer.

The calculation of the rate of heat transfer in film cooling can involve as has been shown, two distinct steps. First, the determination of the adiabatic wall temperature distribution and second, the determination of the local heat transfer coefficient according to equation 2.1. The solution of the second problem has been related directly to that of the first by Spalding (16) by connecting the heat transfer coefficient with film effectiveness. Interpreting effectiveness in items of the coolant mass fraction at the wall, assuming the film is boundary layer-like in velocity profile and therefore, that a similar relationship between Stanton and Reynolds numbers exists as for normal turbulent boundary layers, Spalding derives the relationship,

$$\frac{h_{eff}}{\rho_m u_m c_{p_m}} = A\left[1+\left(\frac{u_c}{u_m}-1\right)\eta\right]\left[1+\left(\frac{T_c}{T_m}-1\right)\eta\right]^{(b\omega-1)} \cdot \left(\frac{\rho_c u_c s}{\mu_m \eta}\right)^{-b} \qquad 2.12.$$

where, A = constant,

w = exponent in temperature viscosity relationship,

b = constant.

In a study of the available data to determine these constants Patel (17) however, was unable to show such a relationship existed, even for large x/s.

2.2.1. Summary and Comments:

Surprisingly little detailed work either theorectical or experimental, has appeared on heat transfer in film cooling. The majority of such work which has been published is related to the wall-jet type of film cooling.

It is established that the local heat transfer coefficient should be defined by equation 2.1 and if this definition is used, accepted turbulent boundary layer relationships may be used under certain conditions. These

conditions are that the mass velocity ratio M should be less than unity and, that the minimum distance from injection for validity should not be less than 70 slot heights. For distances closer to the slot and with $M < 1.0$ still, the heat transfer depends in a complicated manner on M, mainstream conditions and, local flow perculiarities originating in the slot design. For $M > 1.0$, the heat transfer is controlled by the injected flow and is almost independent of the mainstream for several hundred slot heights downstream. For large distances from the injection plane, ($\frac{x}{s} > 40$), Stanton number is a function of slot Reynolds number and distance only; impervious flat-plate relationships do not apply. Evidence on heat transfer very near the slot is vague and scanty but the Seban and Back (1961) empirical correlation appears acceptable down to $\frac{x}{s} = 18$. The Seban and Back semiempirical relationship appears to predict the form of the data well but underestimates the heat transfer by up to 10%.

The comparison of the heat transfer data of Jakob, Seban and, Myers et al is very satisfactory considering the wide range of Reynolds numbers and mass velocity ratio covered. In addition, the data of Myers et al is for constant wall temperature whilst the other data are for constant heat flux and this difference in thermal boundary conditions would account for some small disagreement.

2.2.2. Recommendations:

1. For mass velocity ratio $M = 1$, use equation 2.3.
2. For $M > 1.0$, use equation 2.8.
3. For $M < 1.0$, and $x/s > 770$, use equation 2.3.
4. When using equation 2.3 base property values for Stanton and Reynolds numbers on the reference temperature,

$$T_{Ref} = \tfrac{1}{2}(T_s - T_m) + T_m + 0.22\,(T_{s,ad} - T_m) \qquad 2.13.$$

2.3 Adiabatic Wall Temperature Distribution.

2.3.1. Dimensional Analysis.

Dimensional arguments by Samuel and Joubert (18) yielded the parametric relation for film effectiveness,

$$\frac{T_m - T_{s,ad}}{T_m - T_c} = F\left[G_s, \frac{T_m}{(T_m - T_c)}, Re_s^{-1}, Re_x^{-1}, \frac{x_c}{s}, \frac{X_m}{s}, \frac{x}{s}, \frac{\rho_c u_c}{\rho_m u_m}, \frac{\mu_m c_p}{k}, \right.$$
$$\left. \frac{\mu_c c_p}{k}, \frac{\rho_c}{\rho_m}, \frac{d\nu}{dT}(T_m - T_c)/\nu_c, \frac{d\rho}{dT}(T_m - T_c)/\nu_m \right] \qquad 2.14.$$

which indicates the difficulties associated with any purely empirical approach to the problem. Sufficient experimental work could result in a direct solution of this relationship but dealing with each individual parameter in turn would be a time consuming process and the large set of resulting empirical relations would be extremely unwieldy. In addition, as with any purely empirical approach, application of the relations outside the range of test conditions which yielded them would always be doubtful.

Milford and Spiers (19) quote results of a dimensional analysis by Winter for film effectiveness. Winter (20) assumed that since the processes of convective heat and mass transfer are almost invariably governed by functions of Reynolds, Prandtl and Schmidt numbers, that effectiveness is also. He further postulated that for film cooling, relative effects rather than absolute magnitudes are important. Using the form of the established equations to correlate heat and mass transfer data, together with a data examination, the best correlation was obtained using,

$$\Omega = \left(\frac{Re_m}{Re_c}\right)^{0.8} \cdot \left(\frac{Sc_m}{Sc_m}\right)^{0.44} \cdot \left(\frac{Pr_m}{Pr_c}\right)^{0.3} \cdot \frac{x}{s}^{0.8\,0.2} \qquad 2.15$$

where Reynolds numbers were defined, $Re \equiv \frac{\dot{m} d_e}{A\mu}$, d_e being equivalent diameter. This correlating parameter was applied to results from an un-

obstructed annular gap of heights ranging from 0.075 to 0.20 inches with tangential injection into a 6 inch diameter axisymmetric duct, tested over a wide range of experimental conditions. It was found that the product of the Prandtl and Schmidt number terms was almost constant and could be taken as unity without serious error. With this and the additional assumption that viscosity is a function of the square root of temperature, the simplified correlation group was arrived at as,

$$X = \left[\frac{\dot{m}_m A_s}{\dot{m}_c A_m}\right]^{0.8} \cdot \left(\frac{T_m}{T_c}\right)^{0.6} \cdot \left(\frac{x}{s}\right)^{0.8} \cdot \left[\frac{u_m}{u_c} + 0.2\right]^{-5/4} \qquad 2.16$$

for $0 < {}^{u_m}/_{u_c} < 0.8$ and,

$$X = \left[\frac{\dot{m}_m A_s}{\dot{m}_c A_m}\right]^{0.8} \cdot \left(\frac{T_m}{T_c}\right)^{0.6} \cdot \left(\frac{x}{s}\right)^{0.8} \qquad 2.17$$

for ${}^{u_m}/_{u_c} > 0.8$.

The performance of the slot was represented to ± 10% by,

$$\eta = 1.06 - 0.0092\,X \qquad 2.18$$

Equation 2.17 may be re-arranged if it is assumed that viscosity is proportional to temperature raised to the power 0.6, as,

$$X = \left(\frac{x}{Ms}\right)^{0.8} \cdot \left(\frac{\mu_c}{\mu_m}\right)^{-1} \qquad 2.19$$

2.3.2. Theoretical Approaches to Film Effectiveness Based on the Boundary Layer Model.

A large number of theoretical analyses have been made to predict film effectiveness and the majority of these fall conveniently into two groups:

a) Those which consider the film to develop in a manner predominantly boundary layer-like,

b) and, those which consider film development to be predominantly jet-like.

At large distances from the injection plane it is reasonable to expect the film to attain the characteristics of a thick but otherwise normal, turbulent boundary layer, regardless of the injection characteristics. A number of such asymptotic solutions starting with the energy equation (21), (22), (11), (8), (23), (24), (9), (25), have been made and the final expression achieved can usually be reduced to the form,

$$\eta = \alpha \left(\frac{x}{M s}\right)^{\beta} \cdot \left(Re_s \cdot \frac{\mu_c}{\mu_m}\right)^{\gamma} \qquad 2.20$$

In this equation the values of β and γ depend on the wall shear stress law taken; the constant of proportionality α, depends on the velocity and temperature profiles chosen. The values resulting from re-arrangement of the various versions obtained in these analyses are given in Table 2.1 and some of the various versions of 2.20 are compared in Figure 2.3. The agreement shown in this figure is good although this should not be surprising since the separate analyses have in common the energy balance equation, flat plate 1/7th power law profiles, pipe-flow wall shear stress laws, and are similarity solutions. The differences in the values obtained for α arise from the assumptions made for temperature profile. The temperature profile chosen describes the degree of fluid mixing in the film- the greater the mixing, the lower the value of α . References (23), (9) and (24) for example, have assumed complete mixing so that fluid temperature is uniform across the film at any x- station and a temperature discontinuity appears at the film free surface.

TABLE 2.1

Comparison of values in boundary layer model prediction equation.

Author	Reference	α	β	γ
Wieghardt	21	5.44	-0.80	0.20
Tribus & Klein	22	4.62	-0.80	0.20
Seban	11	3.10	-0.80	0.20
Hartnett et al	8	3.39	-0.80	0.20
Seban & Back	25	11.20	-0.85	0.15
Kutateladze & Leont'ev	23	3.10	-0.80	0.20
Stollery & El-Ehwany	9	3.09	-0.80	0.20
Sturgess	24	-	-0.80	0.20

Attempts have been made to take account of the initial region of the film where a thermal and hydrodynamic potential core region might exist (25),(23), (26), (27). Of these attempts, Seban and Back (25) found they were unable to predict potential core length and abandoned their approach, whilst Spalding et al (26), (27) found it necessary to make a provisional empirical recommendation. A prediction for potential core length through Abramovich's jet-theory (28) was attempted by Kutateladze and Leont'ev (23), but they finally recommended this region be neglected in the interests of simplicity and advocated the use of a simple interpolation formula to link the asymptotic solution to the point known by definition, that effectiveness is unity at the injection plane. Their equation, which was for constant properties is,

$$\eta \simeq \left[1 + 0.24\, Re_s^{-0.25} \cdot \frac{u_m}{u_c} \cdot \frac{x}{s}\right]^{-0.8} \qquad 2.21$$

and may be seen in Figure 2.3.

Attempts to correct for the initial thickness of the film at the injection plane for tangential injection have been made by Stollery and El- Ehwany (9), Seban and Back (25) and Spalding et al, (26). Seban and Back decided they were unable to make a prediction for a suitable correction length. Stollery and El-Ehwany's prediction,

$$\eta = 3.09\left[4.1 + \frac{x}{Ms} \cdot \left(Re_s \cdot \frac{\mu_c}{\mu_m}\right)^{0.25}\right]^{-0.8} \qquad 2.22$$

is also given in Figure 2.3.

A consideration of Figure 2.3 which compares some of the theories based on the turbulent boundary layer model, reveals an agreement in final slope which was to be expected from the common power law assumptions, but a wide divergence in starting point. This difference arises because of the different assumptions made for temperature profile. The predictions of Kutateladze and Leont'ev and, Stollery and El-Ehwany, are different in form to the others for small values of $\frac{x}{Ms}$. This is because of their attempts to account for the film initial regions, which represent a less crude approach than the others but are still not particularly satisfactory since they do not really describe the physical processes taking place.

2.3.3. Theoretical Approaches to Film Effectiveness Based on the Jet Model.

The second group of theoretical models which must be considered is that which treats the film as behaving predominently jet-like.

Velocity maxima in profiles may be expected to exist only for $u_c > u_m$ and in regions relatively near to the injection point.

Seban and Back (12) again used the energy balance as with their asymptotic boundary layer model, in analysis of film cooling by considering the jet-model for the flow. The energy balance,

$$c_{pc}\rho_c u_c s T_c = \rho_m c_p u_{max} T_{s_{ad}} \delta_{m/2} \int_0^\infty \frac{\rho}{\rho_m} \cdot \frac{u}{u_{max}} \cdot \frac{T}{T_{s_{ad}}} \cdot d\left(\frac{y}{\delta_{m/2}}\right) \quad 2.23.$$

where $\delta_{m/2}$ is the distance from wall to point when velocity is equal to half its maximum value, was considerably simplified before integration and experimental temperature profiles together with Glauert's theoretical velocity profiles (2.9) were used to enable the integral to be evaluated. Empiricism was employed to determine both Glauert's velocity profile parameter and, the distance $\sim$ position of maximum velocity relation, which automatically therefore includes a correction for finite initial thickness of the film. Their final result was,

$$\eta = 7.7 \frac{\rho_c}{\rho_m} \cdot \left(\frac{\xi}{s}\right)^{-0.6} \quad 2.24$$

Previously, equation 2.6, Seban and Back were forced to use empirical values for x_o because of their inability to predict it, $x_o/s = 12$ being taken. The empirical data used to obtain this value was for isothermal conditions, as is Glauert's analysis, and because of this, equation 2.24 tends to overestimate measured effectiveness by 11% or more.

Analyses for both jet-like $u_c > u_m$, and wake-like $u_c < u_m$, films were derived by Spalding et al (27) from Spalding's postulate (30) that the film entrains like a jet and, that a jet local entrainment rate depends only on local flow properties. Dimensional analysis was used to

determine the functional relationship between momentum deficit, pressure gradient and, velocity ratio, the constants being evaluated from available experimental data. The analysis for effectiveness depends on the conditions for similarity of momentum and energy equations being fulfilled. The basic relation is extended (26) to incorporate a correction for potential core length, although the resulting equation does not then in itself form a complete solution since it involves potential core length x_p , as an unknown. Spalding et al recommended for solution, a constant value of 14 for non-dimensional potential core length x_p/s . The expression obtained for zero pressure gradient, in terms of enthalpy-based effectiveness is,

$$\eta_h\left(\frac{u_c}{u_m}-1\right) = 2.4\left[\frac{(x-x_p)}{2s}\cdot\frac{C_m u_m^2}{C_c u_c (u_c-u_m)} + \left\{\frac{2.4\,u_m}{(u_c-u_m)}\right\}^2\right]^{-0.5} \quad 2.25$$

In view of their expectation that potential core length would be a function of velocity and density ratios, which implies shear-mixing, Spalding et al's assumption of a constant $\frac{x_p}{s}$ seems unrealistic.

2.3.4. Theoretical Approaches to Film Effectiveness Based on Combinations of the Boundary Layer- and, Jet-Models.

The boundary layer model for flow in the film can reasonably be considered to apply for regions very far downstream from the injection plane whatever the injection conditions and, for $u_c < u_m$ for all distances outside the initial region. The jet-model can reasonably be considered to apply for $u_c \geq u_m$ in regions fairly near to the injection plane only, since a flow originally jet-like can be expected to become

of the boundary layer type at large distances downstream. Generally, a film cooling theory whether for prediction or correlation purposes, will have to fit all velocity ratios and all values of x, so a combination of the boundary layer and jet models to cover the whole flow field would seem a logical step to take.

Such a step as that suggested above was taken by Spalding, Jain and Nicholl (31). For $u_c > u_m$, outside the potential core but not too far downstream, free-jet processes were taken as dominant and to represent this, a version (27) of equation 2.25 was used. Similarly, for $u_c < u_m$ outside the potential core, the boundary layer processes will dominate and a boundary layer-type equation was used, with an empirical constant to improve the fit with available data. These two equations were combined to give a composite formula to fit all available data for both jet and wake cases,

$$\eta_h \simeq \frac{\rho_c u_c / \rho_m u_m \times \text{constant}}{0.295\left\{\frac{\rho_c u_c |(u_c - u_m)|}{\rho_m u_m^2}\right\}^{\frac{1}{2}} \cdot \left(\frac{x}{s}\right)^{\frac{1}{2}} + 0.189 \left(\frac{\rho_m u_m s}{\mu_m}\right)^{-0.2} \cdot \left(\frac{x}{s}\right)^{0.2}} \qquad 2.26$$

For correlation purposes, this equation was used as the basis for Spalding's correlation parameter X (32), where

$$X = 0.91 \cdot \left(\frac{u_m}{u_c} \cdot \frac{x}{s}\right) Re_s^{0.8\,-0.2} + 1.41\left\{\left|\left(1 - \frac{u_m}{u_c}\right)\right| \frac{x}{s}\right\}^{0.5} \qquad 2.27$$

For the data examined, Spalding recommended,

$$\begin{aligned} X &< 0.75 \quad , \quad \eta = 1.0 \\ X &\geq 0.75 \quad , \quad \eta = 7/X \end{aligned} \qquad 2.28$$

A more advanced procedure has been in the course of evolution by Spalding and his group at Imperial College. Spalding commenced with the

postulates (35) that the velocity, temperature and concentration profiles can be described by formulae having two main components, one accounting for effects of momentum, heat and mass transfer to the wall, and the other accounting for interactions with the mainstream, and, that fluid is entrained into the wall layer in the same manner as it is into a turbulent jet: The flow field is then described by the boundary layer model. With these two-parameter profiles, the integral forms of the boundary layer equations were solved first by various approximate methods, (36), (37), (38), (39). Because of the shortcomings associated with these solutions, a finite difference procedure for solving the partial differential equations (40) has been adopted and which is still being developed, e.g. Pai (41).

2.3.5. Other Theoretical Approaches to Film Effectiveness.

A heat balance technique together with a conduction analogy, was used by Hatch and Papell (33) in their analysis of the problem. This theory is unique of those analyses reviewed previously in that it assumes there is no mixing whatsoever between the film and mainstream i.e. the film exists as a discrete layer. This is clearly unsatisfactory in that the model is unrealistically farremoved from the actual physical process which take place even though the existance of a thermal potential core region is recognised and accounted for. The adjustments to the theory are purely empirical using data of Papell and Trout (34), together with some additional data for helium injection, and the resulting form is exceedingly cumbersome to use. It is to be noted that Papell and Trout's experimental starting effectiveness did not have the value of unity, as is required from the definition in equation 2.2. The implication is that the coolant injection temperature was incorrectly measured, perhaps up-

stream of the slot thus neglecting any subsequent heat transfer to the coolant from the hot mainstream through the slot itself. In view of these shortcomings, this method is not discussed further.

2.4.0. Experimental Investigations of Effectiveness in Two-Dimensional, Incompressible, Constant Pressure Turbulent Film Cooling.

A number of experimental investigations into the effectiveness of film-cooling have been carried out and details of the most important of these are contained in Table 2.2.

2.4.1. Slot Geometry Descriptions.

There exist two principal types of injection geometry - a step-down slot such as that of Seban (11) and, surface injection close to tangential. The latter type may be further sub-divided into porous injection areas such as that of Nishiwaki et al (42) and, those similar to that of Hartnett et al (8). Examples of some of these injection geometries are given in figure 2.4. Although figure 2.4 does contain a wide variation of injection geometry, these geometries all have one feature in common; this is, they all present a minimum aerodynamic distance to the coolant flow whilst introducing a uniform, two-dimensional film on the cooled surface. Wiegherdt's (21) injection geometry, figure 2.4a), is unique of those illustrated in that it approximates to that of a likely practical geometry for an aircraft anti-icing system, which problem Wiegherdt was indeed investigating, and the initial parts of the resulting film were therefore three-dimensional in nature.

A practical film cooling slot is designed to suit its application

with considerations of mechanical integrity, ease and cheapness of manufacture, and weight taking precedence over those of an aerodynamic nature. This philosophy results in geometries which are far removed from the majority of those idealised slots illustrated in figure 2.4, and which generally present a complex flow path to the coolant stream. The state of the fluid is highly three- dimensional inside the slot and can be so in the initial regions of the film, although for a properly designed slot it can become quasi-two-dimensional reasonably quickly (45).

It may therefore be seen that, although figure 2.4 does in fact represent a wide variation in injection geometry compared with practical slots, diagrammatically represented in figure 2.5, these slots all present with the exception of 2.4a), a minimum aerodynamic disturbance to the coolant flow as was stated above. To differentiate between these two fundamental classes of slot, the generic names 'clean slots' and, 'dirty slots' are in common usage applied respectively to those like 2.4 and, practical, gas-turbine cooling slots.

The majority of the data reported in the open literature are referred to clean slots.

2.4.2. Correlation of Data.

The experimental data of the various investigators are characterised by their empirical correlation for effectiveness, and some of the major of these are contained in Table 2.3; the ranges of the experiments are to be found in Table 2.2.

Of these correlations, those due to Papell and Trout (34) are not considered further because it is immediately apparent from a persual of their

original report that despite insulation, heat transfer to the coolant through the slot took place and that because of this, the coolant temperature was measured too far upstream from the slot outlet. The wealth of data contained in this work is too great to be completely rejected however. To salvage this valuable data, a correction has been applied so that the effectiveness is always unity at the injection point (46); no correction can be made to the coolant temperature so any blowing group based as this will always be slightly in error. Any use made of the data from reference (34) is always in this corrected form.

Seesa's correlation (6) which is for normal injection, is included for completeness and historical interest.

The correlations of Samuel and Joubert (18) reveal a significant geometry effect, even at large distances from the injection point. In view of their particular slot geometry, figure 2.4.g), with its thick outer lip and ineffectual feathering, this is not perhaps surprising. In the present context therefore, their correlations are not considered relevant.

It should be noted from Table 2.3 that the majority of the correlations are for large distances from the injection plane, thus representing conditions suitable for comparison with the asymptotic solutions represented by equation 2.20 and Table 2.1, and, those illustrated in figure 2.3. These correlations are compared graphically in figure 2.6 where it may be appreciated that for what is nominally the same experiment, there is a wide divergence of results.

The form of the correlation commonly obtained for large x/M_s is,

$$\eta \propto \left(\frac{x}{M_s}\right)^{a} \qquad 2.29$$

which should be compared with equation 2.19.

The value obtained for the exponent 'a' is normally -0.7 to - 0.88 and commonly, - 0.8. It can be seen from figure 2.6 that variation of this exponent does not have too significant an effect compared with that of the "starting point", i.e. the largest value of $\frac{x}{M_s}$ for which film effectiveness η, is still unity. A fairly wide range of values has been obtained for this constant of proportionality in equation 2.29. Indeed it has been suggested that this is not a constant but depends on,

(i) slot Reynolds number according to Seban et al (7),

(ii) mainstream Reynolds number based on upstream boundary layer displacement thickness according to Goldstein et al (43),

(iii) mainstream Reynolds number based on downstream distance from the initial point of injection according to Goldstein et al (43), for the data of Nishiwaki et al (42),

(iv) mass velocity ratio according to Seban (ii) and, Samuel and Joubert, (18),

(v) velocity ratio according to Sturgess (47).

It is to be expected from equation 2.20 that slot Reynolds number would appear in any asymptotic correlation. With the model represented in this equation, Stollery and El-Ehwany (9) used the data of Hartnett et al (8) and Seban (11) to demonstrate that inclusion of slot Reynolds number did bring about a useful improvement in correlation of these data. For the data of Wieghardt (21) and Seban (11), these authors also showed that

even when slot Reynolds number is included in the group, the 'constant' of proportionality is not always a constant but depends on mass velocity ratio, M. Figure 2.7 which is based on Stollery and El-Ehwany's paper illustrates this; also shown in this figure are some additional data due to Whitelaw (44). If constant pressure mixing is assumed, it can be appreciated from figure 2.7, since then for these data $M \simeq u_c/u_m$, that the velocity ratio condition for the boundary layer model to apply is approximately $u_m/u_c \geqslant 0.66$. This was confirmed by Stollery and El-Ehwany (10) who found that the group $(x/M_s)(Re_s \cdot \mu_c/\mu_m)^{-0.25}$ also "successfully" correlated enthalpy-and concentration-based effectivenesses for $0 < M \leqslant 6.1$, provided $u_m/u_c \geqslant 0.66$.

Shown in figure 2.8 are measurements made of this 'constant' for two practical geometry cooling devices actually used in combustion chambers: The source of these data will be discussed in a later section of this thesis. These results were initially reported in reference (46) in the form of a Mach number ratio. However, the tests were all carried out at a constant temperature ratio T_c/T_m, of 0.655 and the results have been here replotted in terms of velocity ratio u_m/u_c. In reference (46), the equation representing effectiveness was arranged in the form,

$$\eta = \left\{1 - C\left[\left(\frac{x}{M_s}\right)\left(Re_s \cdot \frac{\mu_c}{\mu_m}\right)^{-0.25}\right]\right\}^{+0.65} \qquad 2.30$$

From figure 2.8, it can be seen that at a velocity ratio of around 0.6-0.7, the 'constant' does become a constant and below this value, the boundary layer model does not apply.

It would thus appear that opinion (V) above, is confirmed beyond reasonable doubt.

It is indicated by figure 2.7 that for $u_m/u_c \geqslant 0.66$ and all mass velocity ratios, that for clean slot geometry injection, the film effectiveness

is asymptotic to the line given by,

$$\eta = 3.68 \left(\frac{x}{M_s}\right)^{-0.8} \cdot \left(Re_s \cdot \frac{\mu_c}{\mu_m}\right)^{0.2} \qquad 2.31$$

This equation should be compared with equation 2.20 and the numerical values contained in Table 2.1.

In figure 2.9, equation 2.31 is compared with wake-like data from the experimental work of Whitelaw (44), Seban and Back (12), Papell and Trout (34), and, Kacker and Whitelaw (48). Kacker and Whitelaw examined four slots of heights ranging from 0.074 inches to 0.50 inches, so together with figure 2.7, a wide range of slots is represented altogether. It may be seen from this figure that it is therefore reasonable to state that equation 2.31 adequately represents an asymptotic description of all clean-slot data for velocity ratios $\frac{u_m}{u_c} \geq 0.66$ when the group $\frac{x}{M_s}\left(Re_s \cdot \frac{\mu_c}{\mu_m}\right)^{-0.25}$ is greater than about 10.

It may be seen from Table 2.3 that for $R > 1.0$, or, $\frac{u_m}{u_c} < 1.0$, or, small $\frac{x}{M_s}$, i.e. a jet-like flow, only Seban, Chen and Scesa (7) report correlations radically different from equation 2.31. Consideration of figure 2.9 indicates that the description of the flow for small $\frac{x}{M_s}$ is important since the asymptotic solution as represented by equation 2.31, is not adequate in this region. For $\frac{x}{M_s} < 40$ and all R, they suggested the correlation

$$\eta = 0.16 \left(\frac{x}{M_s}\right)^{-0.25} \cdot Re_s^{1/3} \qquad 2.32$$

Examination of this equation reveals a limitation on its use; it cannot be used for slot Reynolds numbers greater than 3.875×10^3 together with the condition $\frac{x}{M_s} \leq 40$ since by definition, η cannot be greater than unity.

Comparison of equation 2.32 with the data of Whitelaw (44) for $0.467 \leq R \leq 2.26$ and $4.035 \leq Re_s \times 10^{-3} \leq 1.95$, shows the existance of such

a region, but correlation was not good for large M. The limiting value of $\frac{x}{Ms}$ = 40 was found to be fairly flexible, a value of 60 being more appropriate for Whitelaw's data. Equation 2.32 did not predict the data well. For small values of the group $(x/Ms) \cdot Re_s^{-0.25}$, i.e. large $\frac{x}{Ms}$, Whitelaw's data showed a trend towards a value of -0.80. the implication of this being that a flow which is originally jet-like eventually becomes boundary layer-like at large distances from the injection plane.

Seban (11) reports a jet-like correlation for M>1.0,

$$\eta = 1.09\left[\left(\frac{\rho_m}{\rho_c}\right)^{1.5} \cdot \left(\frac{u_c - u_m}{u_c}\right)^{0.5} \cdot Re_s^{-0.3} \cdot \frac{x}{s}\right]^{-0.5} \qquad 2.33$$

In figure 2.10, this equation is compared with data from Whitelaw (44) and, Papell and Trout (34). It can be seen that this group does correlate well the data of Papell and Trout but does not predict it, and, does not correlate Whitelaw's data but does represent it.

The sound basis of equation 2.31 would seem to be a reasonable starting point from which to deal with jet-like flows. Figures 2.7 and 2.8 indicate a likely direction to be taken by describing the "constant" equal to 5.68 for wake-like flows, in terms of velocity ratio u_m/u_c, when this ratio is less than 0.66. A simple linear relationship between velocity ratio and this constant of proportionality was assumed in place of the more complicated form suggested by figure 2.8, and using the scanty data of figure 2.7, the following relationship was derived:

$$\eta = \eta\left\{\left(2.374 - \frac{u_c}{u_m}\right)^{-1.25} \cdot \left[\frac{x}{Ms}\left(Re_s \cdot \frac{\mu_c}{\mu_m}\right)^{-0.25}\right]\right\} \qquad 2.34$$

This correlation group was tested against a very wide range of jet-like data taken from the experimental work of Seban (11), Seban and Back (12),

Chin, Skirvin, Hayes and Silver (49), Chin, Skirvin, Hayes and Burggraf (50), Pai and Whitelaw (51), Whitelaw (44), and, Popell and Trout (34). These data not only cover an extremely wide range of the main aerodynamic variables, but the injection of hydrogen, argon, Areton 12 foreign gases in addition to air, and also, injection of air into hot combustion gases.

Results of the correlation are shown in figure 2.11, where it may be seen that in general, the majority of the data agree excellently. A number of test runs however, fall outside the general scatter. One of these tests is for argon injection, the others are for air. There is no systematic variation with velocity ratio, mass velocity ratio or Reynolds number. With one exception, (Popell and Trout), the "wild data" originates from the same laboratory. One of the "wild" test runs (Whitelaw) is also at variance with the general run in figure 2.10 when Seban's correlation group was tested.

If the "wild" data are disregarded, the remaining data are excellently correlated by the relationship of 2.34; to the same degree as the wake-like data shown in figure 2.9.

Similar corrections to that of relationship 2.34 for jet-flow have been proposed by other authors. Winter (20) for example, modified his group which was arrived at by dimensional reasoning and is shown in equation 2.15, by the addition of an empirical factor equal to $\left(\frac{u_m}{u_c} + 0.2\right)^{-1.25}$ for $\frac{u_m}{u_c} < 0.8$, as indicated previously in equation 2.16. The similarity of this factor with that arrived at in relationship 2.34 above is obvious.

2.4.3. Conclusions.

Some of the theoretical correlation groups given above together with the empirical groups, have been tested by their originators against the

experimental data. Reasonable correlation, ± 5-10% has generally been obtained when the data originating from only a single source are used; but when all available data are considered together overall correlation is seldom better than ± 50% of unity.

The use of the boundary layer model and the correlation group based on it are substantiated. The model breaks down as the flow becomes progressively jet-like in nature, but use of correction groups based on velocity ratio, account satisfactorily for this. A flow which is originally jet-like becomes boundary layer-like at large distances from the injection plane.

2.4.4. Recommendations.

(i) For all values of M and $\frac{u_m}{u_c} \geq 0.66$ with clean geometry slots, use:

$$\eta = 3.68 \left(\frac{x}{Ms}\right)^{-0.8} \cdot \left(Re_s \cdot \frac{\mu_c}{\mu_m}\right)^{0.2}$$

for asymptotic solutions.

(ii) For $u_m/u_c < 0.66$ with clean geometry slots,

$$\eta \propto \left\{\left(2.374 - \frac{u_c}{u_m}\right)^{-1.25} \cdot \left[\frac{x}{Ms}\left(Re_s \cdot \frac{\mu_c}{\mu_m}\right)^{-0.25}\right]\right\}^{-0.8}$$

2.4.5. Choice of Coolant Injection Velocity.

It can be intuitively argued that blowing harder in a given cooling situation should result in increased effectiveness at any value of x/s. A more sophisticated line of argument indicates that as mixing of the mainstream with the film will be dominated by velocity and temperature differences between the two, i.e. on mass velocity ratio M for constant pressure mixing, the film effectiveness at any x/s will be a maximum for M equal to unity.

That mixing of the two streams is least and therefore effectiveness greatest, when velocity ratio is unity, was intuitively argued by Bayley (52). From a theoretical study Spalding (53), was able to make two important conclusions,

(i) for the most effective cooling with a restricted quantity of coolant, the slot height should be chosen so as to inject the coolant at the velocity possessed by the mainstream.

(ii) when the slot height is fixed and it is desired to provide the most effective cooling at a given point on the surface irrespective of coolant quantity, the optimum velocity of coolant is also equal to the mainstream velocity in most practical circumstances.

The effect of the parameter M on effectiveness at various stations has been experimentally examined by Whitelaw(44), who found an effectiveness maximum occuring for values of M between 1.0 and 1.2 with the peak becoming more pronounced with increasing x/s ; for x/s of 45, the peak was hardly perceptable. The experimental data of Papell and Trout (54) enables a similar comparison to be made, as in figure 2.12. Considerable differences between these plots and those of Whitelaw may be observed: For the 0.25 inch slot at x/s of 100, the form of the curve is similar to that observed by Whitelaw except that the effectiveness peak occurs at an M of 2.27. For both distances with the 0.125 inch slot, no maximum appears and effectiveness apparently continuously increases with M. The only difference between the results for x/s of 100 is one of slot height, which indicates a possible importance of this parameter. A study using the correlation equations obtained above, indicates that at a given distance outside the film initial

region, the effectiveness ~M relationship should be of the form of an effectiveness maximum around M = 1, followed by a minimum at some greater value of M and then, a steady increase of effectiveness with M, assymptotic to a value associated with choking of the slot.

The later work of Whitelaw with Kacker (48) does show a significant effect of slot height. For a slot height of 0.074 inches, no maximum effectiveness was detected for values of x/s up to 150, for 0.132 and 0.25 inch high slots a maximum was observed when x/s was about 50, and for a 0.5 inch slot, a maximum had appeared as close to injection as an / of 25. The value of M at which the maximum effectiveness occurs is also a function of slot height as is shown by this data and that of Papell and Trout (34), in figure 2.13. For slot heights above about 0.150 inches, increasing slot height reduces the value of M at which maximum effectiveness is attained, towards unity, although the two sets of data do not agree on actual values. This difference is most probably associated with the velocity profiles in the slot exits. Nobbs and Rice (60) show an exactly similar form of result for a practical film cooling gometry of the Rolls Royce machined splash-impingement type, except that there is less sensitivity to slot height.

Hartnett, Birkebak and Eckert (54) state that in their opinion, the optimum mass velocity ratio is close to 0.67, but do not elaborate the point.

A study of combustor cooling by the present author (55) indicates an optimum mass velocity ratio of the order of 1.33.

2.4.6. Effects of Mainstream Turbulence.

In the majority of the literature prior to 1968, turbulence values are not quoted. For these earlier reports and most of the subsequent

reports where values are quoted turbulence intensities $\frac{\sqrt{\overline{u'^2}}}{u_m}$ are appropriate to those of normal wind tunnels, i.e. 0.5 to 2.0 percent. Only one reference with systematic variation of mainstream turbulence has been found, that of Carlson and Talmor (56).

With both streams of gaseous nitrogen, Carlson and Talmor varied mainstream turbulence intensity $\frac{\sqrt{\overline{u'^2}}}{u_m}$ from 5.2 to 22.0 percent for a 0.0625 inch slot in cylindrical flow, where mainstream Mach number was varied from 0.1 to 0.5 together with velocity ratios, $1.492 \leqslant \frac{u_m}{u_c} \leqslant 5.88$. The results obtained can be analysed to show two features as turbulence is increased : first, a considerable reduction in the length of the initial region of the film where effectiveness is at or near, unity, and second, a small increase in downstream mixing as evidenced in a decrease away from zero in the exponent 'a' in equation 2.29. These results are shown in figure 2.14.

Also shown in figure 2.14 are some data derived from the work of Price (57), (58). Two configurations were examined: a ram jet nozzle and, a parallel, axisymmetric duct. In each case, a ramjet colander and flameholder were inserted in the duct upstream of the film cooling slot. The results of the turbulence induced by the colander and flameholder were the same as was observed from the data of Carlson and Talmor - a reduction in initial region and a decrease in exponent 'a'. Price does not quote values of mainstream turbulence intensity so these were estimated for the particular geometries from the data of Meric (59).

Also shown in figure 2.14 are " low turbulence" data as represented by the data of Hatch and Papell (33) and, Chin et al (49). The agreement

of the data is very satisfactory. It is seen that mainstream turbulence can exert a considerable influence on effectiveness, largely through potential core length.

Fig. 2.14 is produced by a "blanket" consideration of the data and the effects of the turbulence at different velocity ratios for example, is not considered. This method is therefore, only a crude indicator of the magnitude and direction of the effect.

2.4.6 . Effects of Slot Turbulence.

Very little work appears to have been carried out into the effects of slot-generated turbulence. Kacker and Whitelaw (48) varied slot turbulence intensity $\sqrt{\overline{u'^2}}/u_c$, from 5.0 to 10 per cent in a 0.25 inch high slot, and were unable to detect any effect of significance.

2.4.7. Effects of Mainstream Boundary Layer Thickness.

Seban (61) added a 2 ft. upstream attachment to his standard test-section (11), together with a sandpaper roughness-strip to investigate the effects of mainstream initial boundary layer. With this modification, boundary layer thickness at the injection plane was of the order of 0.60 inches with velocity profiles of the generally accepted turbulent form. The original boundary layer thickness was 0.06 inches; slot heights were 0.063 to 0.25 inches and $0.25 < R < 0.80$. Seban's experiments thus provided a maximum range of $1 \lesssim \delta_m/s \lesssim 10.0$. The changes in effectiveness resulting from the initial boundary layer proved complicated. For small values of δ_m/s there was but a minor reduction in effectiveness at large x/s , whilst for large values of δ_m/s , there were

reductions of 2.5 per cent of unity but small increases in effectiveness at intermediate x/s . This indicates enlarged initial regions and a higher downstream rate of decay. However, if all the results are correlated using any of the appropriate correlation groups, then the effects of the increased boundary layer thickness are submerged and the correlation of data remains good. Slight decreases in measured heat transfer coefficient were found and the reductions applied for all x/s . Seban notes that these small changes might be interpreted as an indication of a relatively unaltered film hydrodynamic behaviour. However, velocity profiles were found to have been significantly altered and power-law similarity was not attained until much greater distances downstream compared to the thin boundary layer case. Temperature profiles were similar even quite close to the injection plane. This is interpreted as the thermal layer growing more quickly when the hydrodynamic layer is thicker, and that the invariability of effectiveness results from lower wall velocities associated with this layer. When slot size is reduced below 0.25 inch this relationship between the two effects apparently fails at large distances from injection.

Kacker and Whitelaw (62) report an investigation where mainstream velocity was kept constant at 68 ft./sec., as was the slot height at 0.074 inches. Three values of mainstream initial boundary layer were similar to that of Seban. Those tests indicated a general reduction of effectiveness of less than 5 per cent of unity in the range of velocity ratio, $0.35 \leq u_c/u_m \leq 2.05$

In figure 2.15, the reduction in effectiveness as a function of velocity ratio u_c/u_m at three downstream positions is shown for an approximate 8-fold increase in mainstream initial boundary layer thickness; data from Kacker and Whitelaw, and, Seban are used. This figure is not very

precise since values had to be taken from small-scale graphs and, for Seban's data a constant density ratio ρ_m/ρ_c, of 1.12 was assumed.

One other experimental investigation of this nature has been reported; it was in fact, chronologically the first, that of Chin, Skirvin, Hayes and Silver(49). The boundary layer thickness range was $8 \leq \delta_m/s \leq 20$ and the slot height 0.108 inches. Absolute values of effectiveness were generally higher than those of both Kacker and Whitelaw and, Seban. Again, a reduction in effectiveness was noted with increasing initial boundary layer thickness, this effect being of the order of 3.0 per cent of unity at x/s of 200 for a change in thickness equal to about 16 slot heights. The reduction tended to a maximum as velocity ratio tended to unity; For $x/s > 50$, Kacker and Whitelaw's data in figure 2.15 could be interpreted as showing a similar tendency.

The general indication would therefore seem to be that mainstream boundary layer causes an almost negligible change in effectiveness, a reduction by a few per cent of unity at worst.

2.4.8. Effects of Slot Height.

Papell and Trout (34) for a fixed mainstream Mach number of 0.5 plotted effectiveness against x/s for four slot heights of 0.5, 0.25, 0.125 and 0.0625 inches, with mass velocity ratio of unity and fixed temperature ratio T_c/T_m, of 0.36. They concluded that within the precision of their measurements, no effect of slot height was present.

In the above Section 2.4.5., and in figure 2.13, it was suggested that such an effect did in fact, exist. A more detailed study of Papell

and Trout's data demonstrates the existance of a positive effect due to slot height and this is shown in figures 2.16 and 2.17 where as a function of slot height and mass velocity ratio, the effectiveness at two fixed points in the flow field is shown. (The shapes of these curves agrees with that discussed in Section 2.4.5.). The detailed picture is shown in figure 2.18 by cross-plotting. Also shown in this figure are some data due to Whitelaw (63). Further data from Kacker and Whitelaw (48) for fixed mainstream conditions also, are shown in figure 2.19. In figure 2.20, the effect of slot height at fixed positions from injection is shown.

The figures show the following important features:

(i) for slot heights greater than 0.20 inches there is no significant effect of slot height,

(ii) slot heights less than 0.1 inches operate at low values of effectiveness, and small variations in height produce large changes in effectiveness,

(iii) there is an optimum slot height of 0.125 to 0.150 inches,

(iv) these conclusions apply for wide ranges of mass velocity ratio, $0.5 \leq M \leq 3.0$ and position in the flow field, i.e. $25 \leq \frac{x}{s} \leq 100$. They also hold for fixed positions in the flow field, or, distances from injection.

A theoretical study by the present author (55) shows the optimum slot height also applies for the film initial region and, on a coolant efficiency basis.

It is difficult to decide the exact cause of these very significant effects. Whitelaw (63) has discussed this in some detail and concluded he could not decide the exact causes. The present author is also unable to

decide the exact nature of the observed effects (64).

Nobbs and Rice (60) also report a similar pattern for their splash-impingement slot, although the smallest slot height tested was 0.32 inches and therefore the results are not so dramatic.

2.4.9. Effects of Slot Lip Thickness.

The majority of reports in which a variation of the ratio of lip thickness to slot height δ_w/s , e.g. (11), (34) and others, have obtained this variation through slot height changes for fixed lip thickness. Such data then contain in addition to lip thickness effects, those effects due to changes brought about in the slot flow by changing slot height.

Some insight into slot lip thickness effects was unwittingly given by the paper of Samuel and Joubert (18) whose badly designed slot geometry is illustrated in figure 2.4h). Slot lip thickness was 0.125 inches if the feathering used is accepted as ineffectual, as it almost certainly was, giving $0.333 \leqslant \frac{\delta_w}{s} \leqslant 1.0$. Samuel and Joubert found for a mass velocity ratio of 0.88, that velocity profiles showed the existance of an extensive velocity defect associated with the large value of δ_w, and hence, the presence of a velocity maximum in the film even though mainstream velocity was greater than that of the coolant. Thus, the inner parts of the coolant film had the appearance of wall-jet flow for nominal wake-like injection conditions. This jet-like characteristic regardless of velocity ratio was confirmed by the empirical correlations obtained when it was found that,

$$\eta = \eta \left(\frac{x}{s}\right)^{-0.5} \qquad 2.35$$

for all x/s and $M < 1.0$.

A more detailed appraisal of the problem was made by Sivasegaram and Whitelaw (65). Two values of lip thickness, 0.16 and 0.34 inches were used, with a constant slot height of 0.20 inches. Effectiveness was plotted against mass velocity ratio for x/s of 25, 50 and 100, for δ_w/s of 0.82 and 1.60. These plots showed that an increase in δ_w reduced effectiveness slightly for all x/s and M and that this effect was greatest close to the slot and for $1 \leq M \leq 3$. Cross- plots were also presented in the form of effectiveness against δ_w/s for various distances and mass velocity ratios, for these results and also for those from reference (63) where δ_w/s variation occured due to slot height changes with fixed lip thickness. As pointed out above, this is not a valid procedure.

A lip thickness variation of $0.20 \leq \delta_w/s \leq 0.60$ for a 0.32 inch slot at unity velocity ratio was made by Nobbs and Rice (60) for their slot geometry, and a very slight decrease in effectiveness with increasing lip thickness was observed. It was observed that the effect of a thick lip was similar to increasing the slot height and they proposed use of a modified value for slot height,

$$s' = \left[s + \frac{u_c \delta_w}{(u_c + u_m)} \right] \qquad 2.36.$$

Using this modified value with data for $u_m/u_c > 1.0$ with the boundary layer-model correlation group, Nobbs and Rice improved correlation of the data from $\pm$ 10% to $\pm$ 5% of unity.

Use of equation 2.3.6. for slot heights less than about 0.2 inches is not recommended because of the effects shown in figure 2.19.

2.4.10. Importance of Coolant Injection Angle.

Scesa (6) produced the empirical correlation,

$$\eta = 2.20 \left(\frac{x}{Ms} \right)^{-0.5} \qquad 2.37$$

for normal injection. It can be realised by comparing this equation with equation 2.31 that injection at 90^0 reduces effectiveness considerably, thus confirming the intuitive feeling that mixing of the two streams would be a minimum for parallel flows.

A detailed study is carried out by Papell (66) who injected the coolant through slots with nominal angles of 90^0, 60^0 and 30^0. He found the coolant was actually discharged into the mainstream at 90^0, 60^0 and 45^0 respectively, and subsequently referred to these latter values as the injection angles. Papell therefore postulated an effective angle of injection θ_{Eff} which was defined by the vector sum of the mass velocities of the two streams, relative to the test surface in the direction of flow,

$$\text{i.e.} \qquad \theta_{Eff} = \tan^{-1}\left[\frac{\sin\theta}{\cos\theta + 1/M}\right] \qquad 2.38.$$

where θ is the slot geometric angle. He subsequently found effectiveness was proportional to the cosine of θ_{Eff}. The experimental results qualitatively confirmed the conclusion drawn above from equations 2.31 and 2.37 but unfortunately, the test conditions involved relatively large density variations due to compressibility and it is not possible to separate the two effects.

Sivasegarem and Whitelaw (65) reported some further measurements at slot geometry injection angles of 30^0, 60^0 and 90^0 which supported Papell's conclusion that effectiveness was reduced when coolant injection deviates from tangential. Figure 2.21 from Sivasegarem and Whitelaw's curves for $0.3 \leqslant M \leqslant 1.5$; equation 2.31 is also plotted to represent the zero injection angle case. For this equation the slot Reynolds number was taken as 5,000 which is representative of Whitelaw's data (44) with a nominal slot

height of 0.25 inches for which the ratio $\delta_{w/s}$ was about 0.04; with these conditions the equation is valid when $x/M_s \geq 50$. This figure shows dramatic reductions in effectiveness for the range of x/M_s of general practical interest. From this figure a further crossplot is made, which is shown as figure 2.22, where the influence of injection angle is presented directly for unity mass velocity ratio at two distances from the injection plane. This diagram indicates that the reduction of effectiveness is greatest in the region of injection angles from 0^0 to 60^0. This is opposed to Papell's (66) conclusion that the reduction is greatest from about 60^0 to 90^0, (θ - values). The magnitude of the effect according to Sivasegarem and Whitelaw is greater than that indicated by both Scesa's (6) and Papell's (66) data.

Also shown in figure 2.21 are data of Sivasegarem and Whitelaw's for tangential injection from a 0.20 inch slot with a $\delta_{w/s}$ ratio of 0.82. It is clear from this plot that under certain geometric circumstances, it can be <u>detrimental</u> to inject the coolant tangentially and angled injection may be preferable.

2.4.11 <u>Transverse Wall Curvature.</u>

The work discussed above relates to plane-flow films. In many practical applications however, the film will be developing over a wall with transverse curvature at the least. Two cases can exist: flow over concave transverse curvature and, flow over convex transverse curvature, surfaces, (flow over inner and outer surfaces of a cylinder, respectively).

An investigation of the flow of a pure wall jet ($u_m = \frac{u_m}{u_c} = 0$), over axisymmetric, convex transverse curvature surfaces was carried out by Manian, McDonald and Besant (67). These authors report that Singh and, Akatrov showed no effects of curvature for cylinders ranging in diameter from 1 inch to 10 inches. They themselves tested cylinders of 0.125 inch and 0.25 inch in diameter with diameter to slot height ratios of 2.0, 1.0, 0.285, 0.125, 0.666; maximum slot turbulance intensities were measured as 0.8 per cent. Consideration of the results given in this reference indicates that there is a negligible effect of curvature on the hydrodynamic potential core, (slight decrease), but a significant effect on the decay of maximum velocity in the film. Two limiting cases bounding the effect are recognised:

(i) the free, circular jet where $u_{max} \propto (\text{distance})^{-1}$

(ii) the plane wall-jet where $u_{max} \propto (\text{distance})^{-0.5}$

They also found an effect on heat transfer, (indicated here for convenience) empirically expressed,

$$St_s = 1.27 Re_s^{-0.4} \left[\frac{(x+x_o)}{s}\right]^{-0.6} \left(\frac{d}{s}\right)^{0.3} \qquad 2.39$$

The magnitude is such that for d/s of 0.125, Stanton numbers were found to be 1.7 times that of the plane wall-jet. Where the ratio d/s is large, the plane wall-jet is approximated to.

Axisymmetric concave surfaces with d/s values from 50 to 80 were used by Odgers and Winter (68). Price (57), used similar surfaces with a d/s value of 29.5. In the asymptotic region, these authors found no effect of the curvature on film effectiveness; there was some reduction in potential core length which could be attributed to other causes.

For gas-turbine combustion chamber cooling, the curvature can be of either of the two types described depending whether the outer or inner (annular) flametube is considered. Values of d/s will normally be of the order 60 and above, so the assumption of plane-flow conditions would seem reasonable.

2.4.12. Compressibility Effects.

The basic boundary layer analysis has been extended by Holland (69) for compressible flows. For an enthalpy-based effectiveness, he obtained,

$$\eta_h = \left[0.37 - 0.046\left(1+0.8M_{a_m}^2\right)^{-0.44}\right]\left[\frac{x}{Ms}\right]^{-0.8}\cdot\left(Re_s\cdot\frac{\mu_c}{\mu_m}\right)^{0.8} \qquad 2.40.$$

This equation is easily related to the incompressible case, equation 2.31: The first term here includes the effects of Mach number on the shape of the film temperature profiles. This equation was satisfactorily used by Price (57), (58) for correlation of data.

The effects of compressibility on film cooling were experimentally investigated by Papell and Trout (34) who varied mainstream Mach number over the range 0.2 to 0.7 for constant slot height, temperature ratio and mass velocity ratio. The Mach number influence on effectiveness over the limited range covered was observed to be quite small and within the accuracy of the data, was considered negligible. This agrees with equation 2.40 in which the compressibility term is very small for Mach numbers less than unity.

Carlson and Talmor (56) derived a correlation parameter for film effectiveness,

$$X = \frac{Re_m^{0.8}}{Re_s}\cdot\frac{Pr_m}{Pr_c}\cdot\frac{k_m}{k_c} \qquad 2.41.$$

which bears an obvious resemblence to the much earlier Ω group of Winter, (equation 2.15)

This X-group is modified to account for compressibility as follows:

$$X_1 = X\left[\left(P_{.9}/P_{stag}\right)^{A}\right]$$

where; $$A = \left[\frac{1}{4} - \left(\frac{1+\dot{m}_{TOT}}{4}\right)\left(\frac{\gamma-1}{8}\right)\left(1+\frac{\gamma-1}{2}Ma^2\right)^{\frac{1}{2}}\right] / x\,Ma^{27/7}$$

collectively termed, 2.42.

They obtained reasonable effectiveness correlation with this group X_1, but it appears to have little to commend it in comparison with equation 2.40.

2.4.13. The Influence of Pressure Gradient.

Holland (70) further extended his modification (equation 2.40) of the basic boundary layer model to cover weak pressure gradients, i.e.

$$\eta_h = \left[0.37 - 0.046\left(1+0.8Ma_m^2\right)^{-0.44}\right]^{-1} \cdot \left(\frac{x}{Ms}\right)^{-0.8} \left(Re_s \cdot \frac{\mu_c}{\mu_m}\right)^{0.2} \left[\frac{r^{5/4}\left(\frac{Ma_m}{1+0.2\,Ma_m^2}\right)^{4}}{r^{5/4}\left(\frac{Ma_m}{1+0.2Ma_m^2}\right)^{4}}\right]^{0.8} X\left[\frac{r_s}{r_x}\right]^{2} \quad 2.43.$$

where the additional last two terms account for the effects of pressure gradient.

A similar extension for non-zero pressure gradient is also offered by Stollery and El-Ehwany (9). Their boundary layer model analysis incorporates the usual turbulent flow relationship for film thickness,

$$f = 0.37\,x\,Re_{sx}^{-0.2}$$

They suggest that to account for pressure gradient, it can be modified thus,

$$f = 0.37\,X\,Re_x^{-0.2}$$

Where, $$X = P^{-1}\int_0^x P\,dx$$

and, $$P = \left[M_a/\left(1+\frac{\gamma-1}{2}M_a^2\right)\right]^4$$

collectively termed, 2.44.

This is a relationship which may be readily applied to any theory embodying the basic relationship for film thickness.

No data are available to support either of the two modifications given above.

The effects of favourable (accelerating flows) pressure gradients have been experimentally studied by Seban and Back (71) and, Hartnett et al (54). The gradients imposed by these workers are represented through the mainstream velocity distributions shown in figure 2.23. Seban and Back found the effects were small, there being only a slight reduction in effectiveness and departure from linearity in logarithmic plots against distance, in the region of greatest acceleration. An effect of slot height was discernable in the results also. When the blisters were moved forward into the initial mixing region, it was found the effectiveness was further reduced and this was a greater effect than hitherto, the actual amount depending on the blister size. Heat transfer coefficients, (included here for convenience), showed an initial dependence on the slot flow which was maintained up to the end of the initial region; beyond this, the influence of the mainstream predominated. With the largest blister, in the region of acceleration, heat transfer was greatly reduced and the appropriate velocity profile was linear near the wall, these indicating a suppression of turbulence and " relaminarisation" of the flow. The results of Hartnett et al's investigation broadly agreed with those of Seban and Back. They

found that effectiveness decreased up to about 6 per cent with increasing velocity gradient, and obtained a new correlation to account for this effect,

$$\eta^{*} = \eta \left[\frac{u_{Local}}{(u_m)_{x=0}} \right]^{0.2} \qquad 2.45$$

which correlated the data to ± 5 per cent of unity. With uniform heating it was found that heat transfer coefficients agreed with values for an impermeable flat plate to ± 10 per cent provided the distance was greater than about 30 slot heights downstream of injection and, mass velocity ratio was less than unity. Above x/s of 30, the coefficients were extremely susceptable to mainstream velocity variations. For x/s less than 30, the coefficients were dominated by slot flow and were reduced by just a few per cent. For a mass velocity ratio greater than unity, the length to achieve impermeable flat-plate coefficients is considerably increased. These observations should be compared with those given under Section 2.2.

Measurements for compressible flow in a ramjet nozzle have been made by Price (58) and the same author also reports similar measurements made in a parallel duct using the same facility and slot (57). As these two sets of results should be roughly compatiable, (with the exception of shock formation) the nozzle results for film effectiveness have been plotted together with the results for the parallel duct, against the right-hand side of equation 2.43. This group correlates the nozzle results to ± 9 per cent and these effectivenesses are up to 30 per cent lower than these for the parallel duct.

Carlson and Talmor (56) also report measurements of effectiveness made in a half-nozzle with convergence angles of 30^0, 45^0 and 60^0. Their results are somewhat difficult to interprete but show a small reduction in

the initial region of the film and an increasing effect, a reduction in effectiveness, in the main region as convergence angle increases beyond 45^0.

The influence of strong adverse pressure gradients on film effectiveness has been studied by Escudier and Whitelaw (72). The gradients were sufficiently severe to cause separation of the film from the wall and were imposed by a forward-facing step of varying height at the end of the test section. Not until separation is reached does the pressure gradient effect become of major significance. The effect is marginally greatest at high blowing rates. There is a neglible effect on the initial region and only a 10 per cent reduction in effectiveness at separation.

The effects of both favourable and adverse pressure gradients are thus seen to be both small and, of minor importance on effectiveness, Heat transfer coefficients can be significantly influenced by favourable gradients.

2.4.14. Multiple Slots.

Where temperature environmental conditions are particularly severe, or the length to be cooled is large, any practical cooling system will usually consist of more than a single slot. Typically, a number of identical slots are placed in series to ensure that surface temperatures do not exceed a limit determined by the surface material.

Only one investigation of such a multiple-slot cooling system appears in the literature, that carried out by Chin, Skirvin, Hayes and Burggraf (50). A series of 10 identical slots of height 0.115 inches were placed at equal distances apart and could be blanked-off in turn. Adiabatic wall temperatures were measured downstream of the last open slot. The range of velocity ratios covered depended on the number of open slots, being:

$$0.057 \leq u_c/u_m \leq 0.526 \qquad \text{for 10 slots}$$

and,

$$0.304 \leq u_c/u_m \leq 1.134 \qquad \text{for 1 slot.}$$

A correlation group applicable to a single slot (49) was modified to cover multiple slots using the two asymptotic conditions,

(i) when slot spacing is zero, the n- slot assembly is equivalent to a single slot of height ns ,

(ii) when slot spacing approaches infinity, only the last slot is effective.

The final, semi-empirical group obtained was,

$$\eta = \eta(\phi)$$

where,

$$\phi = n^{B} \cdot F\left(\frac{x}{s}\right)$$

and, x = distance downstream from last open slot

n = number of open slots

d = slot spacing

$$B = -\left\{1.3/\left[1+0.02\left(d/s\right)\right]\right\}$$

$$F = A\left(\frac{s}{x}\right)$$

$$A = \left(\rho_c/\rho_m\right)^{-1.5} \cdot \left(\frac{u_c}{u_m}\right)^{-1} \cdot Re_s^{-0.3} \cdot Re_L^{0.19} \cdot \frac{x}{s}$$

Re_L = mainstream Reynolds number based on hydrodynamic starting length,

collectively termed, 2.46

Chin et al found all their data correlated against ϕ to $\pm$ 20% overall, the correlation becoming less satisfactory as the number of slots increased, indicating that the actual behaviour was more complicated than that represented by equation 2.46.

From the data presented, it may be observed that adding more slots increased the extent of the initial regions of the film. Chin et al noted that if sufficient slots, correctly placed, were used, the whole of any surface might be maintained at unity effectiveness. For a given number of slots, increasing the spacing between slots reduces the extent of the initial regions. In the main region of the film where effectiveness is proportional to F (x/s) raised to the power -0.8, increasing the number of slots increases the effectiveness at any x/s for given F ; increasing the spacing between slots for a given number of slots slightly reduces the effectiveness.

The data have been re-examined on a more quantitative basis and the results are shown in figures 2.24 and 2.25. The relative potential core length is here defined as the range of F (x/s) for which $\eta \simeq 1.0$ for n-slots, divided by the range of F(x/s) for which $\eta \simeq 1.0$ for n = 1. The relative transition length is the range of F (x/s) between values for which $\eta \simeq 1.0$ and η where the slope of the data in logarithmic plots is linear with a value greater than -0.8, for n-slots, divided by the same quantity for n = 1. The large effects recorded inthe initial regions of the film may be attributed to dramatic modifications of local injection conditions due to the persisting, preceeding film.

CHAPTER 3.

THE HYPOTHESIS.

3.1. Combustor Cooling.

The example of film cooling to be studied in depth in the present thesis is that of the aircraft gas-turbine combustion chamber. A layout is shown labelled in figure 3.1. although familiarity with the basic component and engine layout is assumed.

The cooling system has to be such that:

(i) oxidation of the wall does not occur,

(ii) temperature gradients do not cause local buckling,

(iii) thermal fatigue cracking does not appear.

Biondi and Draizen (73) report times to steady-state temperature from start-up of the order of 8 seconds so conditions (i) and (ii) may be considered by means of a steady-state analysis at a given design point. They also state that circumferential temperature gradients are generally small in comparison with those in the longitudinal direction, thus confining the analysis to one direction. Some further simplifying assumptions may conveniently be made and justified:

a) due to the thinness of the flametube wall (0.048 to 0.028 inches), no temperature drop across this thickness occurs,

b) there is no heat transfer through the air-casing since it will be insulated and engine-tunnel air will have some elevated temperature (fan by-pass, supersonic cruise for example),

c) the air-casing is at the same temperature as the annulus air as a direct consequence of b).

A steady-state balance of the radiative, convective and conductive heat flows will yield the temperature at a point in the wall. A technique used by the present author establishes an equal-size element system in the wall, where each element is subjected over the whole of its exposed surfaces to the conditions at the nodal point. In practice, to avoid mathematical instability, it is necessary to establish a "preferred path" by considering a "super-element" enclosing three adjacent nodes, as indicated in figure 3.2. Provided element size is small enough, no inaccuracies arise due to the displaced "entry" and "exit" to the considered node.

A steady-state heat balance for the super-element is,

$$R_{in} + C_{in} + Cd_{in} = R_{out} + C_{out} + Cd_{out} \qquad 3.1.$$

where,

R = radiation heat flow

C = convection heat flow

Cd = conduction heat flow

Using the equations for R and C from Lefebvre and Herbert (74), the finite-difference equation may be set up:

$$\sigma\left(\frac{1+E_S}{2}\right)E_m T_f^{1.5}\left(T_f^{2.5} - T_{s_{(n+1)}}^{2.5}\right) + h_{film}\left(T_{s_{(n+1),ad}} - T_{s_{(n+1)}}\right) + \frac{kt}{\Delta x^2}\left(T_{s_{(n+1)}} - T_{s_n}\right)$$

$$= \sigma\left[\frac{E_S E_{Amn}}{E_{Amn} + E_S\left(1-E_{Amn}\right)\frac{d_{mean}}{d_{Amn}}}\right]\left(T_{s_{(n-1)}}^4 - T_{Amn}^4\right) + h_{Amn}\left(T_{s_{(n-1)}} - T_{Amn}\right) + \frac{kt}{\Delta x^2}\left(T_{s_n} - T_{s_{(n-1)}}\right) \qquad 3.2.$$

where,

$$T_f = 3913 + 0.388\,T_3 + 40\left(P_3 - 1\right)^{0.53} \quad {}^{\circ}R$$

the adiabatic flame temperature for stoichiometric mixture

($T_f = T_m$ in the dilution zone of the chamber)

T_3 = compressor delivery temperature, P_3 = compressor delivery pressure in atmospheres.

h_{film} = local heat transfer coefficient in the film

$T_{s_{(n+1),ad}}$ = the adiabatic wall temperature at the (n + 1) th. node.

The hot-gas emissivity E_m may be calculated from the Cohen equation (75),

i.e. $$E_m = 1 - \exp\left[\frac{-3L}{T_f \times 10^{-4}}\sqrt{\frac{P_3 H_d f}{T_f (1 + H_d/L_c)}}\right]$$

L = luminosity (1.7 for kerosine flames)

f = fuel / air ratio

H_d = combustor annular height, ins.

L_c = length of combustor.

It is assumed in writing equation 3.2 that the wall thermal conductivity is independent of wall temperature. Within the temperature ranges encountered, K changes are of the order of one-tenth of one per cent, so this is a valid assumption. For the designs of chamber current, it is not permissible to neglect the conductive terms, as did Lefebvre and Herbert. The annulus-side heat transfer coefficient may be calculated from the Burggraf and Rauf relationship,

$$St\,(Pr)^{2/3} = 0.0355\ Re_x^{-0.2} \qquad 3.4.$$

which includes effects due to the high turbulence to be expected as a result of the annulus flow having passed through the engine compressor.

Equation 3.2 may be solved for any of the wall temperatures $T_{s_{(n-1)}}$,

T_{s_n} or, $T_{s_{(n+1)}}$. However, to avoid "infinite sink" problems in the solution, it is necessary to make an initial guess for all the wall temperatures and then it becomes convenient to solve for T_{s_n} , which is obtained through iteration. The guessed temperatures should fall somewhere between the coolant and maximum permitted wall values. Experience with the computer program to make this solution indicates the number of nodal points should be about 20 per inch of wall, and, 30 iterations are necessary for complete convergence.

It is necessary to enable a complete solution to be made, to provide information on film heat transfer coefficients and adiabatic wall temperatures. In Chapter 2 of this thesis a considerable volume of literature concerning film cooling is reviewed. From this extensive review recommendations are made for equations describing local heat transfer coefficients and film effectiveness over wide ranges of injection conditions. Consideration is given to choice of suitable injection conditions and slot configurations for efficient cooling. The effects on cooling of a wide range of additional parameters and conditions are also covered. The tools would thence appear to be readily available for the successful design and prediction of a discrete-injection, film cooling system to suit any situation.

3.2. Practical Film Cooling Systems.

If the recommended expression for film effectiveness, equation 2.31, is used together with say, equation 2.3 for film heat transfer coefficients, and typical values for slot height and injection conditions are taken, some interesting results are obtained when equation 3.2. is solved.

For an existing design of chamber, the predictions give temperatures much lower than those actually measured, even with allowance for combustion hot-streaks. For a new design, less slots appear to be required to cool the chamber than practical experience indicates even when the basic layout of the chamber is taken into account. Since the other terms in equation 3.2 are either well established or substantiated by recent measurements (75), the discrepancies described must arise in equations 2.31 and, 2.3. However, these equations are themselves justified in Chapter 2 of this thesis. It must be concluded therefore, that some radical difference exists between the experimental researches carried out and the presently considered, practical systems.

An obvious source of difference has been previously alluded to under Section 2.4.1., that of slot geometry, when the class-names 'clean' and 'dirty' slots were introduced. It is worthwhile to describe in some detail, practical cooling devices currently in use. Current practice is to use devices in which the coolant flow through the slot is driven by the sum of the static and dynamic pressures in the annular air passage surrounding the flametube, minus the static pressure inside the flametube. This type of cooling device is referred to by the name "total-head" cooling. A sheet construction flametube thus consists from front to rear, of a series of short frusta of a cone of very small vertex-angle, with generally constant initial diameters in the main part, joined by the cooling devices which are usually welded in place. The resulting form of the slot is probably then a short, spacing and metering device with a vestigial (in length not thickness)

lip to reduce initial hot-gas and possible fuel entrainment. The metering and spacing arrangements may be in one or more stages and might also provide support for an extended lip. The ratio of lip thickness to slot height is of the order 0.3 on all but the smallest chambers. The allowable size of lip and nature of the metering together with outlet shape, are compromised by thermal stress and fatigue, and, manufacturing considerations. On small chambers, the slots may be machined integrally with the complete flametube. Wholly sheet-metal devices may also be fabricated. Schematic drawings which represent respectively, machined and fabricated, devices are given in figures 3.3 and 3.4, and these should be compared with the clean slots shown in figure 2.4.

Systematic studies of the dirty-geometry slot have been extremely rare and of those available, most also have considerable density gradients which render the separation of effects difficult. Wieghardt (21) modified his slot geometry from the two-dimensional one shown in figure 2.4, to the more complex (normal injection) ones also shown in this figure. As the geometry became more complex, the effectiveness for any value of $x/_{MS}$ was reduced and the deviations produced were very large. The effects of complex slot geometry were studied by Whitelaw (76) who concluded in a not very informative paper, that slots of complex geometry give rise to lower downstream values of effectiveness than two-dimensional slots and, that effectiveness is a function of free area ratio k, for tangential injection.

These observations agree with the designer's experience of equation 3.2., and confirm that slot geometry is of equal to or greater importance than, the injection parameters, but offer little to further the design of practical cooling systems.

3.3.. The Differences in Film Development Between Clean and Dirty Slots.

Some measurements of film effectiveness for a number of practical geometry cooling devices were very kindly made available from Bristol Engine Division, Rolls Royce Ltd., through the National Gas Turbine Establishment.

Of these results, those for two devices, Types C and L, respectively fabricated and machined slots, were correlated using correlation groups developed for clean slots. In figures 3.5 and 3.6, these data are shown correlated by and compared with respectively, Kutateladze and Leont'ev's method (23), given as equation 2.21 and, Spaldings method (32), given as equations 2.27 and 2.28.

Consideration of figures 3.5 and 3.6 reveals a number of significant observations:

(i) neither of the formulations successfully correlates the dirty-slot data,

(ii) the equations do not represent the data,

(iii) the region where effectiveness is unity is considerably smaller than that predicted for clean slots,

(iv) the slope of the asymptotic region is smaller (of greater decay) than that predicted for clean slots,

(v) the region between unity effectiveness and the asymptotic condition is very large for dirty slots,

Some of the work contained in the present section has been published as reference (47), in which one further clean slot correlation group was used. This was that of equation 2.20 with constants taken from Table 2.1. Correlation of the data for Types C and L using this group was also unsatisfactory.

It is reasonable to conclude from a consideration of figures 3.5 and 3.6, together with reference (47), that no suitable description exists for effectiveness when the slot geometry is complex - i.e. for the present practical application.

One may reason, Section 2.4.5., that the most important aerothermodynamic parameter governing film effectiveness at any distance from injection, is the injection velocity ratio. A comparison of film decay on this basis for two slots, one clean and the other dirty geometry, has been made. The dirty slot was Type C and the clean slot was that of Seban (ii), shown in figure 2.4.f); it is of course, not possible to show a similar drawing for Type C. Since small differences in temperature ratio and slot Reynolds number exist, the data do not represent perfect back-to-back tests, but are indicative of the differences existing. This study has been published as reference (46), from which figure 3.7 has been reproduced.

Figure 3.7 shows essentially the same features as described previously: For a given velocity ratio, the region where effectiveness is unity is reduced and, an extensive region exists <u>regardless of velocity ratio,</u> where the effectiveness is proportional to $(x/s)^{-0.5}$, i.e. <u>jet-like flow</u>. In the asymptotic region, effectiveness is roughly proportional to $(x/s)^{-0.8}$

3.4. <u>Film Model.</u>

The foregoing remarks lead to the formulation of a mathematical model with which to represent film development from a slot with a practical geometry. The model must successfully account for an initial region of unity effectiveness, followed by a region where effectiveness is proportional to

$(x/s)^{-0.5}$, preceeding an asymptotic region where effectiveness is proportional to $(x/s)^{-0.8}$.

The model proposed is shown in figure 3.8. It was tentatively described in work published as reference (47) and more firmly in work published as reference (77). Subsequent development of the problem is centred around this model.

The model arises from the very simple boundary layer theory of film cooling due to Stollery and El-Ehwany (9). This theory is only suitable for clean geometry slots where the injection velocity ratio u_m/u_c is greater than unity, and is here extended to account for the described differences due to the practical construction of the slot. This is done by relating these differences to a velocity defect which is apparent in the film regardless of injection conditions.

Considerations of figures 3.3 and 3.4 and comparison with figure 2.4 indicates how changes in the film might arise: Amongst other differences, boundary layers will form inside the slot and also on the upstream portion of the flametube wall (this may be the residual film from a preceeding slot or series of slots), which together with a separated flow region immediately downstream of the relatively thick lip, create a defect in the velocity profile. Thus, whatever the velocity ratio at injection, the initial film velocity profiles would be expected to appear quasi-jet-like until this defect is filled-in by turbulent mixing. The inner edge of the turbulent mixing layer will grow towards the cooled wall, whilst along this wall is growing a normal boundary layer which may or may not be turbulent. The intersection of these two layers marks the end of the potential core, x_p,

within which the film velocity will remain substantially constant at the injection value. Following the potential core is a region termed the transition length x_T, where the film inner profiles change from those like a wall-jet to the mathematically similar, asymptotic turbulent boundary layer form. Thereafter, there is no further change except in scale as the film grows in thickness; this is the main region.

From the effectiveness work discussed in Chapter 2, it is clear how this model represents the jet-like and boundary layer-like flows to be accounted for. The potential core is equivalent to the region where effectiveness is unity since there, $u_c / (u_c)_{x=0} \simeq 1.0$, which is equivalent to $\eta = 1.0$ if Reynolds analogy is assumed. (Here, the cooled wall boundary layer is neglected. This is a justified step since it will be extremely small in most cases.). This being so, $x_P = x_{P,T}$, the thermal potential core length.

3.5. Applicability of the Model to Combustion Chamber Cooling.

A study was undertaken to relate the model described above to a practical case of combustion chamber cooling by determining what is the minimum value of film effectiveness permissible in a given situation, and, what proportion of the resulting cooled wall distance is potential core. The case study concerned a hypothetical engine to power a Mach 2.2 cruise supersonic airliner of the (early) Concorde class. The general assumptions made concerning this engine at design point are given in Appendix A1.

Two cooling devices were used in the study, Types C and L, as referred to above under Section 3.3. From the experimental data, measurements were made of the initial region by plotting effectiveness as

ordinate against distance from injection divided by slot height as abscissa, on logarithmic paper and linearly extrapolating the asymptotic region back to the line where effectiveness is unity. The resulting intercept is termed for easy reference, potential core length x'_p/s, although obtained by this method it probably includes not only the true hydrodynamic core but also a considerable proportion of the transition region. These results are shown in figure 3.9, where the pronounced tendancy for a maximum x'_p/s to occur at unity velocity ratio should be noted. The effectiveness data were correlated using the group from equation 2.20, and the results are shown in figure 3.10. Even though the correlation of data so obtained is unsatisfactory, figure 3.10 was used in the present preliminary study. Figures 3.9 and 3.10 are reproduced from reference (77), the published version of this study.

The calculations were made for inner and outerflametubes of the combustor in the primary and dilution zone areas. Mean dimensions were taken for the turbine entry duct. The flow was assumed to be everywhere uniform. Gas temperatures and velocities were assumed constant over the whole of each zone. With these restrictions, the ensuing calculations can only yield indications as to the probable order of the cooling difficulties likely to be encountered in each zone of the chamber.

A simplified version of equation 3.1 was used. Following Lefebvre and Herbert (74), a steady state heat balance was set up with wall conduction being neglected. With the assumption of zero wall conduction, solution of the equation becomes a simple problem and a finite difference form is not necessary. Proceeding to the equivalent of equation 3.2 then, the convective term to the wall was also written differently, as:

$$C_{in} = h_{film}(T_m - T_s) \qquad 3.3.$$

this form being more commonly encountered in heat transfer work.

Thus, if a required maximum wall temperature is specified the heat balance may be solved for h_{film}, the remaining heat fluxes being evaluated by the method suggested by Lefebvre and Herbert(74) for wall temperature T_s, which is now known since it is taken as $T_{s,max}$, the specified value. Hence, typical values of film heat transfer coefficient for each zone of the chambers, to keep the wall just at its maximum permitted value can be found.

It is now required to relate the effective heat transfer coefficients so obtained to appropriate values of film effectiveness. Such a relationship has been proposed by Spalding (16) and which appears as equation 2.12 in the present Literature Survey forming Chapter 2 of this thesis, and abbreviated here as,

$$\frac{h_{film}}{C_m c_p u_m} = a\left(\frac{k\rho_c u_c s}{\eta \mu_c}\right)^b \qquad 3.4.$$

where a, k and b are unknown constants.

To eliminate the constants a and k, the film heat transfer coefficient expressed by equation 3.4 has been divided by a reference heat transfer coefficient which it is assumed can be expressed in exactly the same form as h_{film}. This results in the relationship:

$$\frac{h_{film}}{h_{ref}} = \left[\frac{\eta_{ref}}{\eta_{film}}\right]^b \qquad 3.5.$$

where the simplifying assumption has been made that property values apply to the mainstream state. This approach is permissable from the manner in which Spalding formulated his relationship(16). Spalding suggests a numerical

value of about 0.25 for b and, treating the film as an insulating layer which becomes less efficient as distance from injection is increased, this value is taken as appropriate.

A suitable definition is now required for the reference heat transfer coefficient. A convenient and easily calculable reference is that for the heat transfer coefficient in the total absence of film cooling, i.e. for a normal turbulent boundary layer along the surface. The expression actually taken was that used in the heat balance equation for $C_{,out}$, which is given in reference (74) as,

$$St = 0.0283\, Re^{-0.2} \qquad 3.6.$$

To calculate η_{ref}, the following procedure is adopted:
Seban (11) and, Hartnett et al (54) observed that for all values of free-stream to coolant mass velocity ratio M, the ratio h_{film}/h_{ref} became equal to unity for $x/s \geq 50$ approximately. In the absence of further information, it was decided to take this value for clean slots as applicable to Type C and L slots also. Thus, a distance limit, beyond which the film cooling is no better for reducing wall temperature than a normal boundary layer whatever the blowing conditions, is defined. A desirable velocity ratio is indicated from figure 3.9 where it can be seen that the initial region is a maximum when velocity ratio is unity. This condition was assumed and coolant velocities chosen to meet this requirement. Such an assumption agrees with Section 2.4.5. With existing density ratios, the blowing group:

$$S_1 = \left(\frac{x}{Ms}\right) Re_s^{-0.25} \qquad 3.7.$$

is then worked out for the limiting condition. The value of η_{ref} is then

extracted for each slot from the "correlated" data of figure 3.10 by entering the appropriate values of S_1.

It is now possible to work out from equation 3.5 the appropriate values of η_{film} using the values of h_{film}/h_{ref} calculated from the heat balance equation and, equation 3.6, together with η_{ref} values obtained for each chamber position according to the method set out above. Because of the conditions that η_{ref} represents the effectiveness where the film is no greater resistance to heat transfer than a normal boundary layer, and, that h_{film} is calculated as the heat transfer coefficient to keep the wall just at the specified maximum, η_{film} may be termed the minimum acceptable effectiveness, η_{min}.

Results of this type of calculation applied to the chamber under consideration are summerized in Tables 3.1, 3.2 and 3.3. Note that η_{min} is specified as 1.0 over the dilution zone. This does not mean that all the dilution zone cannot be kept at $T_{S,max}$ or below, as mean dimensions only were taken for it. It does mean that with the limited amount of air available, the <u>whole</u> of the dilution zone cannot be maintained at the specified maximum temperature. The approximate values of the Kutateladze blowing group obtained from figure 3.5 for the appropriate values of η_{min} are also given. From these minimum allowable values of the blowing group, limiting values of x beyond which temperature would be greater than $T_{S,max}$, were estimated and these are given in Table 3.3, together with potential core lengths obtained from figure 3.9.

Consideration of the results shows that the high efficiency cooling

regime immediately downstream of the slot, due to the mixing out of the hydrodynamic potential core and subsequent establishment of a universal velocity profile, is a significant proportion of the cooled region in all cases and cannot be neglected in design and prediction considerations.

3.6. The Hypothesis.

The hypothesis presented from the above studies is that for a practical film cooling system of a gas turbine combustion chamber using discrete injection, air-cooling, the film initial regions are of paramount importance and that the design and calculation of such systems should be based on these regions. In addition, the effects of many of the associated variables on film performance can be described in terms of their effects on these initial regions.

CHAPTER 4.

CORRELATION OF DATA AND PREDICTION OF EFFECTIVENESS.

4.1. Introduction.

One is reluctant to completly abandon the boundary layer approach to the prediction of film effectiveness and as a basis for data correlation, in particular that of Stollery and El-Khwany (9) become of its' elegant simplicity and asymptotic nature. Therefore, suitable modifications were sought to enable application to be made to practical slot geometry data. This was done by taking cognizance of the mathematical model described in Chapter 3.

4.2. Analysis.

For this study, the model is applied as follows: The actual developing film is represented by a potential core region, a zero length transition region and, a main region which retains a "memory" of the previous history of the flow. The growth of the model is then represented by a turbulent boundary layer which has the correct thickness equal to that of the real film, at every point. It is assumed that the temperature and velocity boundary layers have the same thickness and that flows are two- dimensional.

Referring to figure 4.1., the thickness f of the film at any point downstream of the potential core x_p, is, by superpositions, the sum of its thickness at the end of this core f_2, plus the growth since that point, f.

i.e. $$f = f_1 + f_2 \qquad 4.1.$$

If x' represents the origin upstream of the injection plane, of a hypothetical turbulent boundary layer which grows to a thickness equal to f_2 at the point x_p, this growth may be represented by the usual expression derived from the zero pressure gradient, uniform stream, momentum equation as,

$$\frac{f_2}{(x'+x_p)} = k_1 \, Re_{(x'+x_p)}^{-b_1} \qquad 4.2.$$

where K_1 and b_1 are constants which depend respectively, on the velocity profile and wall shear stress law chosen for the boundary layer. $Re_{(x'+x_p)}$ is a length Reynolds number based on the distance $(x' + x_p)$.

Similarly, additional growth of the film after the potential core may be represented by,

$$\frac{f_1}{(x-x_p)} = k_2 \, Re_{(x-x_p)}^{-b_2} \qquad 4.3.$$

Consider now an enthalpy balance for a small element of the film, mean height f and length dx, when the temperature gradient across the film is assumed small, i.e. element temperature is approximately equal to the adiabatic wall temperature, $T_{s,ad}$. This approach thus considers the injected and entrained mass flows in the film to be fully mixed at every point and as a consequence, there will exist a temperature discontinuity at the edge of the film.

$$\dot{m}'_f c_{pc} T_{s,ad} = \dot{m}'_c c_{pc} T_c + \dot{m}'_e c_{pm} T_m \qquad 4.4.$$

where $\dot{m}'_c$ is the mass flow rate of the coolant at temperature T_c injected per unit width of slot, and $\dot{m}'_e$ is the entrained mass flow rate at mainstream temperature T_m, per unit width of film.

For gas turbines operating with liquid hydrocarbon fuels and typical air/fuel ratios, the mean molecular weight of the hot products of combustion may be taken as approximately equal to that of air without introducing serious error. If therefore a like-into-like injection, constant pressure mixing and temperature differences small enough for specific heat at constant pressure c_p, to be considered constant, are assumed, equation 4.4 reduces to,

$$\dot{m}'_f T_{s,ad} = \dot{m}'_c T_c + \dot{m}'_e T_m$$

It is clear therefore, that the present method neglects the effects of specie diffusion on film effectiveness.

Following an idea of Spalding's (78) which was developed in a jet-mixing study concerned with combustion chamber dilution zones (79), and expressing the entrained mass flow rate in terms of the total mass flowing and the injected mass flow rate,

$$\dot{m}'_e = \dot{m}'_f - \dot{m}'_c \qquad 4.5.$$

and substituting,

$$\dot{m}'_f T_{s_{ad}} = \dot{m}'_c T_c + (\dot{m}'_f - \dot{m}'_c) T_m \qquad 4.6.$$

The total mass flowing in the film can be found by integrating the assumed mass velocity profile for the boundary layer across the film.

Thus,
$$\frac{\dot{m}'_f}{\rho_m u_m} = \int_0^f \frac{\rho u}{\rho_m u_m} \cdot dy = \int_0^f \left(\frac{y}{f}\right)^{\frac{1}{n}} dy = \frac{n}{(n+1)} \cdot f$$

if the mass velocity profiles are assumed to obey a power law of the form,

$$\frac{\rho u}{\rho_m u_m} = \left(\frac{y}{f}\right)^{\frac{1}{n}} \qquad 4.7.$$

This passé form of profile is perfectly adequate for the present purposes, as will be seen.

Hence,

$$\dot{m}'_f = \frac{n}{(n+1)} \rho_m u_m f \qquad 4.8.$$

From the conservation of mass,

$$\dot{m}'_c = \rho_c u_c s \qquad 4.9.$$

Equation 4.6. may be rearranged in the form,

$$\frac{T_{s_{ad}} - T_m}{T_c - T_m} = \frac{\dot{m}'_c}{\dot{m}'_f}$$

whence it may be seen that from the definition given in equation 2.2 that,

$$\eta = \frac{\dot{m}'_c}{\dot{m}'_f} \qquad 4.10$$

Substituting for the mass flow rate from equations 4.9 and 4.8, and from equation 4.1 for film thickness, in equation 4.10, the effectiveness is seen to be given by,

$$\eta = \frac{\rho_c u_c}{\rho_m u_m} \cdot \frac{s}{(f_1+f_2)} \cdot \frac{(n+1)}{n} \qquad 4.11$$

Substituting now for f_1 and f_2 from equations 4.2 and 4.3,

$$\eta = \frac{(n+1)}{kn} \cdot \frac{\rho_c u_c}{\rho_m u_m} \cdot s \left[\frac{(x-x_\rho)}{Re^{b_2}_{(x-x_\rho)}} + \frac{(x'+x_\rho)}{Re^{b_1}_{(x'+x_\rho)}} \right] \qquad 4.12$$

where the velocity profiles contributing to f_1 and f_2 have been taken to be the same,

$$\text{i.e.} \quad k_1 = k_2 = K$$

The mass flow rate at the end of the potential core may be also expressed in terms of the injected mass flow rate by letting,

$$K_3 \rho_c u_c s = (\dot{m}'_f)_{x_\rho} \qquad 4.13$$

where K_3 is an unknown greater than unity. As before, $(\dot{m}'_f)_{x_\rho}$ may be found by integration of the mass velocity profile, therefore,

$$K_3 \rho_c u_c s = \int_0^{f_2} \rho u \, dy$$

yielding with the use of equation 4.7,

$$f_2 = \frac{(n+1)}{n} K_3 \cdot \frac{\rho_c u_c}{\rho_m u_m} \cdot s \qquad 4.14$$

But from equation 4.2,

$$f_2 = K_1 (x'+x_\rho) Re^{-b_1}_{(x'+x_\rho)} \qquad 4.15$$

Since the film must be continuous at this point x_ρ, these equations may be equated to enable the Reynolds number based on $(x' + x_\rho)$ to be found and

substituted into 4.12, which then yields upon further algebraic manipulation the final expression for effectiveness,

$$\eta = k_4 \left\{ \frac{nk}{(n+1)k_3} S_N^{(1-b_2)} + 1 \right\}^{-1} \qquad 4.16a)$$

where,

$$S_N = \frac{(x-x_p)}{Ms} \left(Re_s \cdot / \frac{\mu_c}{\mu_m} \right)^{-b_2/(1-b_2)} \qquad 4.16b)$$

and, $k_4 = \frac{1}{k_3}$, $M = \frac{\rho_c u_c}{\rho_m u_m}$, the mass velocity ratio.

For prediction purposes it is desirable to have available a single equation which represents the performance of all slots, or at least all slots of a certain general class. In the foregoing development leading to equation 4.16, only aerodynamic parameters were directly taken into consideration. The underlying premise of the whole approach however, is that slot geometry is one of the dominating factors in the film development subsequent upon injection. The immediate effects will be accounted for by the potential core; here, the effects on the remaining film development are under consideration.

The effects of slot geometry will be experienced through velocity profile and wall shear stress. This relationship between slot geometry and wall shear stress is not at all well understood so detailed modifications are not possible at this stage. Mixing in the film also depends on the turbulence structure, the level of which depends on the initial turbulence generated by the slot; this being in turn a function of the expansion ratio across the slot, for a given slot. On the postulate that the coolant flow experiences expansion in steps throughout the length of the injection device, the ratio of outlet area to slot total effective area A_b'/A_E', was felt to be a suitable

description of geometry in the first instance. Accordingly, equation 4.16b) was modified to,

$$S_{N_2} = \left[\frac{(x-x_p)}{Ms} \cdot \left(Re_s \cdot \frac{\mu_c}{\mu_m}\right)^{-b_2/(1-b_2)} A'_o/A'_E \right] \qquad 4.17$$

4.3. Use of the Analysis.

Refering to equations 4.1 and 4.2, it was stated that the exponent 'b' depended on the wall shear stress law chosen for the boundary layer. This can be realised from a consideration of how the expression linking boundary layer thickness δ, with length Reynolds number is classically derived from the appropriate form of the Von Kármán integral momentum equation. Into this equation a value for wall shear stress is inserted which is based on Blasius' turbulent pipe flow measurements to eventually yield for zero pressure gradient flow, the familiar,

$$\frac{\delta}{x} = \frac{0.37}{Re_x^{1/5}} \qquad 4.18$$

Consideration of the film development described above makes the classical Blasius wall shear stress law,

$$\frac{\tau_s}{\rho u_{max}^2} = 0.0225 \left(Re_{,\delta} \right)^{-0.25} \qquad 4.19$$

where $Re_{,\delta}$ is a Reynolds number based on boundary layer thickness, seem an unrealistic choice for the present situation. Indeed, for the wall-jet, $u_c \gg u_m$, various authors have measured values greatly differing from those given by equation 4.19, e.g. Seban and Back (12), Bradshaw and Gee (80). These latter authors found that equation 4.19 underestimated the measured surface friction by about 25 per cent. An alternative expression for the wall shear stress of a jet-like flow under a co- flowing stream was

recommended (80) as,

$$\frac{\tau_s}{\rho u_{max}^2} = 0.013 \left(Re_{,\delta} \right)^{-0.18} \qquad 4.20$$

If this latter expression is used in the integral momentum equation, the growth of a boundary layer subject to this wall shear stress can be found as,

$$\frac{\delta}{x} = K_5 \, Re_x^{-0.1525} \qquad 4.21$$

We now assume that the fictitious boundary layer with which the real film is being simulated "remembers" that it is trying to represent a quasi-jet like flow and therefore that its growth rate follows equation 4.21 rather than 4.18½ This is a reasonable hypothesis since in the real case, the decay period of the turbulent eddies bearing the "packets" of shear stress will in general be longer than their residence time within the transition region. It is therefore taken that an appropriate value for b_2 is given by equation 4.21 and hence, that

$$\frac{S}{N_2} = \left[\frac{(x - x_p)}{Ms} \cdot \left(Re_s \cdot \frac{\mu_c}{\mu_m} \right)^{-0.18} \cdot A_o'/A_\epsilon' \right] \qquad 4.22$$

An examination of the data indicated that the exponent on the Reynolds number ~ viscosity ratio term should be increased even further towards zero than indicated by equation 4.22. This is not unexpected since the geometry-induced film turbulence associated with any practical injection geometry would be greater than that experienced in reference (80). Separate wall shear stress laws are probably required for each individual geometry variation. However for a series of geometries which are all of a particular class, a blanket law would appear to be acceptable. For all the geometries studied, it was found that acceptable correlation of data was found if equation 4.22 was modified by trial and error, to:

$$S_{N_2} = \left[\frac{(x-x_p)}{M_S} \cdot \left(Re_s \cdot \frac{\mu_c}{\mu_m} \right)^{-0.15} \cdot A_o'/A_E' \right] \qquad 4.23$$

Further increase of the exponent towards zero brought about small but insignificant additional improvements in correlation for certain of the geometries, but completely eliminating the Reynolds number group reduced the degree of correlation for <u>all</u> the geometries.

For correlation of effectiveness data, equation 4.23 may be used to provide a suitable blowing group. It is not necessary to assign a value to 'n' in equation 4.16a) since it is not possible at this stage, to give a value to K_3 and therefore, this equation cannot be used for prediction purposes. Thus we must write,

$$\eta = \eta \left(S_{N_2} \right) \qquad 4.24$$

and determine the form of the relationship from the data. The form of the functional relationship can be based on equation 4.16a),

$$\text{i.e.} \quad \eta = A \left[1 + B S_{N_2}^{C} \right] \qquad 4.25$$

where A, is a constant which from the effectiveness definition ideally should be unity but in fact depends on how acurately the potential core length is determined, B is another constant which depends on the rate of mixing in the film, and C a further constant dependant upon which part of the film is under consideration.

The constant C when applied to practical geometries in the present application, is the mean slope of the data in the transition region. Because of the velocity defect introduced into film profiles by the substantial lip,

the transition region for all velocity ratios commences like a wall-jet and ends asymptotically, like a boundary layer. It has been shown in Chapter 2 that for $u_c > u_m$, the wall-jet case, effectiveness is proportional to $\frac{(x - x_p)}{s}$ raised to the power 0.5; similarly, for the wake-case, $u_c < u_m$, the exponent should have the value 0.8. A compromise value of 0.65 is suggested to cover practical geometries for all velocity ratios. Thus,

$$\eta = A\left[1 + BS_{N_2}^{+0.65}\right] \qquad 4.26$$

Samuel and Joubert (18) who operated a slot with a thick lip, $0.33 \leqslant \delta_w/s \leqslant 1.0$, which resulted in an extensive velocity defect, empirically found that a good compromise was

$$\eta = \eta\left(\frac{x}{s}\right)^{-0.65} \qquad 4.27$$

which is in agreement with the form of equation 4.26..

4.4. Experimental Data.

Data for two basic types of practical cooling slot were available for correlation studies: 6 total-head machined slots and, 3 fabricated sheet stacked-ring slots.

The machined slot data were obtained from a two-dimensional test-rig having a test section of area 6 inches width by 3 inches height, fed with mainstream air from a preheater at temperatures up to 1470°F and 300 ft./sec. velocities. Coolant was available up to 224°F. Discharge was to atmosphere. There was no coolant by-pass flow, the cooled surface being insulated for measurement of adiabatic wall temperatures by surface thermocouples. Adiabatic wall temperatures were taken as the arithmetic mean of three rows of thermocouples placed on the longitudinal centre-line and, symmetrically on either side of it. The present author thanks the Bristol Engine Division, Rolls Royce Ltd., for these data.

The stacked-ring slot data were obtained from a wind-tunnel whose test-section was 16inches in cross-section and, $9\,^{13}/_{16}$ inches in length, with mainstream velocities up to 150 ft./sec. at ambient temperatures. The slot flow was preheated to about 55^{0}F above ambient temperature. There was no bypass flow and adiabatic wall temperatures were obtained from surface thermocouples where averaging was accomplished automatically through lateral copper strips under the thermocouples. This facility was that used and described by Chin et al (49), (50). These data were kindly provided by the Aircraft Engine Division, General Electric Company.

Tables 4.1 and 4.2 show respectively the range of aerothermodynamic and geometric, parameters covered for the machined slots: Similarly, Tables 4.3 and 4.4 for the stacked-ring slots. Aerothermodynamic quantities in these tables are bulk-values.

The overall effective area of a slot is defined by

$$\dot{m}'_c = A'_E \left[\frac{2g_o 144}{R} \cdot \frac{p_c \Delta P}{T_c} \cdot 144 \right]^{1/2} \qquad 4.28$$

where $\dot{m}'_c$ is in units of lb_m/ sec. ft. run of slot, and, pressures are in lb_f/in^2. Experience with the machined slot data indicated that for a given slot over the range of parameters investigated, discharge coefficient was substantially constant. This was because of the zero slot-bypass flow. Such was also found to be the case for the stacked-ring slots. Effective area was therefore found by measuring the gradient $d(\dot{m}'_c) / d\left(\frac{p_c \Delta p}{T_c}\right)^{\frac{1}{2}}$ for each geometry. The procedure is illustrated in figure 4.2. In general, A'_E would be a function of the ratio of wall pressure drop to annulus dynamic head. For combustion chambers, the design is such that this is not the case to ensure constancy of performance.

The Rolls Royce raw data was found to be defective in that at the injection plane, the effectiveness was less than unity. This was traced to an upstream measurement of coolant temperature used to evaluate effectiveness when due to heat transfer, the actual coolant temperature was at a higher value.

To correct the data, the expression,

$$\eta' = \frac{T_{s,ad} - T_s}{T_{s,ad} - T_c'}$$

where η' is the erroneous effectiveness based on the incorrect coolant temperature T_c', is divided by its' $x = 0$ value, since

$$\eta = \eta' / (\eta')_{x=0} = \frac{T_{s,ad} - T_s}{T_{s,ad} - T_c'} \times \frac{T_{s,ad} - T_c'}{T_{s,ad} - (T_s)_{x=0}}$$

where, for an adiabatic wall and unity Prandtl number,

$$(T_s)_{x=0} = (T_c)_{x=0}$$

No specific meaurements were made of potential core in either test series. Potential core length was found therefore in each case by plotting the natural logarithmic values of x/s against effectiveness and making a linear extrapolation back to the line $\eta = 1.0$, as outlined in reference (46). This is illustrated in figure 4.3.

Potential core lengths of the practical slots are shown for each device in figures 4.4 and 4.5. The results are presented in slot heights, as a function of velocity ratio only, other relevant parameters are not accounted for. These figures are to serve only as a convenient presentation of data.

To test the efficacy of the basic analysis, the data were correlated against the group,

$$S_{N_2} = \left[\frac{(x - x_p)}{M s} \left(R_s \cdot \frac{\mu_c}{\mu_m} \right)^{-0.15} \right] \qquad 4.29.$$

for individual devices. The results are shown in figures 4.6 and 4.7.

For all the nine slots, correlation was to within ± 5 per cent of unity. The exponent of 0.65 renders the correlated data linear over the range of the data. For velocity ratios $u_m/u_c \leq 0.5$ an effect of velocity ratio becomes apparent, as had been found earlier in Section 2.4.2. This effect is rather strong for the machined devices but not so pronounced for the stacked ring devices. Figure 4.8 illustrates this by showing the slopes of the data for geometries G1 - G3 as a function of velocity ratio.

The linear equations describing the data were found as follows: The slopes were integrated means,

$$B = \int_1^2 -m \, d\left(u_m/u_c\right) \Big/ \left[u_m/u_c \right]_1^2$$

obtained by numerical integration by Simpson's rule of curves such as these of figures 2.8 and 4.8. The intercepts were random, depending on how well the potential core was determined and how exactly the 0.65 exponent rendered the data linear. The mean intercept was therefore found as a straight arithmetic mean value for all the tests of a particular device. With a form given by equation 4.26, the equation constants are as follows,

Device	A	- B
B1	1.01022	0.25422
B2	1.0251	0.17813
B3	1.0104	0.20047
B4	1.0	0.22432

... Continued/..

Device	A	- B
B5	1.0725	0.22310
B6	1.10	0.22180
G1	0.99808	0.11301
G2	0.99116	0.12641
G3	0.98187	0.10126

Consideration of figures 4.6 and 4.7 reveals that the present model and analysis satisfactorily accounts for variation of the aerothermodynamic parameters. At the present author's request and direction, the correlation group was applied also to the data of Chin et al (50) by Patel (81), and some of these results are presented in figure 4.9 with Mr. Patel's kind permission. Figure 4.9 is particularly interesting in that values of $S_{N_2}^{+0.65}$ are much larger than these obtained in the B and G series of tests presented in figures 4.6 and 4.7. It can be seen that the relationship between effectiveness and the correlation group is linear and the data again correlated to $\pm$ 5 per cent of unity, to $S_{N_2}^{+0.65}$ values up to 10 : For greater values the 0.65 exponent is no longer appropriate since the main region of the film is now being seen and the linearity breaks down. A value of 0.8 would there be more suitable.

4.5. Universal Correlations.

With the efficacy of the basic aerothermodynamic modelling established by figures 4.6 and 4.7, universal correlations using the full blowing group defined by equation 4.23, were attempted.

The results of universal correlation are contained in figures 4.10 and 4.11, respectively for the Rolls Royce and General Electric data. Shown on figure 4.10 is the line representing the Rolls Royce machined slot data as,

$$\eta = 1.0082\left[1.0 - 0.12025\, S_{N_2}^{+0.65}\right] \qquad 4.30$$

found by the methods described in Section 4.4. This line is shown in figure 4.11, together with the line,

$$\eta = 1.00126\left[1.0 - 0.094075\, S_{N_2}^{+0.65}\right] \qquad 4.31$$

representing the G.E. fabricated stacked-ring data. Shown in figures 4.12 and 4.13 are regression plots illustrating the accuracy of equations 4.30 and 4.31 in representing the collected data for each type of cooling device.

Figures 4.12 and 4.13 show that the group S_{N_2} does correlate the data of a given slot-type - i.e. machined or fabricated. For the machined slots of Rolls Royce origin, equation 4.30 represents the data such that 94.58 per cent of all data falls within the 10 per cent of unity bands and, 97.29 per cent of all data falls within the 12 per cent bands. Equation 4.31 represents the General Electric stacked-ring data such that 91.01 per cent of all data falls within the 10 per cent of unity bands and, 94.96 per cent within the 12 per cent bands. For the present application, effectiveness seldom can fall below values of about 0.5; within this range, correlation is very good indeed. Figures 4.10 and 4.11 should be compared with figures 3.10, 3.6 and 3.5 for practical geometries; and, figure 4.9 with figure 2.9 for clean geometries. The contrast in the degrees of correlation achieved is pleasing.

It may be seen from figure 4.11 that the G.E. stacked-ring devices apparently have a better performance, i.e. higher η for a given S_{N_2}, than

the R.R. machined devices. It is difficult to trace the origin of this difference. One obvious source for the difference could arise in the rig facilities, in particular, through the mainstream turbulence. As has been shown by figure 2.14, the effects of mainstream turbulence are described in terms of potential core length and, decay rate of the main film region. Both these regions however, are excluded from the data by the form of the blowing group S_{N_2}, which applies to the transition region only. In any case, such differences would tend to be ruled out by the nature of the stacked-ring data: For the data shown satisfactorily correlated in figure 4.11, tests are included where the mainstream boundary layer starting length was varied from 8 to 29 inches, turbulence - generating screens were placed in the mainstream and, turbulence pins protruded through the cooled wall. Any evidence of these variations is submerged in the general scatter of the data. If some fundamental difference in the performance of the two types of slot does indeed exist, then equation 4.23 is not a universal correlation group. The good correlation of the Rolls Royce data however, which covers an enormously wide range of geometries, (see Table 4.2), validates the correlation group and suggests some unaccounted for difference in either the facilities, the measurement of quantities, or, the reduction of data. In view of the greater range of parameters represented andits conservative predictions, equation 4.30 is therefore recommended for use in design and prediction of film cooling systems for combustion chambers.

4.6. Conclusions.

4.6.1. The simple boundary layer model of film cooling may be extended by relatively slight modifications to correlate satisfactorily, data

from practical cooling slots. The same correlation group may be used with similar success for clean geometries, within its range of applicability

4.6.2. The new group offers considerable improvement in correlation of practical geometry data than previous ones. The modified form still breaks down for flows where $u_c \gg u_m$, but may be used satisfactorily for data where $u_c > u_m$ is included provided $u_m \gg u_c$ is not met with in the same set of data. These conditions are generally complied with in the combustion chamber.

4.6.3. Reliable and simple equations are available for the calculation of film cooling effectiveness. These equations are valid for differing mainstream- side lip boundary layers and, changes in film and mainstream turbulence.

4.6.4. The working hypothesis of the thesis, given in Section 3.6, that account of the film initial region is necessary, has been shown to be the key to dealing with film effectiveness.

The majority of the work presented in this chapter was reported initially in references (82) and (83), for Bristol Engine Division, Rolls Royce Ltd., and, publically in total, as reference (84). For obvious, proprietory reasons the amount of detail given of the Rolls Royce and General Electric Companies work in this and the heat transfer, area must be strictly limited.

Nota Bena.

Since the original preparation of this thesis, the S_{N_2} correlation group has been applied to the effectiveness test-data from three further slots of machined construction, slots G4, G5 and G6. The design of these slots was

different to any of the machined B - series of slot, and the test measurements were made in a third wind-tunnel which has initial mainstream turbulences of the order 20% $\sqrt{u'^2}/u_m$. Excellent correlation of test-data was obtained and equation 4.30 made a good prediction of the results up to the end of the transition region in the film, (See Chapter 12).

CHAPTER 5.

SCALE EFFECT IN COMBUSTOR FILM COOLING.

5.1. Introduction.

From an overall logistics viewpoint, it is extremely desirable to have one (good) slot design which may be applied to all combustion chambers whatever their shape, size and operating conditions. There are double advantages to such a policy in that estimates of the cooling requirements of any chamber may be made from measurements made on one "standard" chamber. The efficacy of such a policy depends on the scaling laws pertinent to film cooling.

It has long been recognised that the scale of the combustor can exercise important effects on overall performance (85), and "PD scaling" or, constancy of the product of static pressure and combustor characteristic dimension, is used for comparing the performance of geometrically similar chambers. It is not possible when using PD scaling, to exactly reproduce wall temperatures. Where constancy of PD is maintained, wall temperatures fall with combustor linear dimension, for constant inlet temperature and velocities.

When assessing the potential performance of a projected combustor against a known standard, very often, the variable is linear scale alone and other conditions are approximately constant, at a given level of combustor technology. This represents a somewhat different kind of scaling. In this case, the equations of reference (85) indicate that convective input to the wall, (see equation 3.1 of present thesis), increases with $(1/K)^{-0.2}$ while radiative input reduces with $(K)^{-0.6}$, where the scale factor K, defined as the ratio of combustor characteristic dimensions, is always greater than

unity. These suggest an increase in wall temperature with decreasing combustor size provided film effectiveness can be shown to scale in the same manner.

5.2. Effectiveness Scaling.

An expression describing film effectiveness for machined construction, practical geometry cooling slots is presented in equation 4.30, given again here,

$$\eta = 1.0082\left[1.0 - 0.12025\, S_{N_2}^{+0.65}\right] \qquad 5.1.$$

As pointed out immediately following equation 4.25, the first of the constants appearing in equation 5.1 should ideally have the value of unity. Taking this to be so, equation 5.1 can be rearranged as,

$$(1-\eta) = 0.12025\; S_{N_2}^{+0.65}$$

where,

$$S_{N_2} = \left[\frac{(x-x_p)}{Ms}\cdot\left(Re_s\,\frac{\mu_c}{\mu_m}\right)^{-0.15}\cdot\frac{A_o'}{A_E'}\right]$$

For a given slot design, the area ratio A_o'/A_E' will be a constant. Since most combustion chambers tend to operate at a constant value of non-dimensional wall pressure drop, the slot Reynolds number will not vary greatly. Because of this and in addition, because of the magnitude of the exponent on the Reynolds number $\sim$ visocsity grouping, this grouping may also be treated as a constant. Thus,

$$(1-\eta) \propto \left[\frac{(x-x_p)}{Ms}\right]^{+0.65} \qquad 5.2$$

Mass velocity ratio M is defined,

$$M = \frac{\rho_c u_c}{\rho_m u_m}$$

Now, using the equation of conservation of mass,

$$\rho_m u_m = \dot{m}'_m / d \qquad \text{and,} \qquad \rho_c u_c = \frac{\dot{m}'_c}{S}$$

where d is a combustion chamber characteristic dimension.

Thus,

$$M = \frac{\dot{m}'_c}{\dot{m}'_m} \cdot \frac{d}{S}$$

Hence, when substituted in equation 5.2,

$$(1-\eta) \propto \left[\frac{(x-x_p)}{d} \cdot \frac{\dot{m}'_m}{\dot{m}'_c} \right]^{+0.65} \qquad 5.3.$$

Usually, the coolant flow tends to be specified as a design parameter in project studies, as a fixed (predjudice value based as previous experience) percentage of core compressor delivery flow,

i.e. $\dot{m}_c / \dot{m}_m$ is constant.

But $\dot{m}_c / \dot{m}_m \propto \dot{m}'_c / \dot{m}'_m$, thus , $\dot{m}'_m / \dot{m}'_c$ is constant also.

Then,

$$(1-\eta) \propto \left[\frac{(x-x_p)}{d} \right]^{+0.65} \cdot \left(\frac{d_{slot}}{d} \right)^{+0.65} \qquad 5.4.$$

From a manufacturing standpoint, it is convenient to have flametube panel lengths, (between slots), which are constant. Such panel lengths will in general, be greater than the slot potential core length. Thus, $x \gg x_p$ and, equation 5.4 becomes,

$$(1-\eta) \propto \left(\frac{1}{d} \right)^{+0.65} \qquad 5.5$$

where for all but the smallest chambers, $\left(\frac{d_{slot}}{d}\right)^{+0.65}$ can be taken as unity.

From equation 5.5, it can be seen that as d increases, $(1-\eta)$ decreases and, η increases. Therefore, it may be concluded:

(i) for a specified coolant ratio, a large chamber will run

cooler than a small one, for the same design of slot and fixed panel length,

(ii) if panel length is made equal to the potential core length, both large and small chambers will run at the same temperature for equal compressor delivery temperature and combustor temperature rise.

To assess the extent of this adverse (for small combustors) scaling effect, consider two designs A and B, and let $d_B > d_A$. The scale factor is,

$$K = (d_B / d_A)$$

and,

$$(1 - \eta_A) = K^{+0.65} (1 - \eta_B) \qquad 5.6$$

from equation 5.5.

Now, let the characteristic dimension be proportional to combustor dome height. For the two chambers under consideration,

Chamber B dome height = 3.25 inches

Chamber A dome height = 2.26 inches

and so,

$$(1 - \eta_A) = 1.2646 (1 - \eta_B) \qquad 5.7$$

Design B may be the "standard" combustor, and design A the one under investigation. In figure 5.1, is shown how the actual film effectiveness in chamber A is reduced from that expected on the basis of experience with chamber B, due to the scale effect which is given in equation 5.7. The importance of scale effect to wall temperatures is shown in figures 5.2 and 5.3 for respectively primary and dilution zones of chamber A. To obtain these temperatures from the effectivenesses shown in figure 5.1, a simplified version of equations 3.1 and 3.2 was used, neglecting wall conduction. It can be seen

that actual wall temperatures can be significantly higher than these expected on the basis of chamber B experience

5.3. Conclusions.

5.3.1. The absolute size of the combustor has a direct bearing on the film effectiveness.

5.3.2. If cooling systems are designed such that the panel length is equal to the potential core length, cooling development experience with one chamber can be read across to another chamber differing in size only, provided the same slot design is used.

CHAPTER 6.

PREDICTION OF LOCAL HEAT TRANSFER COEFFICIENT IN FILM COOLING.

6.1. Introduction.

Consideration of the wall heat balance given in equation 3.2, shows the convective heat input term is based on a temperature difference between the adiabatic wall temperature and the actual wall temperature. This is a somewhat unusual temperature difference to work with compared to normal heat transfer practice and the historical reasons for it are given in Chapter 2 of this thesis. The calculation of heat transfer rate is thus a two-step procedure involving local heat transfer coefficient and film effectiveness. It would be convenient if these two steps could be directly related.

The recommended heat transfer relationship, equation 2.8, is semi-empirical and was obtained for clean geometry slots. It is necessary to be able to account for practical injection geometries in any general relationship.

The object of the present Chapter is to derive a local film heat transfer coefficient which is based on a normal temperature difference by relating the two separate steps described above, and which accounts for slot geometry.

6.2. Analysis.

The film is mathematically modelled (Chapter 3) to consist of a potential core preceeding a transition region, followed by the main region of the film. The flow field is illustrated in figure 3.8. For the potential

core and main region it is reasonable to assume on the basis of the flow model, that local film convective heat transfer coefficients may be predicted satisfactorily from the standard, impermeable wall, turbulent flow relationships. For example, the Colburn relationship, given as equation 2.3 and here as,

$$St = 0.037 \left(Re_x \right)^{-0.2} \qquad 6.1$$

where, for the potential core the Stanton number is based on the injected coolant, and for the main region on hot-gas bulk, conditions. For the transition region, which has been shown (Chapter 4) to be substantial for practical cooling geometries and operating conditions and where this forms the majority of the cooled area in a combustion chamber, a suitable relationship is required. Analysis of this region is presented below.

Consider the film formed from a two-dimensional slot of arbitrary geometry, as shown in figure 6.1: Let the film exist as a discrete layer over an elemental control volume AB of length 2 dx and unit width, at a distance x from the injection plane, but with a mass rate $\dot{m}_e'$ entrained from the mainstream ahead of A. The distance x is greater than the potential core but less than the main region. Consider convective heat transfer to the film from the mainstream. A steady-state heat balance for an element of the wall, dx, is

$$C_{in} = \left(R_{out} + C_{out} \right) + {}_A H_B \qquad 6.2$$

neglecting longitudinal wall conduction, where,

$${}_A H_B = \text{enthalpy increase of the film in passing A to B,}$$

R_{out} , C_{out} = heat flows from the wall to annulus by radiation and and convection.

C_{in} = convective heat flow to film

If the mean temperature of the film at x is T_c, the mean temperatures at A and B are, respectively,

$$\left(T_c - \frac{dT_c}{dx} \cdot dx \right) \quad \text{and,} \quad \left(T_c + \frac{dT_c}{dx} \cdot dx \right)$$

and the enthalpy increase of the film in passing from A to B is,

$$_AH_B = (\dot{m}_c' + \dot{m}_e') \bar{c}_p \left[\left(T_c + \frac{dT_c}{dx} \cdot dx \right) - \left(T_c - \frac{dT_c}{dx} \cdot dx \right) \right]$$

where, $\bar{c}_p$ = mean film specific heat.

i.e. $$_AH_B = 2 (\dot{m}_e' + \dot{m}_c') \bar{c}_p \frac{dT_c}{dx} \cdot dx \qquad 6.3.$$

Now, the average heat flow into the element is given by

$$C_{in} = 2h\, dx (T_m - T_c')$$

where T_c' = some appropriate mean film temperature, the arithmetic mean say, T_c.

thus, $$C_{in} = 2h\, dx (T_m - T_c) \qquad 6.4.$$

Make the assumption that the normal temperature gradient through the film is small, implying that the mean coolant temperature is approximately equal to the wall surface temperature and, that h approximates to the overall effective heat transfer coefficient, including the film resistence to heat flow, and termed h_E .

Then, from equation 6.4,

$$C_{in} = 2h_E dx (T_m - T_s) \qquad 6.5.$$

and,

$C_E = (R_{out} + C_{out})$ from an <u>overall</u> heat balance,

C_E being the overall effective convective input.

Now,

$(R_{out} + C_{out}) \propto C_{in}$ approximately and so from equation 6.5,

$$(R_{out} + C_{out}) = K_1 h_E \, 2\,dx\,(T_m - T_s) \qquad 6.6$$

The above steps avoid the confusing inclusion of unneccessary backside conditions by expressing the total heat flow out through the wall as a fraction of what flows in.

Substituting into the original heat balance equation 6.2, for C_{in} from equation 6.5, for $(R_{out} + C_{out})$ from equation 6.6, and, for H_{AB} from 6.3, we have upon re-arrangement,

$$h_E (T_m - T_s)(1 - K_1) = (\dot{m}'_c + \dot{m}'_e)\,\bar{c}_p \frac{dT_s}{dx} \qquad 6.7$$

K_1 is of course, an unknown constant.

Separating the variables,

$$\frac{dT_s}{(T_m - T_s)} = \frac{h_E (1 - K_1)\,dx}{(\dot{m}'_c + \dot{m}'_e)\,\bar{c}_p} \qquad 6.8$$

The boundary conditions for this differential equation are as follows:

(i) at $x = x_p$, $T_s = T_{c_i}$, the coolant injection temperature

(ii) at $x > x_p$, $T_s = T_s(x)$

Integrating therefore,

$$\int_{T_s = T_{c_i}}^{T_s = T_s} \frac{dT_s}{(T_m - T_s)} = \int_{x = x_p}^{x = x} \frac{h_E (1 - K_1)\,dx}{(\dot{m}'_c + \dot{m}'_e)\,\bar{c}_p}$$

i.e.

$$\ln\left[\frac{(T_s - T_m)}{(T_{c_i} - T_m)}\right] = \int_{x_p}^{x} \frac{h_E (K_1 - 1)\,dx}{(\dot{m}'_c + \dot{m}'_e)\,\bar{c}_p} \qquad 6.9$$

Now, as a consequence of the assumptions, $T_s \simeq T_{s,ad}$, hence equation 6.9 may be written,

$$\ln\left[\frac{(T_{s,ad}-T_m)}{(T_{c_i}-T_m)}\right] = \int_{x_p}^{x} \frac{h_E\,(K_1-1)\,dx}{(\dot{m}'_c+\dot{m}'_e)\,\bar{c}_p}$$

But, $\dfrac{(T_{s,ad}-T_m)}{(T_{c_i}-T_m)} \equiv \eta$, the film effectiveness, according to equation 2.2

Therefore,

$$\ln \eta = \int_{x_p}^{x} \frac{h_E\,(K_1-1)\,dx}{(\dot{m}'_c+\dot{m}'_e)\,\bar{c}_p} \qquad 6.10$$

To proceed with the integration suitable mass entrainment laws are required. Cole (36) found for a distance downstream of the potential core there was a region where Spaldings recommended film entrainment laws (35) were not valid. He suggested this region was the transition length, where constant values of entrainment might be appropriate. To give a good fit to existing (clean slot) data, he found these values depended upon velocity ratio and the relative magnitude of the free-mixing layer component of the velocity profile at the end of the potential core, resulting in an entrainment law,

$$(\dot{m}'_c+\dot{m}'_e) = \left[\dot{m}'_c + (\dot{m}''_e)_{x_p}\,x_p + (\dot{m}''_e)_{x_T}\,(x-x_p)\right] \qquad 6.11$$

where $(\dot{m}''_e)_{x_p}$ and $(\dot{m}''_e)_{x_T}$ are independent of x and represent the entrainment rates in respectively, the potential core and, transition regions.

Laws of this type have been studied (86) in the combustion chamber described in Appendix L of this thesis. Equation 6.10 was simplified by taking $K_1 = 0$ (insulated rear-face wall with heat generation) and solving for effectiveness. The appropriate heat transfer coefficients were calculated such that the wall temperature would nowhere exceed a value of 800°C, by solving the simplified (zero conduction) version of equation 3.2, the heat balance, where the convective flux to the wall was given by $h_{eq}(T_m - T_s)$. The

method is described in detail in reference (86). Constant fractions of the mainstream were entrained,

$$\text{i.e. } (\dot{m}''_e)_{x_p} = A\rho_m u_m \text{ and, } (\dot{m}''_e)_{x_T} = B\rho_m u_m$$

Extreme sensitiveness to the actual values assigned to A and B was observed. As an example, plots representing the required effectiveness (such that wall temperatures do not exceed the specified maximum) for the dilution zone are shown in figures 6.2 – 6.5 inclusive. It can be seen from those figures that entrainment into the potential core region is extremely important.

It is obvious due to the demonstrated sensitivity, that the entrainment laws chosen for equation 6.10 must be closely related to the geometry of the actual cooling devices under consideration. Equation 6.11 cannot be used directly because of the uncertainty of designating appropriate values to $(\dot{m}''_e)_{x_p}$ and $(\dot{m}''_e)_{x_T}$ entrainment rates.

The entrainment of hot gases is represented by,

$$(\dot{m}'_c + \dot{m}'_e) = \dot{m}'_c + (\dot{m}'_e)_T + (\dot{m}'_e)_{x_p} \qquad 6.12$$

where,

$(\dot{m}'_e)_T$ = mass flow rate entrained in transition region up to elemental volume.

$(\dot{m}'_e)_{x_p}$ = mass flow rate entrained by film during potential core development.

From the turbulent boundary layer model used in Chapter 4, the total mass flow rate in the film may be expressed as,

$$\dot{m}_f = (\dot{m}'_c + \dot{m}'_e) = \frac{\dot{m}'_c}{\eta} \qquad 6.13$$

which is derived directly from equation 4.10. It was also shown that for the transition region, film effectiveness for practical slots may be predicted

from the equation,

$$\eta = A\left[1 - B S_{N_2}^{+0.65}\right] \qquad 6.14\ a)$$

where

$$S_{N_2} = \left[\frac{(x-x_p)}{MS}\cdot\left(Re_s\cdot\frac{\mu_c}{\mu_m}\right)^{-0.15}\cdot A_o'/A_E'\right] \qquad 6.14\ b)$$

Equation 6.14 may thus be used in equation 6.13 to provide an entrainment law for the transition region. Within the potential core, η is unity by definition and equation 6.13 yields zero entrainment and so the potential core must be dealt with differently. Thus,

$$(\dot{m}_c' + \dot{m}_e') = \frac{\dot{m}_c'}{\eta} + K_2\dot{m}_c' = \dot{m}_c'\left(\frac{1}{\eta} + K_2\right) \qquad 6.15$$

where K_2 is a 'constant' which may be expected from Cole's work (36), to be a function of velocity ratio, and, slot geometry, and which determines entrainment in the potential core region.

Returning therefore to the differential equation, with equation 6.15 to represent entrainment,

$$\ln.\eta = \frac{-h_E(1-K_1)}{\dot{m}_c'\bar{c}_p}\int_{x_p}^{x}\frac{\eta}{(1+\eta K_2)}\,dx \qquad 6.16$$

Letting,

$$C = B\left[\frac{1}{MS}\cdot\left(Re_s\cdot\frac{\mu_c}{\mu_m}\right)^{-0.15}\cdot A_o'/A_E'\right]^{+0.65} \qquad 6.17$$

and substituting into equation 6.16 for η from equation 6.14, yields,

$$\ln.\eta = \frac{-h_E(1-K_1)}{\dot{m}_c'\bar{c}_p}\int_{x_p}^{x}\left\{\frac{A - D(x-x_p)^{+0.65}}{E - K_2 D(x-x_p)^{+0.65}}\right\}dx \qquad 6.18$$

where,

$$D = AC\ , \qquad E = 1 + K_2 A \qquad 6.19$$

For evaluation of the above integral, let $(x-x_p)^{+0.65} = (x-a)^n$; let $(x-a) = t$ also. Thence, $dx = dt$ and the integral of equation 6.18 trans-

forms to,

$$\int \frac{A - Dt^n}{E - K_2 Dt^n} dt \text{ ; which may be put into partial fractions,}$$

$$\int \frac{A - Dt^n}{E - K_2 Dt^n} dt = \int \frac{A\,dt}{(E - K_2 Dt^n)} - \int \frac{Dt^n}{(E - K_2 Dt^n)} dt \qquad 6.20$$

Treating these integrals separately, the first term represents a standard form which has the general solution,

$$\int \frac{A dt}{(E - K_2 Dt^n)} = A\left[\frac{1}{E}\int dt + \frac{K_2 D}{E}\int \frac{t^n dt}{(E - K_2 Dt^n)}\right] \qquad 6.21$$

Substituting this back into the partial fraction expression, equation 6.20,

$$\int \frac{A - Dt^n}{E - K_2 Dt^n} \cdot dt = \frac{A}{E}\int dt + D\left[\frac{K_2 A}{E} - 1\right]\int \frac{t^n dt}{(E - K_2 Dt^n)} \qquad 6.22$$

Letting now $E/D = b$ and $-K_2 = a$,

$$\int \frac{Dt^n dt}{(E - K_2 Dt^n)} = \int t^n (at^n + b)^{-1} dt \qquad 6.23$$

which is an integral of the binomial differential type for which no stable reduction formulae exist.

Let $t^n = z$, $dt = \frac{dz}{nt^{n-1}}$; thus, transforming yet again,

$$\int t^n (at^n + b)^{-1} dt = \frac{1}{n}\int z^{\frac{1}{n}} (az + b)^{-1} dz = \frac{1}{n}\int z^{\frac{1}{n}} b^{-1}\left(\frac{az}{b} + 1\right)^{-1} dz \qquad 6.24$$

Expanding equation 6.2.4 by the binomial theorem,

$$\int t^n (at^n + b)^{-1} dt = \frac{1}{nb}\int z^{\frac{1}{n}}\left[1 - \frac{a}{b}z + \frac{2}{2!}\left(\frac{az}{b}\right)^2 - \frac{2.3}{3!}\left(\frac{az}{b}\right)^3 + \cdots\right] dz \qquad 6.25$$

which is convergent if $\left(\frac{az}{b}\right)^2 < 1$, i.e. if $\frac{a^2 t^{2n}}{b^2} < 1$, or, if

$$\frac{a}{b^2}(x - x_p) < 1$$

now, $a = -K_2$, which $\leqslant 1.0$ usually,

$b \simeq 1.0$

$(x - x_p)$ has dimensions of feet and is therefore < 1.0 for the present application.

Thus, $\frac{a^2}{b^2}(x - x_p)^{1.2} < 1$ and the series is convergent.

Therefore,

$$\int t^n (at^n + b)^{-1} \cdot dt = \frac{1}{nb}\int \left(z^{\frac{1}{n}} - \frac{a}{b} z^{\frac{n+1}{n}} + \frac{a^2}{b^2} z^{\frac{2n+1}{n}} - \frac{a^3}{b^3} z^{\frac{3n+1}{n}} + \dots\dots\right) dz$$

$$= \frac{1}{nb}\left[\frac{n}{n+1} z^{\frac{n+1}{n}} - \frac{a}{b}\cdot\frac{n}{(2n+1)} z^{\frac{2n+1}{n}} + \frac{a^2}{b^2}\cdot\frac{n}{(3n+1)} z^{\frac{3n+1}{n}} - \frac{a^3}{b^3}\frac{n}{(4n+1)} z^{\frac{4n+1}{n}} + \dots\right.$$

i.e.

$$\int t^n (at^n + b)^{-1} dt = \frac{1}{nb}\left[\frac{n}{(n+1)} t^{n+1} - \frac{a}{b}\cdot\frac{n}{(2n+1)} t^{2n+1} + \frac{a^2}{b^2}\frac{n}{(3n+1)} t^{3n+1} - \frac{a^3}{b^3}\cdot\frac{n}{(4n+1)} t^{4n+1} + \dots\dots\right]$$

or,

$$\int \frac{Dt^n dt}{(E - K_2 Dt^n)} = \frac{D}{nE}\left[\frac{n}{(n+1)} t^{n+1} + \frac{K_2 D}{E}\cdot\frac{n}{(2n+1)} t^{2n+1} + \frac{K_2^2 D^2}{E^2}\cdot\frac{n}{(3n+1)} t^{3n+1} + \frac{K_2^3 D^3}{E^3}\cdot\frac{n}{(4n+1)} t^{4n+1} + \dots\right]$$

Therefore,

$$\int \frac{(A - Dt^n) dt}{(E - K_2 Dt^n)} =$$

$$\left\{\frac{At}{E} + \frac{D}{nE}\left[\frac{K_2 A}{E} - 1\right]\left[\frac{n}{(n+1)} t^{n+1} + \frac{K_2 D}{E}\cdot\frac{n}{(2n+1)} t^{2n+1} + \frac{K_2^2 D^2}{E^2}\cdot\frac{n}{(3n+1)} t^{3n+1} + \frac{K_2^3 D^3}{E^3}\cdot\frac{n}{(4n+1)} t^{4n+1} + \dots\right]\right.$$

Hence,

$$\int \left\{\frac{A - D(x - x_p)^{+0.65}}{E - K_2 D(x - x_p)^{+0.65}}\right\} dx =$$

$$\left\{\frac{A}{E}(x - x_p) + \frac{D}{.65E}\left[\frac{K_2 A}{E} - 1\right]\left[.39394(x - x_p)^{1.65} + .28261\frac{K_2 D}{E}(x - x_p)^{2.3} + .22034\frac{K_2^2 D^2}{E^2}(x - x_p)^{2.95} + \right.\right.$$

$$\left.\left. \dots\dots + .18056\frac{K_2^3 D^3}{E}(x - x_p)^{3.6} + \dots\right]\right\} \qquad 6.25$$

Substituting now into equation 6.18,

$$\ln.\eta = \frac{-h_E(1-K_1)}{\dot{m}'_c\,\bar{c}_p}\left\{\frac{A}{E}(x-x_p)+\frac{D}{.65E}\left[\frac{K_2A}{E}-1\right]\left[f_1(x-x_p)\right]\right\}_{x_p}^{x} \qquad 6.27a)$$

where,

$$f_1(x-x_p)=\left[.39394(x-x_p)^{.65}+.28261F_1(x-x_p)^{2.3}+.22034F_1^2(x-x_p)^{2.95}+.18056F_1^3(x-x_p)^{3.6}+\cdots\right] \qquad 6.27b)$$

and,

$$F_1 = \frac{K_2 D}{E} \qquad 6.27c)$$

Hence,

$$\ln.\eta = \frac{-h_E(1-K_1)}{\dot{m}'_c\,\bar{c}_p}\left\{\frac{A}{E}(x-x_p)+\frac{D}{.65E}\left[\frac{K_2A}{E}-1\right]\left[f_1(x-x_p)\right]\right\}$$

$$= \frac{-h_E(1-K_1)}{\dot{m}'_c\,\bar{c}_p}\left\{\frac{A(x-x_p)}{(1+K_2A)}+\frac{AC}{.65(1+K_2A)}\left[\frac{K_2A}{(1+K_2A)}-1\right]\left[f_1(x-x_p)\right]\right\}$$

$$= \frac{-h_E(1-K_1)A}{\dot{m}'_c(1+K_2A)\bar{c}_p}\left\{(x-x_p)-\frac{C}{.65(1+K_2A)}\left[f_1(x-x_p)\right]\right\}$$

$$= \frac{-h_E(1+K_1)A(x-x_p)}{\dot{m}'_c\,(1+K_2A)\,\bar{c}_p}\left\{1-\frac{C}{.65(1+K_2A)}\left[f_1(x-x_p)\right]\right\}$$

i.e.

$$\ln.\eta = \frac{-h_E(1-K_1)A(x-x_p)}{\dot{m}'_c\,(1+K_2A)\,\bar{c}_p}\left\{1.0-\frac{B}{.65(1+K_2A)}\left[\frac{(x-x_p)}{Ms}\cdot(Re_s\cdot\mu_c/\mu_m)^{-0.15}\cdot\frac{A'_o}{A'_E}\right]\left[f_2(x-x_p)\right]\right\} \qquad 6.28a)$$

where,

$$f_2(x-x_p)=\left[.39394+.28261F_2(x-x_p)^{-.65}+.22034F_2^2(x-x_p)^{1.3}+.18056F_2^3(x-x_p)^{1.95}+\cdots\right] \qquad 6.28b)$$

and,

$$F_2 = \frac{K_2AC}{(1+K_2A)} \qquad 6.28c)$$

Finally,

$$\ln.\eta = \frac{-h_E(1-K_1)A(x-x_p)}{\dot{m}'_c\,(1+K_2A)\,\bar{c}_p}\left\{1.0-\frac{B}{.65(1+K_2A)}S_{N_2}^{+0.65}\left[f_3(x-x_p)\right]\right\} \qquad 6.29a)$$

where,

$$f_3(x-x_p)=\left[.39394+.28261F_3 S_{N_2}^{+0.65}+.22034F_3^2\left(S_{N_2}^{+0.65}\right)^2+.18056F_3^3\left(S_{N_2}^{+0.65}\right)^3+\ldots\right] \qquad 6.29b)$$

and,

$$F_3 = \frac{K_2 A B}{(1+K_2 A)} \qquad 6.29c)$$

Rearranging equation 6.29, the heat transfer coefficient is given by,

$$h_E = -\frac{\dot{m}_e' \bar{c}_p (1+K_2 A) \ln \eta}{(1-K_1) A (x-x_p)} \left\{1.0 - \frac{B}{.65(1+K_2 A)} S_{N_2}^{+0.65} \left[f_3(x-x_p)\right]\right\}^{-1} \qquad 6.30$$

Unknown in this equation are the quasi-constants K_1 and K_2. K_1 does not need to be found directly since it may be accomodated by an iterative loop inside the computer program used to solve the difference equation for wall temperature, with the assumption of an adiabatic rear-faced wall on the first pass. The entrainment constant K_2 however, must be described before solution can be made.

In the absence of any suitable additional information, the approach of Cole (36) must be used. K_2 may be related to Spalding's dimensionless entrainment constant (35) as applied by Cole to the potential core. This is defined as,

$$-\bar{m}_q = \frac{(\dot{m}_e'')_{x_p}}{C_m u_m} \qquad 6.31$$

Now,
$$K_2 = (\dot{m}_e'')_{x_p} \cdot x_p / \dot{m}_c' \qquad 6.32$$

Thus,
$$K_2 = \frac{x_p}{M s} (-\bar{m}_q) \qquad 6.33$$

where M is the mass velocity ratio at injection, and $-\bar{m}_q$ here is considered as a function of velocity ratio only.

This approach still suffers from a serious drawback. Cole showed

the shape of the velocity profiles is important also in determining entrainment. The entrainment laws used in the present analysis, equation 6.33 and 6.15, do not account for this. Equation 6.15 contains equation 6.13 which was derived in Chapter 4 as equation 4.10. This latter equation was derived from an enthalpy balance which assumed the entrained and injected masses were fully mixed at every station and therefore, a uniform film profile. This however, is considerably removed from reality. Any practical slot will have a sharply peaked velocity profile in its exit plane, and, the mainstream will have either a boundary layer or a residual film from a preceeding slot. In addition, the injected and mainstream flows will be separated initially by a partition of substantial thickness, (the slot lip), which produces a marked velocity defect in the initial regions of the film. Temperature gradients in the film also will not be inconsiderable. Uniform profiles are not then, a feature of the real film.

Such effects as described are difficult to account for in a manner other than empirically. Accordingly, if all injection parameters in equation 6.30 are based on nominal values, the slot flow may be defined as

$$\dot{m}_c' = K_3 \rho_c u_c s \qquad 6.34$$

where K_3 is an empirical dimensionless distortion index through which film profile shape is simply and conveniently accommodated. This index may be expected to be at least a function of velocity ratio and, slot lip thickness.

From a subsequent study of the cooling of the combustor described in Appendix I, it was found that the amount of coolant required for a given

surface temperature not to be exceeded was a direct function of slot geometry through the group $(\frac{\delta_w}{s} \cdot \frac{A_o'}{A_\epsilon'})$, as illustrated in figure 6.6. Thus, the distortion index K_3 might be expected to be described by,

$$K_3 = K_3\left[\left(\frac{\delta_w}{s} \cdot \frac{A_o'}{A_\epsilon'}\right), \frac{u_m}{u_c}\right] . \qquad 6.35$$

Unfortunately, suitable experimental data for investigation of equation 6.30 is extremely scarce and almost nothing for practical slot geometries is available in the open literature : Limited data for devices G1 - G3 described in Chapter 4 of this thesis, are used to test equation 6.35. The ranges of variables for the heat transfer tests were within those given for the effectiveness tests in Table 4.1; the geometric variables are described in Table 4.2. Tests were run with an adiabatic wall with heat generation through surface copper strips whichware electrically heated to a constant 200^0F; thus in equation 6.30, $K_1 = 0$.

The entrainment constant K_2 was found for each test run from equation 6.33 in which, $-\bar{m}_{e_1}$ was taken from Cole's curves in reference (36), and, x_p from measured values in figure 4.5, at the appropriate velocity ratios. For a given test run, local K_3 values at regular intervals of x/s were found by matching predicted heat transfer coefficients from equation 6.30 with measured values at a particular x/s : Typical plots for three of the geometries are shown in figure 6.7 where it can be seen that within the transition region and making due allowance for test-scatter, K_3 may be considered constant. The constant value for each K_3 is taken as a straight arithmetic mean of the

local values of the test-run. The mean values of the distortion index K_3, are correlated as a function of the entrainment group,

$$\bar{K}_3 = \bar{K}_3 \left[\frac{u_m}{u_c} \cdot \left(\frac{\delta_w}{s} \cdot A_o'/A_E' \right) \right] \qquad 6.36$$

which was derived on the basis of the arguments given above. The results are shown in figure 6.8 and for the limited amount of data available, the correlation is good.

In figures 6.9 to 6.14 inclusive, are shown comparisons of film heat transfer coefficient between experimental data and predictions made using equation 6.30. For these predictions, K_1 was taken as zero, K_2 was calculated from equation 6.33 using Cole's charts for $-\bar{m}_6$ together with measured α_p's, and, K_3 was found for the particular geometry and injection conditions from figure 6.8; potential core lengths and effective areas were taken from Chapter 4.

Also shown on these figures are predictions made using the Colburn formulation, equation 6.1 and, the recommended Seban and Back relationship, equation 2.8 of Chapter 2. In each case Stanton numbers were based on slot conditions. The experimental tests were run in such a manner that the temperature difference between the heated wall temperature and the equivalent adiabatic wall temperature for similar injection conditions, was approximately equal to the differences between heated wall and injected coolant temperature, and, the difference between heated wall and mainstream, temperatures,

$$\text{i.e. } (T_{s_{heated}} - T_{s_{ad}}) \simeq (T_{s_{heated}} - T_c) \approx (T_{s_{heated}} - T_m) \qquad 6.37$$

Common comparisons are then valid.

Immediately noticeable in all the plots is the large amount of scatter in the test-data. Evident also in the data of each figure to a greater or lesser degree depending on the injection conditions and slot geometry, is a pause in the decrease of film heat transfer coefficient with increasing non-dimensional distance from injection, followed by a step-change to a lower but again almost constant, level. The step-change occurs within the distance range 35-45 slot heights from injection for the six tests examined. The onset of the pause is less clearly defined due to the test-scatter, but appears to be established by 20 slot heights from the injection plane.

According to the recommendations of Chapter 2, the Colburn equation is valid for injection mass velocity ratios of equal to or less than, unity and, x/s greater than 70. It would therefore, not be expected to give good predictions for all of the present test-points. Without exception, it underestimated heat transfer coefficient for x/s less than about 15, and, overestimates it for x/s greater than 40. It best represents the data when M is close to unity, as may be seen from figures 6.11 and 6.12.

For M greater than unity, it was recommended in Chapter 2 that the semi-empirical relationship of Seban and Back might be used. Since the empirical part of this relationship was derived from test-data originating in clean-slot geometries, it might be expected that agreement with the present dirty-slot data would not be good. Agreement however, is very good for all the test-points: The data are invariably underestimated for small x/s , but well estimated for x/s greater than about 25.

Predictions based on equation 6.30 agree admirably with the data for all x/s up to 35 - 40, which region corresponds to the transition region in the mathmatical modelling of the film and for which the equation is valid, for slot geometry G1. Agreement is good up to an x/s of 30 for geometry G2

and to x/s of 25 for geometry 63. These distances cover the range likely to be encountered in any practical case of combustor cooling. The assumption of constant entrainment rate for the potential core seems to be valid and is accounted for by injection velocity ratio and profile distortion index. These limited data do not represent a very stringent test of equation 6.30 and the associated entrainment assumption, and this should be borne in mind. However, the present purpose is only to illustrate the importance of potential core length and the significance, and use to which it can be put. In this endeavour at least, success is achieved.

.....

CHAPTER 7

PREDICTION OF POTENTIAL CORE LENGTH.

7.1. Introduction.

7.1.1. In the preceeding chapters of this thesis, for the film cooling of a high performance gas-turbine combustion chamber by discrete, tangential injection of coolant, it has been demonstrated that only the initial regions of the developing film from an individual slot are relevant. These initial regions have been modelled by a conditional potential core, followed by a so-called 'transition' region. The hypothesis has been advanced that the practical cooling system can be adequately if not completely, described in terms of this potential core. The effects of mainstream turbulence on effectiveness have been described through the potential core length. It has been shown also that the effects of multiple-slot cooling can be accounted for through potential core length. On the basis of the model, both film effectiveness and heat transfer coefficient have been described for the transition region, in terms of the potential core length. These theories have been so developed and tested that, if reliable predictions for potential core can be made, the performance of the practical cooling system can indeed be completely described.

7.1.2. A diagrammatic representation of the film hydrodynamic development is shown in figure 3.8. The region of interest is the potential core length x_p, the extent of which must be predicted for use in equations 4.30 or 4.31, and, 6.30. The formation of the potential core is described in Chapter 3, under Section 3.4.

Re-consideration of figure 3.8 reveals that prediction of x_p involves definition of a wall layer growing along the cooled wall and, a turbulent free mixing layer originating from the slot outer lip. Section

2.4.11 of Chapter 2 indicates that an overall two-dimensional analysis of the flow field is justified for all but the smallest of combustion chambers. Practical considerations of reducing to a minimum initial hot-gas entrainment by the film to avoid streaky-cooling with resulting thermal stress and fatigue problems, cause the designer to seek practical slot geometries which inject the coolant as uniformly as possible. Initial, local three-dimensionalities in the film ideally will be small and can therefore, be neglected for simplicity. Because of the nature of the application under consideration, flows can be considered turbulent.

The wall layer may conveniently be regarded as a normal boundary layer at this point and relegated to the background for the time-being. Additional comment will be made where appropriate, later in the analysis.

7.1.3. Holland (87) and, Whittacker (88) have demonstrated that incomplete knowledge of the mainstream conditions causes the greatest error in calculated wall temperatures. In the combustion chamber, available descriptions of the mainstream conditions are at their best, naïve. These uncertainties associated with the practical application decided the nature of the approach to the problem. Further, 'exact' answers in the potential core region require solution of the hyperbolic formulation of the Navier-Stokes equations. Such a solution technique was not available when the present exercise was made, although considerable progress in this direction is currently being made, (89).

An 'engineering approach' was therefore decided upon: The aim was to provide adequate prediction for given nominal conditions, without necessarily describing or contributing to the understanding of, the actual physical processes involved. In keeping with the aims stated under Section 1.4, the prediction technique should be capable of simple and rapid manipulation to render it germane to the manner in which the industry conducts its business.

7.2. Basic Equations (applied to the Mixing Layer)

7.2.1. The Equations.

In fluid dynamics it is accepted that the entire behaviour of the flow in all regions is implied in the Navier-Stokes equations, together with the equation of continuity. Once turbulence is established in a flow, the flow is inherently non-steady, and the local parameters fluctuate about their mean values. Therefore, even in the case of a flow in which the mean values are constant, the time-derivative must be retained in the fundamental equations.

The conservation of momentum is written, (90),

$$\rho \frac{Du}{Dt} = -\frac{\partial p}{\partial x} + \frac{\partial}{\partial x}\left(\mu \frac{\partial u}{\partial x}\right) + \frac{\partial}{\partial y}\left(\mu \frac{\partial u}{\partial y}\right) + \frac{\partial}{\partial z}\left(\mu \frac{\partial u}{\partial z}\right) + \left(\frac{\partial \mu}{\partial x} \cdot \frac{\partial u}{\partial x}\right) + \left(\frac{\partial \mu}{\partial y} \cdot \frac{\partial u}{\partial y}\right) + \left(\frac{\partial \mu}{\partial z} \cdot \frac{\partial u}{\partial z}\right) \qquad 7.1$$

where the operator,

$$\frac{D}{Dt} \equiv \frac{\partial}{\partial t} + u\frac{\partial}{\partial x} + v\frac{\partial}{\partial y} + w\frac{\partial}{\partial z}$$

there being two similar equations by cyclic interchange for velocity components v and w along the y and z axes respectively. Note that viscosity

μ is dependent on the space co-ordinates since it varies considerably with temperature.

The conservation of mass is,

$$\frac{\partial u}{\partial x} + \frac{\partial v}{\partial y} + \frac{\partial w}{\partial z} = 0 \qquad 7.2$$

Equations 7.1 and 7.2 are for the imposed restriction of constant density.

These general equations cannot be considered further owing to their complexity and our inability to postulate in them realistic, time-dependent boundary and initial conditions.

If the additional assumption of constant fluid properties is made, the momentum equation becomes,

$$\frac{Dc}{Dt} = -\frac{1}{\rho} \text{ grad } p + \nu \nabla^2 c \qquad 7.3$$

where C is a velocity vector.

Assume further that the independent variables in the equations can be represented for a quasi-steady stream as an average value and a fluctuating component, the time average of every fluctuating component converging to zero for large time intervals,

$$\text{i.e.} \quad u = \bar{u} + u' \; ; \quad \overline{u'} = 0$$
$$p = \bar{p} + p' \; ; \quad \overline{p'} = 0 \quad \text{etc.} \qquad 7.4$$

This assumption gives rise to additional "apparent" components, i.e. the equation for the x - component mean velocity in quasi-steady turbulent flow becomes,

$$\bar{u}\frac{\partial \bar{u}}{\partial x} + \bar{v}\frac{\partial \bar{u}}{\partial y} + \bar{w}\frac{\partial \bar{u}}{\partial z} = -\frac{\partial}{\partial x}\left(\overline{u'^2}\right) - \frac{\partial}{\partial y}\left(\overline{u'v'}\right) - \frac{\partial}{\partial z}\left(\overline{u'w'}\right) - \frac{1}{\rho}\frac{\partial \bar{p}}{\partial x}$$
$$+ \nu\left(\frac{\partial^2 \bar{u}}{\partial x^2} + \frac{\partial^2 \bar{u}}{\partial y^2} + \frac{\partial^2 \bar{u}}{\partial z^2}\right) \qquad 7.5$$

Consider now a two-dimensional flow of the mixing layer in the general

direction x. Assume that the mixing layer, of thickness b, is 'thin'. If the thickness is b at a station , y is of order b, $y = O(b)$. Now if x, u, p etc., are of normal order of size, i.e. $x = O(1)$, some approximations can be introduced by estimating terms and deleting those of small order.

By this procedure, it is seen that the rate of change of fluid momentum along the y - axis is of order O (b) compared with O (1) in the x-direction, and so is the force producing this rate of change. This force is the sum of normal and shear forces in direction y. As their sum is neglected, each can be neglected independently. Thus, the static pressure gradient is negligible in the y - direction, (Note: b and x can become of the same order of size at large x in separated flows, so this analysis only applies to the early regions of the mixing layer. As will be shown later, a similar problem can arise at the start of the layer for real slot geometries.), $\frac{1}{\rho}\cdot\frac{\partial p}{\partial x} = O(1)$, but $\nu = O(b^2)$ and O (1) can be neglected when compared with $O(1/b^2)$.

With these assumptions, the conservation of momentum becomes,

$$\rho \bar{u} \frac{\partial \bar{u}}{\partial x} + \rho \bar{v} \frac{\partial \bar{u}}{\partial y} = -\frac{dp}{dx} + \frac{\partial \tau}{\partial y} \qquad 7.6a)$$

Note that equation 7.6 for the incompressible free mixing layer has the same form as that obtained for the attached boundary layer.

The sheer stress may be expressed,

$$\tau = \tau_L + \tau_T \qquad 7.6b)$$

where,

$$\tau_L = \mu \frac{\partial \bar{u}}{\partial y} \qquad 7.6c)$$

and,

$$\tau_T = -\rho(\overline{u'v'}) \qquad 7.6d)$$

The conservation of mass becomes,

$$\frac{\partial \bar{u}}{\partial x} + \frac{\partial \bar{v}}{\partial y} = 0 \qquad 7.7$$

It is not usual to retain the Reynolds stresses as fluctuating terms explicitly in the equation, but to take the Boussinesq analogy (91.), with the coefficient of viscosity in Stoke's law for laminar flow, and introduce,

$$\tau_T = A_\tau \frac{\partial \bar{u}}{\partial y} \qquad 7.8$$

where A_τ is a turbulent mixing coefficient called the eddy viscosity. Use is often made of the eddy kinematic viscosity, $\epsilon = A_\tau / \rho$,

$$\text{i.e. } \tau_T = \rho \epsilon \frac{\partial \bar{u}}{\partial y} \qquad 7.9$$

whence it is seen that,

$$\epsilon = \left(\overline{u'v'} \right) \qquad 7.10.$$

ϵ is not a property of the fluid, but depends on the mean velocity, and, $\epsilon = \epsilon(x)$ only. The assumption that $\epsilon \neq \epsilon$ (y) is known to lead to satisfactory phenomenological descriptions of the flow field.

For constant pressure, it has been shown (92) that equation 7.6a) may be reduced without serious loss of accuracy to the form:

$$\rho u_{ref} \frac{\partial \bar{u}}{\partial x} = \frac{\partial \tau}{\partial y} \qquad 7.11$$

In the mixing layer, $\tau_L \leq \tau_T$, so equation 7.11 can be written,

$$u_{ref} \frac{\partial \bar{u}}{\partial x} = \epsilon \frac{\partial^2 u}{\partial y^2} \qquad 7.12$$

Following Nash (93) the following transformation can be used:

let,

$$\xi = \int_0^x \frac{\epsilon}{u_{ref}} \cdot dx \qquad 7.13$$

Substituting equation 7.13 into 7.12, gives an equation which is the classical non-dimensional diffusion equation, (linear heat conduction equation with unity diffusivity), for which standard solutions are available, (93),

i.e. $$\frac{\partial \bar{u}}{\partial \xi} = \frac{\partial^2 \bar{u}}{\partial y^2} \qquad 7.14$$

The problem thus resolves itself into two parts:-

(i) simultaneous solution of equation 7.14 with appropriate boundary conditions, with the growth of the cooled wall layer,

(ii) interpretation of the ϵ function to derive some plausible relation between ξ and x.

7.2.2. Solution of the Problem Equations.

The partial differential equation of 7.14 is parabolic and may be solved by one of two approaches:

(i) direct solution of a finite - difference version by one of the newer field methods (94),

or,

(ii) an integral method through specification of velocity profiles.

The former method was remote at the time of conception for this prediction so consideration was given to the latter: The velocity field throughout the free mixing layer will be defined once the velocity profile in similar form at the separation point $\xi = 0$, is specified. To do this, it is necessary to consider development of the layer in some detail.

If it is assumed for the purpose of analysis, the pressure is everywhere constant and if there are no solid boundaries downstream of the origin of mixing along which external forces could be allowed to act, (true for within the potential core), the total momentum of the flow is conserved for an ideal mixing layer. Within the conservation of total momentum however, there is a continuous exchange of momentum due to the mixing processes

between the layers of fluid moving at different velocities. Air initially at rest or at low velocity outside the mixing layer is entrained and gathers momentum at the expense of the retardation of air originating in the high-speed side of the layer. As the flow proceeds downstream more and more fluid comes under the influence of the mixing phenomenon and the width of the layer increases steadily; but the width remains small compared with the distance from the origin, making the shear layer a boundary layer type of problem (as was shown in the specification of the Navier-Stokes equations) with large transverse gradients.

Mixing is initiated when the streams separate from a solid partition and boundary layers will have developed inevitably upstream of the separation point. Thus at its' origin, the layer has a non-zero thickness, and the velocity profiles of these initial boundary layers together with their distribution of turbulent shear stress, even when the dividing partition is infinitely thin. These conditions represent important boundary conditions placed on the subsequent development of the layer. The flow in the early part of the mixing layer is dominated by the transition from velocity profiles of a boundary layer type to those corresponding to fully-developed mixing further downstream, (dependent on the extent of the potential core), and in this region, thickness of the initial boundary layers presents a reference dimension which determines the scale of succeeding velocity profiles.

At $\xi = 0$, the velocity profile is discontinuous, for,

$0 < y < +\infty \quad , \quad \bar{u} = u_o(y)$

$0 < y < -\infty \quad , \quad \bar{u} = u_o(-y)$

With these boundary conditions the integration is difficult to evaluate in closed form. Korst and Chow (95) have solved the equation with uniform initial streams (plug-flow), and, an error function velocity profile in the shear layer. Nash(96) has solved the problem for one initial stream only, but was forced to take a boundary layer profile for this stream simplified to a linear form, in order to evaluate the integral.

If the problem is completely generalised, the dividing partition will have finite thickness δ_w, and the boundary conditions become:

For,

$$0 \leq y < +\infty \quad , \quad \bar{u} = u_o(y)$$
$$0 \leq y \leq -\delta_w \quad , \quad \bar{u} = 0$$
$$-\delta_w \leq y < -\infty \quad , \quad \bar{u} = u_o(-y)$$

Korst and Chow (95) attack the idea of an essentially stagnant wake, i.e. $0 \leq y \leq -\delta_w$, $\bar{u} = 0$, and state that finite wake velocities must be used to account for the convective heat transfer known to take place between wake flow and the bounding wall to the separated flow region. However, disregarding this additional complication, the equation cannot be evaluated with the last set of boundary conditions.

These mathmatical difficulties aside, the whole structure of the equation for which solution is sought is invalidated by the realistic boundary conditions. The breakdown arises in two areas:

a) there will be a momentum loss associated with the separated flow region arising from the finite value of δ_w,

b) the initial thickness is no longer small and, because of the values of slot height and lip-thickness in practical use, free mixing layer thickness is <u>nowhere</u> small in comparison with x.

Equation 7.14 is not therefore, directly applicable to the problem.

The core of the second problem, which is concerned with the interpretation of the eddy viscosity function, is that when time averages of the equations of motion are taken to make them more tractable, the Reynolds stresses are left as unknowns, for which hypothetical equations must be derived.

The reference dimension which determines the scale of the velocity profiles and referred to above, is, in general,

$$L = \left[(\delta)_1 + \delta_w + (\delta)_2 \right] \qquad 7.15$$

where, δ_w = lip thickness

δ = boundary layer thickness

subscripts 1,2 refer to the streams on either side of the lip, prior to separation.

The generalised co-ordinate used by Nash (96) becomes,

$$\eta_0 = f\left[(\delta)_1 + \delta_w + (\delta)_2 \right] \qquad 7.16a)$$

where,

$$\eta/\eta_0 = y/L \qquad 7.16b)$$

To determine the relation between η_0 and x, it is necessary to specify the variation of eddy viscosity with downstream distance.

Korst (95) chose,

$$\epsilon = \epsilon_\infty f(\psi)$$

where, $\psi = x/L$ and, $\epsilon_\infty = \frac{1}{46^2} \cdot x \ (\bar{u}_1 + \bar{u}_2)$,

6 being an empirical similarity parameter, collectively termed, 7.17

Nash (96) used Prandtl's mixing length hypothesis of turbulence for the expression,

$$\epsilon = l^2 \left| \frac{\partial \bar{u}}{\partial y} \right| \qquad 7.18$$

where ℓ is the mixing length. For free turbulent flows, Prandtl suggested that the size of the fluid elements which are caused to move in a lateral direction by the turbulent mixing process is of a comparable order to the width b of the mixing layer, and further, that the fluid elements experience an overall velocity gradient which is proportional to the maximum velocity difference across the layer divided by b. From these suggestions, Nash took the modified form of the above statement,

$$\epsilon = K b (u_1 - u_2) \qquad 7.19$$

where K is an unknown constant, and b is here a measure of both mixing length and velocity gradient. The basis for this equation is Prandtl's new mixing length hypothesis, (97).

7.2.3. First Conclusions.

Two important conclusions can be drawn immediately from the foregoing passages:

1. Even gross simplifications made to the Navier-Stokes equations do not lead to forms which are easily solvable.
2. Any suitable theory is likely to depend heavily at the present time on certain empirical incorporations to account for the Reynolds stresses.

7.3 Outline of Solution Method.

7.3.1. Philosophy.

From the fundamental starting point of the Navier-Stokes equations consideration has been given to 'exact' solutions to the problem. Gross simplifications were made to these equations but forms for convenient and easy solution were not obtained. These much simplified but hard or impossible

to solve, parabolic forms were shown not to represent the problem under study: The present problem really requires solution of the hyperbolic forms of the Navier-Stokes equations. Solution of the hyperbolic equations in finite-difference form by a field method was a task beyond the scope of the present thesis. Even these hyperbolic equations would have to accommodate the Reynolds stresses in an empirical manner. Therefore, in line with the general philosophy presented in Sections 1.4 and, 7.1.3, together with the adjunct that to be useful, any solution must be timely, an integral method with empirical incorporations was decided upon.

7.3.2. Solution Technique

The differences between the idealised, asymptotic shear layer for which the parabolic equations are applicable, and the real mixing layer requiring solution of the hyperbolic equations of motion, are itemised in Table 7.1.a), which indicates the mode of attack to be used.

Referring back to the earlier mentioned characteristic dimension which determines the scale of succeeding velocity profiles, as the flow proceeds downstream the influence of this initial disturbance in the shear layer decays and at very large distances from separation the characteristic dimension loses its significance with the velocity profiles approaching similarity. The existance of this asymptotic form has led to the formulation of the usual simplified flow model in which the thickness of the layer is zero at its' origin and similarity of the velocity profiles is assumed throughout, the conditions for which to occur are given above. This model and its' adoption, implies a higher order singularity at the separation plane insofar as there must be a discontinuity in velocity as distinct from one in velocity gradient. However, any difficulties in the solution are purely local, as in the case of

the flow in the boundary layer near the leading edge of a plate.

A simple method of predicting the characteristics of the pre-asymptotic shear layer was proposed by Kirk (98). It was suggested by Kirk that the real mixing layer could be replaced by an equivalent ideal layer growing over a greater distance from zero thickness. In this way, reference could be made to all the results for the asymptotic shear layer and the effects of the finite initial thickness translated into nothing more than a linear shift of the origin.

This suggestion of Kirk's provides the basis for the present method of predicting potential core length. Development of the shear layer produced by the mixing of two uniform but differing velocity streams is calculated and the effects of momentum loss associated with the separated flow wake formed behind the partition lip, and stream velocity profiles, accounted for by a process resulting in a simple, linear shift of the origin. It is assumed that similar profiles are established very soon from the starting point and that error introduced by applying these asymptotic forms over the whole region are negligible.

7.3.3. Starting Point.

A theory for the potential core length of a semi-contained, two dimensional turbulent jet has been developed by Abramovich,, (99). This theory is for incompressible, isothermal flow, uniform streams and a turbulent wall boundary layer growing from the plane of the mixing layer origin. It gives good agreement with experiment over the ranges it would be expected to be valid and forms an excellent starting point for the present theory. The

result can be expressed as:

$$\frac{x_p}{s} = \left[\frac{0.37}{(Re_{x_p})^{0.2}} \pm 0.27(0.416 + 0.134m)\left(\frac{1-m}{1+m}\right) \right]^{-1} \qquad 7.20a)$$

where, $$Re_{x_p} = \frac{\rho_c u_c x_p}{\mu_c} \qquad 7.20b)$$

and, $$m = u_m/u_c \qquad 7.20c)$$

[Nota Bena:

Bars over symbols to denote a time average will be generally dropped henceforth for convenience.]

The theory represented by equations 7.20 is deficient for the present application on a number of counts: It must be made to apply for non-isothermal flows, the origin of the wall boundary layer must be shifted to inside the slot, and, the momentum-loss correction of Kirk must be applied. A further deficiency is that for unity velocity ratio, an infinite potential core is predicted. This does not occur in practice and must be remedied. Some way of accounting for high mainstream turbulences must be found.

7.4. A Semi-Empirical Theory for the Prediction of Potnetial Core Length.

7.4.1. Mixing Expression.

It is necessary initially to obtain a suitable expression to describe the growth of mixing layer width with distance from separation, i.e. $\frac{db}{dx}$.

Abramovich (99) based his expression on Prandtl's mixing length hypothesis (91). This leads to,

$$\frac{db}{dx} \propto \frac{|u_1 - u_2|}{|u|} \qquad 7.21.$$

By defining the characteristic velocity u, as,

$$u = \frac{\int_0^b \rho u \, dy}{\int_0^b \rho \, dy} \qquad 7.22.$$

and as a first approximation redefining this as,

$$u = \frac{\rho_1 u_1 + \rho_2 u_2}{2(\rho_1 + \rho_2)} \qquad 7.23$$

the mixing expression can be extended for non-isothermal flows as,

$$\frac{db}{dx} = 0.27 \cdot \frac{(1+\theta)}{2} \cdot \frac{(1-m)}{(1+\theta m)} \qquad 7.24a)$$

where,

$$\theta = T_1/T_2 \qquad 7.24b)$$

This expression involves the assumption that mixing of the two streams takes place at constant pressure and, that the ratio of molecular weights can be taken as unity without serious error. (This is a reasonable assumption for the combustion chamber when primary and dilution zone overall fuel/air ratios are considered.) The constant of proportionality has been taken as the value used by Abramovich for isothermal mixing, which was evaluated from the experimental results of Zhestkov et al, and also of Albertson et al.

Equation 7.24 represents the simplest manner in which mixing in non-isothermal flows can be accounted for. However, it is unsatisfactory in that it predicts zero mixing for unity velocity ratio, admitting through its' form, no thermal diffusion.

Various suggestions have been offered as to suitable ways to account for the density field: On suggestion (100) is to replace the velocity difference in equation 7.21 with a mass flux difference, and such a formulation has shown agreement with certain experimental data. However, when the mass fluxes of the two streams are equal, no mixing is again predicted and it has been demonstrated that such is not the case, (101). Alpinieri (101), suggests the use of the sum of mass and momentum fluxes, and this is also shown to be in agreement with some experimental data. Abramovich, (102) in a later and undeveloped suggestion, proposed a formulation based on momentum fluxes alone. A comparison has been made of the various suggested

modifications to the basic mixing length approach, by Ragsdale and Edwards (105) which showed when comparisons are made on a consistent basis, the expressions have differences that are more apparent than real. Accordingly, Abramovich's (102) suggestion is selected for development on the grounds of continuity only.

The simplest momentum transfer theory is that due to Prandtl: Prandtl's mixing length hypothesis which arises from the analogy drawn between the behaviour of turbulent fluid flow and the behaviour of the molecules of a gas according to kinetic theory, relates the turbulent shear stress to the mean velocity profile existing at that same point,

$$\text{i.e. } \frac{\tau}{\rho} = l^2 \left|\frac{\partial u}{\partial y}\right| \frac{\partial u}{\partial y} \qquad 7.25$$

where l is the mixing length.

Thus, where the derivative $\frac{\partial u}{\partial y}$ vanishes, the hypothesis predicts zero shear stress. This condition arises for example, at the edge of a turbulent boundary layer where the physical explanation is that beyond the edge the flow is inviscid and no shearing stress can exist. (The significance of this to the potential core problem is that the inner and outer layers of the flow field can be considered independently since there would be no stress interactions at their respective extremities right from the injection plane to intersection at x_p.) At a velocity maximum, it would also be expected that shear stress is zero if the mixing hypothesis is valid. It has been shown (80) however, that the shear stress at the velocity peak in the wall-jet is not zero and in general is not small, being for the pure wall-jet ($u_m = 0$), approximately equal and opposite to the value at the wall.

The concept that the distribution of shear stress through a turbulent

shear layer is determined uniquely by the local velocity profile has been the subject of controversy in recent years. It implies the existance of local equilibrium between the dissipation and production of turbulent kinetic energy. If however, this is so, advection and diffusion of turbulent energy is negligible and Bradshaw and Gee's (80) explanation of the existance of finite shear stress at a velocity maximum is not admissible. As Bradshaw has pointed out (104), the analogy upon which the hypothesis is founded can only be valid if the "mean free path" of turbulent eddies is small compared with the distance over which the mean flow velocity changes appreciably; this is not always so. Bradshaw and Ferris (105), Felsch (106) and Goldberg (107) all conclude that the shear stress in fact must depend not only upon the local velocity profile, but also upon the influencesof the upstream history of the flow, about which unfortunately there is little information. This is gaining acceptance (94).

The Prandtl mixing length hypothesis can thus no longer be considered as a correct representation of the situation, and is roundly condemned by Bradshaw (104). However, a reasonable pragmatic defence of the hypothesis, in the sense of testing its' truth by its' concrete effects, is made for engineering problems at least, by Spalding (108).

Thus, although it is now generally recognized that recent measurements of the detailed structure of turbulent flows are making tenancy of the mixing hypothesis progressively more uncomfortable, the relatively primitive state of experimental research has thus far prevented replacing the theory with one much more satisfactory. The present approach therefore, goes along with

Spalding (108) since the "if it works, use it" attitude fits the philosophy decided for this thesis.

Therefore, proceeding from Prandtl's mixing hypothesis it can be shown that the perturbation component of transverse velocity v', is

$$v' \propto l \frac{du}{dy} \qquad 7.26$$

where l is the mixing length as before.

We assume that,

$$\frac{db}{dt} \propto v' \qquad 7.27$$

Now, $\frac{db}{dt} = \frac{db}{dx} \cdot \frac{dx}{dt}$ and, $\frac{dx}{dt} = u$, 7.28

So, $$\frac{db}{dx} \propto \frac{|v'|}{|u|}$$

where u is again the characteristic velocity of the shear layer.

Abramovich's suggestion (102) may be expressed in the form that the local momentum interchange in the flow direction of the instantaneous mass of a shear layer as a result of neighbouring turbulent fluctuations is proportional to the difference in the velocity heads at a distance equal to Prandtl's mixing length,

$$\text{i.e. } (\rho u)|v'| \propto l \frac{d(\rho u^2)}{dy} \qquad 7.29$$

This is the modified form of the mixing hypothesis which replaces equation 7.26

Applied to the mixing layer equation 7.29 becomes,

$$(\rho u)|v'| \propto \frac{l}{b}(\rho_1 u_1^2 - \rho_2 u_2^2) \qquad 7.30$$

from which the modulus of the fluctuating transverse velocity component is obtained as,

$$|v'| \propto \frac{l}{b} \cdot \frac{(\rho_1 u_1^2 - \rho_2 u_2^2)}{(\rho u)} \qquad 7.31$$

Thus, substituting into equation 7.28, the rate of growth of the mixing layer with distance is obtained as,

$$\frac{db}{dx} \propto \pm \frac{l}{b} \cdot \frac{(\rho_1 u_1^2 - \rho_2 u_2^2)}{(\rho u)(u)} \qquad 7.32$$

It is necessary to define the characteristic values of mass velocity (ρu) and velocity (u), through the mixing layer:

$$\text{i.e. } (\rho u) \equiv \frac{1}{b}\int_0^b \rho u \, dy \qquad 7.33a)$$

$$(\rho) \equiv \frac{1}{b}\int_0^b \rho \, dy \qquad 7.33b)$$

Thus,

$$\frac{db}{dx} \propto \pm \frac{l}{b} \cdot \frac{(\rho_1 u_1^2 - \rho_2 u_2^2)}{\int_0^b \rho u \, dy} \cdot \frac{b\int_0^b \rho \, dy}{\int_0^b \rho u \, dy} \qquad 7.34$$

To proceed further it is necessary to have a detailed knowledge of both velocity and density profiles across the shear layer to evaluate the integrals in equation 7.3.4. A priori, such information is not readily available. Fortunately, if the two stream densities do not differ greatly some simplifying approximations may be made: If the densities do not differ by a factor of more than two,

$$\frac{1}{b}\int_0^b \rho \, dy \simeq \frac{\rho_1 + \rho_2}{2} \qquad 7.35a)$$

and,

$$\frac{1}{b}\int_0^b \rho u \, dy \simeq \frac{\rho_1 u_1 + \rho_2 u_2}{2} \qquad 7.35b)$$

These approximations hold good for combustion chamber dilution zones but only barely so for primary zones.

Substituting equations 7.35 into 7.34,

$$\frac{db}{dx} \propto \pm 2\frac{l}{b} \cdot \frac{(\rho_1 u_1^2 - \rho_2 u_2^2)(\rho_1 + \rho_2)}{(\rho_1 u_1 + \rho_2 u_2)^2} \qquad 7.36$$

Introducing now,

$$n \equiv u_2/u_1 \quad , \quad \bar{\rho} \equiv \rho_2/\rho_1 \qquad 7.37$$

and making the assumptions regarding densities given above, equation 7.36 reduces to,

$$\frac{db}{dx} = \pm \frac{2l}{b} k (1+\theta)(1-\theta_m^2) \Big/ (1+\theta_m)^2 \qquad 7.38a)$$

where $\theta = T_1 / T_2$ 7.38b)

and, k is a constant which is slightly less than unity.

It is necessary to place a value on the group $\frac{2lk}{b}$.

For the outer layer of a boundary layer, a reasonable assumption consistent with the available data is that the dimensionless mixing length λ , where $\lambda \equiv l / y_G$, y_G being some plausible definition of the boundary layer thickness, has a uniform value of about 0.075, (109). For free turbulent flows, constant mixing length is a well-known empirical feature. The presence of a wall linearly reduces the mixing length with distance to the wall. A survey by Escudier (110), of experimental data on mixing length distribution led him to adopt generally a ramp function for both boundary layers and wall-jets with $\lambda_G = 0.075$, although the value on the ramp, λ_G , was about 25% higher for the latter than for the former. Escudier's investigation was for isothermal flows, for which, $\theta \doteq 1$ and equation 7.3.8 becomes,

$$\frac{db}{dx} = \pm \frac{4lk}{b} \frac{(1-m)}{(1+m)} \qquad 7.39$$

If we assume $\frac{lk}{b} = \lambda$, and apply Escudier's ramp value λ_G , the mixing expression is given by,

$$\frac{db}{dx} = \pm 0.300 \frac{(1-m)}{(1+m)} \qquad 7.40$$

This expression agrees very closely with that obtained for isothermal flow by Abramovich in his original analysis (99), the constant being 0.270, obtained from the mixing data of Zhostkov et al, and, Albertson et al. Abramovich found

the value of 0.27 also applied to non-isothermal flows. With such close agreement between Abramovich's and the present mixing expressions for isothermal flow, the assumption that the Escudier-based constant also applies for non-isothermal flows is justified.

Therefore,

$$\frac{db}{dx} = 0.300 \frac{(1+\theta)}{2} \cdot \frac{|(1-\theta_m^2)|}{(1+\theta_m)^2} \qquad 7.41$$

The isothermal form of the mixing expression is equation 7.40 and, for equal stream velocities equation 7.41 becomes,

$$\frac{db}{dx} = \frac{0.300}{2} \frac{(1-\theta)}{(1+\theta)} \qquad 7.42$$

If velocity and temperature ratios are both unity, the basic equation predicts zero-mixing between the two streams. However, since the two streams will inevitably have in them some initial turbulence with a V' component, equation 7.2.8 would give some finite mixing to take place, even at this condition. There is a considerable volume of experimental evidence that such "pre-turbulence" may be the dominant factor if the two streams are at nearly equal velocities, (100), (101), (111), (112).

Ragsdale and Edwards (103) concluded that the initial turbulence present in the two streams contributed significantly to the mixing processes and dominated the situation for the velocity ratio range $0.85 \leqslant u_m/u_c \leqslant 1.52$. Abramovich, using his original mixing expression, found departures from the experimental data for $0.4 \leqslant u_m/u_c \leqslant 2.5$, and explained the discrepancy as being due to pre-turbulence. This explanation was questioned however, by Yakovlevskiy (113) who found instead of the measured values of 1 - 5% "pre-turbulence" intensity, values in the order of 10 - 15% would be required for dominance over this velocity range. It is therefore plain that although

Abramovich's qualitative explanation of pre-turbulence effects was undoubtedly a contributory factor, the wide velocity ratio range is due to incorrect accounting of how the density field influences the growth of the mixing layer.

A number of methods, of varying degrees of sophistication, are available to deal with pre-turbulence. Use of superpositions immediately suggests itself, where to the mixing-derived turbulence, the pre-turbulence is directly added. In this, the Taylor parameter might perhaps be used,

$$\text{i.e. } \left(\frac{db}{dx}\right)_{\text{Preturbulence}} = \left\{1 + f\left[\epsilon\left(\frac{x}{L}\right)^{0.2}\right]\right\}\frac{db}{dx} \qquad 7.43$$

ϵ being the initial turbulence intensity, L is the scale of the turbulence, and, f is an unknown function.

A further choice might be some functional modification to the basic mixing equation to give improved agreement with experimental data, after Ribner's correction (114) for round jets in a pressure gradient.. However, consistent with the general philosophy, the present method of dealing with pre- turbulence is an engineering one which is simple, conservative, and in general accordance with the observed facts. A limiting (minimum) value is set upon $\frac{db}{dx}$ over a range of velocity ratios about unity. The range is that suggested by Ragsdale and Edwards.

7.4.2. Velocity and Temperature Profiles.

Assumption of the Prandtl mixing hypothesis means that the mixing and wall layers in the potential core region can be considered independently.

For the wall layer, representation as a normal boundary layer with a simple power law similarity form is considered adequate, although such a law is now considered passé.

Defining universal non-dimensional profiles in the inner and outer layers of the potential core region is tantamount to assuming that flow similarity is achieved independently in each layer, everywhere, i.e. the validity of Prandtl's mixing hypothesis is implicit in the assumption of similar profiles. That this is certainly not true downstream of the potential core is shown by the experimental data. This reveals that the shape of the non-dimensional velocity curve in the inner layer of a wall-jet flow in fact depends to some degree on the conditions existing external to the shear layer, as would be expected from Bradshaw and Gee's (80) work, and the foregoing comments on the validity of the mixing hypothesis. Gartshore (115) selected an 1/11-th power law and Harris (116), using Bradshaw and Gee's data, selected a 1/10-th power law as a mean representative form. In a later paper (117), Gartshore was able to calculate the actual law as a function of the streamwise co-ordinate using a double momentum - integral technique. In each of the cases cited, there was an abrupt change in profile shape to the power law chosen at the end of the potential core. However, within the potential core, Gartshore (115), represented the profile by a 1/7th. power law profile and gave data which showed reasonable agreement with this assumption. In addition, since the inner layer is almost always a small proportion of the film thickness at x_p, little error is in fact likely to arise from this source in assuming such a representative function and calling it universal. Accordingly,

$$\frac{u}{u_s} = \left(\frac{y}{\delta}\right)^{\frac{1}{7}} \qquad 7.44$$

is assumed for the inner layer.

For the mixing layer, equation 7.41 is strictly only true if similar profiles of temperature and velocity (similar in themselves and not with each

other) are attained very soon after the separation point. This is because of the way (ρu) and (ρ) are defined in equations 7.33; equations 7.35 being only approximations to these integral forms. Similarity is assumed and as mentioned under Section 7.3.2., with the additional assumption of zero thickness of the layer at the separation point, the similar form will exist throughout the region.

It has been found that similarity for the shear layer results if velocity profiles are plotted in the following form:

$$\frac{u_1 - u}{u_1 - u_2} = f\left({}^{y - y_2}/_{b} \right) = f(\eta) \qquad 7.45a)$$

where,

$$\eta \equiv \frac{y - y_2}{b} \qquad 7.45b)$$

The function $f(\eta)$ in equation 7.45 can take several forms. It could be found from the Tollmien-Keuthe theory (118), (119) or, Görtler's theory (120). However these somewhat complicated theories involve the incorporation of an empirical constant and are not considered convenient. Spalding's (121) assumption of a linear relationship for $f(\eta)$ is not considered a satisfactory representation of the profile. Korst (95) elected to use an error function in his studies.

In the present analysis, Schlichting's two-dimensional wake theory (122) is used for $f(\eta)$, since it is based on Prandtl's mixing hypothesis. This wake theory yields the expression,

$$f(\eta) = \alpha(1 - \eta^{3/2})^2 \qquad 7.46$$

where α is a grouping of empirical constants. However, considering the boundary condition $\eta = 0$, at which $f(\eta) = \alpha$ and, $f'(\eta) = 0$, gives $\alpha = 1$. Thus,

$$\frac{u_1 - u}{u_1 - u_2} = (1 - \eta^{3/2})^2 \qquad 7.47$$

Equation 7.47 has the advantage over Korst's error profile that it is much simpler to integrate. In addition, it is the form used by Abramovich in his initial analysis, (99). It has been shown by Vulis (123), Yershin (124) and

Glikman (125) that Schlichting's wake theory for isothermal flows is valid, and that the velocity profile remains the same dimensionless, universal law, when there exist large density gradients in the flow. Therefore, equation 7.47 may be considered valid for the present application.

Temperature profiles are similar when plotted in the form,

$$\frac{T_1 - T}{T_1 - T_2} = \phi(\eta) \qquad 7.48$$

The function $\phi(\eta)$ was found empirically by Yakovlevskiy (99) as,

$$\frac{T_1 - T}{T_1 - T_2} = (1 - \eta) \qquad 7.49$$

7.4.3. Development of Conserved Momentum Shear Layer.

The conservation of mass for the shear layer may be written as:

$$\int_{y_2}^{y_1} \rho u \, dy = \rho_1 (u_1 y_1 - v_1 x) + \rho_2 (-u_2 y_2 + v_2 x) \qquad 7.50$$

Likewise, the conservation of momentum along the x- axis may be written,

$$\int_{y_2}^{y_1} \rho u^2 dy = \rho_1 u_1 (u_1 y - v_1 x) + \rho_2 u_2 (-u_2 y_2 + v_2 x) \qquad 7.51$$

Equation 7.49 can be re-arranged for the temperature ratio T/T_1, and using the previously made assumptions, the density profile can therefore by expressed as,

$$\frac{\rho}{\rho_1} = \frac{\theta}{[1 + \eta(\theta - 1)]} \qquad 7.52$$

Following Abramovich (99), we introduce the transforms,

$$\bar{\eta}_1 \equiv y_1/b \quad ; \quad \bar{\eta}_2 \equiv y_2/b \quad ;$$

$$\bar{v} \equiv \frac{v}{b u_1} \quad ; \quad \bar{b} = b/x \quad , \text{ collectively,} \qquad 7.53$$

Introducing these transforms and dividing both sides by $\rho_1 u_1 b$:

Equation 7.50 becomes,

$$\int_{y_2}^{y_1} \frac{\rho u}{\rho_1 u_1 b} \cdot dy = \bar{\eta}_1 - \bar{v}_1 - (m\bar{\eta}_2 - \bar{v}_2)\theta$$

Changing the integration limits and introducing the velocity profile from equation 7.47, the conservation of mass becomes on rearrangement,

$$\bar{\eta}_1 - \bar{v}_1 - (m\bar{\eta}_2 - \bar{v}_2)\theta = \int_0^1 \frac{\rho}{\rho_1} d\eta - (1-m)\int_0^1 \frac{\rho}{\rho_1}(1-\eta^{3/2})^2 d\eta \qquad 7.54$$

Similarly, for equation 7.51:-

$$\int_{y_2}^{y_1} \frac{\rho}{\rho_1} \cdot \frac{u^2}{u_1^2 b} \cdot dy = \left[\bar{\eta}_1 - \bar{v}_1 - (m\bar{\eta}_2 - \bar{v}_2)\theta_m \right]$$

Changing the integration limits etc., as before, the conservation of momentum becomes,

$$\bar{\eta}_1 - \bar{v}_1 - (m\bar{\eta}_2 - \bar{v}_2)\theta_m = \int_0^1 \frac{\rho}{\rho_0} d\eta + (1-m)^2 \int_0^1 \frac{\rho}{\rho_1} f^2(\eta) d\eta - 2(1-m)\int_0^1 \frac{\rho}{\rho_1} f(\eta) d\eta \qquad 7.55$$

Comparing sides of equations 7.54 and 7.55, reveals common terms so from 7.5.4., equation 7.5.5 can be subtracted. This leads to, upon algebraic manipula

$$(m\bar{\eta}_2 - \bar{v}_2)\theta = (1-m)\int_0^1 \frac{\rho}{\rho_1} f^2(\eta) d\eta - \int_0^1 \frac{\rho}{\rho_1} f(\eta) d\eta \qquad 7.56$$

This is an expression for $\bar{\eta}_2$ and $\bar{v}_2$, a description of one side of the mixing layer, and a similar expression is now required for the other side, i.e. for $\bar{\eta}_1$ and $\bar{v}_1$.

Multiplying equation 7.54 by velocity ratio m, and subtracting equation 7.55 yields,

$$(\bar{\eta}_1 - \bar{v}_1) = \int_0^1 \frac{\rho}{\rho_1} d\eta - (2-m)\int_0^1 \frac{\rho}{\rho_1} f(\eta) d\eta + (1-m)\int_0^1 \frac{\rho}{\rho_1} f^2(\eta) d\eta \qquad 7.57$$

Substituting in these equations the density profile from equation 7.52 yields respectively,

$$m\bar{\eta}_2 - \bar{v}_2 = (1-m)\int_0^1 \frac{f^2(\eta)\, d\eta}{1+(\theta-1)\eta} - \int_0^1 \frac{f(\eta)\, d\eta}{1+(\theta-1)\eta} \qquad 7.58$$

and,

$$\frac{(\bar{\eta}_1 - \bar{V}_1)}{\theta} = \int_0^1 \frac{d\eta}{1+(\theta-1)d\eta} - (2-m)\int_0^1 \frac{f(\eta)d\eta}{1+(\theta-1)\eta} + (1-m)\int_0^1 \frac{f^2(\eta)d\eta}{1+(\theta-1)\eta} \qquad 7.59.$$

Letting now,

$$I_1 \equiv \int_0^1 \frac{f^2(\eta)d\eta}{1+(\theta+1)\eta} \; ; \quad I_2 \equiv \int_0^1 \frac{f(\eta)d\eta}{1+(\theta-1)\eta} \; ; \quad I_3 \equiv \int_0^1 \frac{d\eta}{1+(\theta-1)\eta} \qquad 7.60$$

Thus,

$$m\bar{\eta}_2 - \bar{V}_2 = (1-m)I_1 - I_2 \qquad 7.61.$$

and,

$$\frac{(\bar{\eta}_1 - \bar{V}_1)}{\theta} = I_3 - (2-m)I_2 + (1-m)I_1 \qquad 7.62$$

Outside the shear layer on the wall-side, and between it and the wall boundary layer, the flow is of constant velocity and is conditionally termed "potential" because usually, the initial turbulence there is considerably less than the turbulence arising in the shear layer. In this potential core by definition,

$$u = \text{constant, and, } \frac{\partial u}{\partial x} = 0$$

Thus, if the conservation of mass, equation 7.2, is considered in two-dimensions, it yields, $\frac{\partial v}{\partial y} = 0$ and therefore $V = 0$, for the potential core. If stream 1. is made the coolant stream, from the definition of the transform $\bar{V}$, equation 7.5.3., it can be seen that $\bar{V}_1 = 0$.

Therefore equation 7.62 becomes,

$$\bar{\eta}_1 = \theta\left[I_3 - (2-m)I_2 + (1-m)I_1\right] \qquad 7.63.$$

which describes the development of the inner edge of the shear layer within the potential core region.

Equations of the form of 7.61 and 7.62, together with additional equations representing the conservation of heat and, transverse equilibrium

of the shear layer, were developed by Abramovich (Chapter 7). He solved these equations simultaneously with the (unsatisfactory) mixing expression equation 7.24, to derive the general properties downstream in co-flowing, turbulent, plane-jets of compressible gases. By making the a priori assumption and limitation of a potential core, as in the preceeding paragraph, the cumbersome solution of five simultaneous equations is avoided.

7.4.4. Cooled Wall Boundary Layer.

In general, the cooled wall hydrodynamic boundary layer grows from some point upstream x_s, of the injection plane, $x = 0$, and may undergo transition from laminar to turbulent flow. For convenience in computation, the necessary equations must be developed in closed form.

For the laminar portion of the layer, a Blasius profile is assumed, the thickness being then given by,

$$\frac{\delta_L}{x_1} = \frac{5.2}{Re_{x_1}^{1/2}} \qquad 7.64$$

and for the turbulent portion as suggested above, a 1/7 th. power profile, resulting in a thickness,

$$\frac{\delta_T}{x_2} = \frac{0.37}{Re_{x_2}^{1/5}} \qquad 7.65.$$

The growth of the layer is diagrammatically shown in figure 7.1., where transition takes place at the discrete point C, for the transition Reynolds number Re_c. In fact, usually transition occupies a finite region but Squire and Young (126) showed that the transition point may oscillate appreciably, particularly if the flow outside the boundary layer has some turbulence, this oscillation being so rapid that the idea of a unique transition point - a mean of this oscillation - is justified. Thus, for 0 to C,

equation 7.6.4. holds, and from C to infinity downstream equation 7.65 holds. Therefore if there is to be no finite impulse on the fluid at C, the following condition must be obeyed:

$$\left[Re_{\delta_2}\right]_L = \left[Re_{\delta_2}\right] \qquad 7.66$$

But,

$$\left(\delta_2/\delta\right)_L = \alpha_L \quad \text{and} \quad \left(\delta_2/\delta\right)_T = \alpha_T$$

where the respective constants α , depend on the profiles chosen.

Thus, equations 7.64 and 7.65 become upon substitution and rearrangement,

$$\left(\delta_2\right)_L = \frac{A' x_1}{Re_{x_1}^{1/2}} \qquad 7.67a)$$

and,

$$\left(\delta_2\right)_T = \frac{B' x_2}{Re_{x_2}^{1/5}} \qquad 7.67b)$$

and where,

$$A' = 5.2\,\alpha_L \qquad 7.68a)$$

$$B' = 0.37\,\alpha_T \qquad 7.68b)$$

Thus, the respective Reynolds numbers based on momentum thickness can be found and substituted in equation 7.66, to give:

$$A'\left(Re_{x_1}\right)^{1/2} = B'\left(Re_{x_2}\right)^{4/5} \qquad 7.69$$

From condideration of figure 7.1 ,

$$x_2 = x_1 - a$$

or,

$$Re_{x_2} = Re_{x_1} - Re_a \qquad 7.70$$

Substituting for Re_{x_2} therefore in the equation for the turbulent Reynolds number based on momentum thickness, which is

$$\left[Re_{\delta_2}\right]_T = B'\left(Re_{x_2}\right)^{4/5}$$

yields,

$$\left[Re_{\delta_2}\right]_T = B'\left(Re_{x_1} - Re_a\right)^{4/5} \qquad 7.71.$$

At transition, the momentum thickness is continuous across C and therefore,

$$Re_{x_1} = Re_a \qquad 7.72$$

Thus, from equations 7.66 and 7.71, together with the equation for the laminar Reynolds number based on momentum thickness, which is

$$\left[Re_{\delta_2}\right]_L = A'\left(Re_{x_1}\right)^{1/2},$$

$$A' Re_c^{1/2} = B'\left(Re_c - Re_a\right)^{4/5} \qquad 7.73$$

giving,

$$Re_a = Re_x - \left[\left(\frac{A'}{B'}\right)^2 Re_c\right]^{5/8} \qquad 7.74.$$

Equation 7.65 can now be re-written as,

$$\delta_T = \frac{0.37\,(x_1 - a)}{\left(Re_{x_1} - Re_a\right)^{1/5}} \qquad 7.75.$$

Substituting into this equation, the definition for R ,

$$\frac{\delta_T}{x_1} = \frac{0.37\left(1 - Re_a/Re_{x_1}\right)^{4/5}}{Re_{x_1}^{1/5}} \qquad 7.76$$

If the cooled wall boundary layer grows from a point distant upstream of the slot outlet ($x = 0$) , the relevant equations above can be rewritten when applied for the thickness at the end of the potential core region,

$$\left(\delta_L\right)_p = \frac{5.2\,(x_p + x_s)}{Re_{(x_p+x_s)}^{1/2}} \quad \text{for} \quad \frac{u_c\,(x_p + x_s)}{\nu_c} < Re_c \qquad 7.77$$

and,

$$\left(\delta_T\right)_p = \frac{0.37\,(x_p + x_s)\left[1 - Re_a/Re_{(x_p+x_s)}\right]^{4/5}}{Re_{(x_p+x_s)}^{1/5}} \text{ for } \frac{u_c\,(x_p + x_s)}{\nu_c} > Re_c$$

7.78.

where Re_c is the critical Reynolds number for transition, usually about 3.2×10^5.

$$Re_a = Re_x - \left[\left(\frac{A'}{B'}\right)^2 Re_c\right]^{5/8} \qquad 7.79$$

Empirical values for A' and B' for the profile chosen were taken from reference (127), to give for the group $(A'/B')^2$, the number 322.03.

If the cooled wall boundary layer is wholly turbulent from its commencement, the following equation should be used,

$$(\delta_T)_p = \frac{0.37(x_p + x_s)}{Re_{(x_p+x_s)}^{1/5}} \qquad 7.80$$

7.4.5. Idealised Potential Core Length.

It may be realised from figure 7.2 that the slot height s, is equivalent to,

$$s = (\delta)_p + (y_1)_p \qquad 7.81$$

where as before, the subscript p denotes "at the end of the potential core." This equality may be rearranged to incorporate potential core length as

$$\frac{x_p}{s} = \left[\frac{(\delta)_p}{x_p} + \frac{b_p}{x_p}\cdot\frac{(y_1)_p}{b_p}\right]^{-1} \qquad 7.82.$$

The non-dimensional potential core length for ideal mixing, x_{p_i}, is thus given by,

$$\frac{x_{pi}}{s} = \left\{\left[\frac{(\delta)_p}{x_{pi}} + 0.300\cdot\frac{(1+\theta)}{2}\left|\frac{(1-\theta_m^2)}{(1+\theta_m)^2}\right|\cdot\right]\left[I_3 - (2-m)I_2 + (1-m)I_1\right]\theta\right\}^{-1} \qquad 7.83.$$

having incorporated equations 7.41 and 7.63, for the mixing rate expression and growth of the shear layer inner edge, respectively. The appropriate

expression for $(\delta)_p$ is used from equations 7.77, 7.78 or, 7.80. From the manner in which the transform $\bar{\eta}$ is defined, equation 7.53, and, the choice of stream 1. as the coolant stream in obtaining equation 7.63,

$$\theta = T_c / T_m \qquad 7.84a)$$

and,

$$m = u_m / u_c \qquad 7.84b)$$

The present equation system for x_{p_i} should be compared to Abramovich's original expressions, equation 7.20. The parenthood of equation 7.83 is plain.

7.4.6. Application of Kirk's Suggestion.

In Kirk's suggestion, (described in Section 7.3.2.), the real mixing layer is replaced by an equivalent hypothetical shear layer growing over a greater distance from zero thickness, and the effects of momentum loss are translated into a simple linear shift of the origin. As Lamb (128) has pointed out, although such a technique can be justified on the grounds of expediency, it does not yield any information about the fundamental nature of the developing flow field. For the approach presently followed, such a technique is justified. In fact, use of Kirk's technique has proved rather popular being used to calculate effective origins by Hill and Page (129), Childs, Paynter and Redeker (130), duP. Donaldson and Grey (131), and, Sirierx and Solignac (132), etc. for their particular problems.

With Kirk's technique therefore, the actual potential core length may be expressed as:

$$x_{p_i} = x_{p_i} - x_c \qquad 7.85$$

where, x_c = correction length equal in extent to the distance required for the velocity defect introduced by slot lip and lip boundary layers to be filled, within the potential core,

x_{ρ_r} = the real potential core length,

x_{ρ_i} = the idealised potential core length given by equation 7.83.

7.4.7. Correction for Momentum Loss.

To calculate x_c, it is necessary to analyse the wake development. The two-dimensional wake in isothermal flow is well investigated, e.g. Schlichting (122), and it is only necessary to extend the solutions to isothermal flow.

Consider the non-isothermal, incompressible, two-dimensional wake development shown in figure 7.3. Let $u_2 > u_1$ and, $T_2 < T_1$. The velocity and temperature profiles shown in this figure forms very soon downstream of the lip so therefore, assume it exists from the plane of the lip, i.e. the separated flow is neglected.

The total drag is made up of the boundary layer drags and the base pressure drag, i.e.

$$D_{ToT} = D_{\delta,1} + D_{\delta,2} + D_P \qquad 7.86$$

The boundary layer drag can be found from the integral momentum equation which for two-dimensional, zero mass transfer in zero pressure gradient flow over a flat plate reduces to :

$$\frac{d\delta_2}{dx} + \delta_2 \left[\frac{1}{\rho_e} \cdot \frac{d\rho_e}{dx} \right] = C_f/2 \qquad 7.87.$$

where subscript G implies parameters outside the layer. The ρ_G's remain constants up to the edge of the slot if the lip is considered adiabatic. Beyond the lip, the boundary layers cease to exist as such. Therefore, the above equation reduces to:

$$\frac{d\delta_2}{dx} = c_f/2 \qquad 7.88$$

Now, for a boundary layer,

$$D_\delta = \tfrac{1}{2}\rho u^2 c_f x$$

and from equation 7.88, $c_f = \frac{2\delta_2}{x}$,

hence,

$$D_\delta = (\rho u^2)_s \delta_2 \qquad 7.89.$$

the subscript s denotes surface values.

The minimum velocity in the profile, v_{min}, will lie approximately at the edge of the stream with the greater density, i.e. for equal molecular weight streams and constant pressure mixing, at the edge of the stream with the lower temperature. In other words, there will be flow around the lip. With this statement, it can be assumed that the base pressure drag is proportional to the dynamic pressure of the stream with the smallest mass velocity, i.e. if $\rho_1 u_1 < \rho_2 u_2$, pressure drag is,

$$D_p = \tfrac{1}{2}\rho_1 u_1^2 C_D \delta_w \qquad 7.90$$

where C_D is the coefficient of base pressure drag.

Hence, from equation 7.86, the total drag on the lip is,

$$D_{TOT} = (\delta_2)_1 \cdot (\rho_1 u_1^2)_s + (\delta_2)_2 \cdot (\rho_2 u_2^2)_s + \tfrac{1}{2}\rho_1 u_1^2 C_D \delta_w \qquad 7.91.$$

If the incompressible Bernoulli equation is applied to the system with,

(i) the total pressure in a given stream being constant, and,

(ii) the static pressure constant over the whole field,

it can be written

$$(p - p_s) = \tfrac{1}{2}(\rho_1 u_1^2)_s - \tfrac{1}{2}\rho_1 u_1^2 = \tfrac{1}{2}(\rho_2 u_2^2)_s - \tfrac{1}{2}(\rho_2 u_2^2) \qquad 7.92$$

Now, if as noted above, there is flow around the lip from the lower mass velocity side, the static pressure difference must be proportional to the dynamic pressure of this side, [illegible] the static pressure difference must be proportional to the dynamic pressure of this side,

$$\text{i.e.} \quad (p-p_s) = -a_1 \tfrac{1}{2}\rho_1 u_1^2 \qquad 7.93$$

where a_1 is the constant of proportionality, less than zero usually.

Therefore, combining equations 7.92 and 7.93 yields,

$$\frac{(\rho_1 u_1^2)_s}{\rho_1 u_1^2} = 1 - a \qquad 7.94a$$

and,

$$\frac{(\rho_2 u_2^2)_s}{\rho_1 u_1^2} = \frac{\rho_2 u_2^2}{\rho_1 u_1^2} - a \qquad 7.94b$$

If equation 7.91 is divided by $\rho_1 u_1^2$ and equations 7.94 introduced into it, there results,

$$\frac{D_{ToT}}{\rho_1 u_1^2} = (\delta_2)_1 (1-a) + (\delta_2)_2 \left(\frac{\rho_2 u_2^2}{\rho_1 u_1^2} - a\right) + \tfrac{1}{2} C_D \delta_W \qquad 7.95$$

Now, a general definition of the two-dimensional momentum thickness is,

$$\delta_2 = \int_0^{\delta} \frac{\rho u}{\rho_e u_e}\left(1 - \frac{u}{u_e}\right) dy$$

Therefore, if a power law form of boundary layer velocity profile is assumed,

$$u/u_e = (y/\delta)^n$$

and if as before, $\rho = \rho_e$, the momentum is found as,

$$\delta_2 = \frac{n}{(n+1)(2n+1)}\,\delta \qquad 7.96$$

where δ is the thickness of the boundary layer.

Substituting then for δ_2 in equation 7.95 gives,

$$\frac{D_{ToT}}{\rho_1 u_1^2} = \frac{n}{(n+1)(2n+1)}(\delta)_1(1-a) + \frac{n}{(n+1)(2n+1)}(\delta)_2\left(\frac{\rho_2 u_2^2}{\rho_1 u_1^2} - a\right) + \tfrac{1}{2} C_D \delta_W \qquad 7.97$$

Making the previous assumptions concerning the density field and introducing $\phi = u_1/u_2$ and $\tau = T_1/T_2$, yields,

$$\frac{D_{ToT}}{\rho_1 u_1^2} = \frac{n}{(n+1)(2n+1)}(\delta)_1(1-a) + \frac{n}{(n+1)(2n+1)}(\delta)_2\left(\frac{\tau}{\phi^2} - a\right) + \tfrac{1}{2} C_D \delta_W \qquad 7.98$$

It is observable from the experimental data for blunt bodies that in the wake, $a \ll 1.0$, and, $C_D \rightarrow 1.0$. Assuming therefore that the slot lip behaves like a blunt body and inserting these two conditions into equation 7.98 gives,

$$\frac{D_{ToT}}{\rho_1 u_1^2} = \frac{n}{(n+1)(2n+1)}\left[(\delta)_1 + (\delta)_2 \frac{\tau}{\phi^2}\right] + \tfrac{1}{2}\delta_W \qquad 7.99$$

But drag is a loss in total momentum, so,

$$D_{ToT} = \int_0^{b_1} (u_1 - u)\, dM_1 + \int_0^{b_2} (u_2 - u)\, dM_2 \qquad 7.100$$

where M is a mass flow rate and in writing equation 7.100, constant pressure in the wake is again assumed. For two-dimensional flow, $dM = \rho u\, dy$ so,

$$D_{ToT} = \int_0^{b_1} \rho u (u_1 - u)\, dy + \int_0^{b_2} \rho u (u_2 - u)\, dy \qquad 7.101$$

Non-dimensionalising by $\rho_1 u_1^2$ for compatability with equation 7.100,

$$\frac{D_{ToT}}{\rho_1 u_1^2} = \int_0^{b_1} \frac{\rho}{\rho_1}\cdot\frac{u}{u_1}\left(1 - \frac{u}{u_1}\right) dy + \int_0^{b_2} \frac{\rho}{\rho_1}\cdot\frac{u}{u_1^2}(u_2 - u)\, dy \qquad 7.102$$

It is convenient at this stage to change the variable, i.e. let $\frac{y}{b} \equiv \eta$; thus, $dy = b\, d\eta$ and the limits of integration become,

$$y = 0 \quad , \quad \eta = 0$$
$$y = b \quad , \quad \eta = 1$$

If the assumption is now made that the wake profiles in similar form, can be made up from the same shear layer profiles used in Section 7.4.3., the density fields will be given by equation 7.52.

Thus,
$$\frac{\rho}{\rho_1} = \frac{\tau}{[1 + \eta(\tau - 1)]} \qquad 7.103$$

Also, using equation 7.47,

$$\frac{u_1 - u}{u_1 - u_{min}} = \frac{u_2 - u}{u_2 - u_{min}} = (1 - \eta^{1.5})^2 \qquad 7.104$$

from which it can be shown that,

$$u\left(1 - \frac{u}{u_1}\right) = \left(1 - \frac{u_{min}}{u_1}\right)(1-\eta^{1.5})^2 u_1 - \left(1 - \frac{u_{min}}{u_1}\right)\left[(1-\eta^{1.5})^2\right]^2 (u_1 - u_{min}) \qquad 7.105$$

and,

$$u\left(1 - \frac{u}{u_2}\right) = u_2\left(1 - \frac{u_{min}}{u_2}\right)(1-\eta^{1.5})^2 - (u_2 - u_{min})\left(1 - \frac{u_{min}}{u_2}\right)\left[(1-\eta^{1.5})^2\right]^2 \qquad 7.106$$

Equations 7.103, 7.105 and 7.106 may be substituted into the R.H.S. of equation 7.102:-

1st term:

$$b_1 \int_0^1 \frac{\tau}{[1+\eta(\tau-1)]} \cdot \left\{\left(1 - \frac{u_{min}}{u_1}\right)(1-\eta^{1.5})^2 - \left(1 - \frac{u_{min}}{u_1}\right)\left[(1-\eta^{1.5})^2\right]^2 \left(1 - \frac{u_{min}}{u_1}\right)\right\} d\eta$$

writing $(1 - \eta^{1.5})^2 = f(\eta)$ as before,

$$\equiv b_1 \left(1 - \frac{u_{min}}{u_1}\right) \int_0^1 \left\{\frac{\tau\,[f(\eta)]}{[1+\eta(\tau-1)]} - \frac{\tau f^2(\eta)}{[1+\eta(\tau-1)]} + \frac{u_{min}}{u_1} \cdot \frac{\tau f^2(\eta)}{[1+\eta(\tau-1)]}\right\}$$

Introducing now the integral definitions of equation 7.60 into the above gives for the 1st term on the R.H.S. of equation 7.102 :

$$\underline{b_1 \tau \left(1 - \frac{u_{min}}{u_1}\right)\left[I_2' - I_1' + \frac{u_{min}}{u_1} I_1'\right]}$$

where the dash denotes replacement of θ by τ in the integral definition.

2nd term:

$$b_2 \cdot \frac{u_2^2}{u_1^2} \int_0^1 \frac{\tau}{[1+\eta(\tau-1)]} \left\{\left(1 - \frac{u_{min}}{u_2}\right)(1-\eta^{1.5})^2 - \left(1 - \frac{u_{min}}{u_2}\right)\left(1 - \frac{u_{min}}{u_2}\right)\left[(1-\eta^{1.5})^2\right]^2\right\} d\eta_2$$

$$\equiv \frac{b_2 \tau}{\phi^2}\left(1 - \frac{u_{min}}{u_2}\right) \int_0^1 \left\{\frac{f(\eta)}{[1+\eta(\tau-1)]} - \frac{f^2(\eta)}{[1+\eta(\tau-1)]} + \frac{u_{min}}{u_2} \cdot \frac{f^2(\eta)}{[1+\eta(\theta-1)]}\right\} d\eta_2$$

or,

$$\underline{\frac{b_2 \tau}{\phi^2}\left(1 - \frac{u_{min}}{u_1} \cdot \phi\right)\left[I_2' - I_1' + \frac{u_{min}}{u_1} \phi I_1'\right]}$$

Therefore, the complete equation 7.102 becomes,

$$\frac{D_{TOT}}{\rho_1 u_1^2} = b_1 \tau \left(1 - \frac{u_{min}}{u_1}\right)\left[I_2' - I_1' + \frac{u_{min}}{u_1} I_1'\right] + \frac{b_2 \tau}{\phi^2}\left(1 - \frac{u_{min}}{u_1}\phi\right)\left[I_2' - I_1' + \frac{u_{min}}{u_1}\phi I_1'\right]$$

7.107.

The finite thickness of the slot lip together with the boundary layers existing on it, introduce a velocity defect into the mixing layer, as shown in figure 3.8. The above equations represent the filling-in of this defect. Consider this in relation to figure 7.4. At a distance x_D from the origin of the wake, turbulent mixing will have filled-in the defect; at this station by definition, $(u_{min})_D = u_1$ as the defect is now filled and, let $b_2 \equiv (b_2)_D$ Thus, at x_D equation 7.107 becomes,

$$\frac{D_{TOT}}{\rho_1 u_1^2} \approx \frac{(b_2)_D \gamma}{\phi^2}\left(1-\phi\chi I_2' - I_1' + \phi I_1'\right) \qquad 7.108$$

Now, any region of turbulent mixing regardless of its origin will obey the form of equation 7.41. Therefore, applying this equation gives, for the b_2 part of the wake:

$$\int_{x_0}^{x_D} dx = F_1\left\{\frac{2}{(1+\gamma)}\cdot\frac{(1+\gamma\phi)^2}{|(1-\gamma\phi^2)|}\int_{(b_2)_{x=x_0}}^{(b_2)_D} db_2\right. \qquad 7.109$$

in integral form and where F_1 implies an unknown function.

The limit x_0 represents the plane of the initial cross-section of the wake, and is the plane from which x_D is measured. The assumption that $x_0 = 0$ was implied in the assumption of similar profiles extending through-out the wake region. If $\delta_W < S$, as it usually is, this is a reasonable assumption.

Equation 7.109 may hence be evaluated as,

$$x_D = F_1\left\{\frac{2}{(1+\gamma)}\cdot\frac{(1+\gamma\phi)^2}{|(1-\gamma\phi^2)|}\left[(b_2)_D - (b_2)_0\right]\right\} \qquad 7.110$$

The question of the initial thickness of the wake, $(b_2)_0$ has to be decided. If any flow from stream 2. round the slot edge is completely neglected, at $x = 0$, $(b_2)_0 = (\delta)_2$. For maximum flow round the lip, the velocity of the other stream is required to be zero when, $u_1 = 0$, $u_{min} = u_1 = 0$ and, $(\delta)_1 = 0$, giving $(b_2)_0 = 0$. Thus, $0 < (b_2) < (\delta)_2$. Abramovich for

isothermal flow, took,

$$(b_2)_o = 0.724\ (\delta)_2 \qquad 7.111$$

In the absence of any alternative, this value is taken to hold for non-isothermal flows and $(b_2)_o$ is given by equation 7.111.

The thickness $(b)_{2D}$ now has to be determined. This is done by combining equation 7.108 with equation 7.99, the two drag expressions, i.e.

$$(b_2)_D = \frac{\phi^2}{\tau(1-\phi)(I_2'-I_1'+\phi I_1')}\left\{\frac{n}{(n+1)(2n+1)}\left[(\delta)_1+(\delta)_2\frac{\tau}{\phi^2}\right]+\tfrac{1}{2}\delta_w\right\} \qquad 7.112$$

An additional expression for $(b_2)_D$ can be found by applying the basic mixing expression again, i.e.

$$(b_2)_D = F_2\left\{\left[x_D+x_c\right]\cdot\frac{(1+\tau)}{2}\frac{\left|(1-\tau\phi^2)\right|}{(1+\tau\phi)^2}\right\} \qquad 7.113$$

Equation 7.113 may be arranged for x_c with substitution for x_D from equation 7.110. Thus,

$$F_1 x_c = \frac{2}{(1+\tau)}\cdot\frac{(1+\tau\phi)^2}{\left|(1-\tau\phi^2)\right|}\left\{(b_2)_D\left[1-\frac{F_1}{F_2}\right]+(b_2)_o\frac{F_1}{F_2}\right\} \qquad 7.114$$

The functions F_1 and F_2 are unknown initially. It is a great convenience if equation 7.114 is rearranged as,

$$x_c = \frac{2}{(1+\tau)}\frac{(1+\tau\phi)^2}{\left|(1-\tau\phi^2)\right|}\cdot\left\{(b_2)_D\left[\frac{1}{0.30}-\frac{1}{F_1}\right]+(b_2)_o\frac{1}{F_1}\right\} \qquad 7.115$$

where F_1 is an unknown function to be determined, F_2 is a mixing constant being taken as 0.300 from equation 7.99.

Because the streams mass velocity ratio determines the amount and direction of flow around the slot lip, auxiliary equations arise for $(b_2)_o$ and $(b_2)_D$. When the streams mass velocity ratio is unity, there will be no flow around the lip and $(b_2)_o$ takes up the value,

$$(b_2)_o = (\delta)_2 + 0.5\,\delta_w \qquad 7.116$$

i.e. the pole for u_{mn} now lies at the mid-point of the slot outer wall.

Similarly,

$$(b_2)_D = \frac{\phi^2}{\tau(1-\phi)(I_2'-I_1'+\phi I_1')}\left\{\frac{n}{(n+1)(2n+1)}(\delta)_1 + \frac{n}{(n+1)(2n+1)}(\delta)_2\cdot\frac{\tau}{\phi^2} + 0.5\delta_W\right\} + 0.5\delta_W \qquad 7.117$$

7.4.8. Correction for Non-Parallel Axes.

We have through Kirk's technique embodied in equation 7.85, produced a linear shift of the origin to enable the idealised shear layer to be used. It is however, the potential core length which is of interest, this length being defined as the distance from the geometric slot outlet to the point where the inner-edge of the shear layer intersects the growing cooled wall boundary layer. Thus, a linear shift of the x- axis for the shear layer must also be accompanied by a similar linear shift for the cooled-wall boundary layer since the 'outer-edge' of this layer is acting as a non-parallel, curved axis relative to the shear layer axis. It is hence clear that equation 7.85 should really be written when referred to figure 7.5, as:

$$x_{p_r} = x_{p_i} - x_c + x_B \qquad 7.118.$$

where x_B is an axis correction.

By considering the geometry of figure 7.5, it can be seen that,

$$\frac{[(\delta)_{p,i} - (\delta)_{p,r}]}{x_B} = \tan\alpha \qquad 7.119$$

and,

$$\tan\alpha = \frac{(y_1)_{p,i}}{x_{p_i}} \qquad 7.120$$

since, from equation 7.63, $(y_1)_{p,i}/b_p$ is linear.

Thus,

$$\tan\alpha = \theta\left[I_3-(2-m)I_2+(1-m)I_1\right]\left[0.3\,\frac{(1+\theta)}{2}\,\frac{|(1-\theta_m^2)|}{(1+\theta_m)^2}\right] \qquad 7.121$$

Thus,

$$x_B = \frac{[(\delta)_{\rho,i} - (\delta)_{\rho,r}]}{\theta\left[I_3 - (2-m)I_2 + (1-m)I_2\right]\left[0.3\ \frac{(1+\theta)}{2}\cdot\frac{|(1-\theta_m^2)|}{(1+\theta_m)^2}\right]} \qquad 7.122$$

Defining D as,

$$D = \theta\left[I_3 - (2-m)I_2 + (1-m)I_2\right]\left[0.3\ \frac{(1+\theta)}{2}\cdot\frac{|(1-\theta_m^2)|}{(1+\theta_m)^2}\right] \qquad 7.123$$

and introducing the boundary layer expressions from equations 7.77, 7.78 and 7.79 the following forms of equation 7.122 can be derived:

$$x_B = \frac{5.2(s x_s)^{1/2}}{Re_s^{1/2} D}\left[\left(1 + \frac{x_{\rho i}}{x_s}\right)^{1/2} - \left(1 - \frac{x_{\rho r}}{x_s}\right)^{1/2}\right]$$

for $\dfrac{u_c(x_{\rho i} + x_s)}{\nu_c} < Re_{crit}$ 7.124

$$x_B = \frac{0.37 Re_{s_{cr}}^{1/5}}{Re_s D}\left\{\left[\frac{(x_s + x_{\rho i})Re_s}{s\,Re_{s_{cr}}} - 1\right]^{4/5} - \left[\frac{(x_s + x_{\rho r})Re_s}{s\,Re_{s_{cr}}} - 1\right]^{4/5}\right\} \qquad 7.125$$

for $\dfrac{u_c(x_{\rho i} + x_s)}{\nu_c} \geq Re_c$

If the wall boundary layer is wholly turbulent from its inception at x_s upstream of the plane of injection,

$$x_B = \frac{0.37 s^{1/5} x_s^{4/5}}{Re_s^{1/5} D}\left[\left(1 + \frac{x_{\rho i}}{x_s}\right)^{4/5} - \left(1 + \frac{x_{\rho r}}{x_s}\right)^{4/5}\right] \qquad 7.126$$

7.5. Summary of Equations to be Solved.

The equations for calculating the potential core length are as follows:

$$x_{p_r} = x_{\rho i} - x_c + x_B \qquad 7.127$$

$$x_{p_i} = \frac{s}{\left[\dfrac{5.2 s^{1/2}(x_s + x_{\rho i})^{1/2}}{x_{\rho i}\, Re_s^{1/2}} + D\right]} \qquad 7.128$$

$$x_B = \frac{5.2(s x_s)^{1/2}}{Re_s^{1/2} D}\left[\left(1 - \frac{x_{\rho i}}{x_s}\right)^{1/2} - \left(1 - \frac{x_{\rho r}}{x_s}\right)^{1/2}\right] \qquad 7.129$$

for,

$$\frac{u_c (x_{pi} + x_s)}{\nu_c} < Re_c$$

$$x_{p_i} = \frac{s}{\frac{0.37 s Re_a^{4/5}}{x_{pi} Re_s D}\left\{\left[\frac{(x_s + x_{pi}) Re_s}{s Re_a} - 1\right]^{4/5} + D\right\}} \qquad 7.130$$

$$x_B = \frac{0.37 s Re_a^{4/5}}{Re_s D}\left\{\left[\frac{(x_s + x_{pi}) Re_s}{s Re_a} - 1\right]^{4/5} - \left[\frac{(x_s + x_{pr}) Re_s}{s Re_a} - 1\right]^{4/5}\right\} \qquad 7.131$$

for,

$$\frac{u_c (x_{pi} + x_s)}{\nu_c} \gg Re_c \qquad 7.132$$

$$x_{p_i} = \frac{s}{\left[\frac{0.37 (x_{pi} + x_s)^{4/5} s^{1/5}}{x_{pi} Re_s^{1/5}} + D\right]}$$

$$x_B = \frac{0.37 s^{1/5} x_s^{4/5}}{Re_s^{1/5} D}\left[\left(1 + \frac{x_{pi}}{x_s}\right)^{4/5} - \left(1 - \frac{x_{pr}}{x_s}\right)^{4/5}\right] \qquad 7.133$$

for wholly turbulent flow.

$$D = \left[0.30 \cdot \frac{(1+\theta)}{2}\left|\frac{(1-\theta m^2)}{(1+\theta m)^2}\right|\right]\left[I_3 - (2-m) I_2 + (1-m) I_1\right]\theta \qquad 7.134.$$

$$m = u_m / u_c \qquad 7.135.$$

$$\theta = T_c / T_m \qquad 7.136.$$

$$I_1 = \int_0^1 \frac{f^2(\eta)\, d\eta}{\left[1 + (\theta - 1)\eta\right]} \qquad 7.137a)$$

7.137b)

$$I_2 = \int_0^1 \frac{f(\eta)\, d\eta}{\left[1 + (\theta - 1)\eta\right]} \qquad 7.137b)$$

$$I_3 = \int_0^1 \frac{d\eta}{\left[1 + (\theta - 1)\eta\right]} \qquad 7.137c)$$

$$Re_a = Re_c - \left[322.03\, Re_c\right]^{5/8} \qquad 7.138$$

$$x_c = \frac{2}{(1+\gamma)} \cdot \frac{(1+\gamma\phi)^2}{\left|(1-\gamma\phi^2)\right|}\left\{(b_2)_D\left[\frac{1}{0.31} - \frac{1}{F_i}\right] + (b_2)_{\infty}\frac{1}{F_i}\right\} \qquad 7.139$$

$\tau = T_1/T_2$ where subscripts 1, 2 are defined by 7.140

$\phi = u_1/u_2$ the boundary conditions. 7.141

$$(b_2)_D = \frac{\phi^2}{\tau(1-\phi)(I_2'-I_1'+\phi I_1')} \cdot \left\{ \frac{n}{(n+1)(2n+1)} \left[(\delta)_1 + (\delta)_2 \frac{\tau}{\phi^2} \right] + \frac{1}{2}\delta_W \right\} \quad 7.142.$$

$$(b_2)_0 = 0.724\ (\delta)_2 \quad 7.143$$

$$(b_2)_D = \frac{\phi^2}{\tau(1-\phi)(I_2'-I_1'+\phi I_1')} \left\{ \frac{n}{(n+1)(2n+1)} \left[(\delta)_1 + (\delta)_2 \frac{\tau}{\phi^2} \right] + \frac{1}{2}\delta_W \right\} + \frac{1}{2}\delta_W \quad 7.144.$$

$$(b_2)_0 = (\delta)_2 + 0.5\,\delta_W \quad 7.145.$$

when $C_c u_c = u_m u_m$

For τ and ϕ, $I' = I$.

Solution of these equations is discussed in Appendix A2.

The boundary conditions are:

If,

$\frac{u_m}{u_c} \cdot \frac{T_c}{T_m} < 1.0$, $\tau = T_m/T_c$, $\phi = u_m/u_c$

$\frac{u_m}{u_c} \cdot \frac{T_c}{T_m} > 1.0$, $\tau = T_c/T_m$, $\phi = u_c/u_m$

$\frac{u_m}{u_c} \cdot \frac{T_c}{T_m} = 1.0$, with $\frac{u_m}{u_c} < 1.0$, $\tau = T_c/T_m$, $\phi = u_c/u_m$

$\frac{u_m}{u_c} \cdot \frac{T_c}{T_m} = 1.0$, with $\frac{u_m}{u_c} > 1.0$, $\tau = T_m/T_c$, $\phi = u_m/u_c$

$\frac{u_m}{u_c} \frac{T_c}{T_m} = 1.0$, with $0.85 < \frac{u_m}{u_c} \leq 1.0$, $\tau = T_c/T_m$, $\phi = 0.85$, $m = 0$

$\frac{u_m}{u_c} \cdot \frac{T_c}{T_m} = 1.0$, with $1.0 \leq \frac{u_m}{u_c} < 1.5$, $\tau = T_m/T_c$, $\phi = 1.5$, $m = 1$

Collectively termed, 7.146

The solution of the integral equations 7.137 is given in Appendix A2. A flow diagram and listing of a computer program to solve the complete set of equations from 7.27 to 7.146 inclusive is also given in this appendix.

Appendix A3 discusses the principle of flow similarity and relates the general to the particular of the present problem, enabling the thermal

potential core lengths to be found under certain circumstances.

.....

CHAPTER 8.

DESIGN AND CONSTRUCTION OF A FILM COOLING WIND TUNNEL.

8.1.0. Introduction.

To test the theory developed in Chapter 7 and to provide information on film development and effects of various design parameters, a suitable test facility was required. A wind-tunnel was designed to satisfy these purposes.

The wind tunnel is a horizontal, subsonic, open return, closed rectangular working-section, suction-type tunnel with a secondary air supply to blow a slot in the front floor of the working section, for the purpose of simulating film-cooling. The tunnel was designed to be extremely flexible in capability to permit aerodynamic, adiabatic-wall and, heat transfer studies to be carried out in the one facility. The main aim of the project was to study the effects of injection geometry on the film cooling process and this required an additional variability in the slot configuration. The resulting design required some compromises to be made to the usual standards of wind tunnel aerodynamics, but produced a compact, multi-purpose facility capable of extremely wide variation of all the necessary parameters. An unavoidable penalty was incurred in mechanical complexity which has caused some difficulties in manufacture.

8.2. General Description.

Certain basic considerations governed to a large extent the overall layout and many of the design descisions taken.

In the building in which it was intended to house the facility, there was a limitation on the electrical supply bus-bars of 15 horse - power equivalent. It was decided that the wind tunnel fan therefore, should not absorb more than 12 horse-power at maximum speed. The investigations were to be made for subsonic flow and a maximum, (to avoid compressibility effects), mainstream velocity of 250 ft./sec. was chosen as acceptable. Because of instrumentation size problems, the minimum height for a slot was taken as 0.25 inches and since at least three slot heights were desirable, the maximum slot height was fixed at 0.75 inches. For the film to be effectively two-dimensional along its centreline, a slot width to height ratio of at least 8 was considered necessary. Thus, for the maximum slot height, a duct width of 7 inches was chosen giving a ratio of 9.34 : 1. The maximum height of the duct was then fixed by the maximum mainstream velocity, the fan power limit and the duct width, a resulting value of 5 inches for the conditions described. The length of the working section had to be a compromise between the ability to acquire the maximum amount of information, a basic overall size limitation posed by the space available, and, the length within which the injected film could be considered two-dimensional. A final working section length of 36 inches was selected and all slot geometry changes were to be accommodated within this length.

Due to severe building-space restrictions, it was clear that only one facility could be accommodated and this must perform all the aerodynamic and heat transfer functions required. Interchangeable floors for the working

section were thus determined from the beginning and the main geometry changes in slot configuration had to be engineered around a moveable floor, so resulting in location problems which ultimately led is the "Meccano-set" system to be described later.

The experimental programme envisaged was large and it was clear that as much as possible of the data acquisition and handling should be automatic to permit the work to proceed within an acceptable time-scale. Instrumentation was therefore considered in relation to a data-logging system. Thermocouples in an adiabatic wall, as opposed to other approaches, were considered necessary for describing the results of coolant injection to be compatiable with the data-logger. As hot-wire anemometers were in any case necessary to acquire measurements of the turbulence parameters, they were also chosen as the means of measurement for velocities; the whole system was to be designed to function in conjunction with a data-logger. It was anticipated that some time and effort would be necessary in proving this instrumentation but it was felt that there would be an ultimate saving in time once the programme was commenced. In the event, considerable practical difficulties were encountered with this system of velocity measurement, resulting in accuracy and repeatability problems. These are briefly alluded to in Appendix A4. For the present tests, a manual approach was used with boundary layer-type total pressure probes.

Use of an adiabatic wall to characterise the injection process implies a suitable temperature difference between injected and main-streams. As a matter of convenience and cost, it was decided to heat the injected stream only. The problem under investigation then becomes one of film-heating

rather than film-cooling but the two problems are similar provided the actual streams temperature difference is not too large.

The final design of the facility is described in detail below; brief mention is made to all the options available for the sake of completeness although not all are used in the present work.

8.3. Detail Description.

A schematic drawing of the facility layout is given in figure 8.1, from which the main components can be identified.

8.3.1. Intake.

The intake to the tunnel is in the form of a bellmouth of maximum width in a plane normal to that of the required two-dimensionality, and equal to 1.8 times the maximum width in the same plane of the tunnel, with a lip radius equal to one half the difference between the half width of the bellmouth and the maximum half-width of the tunnel. In the throat of the bellmouth at a distance of 0.25 inches from the commencement of parallel walls, four static pressure tappings of 0.020 inches in diameter are symmetrically disposed and connection is made to a piezometer ring round the rear of the bellmouth. The bellmouth lips were manufactured from lacquered mahogany mounted on a hydulignum support which carried the static tappings.

Two phosphor-bronze, square mesh, plain weave wire screens are provided on a plywood support which is bolted to the rear of the bellmouth support. The first (upstream) screen is of 40 mesh, 34 gauge wires and the second of 60 mesh, 42 gauge wire. The distance between the two screens is 1.0 inch and the second screen is 1.5 inches downstream from the bellmouth throat.

This simple form of intake system was chosen for its ease of removal so enabling additional lengths of ducting to be conveniently added to the working section in order to increase when appropriate, the mainstream approach boundary layer thickness.

8.3.2. Filter.

Surrounding the bellmouth is a low pressure loss filter. It consists of a large 2 X 2 inch wooden-frame box with filtration panels on five of the six sides. The filtration panels consist of two layers of cheesecloth separated by 3/8ths. of an inch, and mounted on removeable frames fitting in foamed-plastic seals in the supporting box. The sixth side is closed-off with a two-piece fibre-board sheet with a cut-out containing a sealed - cell, foamed-rubber ruff which fitted tightly around the wind-tunnel, downstream of the piezometer ring.

8.3.3. Working Section.

The length of the working section is 69.625 inches between flanges and its width is a constant 7.0 inches. The maximum possible depth is 5.0 inches. The roof is of polished 0.25 inches thick aluminium alloy and contains a central, 0.75 inch wide slot of 56.0 inches length, commencing 8.375 inches from the front edge. This slot permits fore-and-aft movement of a traverse gear. A similar but cross-stream, slot permits traverse of the slot outlet for 2.0 inches on either side of the centre-line. When not occupied by traverse gear, both slots are sealed by rolling mats of sealed-cell, expanded Rubazote neoprone X858 of 0.1875 inches thickness, which are

held firmly in position by the pressure difference across them between the atmosphere and tunnel working section. The side-walls allow visual observation of the working-section and are of polished perspex, 0.375 inches thick with 0.75 X 0.0625 inch vertical reinforcing strips at 6.0 inch intervals, cemented in place. These side-walls provide location for a floor and allow this floor to be in one of three vertical positions depending on the slot height chosen. The actual floor location is in 0.25 inch deep slots machined along the inside of the walls. A carefully designed grid-system based on the 'Meccano' set, of accurately located holes is provided within these slots, permitting location of the floor in any fore-aft position on any of the three levels. This system is the key to the polymorphic nature of the tunnel and provided considerable difficulties in manufacture to the necessary standards of tolerance over the not inconsiderable length.

Three alternative and completely interchangeable floors are available, for aerodynamic, adiabatic wall or heat transfer studies respectively. All these floors have the same dimensions of 36.125 inches overall length, 0.375 inches thickness and, 7.5 inches width. Dummy spacer-floors of Adder-brand, high temperature 'Tufnol', are available in assorted lengths to make up the overall working section length depending on the actual position within this length of the particular floor fitted. The aerodynamic floor is of polished aluminium alloy and in its present form, contains 0.0175 inch diameter static pressure tappings along its centreline and, on lines 1.5 inches on either side of the centreline. This floor is also to serve at a later stage in the investigation as a support for Stanton probes to determine wall shear stress laws. Its present purpose is to assist in establishing the extent of flow

two-dimensionality and, the overall pressure gradient. The adiabatic-wall floor is cast in low thermal conductivity, glass-fibre re-inforced, expoxy resin and contains a total of 92 thermocouples placed along the centre-line and along lines 1.5 inches either side of it. On the centreline, 60 of these thermocouples are spaced as follows: 0.25 inch intervals over first 6.0inches, 0.5 inch intervals over next 11.0 inches, 1.0 inch intervals over next 10.0 inches and, 2.0 inch intervals thereafter. Along the other lines, they are spaced at 2.0 inch intervals for the first 26.0 inches, then 3.0 inches and finally, 4.0 inches apart for the remainder of the floor. The thermocouples are made from 30 s.w.g. chromel- constantan 'insuglas' covered wires, and are spot-welded together and cast integral with the floor in a vacuum autoclave. The rear-face of the adiabatic floor is insulated with standard glass-fibre blanket. To reduce conduction from the thermocouple junctions along the connecting leads, these leads are arranged to lie along isotherms for 3 inches from the actual junctions before being led through the rear face of the floor.

The heat transfer floor is very similar in construction to the adiabatic floor but in this case the resin is changed for Araldite HY 750/ HY 906 / DY 062 which is suitable for higher temperatures up to 145^{0}C. The working surface has vacuum deposited on it, a copper film a few microns thick and in electrical contact with steel bus-bars, cast integrally into each end of the floor. The power input to the film is through alternating current, controlled by a variac and in this manner, enables heat transfer studies to be made with a constant heat flux boundary condition. To measure surface temperatures, 45 of the previously described thermocouples are cast integrally in the floor on

the centre-line and on lines 1.0 inch on either side of it. The casting is arranged so that the junctions are immediately beneath the film, but electrically insulated from it; care is taken to avoid A.C. pick-up by the junctions Along the centreline, the thermocouples are spaced as follows, 0.5 inch intervals for the first 6.0 inches, 1.0 inch intervals for the next 6.0 inches and, 2.0 inch intervals for the remainder of the length. At check points, lines of three thermocouples are placed in the thickness of the floor to measure any heat loss through the rear-face, which is insulated with standard glass-fibre blanket. The applied heat flux is measured electronically by watt-meters.

All thermocouples were resistance-checked before and after casting for open circuits, and a 10% sample was calibrated against laboratory-standards mercury-in-glass thermometers in a water-bath, prior to casting.

Only the aerodynamic floor was used for the present series of tests.

Because of the many geometry changes possible within the working section, provision of corner fillets to reduce roll-up of the flow and eventual loss of two-dimensionality, would have been extremely difficult. These were therefore dispensed with and as described above, precautions taken to determine the limit of effective two-dimensionality along the centreline of the working section floor.

8.3.4. Honeycomb Holder.

To prevent swirl from the fan being propagated back into the working-section, a resin re-inforced paper hexagonal honeycomb of $2\frac{1}{2}$ cells per inch, and 3.0 inches length is provided in a constant 7x5 inch section glass-fibre holder, at the rear of the working section prior to the junction piece.

8.3.5. Junction Piece.

A change of section from rectangular to circular was required for entry to the fan. This is provided in a length of 12.0 inches by a constant area glass-fibre junction-piece.

8.3.6. Diffuser.

An increase in duct diameter was necessary for entry to the fan and this is provided in a 3.4:1 area ratio conical diffuser of 8^0 total included angle in a length of 40.3 inches. The diffuser is constructed of glass-fibre and a short, 3.5 inch tailpipe is provided by the sheet-metal intake to the fan. The diffuser bolts between the junction-piece and this tailpipe. Between the flanges of the tailpipe and the diffuser, is a $\frac{1}{2}$ inch thick, soft, sponge-rubber anti-vibration gasket.

8.3.7. Fan.

The fan is a 20 inch Blackman Type 14 high-efficiency blower which absorbs 10 B.H.P at 2,860 r.p.m. against 28 inches water-gauge pressure. It is directly driven by a Brooks D 256 enclosed fan-cooled slip-ring motor which is controlled by an Airedale Type 51G2 starter/speed regulator designed to give a continuously variable reduction in speed down to 40% of the maximum. Additional speed reduction was provided where necessary by throttling the fan discharge. To the motor through a rear wards extension of the driveshaft, is fitted a Record Electrical tacho-transmitter Type ACA2 driving a remote $3\frac{3}{4}$ dial Cirscale tachometer indicator mounted on the regulator casing.

Fan and motor are mounted on a stand of 2x2x0.25 inch mild-steel angle, provided with four adjustable levelling bolts in its base. The fan and

tunnel centrelines are then nominally 52 inches from test-cell floor level. The outlet from the fan is connected to a 15 foot length of 10-inch diameter. Thermaflex flexible ducting which carries away the discharge to avoid immediate recirculation of flow back to the tunnel intake.

8.3.8. Slot Box.

The slot is blown by air from four, water-cooled Whittacker-Hall sliding-vane compressors ganged to supply air at pressure, 11bm/sec. at 50 p.s.i.g., or, more mass flow at lower pressure. From the compressor-house, the air for the slot is ducted to the test-cell housing the facility and enters via a large, pneumatically-controlled gate-valve. In the cell, it is passed to the slot-box first through a 2-inch diameter main containing a Deltech Model 170 compressed air combined cyclone and chemical-element filter with a quoted filtration efficiency of 99.4% for 0.5 micron diameter lubricating oil aerosol. Either side of the filter are isolating valves. Downstream of the downstream isolating valve is a bleed-valve and a 10^0 included angle conical diffuser to a 4-inch diameter main containing an orifice plate and thermocouple in a measuring section designed according to British Standards instruction BS 1042. A 15 kilowatt heater is situated in the main downstream of the flow-measuring section before a convergence down to $1\frac{1}{2}$ inch diameter, and final connection to the slot-box is made through a 6 foot length of double wire braid, butyl-lined and covered, flexible hosing made up with end-fittings by British Ermeto Corp. Ltd.

The slot-box forms a plenum chamber having an expansion ratio of 31.7 : 1 with a length of 4.67 entry diameters, and contains two phosphor-bronze,

square mesh, plain weave screens of 40 mesh, 34 gauge wire separated by 2 inches and situated 2.5 inches from the inlet. A similar screen is mounted in the circular inlet connection. The outlet from the slot-box serves to turn the slot air through an angle of 90^0 for tangential injection and to accelerate it smoothly to the injection velocity. These requirements must be carried out keeping the wall boundary layers thin to give a flat velocity profile at the injection plane, avoiding flow separation or vortex development, and with low turbulence levels. Provision must also be made for changes in slot height and accomodation of other rig geometry changes without compromising these requirements. In practice, the layout of the wind-tunnel together with the geometry changes, dictated the general form of the convergence and sophisticated design procedures were not considered worthwhile. It was eventually decided that the minimum contraction ratio should not be less than 2:1, that the area changes at either end of the contraction should be kept as gradual as possible and, that there should be a small length of constant area flow at the outlet end prior to injection. In the resulting design, the minimum contraction ratio occurs with the 0.75 inch slot height and is 2.66:1; the maximum which arises with the 0.25 inch slot is 8:1
The surfaces forming the contraction were designed from straight lines and circular arcs to simplify manufacture.

The material of the slot-box is Hydulignum, a resin impregnated wood laminate. This was chosen to take advantage of the constancy of contour ensured by bulk, without the problems of permeability and warping due to drying which are present with pure wood. Hydulignum is also a reasonable thermal

insulator and has the precision - machinability of a metal.

The slot-box remains fixed in position and slot height variations are accommodated by interchangeable convergences. The flow areas normal to the walls forming the convergences are given in figure 8.2, and the flow path for the 0.25 inch slot is shown in figure 8.3. The same convergence contours are used for each slot height, but the length of the constant flow-area portion is extended by 0.25 inch steps as the slot height is increased by 0.25 inch increments, to a maximum of 0.75 inches.

The outer contour of the convergence is made in two parts, aerodynamic continuity of the surface being assured by rabbit and dowel location, together with clay-sealing of the remaining hairline crack between the parts. The upper part forms the slot lip and is variable independently of the slot height. The convergence contour remains fixed and thicker lips are produced by moving slightly further out into the mainstream through increased material thickness. Constancy of the main-stream boundary layer thickness whichever lip is used is assured by beginning this layer at a leading-edge formed by the lip-part itself at a distance of 7 inches upstream of its trailing edge, which forms the end of the slot and the injection plane. This leading-edge always stands proud of the tunnel front-floor, which is fixed in position. Three lip thickness of 0.020, 0.050 and, 0.150 inches respectively, were available. The material for the lips was 70/30 brass for ease of machining; a perspex lip of the greatest thickness was made for assessment of effects on temperature profile at injection of the non-adiabatic brass lips.

Other lips were manufactured with extended lengths giving tangential, parallel flow up to 10 inches before injection into the mainstream. These

were for studies on the effects of slot injection profiles. Also available were inserts into any slot, containing wire grids to vary slot turbulence and, metering-hole arrays to simulate practical injection geometries. These however, did not play any part in the present programme.

8.4. Instrumentation.

8.4.1. Traverse Gear.

Access to the interior of the working section was provided through the two slots machined in the roof and described under Section 8.3.3. Accurate traverse perpendicular to the floor at a particular downstream location was provided through a traverse gear. This traverse gear was designed to accommodate a variety of probes with the minimum of trouble, and was also required to provide an accurate normal profile traverse in 0.001 inch steps, holding the sensor always into the flow direction.

The core of the traverse gear was a Moore and Wright 952A/2 micrometer head with 2 inches of 0.001 inch calibrated travel, which could be clamped firmly in any vertical position on a column. The column, a 10 inch long rod of 0.375 inch diameter silver steel, was brazed in a 5.5 x 4.75 inch solid brass pad of 0.25 inch thickness. On the underside of this pad was machined a discontinuous, sliding-fit, 0.25 inch deep tongue running in the roof slot to ensure constant probe direction once mounted. A slot was machined in the pad through which the probe and lower end of the movement travel during operation. Two such pads and column assemblies were manufactured but with the tongues running in directions different by 90^0 to permit travel along the mutually perpendicular roof slots. The common movement was clamped to the

column of whichever pad was in use.

The movement consisted of two short rectangular bars of brass rigidly joined on one side by a 4 inch long brass plate. Two sets of parallel holes were drilled and reamed in these bars, one set being bearing surfaces for the silver steel column. This set of holes was opened to the outer edges of the bars with a fine, milled slot and Allen screws were provided so that this frame for the movement could be firmly clamped in any vertical position on the column. Position above the pad was accurately determined by placing slip-gauges between the pad and the underside of the lower bar. In this manner, the two inches of fine travel were available anywhere across the tunnel height, with accurate positioning.

The remaining hole in the upper bar accommodated the micrometer which was clamped by an Allen-screw closing the hole through a slot, as previously described. The other hole in the lower bar formed a bearing surface for a 0.25 inch diameter silver steel rod which carried the probe from its lower end. This rod was brazed to a floating brass steady bearing off the column, the whole being supported by a spring between the steady and lower bar. The spring stiffness was chosen to support the heaviest probe, (200 grammes), to be used. Movement of the probe-rod was affected through the spindle-pad of the micrometer operating on the upper surface of the steady, and, against the spring. Probes were carried off the lower end of this rod in interchangeable shoes held in place by a grub-screw.

The shoes extended sufficiently far forward that movement did not cause the upper ends of the probes to foul the traverse gear. Shoes were available with housings for DISA 55 A30 and 55 A21 hot-wire probe supports,

and, boundary layer total pressure and static pressure probes. Probes were firmly clamped in the shoes by Allen-screws closing the holes through a slot.

To eliminate leakage through the slot in the pad, the whole traverse gear was enclosed in a perspex pressure chamber 16 inches high, which was screwed with a soft rubber sealing gasket to the pad. To ensure the scales were readable, the whole interior and exterior surfaces of the perspex were polished to provide optical surfaces. Mounted on the chamber are connectors for coupling to whatever probe is fitted in the shoe. Remote operation of the gear is provided by a special screwdriver operating in a slot machined in the top of the micrometer; coarse and fine drives are provided on the screwdriver shaft external to the pressure chamber, through which it passes via a stuffing gland.

For downstream and transverse location of the traverse gear, rules calibrated in tenths of an inch were screwed in the roof of the tunnel, and reference marks scribed on the pad.

8.4.2. Turbulence Measurements.

The layout for the hot-wire equipment is shown in figure A4-1 of Appendix 4. Because of the difficulties encountered and described in that Appendix, this equipment was only used for turbulence measurements and a somewhat simpler set-up was used.

To measure turbulence intensities in the direction of flow and normal to it, DISA 55 A 32 X-array hot-wire probes were used. These were mounted

in a 55 A 30 X-probe Support carried in the traverse gear and fitted with a 55 A 33 X-Probe 90^0 Adaptor. These probes were used in conjunction with a 55 A 34 X - Shorting Probe. For the abortive velocity measurements, 55 A 25 Miniature Hot-Wire Probes were used, in a 55 A 21 Miniature Probe Support with a 55 A 28 Miniature 90^0 Adaptor. A 55 A26 Miniature Shorting Probe was used with these.

For the turbulence measurements, two DISA Constant Temperature 55A01 Anemometers were used together with one DISA 55 A06 Random Signal Indicator and Correlator. The output signals were monitored on a twin-beam Solartron Oscilloscope.

8.4.3. Static Pressure Measurements.

Wall static tappings were located in the wind tunnel aerodynamic floor and, side wall in the plane of the slot outlet, as indicated in Section 8.3.3. The diameter of these tappings are 0.0175 inches in the floor and, 0.020 inches in the wall. The floor tappings were connected to a multi-tube, tilting-board water manometer, and the wall tappings to a 6-position pressure selector switch which led to a Betz-type projection water manometer.

The static pressure field in the injection plane was surveyed using a static pressure probe in the traverse gear. This probe was based on that used by Trentacoste and Sforza (136) and is shown in figure 8.4.

8.4.4. Total Pressure Measurements.

A standard boundary layer-type total pressure probe was used in place of the hot-wires, to measure profiles in the film. It was similar to that used by Hartnett et al (8) and the design is shown in figure 8.5. Read-out

was on a Betz-type manometer.

A pyrometer was adopted from the same design by inserting a thermocouple junction just indide the intake. The forward-facing tube was opened at its rear-end to allow through-flow of air past the junction and, passage for the leads.

The total pressure probe, static pressure probe and pyrometer, were all made the same length and had an identical collar at the upper end for mounting in the shoe of the traverse gear.

8.5. Visual Presentation.

The test facility is illustrated in a series of photographs, figures8.6 to 8.14 inclusive.

Figure 8.6.

A general view of the rig from the rear. From left to right are the transition piece, honeycomb holder, working section with traverse gear, and, slot-box and filter.

Figure 8.7.

View of bellmouth intake from inside filter box with side panel removed. The gauzes and piezometer ring can clearly be seen. Visible also are the rubber collar around the intake, and, the cheese-cloth filter panels.

Figure 8.8:

A close-up of the injection plane showing the convergence, interchangeable slot-lip, "Meccano" hole system in the side wall, aerodynamic floor, wall statics and, in the roof, the traverse slots.

Figure 8.9:

Tunnel roof showing the traverse gear. The rule for downstream location can be seen together with the rubber mats for sealing the slot. On

the perspex pressure chamber can be seen the stuffing gland for the screw driver remote drive, and, electrical and pressure connections. Fine and coarse drives on the screw driver shaft are visible.

Figure 8.10:

A close up of the traverse gear showing micrometer, column, and movement with steady, spring, carrying rod and shoe. Mounted is a 55 A 30 X-Probe Support.

Figure 8.11:

View of traverse gear showing fixture of pressure chamber to pad. Mounted is a 55 A 30 X-Probe Support with a 55A33 X-Probe 90^0 Adaptor carrying a 55 A 32 X-array probe.

Figure 8.12:

Total pressure , static pressure probes and, pyrometer, showing common collars.

Figure 8.13:

Close up of probe heads, left to right, pyrometer, static pressure probe and, total pressure probe.

Figure 8.14:

Turbulence measuring equipment.

.....

CHAPTER 9.

CALIBRATION AND CHECK-OUT OF THE TEST FACILITY.

9.1. Calibration.

9.1.1. Slot-Flow Measuring Section.

The slot flow was measured by a 2.9420 inch, square-edged orifice plate in a 4 inch diameter standard measurement section designed according to British Standards, Flow Measurements, BS.1042. Static pressure taps are 0.10 inches in diameter, situated 4 inches upstream and, 1.5 inches downstream, of the plate: A thermocouple on the centreline is provided 15 inches upstream. The 2 inch diameter main from the filter is joined to the 4 inch diameter measuring section by an 8.25 inch long diffuser at a distance 30 inches upstream of the orifice plate. Following the plate, the measuring section is straight for 18 inches and then has a 90^0, circular arc elbow, the outlet from which leads into the heater, also of 4 inches diameter. A gauze screen is provided at the flange of the elbow and heater.

The orifice was calibrated according to recognised British Standards practice, by diametral traverses with an NPL pitot-static tube across the open outlet of the heater, with the elements removed. The resulting calibration curve is shown in figure 9.1.

Prior to installation and, calibration of the orifice plate, the measuring section thermocouple was calibrated in a water-bath against the laboratory standards mercury-in-glass thermometers. This calibration is given in figure 9.2.

9.1.2. Bellmouth Intake.

For convenience in setting-up a test-point, the bellmouth intake piezometer ring was calibrated against the total pressure probe which was

positioned clear of the mainstream boundary layer and, in the injection plane. The calibration curve is shown in figure 9.2.

9.2. Check-Out.

9.2.1. Leaks.

A thorough check was made for leaks using a soap solution brush and spray. Leaks on the pressure side were sealed with a silicone-rubber compound, and, plasteraine, and on the vacuum side with vacuum wax. Periodic leak checks were made as part of routine rig maintenance and, following upon any geometry changes.

9.2.2. Downstream Static Pressure Gradient.

The static pressure gradient downstream along the aerodynamic floor centreline in the working section for various blowing rates and mainstream velocities was measured using the floor statics which were conducted to a multi-tube, inclined board manometer at an angle of 20^0. A sample of the plots obtained is shown in figure 9.4. It was concluded that the pressure gradient was effectively zero.

9.2.3. Transverse Static Pressure Gradients in the Injection Plane.

Static pressure traverses on the rig centreline were made in the slot and, on the slot lip, and compared with the wall static readings in the injection plane. To illustrate these, typical comparisons are shown in figures 9.5 and 9.6. It can be seen from figure 9.5 that as the blowing is increased, a gradient across the slot is set up. However, it is small and can be considered negligible, particularly since the comparisons are made directly on the basis of gauge pressures. Figure 9.6. shows that there are significant transverse static pressure gradients in the mainstream.

With these two conclusions, the wall static tappings may be used in conjunction with the total pressure probe to calculate centreline velocities in the injection plane. Using check static tappings provided in the floor on either side of the centreline, no significant transverse pressure gradients were found at downstream locations, either.

Detailed consideration is given to transverse pressure gradients in the flow field immediately downstream of the slot-lip. Static pressure traverses normal to the floor were made on, and 2.075 inches either side of, the centreline at a station 0.61 inches downstream from the slot lip. Traverses were made for several injection conditions and with the three lip thicknesses. No gradients of any significance were found. Examples of these traverses, for the thinnest of the lips, are shown for different injection conditions, in figures 9.11 - 9.13 inclusive.

9.2.4. Normal Static Pressure Gradients at Downstream Locations.

For calculation of velocities in downstream profile traverses, it was desired to use the static tappings in the working section aerodynamic floor. In order for this to be valid, there must be no normal static pressure gradients. This was tested by comparing centreline, normal traverse and, floor static gauge pressures, at different stations for different injection conditions.

Some results of these comparisons are given in figures 9.7 to 9.10 inclusive. Figures 9.7 and 9.10 show that use of the floor static tapping

is permissible at all distances from injection for wide blowing rate variation when the mainstream velocity is high. For low mainstream velocities and low blowing rates, use is acceptable but the discrepancies do increase with increasing distance from injection. For low mainstream velocities together with high blowing rates, the discrepancies between the traverse and the wall static become relatively large; the distance effect is not so noticeable however. Because the comparisons were made on the basis of gauge pressures and, because the investigations were to be concerned primarily with near-field film measurements, use of the floor statics in conjunction with the total pressure probe was considered acceptable.

The figures show a probe pressure which is always greater than the floor pressure, even when the probe is on the floor surface. Since it is relatively easy to measure wall static pressures, it must be therefore assumed that some defect exists in the static probe. As the pressures used are gauge pressures in a suction-tunnel, this supposed defect cannot be the pick-up of some dynamic head, which is a common fault with static probes.

9.2.5. Two-Dimensionality of Velocity in the Injection Plane.

Figures 9.11 to 9.13 inclusive, indicate that flow in the injection plane should be two-dimensional. The two-dimensionality was checked with total pressure traverses on the centreline and on either side of it, at a distance of 0.33 inches downstream of the lip.

Some of the calculated velocity profiles are shown in figures 9.14 to 9.17, for the thinnest of the lips, (δ_w = 0.055 ins). These figures verify the two-dimensional nature of the flow with for the injection conditions shown,

maximum deviation from centreline velocities of 5 ft./sec. in the mainstream and 4 ft./sec. in the slot flow: This is across the central 4.15 inches of the tunnel. For the mainstream, a slight peak in transverse velocity profile occurs; the slot profile is almost completely flat in the transverse direction.

The traverses also demonstrate the flatness of the slot velocity profile for both high and low blowing rates.

9.2.6. Check on Tunnel Overall Performance.

An assessment of the tunnel overall performance was made by operating it as a normal facility with zero blowing, and measuring velocity profiles at downstream locations. If there are no tunnel peculiarities, profiles should be obtained which agree with the classical universal velocity profiles obtained for turbulent boundary layers.

Velocity profiles were measured at two downstream locations, 28 and 34 inches downstream from the slot lip. A Clauser plot (137) was constructed by plotting the measured profiles in the form of u/u_G against $\log_{10}(u_G y/\nu)$ over a grid of constant skin friction coefficient c_f, which were calculated from:

$$u/u_G = \sqrt{c_f/2} \cdot 4.9 \log_{10}\left(\frac{u_G y}{\nu}\sqrt{c_f/2}\right) + 5.9\sqrt{c_f/2} \qquad 9.1$$

This plot is shown in figure 9.18, from which it can be estimated that,

at $x = 28.0$ inches, $c_f = 0.0012$

and,

at $x = 34.0$ inches, $c_f = 0.00225$

The measured velocity profiles were recalculated using these values in the form of U^+ and y^+, defined as,

$$u^+ \equiv \frac{u}{\sqrt{\frac{\tau_s}{\rho}}} \quad ; \quad y^+ \equiv \frac{y\sqrt{\tau_s \rho}}{\mu} \qquad 9.2$$

The wall shear stress τ_s, values were found from the definition,

$$\frac{c_f}{2} = \tau_s / \rho u_\infty^2 \qquad 9.3$$

The particular version of the universal velocity profile chosen was that of Von Kármán (1939), which has the form:

$$0 \leq y^+ \leq 25 \quad , \quad u^+ = y^+ \qquad 9.4a)$$

$$5 \leq y^+ \leq 30 \quad , \quad u^+ = 5 \ln y^+ - 3.05 \qquad 9.4b)$$

$$30 \leq y^+ \qquad u^+ = 2.5 \ln y^+ + 5.5 \qquad 9.4c)$$

This profile is plotted in figure 9.19, and compared against the experimental data.

It can be seen from figure 9.19 that although there is some scatter, the data agree tolerably well with the profile represented by equation 9.4, at least to a value of $\ln y^+$ of about 4. This represents the inner regions of the layer, including the viscous sub-layer, the transition layer, and part of the main region. Departure from the universal profile occurs at large y^+ and represents the wake part of the boundary layer. The amount and direction of the departure from the universal profile in a free-stream, (present case is duct-flow), in the wake region depends on the pressure gradient, deflection upwards indicating an adverse pressure gradient. (The traverses were taken towards the rear of the working section which was followed by a honeycomb and diffuser. In addition, with the 0.25 inch slot fitted, there was a 0.5 inch step-down at the rear of the working section). Spalding's two-parameter profile (35) shows departures from the log-law for

values of $\ln y^+$ greater than 3.8, which is in agreement with the present results.

9.3. Conclusions.

The very careful checks on the facility reported in this chapter, indicated that all was satisfactory with the tunnel performance, and that the test programme could proceed.

.....

C H A P T E R 10.

TESTING AND TEST RESULTS.

10.1 Test Procedure.

10.1.1. Set Up (Velocity Profile Measurement.)

The slot lip fitted was measured at three stations distributed across its width and the arithmetic mean lip thickness determined. The slot height was measured in situ with slip gauges, again in three locations equally spaced across the slot width.

The pressure probe was fitted in the traverse gear and the traverse gear movement set with slip gauges so that the two-inch calibrated traverse was available where required. Setting the probe sensing-head on a level with the slot lip, the traverse gear was moved forward in the roof central slot so that the head just touched the lip. The zero on the longitudinal scale was then noted by the scribe-mark in the traverse-gear pad. To obtain the normal zero on the micrometer scale, the gear was operated such that the bottom of the probe just touched the working section floor. Thickness of the probe was checked with a micrometer, prior to installation.

Illumination of the Betz-type projection micro-manometers was switched on, the manometers levelled and after due period for thermal stabilization, the zeros were set. Zero levels of the multi-tube and U-tube manometers were taken after levelling.

Vacuum bottles holding the thermocouple cold-junctions were filled with freshly crushed melting ice and, water, and were sealed.

The pneumatic gate-valve into the test-cell was opened fully, as were the isolating valves on either side of the filter and, the bleed valve. The

electrical isolator-switch was thrown, the fan-motor regulator set to idle (about 120 R.P.M.) and the fan started. Depending on the slot mass flow rate required for the test, the requisite number of Whittacker-Hall compressors were started in the compressor house and set to give approximately the right flow. The inter-and, after-coolers of these compressors were set to give delivery at a constant temperature of 15^{0}C. The bleed valve was partially closed to divert flow through the rig, and a warm-up period of 30 minutes allowed for the rotating machinery. During this period the oil drain valve on the filter was left open to blow out any residual deposits from the previous test.

When steady conditions were observed the oil drain valve was closed and the fan speed adjusted to give the correct bellmouth pressure drop for the mainstream velocity required in the test. The bleed-valve was adjusted to set the required slot flow. Atmospheric pressure and temperature were recorded at an adjacent barometer.

10.1.2. Test Run (Velocity Profiles).

The traverse was conducted in 0.020 inch steps in most cases. Total pressures were indicated in millimeters of water gauge pressure on a Betz-type projection micrometer.

In the injection plane, the wall statics were used in conjunction with the total pressure probe. The tappings led to a 6 - point rotary pressure switch which was connected to a further Betz-type micromanometer. The tapping nearest to the probe position was used, and a reading was taken every 10 traverse points. For downstream traverses, the nearest floor static was

read, again on a Betz-type micromanometer, at the beginning and end of a traverse.

The slot-flow temperature was taken as being equal to that at the orifice station, and was read from that thermocouple. Mainstream temperatures were found by an unshielded mercury-in-glass thermometer inserted at the traverse station through the roof traverse slot, with the bulb extending to the centre of the working section. Readings were taken at the commencement and end of a traverse at the station.

The barometric pressure and ambient temperature were read at the beginning of each normal traverse.

The normal zero on the traverse gear was found anew for each downstream traverse station.

A continual monitoring of the bellmouth pressure drop, fan R.P.M. and orifice plate flow function, $(\rho \Delta P/T)^{\frac{1}{2}}$, and, slot-flow temperature, was carried out.

A near-field velocity profile survey suitable for determination of the hydrodynamic potential core length was found to take of the order of 7 hours, excluding set-up, warm-up and shut-down, periods. For this reason, a number of tests were conducted where complete velocity profiles were interspersed by "half-profiles" where just sufficient data were gathered to cover the inner edge of the developing mixing layer. By this method it was possible to cover two test-points in one working day.

10.1.3. Set Up and Test Runs (Turbulence Profiles).

The traverse longitudinal zero was established with the shorting probe fitted in the holder in place of the hot-wire, and the first downstream station set. This was to avoid possible damage of the delicate wires on the slot lip. The normal zero of the traverse was set as described under Section 10.1.1.

All electronic equipment was turned on and allowed to warm up, after checking and adjusting zeros. Manometers and other instrumentation in use were set as previously described.

The hot-wire anemometers were checked, set and balanced according to maker's (DISA) recommendations. The shorting probe was replaced by the hot wire probe and the wire resistances measured. The wire overheat ratios were set by setting 1.5 times the measured probe values on the anemometer resistance decades. (Ambient temperature was taken into account at this stage by measuring the Bridge DC volts at zero velocity.)

The wind-tunnel and slot flows were set up as described in Section 10.1.1. When the test point was established, the anemometers were switched from 'Standby' to 'Operate' and the Bridge-voltmeter set to a sensitive range by adjusting the meter range together with the voltage suppressor. The R.M.S. voltmeter on the correlator was set in a protective range and the A and B signals from the two anemometers switched-in, in turn. A suitable voltage range was set. The suitability of this range was verified for the A+B and A-B signals generated within the correlator. The A and B signals from the anemometers were monitored on the twin-beam oscilloscope, whilst the A and B signal DC Bridge-volts and, the A+B and A-B R.M.S. volts were recorded.

Normal traverses at different downstream stations were taken, as described previously for the velocity profile traverses. A complete survey could be made in two hours.

10.2. Scope of Tests.

Since difficulties arise concerning the validity of scaling laws for film cooling and as the complete range of aero-thermal parameters for a practical case could not be simulated, the aim was to establish the efficacy of the theory for potential core over as wide a range of parameters as possible. When sufficient confidence has been accummulated in a theory by such an approach, it may be applied with a fair expectation of success to other, untested, situations.

A total of 60 test points were run, excluding rig development, and represented some 322 hours of testing. A few turbulence profile runs were made, but the majority of the tests were run for velocity profiles from which the hydrodynamic potential core could be determined. Due to external committments which restricted the total time available for the experimental study, the scope of the test programme had to be narrowed down considerably. At the time, it appeared that lip thickness was a most important geometrical parameter so the investigation was concentrated in this area.

Tests were run with a constant slot height of 0.25 inches nominal dimension, and three lip thickness of 0.050, 0.100 and, 0.150 inches, nominally. These lips gave values of lip thickness to slot height ratio in the range $0.2 \leqslant \frac{\delta_w}{s} \leqslant 0.6$, which covers current practical, slot design

values. The value of slot height was the nearest to current (U.K.) big engine practice and in view of the 'scale' effect shown in figures 2.18 and 2.19, seemed appropriate.

Three levels of slot Reynolds number were chosen, 9,500, 15,000 and, 23,000 respectively, to represent the complete range likely to be encountered in modern high-pressure engines. In view of the comments made in Chapter 6 on entrainment, it was felt that to present an adequate picture, tests at a given Reynolds number should be made over as wide a range of injection velocity ratio as possible. The total range of velocity ratio was $0.17 \leqslant u_m/u_c \leqslant 1.5$ over the Reynolds number range, but due to power limitations and the high losses associated with the intake filter and gauze screens, this could not be covered for each of the Reynolds numbers.

The tests reported here were all made in what was effectively isothermal flow. Mainstream boundary layer thickness was proportional to mainstream velocity and was generally of the order of one third of a inch in thickness. Some tests were made with thickness up to one inch, and, one down to 0.03 of an inch.

10.3. Test Results.

The tests carried out are summerized in Tables 10.1, 10.2 and, 10.3. Assistance with testing for runs 53 to 77 was kindly provided by H. Patel. The velocity for slot Reynolds number is based on the plateau value in the injection plane. Boundary layer thicknesses are taken where the local velocity equals 99% of the maximum. Mainstream and coolant velocities, u_m and u_c respectively, were taken outside the boundary layers. The velocity $\bar{u}_c$ is based on the equation of mass conservation.

The tables also contain statements of measured and predicted core lengths, non-dimensionalised in terms of slot height. A complete tabular presentation of all the data collected would be impossibly bulky. Representative data only is therefore presented in a graphical form. A constant slot velocity around 70 ft./sec. is chosen and graphs of downstream film development are presented. For this presentation values of injection velocity ratio less and greater, than unity for each of the slot lip thickness are used, except for the largest of the lips, where only half-profiles were taken for most of the tests. Figures 10.1, 10.2 and 10.3 are for the 0.0550, 0.0995 and 0.1525 inch thick lips respectively. In figure 10.4, profiles for injection at near-unity velocity ratio from the thin-lipped slot are given. Together, these figures illustrate the type of the measurements taken and show representative film development.

For all the lips, injection at $u_m/u_c < 1.0$ produces film development characteristic of wall jet-like flow and, injection at $u_m/u_c > 1.0$ produces wake-like development. The finite thickness of the lip introduces a deficit into the profile, which is evident whatever the injection velocity ratio. As the flow proceeds downstream this deficit is progressively filled by turbulent mixing. Generally, the deficit is filled relatively quickly. With increasing lip thickness, no significant change in the profiles is apparent. With almost unity velocity ratio however, even for the thinnest lip, the deficit exists for many slot heights downstream.

Measurements of the hydrodynamic potential core length are made by plotting from the velocity profiles in the manner described above, the loci

of the points on the inner-edge of the mixing layer and, the outer-edge of the wall boundary layer. The plots for each test run are shown in figure 10.5. The theoretical equation derived in Chapter 7 showed that except in the region of flow round a substantial lip, the spread of the inner edge of the mixing layer is linear with distance from the lip. Consequently, a straight line is used to join these points; the best curve is drawn through the points marking the edge of the wall boundary layer. Where these two lines intersect is taken as the end of the potential core. It can be seen and appreciated that measurement of potential core is not a precise procedure and a plus or minus one slot scatter band is therefore attached to the measurements.

In figures 10.6 and 10.7 are shown turbulence profiles obtained with the 0.0550 and 0.0995 inch lipped slots. The results are for two injection conditions, with $u_m < u_c$ and, $u_m \simeq u_c$.

Turbulence intensity is plotted as a percentage of the local x-direction velocity. For flows past a solid boundary, it is usual to reference the fluctuating component of velocity to the friction velocity u^*, since the entire velocity profile existing must depend on the local rate of energy dissipation and therefore, on the flow in the viscous sub-layer. The viscous sublayer is defined by a Reynolds based on the friction velocity, which is defined as $\sqrt{\tau_s/\rho}$. Such a characteristic velocity for a defect-type distribution is less easily identified. The present profiles are referred to the local u, largely for convenience and in the absence of a suitable alternative.

It can be seen that the slot turbulence is homogeneous of intensity around 4.0%; the mainstream turbulence is also homogeneous at about 1.2%. In the remenants of the mainstream boundary layer which forms the outer part of the mixing layer, the suppression of the normal fluctuating velocity

component by the upper surface of the slot lip is evident. A peak of turbulence is formed in the wake downstream from the lip, and decays with increasing distance from the lip. When the mainstream and coolant velocities are very nearly equal, the turbulence decays much more rapidly than otherwise. This behaviour accounts for the prolonged existance of the wake at unity injection velocity ratio. Whatever the velocity ratio the normal component of the fluctuating velocity in the wake decays more rapidly than the longitudinal.

Measurement from additional tests is presented under appropriate section headings in the following Chapter where the results are analysed.

.....

CHAPTER 11.

ANALYSIS OF RESULTS.

11.0. Test of Assumptions in Potential Core Theory.

The developing film from a slot has been mathmatically modelled in terms of a potential core length, and a theory derived to predict the extent of this region. A number of assumptions were necessarily made during developmen of the theory. The validity of these assumptions must be established as a preliminary to using the theory for prediction purposes. Not least of the things to be proved, is the physical existance of the core itself.

11.1. Existance of the Potential Core Region.

The substance of the present approach to film cooling is that from the injection plane, and between the growing boundary layer on the cooled wall and the inner edge of the mixing layer developing from the slot lip, the flow is of constant velocity. This constant velocity flow is conditionally termed potential because the initial turbulence there is considerably less than the turbulence arising in the mixing layer.

Substantial evidence of an indirect nature was obtained in Chapter 4 where successful correlation of effectiveness data was obtained by introducing the thermal potential core in the blowing groups S_N and S_{N_2}. Consideration of the shapes of the velocity profiles shown in figures 10.1 to 10.3, suggests the hypothesis does indeed have some foundation in fact. The turbulence profiles of figure 10.6 and 10.7 show an initial region where intensities remain close to the initial slot values. Turbulence from the mixing and,

wall boundary, layers does not diffuse completely across the film for some distance downstream from injection. This is also in keeping with the existance of a potential core.

By definition, within the potential core,

u = constant = u_c and, $\frac{\partial u}{\partial x} = 0$

For the confined flow which forms the potential core, the condition $\frac{\partial u}{\partial x} = 0$ obviously cannot be exactly satisfied since both the cooled wall boundary layer and the mixing layer, entrain mass from this flow. Within the relatively short distance of the core however, it is substantially valid to make this assumption, as is shown in figures 11.1, 11.2 and 11.3, where it may be seen that for all the tests, $\partial u/\partial x \simeq 0$ and u_c is not less than 95.5% of the injection value, at the end of the core, with due allowance for some test scatter. These figures were constructed by dividing the maximum velocity just outside the wall boundary layer, by the value at injection, and plotting against downstream distances expressed in terms of the measured potential core length obtained from the appropriate plot in figure 10.5.

The conditions of velocity profile, turbulence structure, velocity gradient and, constancy of velocity being satisfied, it must therefore be concluded that all the assumptions regarding the existance of a potential core as described, are justified and the reality of the core is established. The measurements made in figure 10.5 thus do describe a real, physical phenomena.

11.2. Similarity of Mixing Layer Velocity Profiles.

The theory given in Chapter 7 considers that the free, turbulent flow, mixing layer developing from the slot lip can be of two forms;

an idealised shear layer of zero starting thickness and, a wake flow arising from the separated flow region which exists immediately downstream of a real lip. For the velocity profiles, Schlichting's two- dimensional, isothermal wake theory was used and expressed as equations 7.47 and, 7.45b).

Consideration of the form of the profiles shown in figures 10.1 to 10.4 reveals that both wake and shear-flow component forms of velocity profile can be exhibited in the same test. For the wake profiles, the profile is divided into inner and outer portions by the minimum of the velocity defect and equation 7.47 applied as follows:

for the inner layer, $$\frac{u_c - u}{u_c - u_{min}} = f\left(y/b_c\right) \qquad 11.1$$

for the outer layer, $$\frac{u_m - u}{u_m - u_{min}} = f\left(y/b_m\right) \qquad 11.2$$

where,

b_c, b_m are the respective thicknesses of the inner and outer layers, and, u_{min} is the minimum velocity in the defect. For the pure shear profiles, equation 7.47 was applied as,

$$\frac{u_1 - u}{u_1 - u_2} = f\left(1-\eta\right) \qquad 11.3$$

where,

subscripts 1 and 2 were applied to coolant or mainstream according to the velocity ratio at injection.

In figure 11.4 are shown examples of shear-type universal velocity profiles for the thin-lipped slot; shown also in this figure is equation 7.47. Profiles for both jet-like and wake-like flows, taken at different downstream stations are given. It may be seen that when plotted in this form, the profiles are similar and, that the equation 7.47 does satisfactorily represent them.

Wake-type profiles in similar form are shown in figures 11.5, 11.6, and 11.7, for the thin-lipped slot. Both jet-like and wake-like flows are represented by profiles taken at downstream distances ranging from 0.5 inch from the lip, to 5.0 inches. All three slot Reynolds number ranges are covered. When the data are plotted in the form of equations 11.1 and 11.2, the profiles are similar and, equation 7.47 which is also given, is seen to adequately represent the data. Similarity is established at least as close as two slot heights downstream from the lip.

The assumptions made in Chapter 4 concerning the universality and form of the mixing layer profile are seen to be valid for the thin-lipped slots where the ratio of lip thickness to slot height is 0.2146.

The implicit assumption is made in Chapter 4 that the similar profiles were also held regardless of slot lip thickness to height ratio.

For the intermediate thickness lip where the ratio of lip thickness to slot height was 0.379 for a 0.0995 inch thick lip, the profile traverses were restricted to the near flow-field. Consequently, because of the enlarged width of the velocity defect, no pure shear-type profiles were obtained. Wake profiles were obtained.

In figures 11.8, 11.9 and 11.10, wake profiles for three injection velocity ratios in the 9,000 range slot Reynolds number are shown. A somewhat complex pattern is seen which however, can be interpreted as following a logical sequence: For the outer layer, similarity and good representation by equation 7.47 is seen to be established for all velocity ratios by 1.25 inches or 5 slot heights, downstream from the lip. For the inner layer, the position of establishment of similar profiles and representation by equation

7.47 depends on injection velocity ratio. The distances to representation increase with increasing velocity ratio being 1.25 inches for u_m/u_c =0.5075, 2.25 inches for u_m/u_c = 0.9073 and, greater than 2 inches for u_m/u_c = 1.4257. The dependency on velocity ratio can be attributed to flow round the lip, as described in Section 7.47.

Figure 11.11 tells an exactly similar story for the 15,000 slot Reynolds number range at a velocity ratio of 0.7946, the outer layer profiles are similar by about 0.75 inches and, the inner at 1.5 inches downstream; which are in agreement with the lower Reynolds number results.

The majority of the runs carried out, with the thickest (0.1525 inch) of the lips were the 'half-traverses' described under Section 10.12 and, only limited full velocity profiles were obtained.

Only a single ideal shear layer-type profile was obtained and this is shown in figure 11.12 together with equation 7.47, which is seen to be a good representation of the data. This profile was taken at 1.0 inch downstream from the lip, at a slot Reynolds number of 22,652 for a velocity ratio of 0.2303. That a shear layer-type profile is obtained so close to the slot is explained by the high rate mixing due to the injection conditions. These injection conditions are such that even allowing for the increased lip thickness, from the previous data in figures 11.8 - 11.10 inclusive, similar profiles could be expected reasonably close to the injection plane.

Figures 11.13 - 11.15 inclusive, present examples of wake-type similar profiles obtained for the thick-lipped slot. It can be seen that similarity and reasonable agreement with the equation is obtained in the outer layer of the wake by 1.0 inch from injection fortthe low-rate mixing case shown in

figure 11.3. Rather surprizingly, the inner layer appears similar by 0.5 inch from injection with again, reasonable agreement with the equation. The similarity of the inner layer for the high-rate mixing cases of figures 11.14 and 11.15, by 0.5 inch from injection, is to be expected from the previous data pertinent to the other lips.

For the thick lip, the outer layer of the wake appears to be but poorly represented by the chosen universal velocity profile. This could be explained by some changes in the upstream boundary layer flow inherited by the potential core field. Such changes could arise from the manner in which the lip thickness was varied - by changing the combined lip, slot inner contour and, approach plate, as described in Chapter 8. The approach velocity profiles are examined in a later section of the present chapter.

It may be seen from figures 11.4 through 11.15, that the assumption of a similar velocity profile in the wake and pure shear parts of the developing film, and, that such a universal form applies over the whole of the considered region, is substantially true except for the limitations pointed out above. Where the profiles are similar, the assumed form, equation 7.47, does indeed give a good description of the experimental data. It is reasonable on this basis therefore, to expect the theory to give good predictions, except in the region of u_m/u_c near or greater than unity with 9,000 slot Reynolds number, for the intermediate lip thickness to slot height ratio.

11.3. Initial Boundary Layer Velocity Profiles at the Slot.

It was assumed that the slot lip and cooled wall initial boundary layers could be expressed in terms of a simple power law velocity profile of the form,

$$y/y_{max} = (u/u_{max})^{\frac{1}{n}} \qquad 11.4.$$

The mainstream approach boundary growing on the upper surface of the lip, was a function of injection velocity ratio and, the lip fitted. Profiles plotted in the non-dimensional form, off the thinnest lip are shown in figure 11.16 for a selection of test points covering the range of velocity ratios and slot Reynolds numbers. It can be seen that when plotted in this form, the profiles are similar. Shown also is equation 11.4 with the index n equal to 7, the value appropriate for a normal turbulent boundary layer: Agreement of the data with this equation is good. In figure 11.17 are the same plots off the intermediate lip; again, good agreement with the turbulent power law equation is obtained. The plots for the thickest lip are shown in figure 11.18.

It is clear from the plots presented in figures 11.16 to 11.18 inclusive, that the mainstream approach boundary layer is turbulent and is adequately represented by the simple power law form chosen.

For the cooled wall boundary layer, the 'universal' power law profile was found to be a function of slot Reynolds number: For low Reynolds numbers, $Re_s < 10X10^3$, it was found that $n = 9 \sim 11$ and for high Reynolds numbers, $10X10^3 < Re_s < 25X10^3$, $n = 25$ was appropriate. This is illustrated in figures 11.19 and 11.20 for, thin and intermediate lip thicknesses respectively. The slot flow path is shown in figure 8.3 and the flow areas given in figure

8.2. From these figures and the description given in Section 8.38, it can be realised that the layer originates on a convex surface. The dependency of the index n on Reynolds number has been demonstrated for smooth pipes in turbulent flow, by Nikuradse (138). Nikuradse also demonstrated a dependency of 'n' on pressure gradient (139), the index decreasing for divergent flows and increasing for convergent flows: Values of $n \simeq 25$ were obtained for a 2 degree equivalent included half- angle channel. The design of the present injection geometry consists of a constant area discharge preceeded by a smooth convergence and Nikuradse's data indicates the boundary layers are consistent with this type of geometry.

In figure 11.21 are shown in non-dimensional form, the profiles on the slot lip inner surface for most of the tests made with the thinnest lip: Also shown is equation 11.4 with two values of n, 25 and 30. The profiles exhibit some scatter and the simple power law as always, is not capable of representing the data right across the profile, but with these values of the index , provides a crude approximation. Similar data for the intermediate thickness lip is given in figure 11.22, and the same conclusions apply. Representation of the lip velocity profiles by a simple power law with $n = 25$-30 is seen to be satisfactory.

11.4. Growth of Cooled Wall Boundary Layer.

To calculate potential core length, it is also necessary to be able to predict growth of the cooled wall boundary layer. The theory assumes this boundary layer and the lip wake, separated by the potential region, grow independently of each other and the boundary layer growth may be obtained from the uniform stream, zero pressure gradient, two-dimensional flow,

integral momentum equation using Blasius turbulent pipe-flow measurements for wall shear stress, i.e.

$$\frac{(\delta)_{wall}}{(x+x_s)} = 0.05815 \left[\frac{(z+1)(2z+1)}{z}\right]^{4/5} \cdot Re_{(x+x_s)}^{-1/5} \qquad 11.5$$

where,

$z = \frac{1}{n}$ and, x_s = upstream apparent origin of layer. The apparent origin was found by solving equation 11.5 for the distance x_s with the measured injection-plane values of z and (δ) wall. Predictions of (δ) wall were then made using this value.

In figure 11.23 are shown examples of cooled wall boundary layer velocity profiles in non- dimensional form, at increasing stations downstream from the injection plane. It can be seen, that as the distance increases, the appropriate power law index 'n' progressively decreases. As was described previously, the cooled wall boundary layer for this particular slot geometry originates on a convex wall in a region of strong favourable pressure gradient. In the slot discharge, the layer is then growing on a flat wall in a region of effectively zero pressure gradient. The overfull profile, resulting as described in Section 11.4, in the injection plane, therefore reverts along the cooled wall towards the normal turbulent form. Thus, although velocity pro- may be 'universal' initially, this similarity is not subsequently held until a normal turbulent boundary layer is established, and equation 11.5 may not as a result, be considered a good estimate of growth in the present case.

A comparison of predicted and measured cooled wall boundary layer growths is made in figure 11.24, where it may be seen that equation 11.5 over-estimates the growth by an amount depending on Reynolds number. Since the growth rate of the inner edge of the lip mixing layer is almost always greater than that of the wall boundary layer, the error in predicted, absolute

potential core length arising from this source in assuming such a representative function is however, likely to be small. Consideration of Table 10.1 shows the predictions for these runs agree with the measured value for No.16 and, underestimate for Runs 23 and 27, as figure 11.24 would indicate.

11.5. Effective Origin of Lip Wake.

As has been described in Section 7.2.2., an inevitable separated flow region is formed in the wake behind the slot lip. The theory of Chapter 7 assumes that the velocity profiles are similar in form right from the lip and hence, that the region of separated flow is negligibly small. This was taken to be the case if the lip thickness is less than the slot height.

In the previous section the similarity of the profiles was examined and although similarity was generally obtained, the closest profile was taken at only two slot heights from the lip. The distance x_o, which represents the effective origin of the wake in equation 7.109 was therefore assessed by plotting the locus of the minimum velocity in the wake and extrapolating back until it intersects the forward extension of the appropriate lip edge. As an additional check, the inner edge of the mixing layer was constructed and extrapolated back to intersect the forward horizontal extension of the lip boundary layer thickness at injection. Both intersections represent a measure of x_o, as shown in figure 7.4. The technique is illustrated in figure 11.25 for Test Run 41 where δ_w/s is 0.379. It can be appreciated from this figure that measurements of x_o by this method could not be particularly precise.

Not each test run had sufficient profiles to enable x_o to be estimated: of the remainder, those where test scatter produced considerable disagree-

ment between the two ways of obtaining x_o were rejected. The rather limited data resulting are shown in figure 11.26. In this figure, x_o is related to the characteristics dimension δ_w, and is shown as a function of the parameter $u_m/u_c \cdot Re_s$. The form of the abscissa in figure 11.26 was arrived at from the argument that the extent of the separated flow should be dependent on the rate of mixing, which is proportional to the velocity ratio, and, the absolute scale of the system in velocity and size, characterised by slot Reynolds number.

Figure 11.26 shows a pleasing agreement of the data for the three lip thicknesses tested and, that

$$\frac{x_o}{\delta_w} \propto \left(u_m/u_c \cdot Re_s\right) \qquad 11.6$$

Both jet-like and wake-like, flows are included.

When $u_m/u_c \cdot Re_s$ is small, the separated flow region is a small fraction of the slot height, even for the thickest of the lips, and may be considered negligible. For large values of $u_m/u_c \cdot Re_s$, x_o can become considerable and if the slip is thick, the accuracy of the potential core length prediction could be affected.

The rather surprising profile similarity found in Section 11.4 for the 0.1525 inch lip is explained by figure 11.26: The injection conditions for all the tests were such that the largest separated flow region was just less than 1 slot height, and had long vanished at the position of the first velocity traverse.

It is concluded that for the present series of tests, the distance x_o was always small enough for the predictions of potential core length not to be greatly affected.

11.6. Rate of Growth of Lip Wake.

In deriving equation 7.11.5 for x_c the correction length, a blanket form of the basic mixing expression, 7.41, was used. A more reasonable approach to the asymmetric wake from the lip would be to divide the defect profile into two shear layers, as was done with the velocity profiles, and assume the turbulence causing the mixing is determined by the largest gradient, i.e. for isothermal flow,

$$\left(db/dx\right)_{\text{outer}} = \frac{.3\left|\left(1-\phi_o^2\right)\right|}{\left(1+\phi_o\right)^2} \qquad 11.7a)$$

$$\left(db/dx\right)_{\text{inner}} = \frac{.3\left|\left(1-\phi_I^2\right)\right|}{\left(1+\phi_I\right)^2} \qquad 11.7b)$$

where, $\phi_o = \frac{u_{min}}{u_m}$, and $\phi_I = u_{min}/u_c$

However, such an approach results in a cumbersome set of equations which present considerable awkwardness in solution. It is also impossible to establish in general form the conditions necessary for determination of the flow parameters at the origin of the wake. Because of these difficulties, the present approach was used in equation 7.109 and introduced the unknown function F_1 .

The unknown function F_1 introduced should of course, be a constant since constant mixing length constant is a well-known empirical feature of free turbulent flows. If the overall velocity ratio across the wake is very far removed from unity, the blanket approach is valid and F_1 would be expected to be close to the familiar 0.3 derived in Chapter 7. However, velocity ratios close to unity are of interest in film cooling and a suitable description of F_1 must be obtained for such injection conditions. Obviously, at unity velocity ratio expressions based on overall conditions will be completely unrepresentative.

Since we are forced by the intractable nature of the alternative equations, 11.7, into using the blanket mixing approach and as this has to work for situations where it is patently incorrect, it is therefore logical in the context of the presently adopted philosophy, (outlined in Chapter 7), to abandon the real physical phenomenum for a mathmatical convenience to side-step those difficulties. In doing this, F_1 will not be a constant, but becomes a function of both overall temperature and velocity ratios.

From the work of Zhestkov reported by Abramovich, the correction length x_c was empirically shown to be a function of velocity ratio and, the sum of lip thickness and boundary layer displacement thicknesses, for velocity ratios less than unity in isothermal flows. This equation is,

$$x_c = \phi_1 \left[\delta_w + (\delta)_2 \left(\frac{m}{m+1} \right)_2 + (\delta)_1 \left(\frac{m}{m+1} \right)_1 \right] \qquad 11.8$$

where m describes the appropriate velocity profile shape.

Zhestkov's empirical equation for x_c was simultaneously solved with equation 7.11.5 of the present theory, to yield F_1 values. This procedure was carried out for a wide range of velocity ratios less and greater than, unity, and for slot Reynolds numbers in the range 8,000 to 25,000. The calculation was carried out taking two lip thicknesses of 0.0550 and 0.0995 inches; boundary layer thicknesses representative of those measured in the present tests were used. The results of the study when presented in terms of the overall injection velocity ratio u_m/u_c, were found to be a unique function of this ratio, as is shown in figure 11.27. The function was curved-fitted with a 9th. order polynomial for $u_m/u_c > 0.75$ and another of 9th. order for $u_m/u_c < 0.75$.

The coefficients in these empirical functions are:

if $\frac{u_m}{u_c} < .75$,

$A_1 = -109.60742$ $A_2 = 2268.883$ $A_3 = -20665.639$

$A_4 = 108286.53$ $A_5 = -358766.76$ $A_6 = 778528.76$

$A_7 = -1106212.7$ $A_8 = 992655.0$ $A_9 = -510709.89$

$A_{10} = 114858.23$

and, if $u_m/u_c > .75$,

$A_1 = 538.7938$ $A_2 = -4259.6355$ $A_3 = 14851.5$

$A_4 = -29950.40$ $A_5 = 38488.911$ $A_6 = -32672.695$

$A_7 = 18312.651$ $A_8 = -6532.1766$ $A_9 = 1345.1347$

$A_{10} = -121.8105$

Unfortunately, equation 7.11.5 can involve the small difference of two large numbers which, for certain combinations of numbers, can in a few cases, cause the iterative processes for x_p to go unstable, diverge and in a computer solution, produce a tightloop. In this event, in the absence of a detailed study of the mixing phenomena, the computer program ceases the iteration, side-steps the present theory, calculates x_c according to equation 11.8, assumes this is valid for the case temperature and velocity ratios, and then resumes the calculation procedure using this value of Kirk's method.

11.7. Effects on Measured Potential Core of Parameter Variations.

The collected experimental data in the form of measured potential core lengths, is plotted in figures 11.28 to 11.35 inclusive. These data trends enable qualitative assessment to be made concerning the effects on potential core of velocity ratio, lip thickness, mainstream boundary layer and, slot Reynolds number.

Slot Reynolds number was set by changing the pressure drop across the slot. Once the slot flow was established, it was maintained constant and velocity ratio was varied by adjusting the speed of the motor driving the

wind-tunnel fan. The experiments were all performed for effectively isothermal flows. Slot height remained constant at a nominal value of 0.25 inches.

11.7.1. Injection Velocity Ratio.

The effects of velocity ratio are seen in figures 11.28 to 11.33: Potential core tends to a maximum in the neighbourhood of unity velocity ratio and is relatively insensitive to it at extreme values. There are insufficient data points to exactly establish the position in terms of velocity ratio, at which the maximum occurs.

11.7.2. Slot Lip Thickness.

The effects of lip thickness are shown in figures 11.28, 11.29, and 11.30, as a function of slot Reynolds number. Figure 11.28 shows the data for the lowest of the three Reynolds numbers. Increasing the ratio δ_w/s reduces potential Λ_{core} at all Reynolds numbers. The lip thickness does not appear to affect the sensitivity to velocity ratio. The influence of lip thickness is seen to be relatively large.

Figures 11.29 and 11.30 shows that as Reynolds number is increased, the importance of lip thickness is reduced. It is barely significant for the highest of the Reynolds numbers.

These points are emphasized by the cross-plot given as figure 11.35 which at a velocity ratio u_m/u_c, of 0.6, shows directly the effect of slot lip thickness on potential core, as a function of slot Reynolds number. At 23,000 Reynolds number, trebling the lip thickness changes x_p by less than

one quarter of a slot height. At a Reynolds number of 9,000, the same increase in lip thickness reduces x_p by nearly 3 slot heights, a significant change.

11.7.3. Slot Reynolds Number.

The effects on potential core of slot Reynolds number for the three lip thicknesses, in figures 11.31, 11.32 and 11.33.

In all cases, increasing slot Reynolds number Re_s, reduces potential core length although the effect is greater for the thinner lips and velocity ratios around unity, becoming progressively less as both Reynolds number and lip thickness are increased. This is seen in figure 11.34, which is cross-plotted from figures 11.31 - 11.33 at a velocity ratio u_m/u_c, equal to 0.5.

This effect of reducing potential core with increasing slot Reynolds number is contrary to the theoretical predictions of Korst (140) and Cole (36). Such disagreement may be explained however, since slot Reynolds number is a dependent and not independent, variable. This is shown in detail in figure 11.36 which was constructed from calculated values from the theory. The response of potential core to slot Reynolds number depends on how the dependent variable is changed. The predicted trend with increasing wall pressure drop shown in figure 11.36 is confirmed by the experimental trends shown in figure 11.34.

11.7.4. Mainstream Boundary Layer Thickness.

Some very limited data available which show the effect of increasing the mainstream boundary layer thickness on potential core. The

thickness of the mainstream boundary layer for the majority of the test runs was of the order of 1. slot heights; for a few tests however, it was increased to the order of 4.1 slot heights and these points are represented by the tagged symbols in figures 11.28, 11.29 and, 11.33.

It can be seen that increasing mainstream boundary layer thickness reduces potential core length by a small amount at higher Reynolds numbers and by a larger amount at lower values.

11.8. Predictions of Potential Core Length.

11.8.1. Predictions.

As a preliminary test of the present theory, predictions were made for potential core lengths measured from data in the published literature.

Data were taken from the work of Papell and Trout (34), Cartshore (115), Seban (11), Seban and Back (25), Whitelaw (63) and, Sivasegaren and Whitelaw (65). Of these data, references (34), (11) and (25) yielded thermal potential cores, reference (115) hydrodynamic cores, and, (63) and (65), impervious wall cores; no corrections were applied and the principle of field similarity with equality of Prandtl and Lewis numbers with unity, was assumed. Papell and Trout's data contained an incorrect measurement of coolant temperature and was corrected in the manner described in Section 4.4. Potential core lengths were measured by linear extrapolation of effectiveness values back to $\eta = 1.0$ on semi-logarithmic paper, as described in Chapter 4. With the exception of reference (34), all the data are for effectively iso-

thermal flows: Papell and Trouth's data had temperature ratios T_c/T_m, down to 0.358.

For the predictions, it was necessary to estimate the boundary layer thicknesses on the lips at injection, where these were not fully quoted. Origins of the boundary layers were based on the slot geometry layouts given, and growths were estimated from the usual simple equations with transition from laminar to turbulent flow taking place at a length Reynolds number of 3.2×10^5.

In figures 11.37 and 11.38 are regression plots showing a comparison of predicted non-dimensional potential core lengths, with measured values. The test data cover extremely wide ranges of slot height, ratio of lip thickness to slot height, slot Reynolds number and, velocity ratio. Despite this, the figures show extremely good agreement of the predictions with the measurements.

Shown in figure 11.39 is the regression plot giving the comparison of the hydrodynamic non-dimensional potential cores by measurement and prediction, for the present set of experimental data. In general, there is good agreement between predictions and experiment, except for large values of x_p/s obtained at a slot Reynolds number of 9,000 for lip thickness to slot height ratios of 0.379 and 0.584. This will be examined in more detail in the following section.

11.8.2. Error Analysis.

For the present set of experimental data, an error analysis was made to determine the limitations of the theory in successfully predicting potential core length. The results of this error analysis are contained

in figures 11.40 to 11.45 inclusive, where the difference between predicted and measured potential core length is plotted against injection velocity ratio as a common abscissa, for various functions of slot Reynolds number and slot lip thickness. Shown in the figures is the estimated uncertainty band for measured values of x_p/s.

A consideration of the figures reveals that:

(i) The theory may be used with confidence for all velocity ratios and slot Reynolds numbers for slot lip to height ratios less than 0.2146, and, for all velocity ratios and slot lip to height ratios provided the slot Reynolds number is above or equal to, 23,000.

(ii) If the ratio of slot lip to height is greater than 0.2146, the theory should be used with caution for velocity ratios $0.5 \leq u_m/u_c \leq 1.9$ when slot Reynolds number is below 9,000.

(iii) If the ratio of slot lip to height is greater than 0.4, the theory should be used with caution for velocity ratios $0.8 \leq u_m/u_c \leq 1.3$ when slot Reynolds number is below 14,000.

These limitations are derived from data which is somewhat narrow in range; the maximum variation of parameters for this series of tests is contained on figure 11.39. Figures 11.37 and 11.38 suggest that the predictions can still be reasonably satisfactory if a somewhat greater loss in accuracy is acceptable, outside these conditions. How accurate predictions of potential core actually need to be for the considered application will be discussed in a later Section.

Failure of the theory in the neighbourhood of unity velocity ratio is not completely unexpected since the mixing model used in the analysis resulting in equation 7.41, there breaks down for isothermal flows. The crude method of accounting for mixing due to "pre-turbulence" in the streams

at these velocity ratios, must be improved if possible. Break-down as the ratio of lip thickness to slot height increases is also to be expected, due to the progressive failure to establish within the potential core region, the postulated wake similar profiles. In the limit, which is $\delta_w \gg s$, the basic flow model itself breaks down and the problem becomes one of a rearward-facing step with base bleed. The Reynolds number effect observable in the accuracy of prediction, was not expected. Its' cause however, can be traced directly to the non-establishment of similar profiles at these conditions, as seen in figures 11.5, 11.8-11.11 inclusive, and, 11.13. The reason for this occurence is not immediately apparent and it may be associated with the form of the lip (interior) boundary layer. An additional effect of Reynolds number could be associated with the cooled wall boundary layer which is discussed in Section 11.4. The relative success of the method across these Reynolds number restrictions as evidenced in figures 11.37 and 11.38, suggests that the effect may be due to some undisclosed rig perculiarity, and not the theory.

11.9. Prediction of Film Development.

A number of relatively simple theories are available which predict film development, those for example, of Hartnett (117), Nicoll and Whitelaw (38) and, Harris (116). These theories require as starting input empirical relationships between the specified quantities at the slot and the properties of the velocity and temperature profiles at some distance downstream. Use can be made of these methods to test how accurately potential core length has to be specified to result in satisfactory predictions of downstream film development. Agreement of downstream predictions with measured data provides an additional check on the validity of the data.

Bertshore's method was selected for this test and was written into a computer program which prepares the input data in a form for solving the integral equations which it does by a 4-point Runge-Kutta numerical technique. Input to this program consists of non-dimensional potential core length x_p/s, slot Reynolds number Re_s, the maximum velocity in the film at x_p, $(u_{max})_{x_p}$, the normal position of this maximum velocity $(d_{max})_{x_p}$, injection velocity ratio u_m/u_c, and, the velocity profile existing at x_p.

It is necessary to attempt a description in general form of the flow conditions at the end of the potential core, to adequately specify the starting point for the integration. This has been done empirically in terms of potential core length itself. From the potential core computer program come values of x_p/s and $\frac{(d_{max})_{x_p}}{s}$ directly. Figures 11.1 to 11.3 inclusive show that $(u_{max})_{x_p}/u_c = 0.955$. The position of the minimum velocity in the profile may be calculated from the empirical equation.

$$(y_{min})_{x_p} = 1.3015\,(s + \delta_w)(u_m/u_c)^{-0.2433} \qquad 11.9$$

the basis for which is represented in figure 11.46. This equation is based on limited data and should be regarded as tentive. Filling of the velocity defect conforms to $(u_{min}/u_3)_{x_p} = 0.92$ where $u_3 = u_m$ for $u_m < u_c$ and, $u_3 = u_c$ for $u_m > u_c$, and is illustrated in figure 11.47. With the positions and magnitudes of the maximum and minimum velocities in the profile at x_p defined, the profile itself was specified through the Schlichting wake profile applied to inner and outer layers; the wall layer was assumed to have a typical turbulent boundary layer form.

As a description of development, decay of the maximum velocity in the downstream film profiles expressed in the form u_{max}/u_c, together with the position of this maximum velocity normal to the wall in the form d_{max}/s, were taken from the total output as representative. As programmed, Gartshore's theory is for isothermal, jet-like flows only, and predictions were made for all such tests for which downstream data were available. For each test point, three predictions were made:

(i) where the input was solely empirical, taken from the measured values for each test,

(ii) a mixed input consisting of predicted x_p/s and, empirical velocity profiles taken from the measured values for each test,

(iii) a wholly predicted input, as outlined above.

Comparisons of the three predictions with themselves and the experimental data, enables the basic accuracy of the method (Gartshore's), the sensitivity to and accuracy of, predicted potential core lengths, and, the accuracy of the theoretical velocity description, to be assessed.

The comparisons of predictions and measured data are given in figures 11.48 to 11.57 inclusive: for figures 11.56 and 11.57 only the wholly theoretical prediction was made. With input type (i) above, agreement with the experimental points is extremely good indeed and excellent up to about 50 slot heights from injection, for both the thin and intermediately thick lips. This verifies the validity of the experimental measurements. It is seen that the predictions with input type (ii) are almost co-incident in all cases, with the type (i) -based predictions. This indicates that the potential core predictions by the present method are perfectly adequate to enable predictions of downstream film development to be made. The actual non-dimensional

core lengths, predicted and measured, used in these present predictions can be compared in Tables 10.1 and 10.2; the maximum difference of these is 1.67 slot heights. A greater effect is observed when predictions based on type (iii) input are attempted. This is because it is difficult to describe velocity profiles at x_p in completely general form. Even so, the maximum difference between predictions of u_{max}/u_c based on all types of input is only about 6% of unity, i.e. of the initial value. For engineering purposes at least, downstream predictions based on type (iii) input, i.e. wholly predicted, are satisfactory up to again, about 50 slot heights from injection.
The complete predictions are seen to consistently under-estimate the actual decay by up to 7.5% of unity, occuring at downstream locations.

.....

CHAPTER 12.

CONCLUSIONS.

12.1. The Hypothesis.

It was postulated for the conditions and geometries associated with gas-turbine combustion chamber cooling using discrete injection systems that, whatever the velocity ratio, the film will appear jet-like initially. It was further postulated that order, understanding, and complete description could be brought to the measured data if it was considered in light of a mathmatical model derived from jets, and which consisted of a potential core, followed by a transition region proceeding a downstream, main region.

On the basis of the model, expressions were developed for film effectiveness, equation 4.2.6 and, film heat transfer coefficient, equation 6.30. A large amount of experimental film effectiveness data for nine different, practical slots and covering wide ranges of injection conditions, was brought into order by the derived theory and resulted in simple, semi-empirical equations suitable for engineering predictions, equations 4.30 and 4.31. Only a very limited amount of data was available against which to test the film heat transfer coefficient theory and the same spectacular success was not achieved. A good representation of the experimental data up to about 40 slot heights from injection was obtained however. Both the effectiveness and heat transfer coefficient expressions are suitable for use up to the end of the transition region of the film, but not beyond. However, for the chosen application, this is quite sufficient since it is necessary due to increasing wall temperatures, to renew the film before this point.

The experimental work carried out verifies hydrodynamically, the existance of the potential core and the complete model. This is for the smoothly-fed slot used The existance of the thermal potential core for practical injection geometries was verified by the sucessful correlation of effectiveness data when the potential core model was used, (Chapter 4).

The two postulates can therefore be regarded as substantiated.

12.2. Potential Core Theory and Prediction of Effectiveness.

The equations for film effectiveness and, heat transfer coefficient are developed in terms of the potential core length. To enable complete predictions to be made it was necessary to describe the potential core length. A theory was developed (Chapter 7) to predict hydrodynamic potential core for slots having thick lips and, boundary layers on the lip. Thermal potential cores could be found from the predicted hydrodynamic values by assuming either, Reynolds analogy or, a Prandtl-Taylor flow, as described in Appendix A3.

In Chapter 11. the theory is subjected to a number of tests which are quite severe. All the assumptions made in the derivation were first examined and substantiated against the measurements taken. Then, comparisons between measurement and prediction were carried out. The initial batch of data was taken from six different sources and is for hydrodynamic, thermal and impervious wall measurements. Geometrically, slot height variation was eight to one, from 0.063 to 0.502 inches, and the ratio of lip thickness to slot height variation was forty-two to one, from 0.04 to 1.70. Aero-thermodynamically,

the variation of slot Reynolds number was sixty-two to one, from 1,210 to 75,380, velocity ratio was seventy-one to one, from 0.071 to 5.042, and, temperature ratio was two to one, from 0.56 to 1.2. Considering the assumptions concerning boundary layers which had to be made, and the wide ranges of the relevant parameters, the agreement between predictions and measurements, shown in figures 11.37 and 11.38, is very satisfactory and the theory can be said to have passed this test. The second batch of data against which the theory was tested was that presently measured. As is shown in figure 11.39, agreement is generally good, with some exceptions which can be explained with reference to Section 11.2. The error analysis led to the tentative recommendations (i) to (iii) of Section 11.8.2, for use of the Theory.

Some understanding of how accurate the predictions of potential core had to be, was obtained in Section 11.9 where the downstream development of the film was examined using Gartshore's theory with predicted x_p's forming the input. As figures 11.48 to 11.57 show, the predictions of potential core are perfectly adequate to result in satisfactory engineering predictions of downstream maximum film velocity decay and position. This study however, was applied for injection conditions where $u_c > u_m$ and, for a smoothly-fed slot and is not therefore, general enough to be completely conclusive.

The main use of potential core is in equation 4.26., to give predictions of film effectiveness for different injection conditions. These predictions will of course, have to be made for practical slot geometries and as such, form the real and major test of the potential core theory. Suitable data for such a test are limited and availability is generally restricted. In figures

12.1 to 12.7 inclusive, some such data are presented for three different, practical slots of machined construction. In the present author's opinion, the measurements were made without overmuch concern about experimental precision, and the scatter in the data reflects this. For each case, a prediction of effectiveness is made from equation 4.30 with the x_p values being obtained for the slot and injection conditions from the computer program given in Appendix A2; a Prandtl-Taylor type flow was assumed a mainstream turbulence (which was measured) correction was applied as indicated in figure 2.14. The scale of the abscissa in the plots of the figures is removed for proprietory reasons.

For slot G4 the agreement of the predictions with the experimental data is extremely good: Down to 0.60 effectiveness, the maximum disagreement is 5% of unity, i.e. of the maximum value. Below 0.60 effectiveness, the prediction becomes conservative, i.e. predicts a greater decay than actually occurs. This arises for two reasons: It will occur beyond the transition region of the film because the exponent on the group S_{u_2} in equation 4.30 becomes inappropriate, and, there is an apparent tunnel perculiarity associated with the turbulence generated by an intake grid, as was observed in Chapter 4.

The plots for slot G5 accord with those for G4, again with excellent agreement between predictions and measurements, except for figure 12.6 where the prediction is severely conservative at downstream stations although the starting point appears correct. This is due to the injection condition at an

M of 0.295 being outside the range of the original data which yielded the empirical constant in equation 4.30.

Figure 12.7 shows the comparison for slot G6, with again, excellent agreement of prediction with measurements.

As Whittacker (88) has shown, a 10% change in film effectiveness causes only a 2 - 3% change in predicted wall temperature. Thus, by this standard, thepotential core theory and semi-empirical equation have held up when applied in real situations. It is worthwhile emphasizing that slots G4, G5 and G6 are real, practical slots, and, G4 and G6 are running in advanced engine combustion chambers; G5 was a development design. Slots G5 and G6 were designed using the information contained in this thesis.

In work subsequent to that reported in this thesis the present author has shown that curves equivalent to those shown in 2.16, 2.17, and, 2.18, 2.19 also exist for the data measured from practical slots. Optimum slot heights and injection mass velocity ratios are in close agreement. Parametric studies using the potential core theory in a typical combustion chamber dilution zone give optima which also agree closely with these. Such being the case,design rules can, and have been, formulated which specify either M or s ,or both, depending upon how much coolant is available and, how severe the heating problem is. The outcome of such rules is that cooling systems are now uniformly being designed with M values in the range 1.0 to 2.0, where the empirical constants in equation 4.30 are appropriate. The combination of optimum M and optimum s , with typical combustor temperature ratios and mainstream flow velocities, together with operation at high pressures, gives slot Reynolds numbers above the potentially troublesome range given in Section 11.8.2.

Thermal stress considerations for the slot lip suggest that in order to limit closure of the slot due to creep of the lip, the lip should be tapered towards it's free end. If an optimum slot height is used, the ratio of lip thickness to slot height will therefore, be usually less than 0.4, thus avoiding another potentially troublesome range indicated in Section 11.8.2.

It can be fairly concluded therefore that reliable predictions of film effectiveness can be made for practical geometry injection slots in combustion chambers by using equation 4.30 in conjunction with the potential core theory.

12.3. Recommendations for Future Work.

The present thesis puts practical film cooling theory on a sound basis and, carries the design and prediction of gas-turbine combustor cooling systems forward considerably. However, many important questions remain to be answered. Some such questions are given below:

(i) How can the combustion chamber conditions be understood and defined to ensure representative input to the film cooling theory?

(ii) What is the effect of a residual preceeding film on specification of the theory input conditions?

(iii) How does the practical slot geometrical structure affect the turbulence generated in the injected coolant and how is the film development changed?

(iv) How is flame luminosity related to fuel injection technique and, operating pressure?

To the practicing combustor engineer, answers to these questions alone would provide the major breakthrough so badly needed in this area.

REFERENCES.

1. P.Lloyd : Engine Development Under the Ministry of Aviation, J.R.Ae.S. Vol. 72, No. 686, pp.132 -140; Feb.1968.

1A. Tu Chung-tse, Yin K'otao and, Ch'en Neng-k'un: Heat Transfer in Turbo Jet Combustion Chambers and Experimentation on Film Cooling Effects, paper read to 1st All-China Applied ThermoPhysics Symposium, August 1965 (available as AFSC FTD HT-23.958.67, AD 669427, Sept. 1968)

2. G.A. Halls : Air cooling of Turbine Blades and Vanes, Aircraft Engineering. pp.4 -14, August 1967.

3. H. Davies : Some Thoughts about the Future of European Aeronautics, J.R. Ae. S, vol.72, No. 689, pp.385 -395, May 1968.

3A. W.H. Roudebush : State of the Art in Short Combustors, NASA TM X-52449, September 1968.

4. S.R. Jackson and J.Odgers : Factors Influencing Heat Release in Combustion Chambers and Consideration of the Related Materials and Structures, Paper read to International Propulsion Symposium, College of Aeronautics, Cranfield, April 1967.

5. L.F. Bell : Design Requirements of Small High Temperature Rise Combustors, SAE Paper 680447, May 1968.

6. S. Scesa : Effects of Local Normal Injection on Flat Plate Heat Transfer, Ph.D.Thesis, University of California, Berkeley, 1954.

7. R.A. Seban, H.W. Chan and S. Scesa : Heat Transfer to a Turbulent Boundary Layer Downstream of an Injection Slot, ASME Paper No. 57-A-36, 1957.

8. J.P. Hartnett, R.C. Birkebak and E.R.G. Eckert : Velocity Distributions Temperature Distributions, Effectiveness and Heat Transfer for Air Injected Through a Tangential Slot into a Turbulent Boundary Layer,

Trans. ASME, Series C, Journal of Heat Transfer,pp.293-306, August 1961

9. J.L. Stollery and A.A. El-Ehwany : A Note on the Use of a Boundary Layer Model for Correlating Film Cooling Data, Int. J, Heat Mass Transfer, Vol.8, pp 55-65, 1965.

10. J.L. Stollery and A.A. El-Ehwany : On the Use of a Boundary Layer Model for Correlating Film Cooling Data, Int. J. Heat Mass Transfer, Vol.10,pp.101 - 105, 1967.

11. R.A. Seban : Heat Transfer and Effectiveness for a Turbulent Boundary Layer with Tangential Fluid Injection, Trans. ASME, Series C, Journal of Heat Transfer, pp.303-312, November 1960.

12. R.A. Seban and L.H. Back : Velocity and Temperature Profiles in a wall Jet, Int. J. Heat Mass Transfer; Vol.3, pp.255 -265, 1961.

13. G.E. Myers, J.J. Shauer and R.H. Eustis : Heat Transfer to Plane Turbulent Wall Jets, Trans. ASME, Series C, Journal of Heat Transfer, pp 209 - 214, August 1963.

14. G.E. Myers. J.J. Shauer and R.H. Eustis : Plane Turbulent Wall-Jet Flow Development and Friction Factor, ASME Paper No.62 - Hyd. - 4.

15. C.J. Akfirat : Transfer of Heat from an Isothermal Flat Plate to a Two-Dimensional Wall Jet, Proc. 3rd. Intl. Heat Transfer Conference, Vol. pp.274 -279, August, 1966.

16. D.B. Spalding : A Relation Between the Effectiveness and the Heat Transfer Coefficient in Film Cooling, unpublished Imperial College report, October 1963.

17. H. Patel : Investigation of the Spalding Relationship between Effectiveness and Heat Transfer Coefficient in Film Cooling, unpublished work, Loughborough University, 1968.

18. A.E. Samuel and P.N. Joubert : Film Cooling of a Adiabatic Flat Plate in Zero Pressure Gradient in the Presence of a Hot Mainstream and Cold Tangential Secondary Injection, Trans. ASME, Series C, Journal of Heat Transfer, pp.409-418, August 1965.

19. C.M. Milford and D.M. Spiers : An Investigation in Film Cooling by Slots, Paper 79; Intl. Heat Transfer Conference, University of Colorado, Boulder, Colorado, 1961.

20. J.Odgers and J.Winter : unpublished work at Lucas Gas Turbine Research Laboratories, November 1963.

21. K.Wieghardt : Hot Air Discharge for De-Icing, AAF Trans. F-TS - 919Re, Wright Field, 1946.

22. M. Tribus and J.Klein : Forced Convection from Non-Isothermal Surface, Heat Transfer-A Symposium, University of Michigan Press, Ann Arbor, 1953.

23. S.S. Kutateladze and A.I. Leont'ev : Film Cooling with a Turbulent Gaseous Boundary Layer, Academy of Sciences of U.S.S.R., Thermal Physics of High Temperatures, Vol.1, No.2, pp.281-290,1963.

24. G.J. Sturgess, unpublished work, 1964.

25. R.A. Seban and L.H.Back : Velocity and Temperature Profiles in Turbulent Boundary Layers with Tangential Injection, Trans. ASME, Series C, Journal of Heat Transfer, pp.45 -54, February 1962.

26. D.B.Spalding, V.K. Jain, E.H.Cole and J.L.Stollery : Film Cooling in Incompressible Turbulent Flow - Representation of the Data of IC/HRJ/10 with Allowances for Potential Core Corrections, unpublished Imperial College report IC/HRJ/14, July 1963.

27. D.B. Spalding, J.L. Stollery, E.H. Coles, V.K. Jain and S.J. Peerless : Film Cooling in Incompressible Turbulent Flow- Proposals for Theoretical Models of the Film-Cooling Process, ARC 25309, HMT 14, November 1963.

28. G.N. Abramovich : The Theory of Turbulent Jets, M.I.T. Press,1963.

29. M.B. Glauert : The wall-Jet, J.Fluid Mechanics, Vol.1, p.525, 1956

30. D.B. Spalding : Theory of Rate of Spread of Confined Turbulent Pre-Mixed Flames, 7th. Symposium on Combustion, Butterworths Scientific Press, London. 1958.

31. D.B. Spalding, V.K. Jain and W.B. Nicholl : Film Cooling in Incompressible Turbulent Flow- Examination of Experimental Data for the Adiabatic Wall Temperature, ARC 2531, HMT 16, July 1963.

32. D.B. Spalding : Prediction of Adiabatic Wall Temperatures in Film Cooling Systems, AIAA J. Vol.3, pp.965 -967, 1965.

33. J.E. Hatch and S.S. Papell : Use of a Theoretical Flow Model to Correlate Data for Film Cooling or Heating an Adiabatic Wall by Tangential Injection of Gases of Different Fluid Properties, NASA TN D- 130, November 1959.

34. S.S. Papell and A.M. Trout : Experimental Investigation of Air Film Cooling Applied to an Adiabatic Wall by Means of an Axially Discharging Slot, NASA Tech Note, D-9,1959.

35. D.B.Spalding : A Unified Theory of Friction, Heat Transfer and Mass Transfer in the Turbulent Boundary Layer and Wall Jet, ARC Report No. 25,925 March 1964, revised December 1964.

36. E.H. Cole: A Procedure for Predicting the Adiabatic Wall Temperature in the Film Cooling Process, Based on the Unified Theory, ARC 27,374, HMT 79, November 1965.

37. S.V. Patankar and D.B. Spalding : A Calculation Procedure for Heat Transfer by Forced Convection Through Two-Dimensional Uniform-Property Turbulent Boundary Layers on Smooth, Impermeable Walls, ARC 27,432,HMT 85, November 1965.

38. W.B. Nicoll and J.H. Whitelaw : The Effectiveness of the Uniform Density, Two-Dimensional Wall-Jet, Int.J.Heat Mass Transfer, Vol. 10, pp.623-639, 1967.

39. M.P. Escudier, W.B. Nicoll, D.B. Spalding and J.H.Whitelaw: Decay of a velocity Maximum in a Turbulent Boundary Layer, The Aeronautical Quarterly, Vol. XVIII, pp.121 -132, May.1967.

40. S.V. Patankar and D.B. Spalding: A Finite-Difference Procedure for Solving the Equations of the Two-Dimensional Boundary Layer, Int. J. Heat Mass Transfer, Vol. 10, pp.1389-1411, 1967.

41. B.R. Pai : The Application of the Boundary Layer Model to Predict the Influence of Slot Boundary Conditions on Film Cooling, Imperial College Report EHT/TN/9, February 1968.

42. M. Nishiwaki, M. Hirata and A.Tsuchida : Heat Transfer on a Surface Covered by a Cold Air Film, Paper 80, 1961 International Heat Transfer Conference, University of Colorado, U.S.A.

43. R.J. Goldstein, G. Shavit and T.S. Chen : Film Cooling Effectiveness with Injection Through a Porous Section, Trans. ASME, Series C, Journal of Heat Transfer, pp. 353-361, August 1961.

44. J.H. Whitelaw: An Experimental Investigation of the Two-Dimensional Wall-Jet, ARC 28, 179, HMT 106, April 1966.

45. R. Krystantas: The Turbulent Jet from a Series of Holes in Line, Aeronautical Quarterly, Vol.15, pp 1-28, 1964.

46. G.J. Sturgess: Some Observations on the Behaviour of Practical Film Cooling Devices for Aircraft Gas-Turbine Combustion Chambers, ARC 27,399 HMT 81, December 1965.

47. G.J. Sturgess: Comment on the Prediction of Adiabatic Wall Temperatures in Film-Cooling Systems, AIAA Journal, Vol.4, No.4, pp. 763 -765, April 1966.

48. S.C. Kacker and J.H. Whitelaw: The Effect of Slot Height and Slot Turbulence Intensity on the Effectiveness of the Uniform Density, Two-Dimensional Wall-Jet, J. Heat Transfer, Trans. ASME, Series C, pp. 469-475, November 1968.

49. J.H.Chin ; S.C. Skirvin, L.E. Hayes and A.H. Silver: Adiabatic Wall Temperature Downstream of a Single, Tangential Injection Slot, ASME Paper No. 58-A-107.

50. J.H. Chin, S.C. Skirvin, L.E. Hayes and F.Burggraf: Film Cooling with Multiple Slots and Louvres -Part 1, Multiple Continuous Slots, Trans ASME, Series C, Journal of Heat Transfer, pp.281-292, August 1961.

51. B.R.Pai and J.H. Whitelaw: The Influence of Density Gradients on the Effectiveness of Film Cooling, G.T.C.C. Combustion Sub-Committee Paper No. 258, December 1967.

52. F.J. Bayley: Air Cooling Methods for Gas-Turbine Combustion Systems, R & M 3110, 1959.

53. D.B. Spalding: Recommendations for the Choice of the Velocity of Injection of a Film Coolant, ARC 25312, HMT 17, October 1963.

54. J.P. Hartnett, R.C. Birkebak and E.R.G. Eckert: Velocity Distributions, Temperature Distributions, Effectiveness and Heat Transfer in Cooling of a Surface with a Pressure Gradient, Paper 81, 1961 International Heat Transfer Conference, University of Colorado, U.S.A.

55. G.J. Sturgess: Unpublished work, 1969.

56. L.W. Carlson and E.Talmor: Gaseous Film Cooling at Various Degrees of Hot-Gas Acceleration and Turbulence Levels; Int. J. Heat Mass Transfer, Vol.11, No.11, pp 1695 -1713, November 1968.

57. R.B. Price: Unpublished Rolls Royce report, Bristol Engine Division, 1965.

58. R.B.Price: Unpublished Rolls Royce report, Bristol Engine Division 1965.

59. R.A. Meric: Turbulence in a Flameholder Wake, Master's Thesis, University of New Hampshire, May 1969.

60. K.W.Nobbs and P.R.Rice: The Performance of Splash Impingement Cooling Devices, College of Aeronautics CoA Memo. No. 146, Cranfield, January 1968.

61. R.A. Seban: Effects of Initial Boundary Layer Thickness on a Tangential Injection System, Trans. ASME, Series C, Journal of Heat Transfer,pp.392-393, November 1960.

62. S.C. Kacker and J.H. Whitelaw: The Dependence of the Impervious Wall Effectiveness of a Two-Dimensional Wall Jet on the Thickness of the Upper Lip Boundary Layer, Imperial College Report EHT/TN/1, London, December 1966.

63. J.H. Whitelaw: The Effects of Slot Height on the Effectiveness of the Uniform Density, Two-Dimensional Wall-Jet, Imperial College Report EHT/TN/4, February 1967.

64. G.J. Sturgess: Unpublished work, 1967.

65. S. Sivasegaram and J.H. Whitelaw: Film-Cooling Slots: The Importance of Lip Thickness and Injection Angle, Imperial College Report EHT/TN/6, October 1967.

66. S.S. Papell: Effect on Gaseous Film Cooling of Coolant Injection Through Angled Slots and Normal Holes, NASA Tech. Note D-299, September 1960.

67. V.S. Manian, T.W. McDonald and R.W. Besant: Heat Transfer Measurements in Cylindrical Wall Jets, Int.J. Heat Mass Transfer, Vol.12, No.6, pp 673-679, June 1969

68. J. Odgers and J. Winter: unpublished work at Lucas Gas Turbine Research Laboratories, December 1963.

69. M.J. Holland: unpublished work at Bristol Engine Division, Rolls Royce, October 1963.

70. M.J. Holland: private communication, 1966.

71. R.A. Seban and L.H. Back: Effectiveness and Heat Transfer for a Turbulent Boundary Layer with Tangential Injection and Variable

Free-Stream Velocity, Trans. ASME, Series C, Journal of Heat Transfer, pp.235-244, August 1962.

72. M.P. Escudier and J.H. Whitelaw: The Influence of Strong Adverse Pressure Gradients on the Effectiveness of Film Cooling, Imperial College Report EHT/TN/7, October 1967.

73. D. Biondi and S. Draizen: Development of a Turbojet Combustor with a Segmentally Constructed Liner, NASA CR -54635, WAD R-437, June 1968.

74. A.H. Lefebvre and M.V. Herbert: Heat Transfer Processes in Combustion Chambers, Proc. Inst. Mech. Engrs. (London) Vol.174, No.12, 1960.

75. D. Cohen: private communication, 1969.

76. J.H. Whitelaw: The Effect of the Geometry of the Injection Region on Wall Cooling Processes ARC 27373, HMT 78, September 1965.

77. G.J. Sturgess: Application of Film Cooling Theory to the Cooling of Aircraft Gas Turbine Chambers, J.R. Ae.S., Vol.71, pp.430-434, June 1967.

78. D.B. Spalding: Theory of Rate of Spread of Confined Turbulent Pre-Mixed Flames, 7th Symposium on Combustion, Butterworths Scientific Press. London, 1958.

79. G.J. Sturgess: A Mixing Parameter and Correlation for Multi-Jet Mixing in a Duct, unpublished work, 1964.

80. P.Bradshaw and M.T.Gee: Turbulent Wall-Jets With and Without an External Stream, R & M No.3252,1962.

81. H. Patel: A Note on Correlating Film Cooling Data, unpublished work, Loughborough University, 1967.

82. G.J. Sturgess: Correlation of Film Cooling Data from Combustion Chamber Experimental Devices, unpublished report, 1966.

83. G.J. Sturgess: Correlation of Film Cooling Data from Combustion Chamber Experimental Devices,- Part 2, unpublished report 1968.

84. G.J. Sturgess: Correlation of Data and Prediction of Effectiveness from Film Cooling Injection Geometries of a Practical Nature, paper read to Cranfield International Propulsion Symposium, April 1969, (to be published).

85. A.H. Lefebvre and G.A. Halls: Some Experiences in Combustion Scaling, Advanced Aero Engine Testing (Edit. Morley and Fabri), AGARDograph 37, pp.177-204, Pergamon Press 1959.

86. G.J. Sturgess: Combustion in Advanced Gas Turbine Systems (Edit. I. Smith), Pergamon Press, pp 347-376, 1968.

87. M.J. Holland: Film Cooling in Air Breathing Engines, ARC 27,379, HMT 80, December 1965.

88. M. Whittacker: Theoretical Assessment of Flametube Temperatures in a Combustor Operating at Typical SST Conditions, paper read to Cranfield International Propulsion Symposium, April 1969, (to be published).

89. A.D. Gosman, W.M. Pun, A.K. Runchal, D.B. Spalding and M. Wolfshtein: Heat and Mass Transfer in Recirculating Flows,

Academic Press, 1969.

90. H. Schlichting: Boundary Layer Theory, 4th Edition, McGraw Hill, p.51, 1960.

91. ibid, p. 475.

92. J.F. Nash: Laminar Mixing of a Non-Uniform Stream with a Fluid at Rest, ARC CP. 613, September 1960.

93. J. Crank: The Mathematics of Diffusion, O.U.P. 1957.

94. Proceedings: Computation of Turbulent Boundary Layers - 1968 AFOSR - IFP- Stanford Conference, Thermosciences Division, Dept. Mech. Eng., Stanford University, 1969.

95. H.H. Korst and W.L. Chow: Non- Isoenergetic Turbulent ($Pr_{t*} = 1$), Jet Mixing Between Two Compressible Streams at Constant Pressure, NASA CR - 419, April 1966.

96. J.F. Nash: The Effect of an Initial Boundary Layer on the Development of a Turbulent Free Shear-Layer, ARC Current Paper CP. No.682, 1963.

97. H. Schlichting: Boundary Layer Theory, 4th Edition, McGraw Hill, p.481, 1960.

98. F.N. Kirk: An Approximate Theory of Base Pressure in Two-Dimensional Flow at Supersonic Speeds, RAE. TechNote Aero 2377, 1954.

99. G.N. Abramovich: The Theory of Turbulent Jets, pp.475-478, Scripta Technica, M.I.T. Press, 1963.

100. A. Ferri, P.A. Libby, and V. Zakkay: Theoretical and Experimental Investigation of Supersonic Combustion, pp.55-118, High Temperatures in Aeronautics, Pergamon Press, 1962.

101. L.J. Alpinieri: Turbulent Mixing of Coaxial Jets, AIAA Journal, Vol. 2, No.9, pp.1560,- 1567, 1964.

102. G.N. Abramovich: Mixing Turbulent Jets of Different Density, Izvestiya Akademii Nauk, U.S.S.R., Oldeleniye Tekhnicheskitch Nauk, Mekhanika i Mashinostroyeniye, No.3, pp.55-57, 1961. (English Trans. AFSC, FTD-TT -63 -222, March,1963).

103. R.G. Ragsdale and O.J. Edwards: Turbulent Coaxial Mixing of Dissimilar Gases at Nearly Equal Stream Velocities, NASA TM X -52082, June 1965.

104. P. Bradshaw : Turbulent Boundary Layers, J.R. Ae.S., Vol 72, No. 689, pp. 451- 459, May 1968.

105. P. Bradshaw and D.H. Ferriss: The Response of a Retarded Equilibrium Turbulent Boundary Layer to the Sudden Removal of Pressure Gradient, NPL Aero. Dept. 1145, 1965.

106. K.O. Felsch : Beitrag zur Bereohnung Turbulenter Grenzschiohten in Zweidiminsionaler Inkompressibler Stromung, Teohnischen Hochschule Karlsruhe, Dr.- Ing. Dissertation, 1965.

107. P. Goldberg : Upstream History and Apparent Stress in Turbulent Boundary Layers, MIT, GTL Dept. 85, 1966.

108. D.B. Spalding : Theories of the Turbulent Boundary Layer, Appl. Mech. Rev. Vol.20, p.735, 1967.

109. M.P. Escudier: The Turbulent Incompressible Hydrodynamic Boundary Layer, Imperial College Report TWF/R/6, October, 1967.

110. M.P. Escudier: The Distribution of the Mixing Length in Turbulent Flows Near Walls, Imperial College Rept. TWF/TN/1, 1965.

111. R. Curtet and R.P. Ricou : On the Tendency to Self- Preservation in Axisymmetric Ducted Jets, Trans.ASME, J. Basic Engineering, Vol.86, No.4, pp.765-776, December 1964.

112. R.G. Ragsdale, H. Weinstein and C.D. Lanzo : Correlation of a Turbulent Air-Bromine Coaxial-Flow Experiment, NASA TN D-2121, February 1964.

113. O.V. Yakovlevskiy : An Hypothesis on the University of Ejection Properties of Turbulent Gas Jets and Its Application, Izvestiya Akademii Nauk SSSR, Otdeleniye Tekhnicheskikh Nauk, Mekhanika i Mashinostroyeniye, No.3, pp.40-54, 1961.

114. H.S. Ribner : Field of Flow About a Jet and Effects of Jets on Stability of Jet-Propelled Airplanes, NACA WR.L -213, 1946.

115. I.S. Gartshore: Jets and Wall-Jets in Uniform Streaming Flow, Report 64-4, McGill University, May 1964.

116. G.L. Harris : The Turbulent Wall-Jet in a Moving Stream, AGARDograph 97, Recent Developments in Boundary Layer Research, Part 1, P-159-191, May 1965.

117. I.S. Gartshore : The Streamwise Development of Certain Two-Dimensional Turbulent Shear Flows, Report 65-3, McGill University, April 1965.

118. W. Tollmien : Berechnung tubulenter Ausbreitungs-vorgänge, ZAMM Vol 6, No.6, p.468, 1926.

119. A. Kuethe : Investigation of the Turbulent Mixing Regions Formed by Jets, J.Appl. Mech. Vol 11, No.3, A87, 1935.

120. H. Görtler : Berechnung von Aufgaben der freien Turbulenz auf Grund eines neuen Naherungsansatzes, ZAMM Vol 22, No.5, 1942.

121. D.B. Spalding : The Plane Turbulent Mixing Layer with Non-Uniform Density, author's manuscript, July 1964.

122. H. Schlichting : Boundary Layer Theory, 4th,Edit. McGraw-Hill, pp 600-604, 1960.

123. L.A. Vulis: Krascheta Turbulentnykh Svobod -uykh Struy Szhimay-emogo Gaza. Izv. AN Kaz SSR, ser. Energeticheskaya, No.10, 1956.

124. Sh. A. Yershin : Eksperimental' no-teoreticheskoye Issledovaniye Turbulentnogo Gazovogo Fakela, Izv. AN. Kaz SSR, ser. Energetich-eskaya, No.1, 1960

125. B.F. Glikman : Eksperimental' noye Issledovaniye Kondensatsii Strui Para V Prostranstve, Zapolnennan Zhidkost'yu, Izv. AN. SSR, OTN, Energetika i Artomatika, No.1, 1959.

126. H.B. Squire and A.D. Young : The Calculation of the Profile Drag of Aerofoils, R&M 1838, November 1937.

127. A.R. Collar : A Closed Formula for the Drag of a Flat Plate with Transition in the Absence of a Pressure Gradient, J.R.Ae.S., Vol.64, pp.38-39, January 1960.

128. J.P. Lamb : The Development of Free Turbulent Shear Layers, AEDC -TR-65-184, December 1965.

129. W.G. Hill Jr. and R.H. Page : Initial Development of Turbulent Compressible Free Shear Layers, Trans. ASME, J. Basic Engineering Vol. 19, Series D, No.1, pp. 67-73, March 1969.

130. M.E. Childs, G.C. Paynter and E. Rodeker : The Prediction of Separation and Reattachment Flow Characteristics for Two-Dimensional Supersonic and Hypersonic Turbulent Boundary Layers, AGARD CP-4, pp.325-352, May 1966.

131. C. duP. Donaldson and K.E. Grey: Theoretical and Experimental Investigation of the Compressible Free Mixing of Two Dissimilar Gases, AIAA Paper 65-822, December 1965.

132. M. Sirierx and J.L. Solignac : Contribution A L'Etude Experimentale De La Couche De Melange Turbulent Isobare D'Un Ecoulement Supersonic, AGARD CP-4, pp. 241-270, May 1966.

133. H. Schlichting : Boundary Layer Theory, 4th. Edit., McGraw Hill, pp 292, 1960.

134. J. Kestin and P.D. Richardson : Heat Transfer Across Turbulent, Incompressible Boundary Layers, Int.J. Heat Mass Transfer, Vol.6. pp.147 -189, 1963.

135. E.R.G. Eckert and R.M. Drake : Heat and Mass Transfer, 2nd. Edit., McGraw Hill, p , 1959.

136. N. Trentacoste and P.M. Sforza : An Experimental Investigation of Three-Dimensional Free-Mixing in Incompressible, Turbulent, Free Jets, Polytechnic Institute of Brooklyn, PIBAL Report No. 871, March 1966, (AFOSR 66-0651).

137. F.H. Clauser : Turbulent Boundary Layers in Adverse Pressure Gradients, J. Aero. Sc., Vol.21, No.2, February 1954.

138. H. Schlichting : Boundary Layer Theory, p.505, 4th. Edition, McGraw Hill, 1960.

139. ibid, p. 568.

140. H.H. Korst : Discussion on paper of Seban & Back, Trans. ASME, Series C, J. Heat Transfer, Vol.84, No.3, pp.242-243, August 1962.

.....

NOMENCLATURE

Some commonly used symbols; others are defined in the text.

Higher Case.

A	area
A'_o	slot outlet area per unit width
A'_E	slot overall effective area per unit width
C_D	drag coefficient
D	drag
DZ.	dilution zone
E	emissivity
H_d	combustor dome height
L	luminosity
L_c	combustor length
M	mass velocity ratio, coolant to mainstream
Ma	Mach number
Nu	Nusselt number
P	total pressure
Pr	Prandtl number
P.Z.	primary zone
R	gas constant
Re_δ	Reynolds number based on boundary layer thickness, δ
Re_s	Reynolds number based on slot height, s
Re_x	Reynolds number based on downstream distance, x
Sc	Schmidt number
S.F.C.	specific fuel consumption

St	Stanton number
T	temperature
T.E.T.	turbine entry temperature
$Ts_{,_{ad}}$	adiabatic wall temperature

Lower Case.

b	width of mixing layer
cp	specific heat at constant pressure
cf	skin friction coefficient
d	diameter
f	film thickness, fuel/air ratio
g_o	Newton's constant of proportionality
h	heat transfer coefficient
k	thermal conductivity
l	Prandtl's mixing length
m	velocity ratio, u_m/u_c
$\dot{m}$	mass flow rate
$\dot{m}'_e$	mass flow rate entrained per unit width of film
$\dot{m}''_e$	mass flux entrained per unit area of film
$\dot{m}'_f$	film mass flow rate per unit width
n	boundary layer profile velocity index
p	static pressure
$\dot{q}$	heat flux
r	radius
s	slot height
t	time

u	downstream velocity
u_G	velocity just outside the boundary layer
$\sqrt{\overline{u'^2}}$	r.m.s. value of fluctuating downstream velocity component
v	velocity along y - axis
w	velocity along z - axis
x	distance downstream from injection plane
x_B	non-parallel axes correction length
x_c	momentum loss correction length
x_o	effective origin of wake
x_p	potential core length
x_{pi}	idealised potential core length
x_{pr}	potential core length corrected for momentum loss.
x_s	upstream apparent origin of boundary layer
x_T	transition length
y	distance normal to x - axis
z	distance mutually perpendicular to x and y axes

Greek.

γ	ratio of specific heats
δ	boundary layer thickness
δ_2	boundary layer momentum thickness
δ_w	slot lip thickness
ΔP	pressure drop across slot
θ	temperature ratio
η	film effectiveness
ρ	density
σ	Stefan - Boltzmann constant
τ_s	surface shear stress

μ	viscosity
ν	kinematic viscosity

Subscripts.

ad	adiabatic
c	coolant stream
Eff	effective
m	mainstream
s	surface.

Units.

The bulk of the present work was completed before the S.I. units were adopted. Where units do appear, those of the source data are retained.

.....

APPENDIX A1.

GENERAL ASSUMPTIONS MADE FOR S.S.T. COMBUSTION CHAMBER.

Design Point.

Engine thrust (take-off)	29,300	lb_f (dry)
	35,000	lb_f (reheated)
Engine airflow (compressor delivery)	356	lbm/sec.
Combustor airflow	342	lbm/sec.
Fuel flow	420	lbm/min.
Bleed for turbine cooling	10.25	lbm/sec. from rear of inner annulus.
Turbine entry temperature	1422	°K
Compressor delivery temperature	715	°K
Maximum bulk temperature	1726	°K
Primary Zone combustion efficiency	80	%
Overall combustion efficiency	99	%
Compressor delivery pressure	217	p.s.i.a.
Overall loss in total pressure	$\Delta P / P_2$ = 10%	losses made up of 50% in the diffuser; of the total pressure drop across the flametube wal 53% is due to mixing in the dilution zone.

Flametube (axial) length	20.5 inches
Outer flametube diameter at primary zone	3.083 feet
Inner flametube diameter at primary zone	1.832 feet.

The gas constants for combustion products and air were taken as respectively. 100 and 96 ft.lb$_f$ / lb$_m$ deg K.

Overall fuel/air ratio	0.02
Primary Zone fuel/air ratio	0.44
Primary Zone airflow	45% total combustor flow
Dilution airflow for mixing	32% total combustor flow
Material	Nimonic 75
Wall temperature limit	800^{0}C
Primary Zone mean Mach number	0.06
Dilution Zone mean Mach number	0.30

.....

A P P E N D I X A2.

SOLUTION OF THE EQUATIONS.

A.1.0. Evaluation of Integrals.

Integrals of the form of equations 7.13/ have been solved by Abramovich analytically,

i.e.

$$I_1 = \frac{-25}{18(\theta-1)} + \frac{208}{35(\theta-1)^2} + \frac{93}{20(\theta-1)^3} + \frac{7}{(\theta-1)^4} - \frac{15}{2(\theta-1)^5} - \frac{1}{(\theta-1)^6} + \frac{\ln\theta}{(\theta-1)} - \frac{6\ln\theta}{(\theta-1)^4} + \frac{\ln\theta}{(\theta-1)^7} - \frac{8\arctan\sqrt{\theta-1}}{(\theta-1)^{5/2}} + \frac{8\arctan\sqrt{\theta-1}}{(\theta-1)^{11/2}} \quad \text{A1.}$$

$$I_2 = \frac{-1}{(\theta-1)} + \frac{7}{2(\theta-1)^2} + \frac{1}{(\theta-1)^3} + \frac{\ln\theta}{(\theta-1)} - \frac{\ln\theta}{(\theta-1)^4} - \frac{4\arctan\sqrt{\theta-1}}{(\theta-1)^{5/2}} \quad \text{A2.}$$

$$I_3 = \frac{\ln\theta}{(\theta-1)} \quad \text{A3.}$$

And,

$$I_1' = \frac{-25}{18(\tau-1)} + \frac{208}{35(\tau-1)^2} + \frac{93}{20(\tau-1)^3} + \frac{7}{(\tau-1)^4} - \frac{15}{2(\tau-1)^4} - \frac{1}{(\tau-1)^6} + \frac{\ln\tau}{(\tau-1)} - \frac{6\ln\tau}{(\tau-1)^4} + \frac{\ln\tau}{(\tau-1)^7} - \frac{8\arctan\sqrt{\tau-1}}{(\tau-1)^{5/2}} + \frac{8\arctan\sqrt{\tau-1}}{(\tau-1)^{11/2}} \quad \text{A4.}$$

$$I_2' = \frac{-1}{(\tau-1)} + \frac{7}{2(\tau-1)^2} + \frac{1}{(\tau-1)^3} + \frac{\ln\tau}{(\tau-1)} - \frac{\ln\tau}{(\tau-1)^4} - \frac{4\arctan\sqrt{\tau-1}}{(\tau-1)^{5/2}} \quad \text{A5.}$$

$$I_3' = \frac{\ln\tau}{(\tau-1)} \quad \text{A6.}$$

Unfortunately, equations A1, A2, A3, A4, A5 and A6, involve the small difference of two large numbers when θ and τ respectively, become less than 2.0 and the iterative processes for x_{p_i} and x_{p_r} go unstable, diverge and in a computer, produce a tight-loop. When this occurs, the following infinite series equations must be used:

$$I_1 = 0.316 + 486.0\left[\sum_{j=1}^{\infty}{}' \frac{(-1)^j(0-1)^j}{(j+1)(j+4)(j+7)(2j+5)(2j+1)}\right] \quad \text{A7.}$$

$$I_2 = 0.45 + 90\left[\sum_{j=1}^{\infty}{}' \frac{(-1)^j(0-1)^j}{(j+1)(j+4)(2j+5)}\right] \quad \text{A8.}$$

and,

$$I_1' = 0.316 + 486.0\left[\sum_{j=1}^{\infty}{}' \frac{(-1)^j(\tau-1)^j}{(j+1)(j+4)(j+7)(2j+5)(2j+1)}\right] \quad \text{A9.}$$

$$I = 0.45 + 9.0\left[\sum_{j=1}^{\infty}{}' \frac{(-1)^j(\tau-1)^j}{(j+1)(j+4)(2j+5)}\right] \quad \text{A10.}$$

For isothermal flows,

$$I_1 = I_1' = 0.316 \quad \text{A11.}$$

$$I_2 = I_2' = 0.45 \quad \text{A12.}$$

$$I_3 = I_3 = 1. \quad \text{A13.}$$

A.2.0. Computer Program Symbols.

An early version, GJS5D4, of the computer program used in the solution of the equations is presented overleaf. It is written in General Electric Time-Sharing Fortran II language. Later versions incorporate minor changes which improve the procedure and have superceeded this version which however, contains the essential substance of the solution. The later variations are written in General Electric Time-Sharing Fortran IV language. The earliest version of all was written in ICT ASA 40 Fortran IV, from which GJS5D4was adopted, and contained F_1 in equation 7.139 as a constant equal to 0.58: This is no longer considered valid and should not be used.

As the quantity x_B is usually a small quantity for the present practical application it is not included in GJS 5D². Also, the manner in which some of

the equations are handled in GJS 5D* ocn, for certain input conditions, result in failure of the solution. This defect, which occurs for low slot Reynolds numbers at high velocity ratio, is an accuracy problem arising in the subtraction of two very nearly equal numbers and is not of real significance for combustion chamber cooling. Failure is immediately evident from the output when it occurs. In later versions, the equations are handled differently.

Major symbol definitions for the program are:

INPUT

AM	velocity ratio, u_m/u_c
ARES	slot Reynolds number, Re_s
TH	temperature ratio, T_c/T_m
QC	profile $\frac{1}{n}$ power law for slot lip boundary layer on coolant side
QM	profile $\frac{1}{n}$ power law for mainstream boundary layer
QW	profile $\frac{1}{n}$ power law for cooled wall boundary layer
DC	thickness of slot lip boundary layer on coolant side, ft., $(\delta)_c$
DM	thickness of mainstream boundary layer , ft., $(\delta)_m$
DWALL	thickness of cooled wall boundary layer, ft., $(\delta)_w$
S	slot height, s, ft.
W	lip thickness, δ_w, ft.
CONST	0.3000
N	number of data inputs
RUN	input number

OUTPUT.

ARES	slot Reynolds number, Re_s
AM	velocity ratio, u_m/u_c

Q	$(\delta)_p / s$,	non-dimensional cooled wall boundary layer at x_p
DA	$(\delta)_m / s$	non-dimensional mainstream boundary layer thickness
DB	$(\delta)_c / s$	non-dimensional slot-lip boundary layer thickness
WW	δ_w / s ,	ratio of lip thickness to slot height
TH	T_c / T_m	temperature ratio
R	x_{pr} / s	non-dimensional potential core length.
RUN		output number.

The coolant velocity for the input velocity ratio and slot Reynolds number should be based on the peak in the slot outlet profile. The predicted values for non-dimensional potential core length in the output should be corrected for mainstream turbulence if this is greater than 1.5-2.0 %, from figure 2.14 and, by the Prandtl number ratio as indicated in Appendix A3 if thermal values are required.

.....

FLOW DIAGRAM FOR PROGRAM GJS5D*

MASTER BLOCK 'POTCOR'

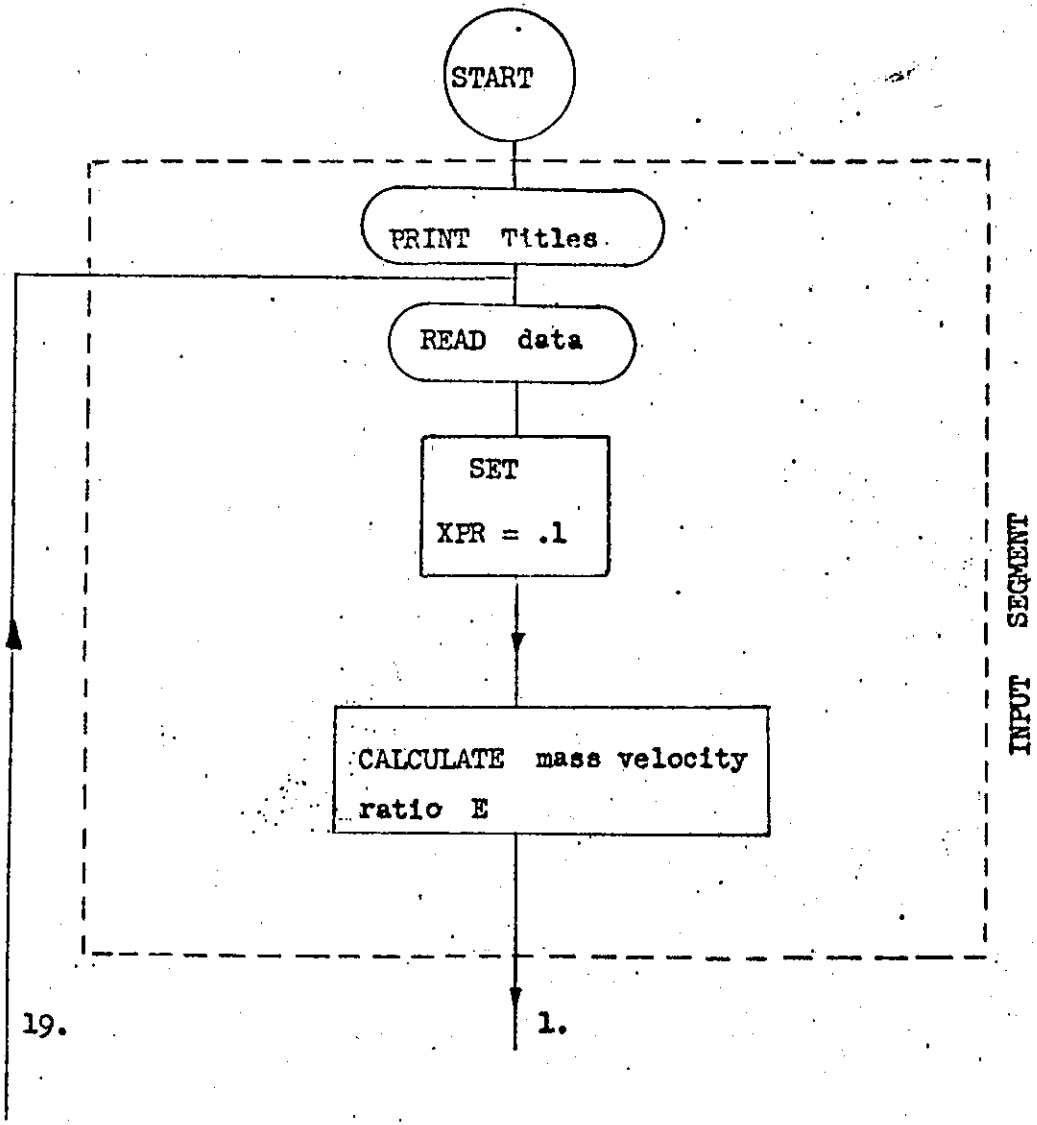

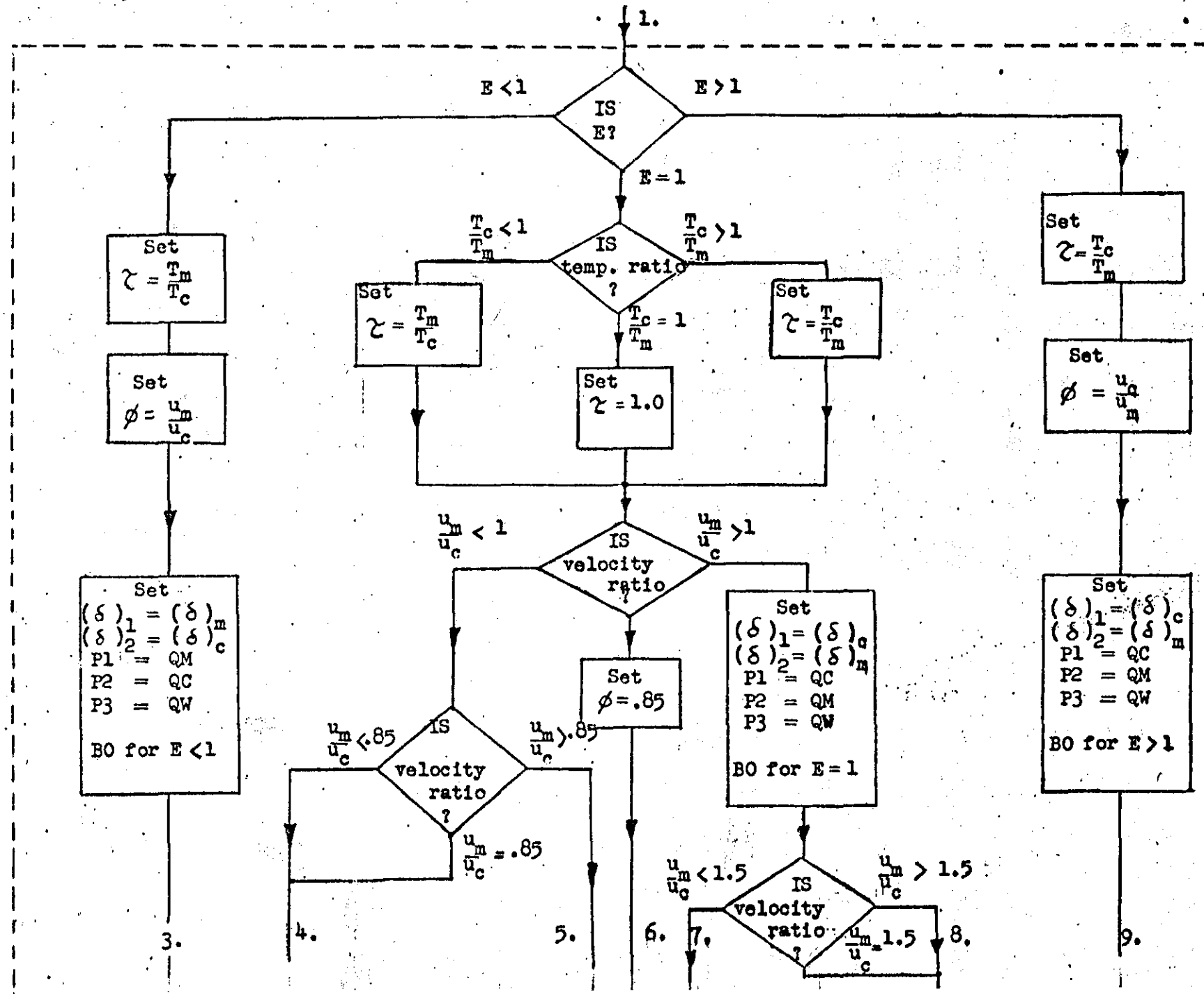

SPECIFICATION OF BOUNDARY CONDITIONS SEGMENT

SPECIFICATION OF BOUNDARY CONDITIONS SEGMENT

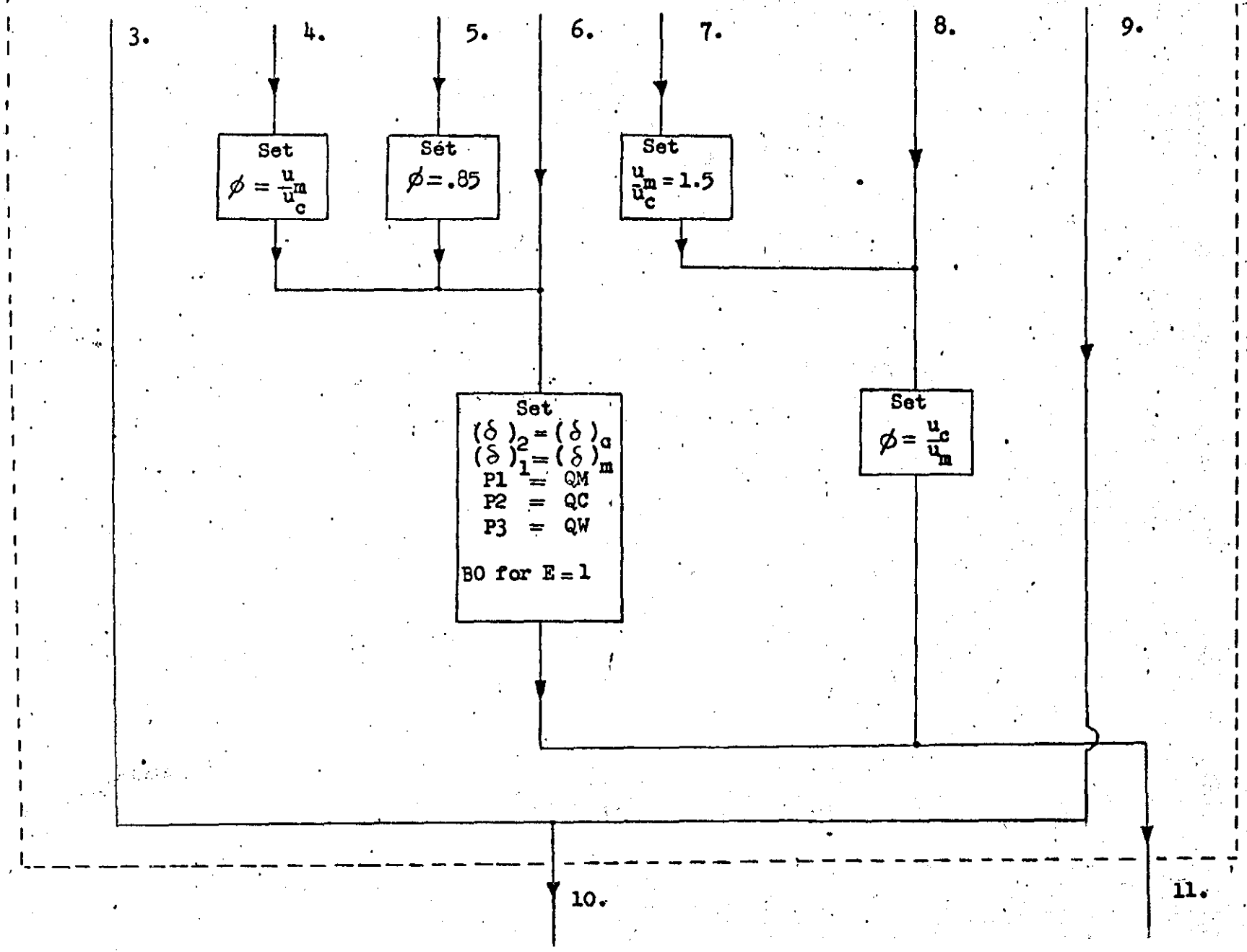

ACCOUNT OF PRETURBULENCE SEGMENT

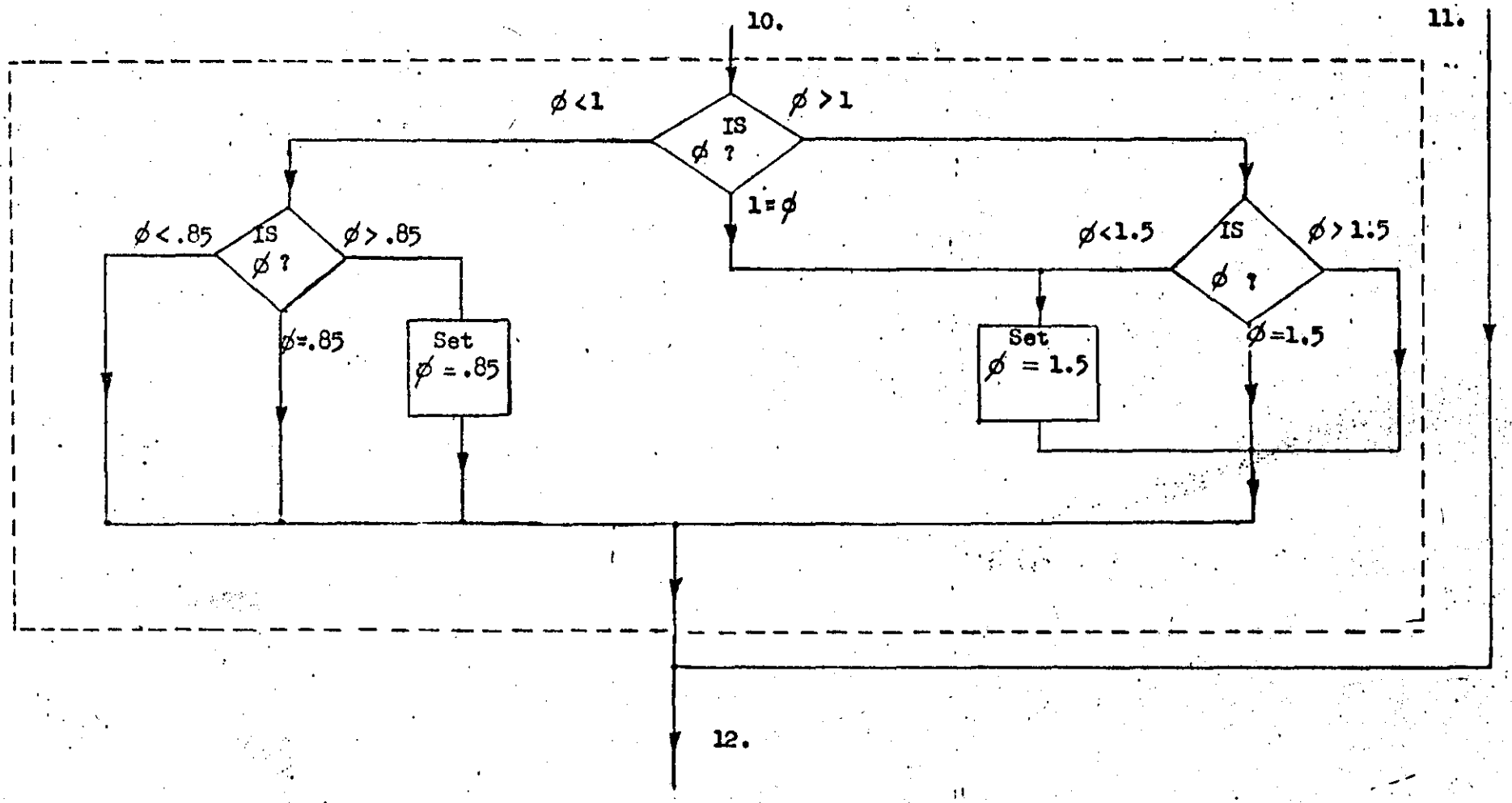

EVALUATION OF WAKE MOMENTUM LOSS AND KIRK'S CORRECTION LENGTH SEGMENT

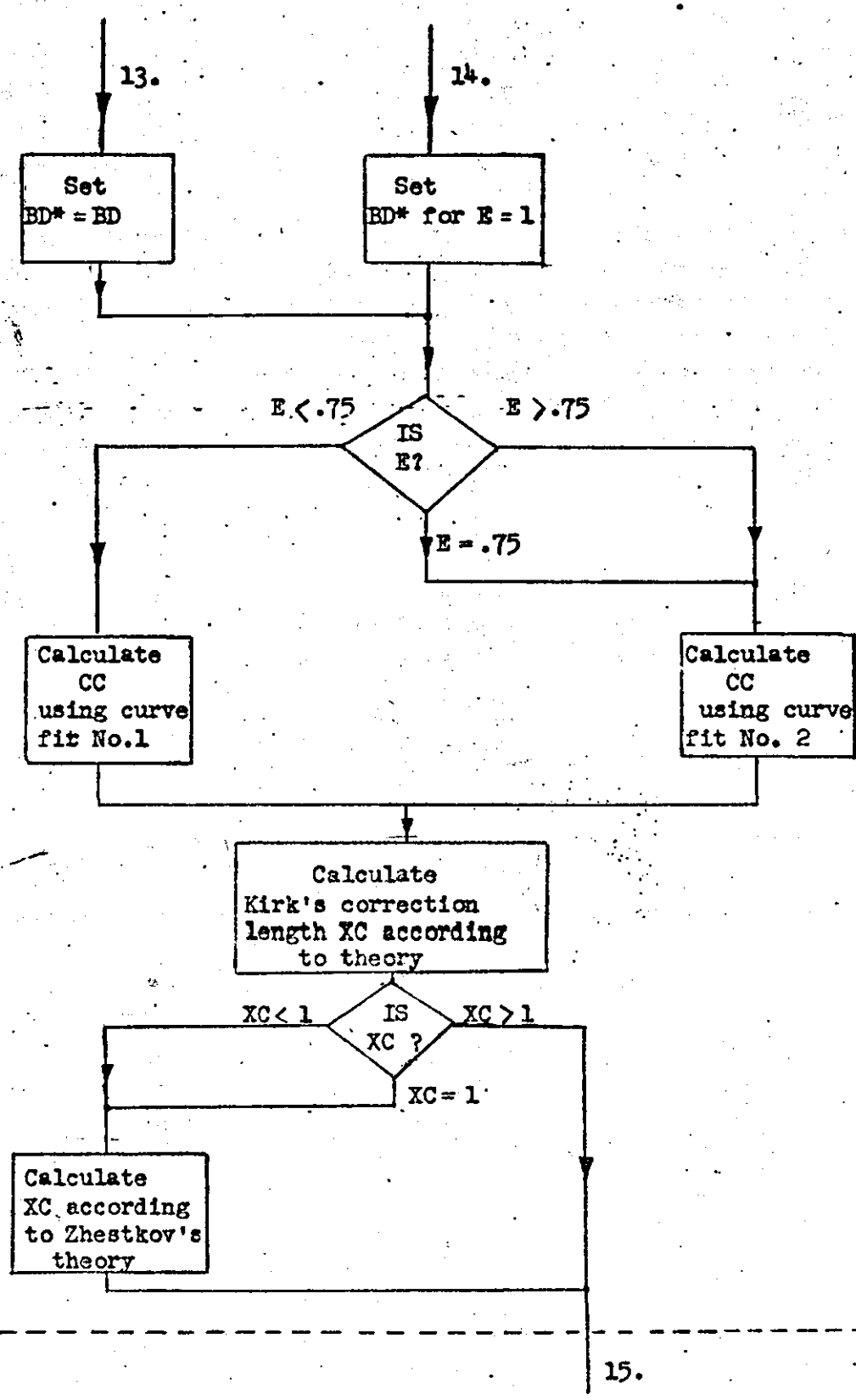
13.
14.
Set BD* = BD
Set BD* for E = 1
E < .75
IS E?
E > .75
E = .75
Calculate CC using curve fit No.1
Calculate CC using curve fit No. 2
Calculate Kirk's correction length XC according to theory
XC < 1
IS XC ?
XC > 1
XC = 1
Calculate XC according to Zhestkov's theory
15.

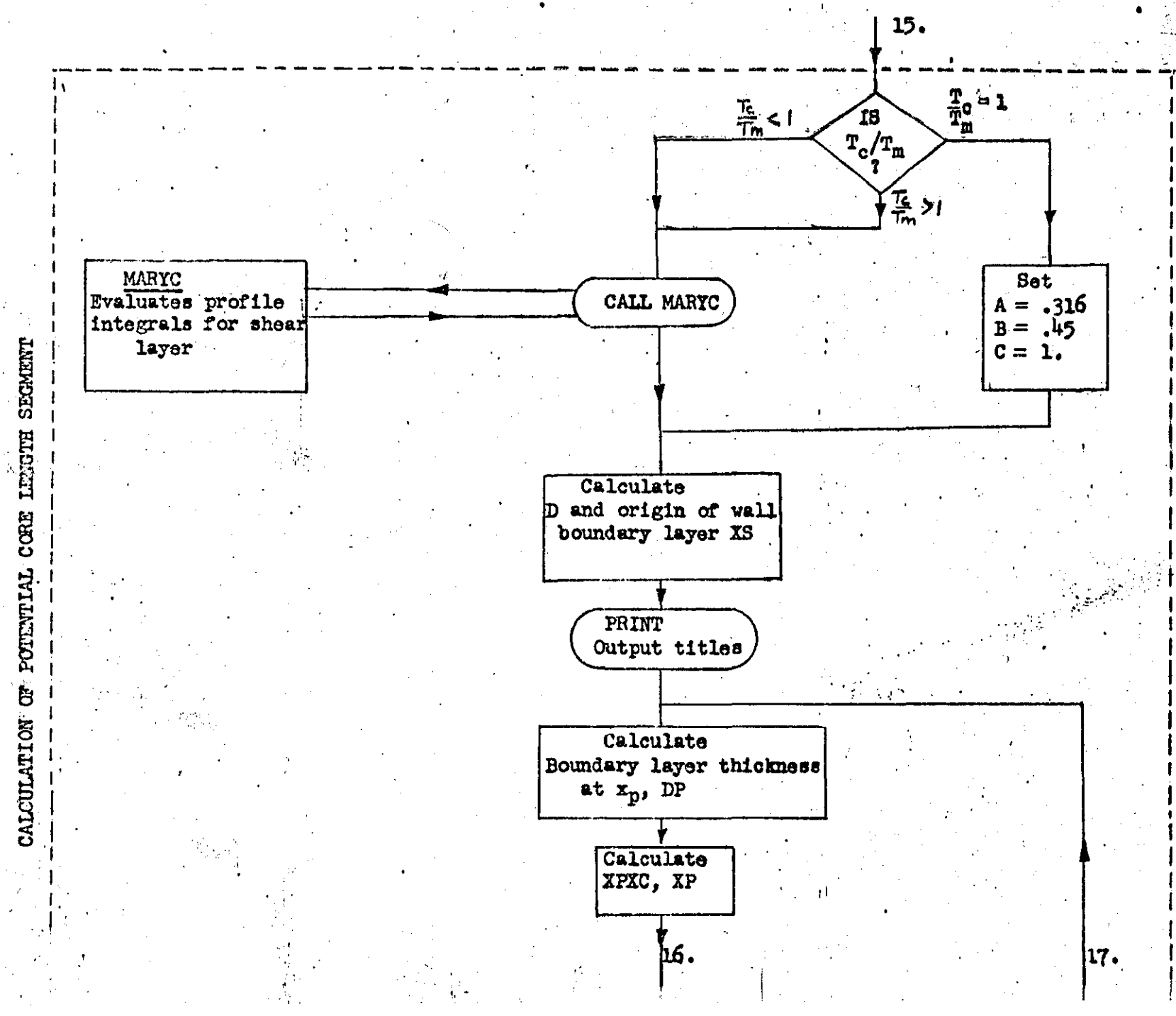
CALCULATION OF POTENTIAL CORE LENGTH SEGMENT
15.
IS Tc/Tm ?
Tc/Tm < 1
To/Tm = 1
Tc/Tm > 1
MARYC
Evaluates profile integrals for shear layer
CALL MARYC
Set
A = .316
B = .45
C = 1.
Calculate
D and origin of wall boundary layer XS
PRINT
Output titles
Calculate
Boundary layer thickness at xp, DP
Calculate
XPXC, XP
16.
17.

CALCULATION OF POTENTIAL CORE LENGTH SEGMENT

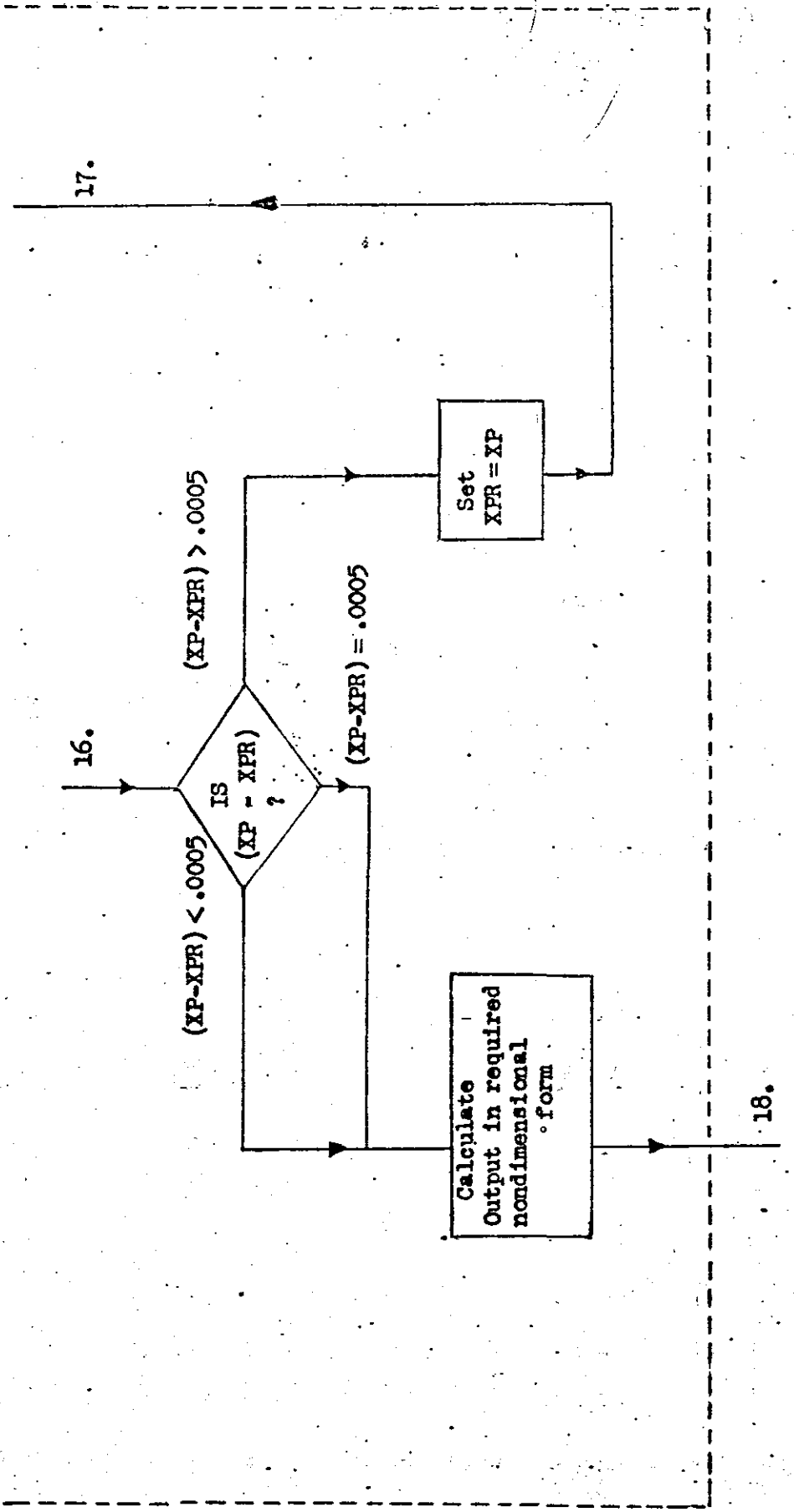

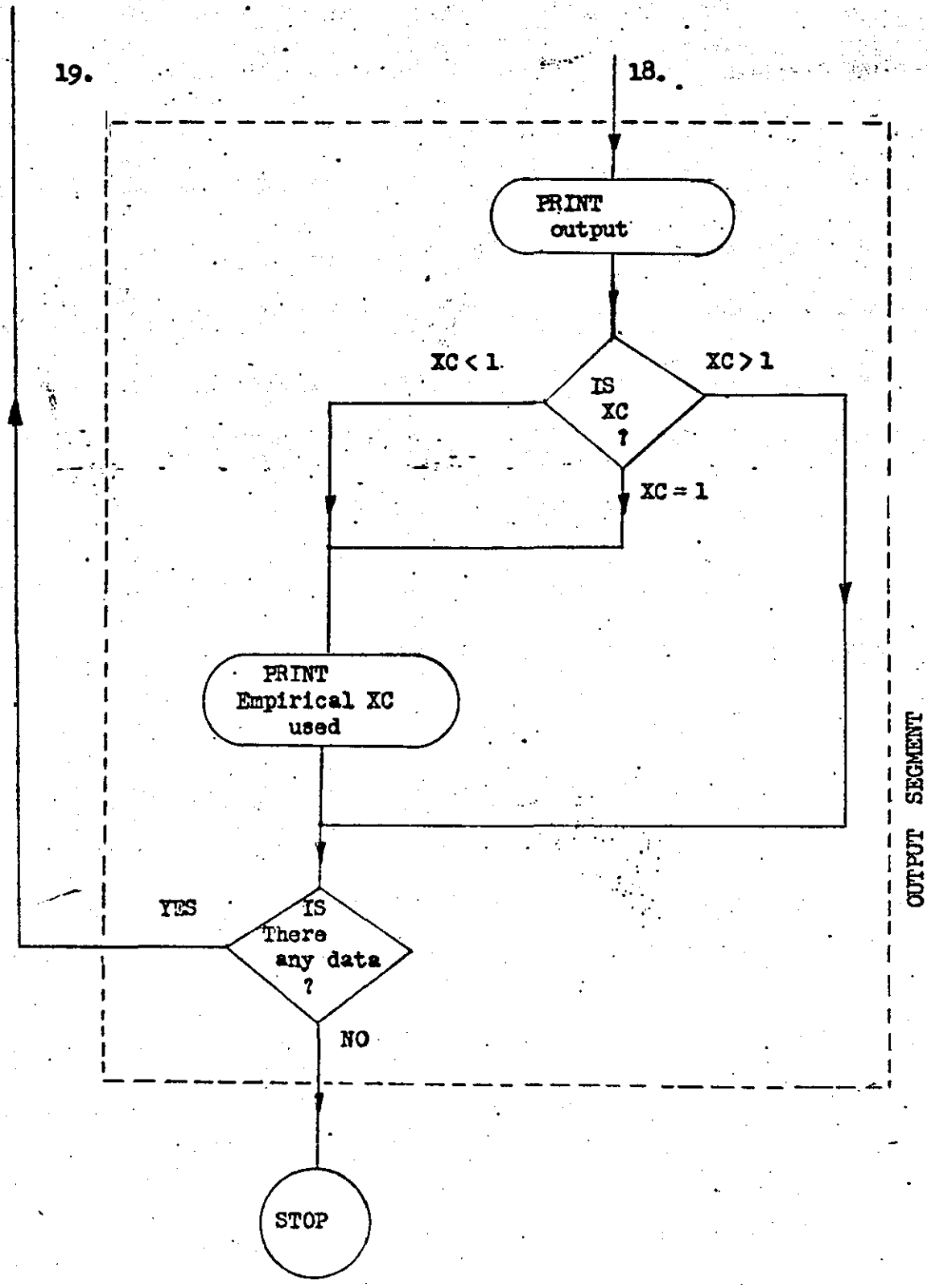
19.
18.
PRINT output
XC < 1
IS XC ?
XC > 1
XC = 1
PRINT Empirical XC used
YES
IS There any data ?
NO
STOP
OUTPUT SEGMENT

SUBROUTINE MARYC

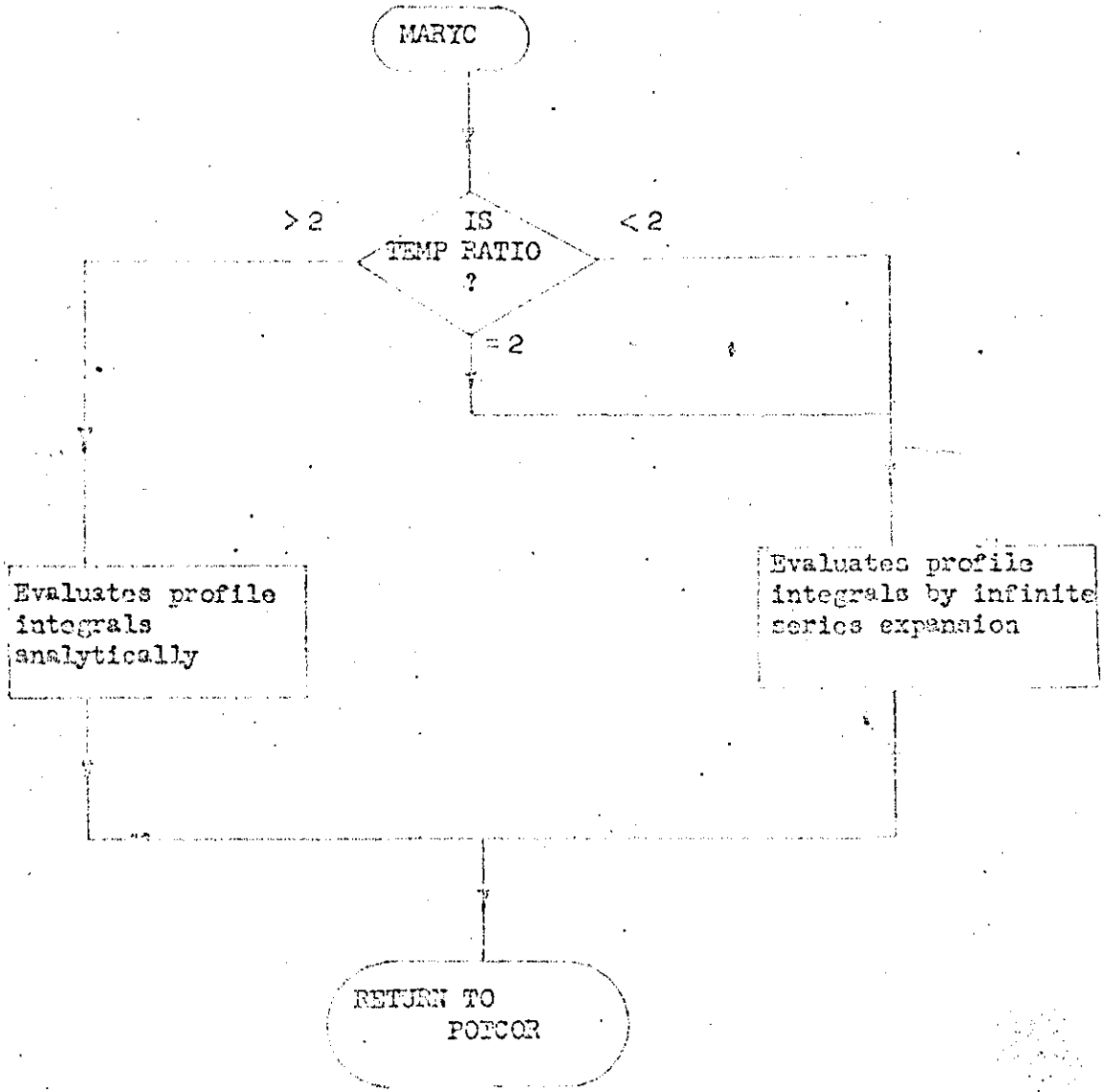

GJS5 D*

```
0000 $FILE GJS5DA
001 'PROGRAM CALCULATES POTENTIAL CORE PREDICTIONS FROM EXPERIMENTAL DATA
002 '[redacted]
004  DIMENSION AM(15),ARES(15),QC(15),QM(15),DC(15),DM(15),DWALL(15),
005 +QW(15),RUN(15),E(15),DTWO(15),P2(15),DWUN(15),P1(15),CM(15),
006 +BO(15),BD(15),BDSTAR(15),XC(15),C(15),D(15),DP(15),XS(15),P3(15),
007 +XP(15),XD(15),R(15),Q(15),DA(15),DB(15),WW(15),XPR(15),XPXC(15),
008 +CC(15),XC1(15)
010  COMMON Y(15),F(15),AA(15),BB(15),Z(15),TH(15),A(15),B(15)
015  INTEGER RUN,DATARUN
020  PRINT 20;20: FORMAT(61H          PREDICTION OF POTENTIAL CORE
022 +  FROM EXPERIMENTAL DATA//)
025 25: READ(1),DATARUN,S,W,N,CONST
026  PRINT 26,DATARUN;26: FORMAT(2X,13HDATA RUN NO.=I4);PRINT
027  PRINT 27;27: FORMAT(3X,2HAM,6X,2HCC,6X,2HXC,6X,2HXS,6X,2HBO,6X,
028 +3HBD*,4X,3HRUN)
030  READ(1),(AM(I),ARES(I),TH(I),QC(I),QM(I),DC(I),DM(I),DWALL(I),
032 +QW(I),RUN(I),I=1,N)
035  DO 207 I=1,N
040  XPR(I)=.1
045  E(I)=AM(I)*TH(I)
050  IF(E(I)-1)55,65,125
055 55: F(I)=1/TH(I): DTWO(I)=DC(I); P2(I)=QC(I); P3(I)=QW(I); DWUN(I)=DM(I)
060  P1(I)=QM(I): CM(I)=AM(I); BO(I)=.724*DTWO(I); GO TO 133
065 65: IF(1-TH(I))70,75,80
070 70: F(I)=TH(I): GO TO 82
075 75: F(I)=1; GO TO 82
080 80: F(I)=1/TH(I); 82: IF(1-AM(I))85,100,105
085 85: DWUN(I)=DC(I); P1(I)=QC(I); DTWO(I)=DM(I): P2(I)=QM(I); P3(I)=QW(I)
090  BO(I)=DTWO(I)+.5*W; IF(AM(I)-1.5)90,95,95; 90: AM(I)=1.5
095 95: CM(I)=1/AM(I); GO TO 138
100 100: CM(I)=.85: GO TO 120
105 105: IF(.85-AM(I))110,115,115
110 110: AM(I)=.85: GO TO 120
115 115: CM(I)=AM(I)
120 120: DTWO(I)=DC(I); P2(I) 0 138; 125: F(I)=TH(I); CM(I)=1/AM(I)
130  DTWO(I)=DM(I); P2(I)=QM(I); DWUN(I)=DC(I); P1(I)=QC(I); P3(I)=QW(I)
132  BO(I)=.724*DTWO(I)
133 133: IF(1-CM(I))134,135,136
134 134: IF(CM(I)-1.5)135,138,138
135 135: CM(I)=1.5; GO TO 138
136 136: IF(CM(I)-.85)138,138,137
137 137: CM(I)=.85
138 138: IF(F(I)-1)140,145,140
140 140: Y(I)=F(I)-1; CALL MARYC(Y(I),F(I),AA(I),BB(I)); GO TO 150
145 145: AA(I)=.316; BB(I)=.45
150 150: BD(I)=(CM(I)↑2)*(P1(I)/((P1(I)+1)*(2*P1(I)+1))*DWUN(I)+P2(I)/
155 +((P2(I)+1)*(2*P2(I)+1))*DTWO(I)*F(I)/(CM(I)↑2,-.5*W)/(F(I)*(1-CM(I))
156 +*(BB(I)-AA(I)+CM(I)*AA(I)))
```

GJS5D* CONTINUED

```
160 IF(E(I)-1)160,162,160;160:BDSTAR(I)=BD(I);GO TO 165
162 162:BDSTAR(I)=BD(I)+.5*W
165 165:IF(E(I)-.75)168,172,172
168 168:CC(I)=-109.60542+2268.8830*E(I)-20665.639*E(I)↑2+
169 +108286.53*E(I)↑3-358766.76*E(I)↑4+778528.76*E(I)↑5-
170 +1106212.7*E(I)↑6+992655*E(I)↑7-510709.89*E(I)↑8+114858.23*E(I)↑9
171 GO TO 176
172 172:CC(I)=533.7938-4259.6355*E(I)+14851.5*E(I)↑2-
173 +29950.40*E(I)↑3+38488.911*E(I)↑4-32672.695*E(I)↑5+
175 +18312.651*E(I)↑6-6532.1766*E(I)↑7+1345.1347*E(I)↑8-121.8105*E(I)↑9
176 176:XC(I)=(2*((1+F(I)*CM(I))↑2)*(BDSTAR(I)*(1/CONST-1/CC(I))+
177 +BO(I)*1/CC(I)))/((1+F(I))*ABS(1-F(I)*CM(I)↑2))
178 XC1(I)=XC(I):IF(XC1(I))178,178,180;178:XC(I)=3*CM(I)*(W+DTWO(I)*
179 +P2(I)/(P2(I)+1)+DWUN(I)*P1(I)/(P1(I)+1))
180 180:IF(1-TH(I))184,190,184
184 184:Z(I)=TH(I)-1
185 CALL MARYC(Z(I),TH(I),A(I),B(I));C(I)=LOG(TH(I))/Z(I)
186 GO TO 195
190 190:A(I)=.316;B(I)=.45:C(I)=1
195 195:D(I)=(CONST*(1+TH(I))/2*ABS(1-TH(I)*AM(I)↑2)/(1+TH(I)*AM(I)
200 +)↑2)*(C(I)-(2-AM(I))*B(I)+(1-AM(I))*A(I))*TH(I)
205 XS(I)=(DWALL(I)/.05815)↑1.25*(ARES(I)/S)↑.25*P3(I)/((P3(I)+1)*
206 +(2*P3(I)+1))
207 207:CONTINUE
208 PRINT 209,(AM(I),CC(I),XC(I),XS(I),BO(I),BDSTAR(I),RUN(I),I=1,N)
209 209:FORMAT(2F7.4,4F8.4,I7);PRINT;DO 260 I=1,N
210 210:DP(I)=.05815*((P3(I)+1)*(2*P3(I)+1)/P3(I))↑.8*S↑2*
215 +(XS(I)+XPR(I))↑.8/ARES(I)↑.2
220 XPXC(I)=S/(DP(I)/(XPR(I)+XC(I))+D(I))
230 XP(I)=XPXC(I)-XC(I)
235 IF(ABS(XP(I)-XPR(I))-.0005)245,245,240
240 240:XPR(I)=XP(I):GO TO 210
245 245:R(I)=XPR(I)/S:Q(I)=DP(I)/S;WW(I)=W/S;DA(I)=DM(I)/S;DB(I)=DC(I)/S
260 260:CONTINUE;PRINT 261:261:FORMAT(3X,2HAM,5X,4HXPXC,5X,3HXPR,
261 +5X,2HXP,5X,3HXC*,5X,3HRUN)
262 PRINT 264,(AM(I),XPXC(I),XPR(I),XP(I),XC1(I),RUN(I),I=1,N)
264 264:FORMAT(2F7.4,F9.4,2F7.4,I7);PRINT
265 PRINT 265;265:FORMAT(2X,4HARES,5X,2HAM,7X,1HQ,6X,2HDA,6X,2HDB,
266 +6X,2HWW,6X,2HTH,7X,1HR,5X,3HRUN)
270 PRINT 275,(ARES(I),AM(I),Q(I),DA(I),DB(I),WW(I),
272 +TH(I),R(I),RUN(I),I=1,N)
275 275:FORMAT(F8.0,F7.4,F7.3,3F8.3,F9.2,F8.4,I6)
280 PRINT;DO 290 I=1,N;IF(XC1(I))285,285,290
285 285:PRINT 288,I:288:FORMAT(2X,28HEMPIRICAL DATA TAKEN FOR XC(,I2,1H))
290 290:CONTINUE;PRINT;GO TO 25
298 $USE MARYC*
```

MARYC*

```
500 SUBROUTINE MARYC(YZ,FTH,AI,BI)
505 COMMON Y(15),F(15),AA(15),BB(15),Z(15),TH(15),A(15),B(15)
507 YY=11/2
510 IF(2-FTH)515,540,540
515 515: AI=-25*(18*YZ)+208/(35*YZ↑2)+93/(20*YZ↑3)+7/YZ↑4-
520 +15/(2*YZ↑5)-1/YZ↑6+LOG(FTH)/YZ-6*LOG(FTH)/YZ↑4+LOG(FTH)/YZ↑7-
525 +8*ATAN(SQRT(YZ))/YZ↑0.5+3*ATAN(SQRT(YZ))/YZ↑YY
530 BI=-1/YZ+7/(2*YZ↑2)+1/YZ↑3+LOG(FTH)/YZ-LOG(FTH)/YZ↑4-4*
535 +ATAN(SQRT(YZ))/YZ↑2.5;RETURN
540 540: AI=.316+486*(-YZ/7280+YZ↑2/21870-YZ↑3/52360+YZ↑4/
545 +108680-YZ↑5/204120+YZ↑6/355810-YZ↑7/585200)
550 BI=.45+9*(-YZ/70+YZ↑2/1.62-YZ↑3/308+YZ↑4/500-YZ↑5/810+
555 +YZ↑6/1190-YZ↑7/1672);RETURN
```

APPENDIX 3.

SIMILARITY OF HYDRODYNAMIC AND THERMAL POTENTIAL CORES.

A.1.0. Principle of Similarity.

The equations of Chapter 7 are solved for the hydrodynamic potential core length; the thermal potential cores measured in Chapter 4, are required. The relationship between these two cores is required.

To determine the relationship between the thermal and the hydrodynamic cores, the principle of similarity is used. From equation 7.3, the x- component of the momentum equation can be written:

$$\frac{Du}{Dt} = -\frac{1}{\rho}\ \text{grad}\ p + \nu\nabla^2 u \qquad \text{A.14}$$

The energy equation for incompressible flow can be written (133) as follows:

$$\rho\frac{D}{Dt}(c_p\theta) = \left[\frac{\partial}{\partial x}\left(k\frac{\partial\theta}{\partial x}\right) + \frac{\partial}{\partial y}\left(k\frac{\partial\theta}{\partial y}\right) + \frac{\partial}{\partial z}\left(k\frac{\partial\theta}{\partial z}\right)\right] + \mu\Phi \qquad \text{A.15}$$

where, $\theta = (T_s - T)$ and,

$$\Phi = 2\left[\left(\frac{\partial u}{\partial x}\right)^2 + \left(\frac{\partial v}{\partial y}\right)^2 + \left(\frac{\partial w}{\partial z}\right)^2 + \left(\frac{\partial v}{\partial x} + \frac{\partial u}{\partial y}\right)^2 + \left(\frac{\partial w}{\partial y} + \frac{\partial v}{\partial z}\right)^2 + \left(\frac{\partial u}{\partial z} + \frac{\partial w}{\partial x}\right)^2\right]$$

If equation A.15 is compared with equation 7.1, it can be observed:-

(i) as pointed out in Chapter 7, the flow field depends on the variation of viscosity and hence, temperature, with position, so the velocity and temperature fields are linked,

(ii) the two fields are not similar because in addition to the inclusion of certain terms which preclude similarity, the viscosity μ and thermal conductivity k depend on different functions of temperature.

Following now Kestin and Richardson (134), equation A.15 can be rewritten by assuming constant fluid properties, in the form of equation A.14.

i.e. $$\frac{D\theta}{Dt} = \alpha\nabla^2\theta + \frac{\nu}{c_p}\Phi \qquad \text{A.16}$$

where, $a = \frac{k}{\rho c_p}$, the thermal diffusivity.

By comparing equations A.14 and A.16, it can be seen that the velocity field is now entirely independent of the temperature field. Also, but for the presence of a pressure gradient term and the term ϕ , the two equations have the same mathmatical form. Assume therefore that the pressure gradient term is small everywhere compared with the remaining terms, i.e. flat plate at zero or near-zero incidences, or surfaces of large radius of curvature. The term ϕ is known as the dissipation function. In a flow with a large Reynolds number of turbulence, the energy dissipation in large eddies can be neglected as compared to the energy passed from the large eddies to the smaller ones. In such a flow, the energy passed to the smaller eddies will be equal to the energy which is dissipated by viscous effects into heat since there are no external energy sources or sinks. Thus, if the fluid viscosity is not large, the dissipation function can be considered small in comparison with the other terms and the product $\mu\phi$, negligible.

With these assumptions therefore, equations A.14 and A.16 become respectively,

$$\frac{Du}{Dt} = \nu\nabla^2 u \qquad \text{A.17}$$

$$\frac{D\theta}{Dt} = a\nabla^2\theta \qquad \text{A.18}$$

and these equations will be exactly similar when $\nu = a$, or,

$$\frac{\nu}{a} = 1.0$$

Now, $\nu = \frac{\mu}{\rho}$, the kinematic viscosity, $a = \frac{k}{\rho c_p}$, the thermal diffusivity.

Thus, $\frac{\nu}{a} = \frac{\mu c_p}{k}$, the Prandtl number.

Hence, the conditions for similarity are these:

a) the flow is incompressible and of 'constant' density,

b) fluid properties can be considered constant,

c) pressure gradient is small,

d) the fluid has a low viscosity.

e) Prandtl number can be considered unity.

f) there is no thermal entry length involved.

A.2.0 Application to Theory.

The theory was developed for incompressible flow with constant pressure mixing and like-into-like injection, so the validity of both 'constant' density and constant fluid properties assumptions depends on the temperature ratio of the two streams. Pressure gradient has been assumed constant (zero), and to have zero effect on the rate of mixing in the mixing layer, and the fluids are both taken as gases so having low viscosity and a Prandtl number not far removed from unity. There will be a small thermal entry length effect due to the radiation-induced thermal boundary layer on the cooled wall beginning at $x = 0$ instead of x_s. This however, will be reduced by conduction upstream in the cooled wall, and may be considered negligible, particularly since the thermal layer will grow at a faster rate than the velocity layer.

Whether or not the two potential cores are similar then depends solely on the temperature ratio of the two initial streams contributing to the flow. Table A3-1 presents fluid property variations with temperature, at two temperature levels. This table reveals that for similarity to be a reasonable approximation, the temperature difference between the two streams should be less than about 50^0C at lower temperatures, and less than about 200^0C at higher temperatures. Generally, the higher the temperature level,

the gr ater the permissible temperature difference. A crude correction to give thermal potential core, would be to multiply the predicted hydrodynamic potential core by a Prandtl number, thus treating the field as one of Prandtl-Taylor flow. The Prandtl number should be based on a mean temperature, say, $(T_c + T_m)/2$.

.....

TABLE A3 - 1 : Variation of Fluid Properties with Temperature.

Data at 1 atmosphere.

a) $T_{ref} = 300^0K.$

T ^0K	T/T_{ref}	$\frac{c_{p_{ref}}}{c_p}$	$\frac{\mu_{ref}}{\mu}$	$\frac{\nu_{ref}}{\nu}$	$\frac{k_{ref}}{k}$	$\frac{a_{ref}}{a}$	$\frac{Pr_{ref}}{Pr}$
350	1.166	1.0	0.850	0.754	0.874	0.743	1.036
400	1.333	0.992	0.808	0.605	0.780	0.589	1.028
450	1.500	0.985	0.744	0.543	0.708	0.525	1.037
500	1.666	0.977	0.691	0.414	0.650	0.398	1.041
550	1.833	0.968	0.648	0.354	0.602	0.339	1.041

b) $T_{ref} = 800^0K$

T ^0K	T/T_{ref}	$\frac{c_{p_{ref}}}{c_p}$	$\frac{\mu_{ref}}{\mu}$	$\frac{\nu_{ref}}{\nu}$	$\frac{k_{ref}}{k}$	$\frac{a_{ref}}{a}$	$\frac{Pr_{ref}}{Pr}$
850	1.062	0.989	0.963	0.907	0.959	0.913	0.996
900	1.125	0.979	0.930	0.829	0.920	0.837	0.990
950	1.188	0.970	0.901	0.760	0.886	0.770	0.986
1000	1.250	0.961	0.873	0.699	0.856	0.712	0.981
1100	1.375	0.946	0.824	0.599	0.799	0.615	0.976

Data from reference (135).

APPENDIX A4.

PRACTICAL PROBLEMS ASSOCIATED WITH HOT-WIRE VELOCITY MEASUREMENTS.

A4 - 1. Introduction.

It was intended to obtain film velocity profiles using a hot-wire sensor ~ anemometer system, with automatic recording of output on punched paper tape through a digital voltmeter. This set-up was considered necessary because of the comprehensive investigation of the film required and, the large number of test-points to be covered with each of many geometrical set-ups. The limitations of this system severely curtailed the experimental work, and the following notes are primarily for the guidance of those tempted to wander in innocence down a similar track.

A4 - 2. Data Logging System.

The relevant part of the total data-logging system is illustrated in figure A4-1. The logger itself was a Dynamco Systems Ltd., Series 6000 and consisted of a 100 channel low-level scanner DM 5011 driven by a DM 5002 Scanner Drive with preset scanning rates of 1,2, 4 or 10 channels / sec. and manual overide with provision for external triggering, feeding a DM 2006 Analogue to Digital Converter with 6-digit display which operated a DM5021 Punch Drive Set for ICT 1905 5-hole code, driving a Creed 25 Tape Punch in 5-hole coding. It is shown in figure A4-2 . The system handles all signals in a continuous scan. The voltmeter was multi-ranging from 1 milli-volt up to 100 volts with a maximum resolution of 1 milli-volt full scale; integrating time was over 40 micro-seconds. No operational problems were encountered with the logger.

The hot-wire equipment is described in detail in Chapter 8.

A4 - 2 Measurement of Profiles.

The digital voltmeter output was calibrated on line against anemometer D.C. bridge volts. The calibration was carried out using two hot-wire probes of different design and, the same probe on different days with intermediate running of both probe and logger. The resulting calibration curve which is held to be universal, is shown in figure A4-3.

It is found that the integrating time constant of the D.V.M. was too small for the total time constant of the system. The input to the logger was therefore corrected by adding a smoothing capacitor to the output of the anemometer. This capacitor was switchable so the same anemometer could be used for turbulence measurements, with the capacitor out of circuit. The effects of this capacitor on output is illustrated in figure A4-4. Additional smoothing was incorporated by modifying the scanner-drive control cards to have 5-point sampling at 1 second intervals which were automatically averaged in the data-reduction computer program. This smoothing was incorporated in the calibration curve of figure A4-3. In figure A4-5, the importance of the 5 - point averaging is shown in a velocity profile traverse of the mainstream on the slot lip, but with zero blowing of the slot. The smoothed and averaged profiles exhibited a scatter of $\pm$ 2.0% at about 100 ft./sec., which is just acceptable.

A4 - 3 Calibration of Hot-Wire Sensors.

The hot-wires were calibrated in a relatively low turbulence wind-tunnel, (see figure A4 - 6), which was initially calibrated against a standard NPL - designed pitot-static tube. The hot-wire to be calibrated was placed in the calibration tunnel at exactly the same position as the pitot-static

tube. The tunnel calibration is shown in figure A4-7.

It was discovered that considerable drift of the hot-wire calibration occurred with cumulative running time. This is shown in figure A4-8, where at 100 ft./sec., the average drift means ± 4.0% over 6 hours. A given calibration had at the very worst, ± 3.0% scatter at 100 ft./sec. All calibration readings were made manually and not using the data-logger.

Examination of the hot-wires revealed that contamination of the fine wire with a consequent charge in its heat transfer characteristics, was responsible for the calibration changes. The contamination was both macroscopic and microscopic; microscopic contamination was always present and the macroscopic only sometimes. Macroscopic contamination consisted of small hairs which were visible to the naked eye and could usually be removed with care, by forceps. Under a microscope the wires were found to be covered with mainly clear, transparent oily droplets and occasional opaque, solid dust particles. Operation of a diesel engine in a laboratory 50 yards from the room housing the calibration tunnel brought about rapid calibration change and a noticeable increase in microscopic contamination with an increase in the ratio of solid to liquid in the deposits.

Appearance of the small hairs seemed random and interception could usually be detected on the monitoring oscilloscope. It would be expected that X-array probes would be more susceptable to picking up hairs, and this was the case. When a hair was picked up, it caused a dramatic change of calibration, of the order + 20 - 30%. X - array and single-wire probes were equally sensitive to

microscopic contamination. For an X-array probe, the individual wires were not equally affected by the contamination. Shown in figure A4 - 9 is the effect of cumulative running time on calibration drift for an X-array probe.

A washing technique was devised for the hot-wire probes. This was standardised as a 1-hour soak in pure benzene, followed by a 10 minute wash with acetone to effect final cleaning and removal of the benzene. To ensure consistent results it was found necessary to use the washing treatment and re-calibrate the probe at 60 minute intervals of running time. Figure A4-10 shows the washing technique as holding a calibration to ± 3% at 100 ft./sec., i.e. to the scatter of the calibration curve, for 1 hour periods. It also indicates that a probe may not be free from contamination initially, i.e. at zero running time. The washing technique should therefore, be carried out before initially calibrating a new probe. The figure also shows that with a carefully controlled handling procedure, the so-called fragile hot-wire probes can be run for many hours, survive repeated washing treatments, and, building -to building transport with intermediate mounting and dismounting.

It was determined that to be useful in the present programme, a given probe and output system would be required to hold a net calibration within ± 3% at all velocities for periods not less than two hours duration. There was a possibility that with further development of the instrumentation and intake filter, together with effective phasing of tests with the nearby diesel-engine tests, that this requirement could have been met. However, time did not permit this possibility to be explored. The probability of random encounter with a hair of course, would always be present.

The contamination does affect the dynamic performance of the wires but not significantly, as is shown in figures A4 - 11 and A4 - 12.

.....

FIG. A4-1: HOT WIRE ELECTRONICS

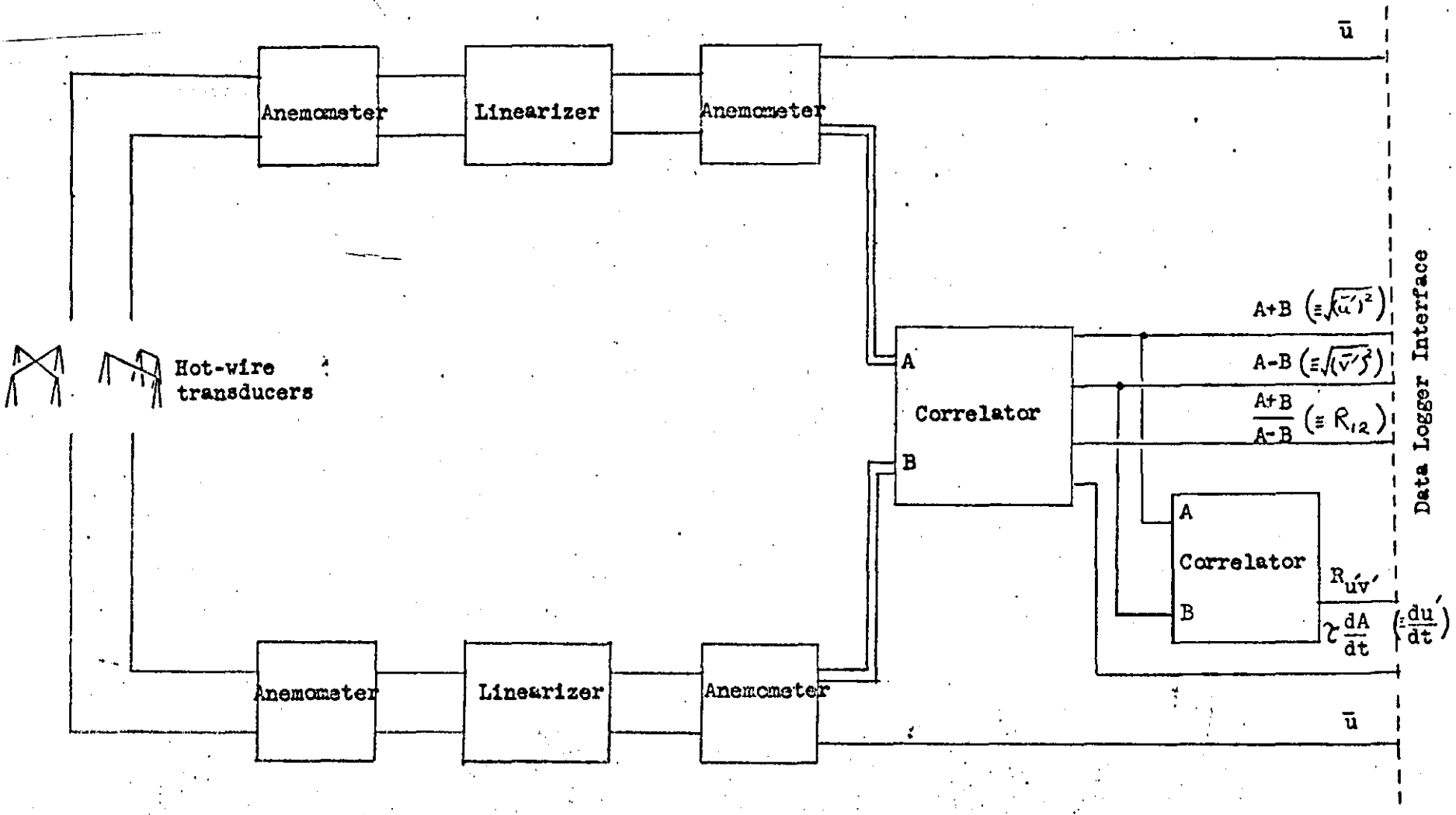

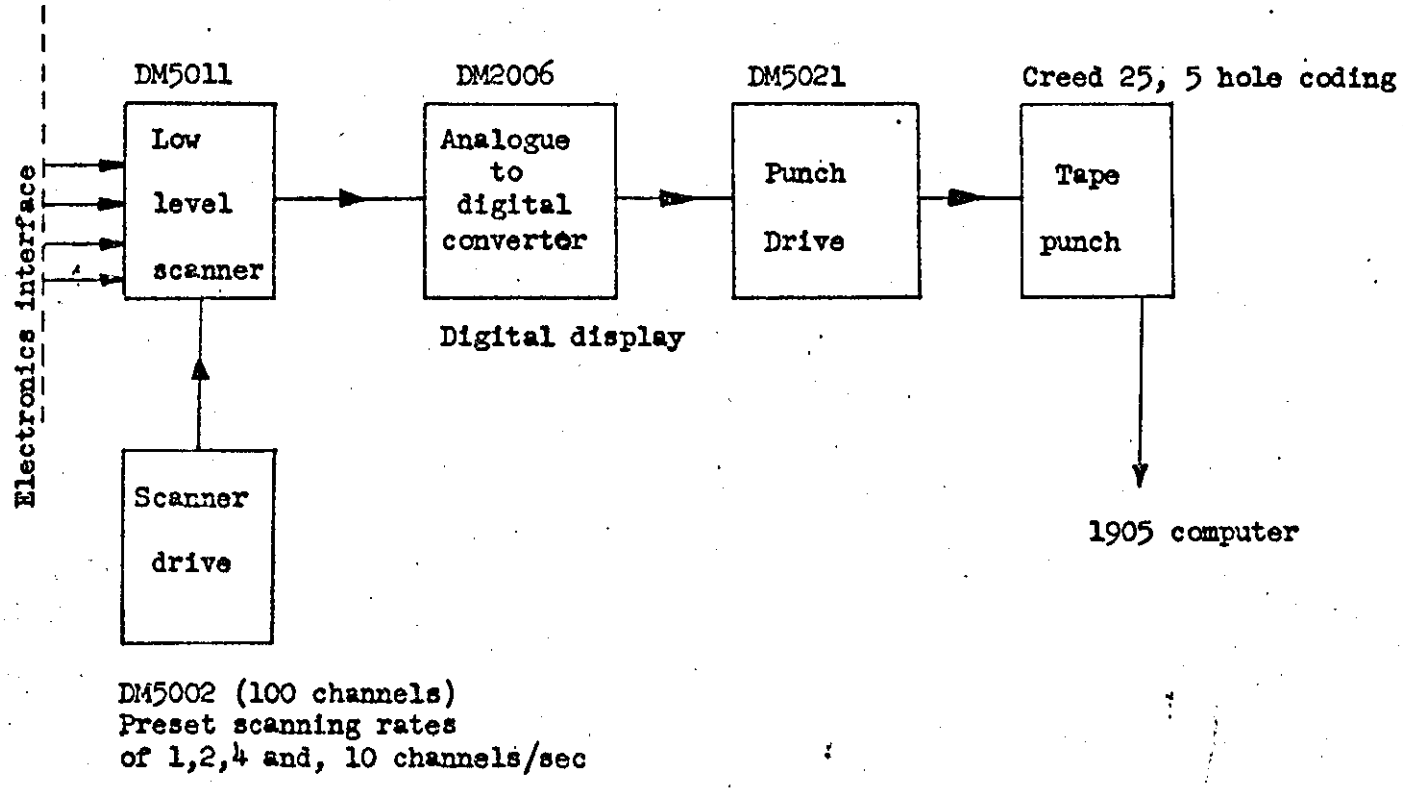

FIG. A4-2: DIGITAL MEASUREMENTS DATA LOGGING SYSTEM

FIG. A4-3: CALIBRATION OF D.V.M. OUTPUT AGAINST ANEMOMETER BRIDGE VOLTS

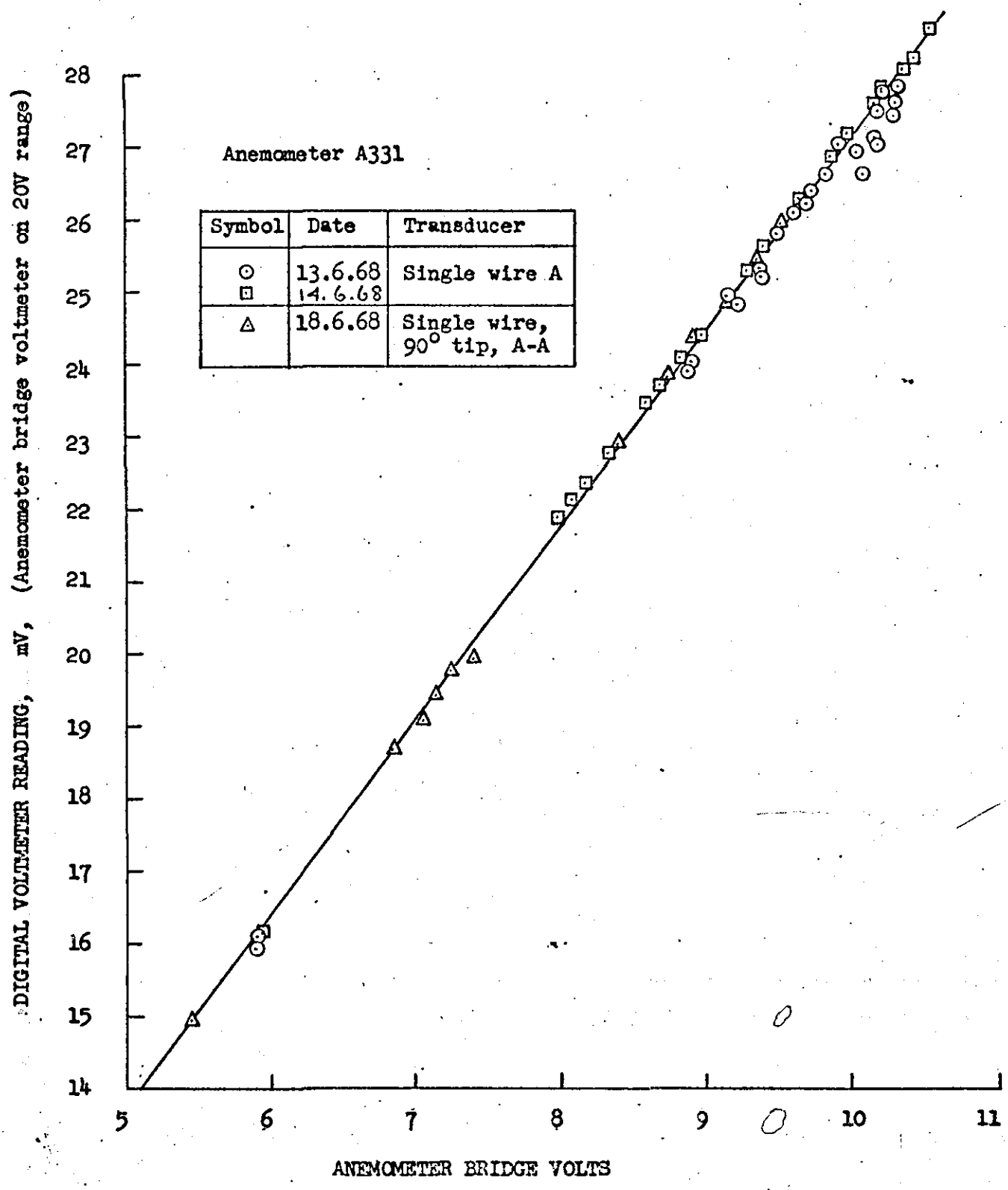

FIG. A4-4: EFFECT OF DAMPING ON ANEMOMETER BRIDGE VOLTS AS RECORDED ON PUNCHED PAPER TAPE BY D.V.M.

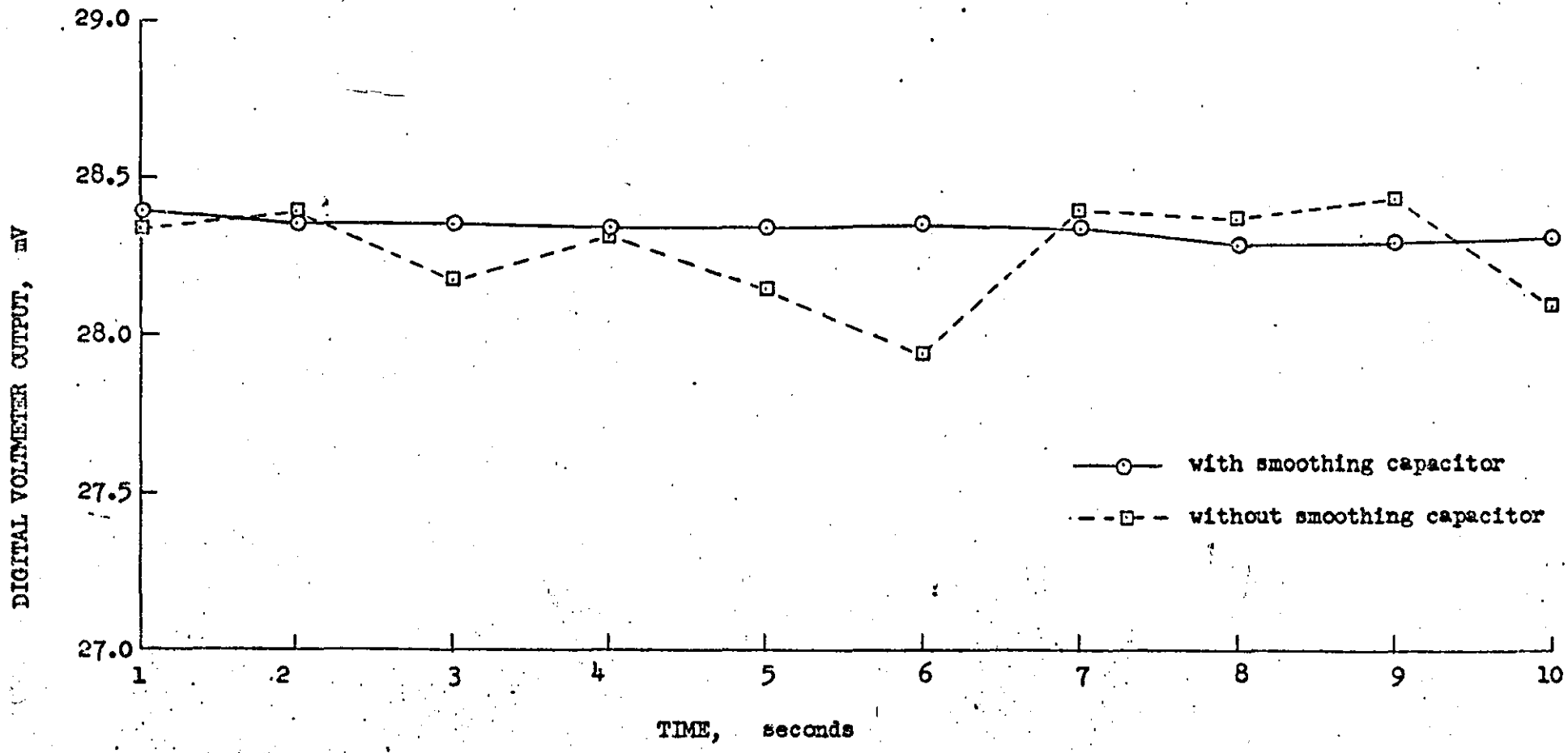

FIG. A4-5: EFFECT OF TIME AVERAGING ON MEASURED VELOCITY PROFILE

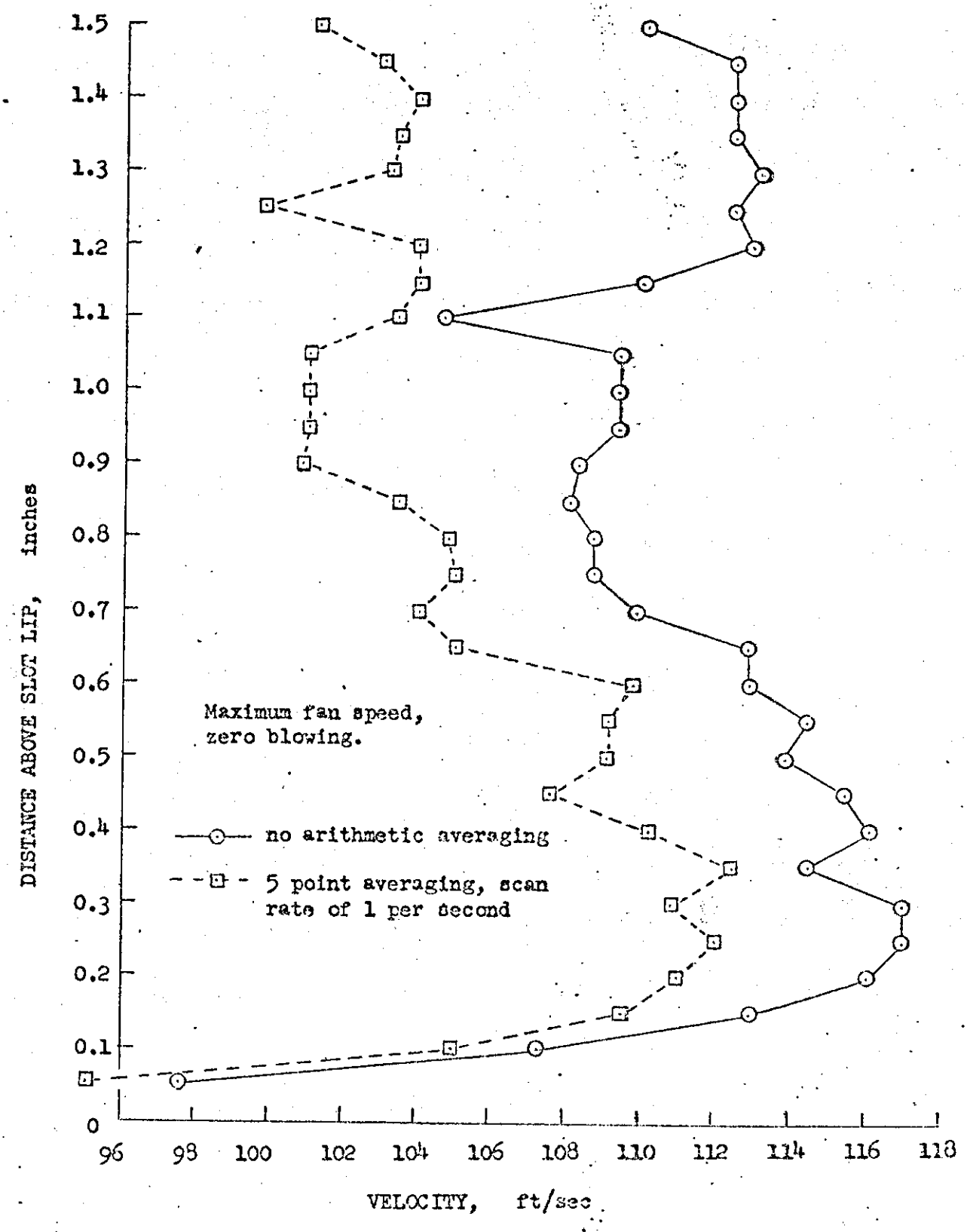

FIG. A4-6: TURBULENCE OF CALIBRATION WIND TUNNEL

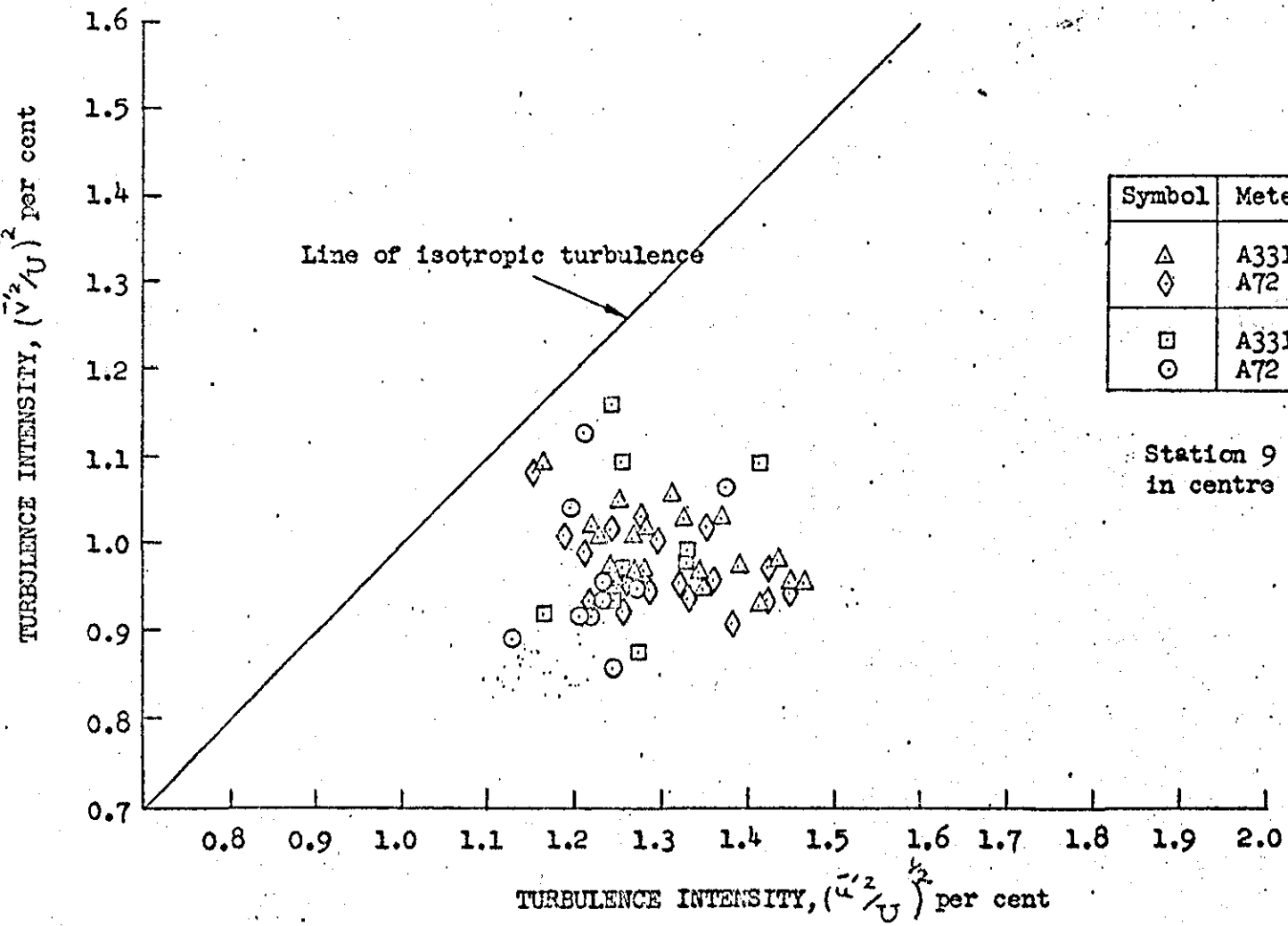

Symbol	Meter	Date	Probe	Array
△ ◇	A331 A72	18.3.68	B	X
⊡ ⊙	A331 A72	29.3.68 20.3.68	A A	X X

Station 9 ins. from tunnel roof, an in centre of working section.

FIG. A4-7: CALIBRATION OF CALIBRATION TUNNEL WORKING SECTION

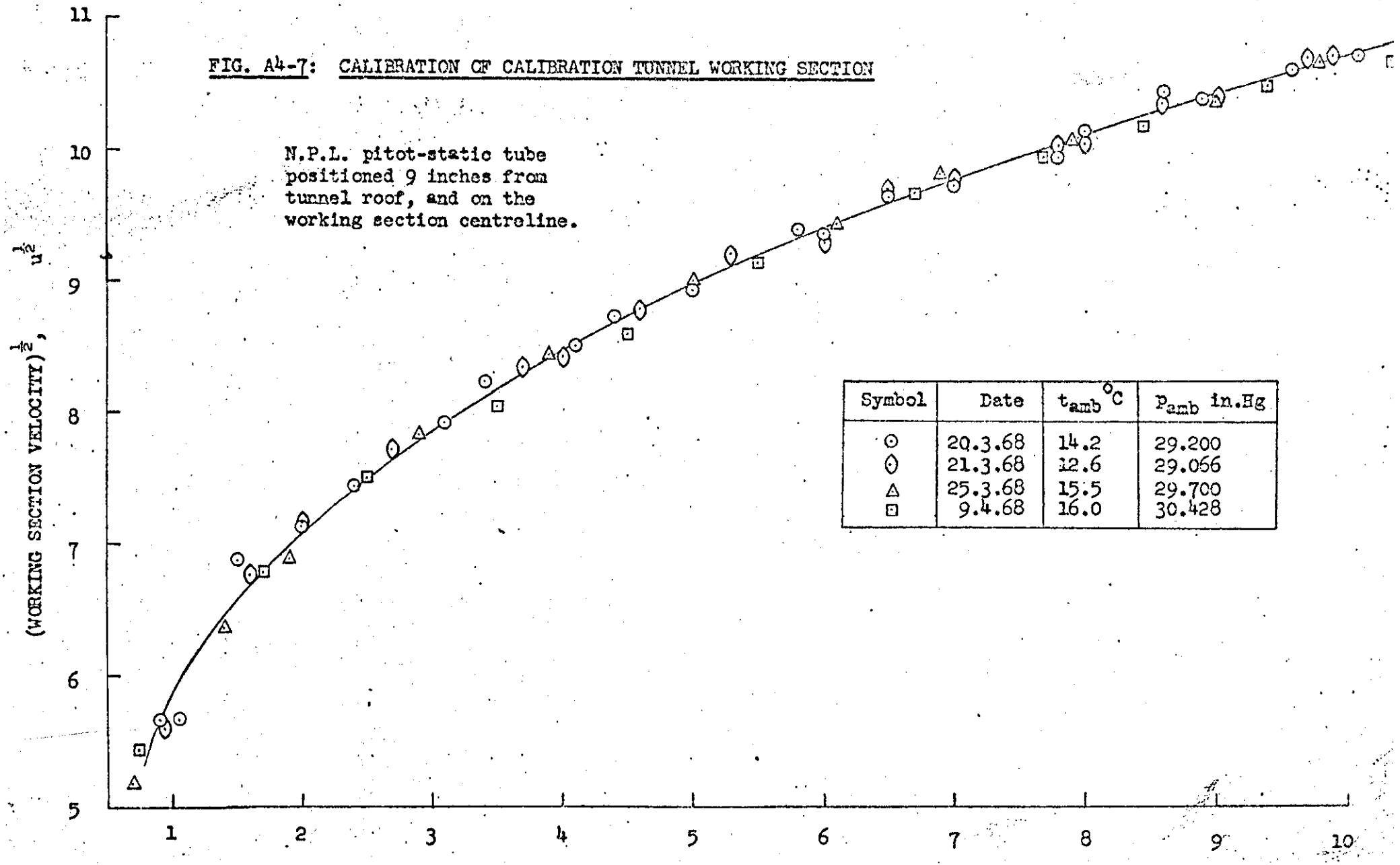

Symbol	Date	t_{amb} °C	p_{amb} in.Hg
⊙	20.3.68	14.2	29.200
◇	21.3.68	12.6	29.066
△	25.3.68	15.5	29.700
⊡	9.4.68	16.0	30.428

FIG. A4-8: VARIATION OF HOT WIRE VELOCITY CALIBRATION WITH CUMMULATIVE RUNNING TIME

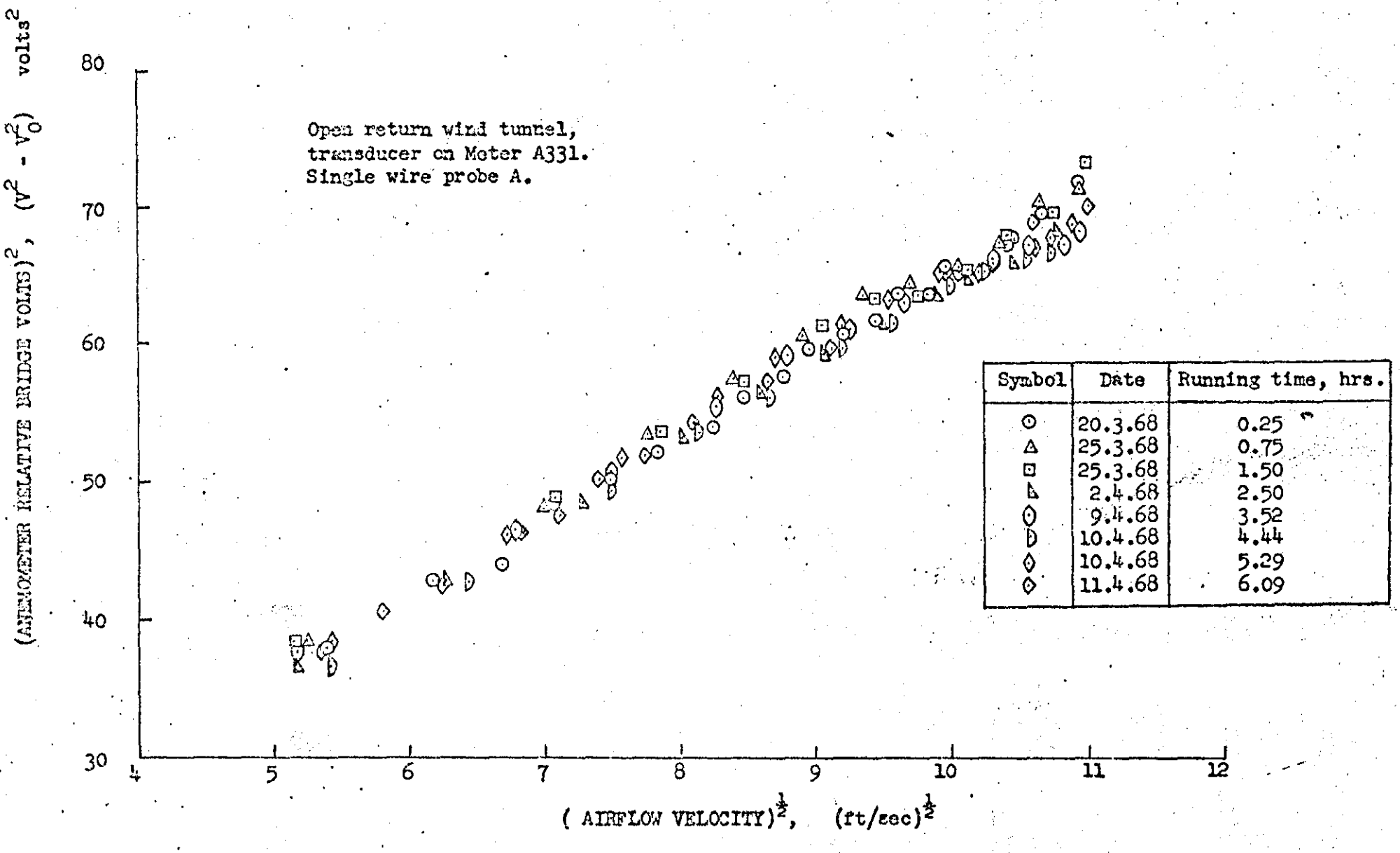

Symbol	Date	Running time, hrs.
○	20.3.68	0.25
△	25.3.68	0.75
□	25.3.68	1.50
◺	2.4.68	2.50
⬯	9.4.68	3.52
▷	10.4.68	4.44
◇	10.4.68	5.29
◇	11.4.68	6.09

FIG. A4-9: DECAY OF VELOCITY CALIBRATION WITH CUMULATIVE RUNNING TIME

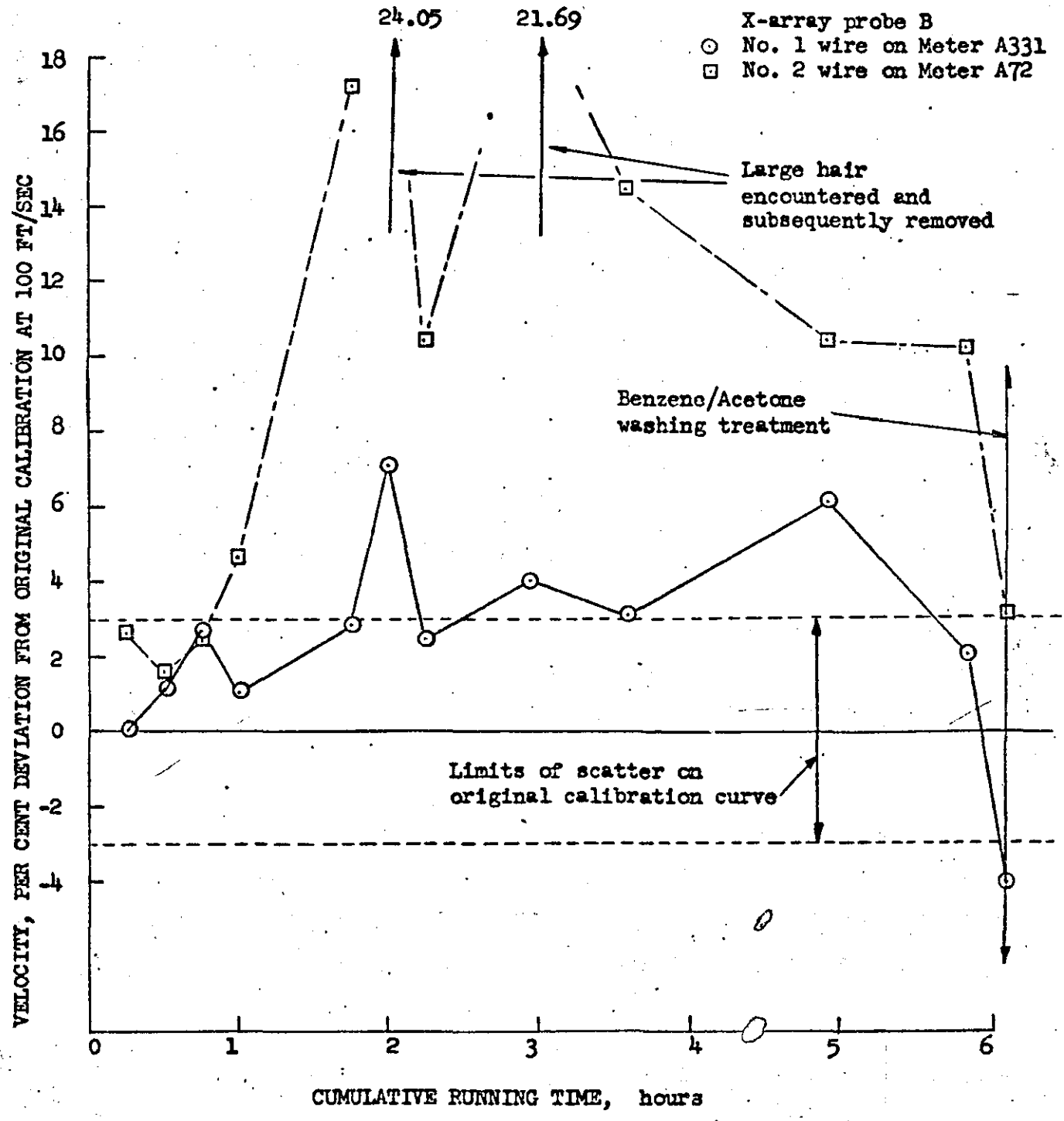

FIG. A4-10: EFFECT OF WASHING EFFICIENCY ON CALIBRATION AFTER CLEANING

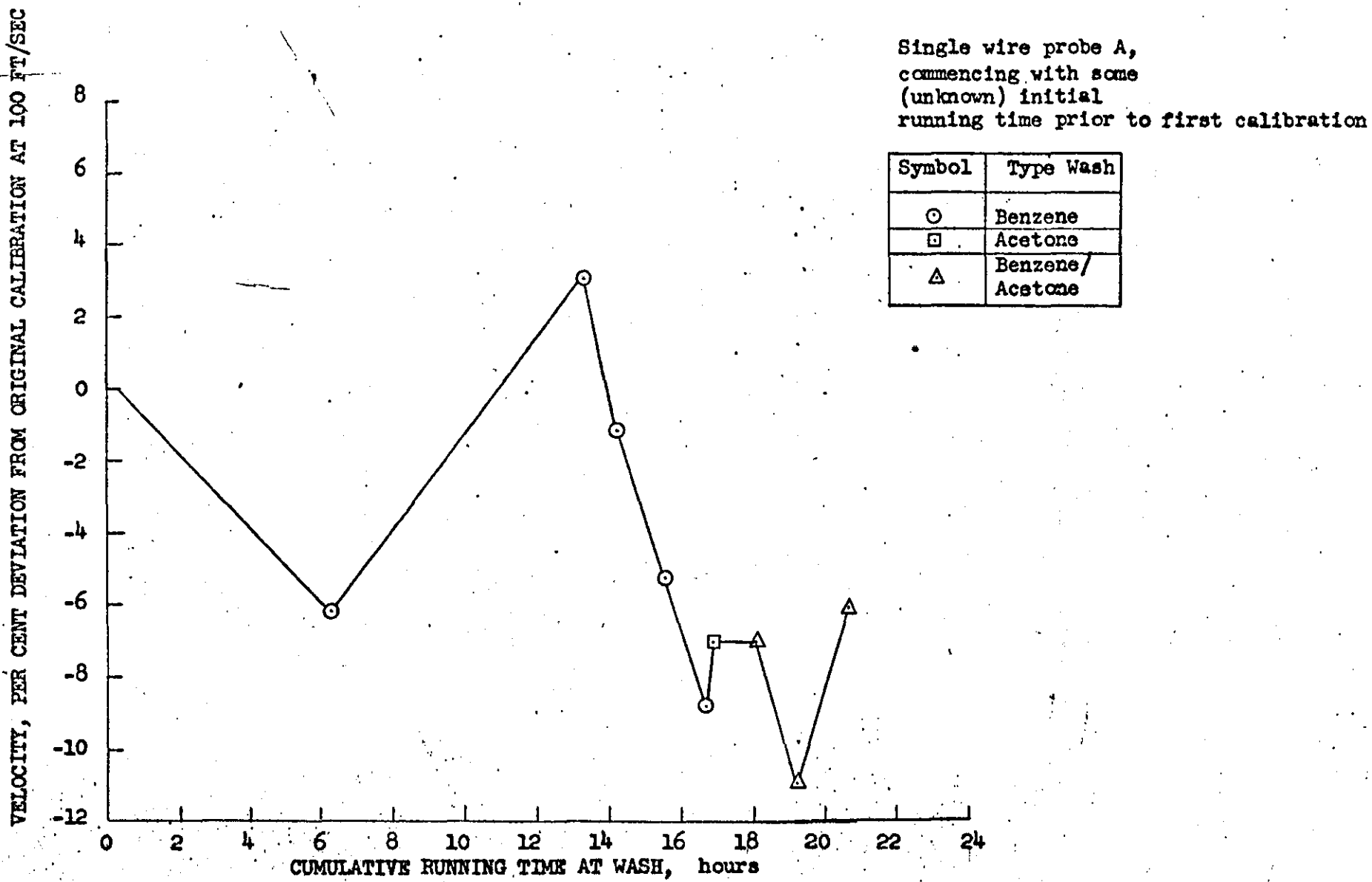

FIG. A4-11: VARIATION OF HOT WIRE DYNAMIC PERFORMANCE WITH CUMULATIVE RUNNING TIME

Symbol	Date	Run Time, hrs.
⊙	28.3.68	0.75
△	29.3.68	1.00
⊡	3.4.68	2.00
◇	5.4.68	4.92
▷	8.4.68	5.84
◇	9.4.68	6.09

X probe B, wire no. 1 on Meter A331; Wire no.2 on Meter A72. Test in calibration tunnel, probe 9 ins. from roof centreline.

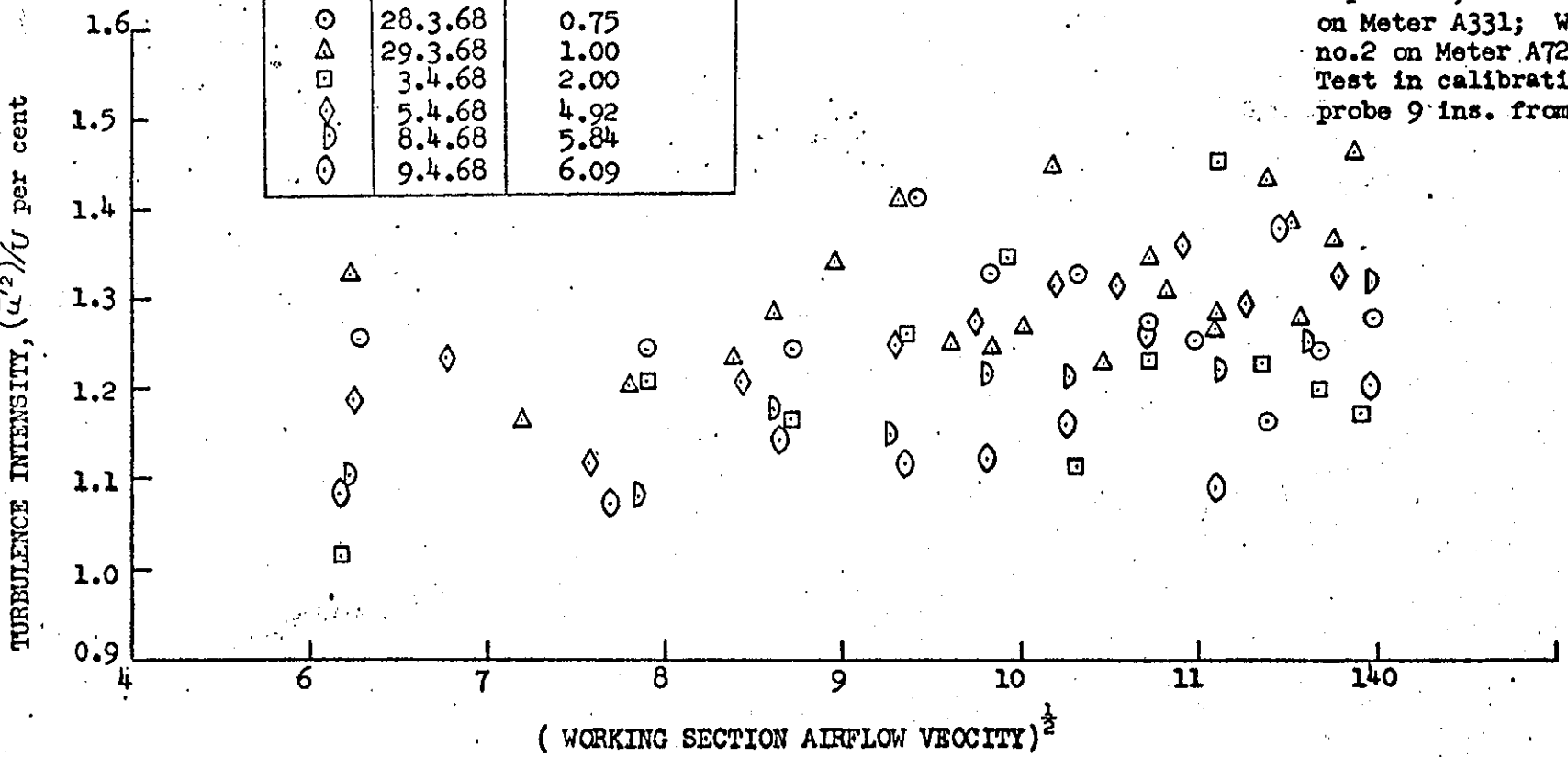

FIG. A4-12: VARIATION OF HOT WIRE DYNAMIC PERFORMANCE WITH CUMULATIVE RUNNING TIME

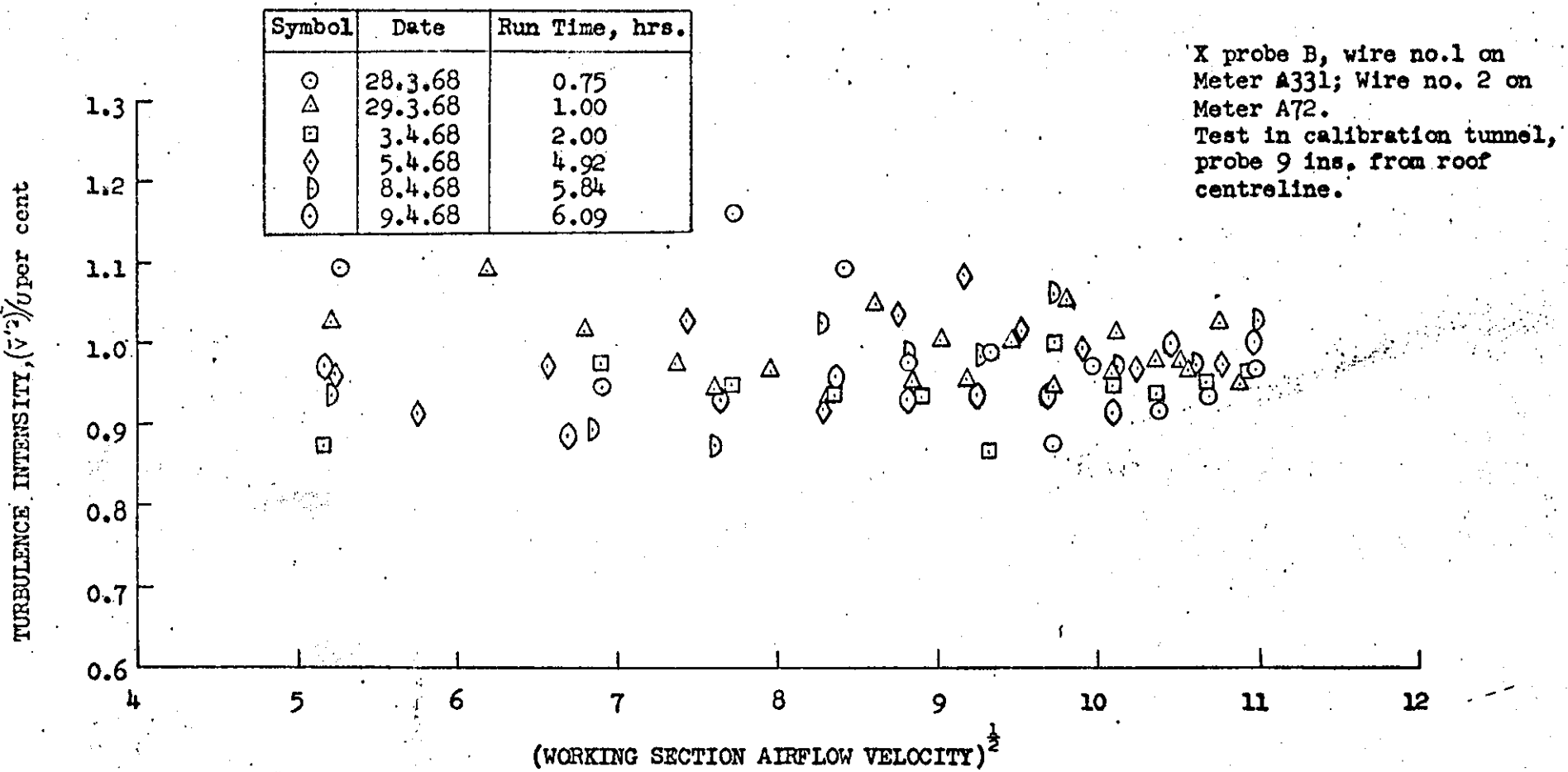

TABLE 2.2

RANGE OF EXPERIMENTAL PARAMETERS FOR PRINCIPAL TWO-DIMENSIONAL,

TURBULENT FLOW FILM COOLING INVESTIGATIONS

Worker	Reference	s inches	x/s	M	Re_s	$(T_c - T_m)$ deg F	u ft/sec	$T_{\delta m}$ F
Wieghardt	21	0.195-0.42	800	0.22-0	3700-12600	-28-(-60)	52-105	32
Seban, Chan & Scesa	7	0.125	120	0.08-0.916	580-2600	50-135	100	50-70
Papell & Trout	34	0.063-0.50	68	0.02-9.34	-	-130-(-430)	-	70-1540
Hartnett, Birkebak & Eckert	8	0.123	120	0.28	2100	10-148	165	70
Nishiwaki, Hirata & Tsuchida	42	0.197-1.97	42	0.04-0.18	700-3500	39-50	20-98	59-74
Seban	11	0.063-0.25	3-300	0.17-20.8	620-6960	70	50-150	50-70
Goldstein, Shavit & Chen	43	1.6875	15	0.12-0.04	1000-5000	32-112	100-185	60-85
Samuel & Joubert	18	0.125-0.375	3.6-275	0.25-3.18	-	-	50-100	122-200
Whitelaw	44	0.248-0.253	4-218	0.47-2.24	4035-19500	0	69	atmos.

WORKER	REFERENCE	EFFECTIVENESS EMPIRICAL CORRELATION	APPLICATION	LIMITS
Wieghardt	21	$\eta = 21.8(x/Ms)^{-0.8}$	$x/Ms \geq 100$	-
Seban, Chan and Scesa	7	$\eta = 0.83(x/Ms)^{-0.7}\,Re_s^{1/3}$ $\eta = 0.16(x/Ms)^{-0.25}\,Re_s^{1/3}$	$x/Ms \geq 40$ $x/Ms < 40$	- -
Papell and Trout	34	$\eta = 12.6(x/Ms)^{-0.72}\,M^{.28}\,(T_c/T_m)^{0.5}$	$0.7>\eta\geq 0.1$, $x/Ms > 3.5$	92.2% data in ± 0.06 band
		$\eta = 1.86(x/Ms)^{-0.36}\,0.08^{M}$	$0.7>\eta>0.1$, $x/Ms < 3.5$	87.0% data in ± 0.08 band
		$\eta = 1.15(x/Ms)^{-0.11}\,M^{0.07}$	$0.7>\eta>1.0$, $x/Ms > 4.65$	89.3% data in ± 0.08 band
		$\eta = 0.83(1/M)^{0.18}$	$0.7>\eta>1.0$, $x/Ms < 4.65$	93.7% data in ± 0.08 band
Harnett, Birkebak and Eckert	8	$\eta = 16.9(x/Ms)^{-0.8}$	$x/Ms \geq 60$	$\pm 40\%$
Nishiwaki, Hirata and Tsuchida	42	$\eta = 7.6(x/Ms)^{-0.75}$ *1. $\eta = 1.77(x/Ms)Re_x^{0.16}$ *2.	$x/Ms > 30$ -	- -
Seban	11	$\eta = 25(x/Ms)^{-0.8}\,M^{0.4}$	$M < 1.0$	-
		$\eta = 1.09\left[(\rho_m/\rho_c)^{1.5}\{(u_c - u_m)/u_c\}^{0.5}\cdot (Re_s)^{-0.3}\,x/s\right]^{-0.5}$	$M > 1.0$	$\pm 5\%$ for $M > 2.5$
Goldstein, Shavit and Chen	43	$\eta = 23.5(x/Ms)^{-0.88}$ $\eta = 0.94(Re_{\delta_1})^{0.39}(x/Ms)^{-0.88}$	$x/Ms \geq 40$	-

WORKER	REFERENCE	EFFECTIVENESS EMPIRICAL CORRELATION	APPLICATION	LIMITS
Samuel and Joubert	18	$\eta = 1.0$ for $m_c^{-1.75}x/s < 40$	$m_c < 1.0$, $s = 0.312$ ins.	-
		$\eta = 10.8(m_c^{-1.75}x/s)^{-0.65}$ for $40 < m_c^{-1.75} < 400$		
		$\eta = 1.0$ for $m_c^{-1.75}x/s < 18$	$m_c < 1.0$, $s = 0.115$ ins.	-
		$\eta = 4.2(m_c^{-1.75}x/s)^{-0.5}$ for $18 < m_c^{-1.75} < 600$		
		$\eta = 1.0$ for $m_c^{0.375}x/s < 30$	$m_c > 1.0$, $s = 0.312$ ins.	-
		$\eta = 3.2(m_c^{0.375}x/s)^{-0.35}$ for $30 < m_c^{0.375}x/s < 150$		
		$\eta = 1.0$ for $m_c^{0.375}x/s < 25$	$m_c > 1.0$, $s = 0.115$ ins.	-
		$\eta = 3.0(m_c^{0.375}x/s)^{-0,35}$ for $25 < m_c^{0.375}x/s < 400$		
Scesa	6	$\eta = 2.2(x/Ms)^{-0.5}$	normal injection	-

*1. according to Whitelaw(76.)
*2. according to Goldstein et al (43.)

TABLE 2.3: EMPIRICAL CORRELATIONS FOR PRINCIPAL TWO-DIMENSIONAL TURBULENT FLOW FILM COOLING INVESTIGATIONS

	Position	Required effective heat transfer coefficient, CHU/ft² sec deg K	$\alpha_{Eff}/\alpha_{Ref}$
PRIMARY ZONE	Outer flame tube	0·01246	0·8713
	Inner flame tube	0·01329	0·9294
DILUTION ZONE	Outer flame tube	0·00825	0·2130
	Inner flame tube	0·02081	0·5380

TABLE 3.1

	Position	$\alpha_{Eff}/\alpha_{Ref}$	$\eta_{Ref} \times 100\%$	$\eta_{Min} \times 100\%$	Kutateladze group	
					Type C	Type L
PRIMARY ZONE	Outer flame tube	0·8713	52·0	90·0	0·7	0·8
	Inner flame tube	0·9294		70·5	1·9	2·4
DILUTION ZONE	Outer flame tube	0·2130	16·5	100·0	0·0	0·0
	Inner flame tube	0·5380		100·0	0·0	0·0

TABLE 3.2

	Position	$(x/s)_{max}$		x_{max} in		x_p'/s at $\mu_m/u_c = 1·0$		$x_p'/x_{max} \times 100\%$	
		Type C	L	C	L	C	L	C	L
PRIMARY ZONE	Outer flame tube	10·46	11·23	1·7	1·4	about 12·0	about 25·0	100·0	100·0
	Inner flame tube	28·38	33·69	4·54	4·2			42·3	74·2

TABLE 3.3

TABLE 4.1

AEROTHERMODYNAMIC PARAMETERS FOR MACHINED SLOT TESTS

Device	u_m/u_c	T_c/T_m	$Re_s \times 10^{-3}$	No. Tests
B1	0.370-1.573	0.417-0.456	7.047-23.690	9
B2	0.279-1.680	0.466-0.622	2.041-6.850	17
B3	0.379-1.499	0.411-0.454	10.71-36.38	17
B4	0.341-1.766	0.412-0.585	6.900-27.00	18
B5	0.391-2.072	0.441-0.581	5.981-22.35	22
B6	0.522-3.468	0.420-0.573	6.072-26.22	23

TABLE 4.2

RELATIVE GEOMETRIC PARAMETERS OF MACHINED SLOTS

Device	$s/(s)_{B1}$	$A_o/(A_o)_{BL}$ unit length	$A_E/(A_E)_{B1}$ unit length	Type Outle
B1	1.000	1.000	1.000	discrete
B2	0.429	0.285	0.272	discrete
B3	1.179	1.780	1.129	slotted
B4	0.892	0.784	0.855	discrete
B5	1.142	1.780	0.801	slotted
B6	1.650	2.253	1.538	obround

TABLE 4.4

AEROTHERMODYNAMIC PARAMETERS FOR STACKED RING TESTS

Device	u_m/u_c	T_c/T_m	$Re_s \times 10^{-3}$	No. Tests
G1	0.370-0.803	1.060-1.453	2.290-8.780	12
G2	0.490-1.020	1.042-1.071	2.330-8.760	3
G3	0.588-1.020	1.042-1.071	2.330-8.760	4

TABLE 4.4

GEOMETRIC PARAMETERS FOR STACKED RING DEVICES (RELATIVE)

Device	$s/(s)_{G1}$	$A_o/(A_o)_{G1}$ unit length	$A_E/(A_E)_{G1}$ unit length	Type Outlet
G1	1.000	1.000	1.000	plain
G2	1.250	1.250	1.1003	plain
G3	1.500	1.500	1.2494	plain

TABLE 10.1

TEST INFORMATION FOR THIN LIPPED SLOT

Run	s inches	δ_w inches	u_m ft/sec	$u_c/\bar{u}_c$	u_m/u_c	Re_s	$(\delta)_m$ inches	$(\delta)_c$ inches	$(\delta)_{wall}$ inches	x_p/s measured	x_p/s predicted	T_{o_m} °C	T_{o_c} °C
15	0.2563	0.0550	40.0	-	0.5500	9415	0.314	0.0663	0.054	10.34	8.85	20.5	19.4
16	0.2563	0.0550	64.0	1.2992	0.8951	9416	0.399	0.0810	0.057	15.61	15.95	20.3	19.15
17	0.2563	0.0550	77.0	1.1679	1.1129	9115	0.379	0.0513	0.090	14.12	16.00	22.8	20.40
18	0.2563	0.0550	68.0	-	0.5290	9120	-	-	-	-	-	18.8	17.70
19	0.2563	0.0550	92.0	1.2414	1.3004	9886	0.530	0.0363	0.075	13.24	12.20	21.5	20.10
20	0.2563	0.0550	106.0	1.2937	1.5078	9520	0.3137	0.0363	0.034	9.85	8.20	24.1	23.10
21	0.2563	0.0550	36.5	1.1263	0.3333	14590	0.3337	0.0443	0.077	5.94	4.77	21.8	20.10
22	0.2563	0.0550	47.9	1.0779	0.4279	14700	0.3457	0.0563	0.083	6.43	5.10	21.7	20.10
23	0.2563	0.0550	74.0	1.1543	0.6526	15120	0.3567	0.0333	0.074	7.13	6.87	20.0	19.60
24	0.2563	0.0550	102.0	1.1783	0.9095	15260	0.3740	0.0413	0.080	9.26	9.15	20.0	20.00
25	0.2563	0.0550	39.5	1.1021	0.2240	23260	0.3190	0.0463	0.082	5.03	4.45	19.2	19.50
26	0.2563	0.0550	51.5	1.1198	0.2901	23630	0.3890	0.0333	0.080	5.06	4.65	21.1	20.73
27	0.2563	0.0550	67.6	1.1309	0.3808	23780	0.3490	0.0333	0.095	5.26	3.95	21.2	20.80
28	0.2563	0.0550	95.0	1.1627	0.5269	24570	0.3140	0.0163	0.140	5.36	4.00	24.8	22.20
29	0.2563	0.0550	41.6	1.1974	0.5846	9582	0.3490	0.0640	0.067	6.83	5.73	21.0	20.00
30	0.2563	0.0550	89.9	1.2749	1.2086	9966	0.3510	0.0390	0.058	13.67	?	25.25	23.10
31	0.2563	0.0550	87.9	1.1318	1.1318	23840	0.2890	0.0390	0.076	6.10	6.15	24.85	22.15
32	0.2563	0.0550		-	0.5734	9400	-	-	-	-	-	-	20.10

TABLE 10.2

TEST INFORMATION FOR INTERMEDIATE LIPPED SLOT

Run	s inches	δ_w inches	u_m ft/sec	$u_c/\bar{u}_c$	u_m/u_c	Re_s	$(\delta)_m$ inches	$(\delta)_c$ inches	$(\delta)_{wall}$ inches	x_p/s measured	x_p/s predicted	T_m °C	T_c °C
34	0.2625	0.0995	98.6	1.2622	1.4257	9477	0.5190	0.0520	0.0800	9.48	8.30	25.0	24.2
35	0.2625	0.0995	87.5	1.2916	1.2471	9564	0.4660	0.0440	0.0900	10.44	11.00	21.7	20.7
36	0.2625	0.0995	75.0	1.3552	1.0204	9892	0.5080	0.0670	0.0920	12.33	16.95	21.4	21.3
37	0.2625	0.0995	65.7	1.2323	0.9073	9806	0.3640	0.0870	0.0850	11.48	14.60	21.5	21.0
38	0.2625	0.0995		-	0.9405	9800	-	-	-	-	-		19.9
39	0.2625	0.0995	45.7	1.1754	0.6621	9353	0.4380	0.0790	0.0900	6.64	8.40	21.7	20.8
41	0.2625	0.0995	37.0	1.2088	0.5075	9635	0.3930	0.0970	0.1000	6.64	7.20	20.4	20.5
42	0.2625	0.0995	88.5	1.1711	0.7946	15940	0.5580	0.0325	0.1200	7.02	6.25	22.8	20.8
43	0.2625	0.0995	81.0	1.1353	0.7344	15090	0.4880	0.0175	0.1000	4.75	6.42	23.0	21.2
44	0.2625	0.0995	60.9	1.0873	0.5527	14430	0.0303	0.0570	0.0770	5.50	4.42	21.0	22.2
45	0.2625	0.0995	41.9	1.0737	0.3754	14120	0.2880	0.0625	0.0800	6.64	5.85	22.0	20.9
46	0.2625	0.0995	35.1	1.1393	0.3180	14790	0.3130	0.0800	0.0800	5.62	4.40	20.5	20.1
47	0.2625	0.0995	70.0	-	0.3867	22988	0.2130	0.0325	0.0800	5.25	5.47	23.1	19.8
48	0.2625	0.0995	64.0	-	0.3596	23216	0.3080	0.0475	0.0900	4.76	4.80	21.0	18.5
49	0.2625	0.0995	52.0	-	0.2873	23438	0.3630	0.0265	0.0750	4.86	4.86	22.2	21.2
50	0.2625	0.0995	42.0	-	0.2320	23724	0.2130	0.04142	0.0900	4.28	4.28	21.0	19.0
51	0.2625	0.0995	31.0	-	0.1769	22824	0.3080	0.0375	0.0750	4.28	4.17	21.0	20.8

TABLE 10.3

TEST INFORMATION FOR THICK LIPPED SLOT

Run	s inches	δ_w inches	u_m ft/sec	$u_c/\bar{u}_c$	u_m/u_c	Re_s	$(\delta)_m$ inches	$(\delta)_c$ inches	$(\delta)_{wall}$ inches	x_p/s measured	x_p/s predicted	^oT_m	^oT_c
53	0.2620	0.1525	73.0	-	1.0429	9043	0.3555	0.0620	0.0730	10.77	19.86	22.2	19.8
55	0.2620	0.1525	50.3	-	0.7290	9015	0.3355	0.0620	0.0770	8.03	11.84	18.5	17.7
56	0.2620	0.1525	37.3	-	0.5567	8872	0.3545	0.0620	0.0600	7.48	9.23	17.5	17.2
57	0.2620	0.1525	39.0	-	0.5571	9137	0.2255	0.0270	0.0650	6.34	9.67	21.0	20.0
58	0.2620	0.1525	31.0	-	0.4572	8878	0.2905	0.0420	0.0830	5.35	7.67	21.0	20.7
59	0.2620	0.1525	63.6	-	0.5579	14592	0.4155	0.0320	0.0690	5.77	6.04	22.0	20.0
60	0.2620	0.1525	71.3	-	0.6254	14350	0.3975	0.0400	0.0750	6.35	6.77	21.5	20.8
61	0.2620	0.1525	51.0	-	0.4501	13944	0.3155	0.0320	0.0550	5.19	5.74	21.7	19.5
62	0.2620	0.1525	47.2	-	0.4222	14392	0.4025	0.0390	0.0620	5.80	5.42	22.0	20.8
63	0.2620	0.1525	37.0	-	0.3333	14302	0.3305	0.0420	0.0700	4.32	4.80	21.0	22.6
64	0.2620	0.1525	61.0	-	0.3389	22491	0.3355	0.0420	0.0750	4.92	4.96	21.8	22.0
65	0.2650	0.1525	41.0	-	0.2303	22652	0.2855	0.0220	0.0800	4.69	3.50	23.0	20.8
66	0.2650	0.1525	70.0	-	0.3855	23200	0.3655	0.0420	0.0800	4.21	5.12	18.3	18.5
67	0.2650	0.1525	30.0	-	0.1739	23214	0.3655	0.0420	0.0750	4.25	4.27	17.0	18.0
68	0.2650	0.1525	34.0	-	0.1977	23105	0.3755	0.0420	0.0800	4.03	4.15	16.0	18.0
69	0.2650	0.1525	41.0	-	0.2323	23295	0.3455	0.0420	0.0850	3.89	3.50	18.0	18.0
70	0.2650	0.1525	25.0	-	0.2315	14453	0.2855	0.0520	0.0700	4.14	3.99	18.0	18.0
75	0.2600	0.1525	100.0	-	0.8772	13889	1.0955	0.0620	0.0700	6.93	8.94	21.0	21.2
71	0.2600	0.1525	105.0	-	1.4894	8923	0.3355	0.0420	0.0850	7.69	8.69	21.0	21.0
72	0.2600	0.1525	94.0	-	1.3390	8930	0.3955	0.0420	0.0900	5.77	10.45	21.0	21.0
73	0.2600	0.1525	60.5	-	0.8718	8977	1.0355	0.0420	0.0730	6.50	14.33	21.0	21.2
74	0.2600	0.1525	81.5	-	1.1760	8888	1.0655	0.0420	0.0675	6.92	9.46	21.0	21.2
76	0.2600	0.1525	93.5	-	0.8252	13885	1.0355	0.0420	0.0800	6.46	7.77	21.0	21.2
77	0.2590	0.1525	99.0	-	0.5500	22245	1.0255	0.0420	0.0470	6.59	6.79	22.0	18.0

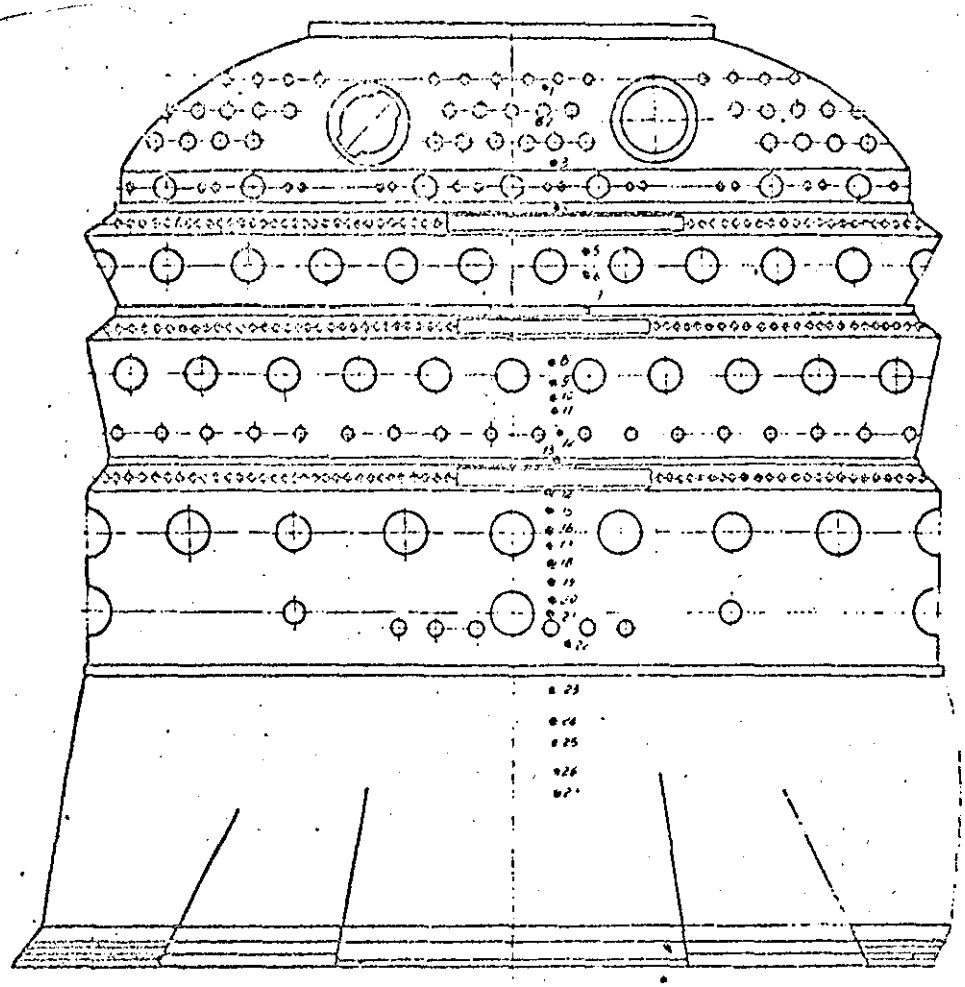

Thermocouple numbers 1 - 26, front to rear

FIG. 1.0b): TYPE B CHAMBER LAYOUT AND THERMOCOUPLE POSITIONS

FIG: 1.0a) EFFECT ON FLAMETUBE SKIN TEMPERATURES OF FILM COOLING

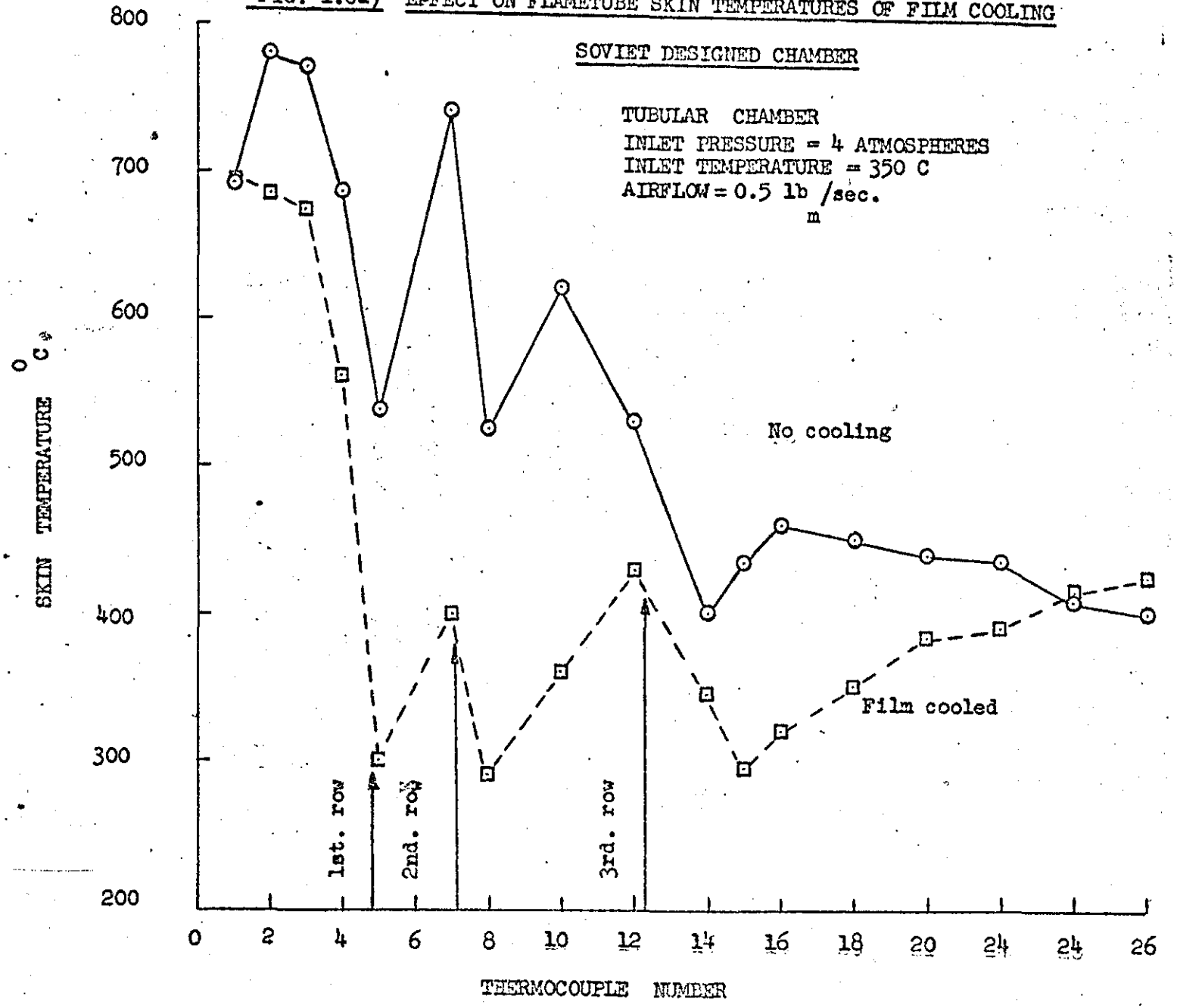

FIG. 1.1: IMPROVEMENT IN ENGINE SPECIFIC WEIGHT WITH TIME

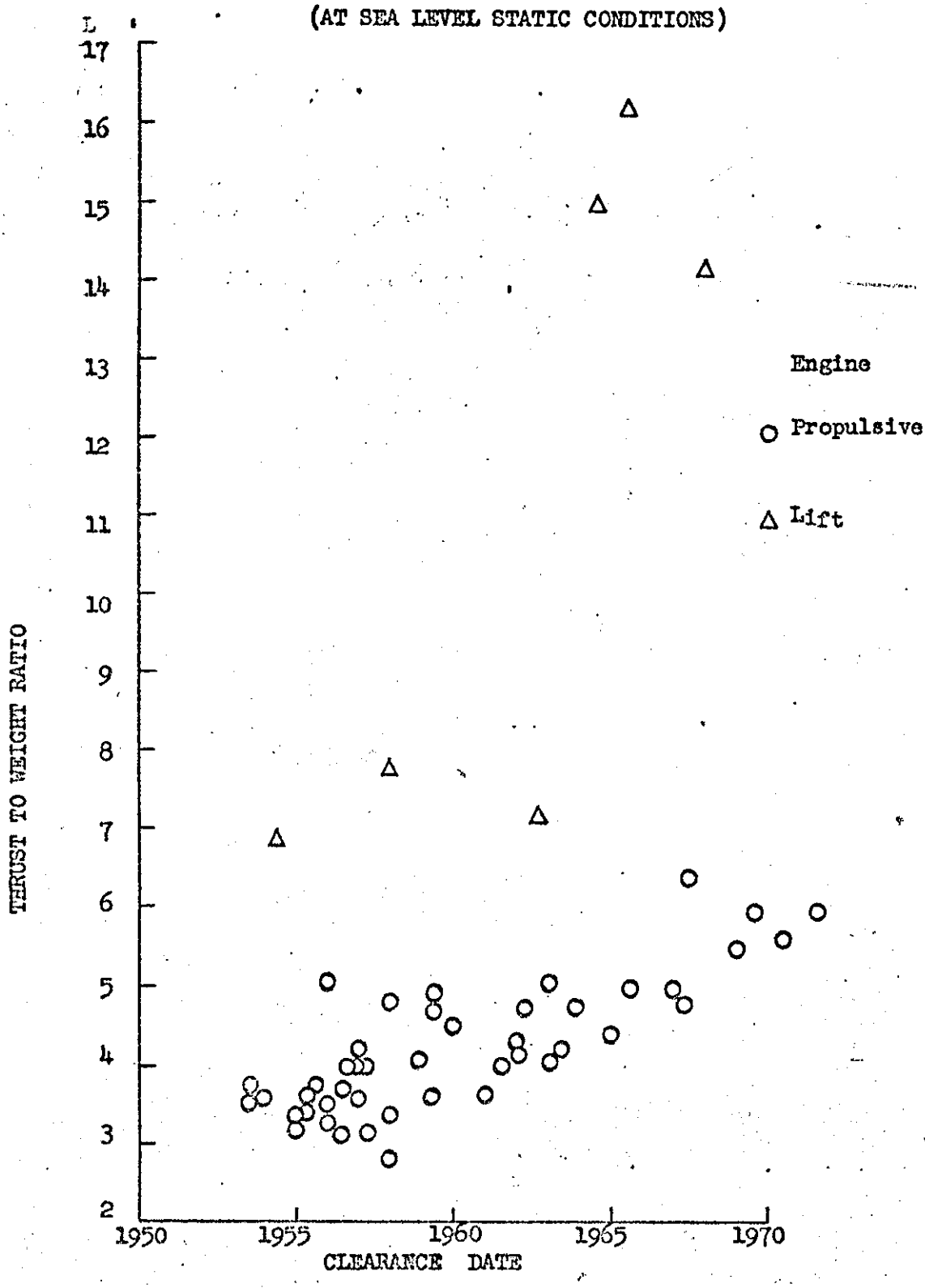

FIG. 1.2: EFFECT OF TURBINE ENTRY TEMPERATURE ON SPECIFIC THRUST FOR SIMPLE TURBOJET

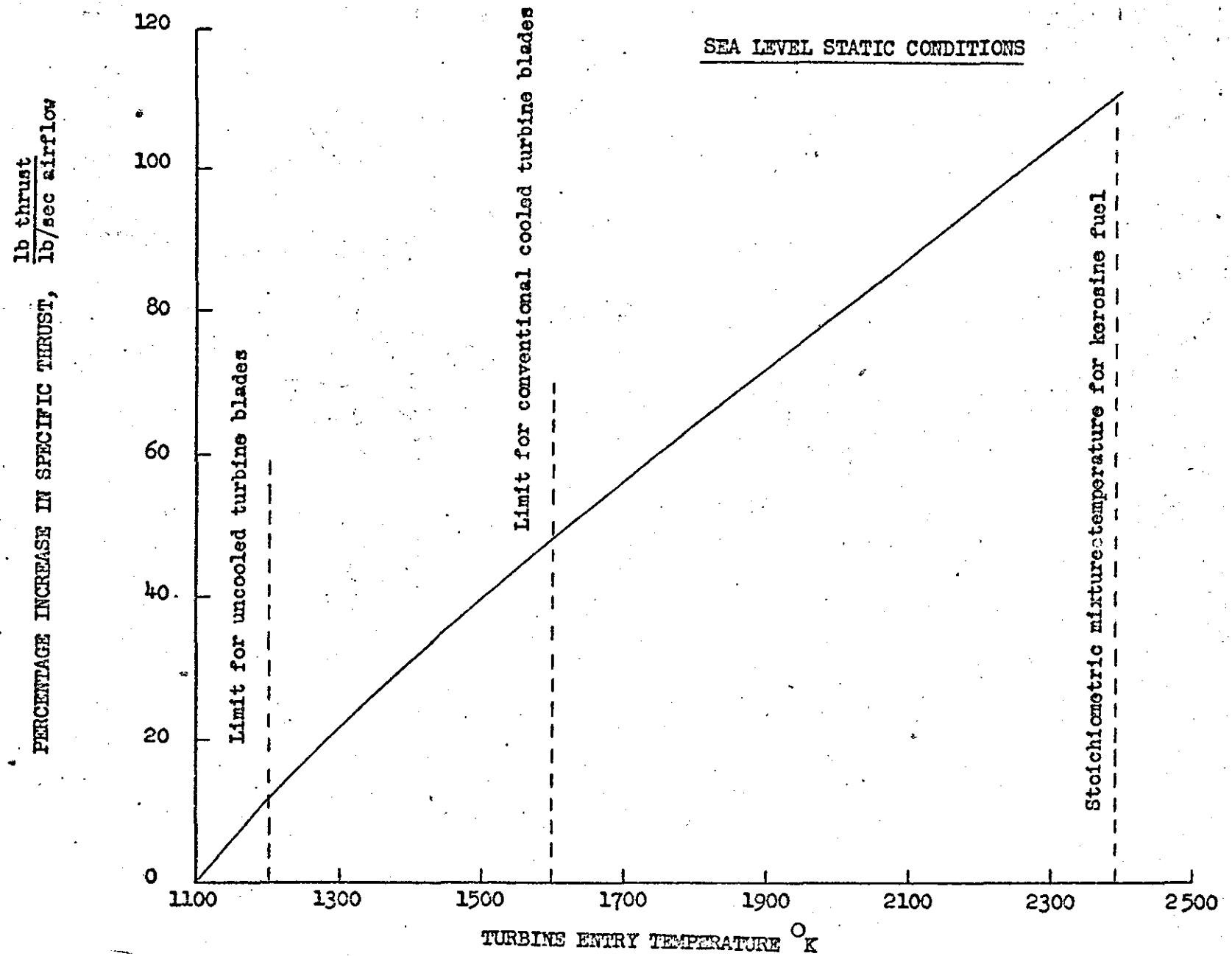

FIG. 1.3: EFFECT OF TURBINE ENTRY TEMPERATURE ON SPECIFIC THRUST FOR TWIN SPOOL BYPASS ENGINE

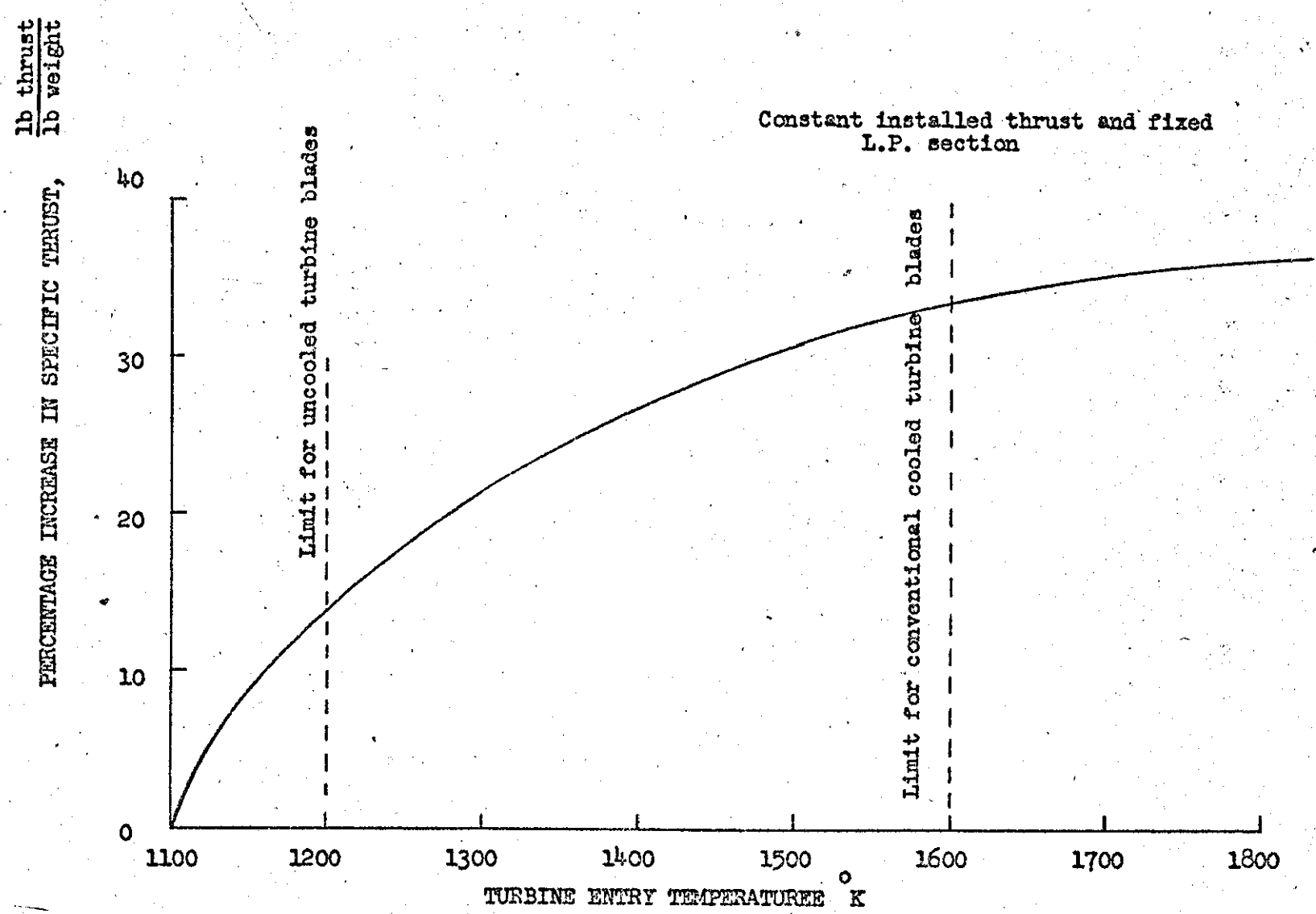

FIG. 1.4: EFFECT OF TURBINE ENTRY TEMPERATURE ON SPECIFIC FUEL CONSUMPTION FOR TWIN SPOOL BYPASS ENGINE

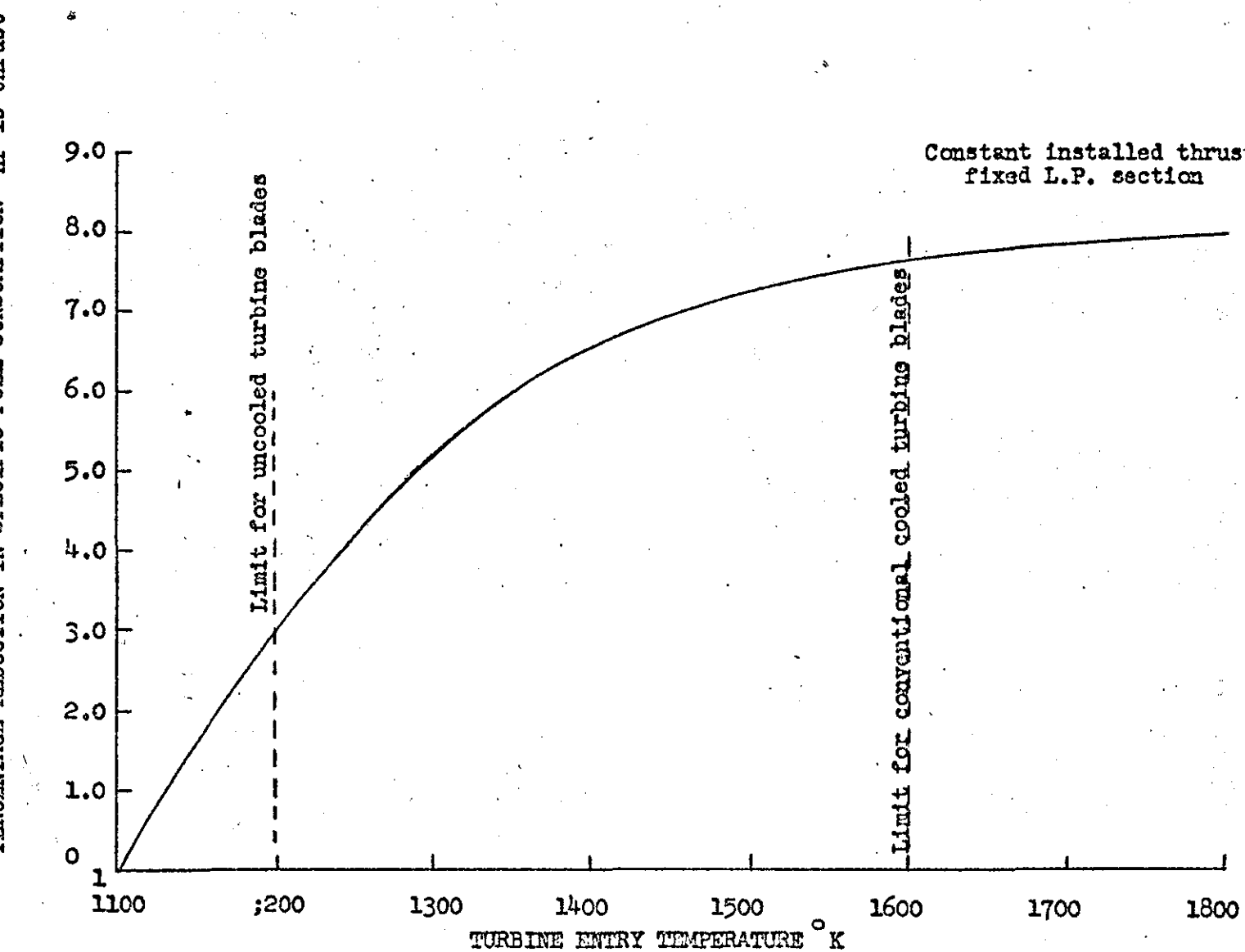

FIG. 1.5: INCREASE IN TURBINE ENTRY TEMPERATURE WITH TIME

(AFTER HALLS)

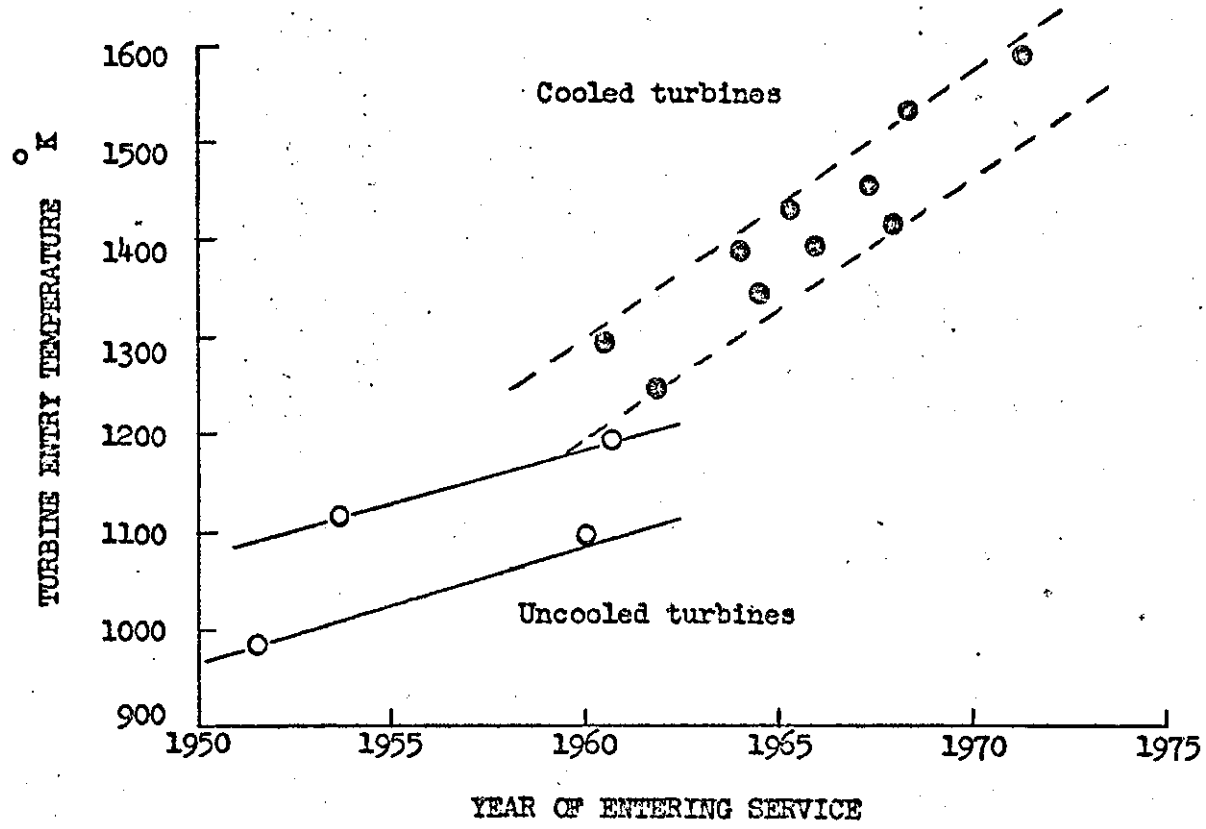

FIG. 1.6: INCREASE IN COMBUSTION CHAMBER ENTRY TEMPERATURES WITH TIME

(AFTER JACKSON AND ODGERS)

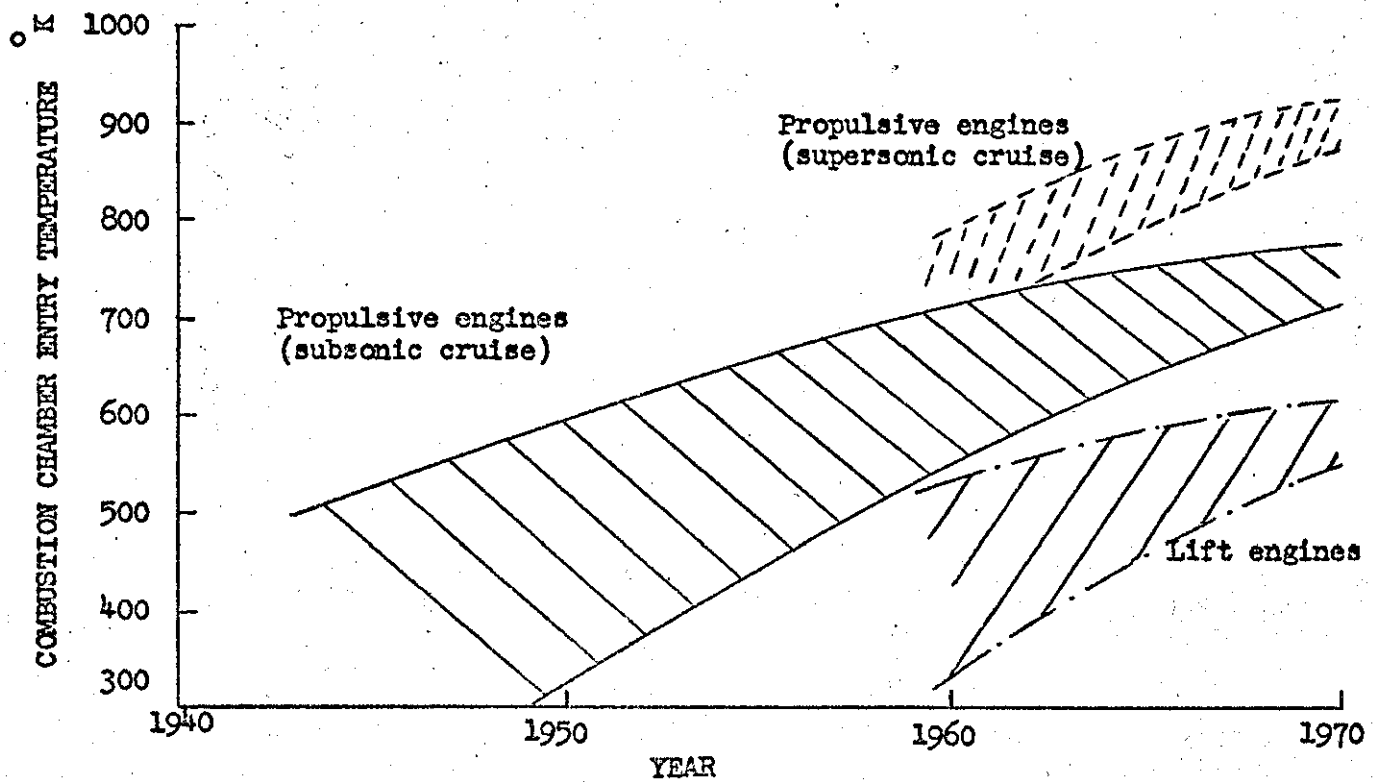

FIG. 1.7: EROSION OF COOLING POTENTIAL WITH TIME

NIMONIC 75 FLAMETUBE

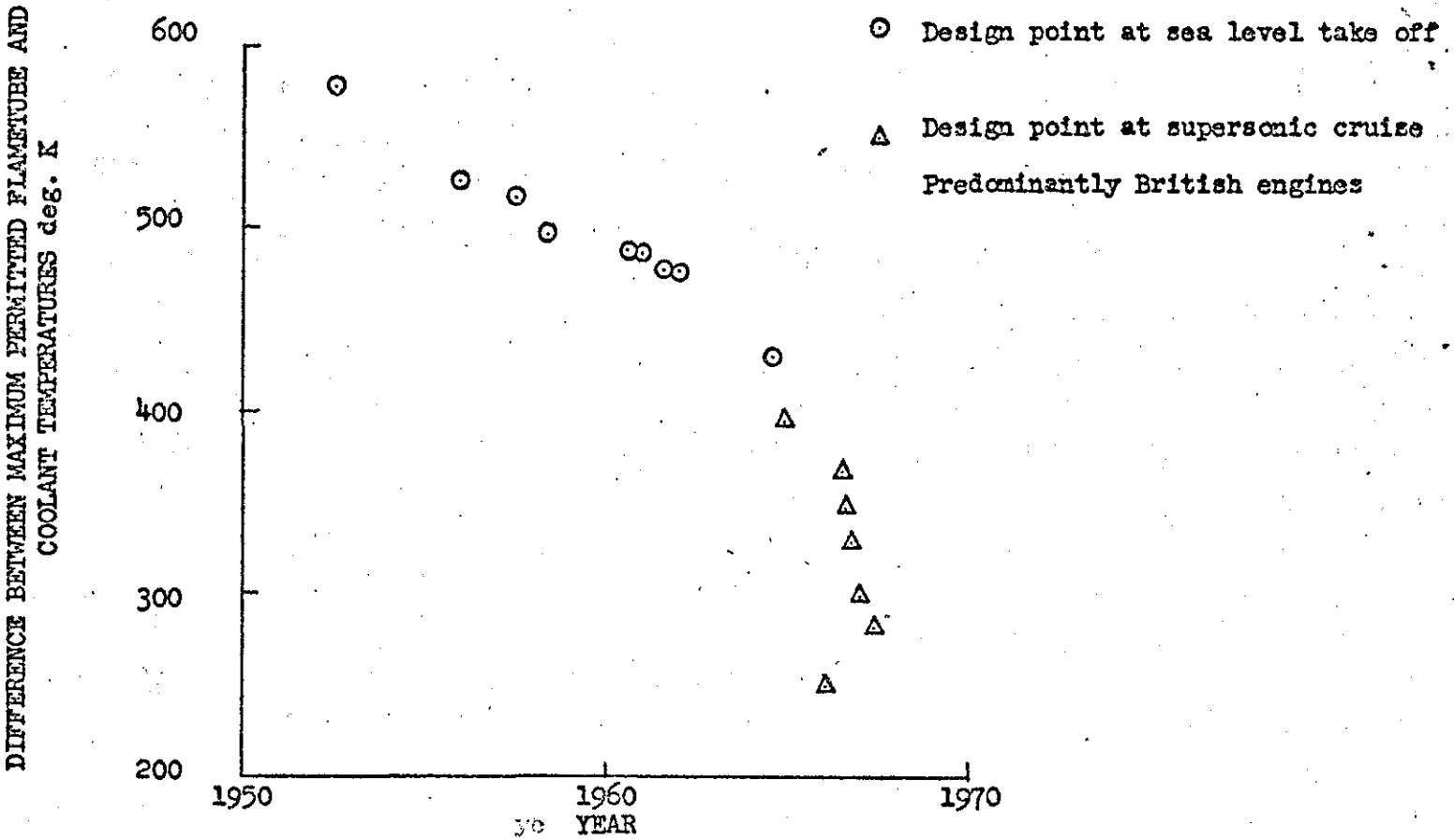

FIG. 1.8: INCREASE IN COOLANT FLOW WITH INCREASE IN COOLANT TEMPERATURE

(AFTER JACKSON AND ODGERS)

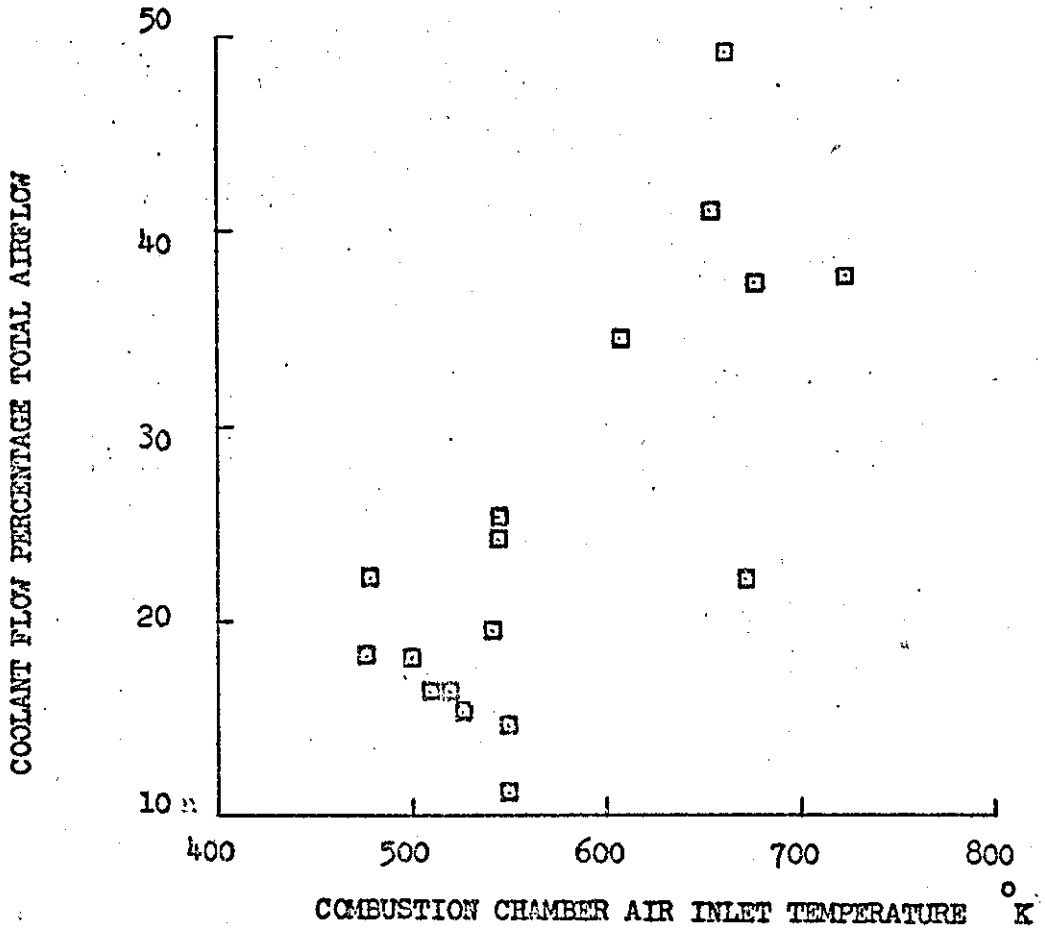

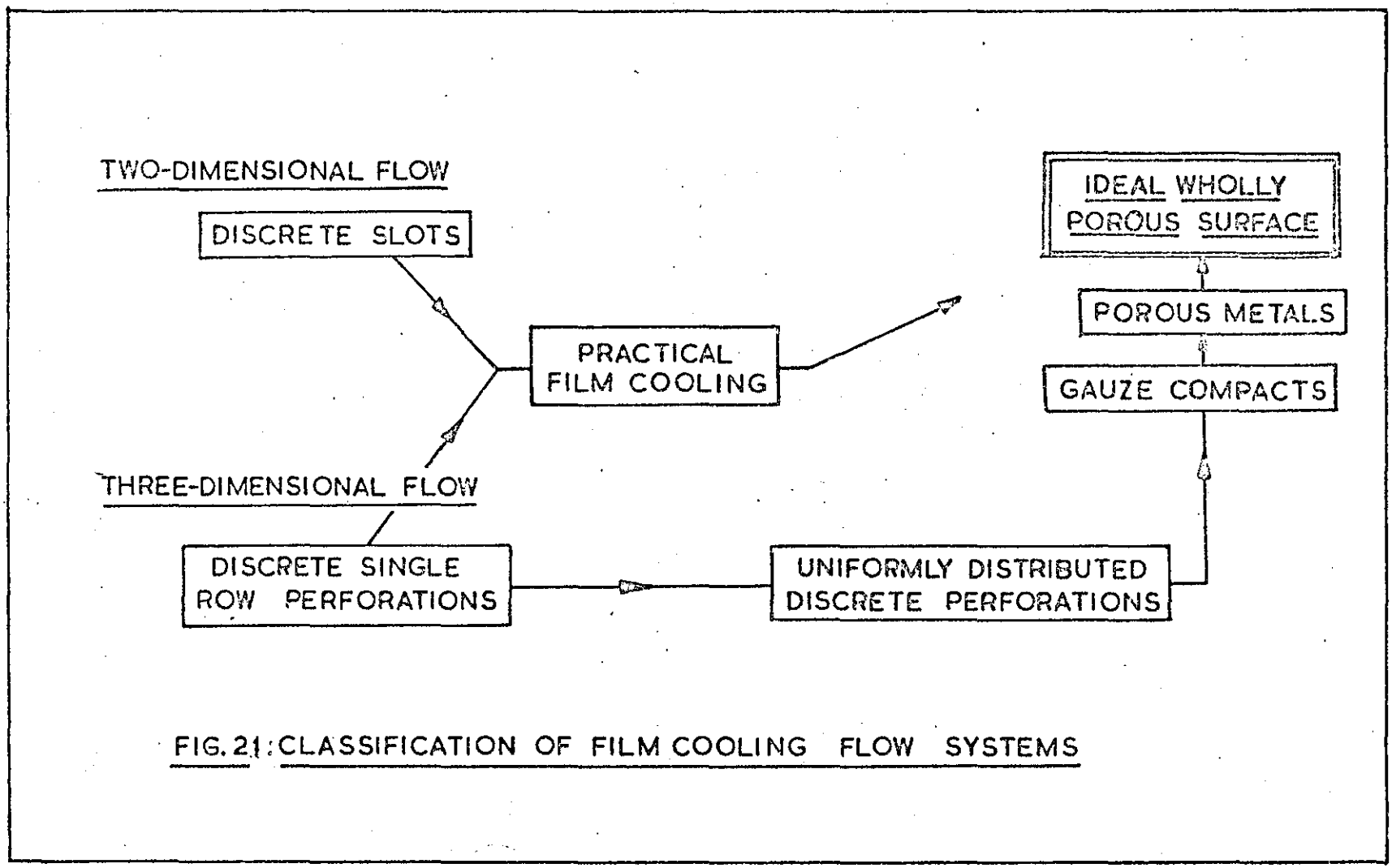

FIG. 21: CLASSIFICATION OF FILM COOLING FLOW SYSTEMS

FIG. 2.2; COMPARISON OF HEAT TRANSFER RELATIONSHIPS FOR MASS VELOCITY RATIOS GREATER THAN UNITY

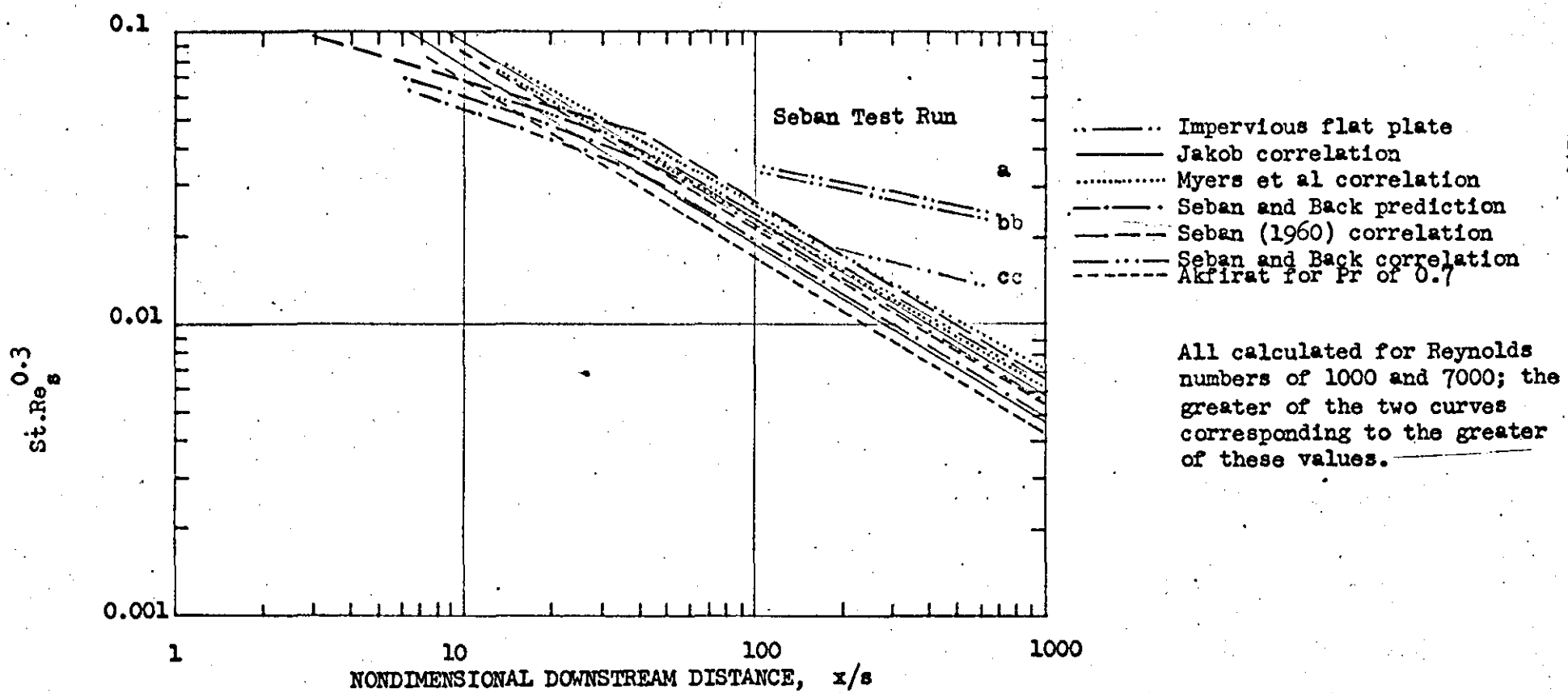

FIG. 2.3: COMPARISON OF SOME TURBULENT BOUNDARY LAYER BASED FILM COOLING THEORIES

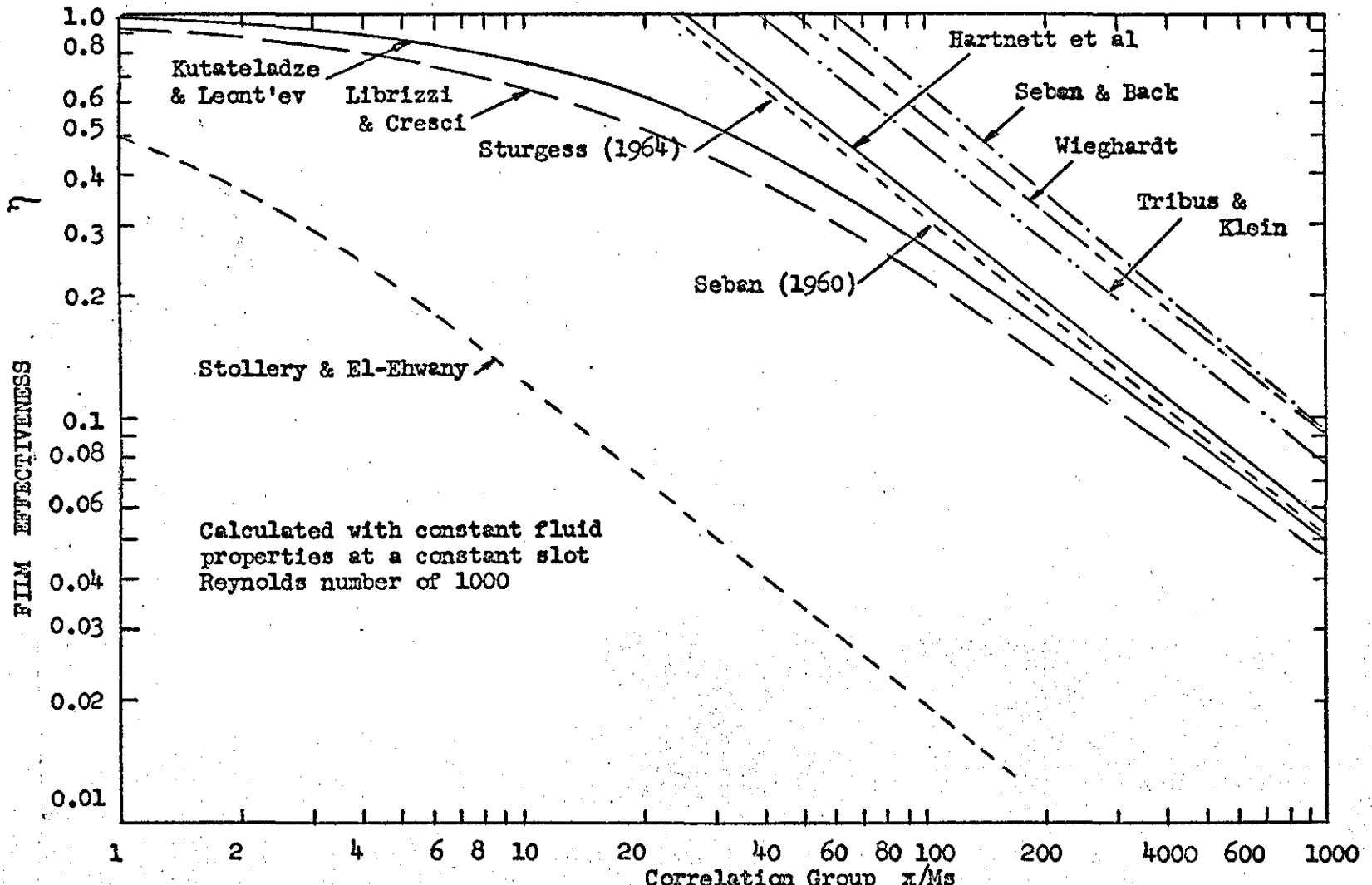

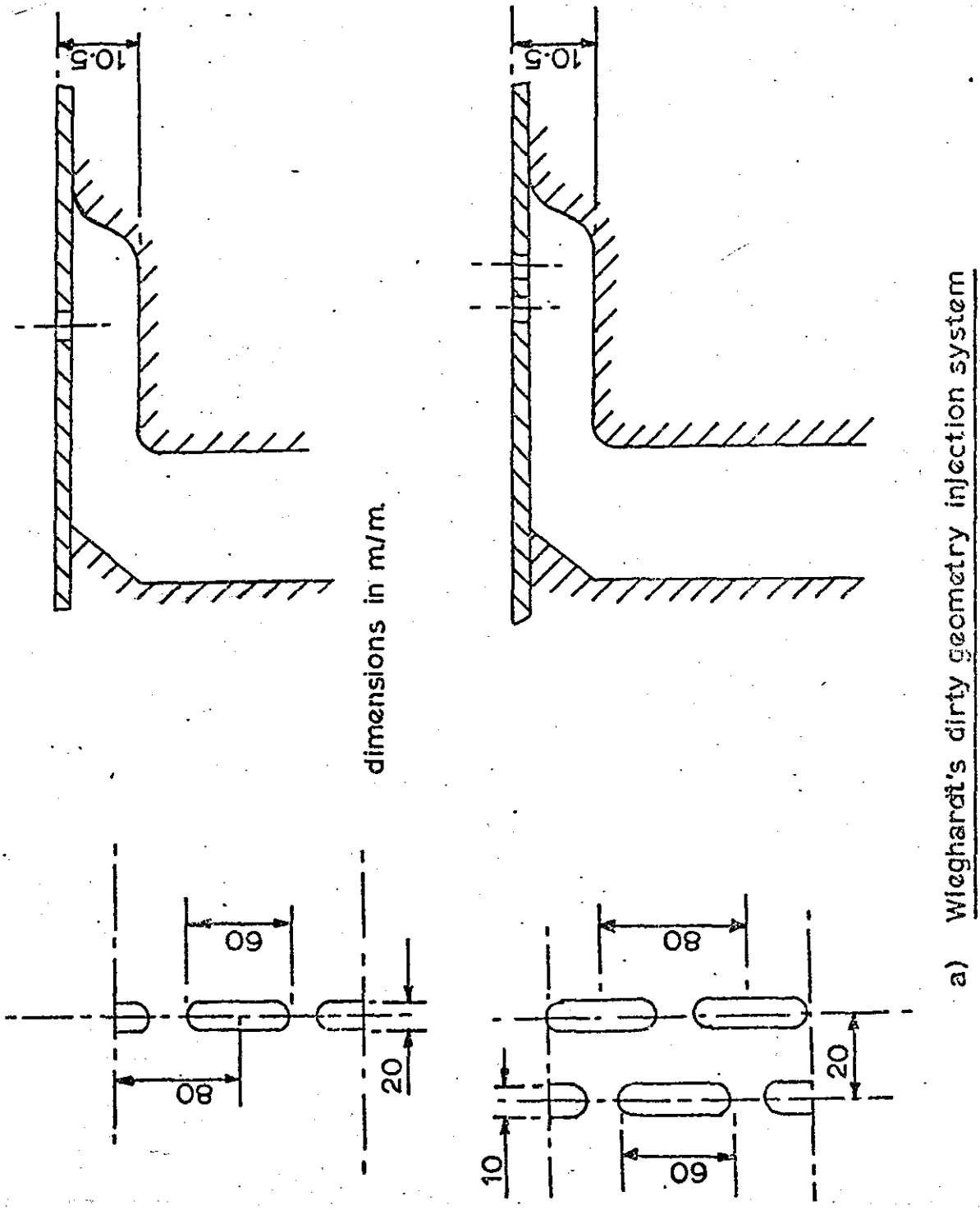

a) Wieghardt's dirty geometry injection system

FIG. 2.4:

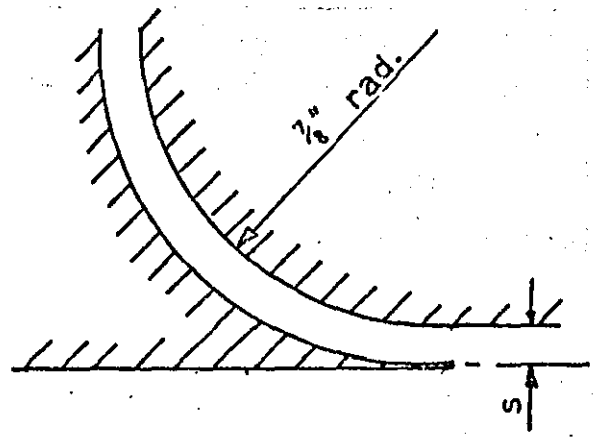

b) Injection geometry of Seban, Chan & Scesa.

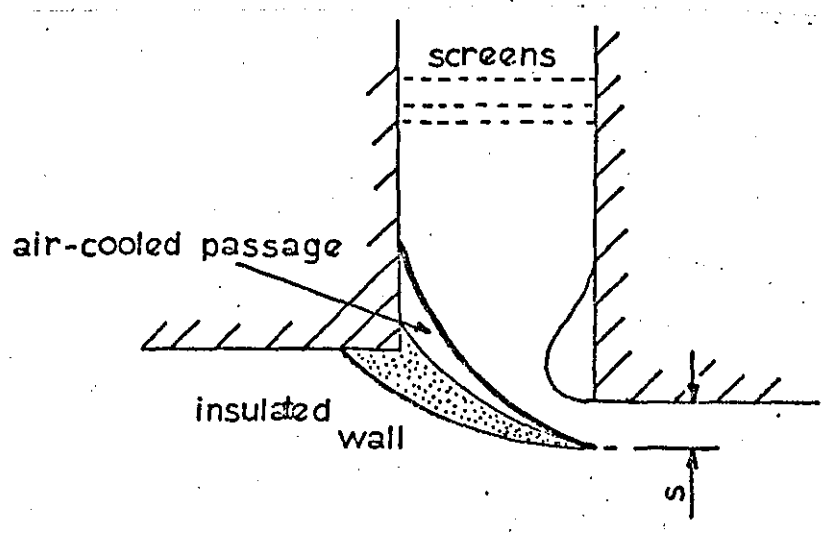

c) Injection geometry of Papell & Trout

FIG. 2.4:

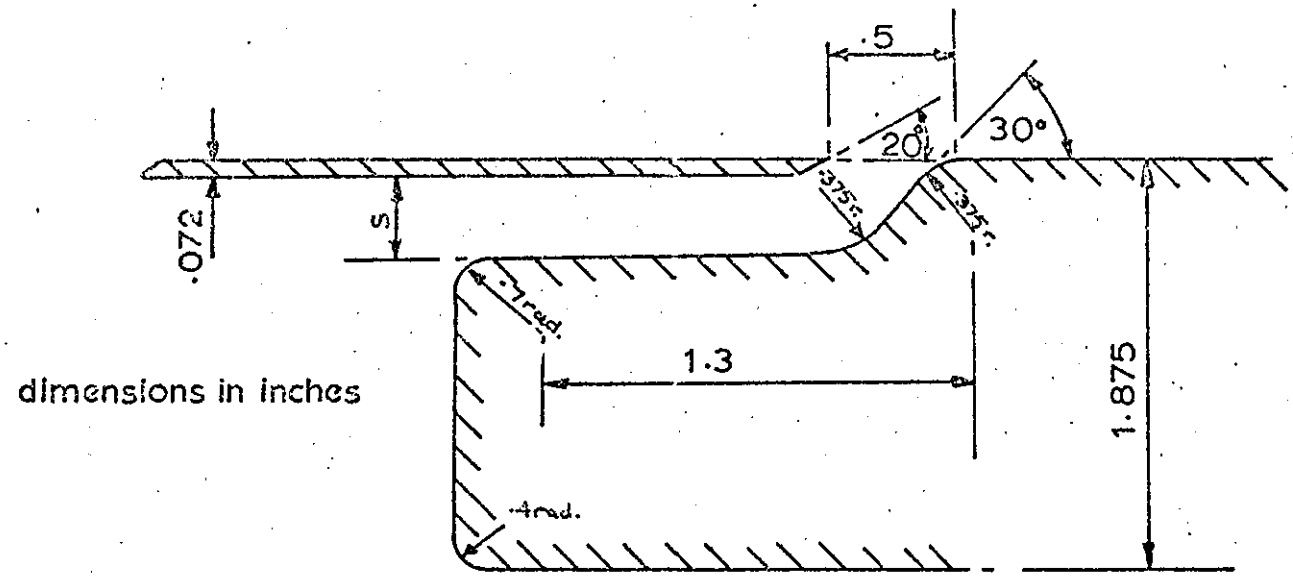

d) Injection geometries of Wieghardt and, Hartnett, Birkebak & Eckert

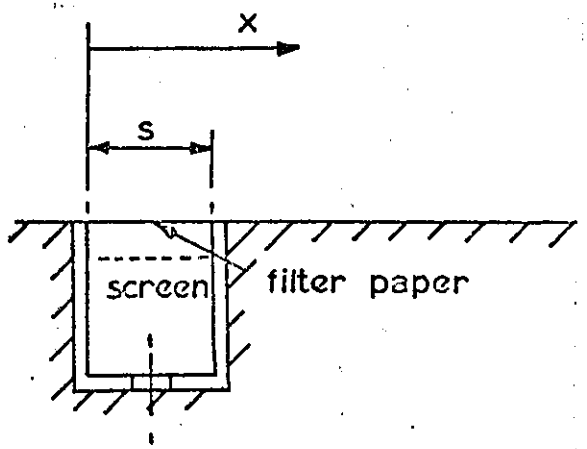

e) Injection geometry of Nishiwaki, Hirata & Tsuchida

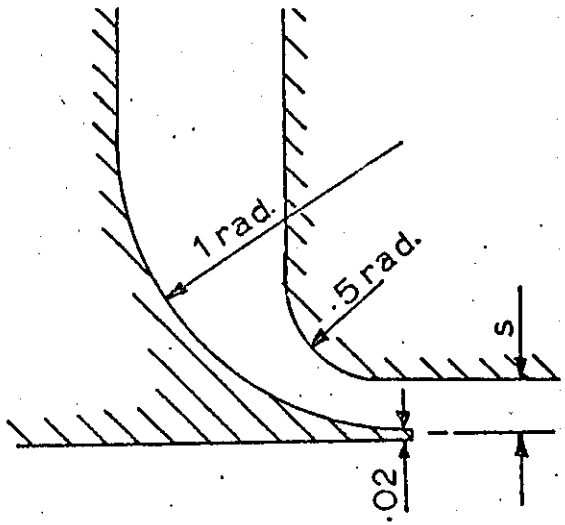

f) Injection geometry of Seban

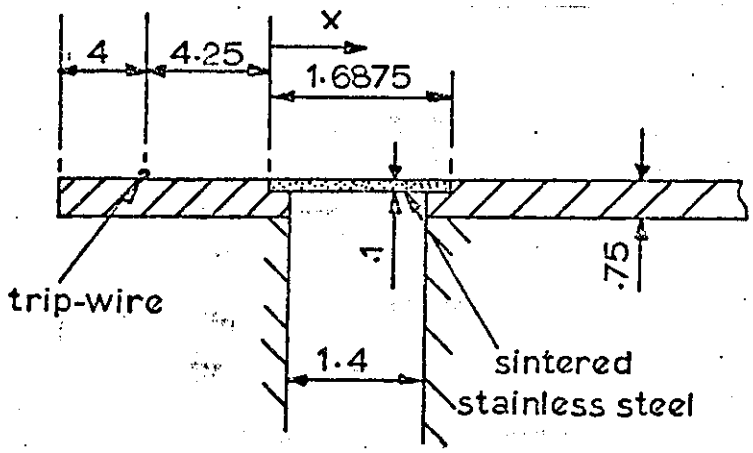

g) Injection geometry of Goldstein, Shavit & Chen

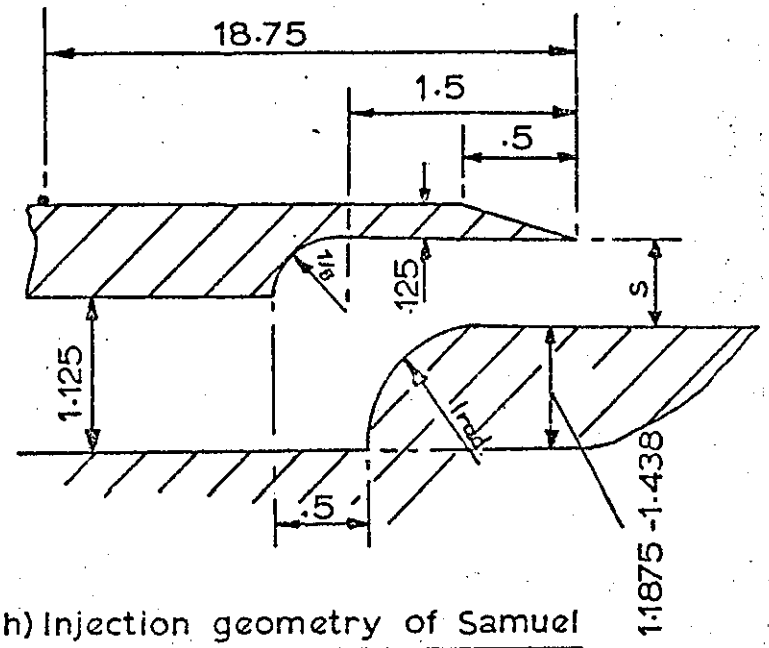

h) Injection geometry of Samuel & Joubert

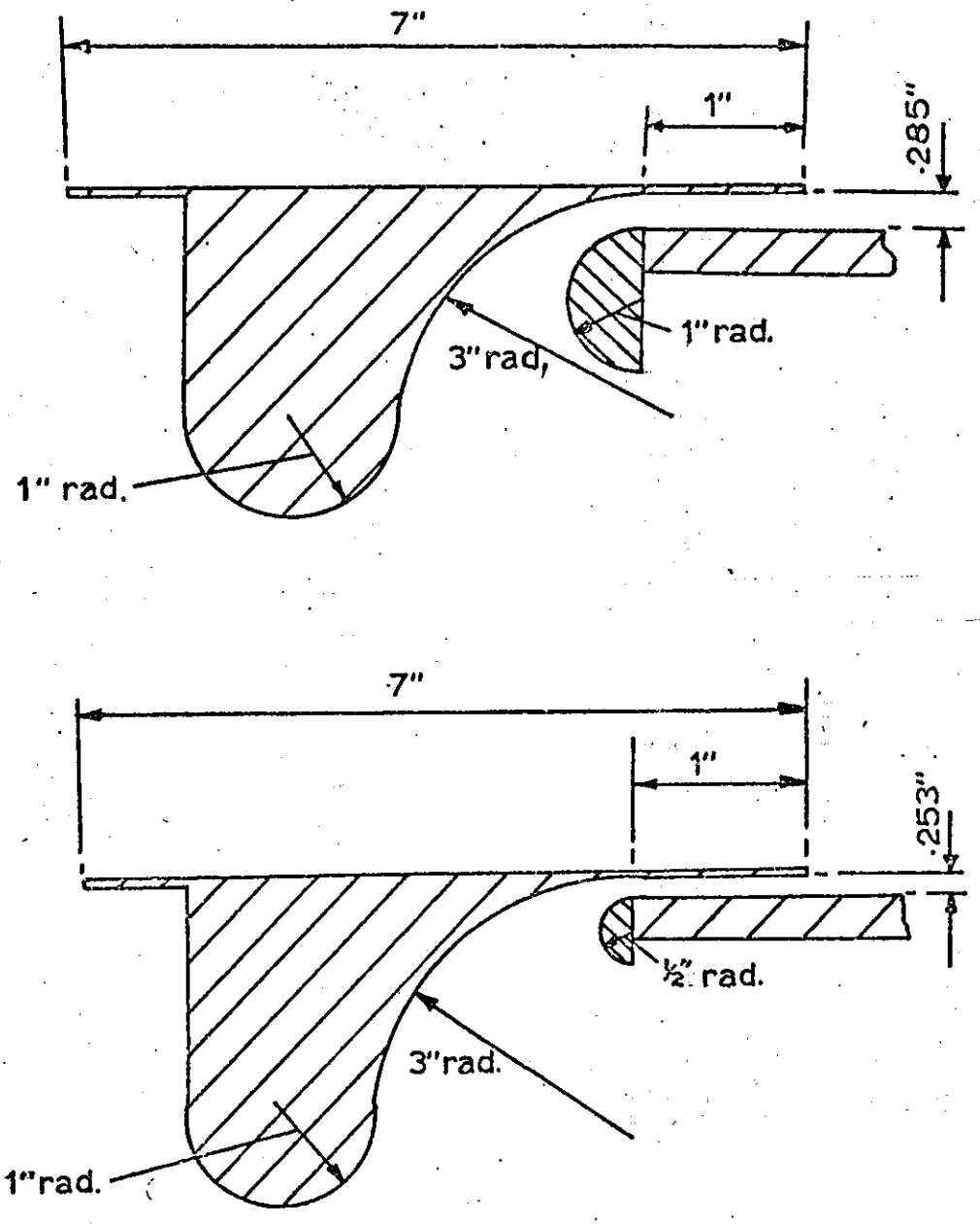

i) Whitelaw's injection geometries

FIG. 2.4: INJECTION GEOMETRIES OF PRINCIPAL INVESTIGATORS

FIG. 2.6: COMPARISON OF SOME EMPIRICAL EFFECTIVENESS RELATIONSHIPS FOR FILM COOLING DATA

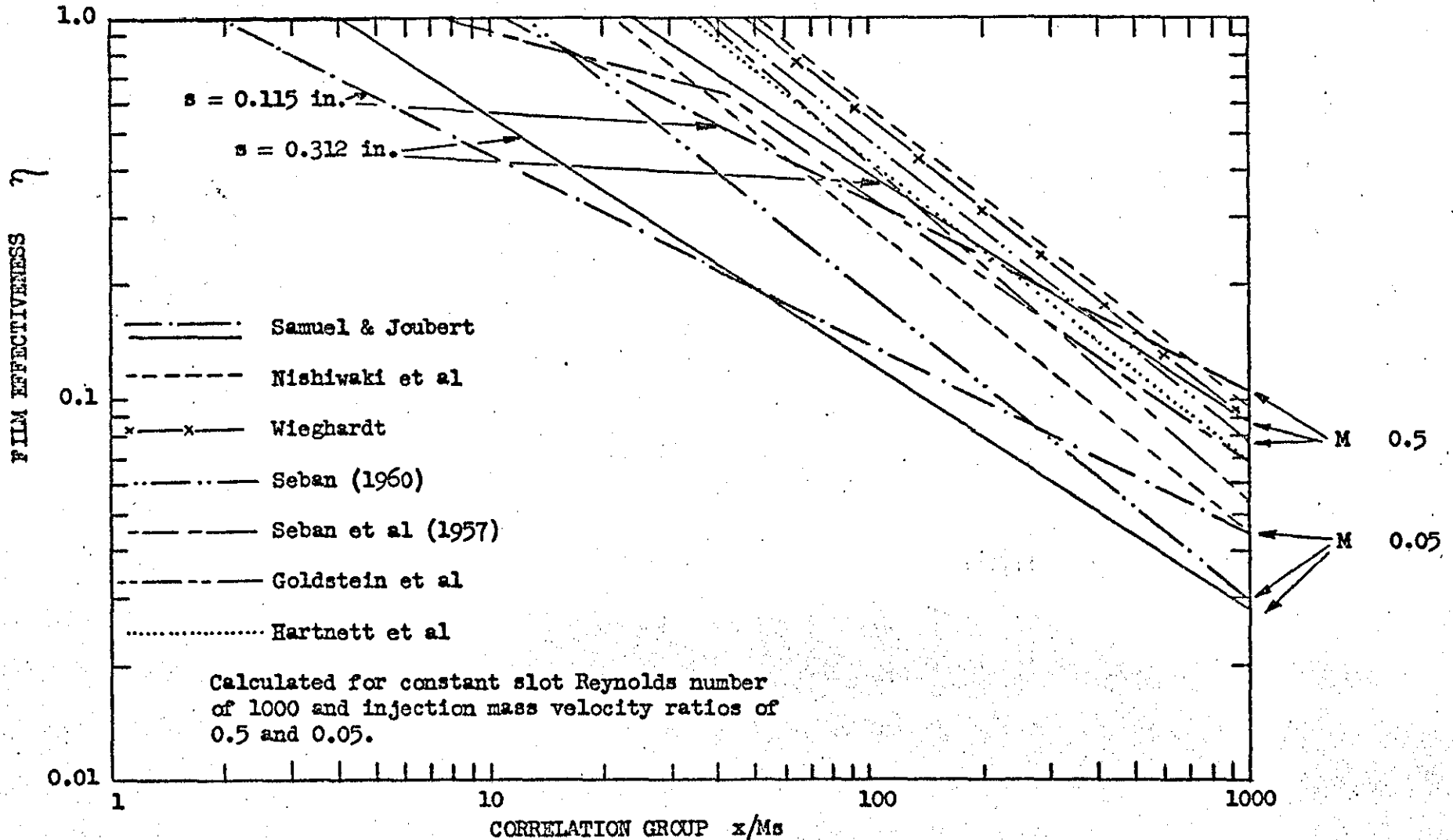

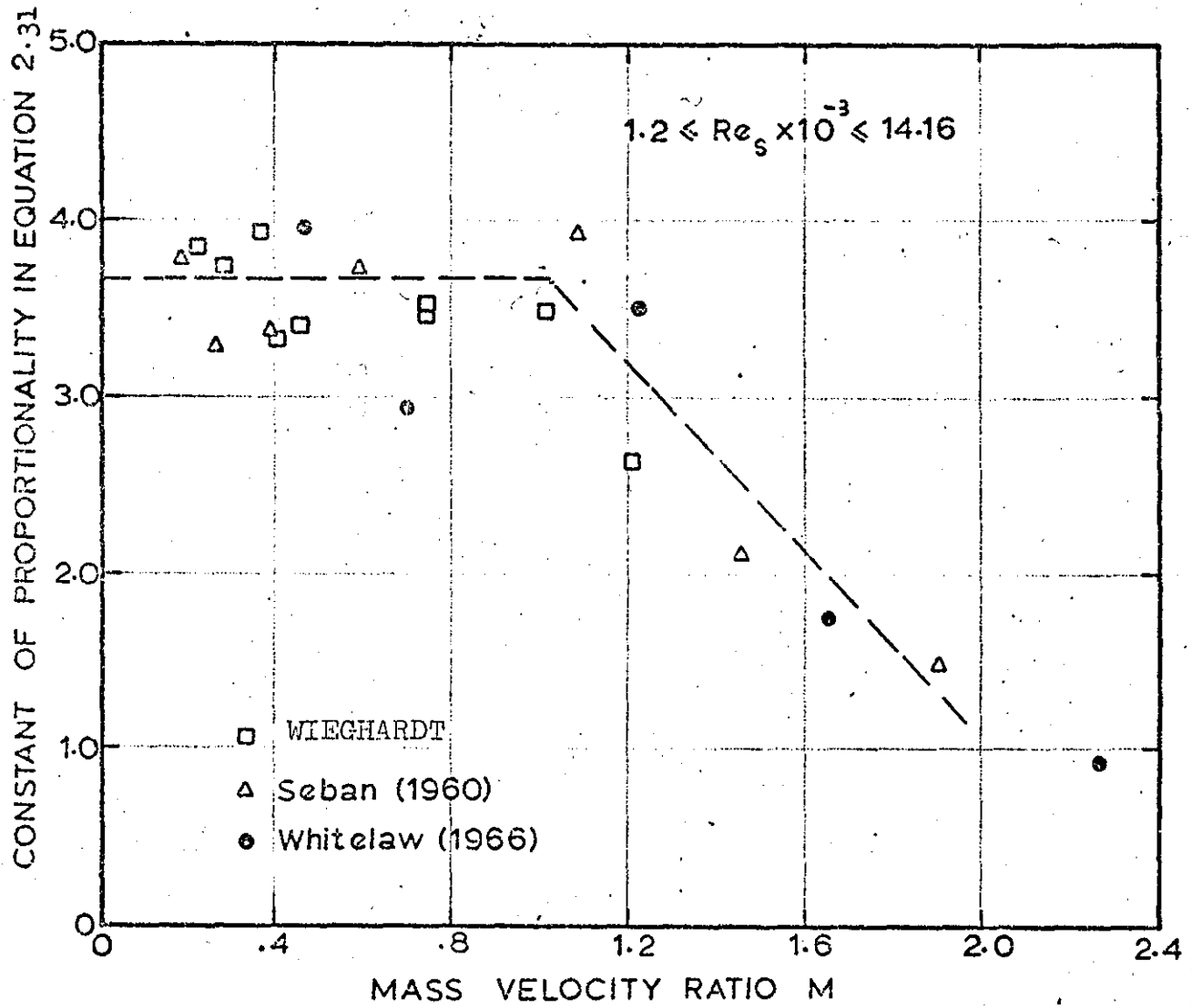

FIG. 2.7 : RANGE OF VALIDITY FOR BOUNDARY LAYER MODEL

FIG. 2.8: DEPENDENCY OF CORRELATION CONSTANT ON INJECTION VELOCITY RATIO FOR TWO PRACTICAL INJECTION GEOMETRIES

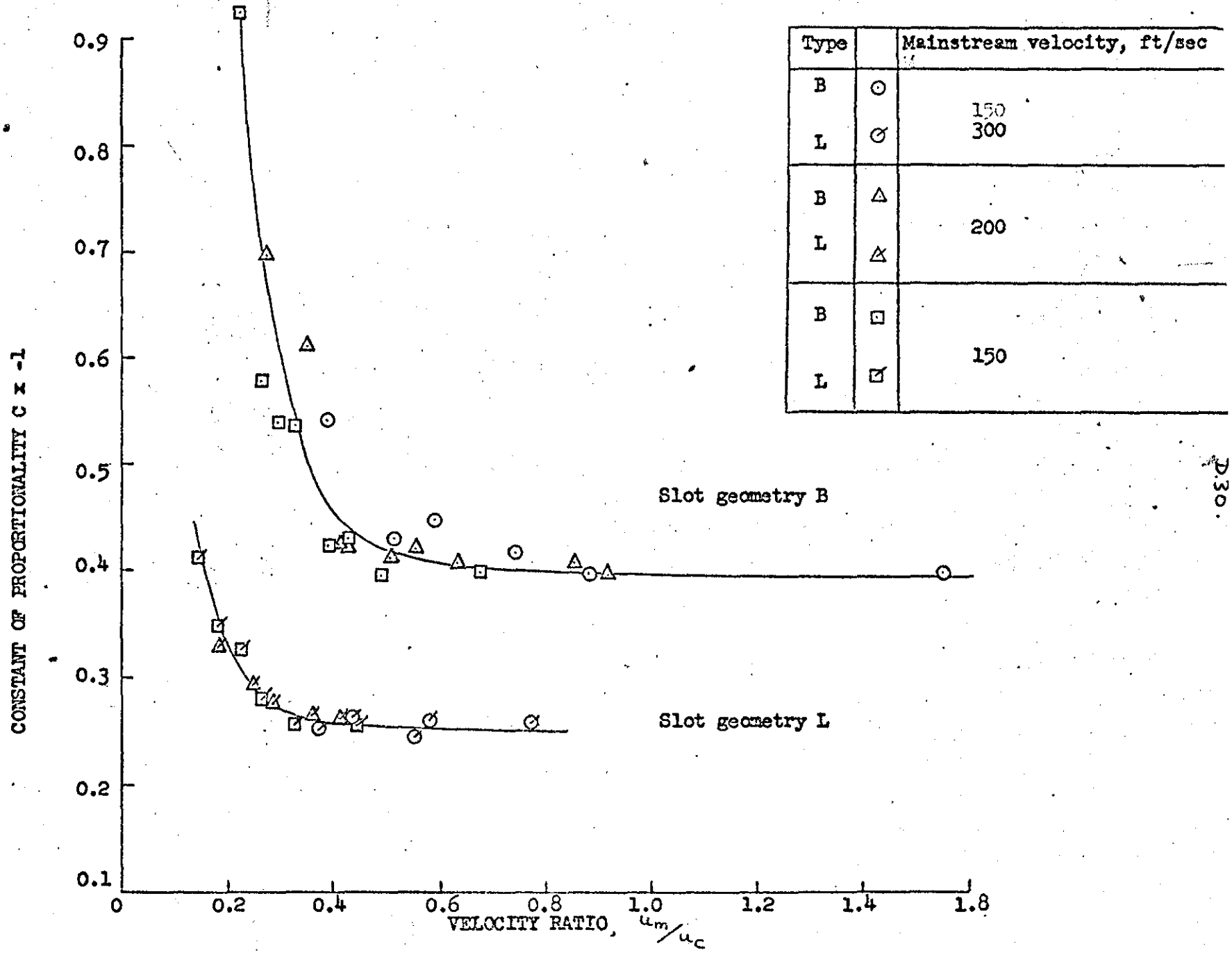

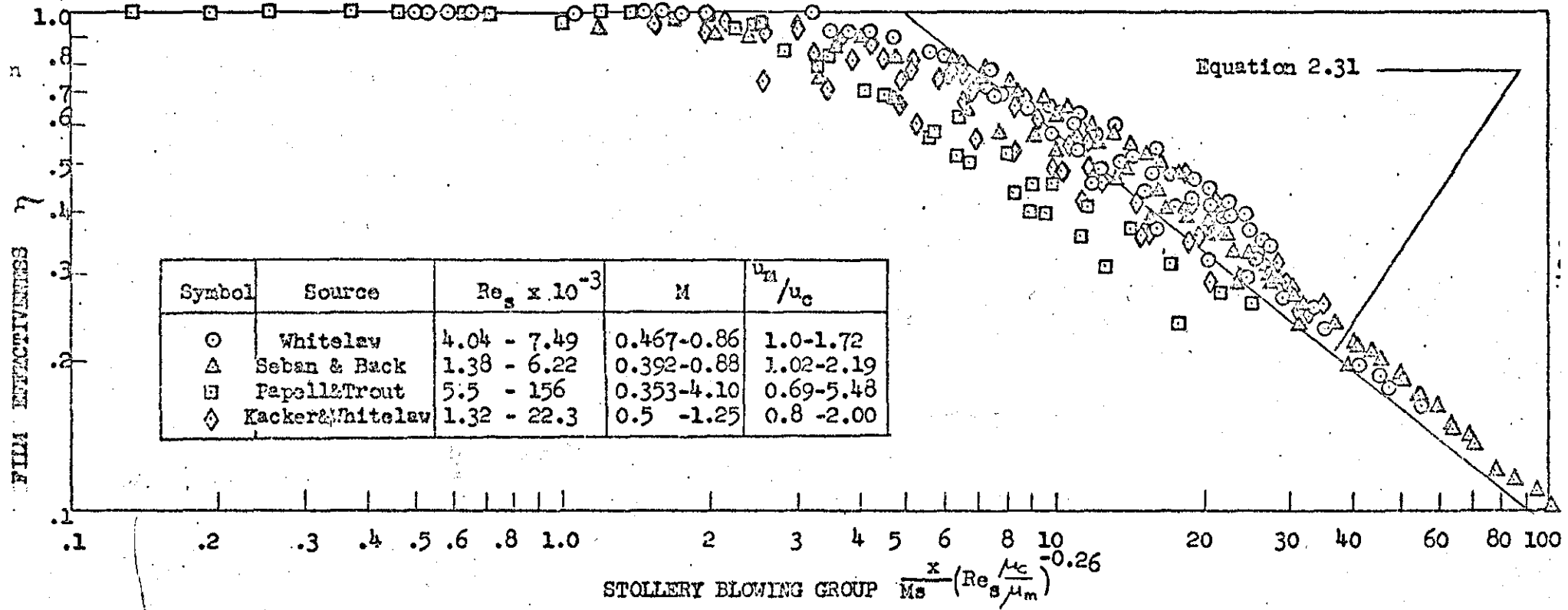

Symbol	Source	$Re_s \times 10^{-3}$	M	u_m/u_c
⊙	Whitelaw	4.04 - 7.49	0.467-0.86	1.0-1.72
△	Seban & Back	1.38 - 6.22	0.392-0.88	1.02-2.19
□	Papell&Trout	5.5 - 156	0.353-4.10	0.69-5.48
◇	Kacker&Whitelaw	1.32 - 22.3	0.5 -1.25	0.8 -2.00

FIG. 2.9: USE OF BOUNDARY LAYER MODEL FOR CORRELATION AND PREDICTION OF WAKE-LIKE EFFECTIVENESS DATA

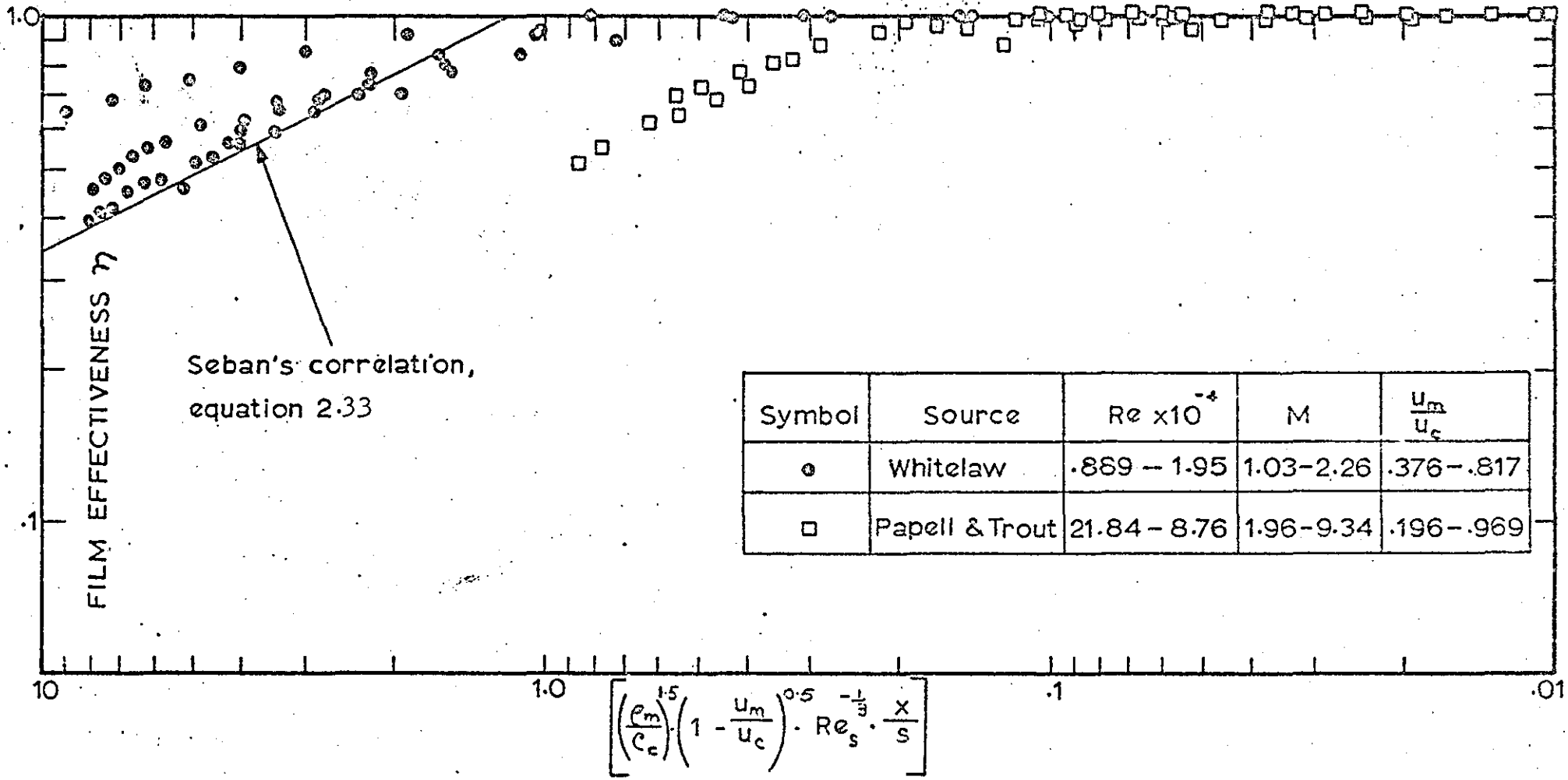

Symbol	Source	Re x10^{-4}	M	$\frac{u_m}{u_c}$
⊙	Whitelaw	.889 – 1.95	1.03–2.26	.376–.817
□	Papell & Trout	21.84 – 8.76	1.96–9.34	.196–.969

FIG. 2.10: USE OF SEBAN'S CORRELATION EQUATION FOR PREDICTION OF DATA FROM JET-LIKE FLOWS.

FIG. 2.11: CORRELATION OF JET-LIKE EFFECTIVENESS DATA WITH MODIFIED BOUNDARY LAYER MODEL

Source		$Re_s \times 10^{-3}$	M	u_m/u_c
Seban & Back	⊙	3.53 - 6.96	4.90 - 12.6	0.071 - 0.196
Chin et al	△	6.16 - 9.27	1.02 - 2.4	0.348 - 0.884
Pai & Whitelaw	◇	0.28 - 14.3	0.09 - 6.87	0.321 - 0.813
Whitelaw	□	10.5 - 19.5	1.22 - 2.26	0.376 - 0.666
Papell & Trout	⊙	88.2 - 218.	4.05 - 9.34	0.197 - 0.691

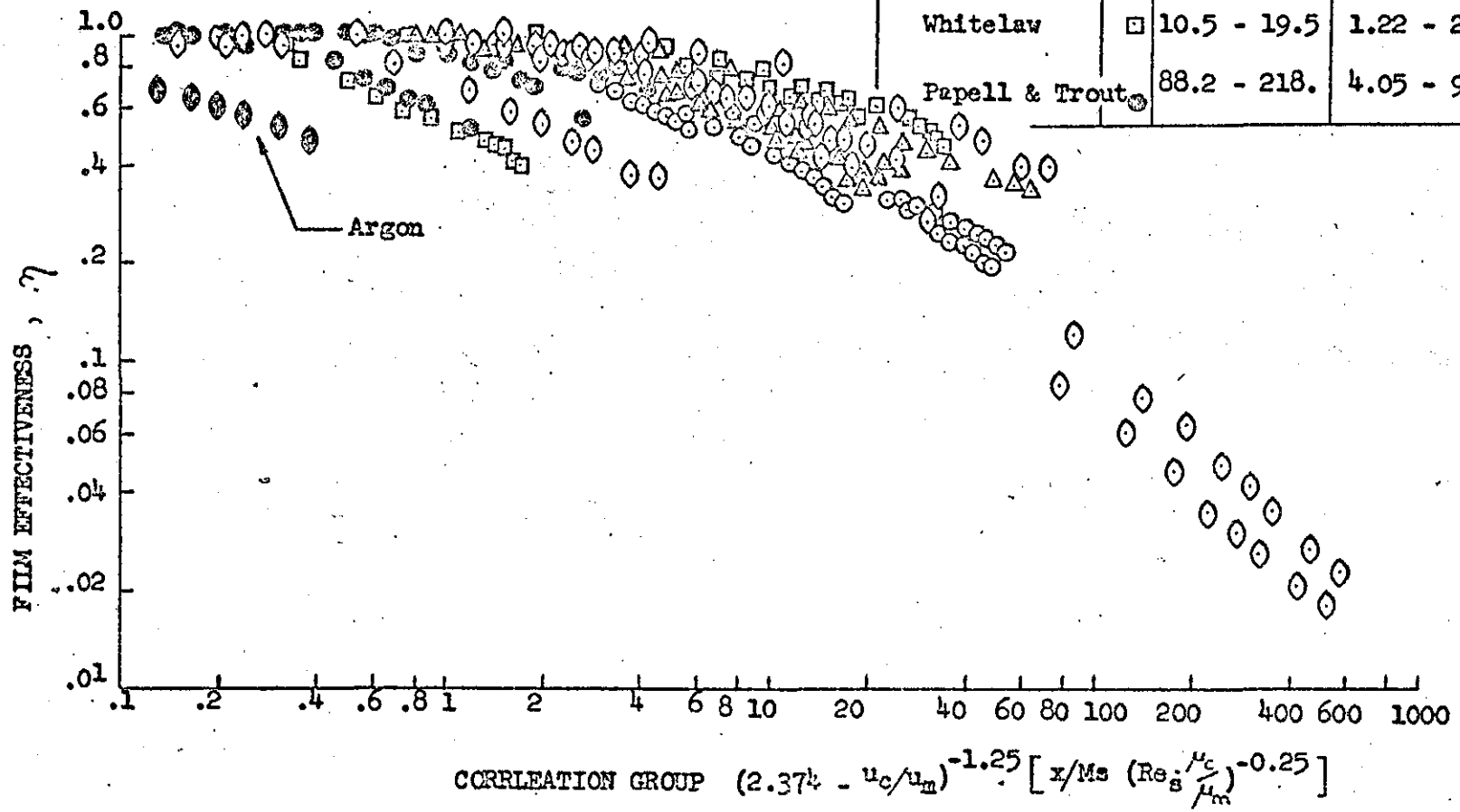

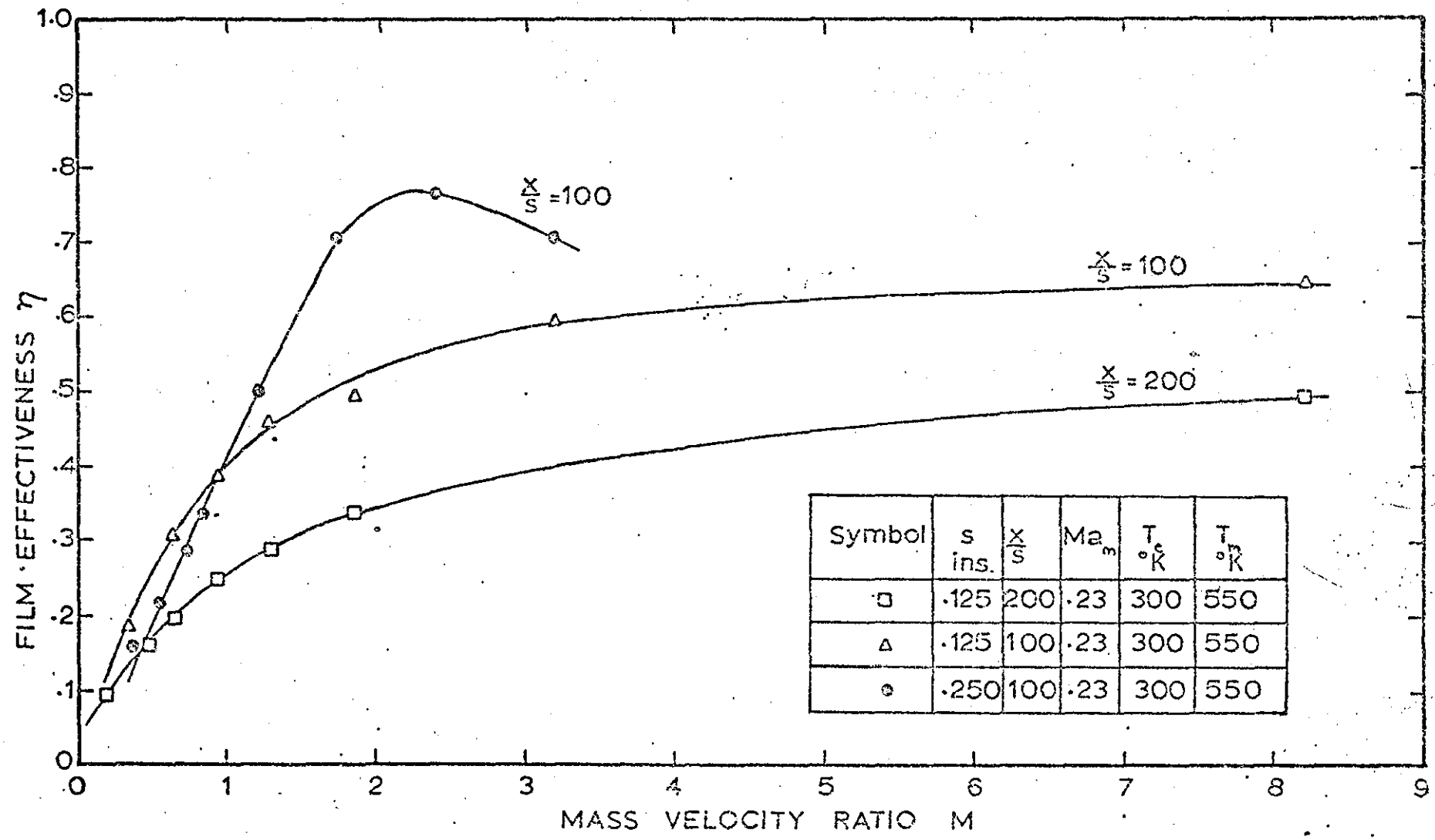

FIG. 2.12: EFFECT OF MASS VELOCITY RATIO ON EFFECTIVENESS USING PAPELL AND TROUT'S DATA

FIG. 2.13: VARIATION OF OPTIMUM FILM EFFECTIVENESS

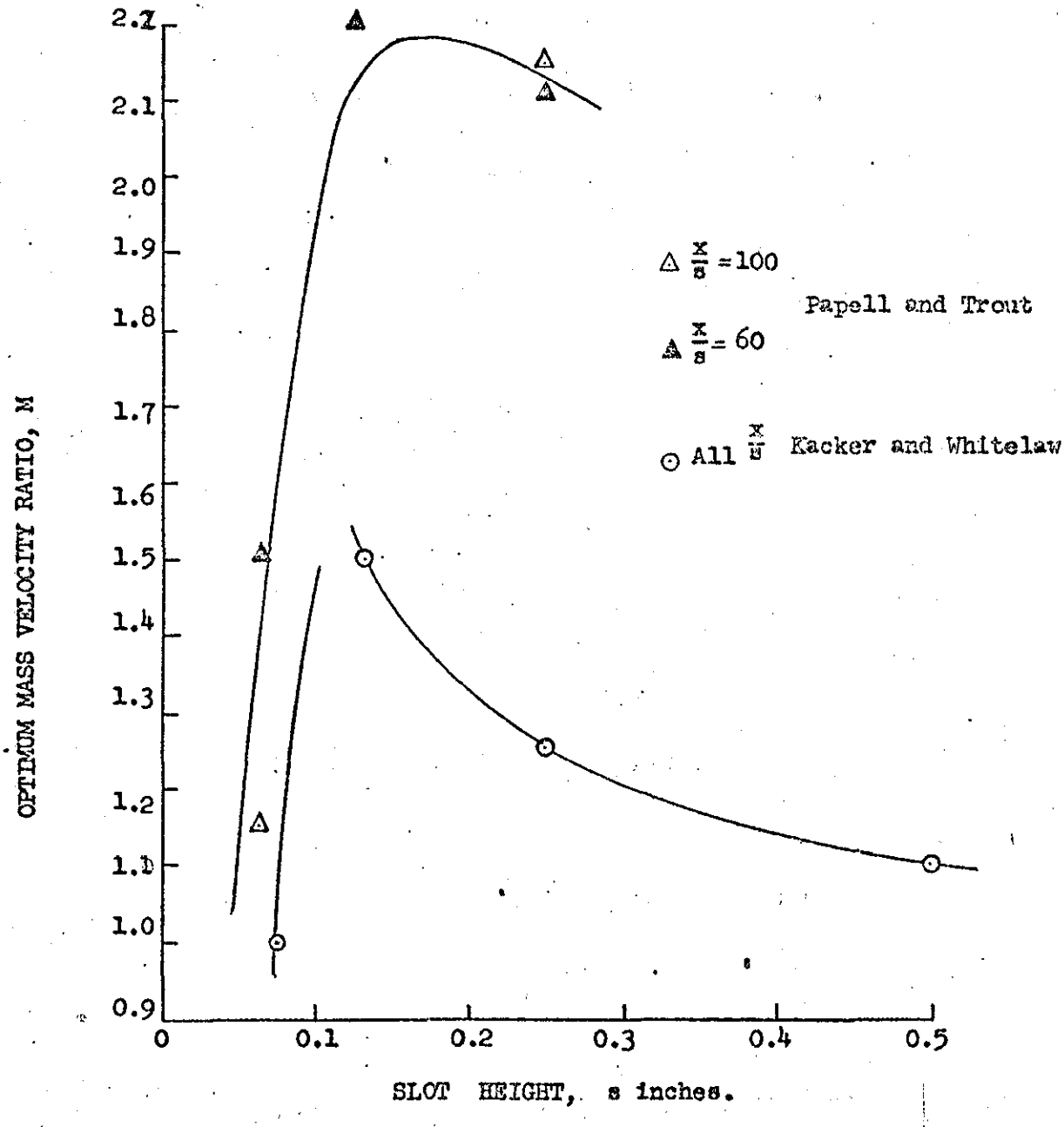

FIG. 2.14: EFFECT OF MAINSTREAM TURBULENCE ON POTENTIAL CORE LENGTH

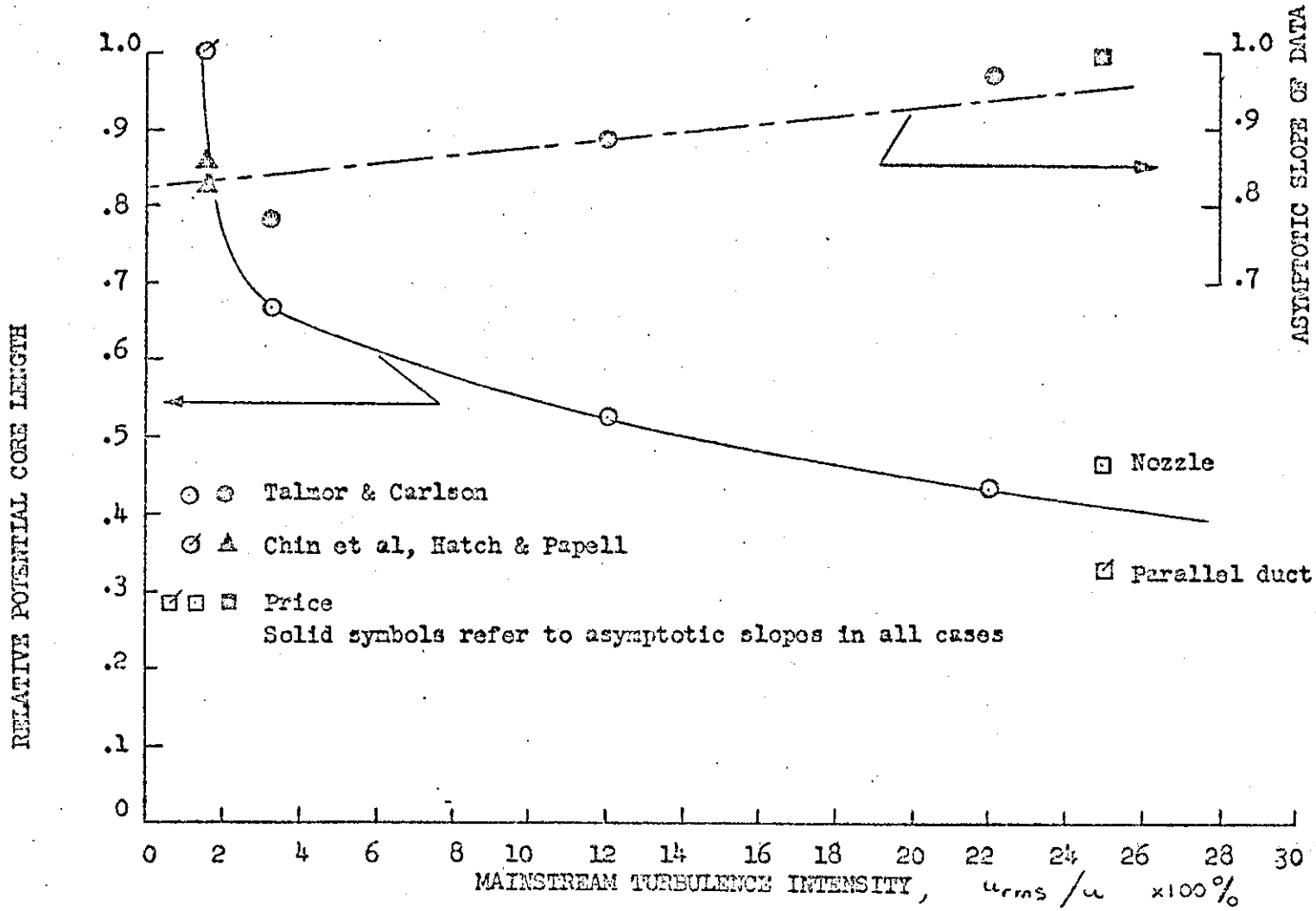

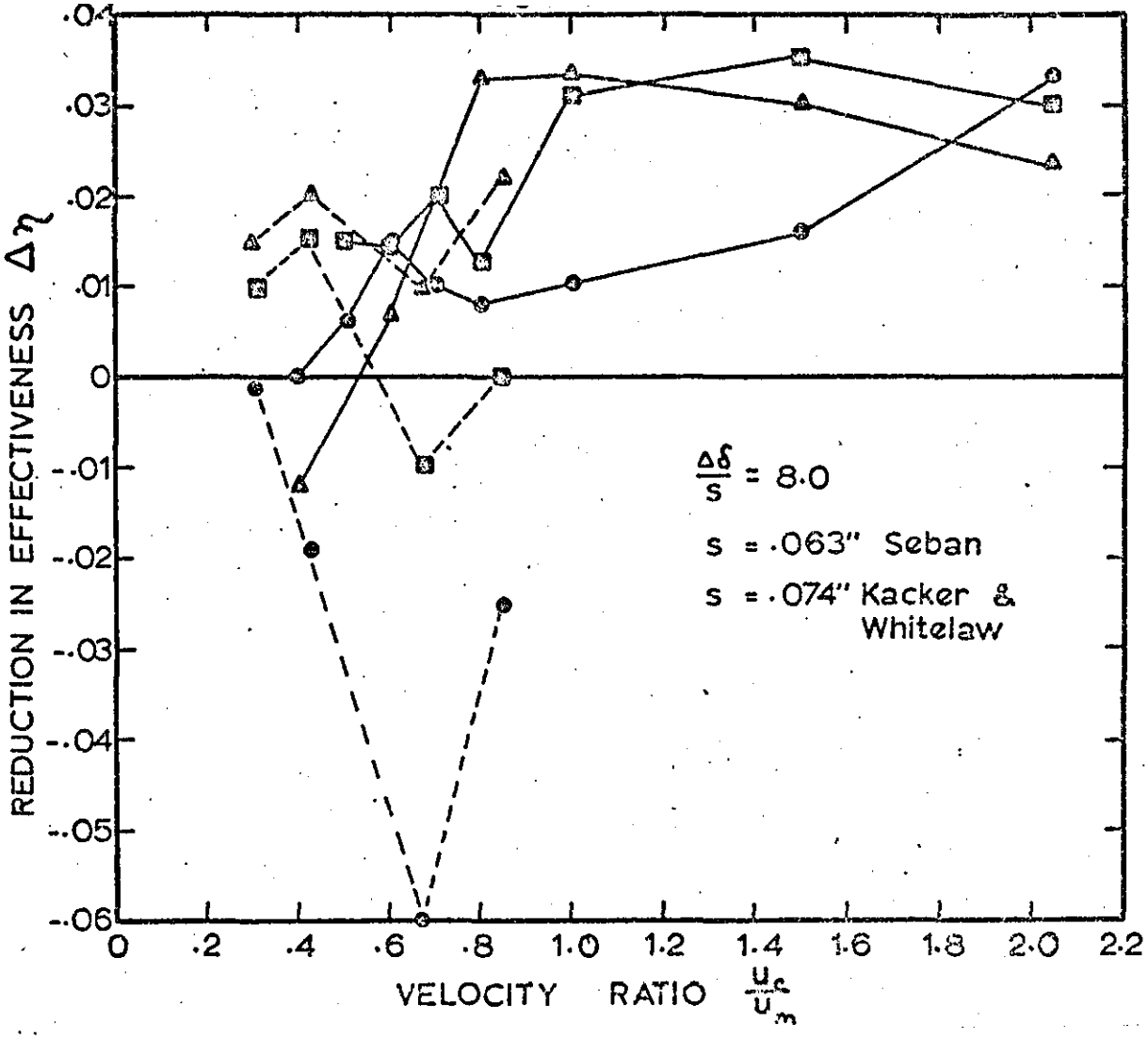

Symbol	Source	$\frac{x}{s}$
---⊙---	Seban	50
——⊙——	Kacker-Whitelaw	50
---□---	Seban	100
——▣——	Kacker-Whitelaw	100
---△---	Seban	200
——▲——	Kacker-Whitelaw	200

FIG. 2.15: EFFECT OF MAINSTREAM INITIAL BOUNDARY LAYER ON FILM EFFECTIVENESS

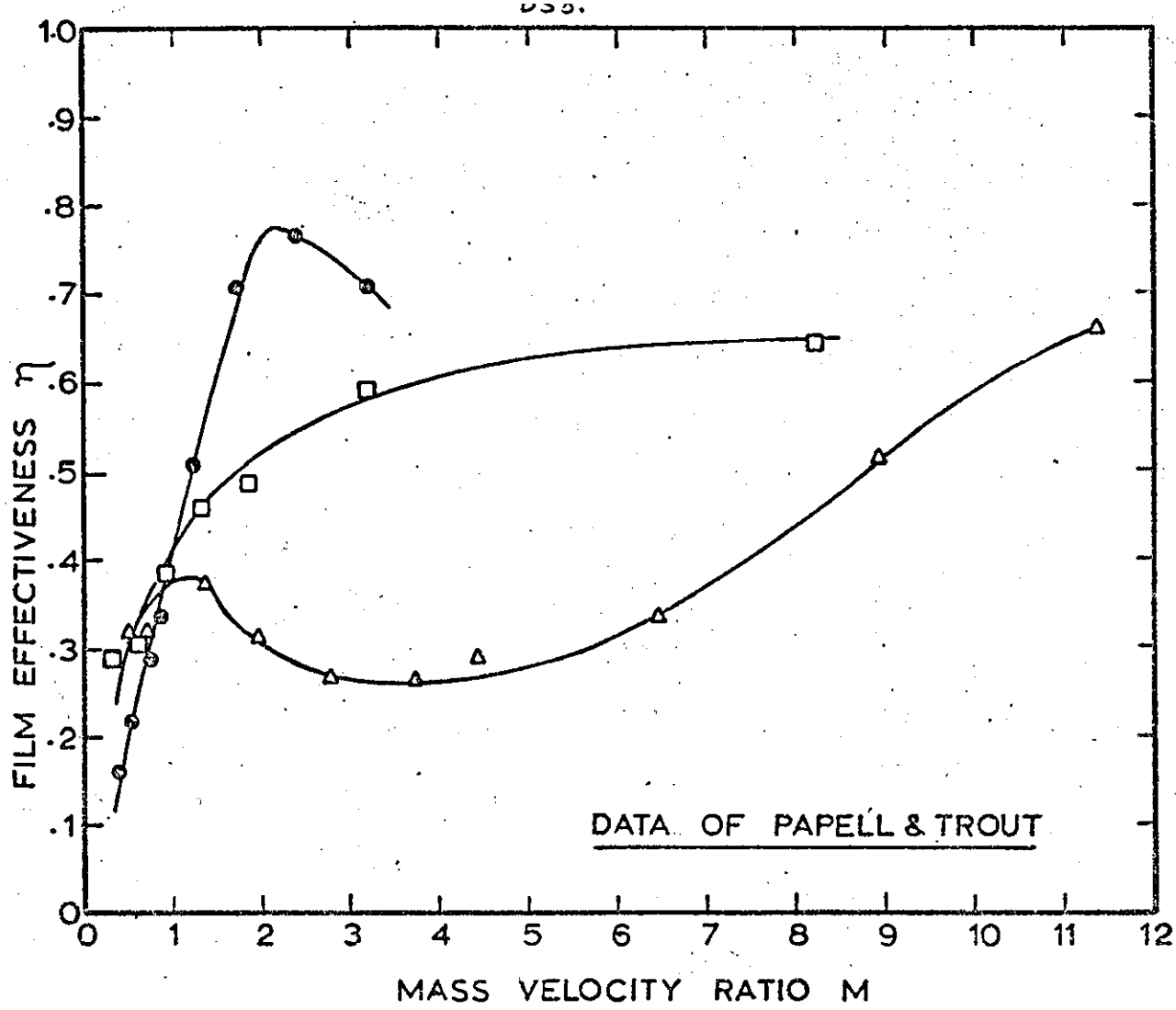

Symbol	s ins.	$\frac{x}{s}$	Ma_m	T_c °K	T_w °K
⊙	0·25	100	0·23	300	550
□	0·125	100	0·23	300	550
△	0·0625	100	0·20	301	561

FIG. 2.16: EFFECT OF MASS VELOCITY RATIO AND SLOT HEIGHT ON EFFECTIVENESS AT x/s OF 100

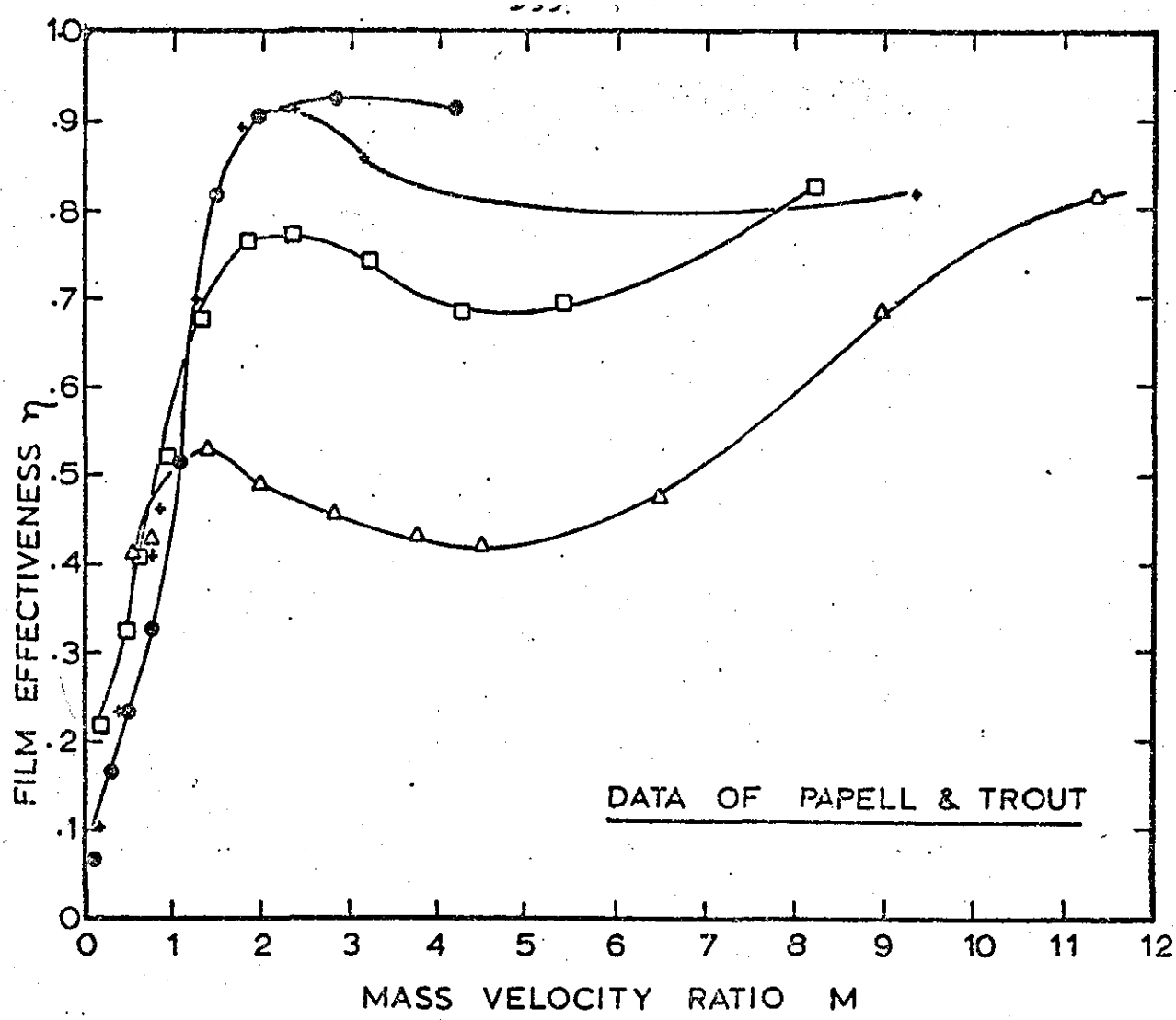

Symbol	s ins.	$\frac{x}{s}$	Ma_m	T_c °K	T_m °K
⊙	0.50	60	0.22	302	566
✦	0.25	60	0.23	300	550
□	0.125	60	0.23	298	561
△	0.0625	60	0.20	301	561

FIG. 2.17: EFFECT OF MASS VELOCITY RATIO AND SLOT HEIGHT ON EFFECTIVENESS AT x/s OF 60

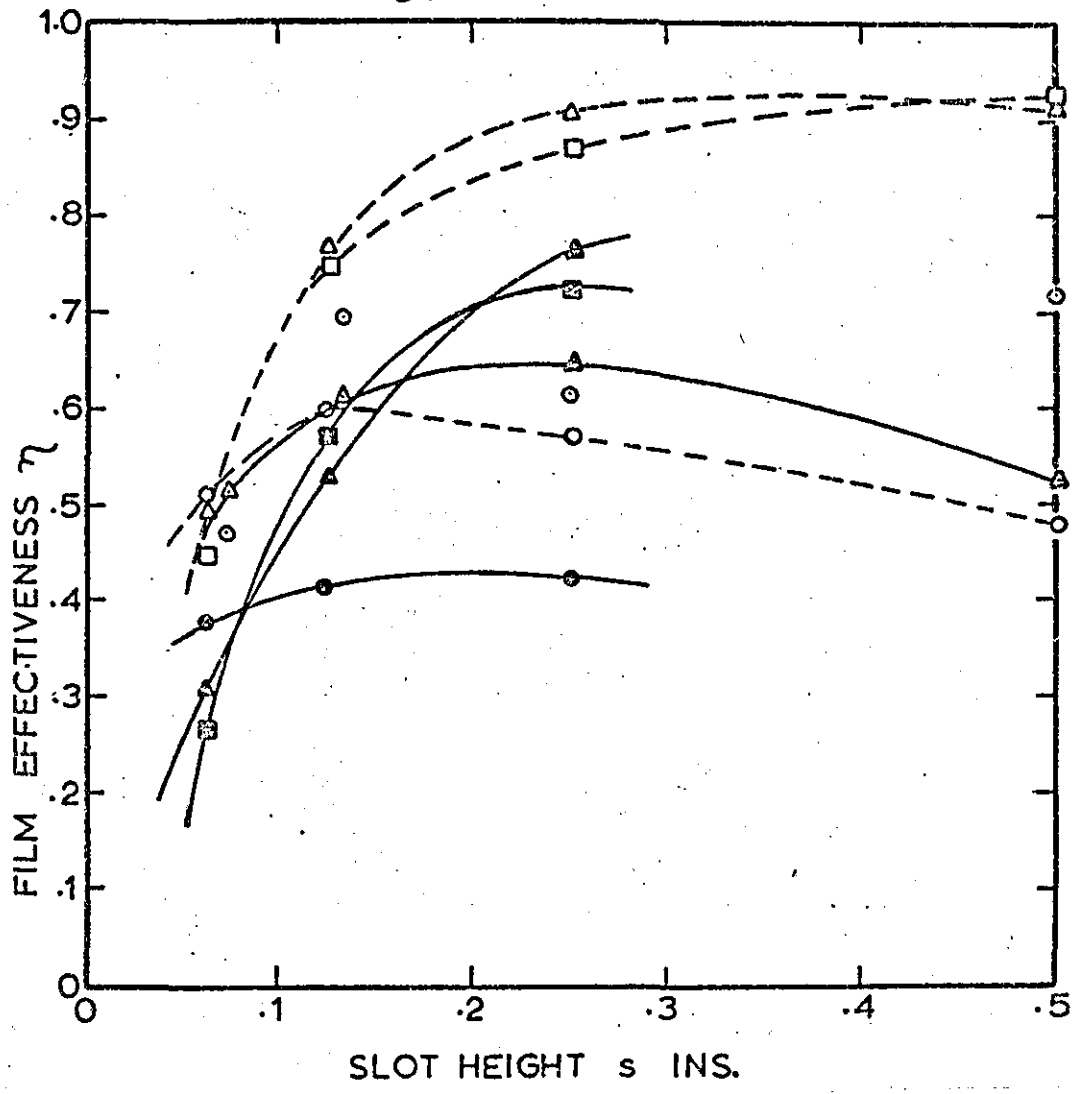

Symbol	M	$\frac{x}{s}$	AUTHOR
—○—	1	100	PAPELL & TROUT
—△—	2	100	
—□—	3	100	
--○--	1	60	
--△--	2	60	
--□--	3	60	
—○—	1	100	Whitelaw
—△—	2	100	

FIG. 2.18: EFFECT OF SLOT HEIGHT CROSS- PLOTTED FROM PAPELL & TROUT'S DATA AND THAT OF WHITELAW

FIG. 2.19: OPTIMUM SLOT HEIGHT (CONSTRUCTED FROM THE DATA OF KACKER & WHITELAW)

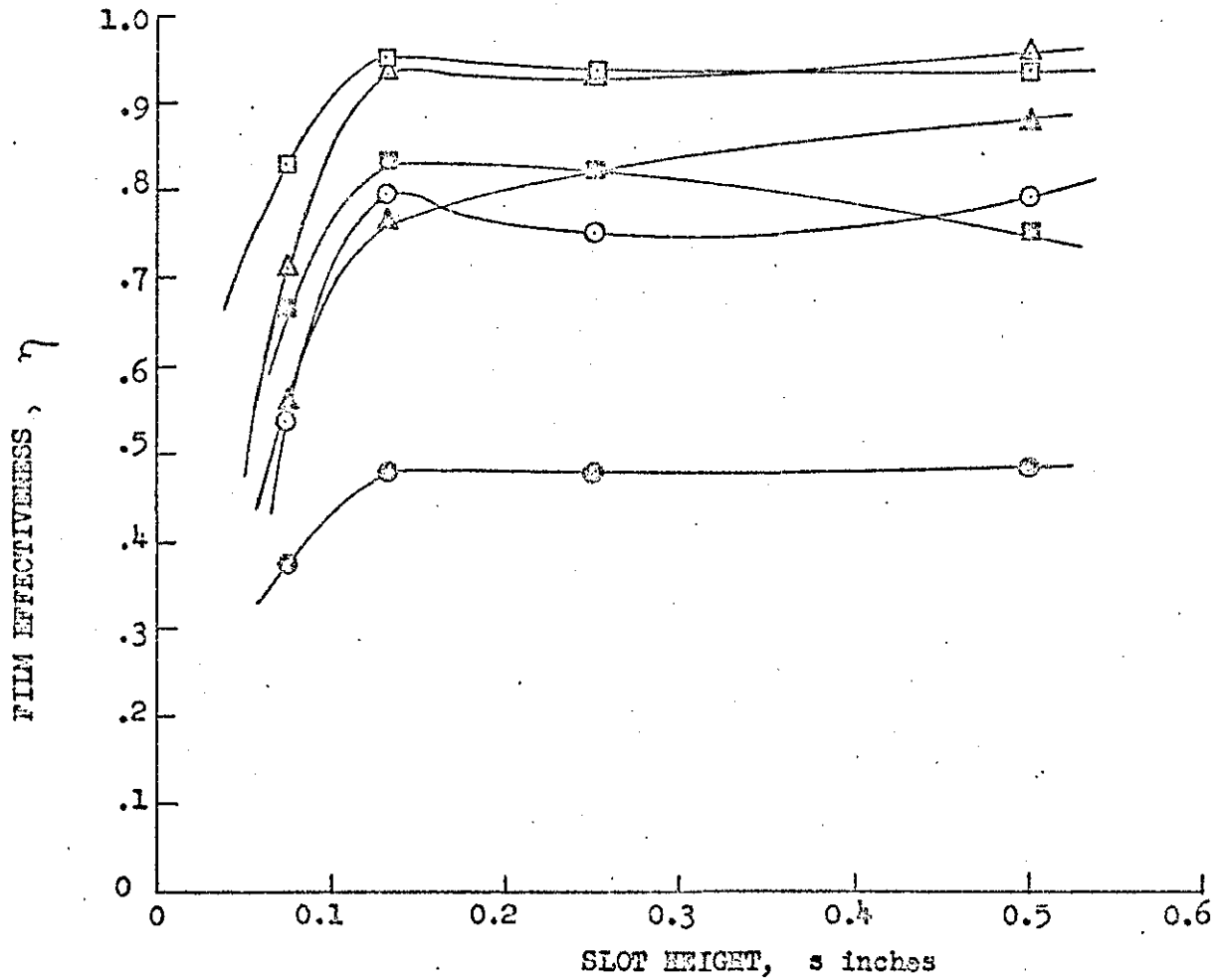

Symbol	M	x/s
⊙	0.5	25
△	1.0	25
⊡	2.0	25
⊙	0.5	50
△	1.0	50
⊡	2.0	50

Fixed mainstream conditions

FIG. 2.20: DEMONSTRATION OF SLOT HEIGHT OPTIMUM AT FIXED DISTANCES FROM INJECTION

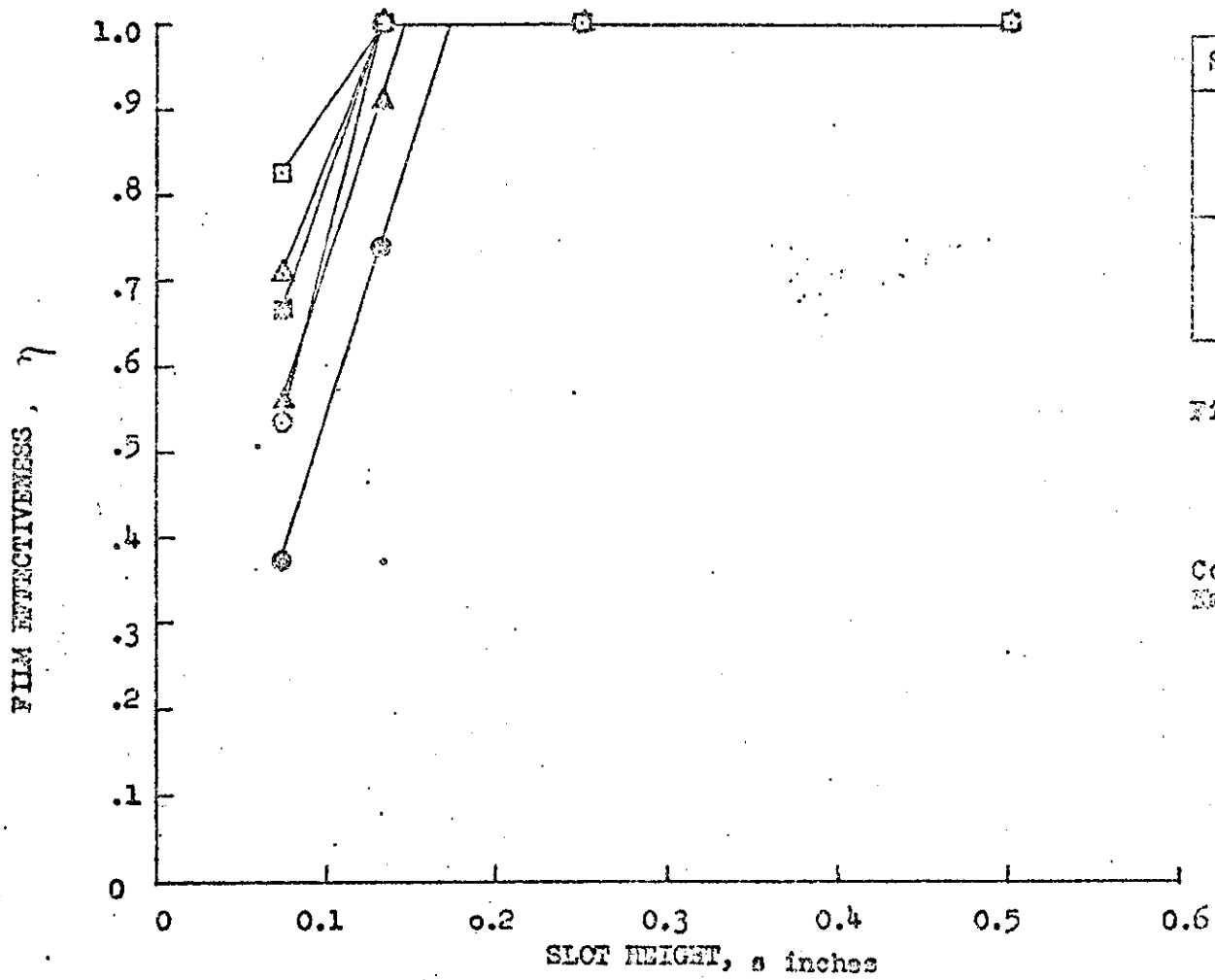

Symbol	M	x ins.
⊙	0.5	1.85
△	1.0	1.85
⊡	2.0	1.85
⊙	0.5	3.70
△	1.0	3.70
⊡	2.0	3.70

Fixed mainstream conditions

Constructed from the data of Hacker and Whitelaw

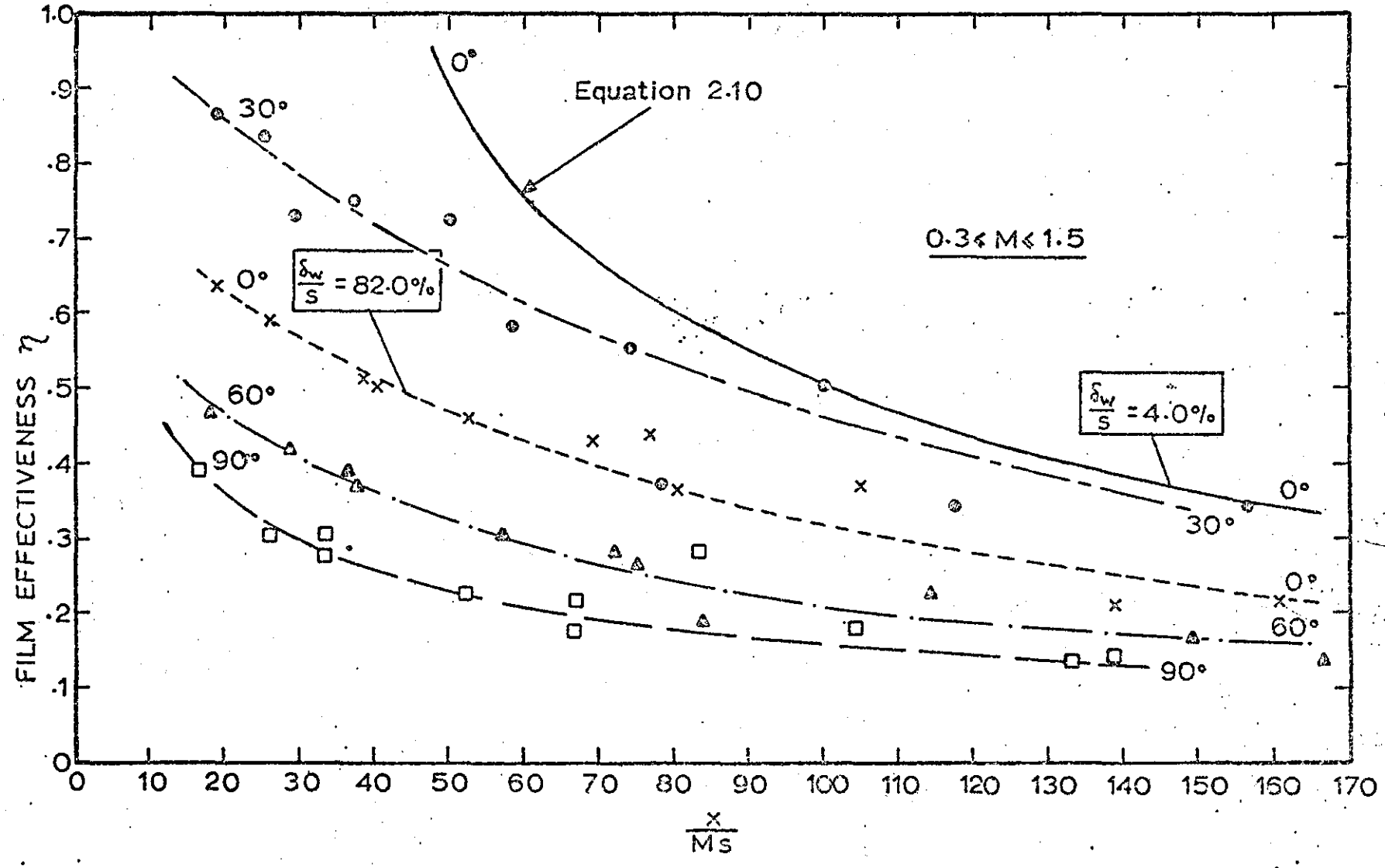

FIG. 2.21: INFLUENCE OF COOLANT INJECTION ANGLE ON EFFECTIVENESS FROM SIVASEGAREM AND WHITELAW

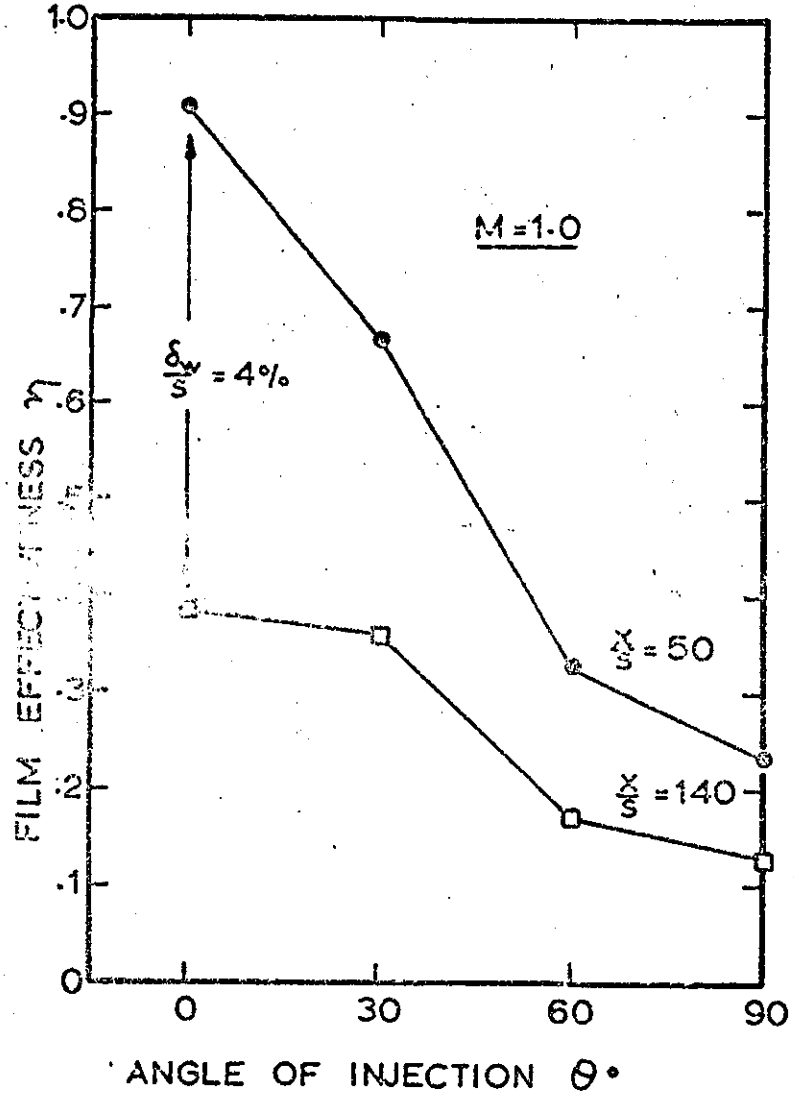

FIG. 2.22: INFLUENCE OF INJECTION ANGLE ON EFFECTIVENESS ACCORDING TO DATA OF SIVASEGAREM AND WHITELAW

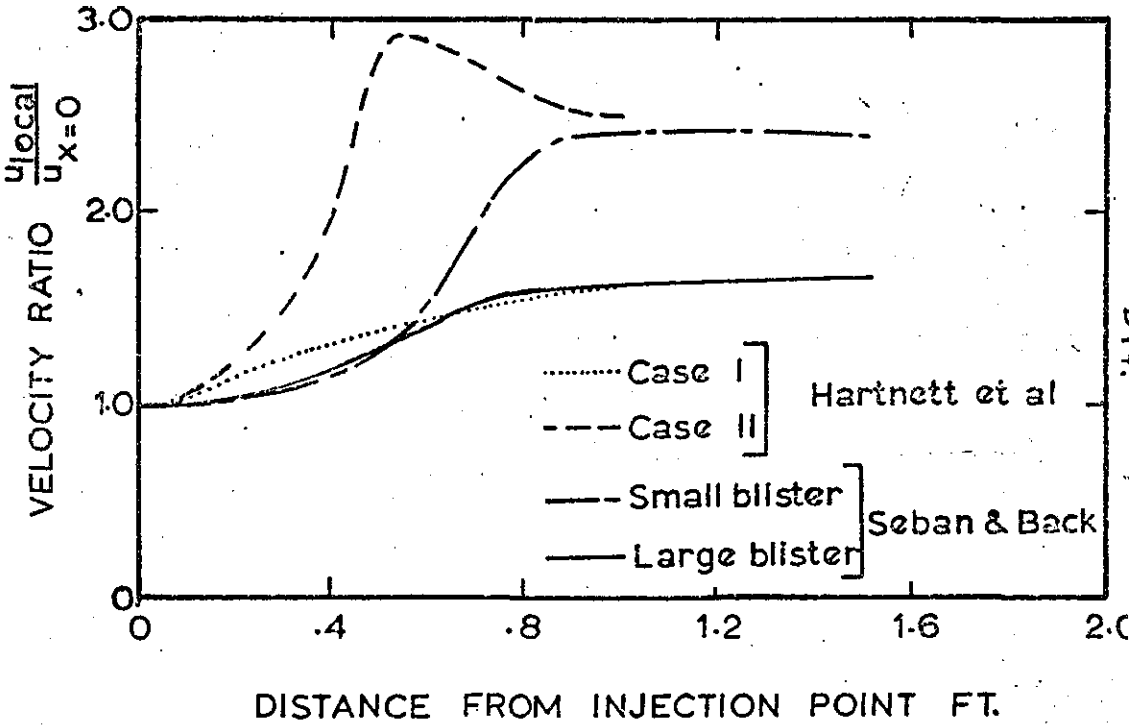

FIG. 2.23: APPLIED VELOCITY GRADIENTS FOR THE EXPERIMENTS OF SEBAN AND BACK, AND, HARTNETT ET AL

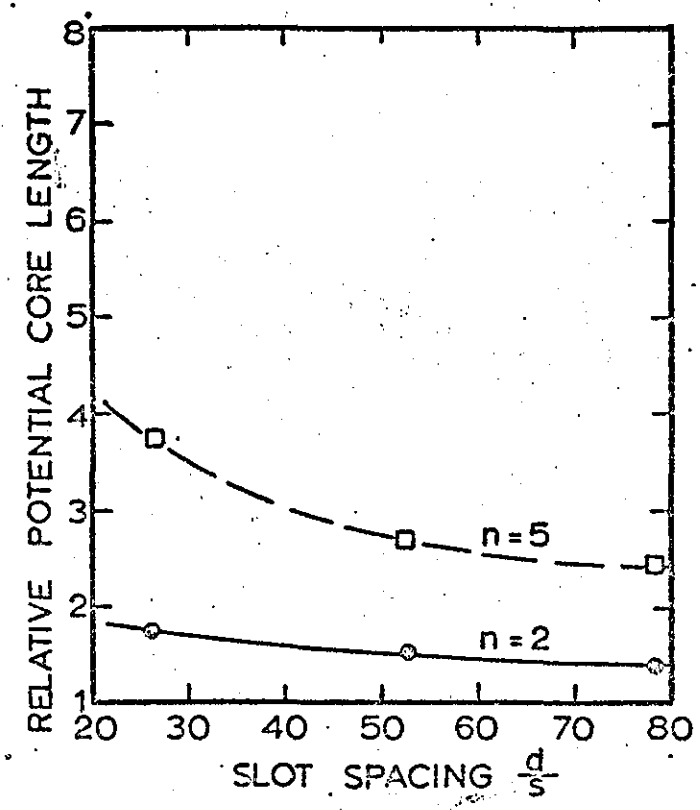

a) SLOT SPACING EFFECT

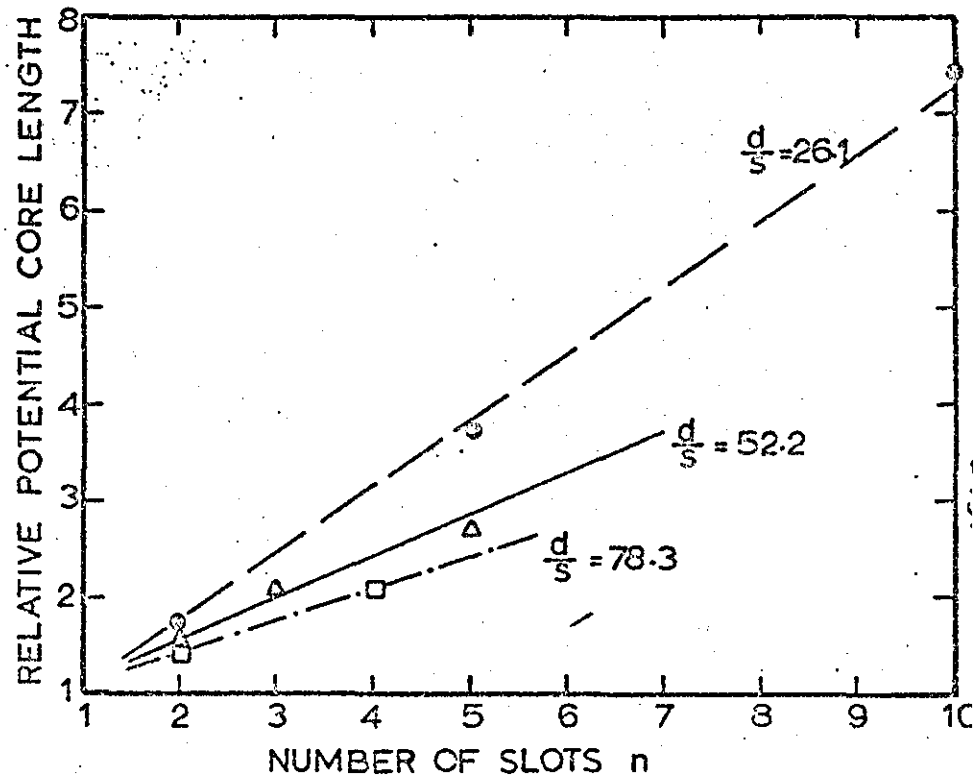

b) SLOT NUMBER EFFECT

DATA OF CHIN ET AL

FIG. 2.24: EFFECT OF NUMBER OF SLOTS AND SLOT SPACING ON POTENTIAL CORE LENGTH

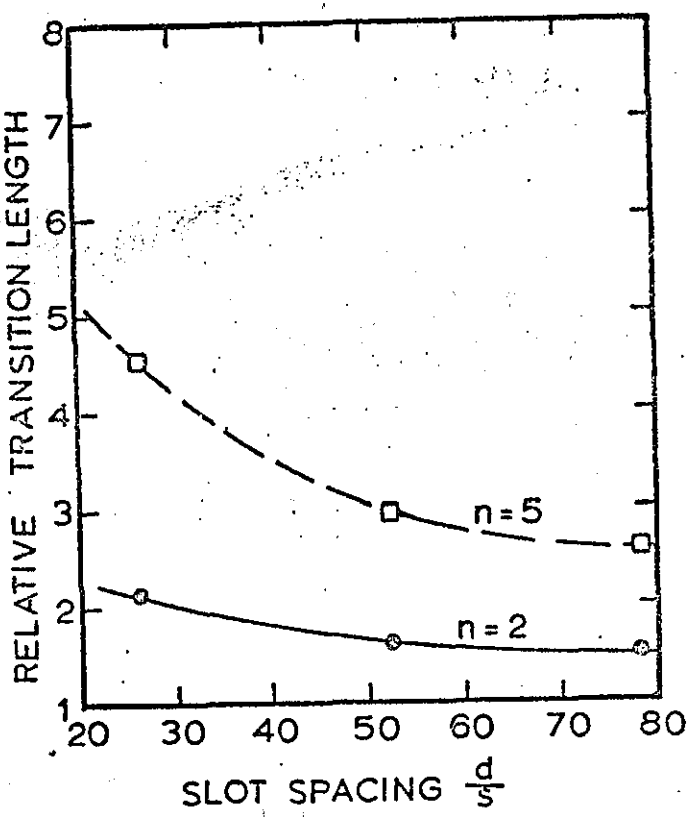

a) SLOT SPACING EFFECT

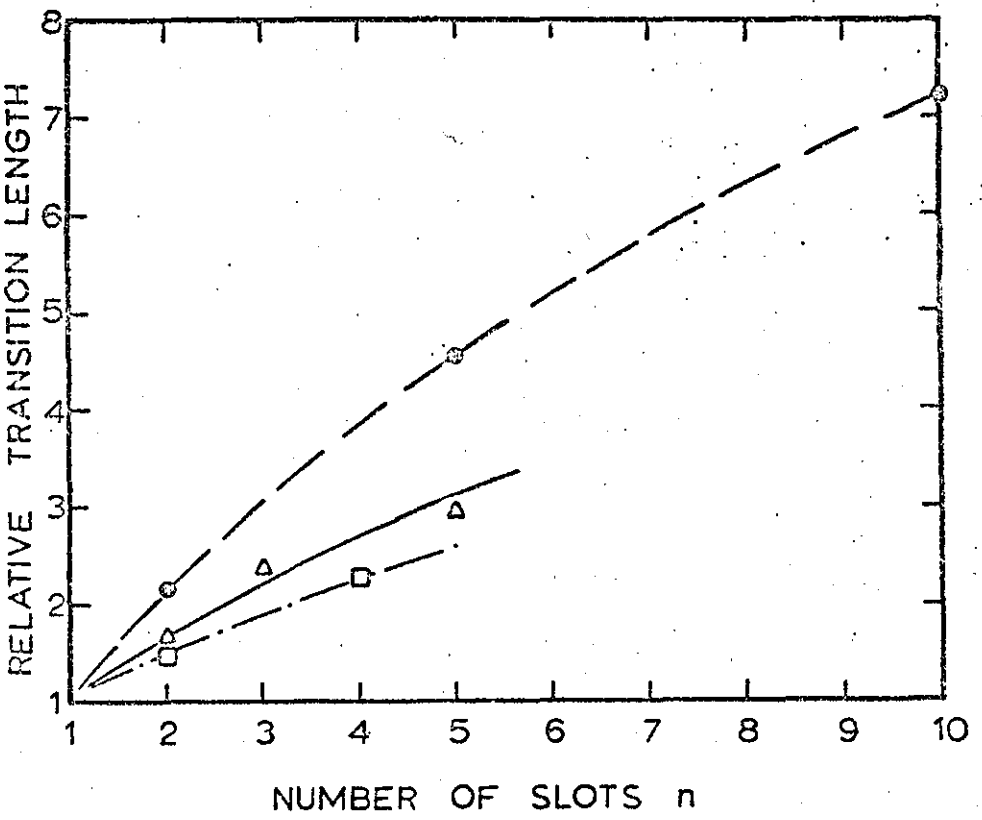

b) SLOT NUMBER EFFECT

DATA OF CHIN ET AL

FIG. 2.25: EFFECT OF NUMBER OF SLOTS AND SLOT SPACING ON TRANSITION LENGTH

FIG. 3.1: TYPICAL GAS TURBINE COMBUSTION CHAMBER FLOW PATTERNS

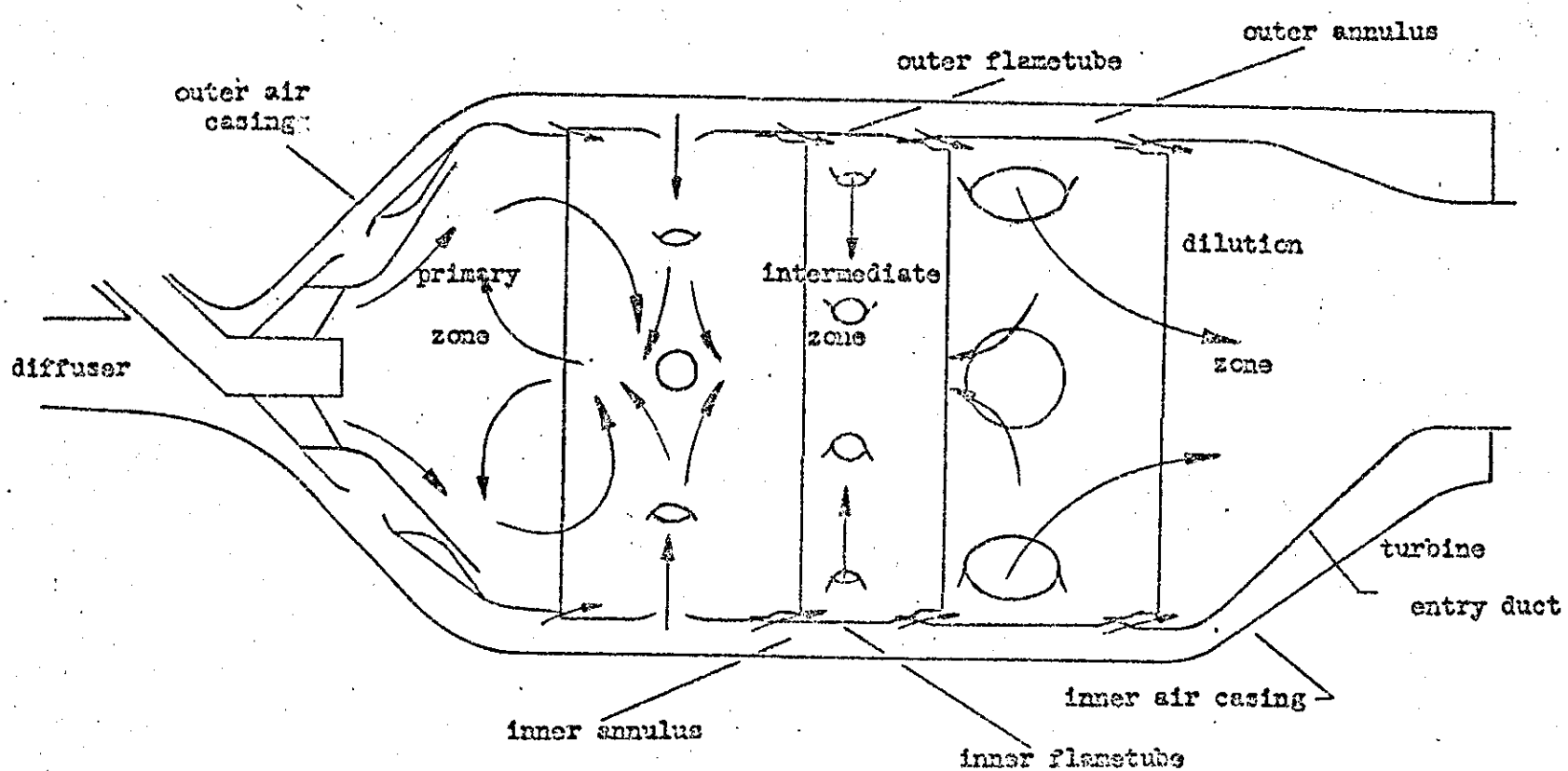

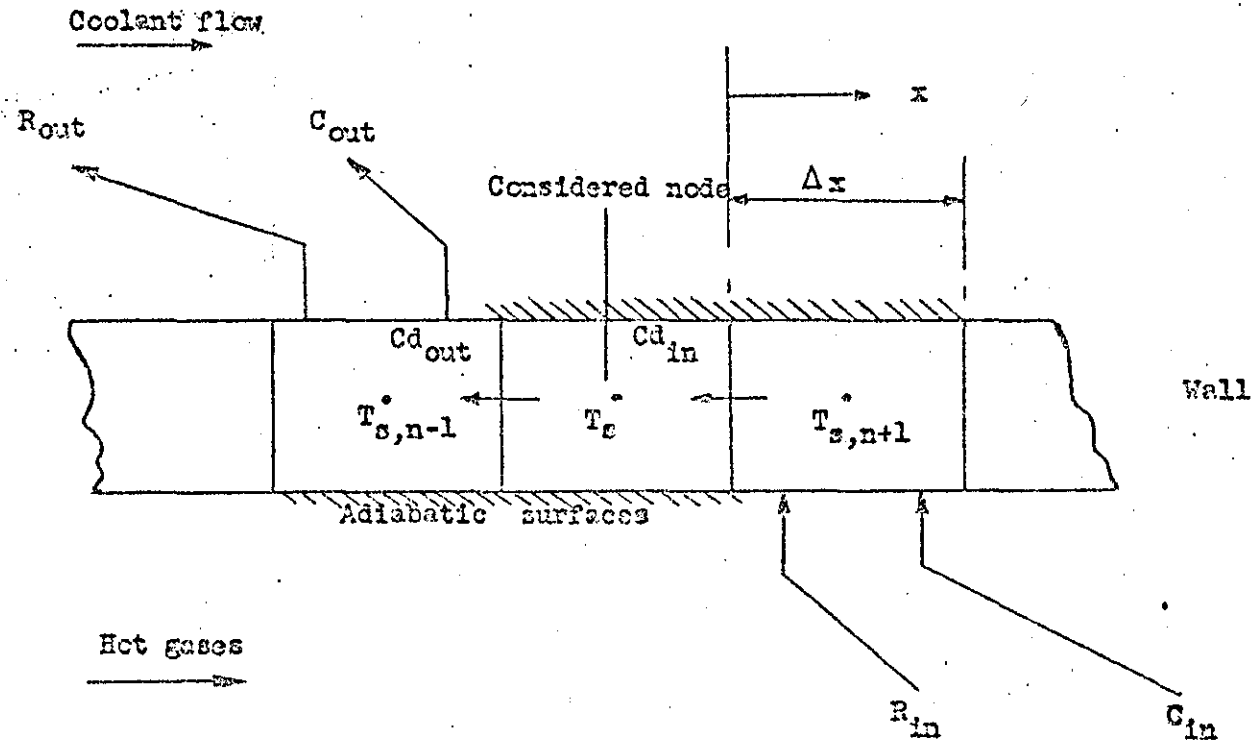

FIG. 3.2: PREFERRED PATH SUPER ELEMENT MODEL

NOT TO SCALE

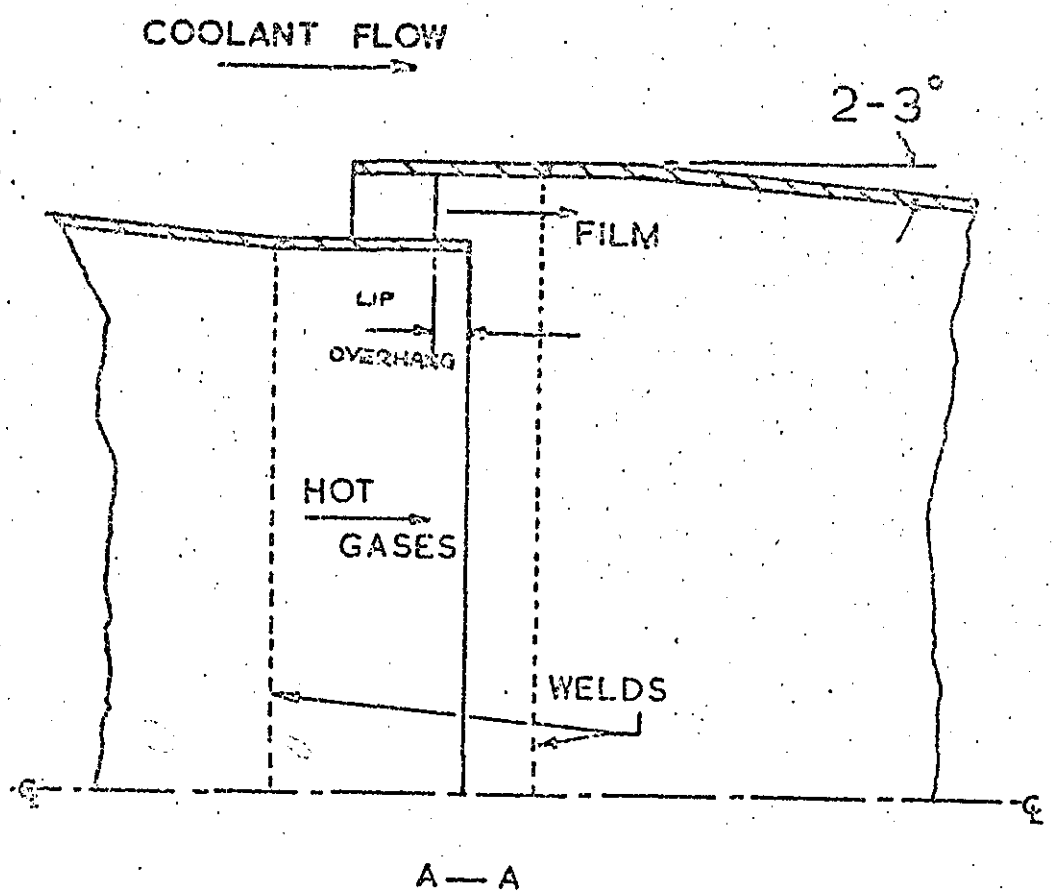

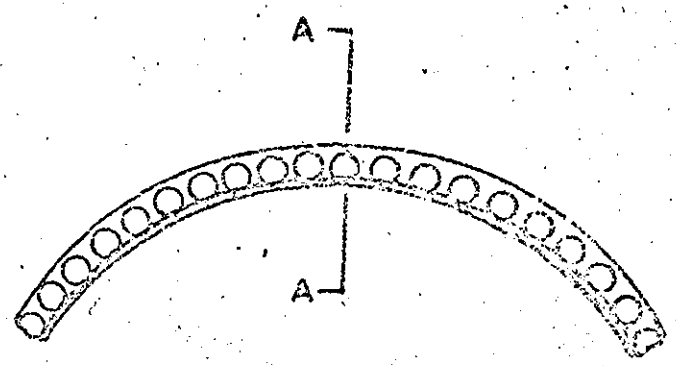

FIG. 3.3: SECTIONS THROUGH A TYPICAL MODERN PRACTICAL COOLING DEVICE IN A FLAMETUBE WALL

Not to scale

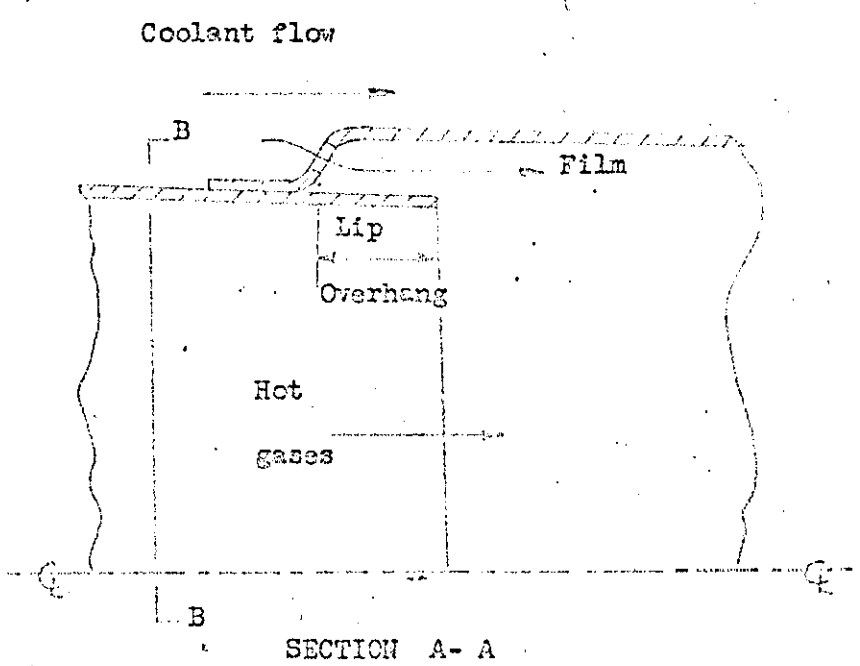

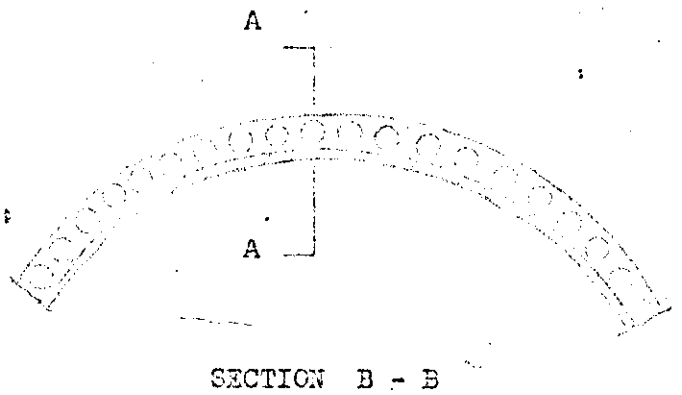

FIG. 3.4: SECTIONS THROUGH A TYPICAL STACKED RING COOLING DEVICE

These figures are reproduced from reference (77), the published version of this part of the work.

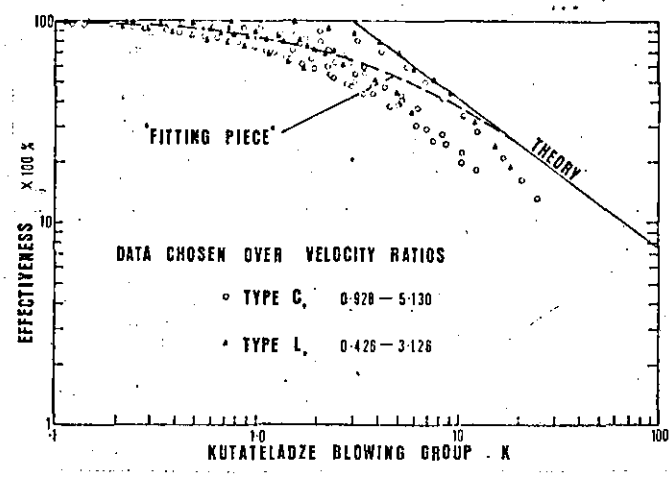

FIG. 3.5: CORRELATION AND PREDICTION OF PRACTICAL SLOTS C AND L USING THE KUTATELADZE BLOWING GROUP AND EQUATION FOR FILM EFFECTIVENESS.

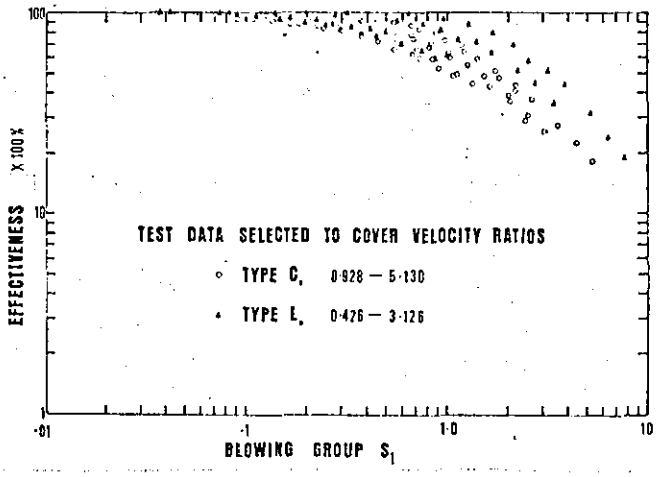

FIG. 3.10: CORRELATION OF PRACTICAL SLOTS C AND L USING THE BLOWING GROUP OF EQUATION 2.20 FOR FILM EFFECTIVENESS

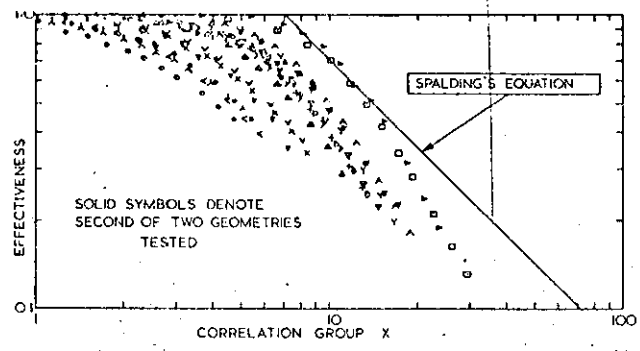

FIG. 3.6: CORRELATION OF PRACTICAL SLOT DATA USING SPALDING'S X PARAMETER AND EQUATION

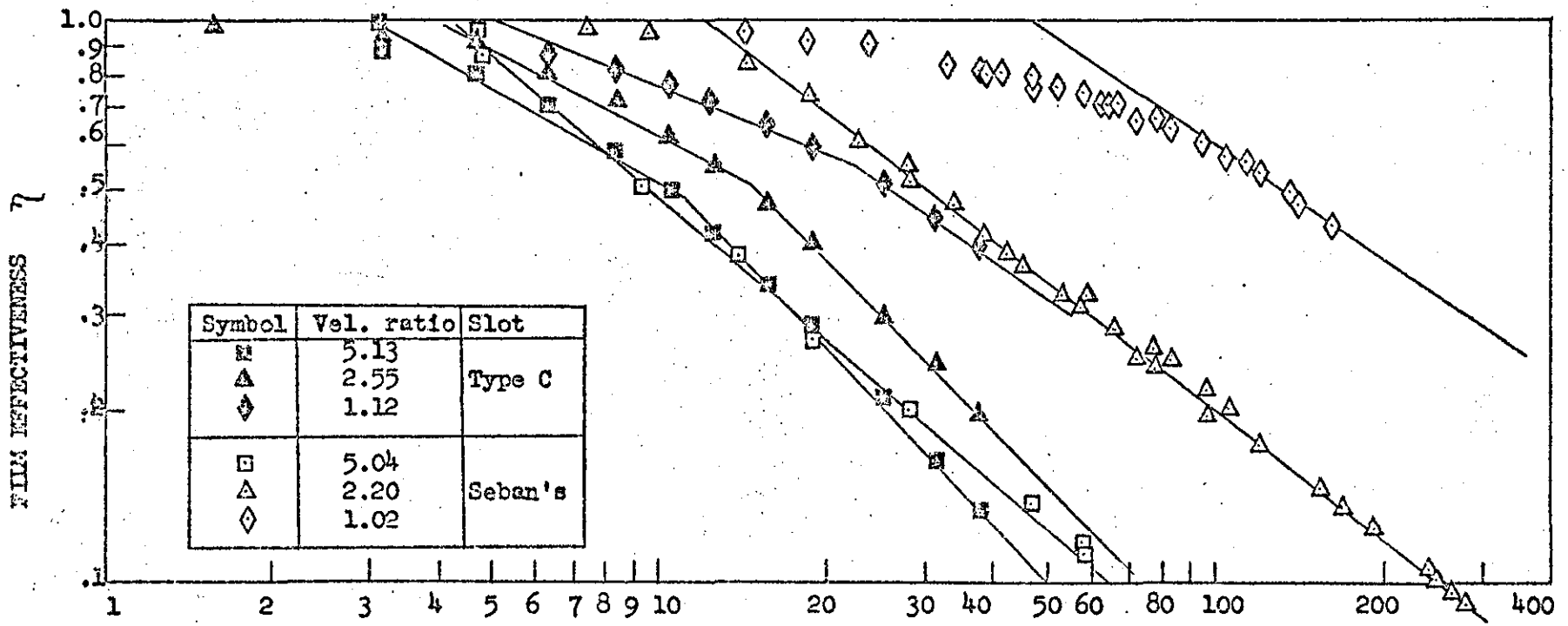

FIG. 3.7: COMPARISON OF DIRTY SLOT DATA WITH SEBAN'S CLEAN SLOT RESULTS

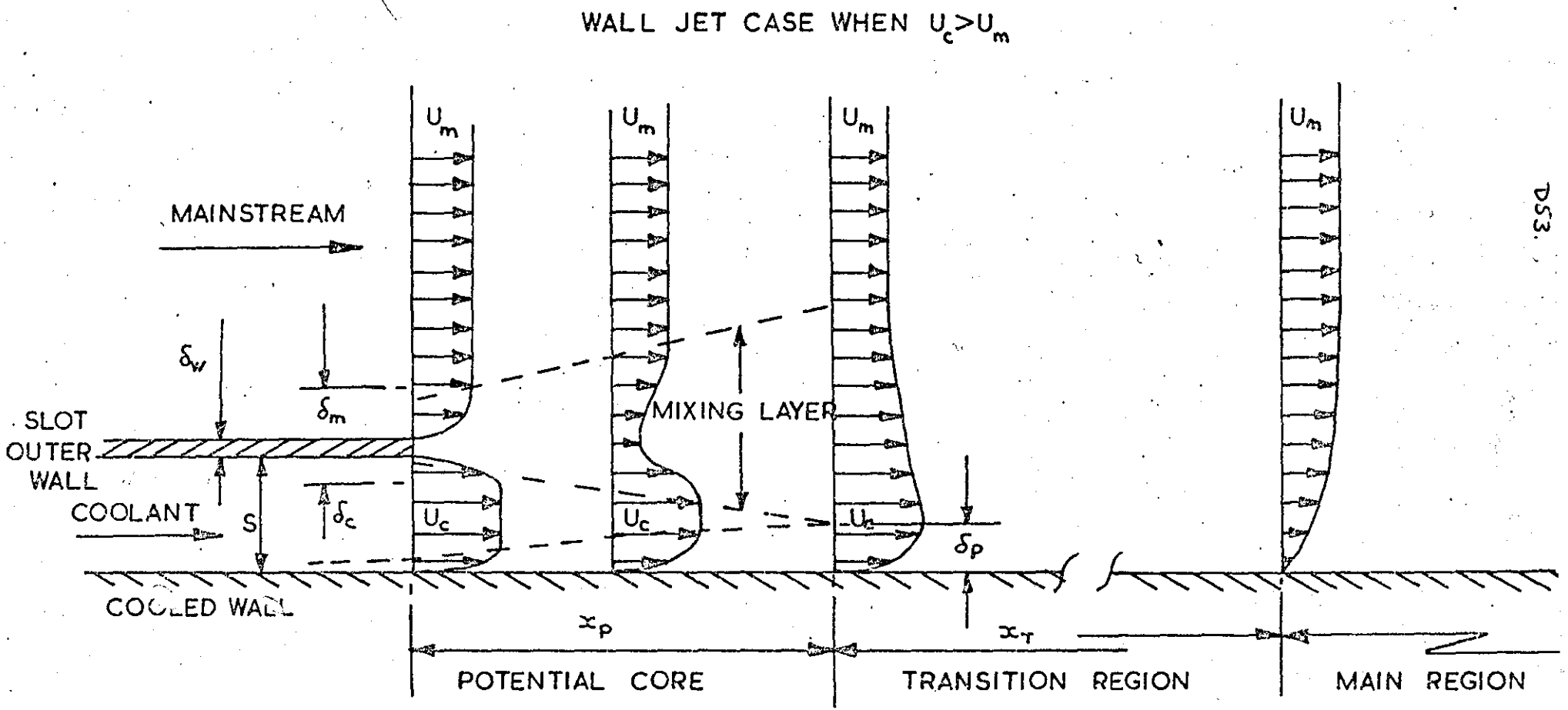

FIG. 3.8: MODEL OF INJECTED FILM HYDRODYNAMIC DEVELOPMENT

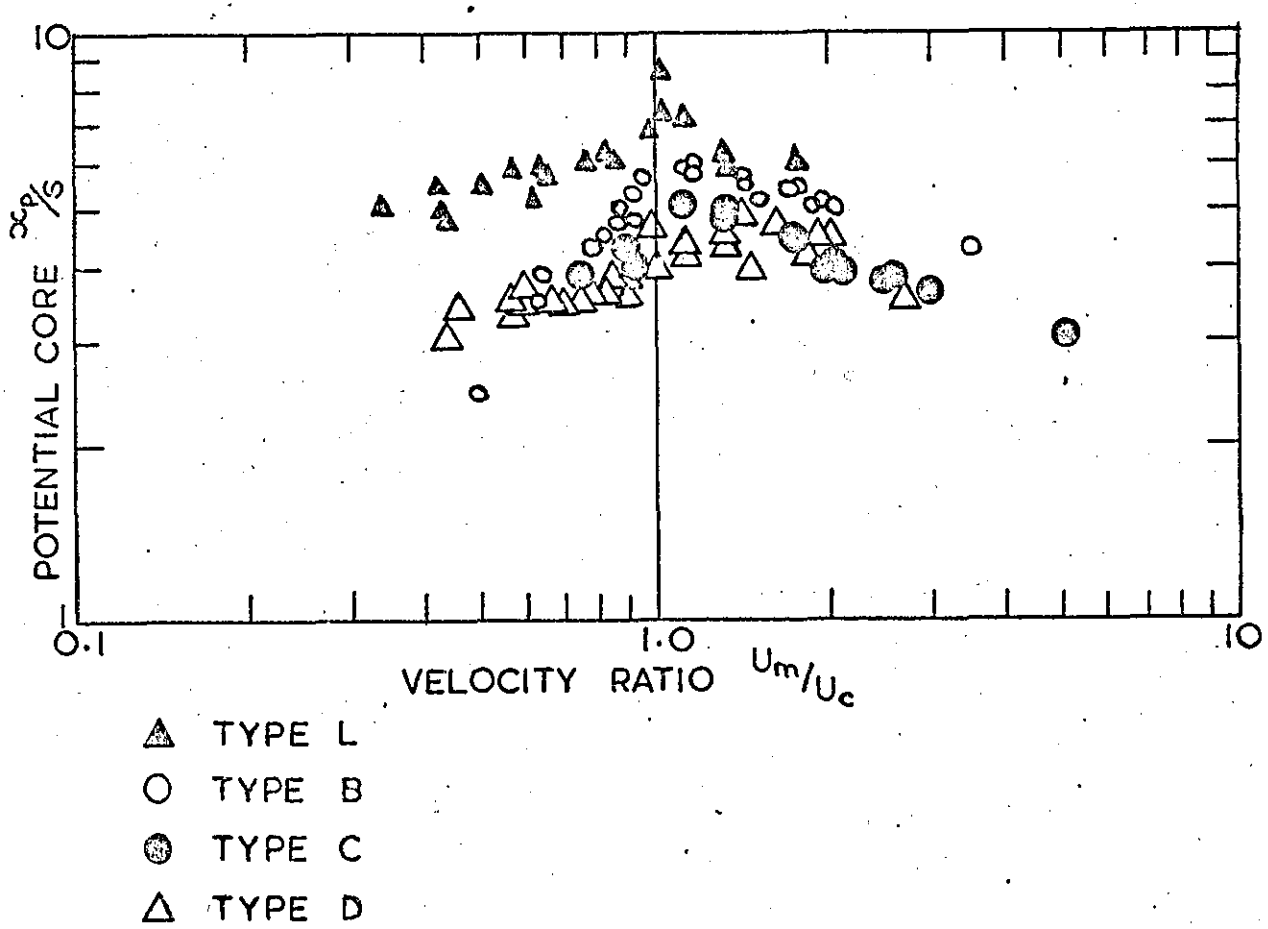

FIG. 3.9: NON-DIMENSIONAL POTENTIAL CORE LENGTH AS A FUNCTION OF VELOCITY RATIO AND GEOMETRY FOR SOME PRACTICAL SLOTS

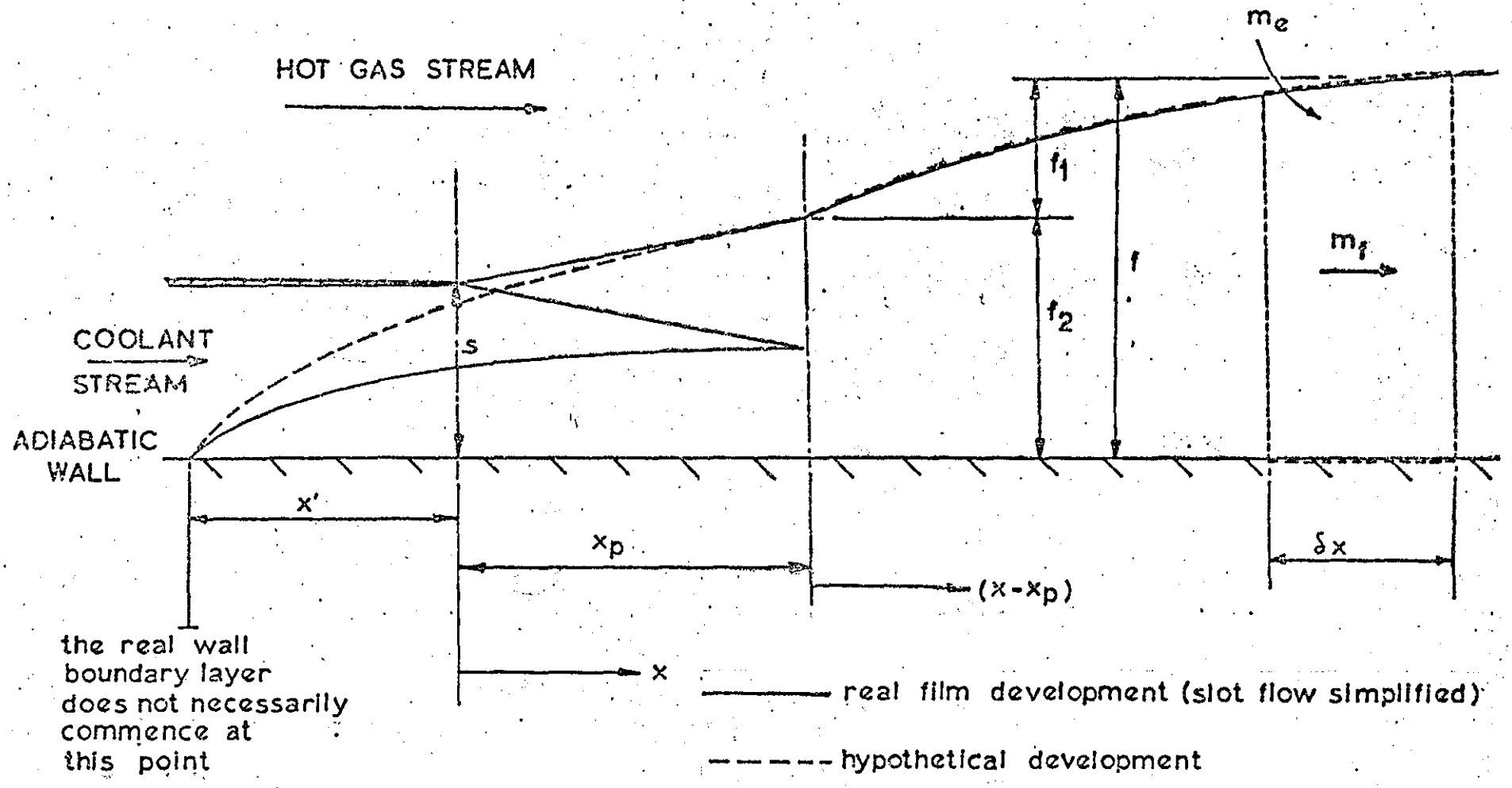

FIG. 4.1: NOMENCLATURE FOR MODEL OF DEVELOPING FILM AND ITS SIMULATION

FIG. 4.2: ASSESSMENT OF OVERALL EFFECTIVE AREA FOR STACKED RING SLOT G1

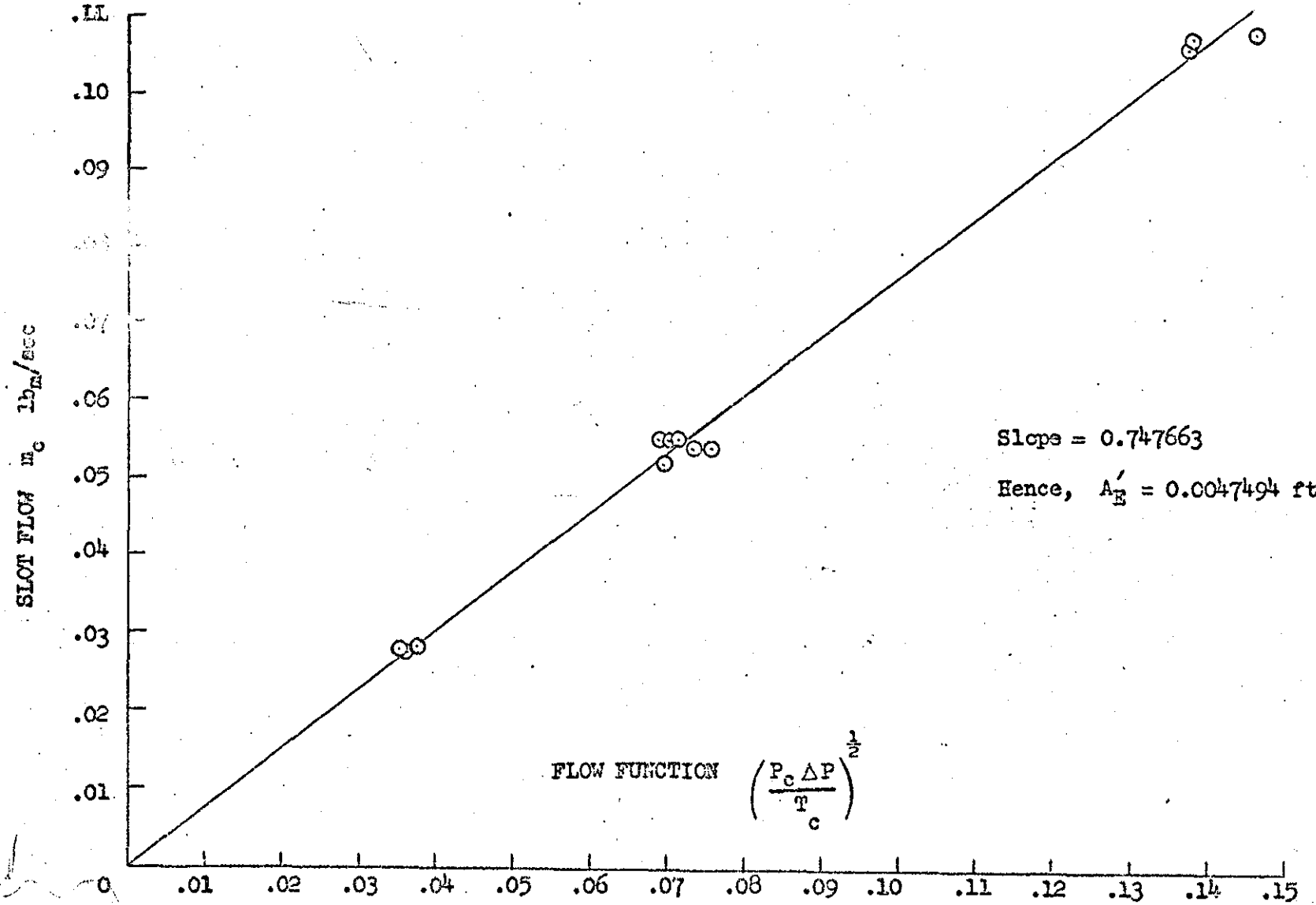

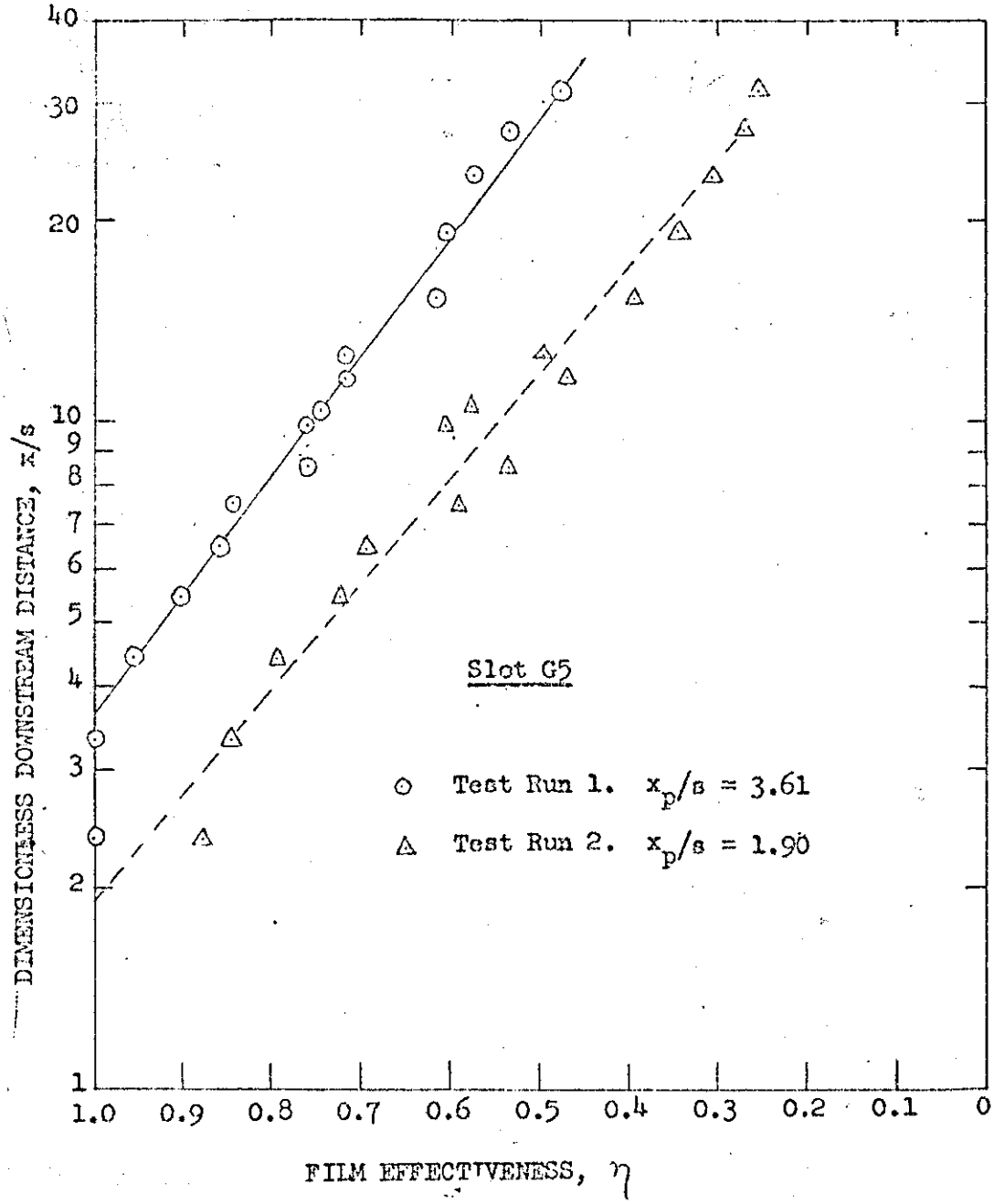

FIG. 4.3: MEASUREMENT OF THERMAL POTENTIAL CORE LENGTH

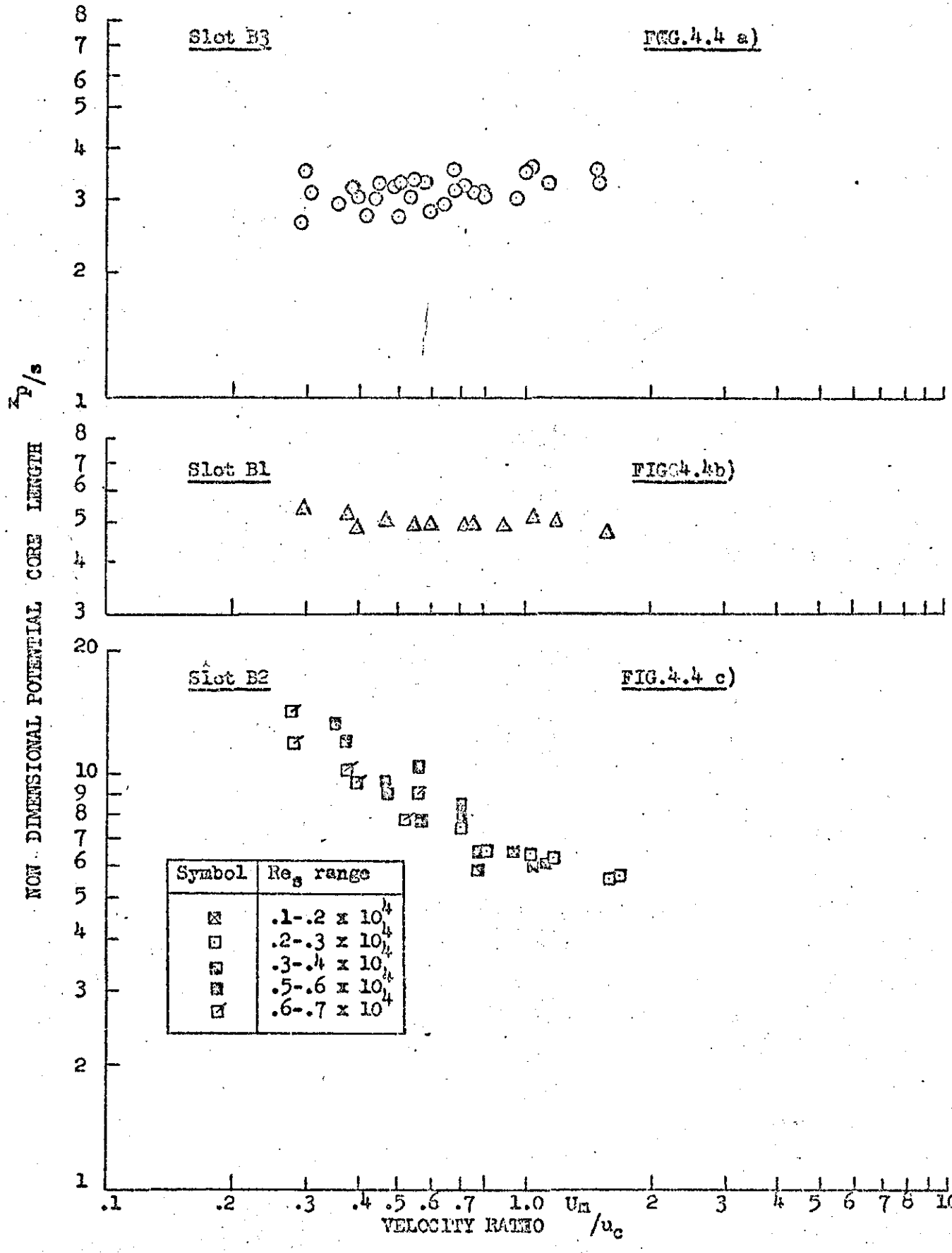
Slot B3
FIG.4.4 a)
Slot B1
FIG4.4b)
Slot B2
FIG.4.4 c)
NON DIMENSIONAL POTENTIAL CORE LENGTH $z_{p/s}$
VELOCITY RATIO U_m/u_c
Symbol
Re_s range
.1-.2 x 10^4
.2-.3 x 10^4
.3-.4 x 10^4
.5-.6 x 10^4
.6-.7 x 10^4

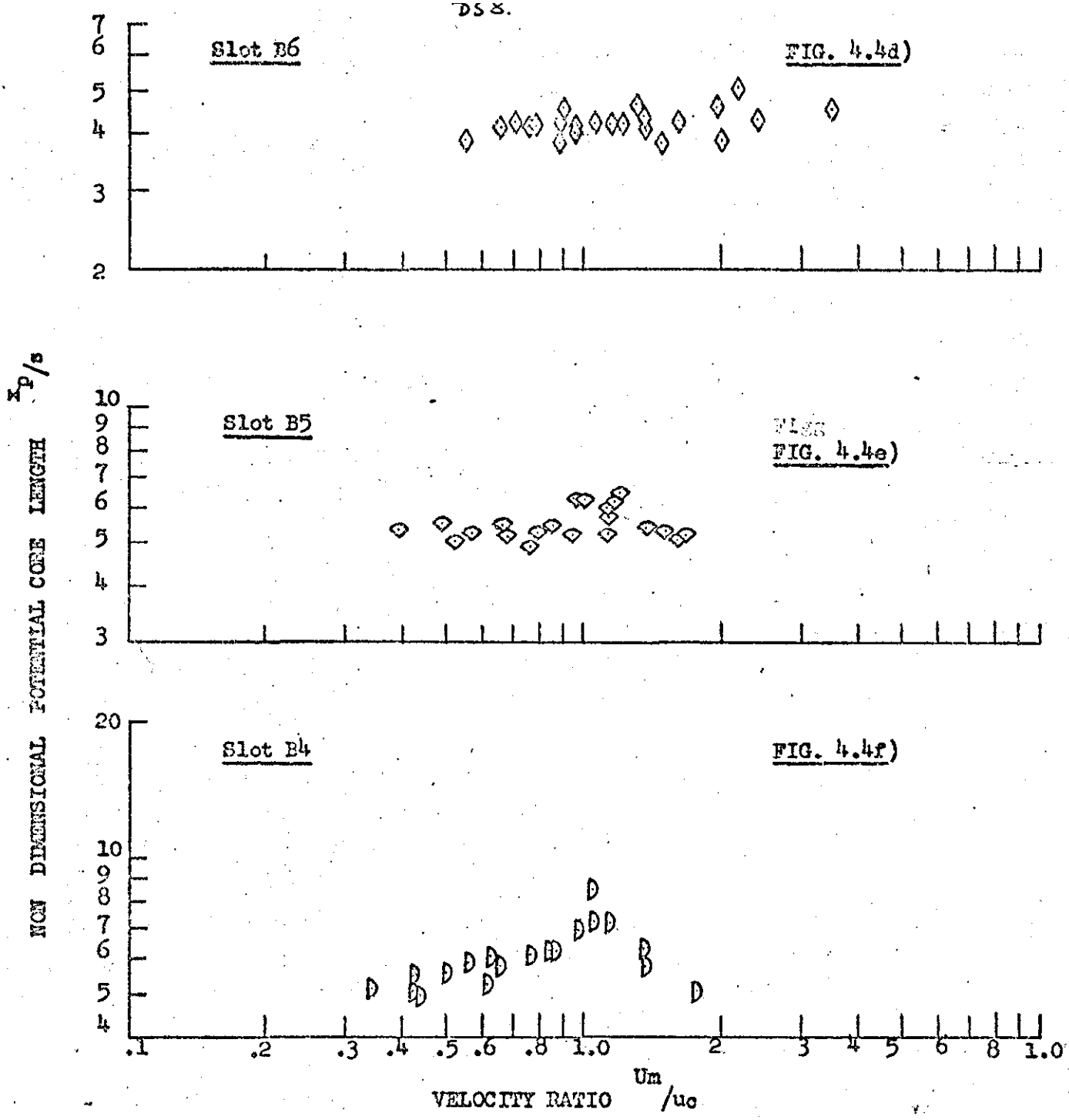

FIG. 4.4: MEASURED THERMAL POTENTIAL CORES FOR SOME MACHINED PRACTICAL GEOMETRIES

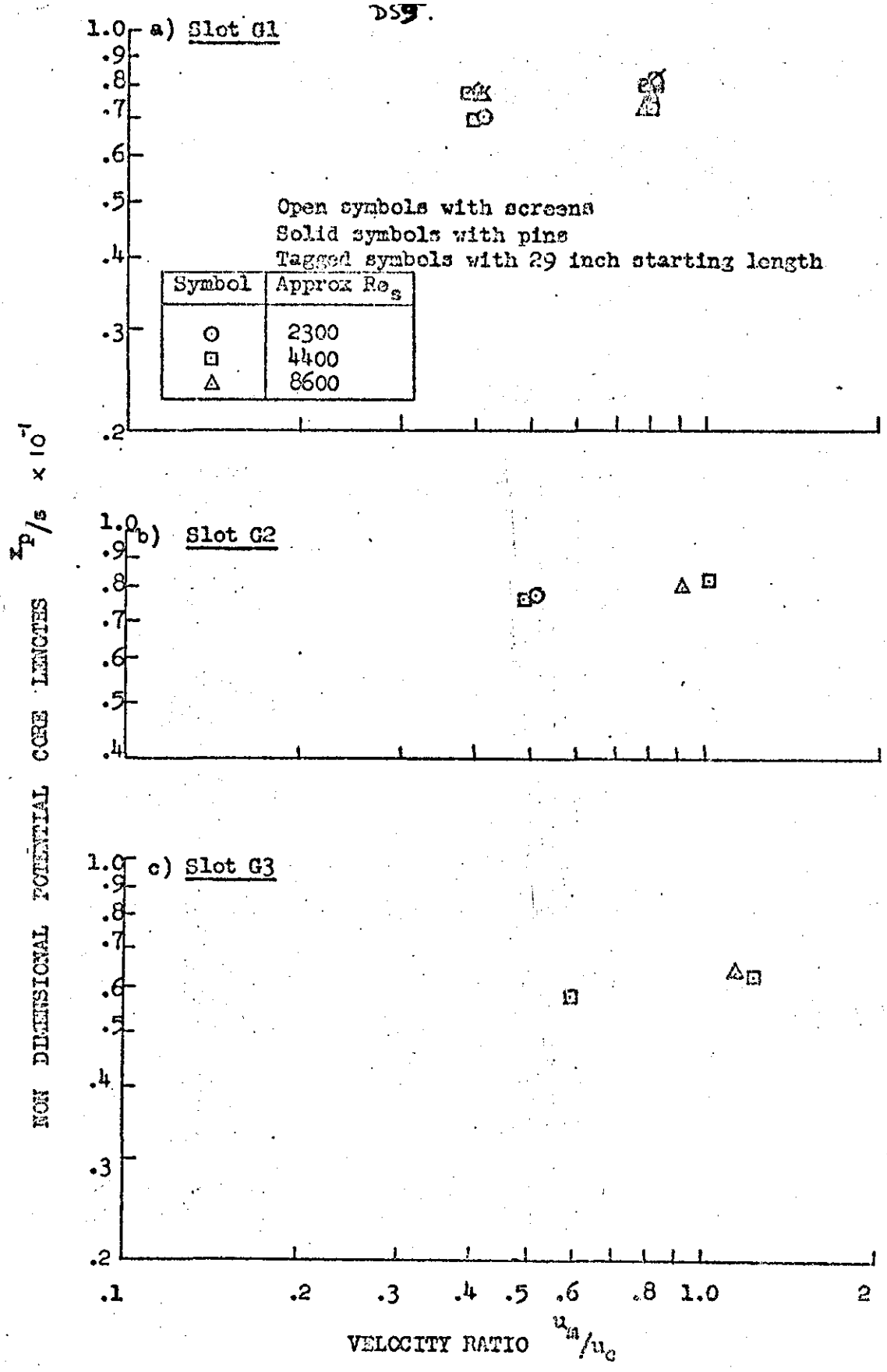

FIG. 4.5: MEASURED THERMAL POTENTIAL CORES FOR SOME STACKED RING SLOTS

FIG. 4.6 a): CORRELATED DATA FOR MACHINED SLOT BL-

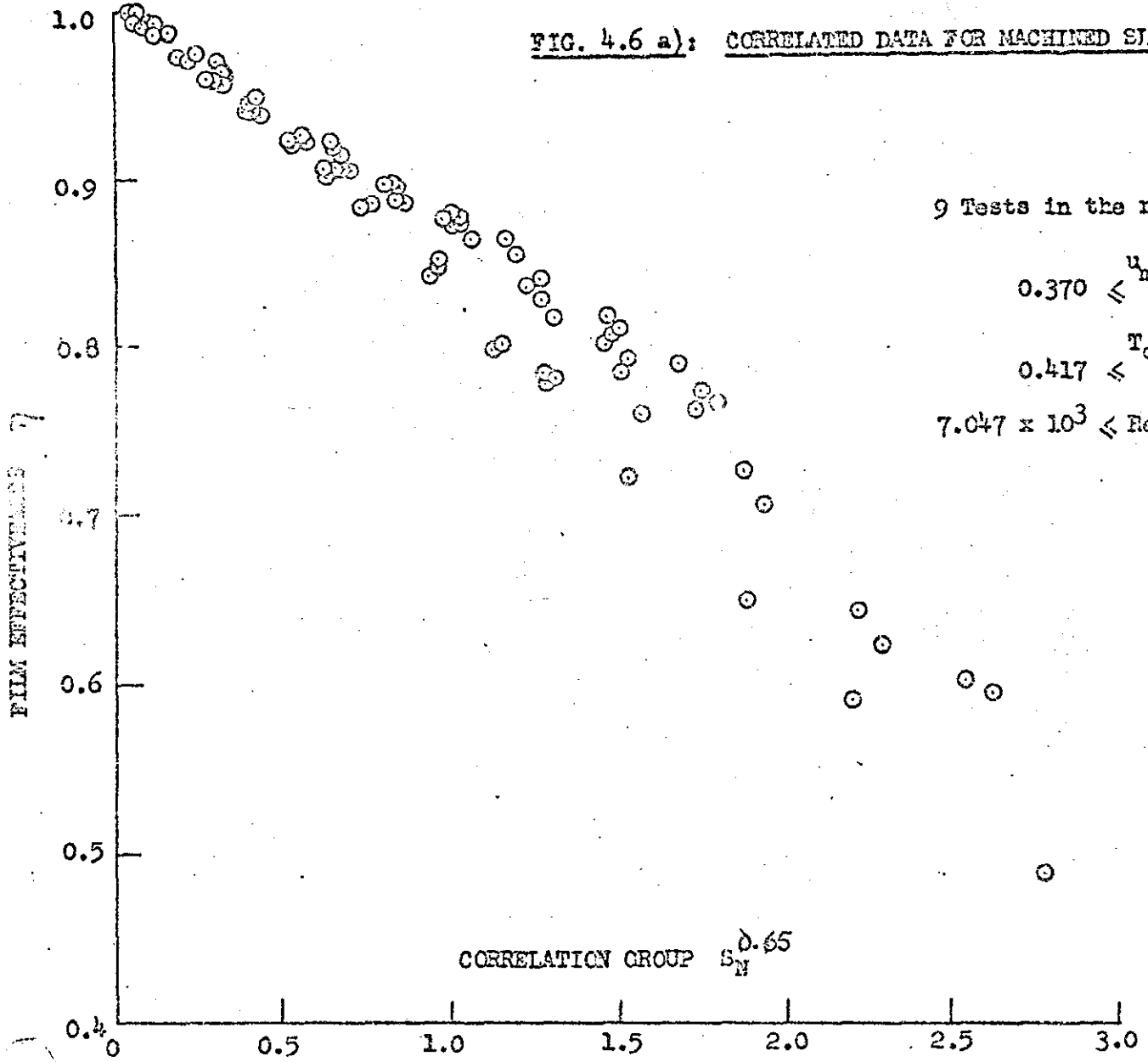

9 Tests in the ranges:

$$0.370 \leqslant {}^{u_m}/_{u_c} \leqslant 1.573$$

$$0.417 \leqslant {}^{T_c}/_{T_m} \leqslant 0.456$$

$$7.047 \times 10^3 \leqslant Re_s \leqslant 23.69 \times 10^3$$

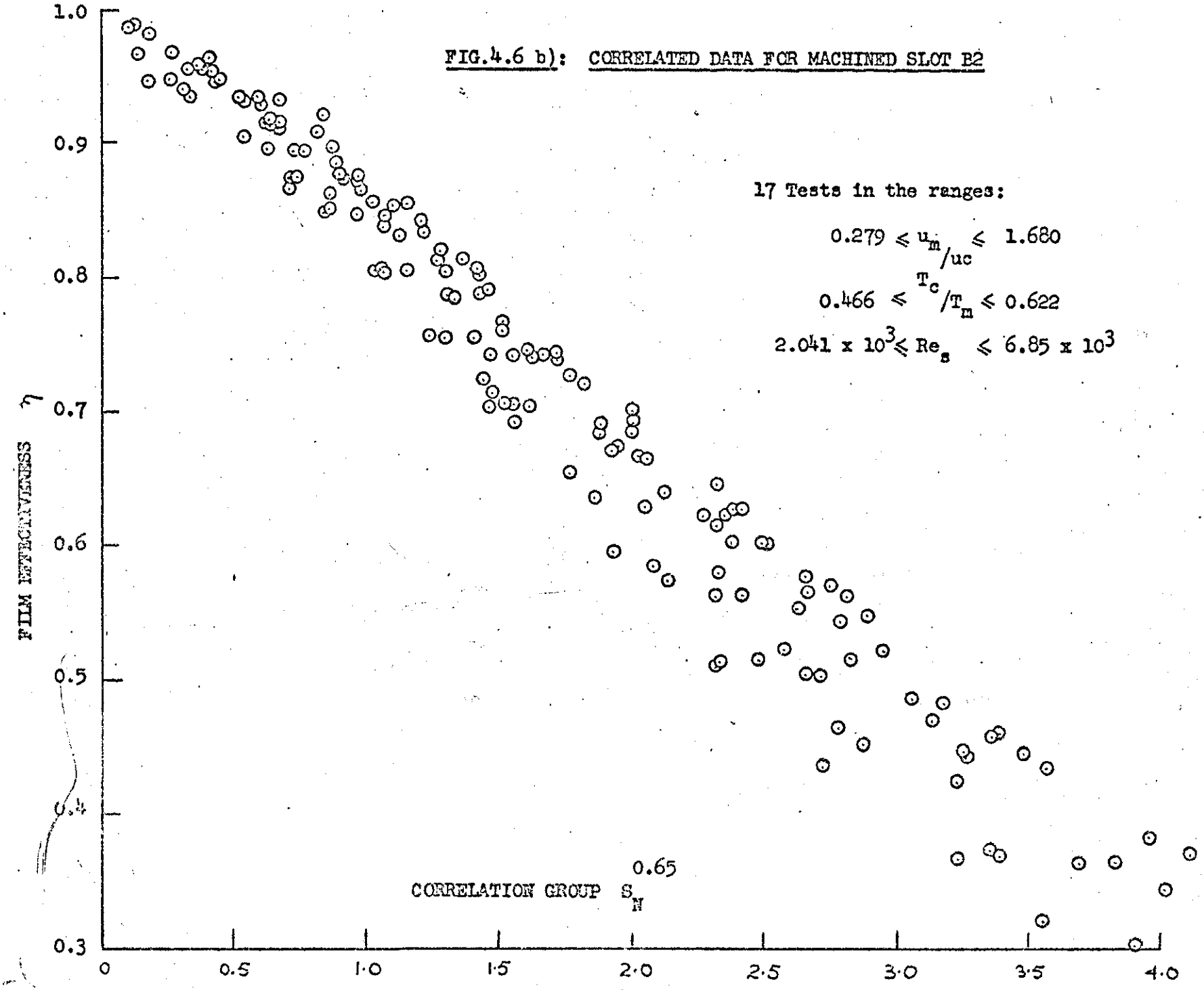
FIG.4.6 b): CORRELATED DATA FOR MACHINED SLOT B2
17 Tests in the ranges:
$0.279 \leqslant u_m/uc \leqslant 1.680$
$0.466 \leqslant T_c/T_m \leqslant 0.622$
$2.041 \times 10^3 \leqslant Re_s \leqslant 6.85 \times 10^3$
FILM EFFECTIVENESS η
CORRELATION GROUP $S_N^{0.65}$
1.0
0.9
0.8
0.7
0.6
0.5
0.4
0.3
0
0.5
1.0
1.5
2.0
2.5
3.0
3.5
4.0

FIG. 4.6 c): CORRELATED DATA FOR MACHINED SLOT B3

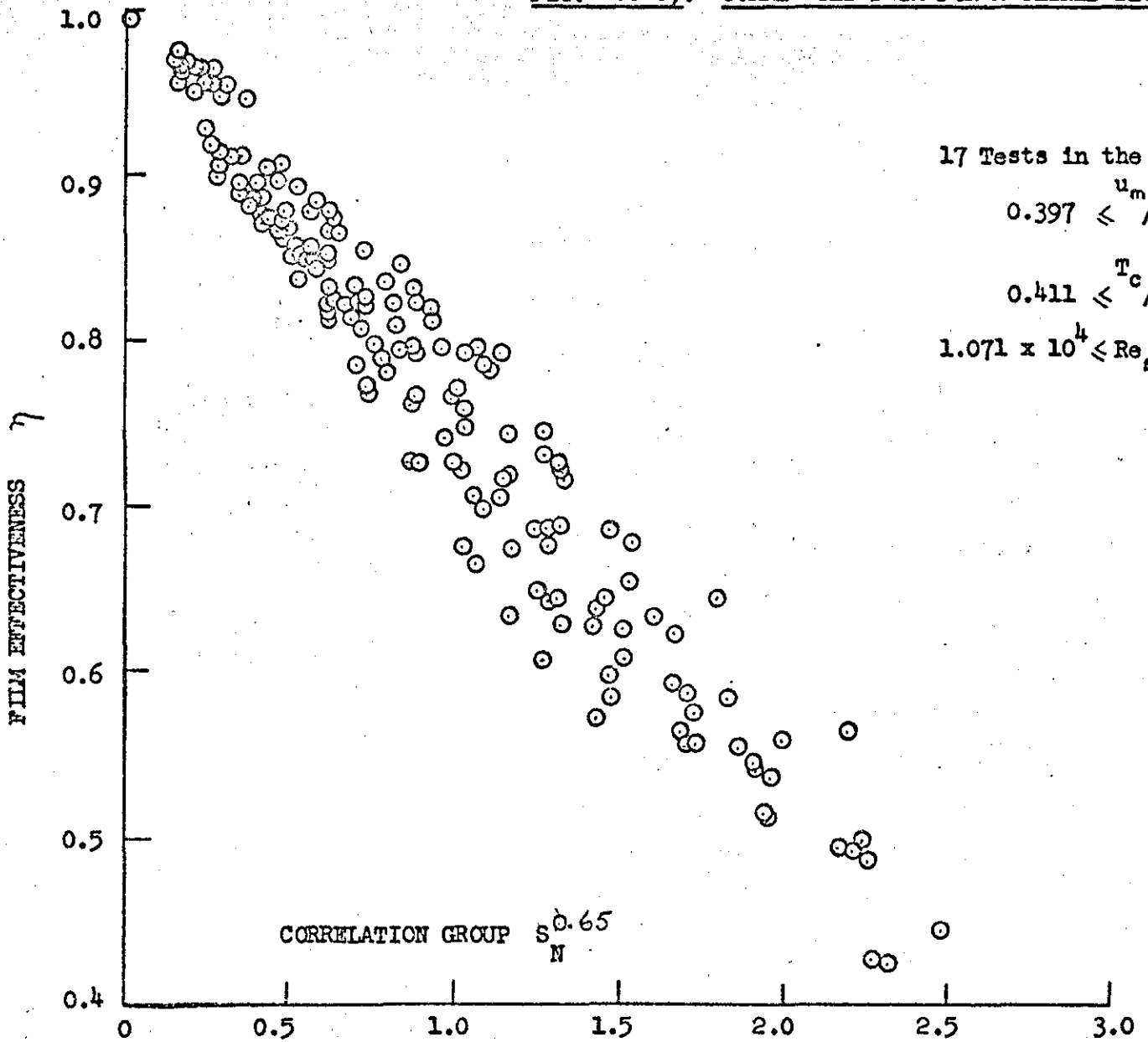

17 Tests in the ranges:

$0.397 \leqslant {}^{u_m}/_{u_c} \leqslant 1.499$

$0.411 \leqslant {}^{T_c}/_{T_m} \leqslant 0.454$

$1.071 \times 10^4 \leqslant Re_s \leqslant 3.638 \times 10^4$

FIG. 4.6 d): CORRELATED DATA FOR MACHINED SLOT B4

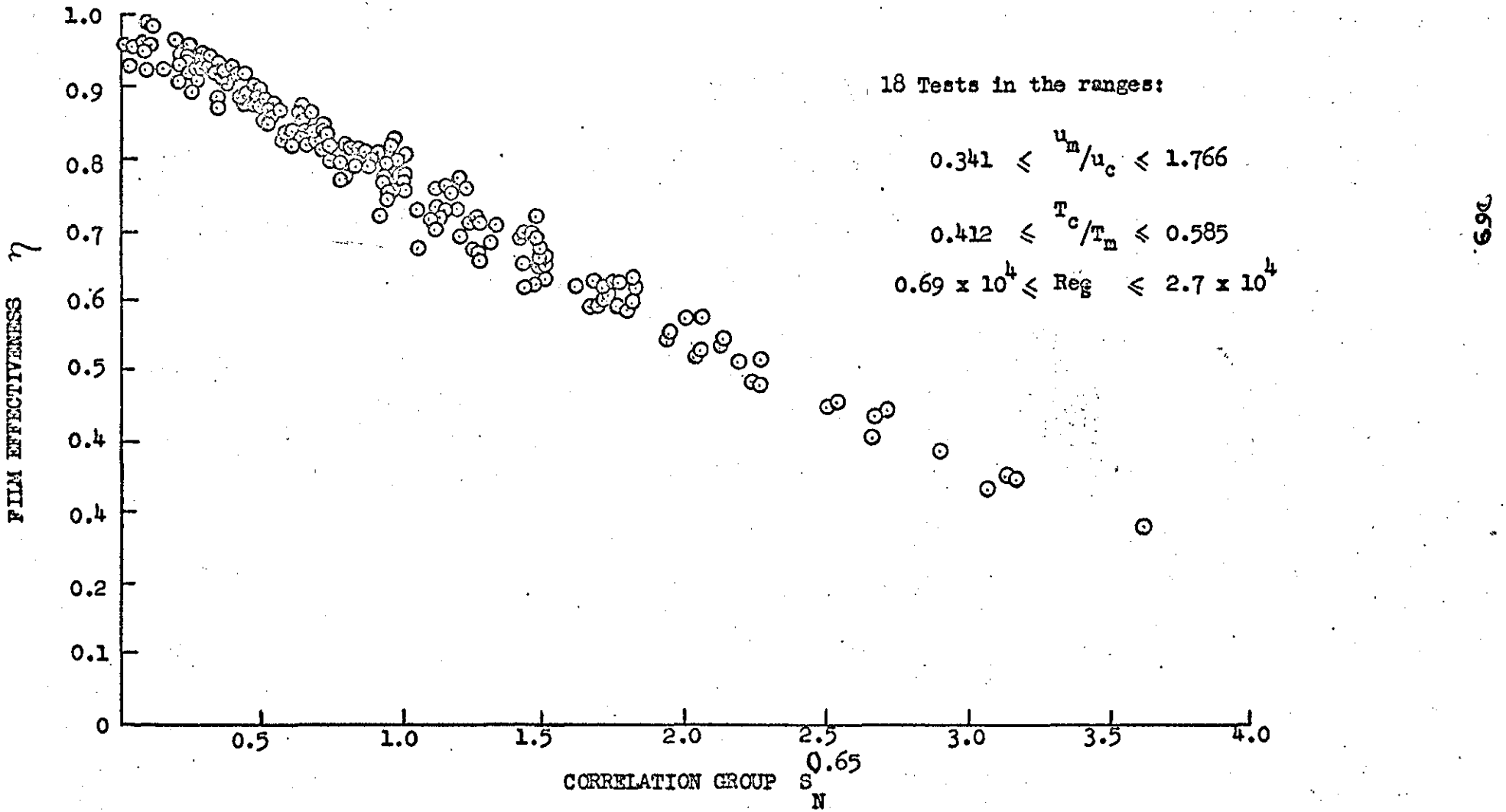

69c

FIG. 4.6 e): CORRELATED DATA FOR MACHINED SLOT B5

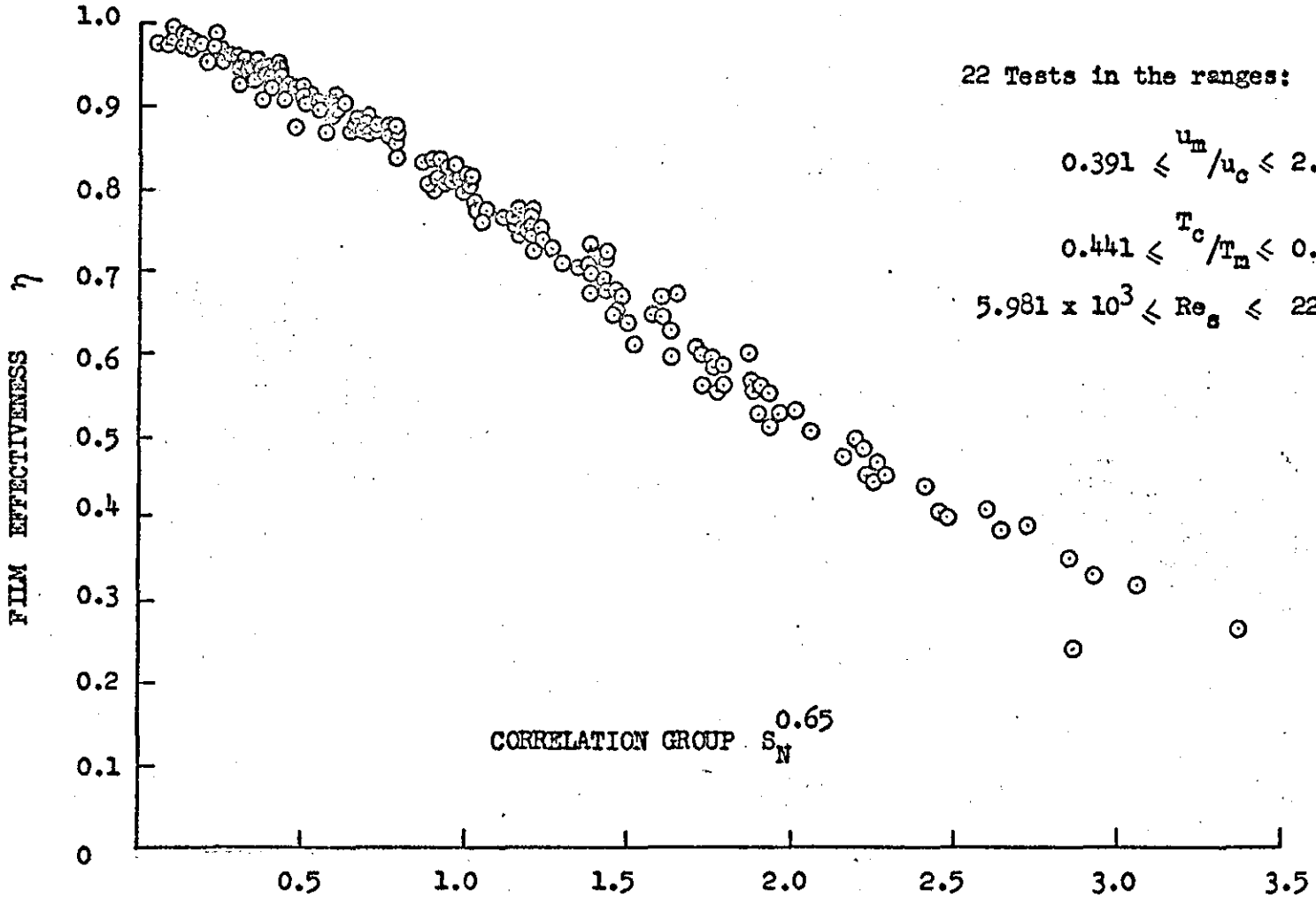

FIG. 4.6 f): CORRELATED DATA FOR MACHINED SLOT $B6_T$

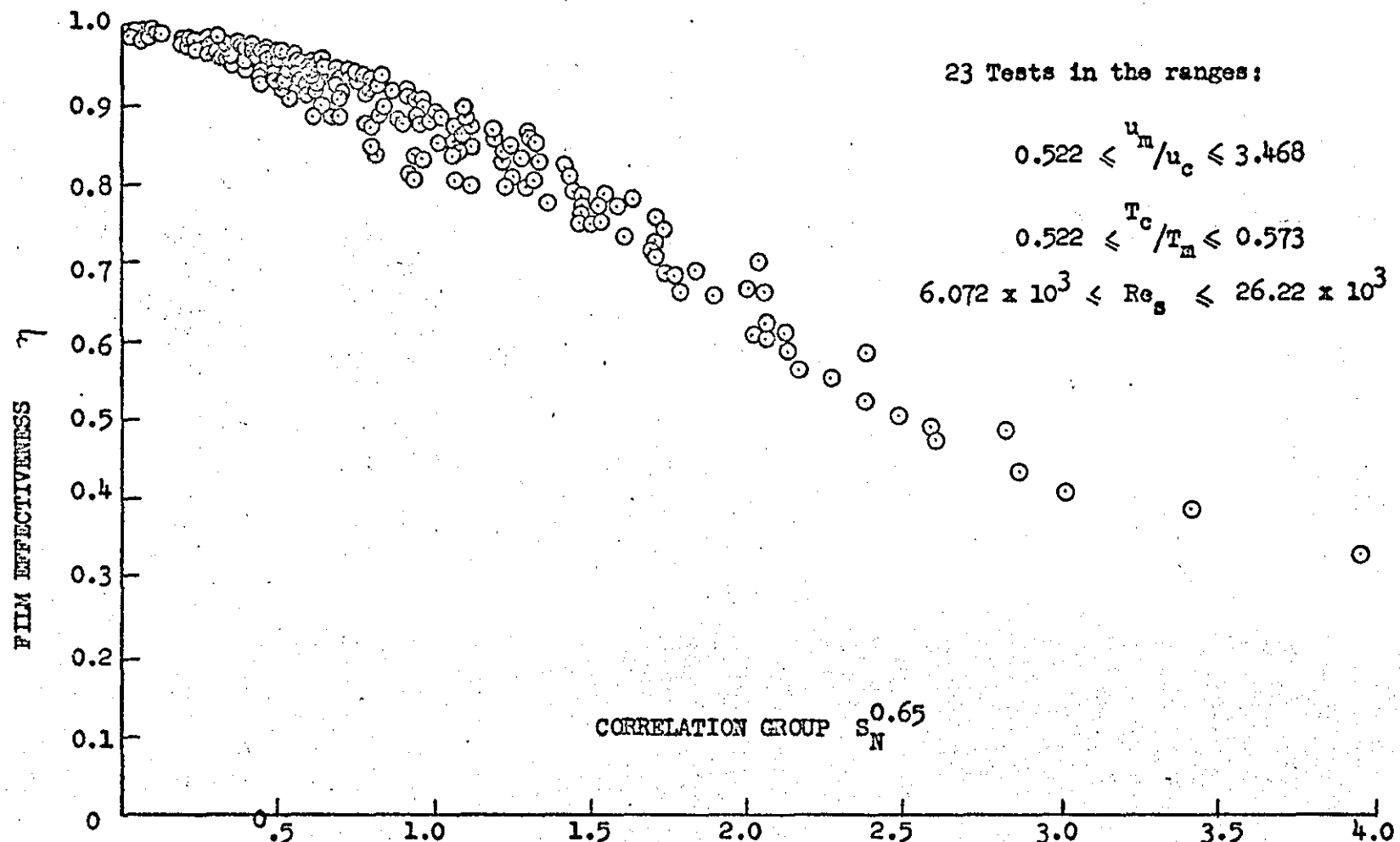

FIG. 4.7 a): CORRELATED DATA FOR STACKED RING SLOT G1

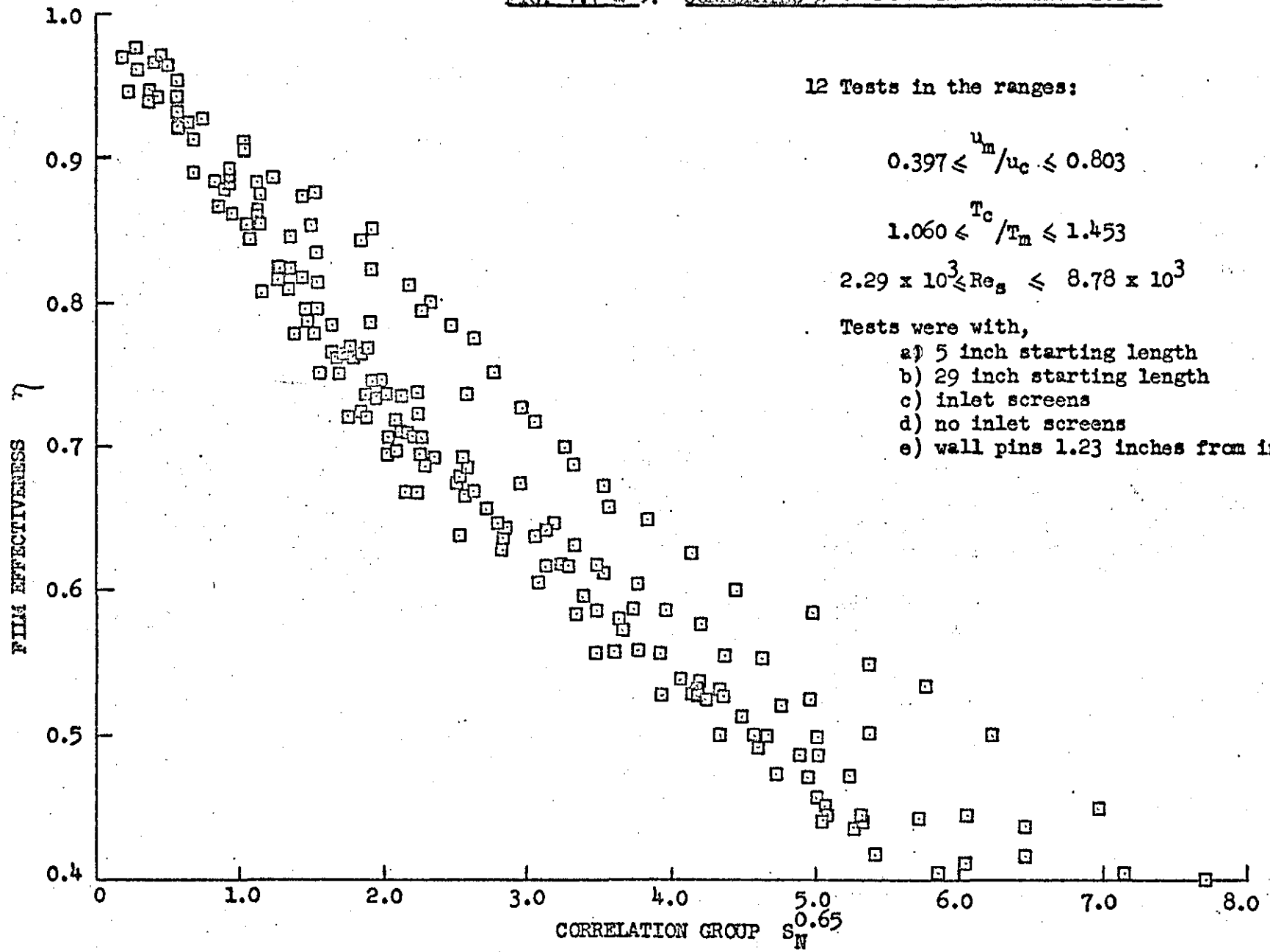

12 Tests in the ranges:

$$0.397 \leq {}^{u_m}/_{u_c} \leq 0.803$$

$$1.060 \leq {}^{T_c}/_{T_m} \leq 1.453$$

$$2.29 \times 10^3 \leq Re_s \leq 8.78 \times 10^3$$

Tests were with,

a) 5 inch starting length
b) 29 inch starting length
c) inlet screens
d) no inlet screens
e) wall pins 1.23 inches from injection

FIG. 4.7 b): CORRELATED DATA FOR STACKED RING GEOMETRY G2

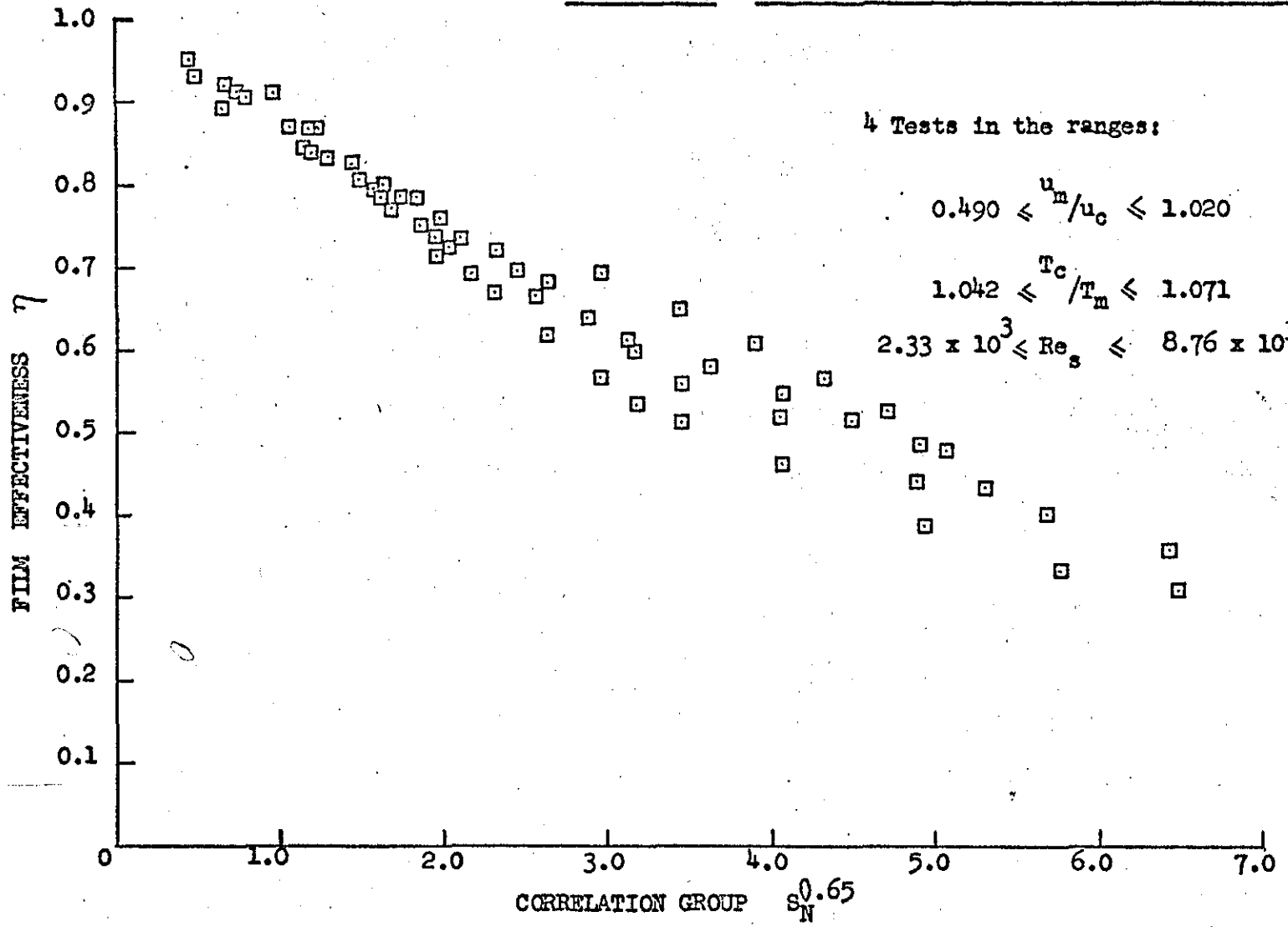

FIG. 4.7 a): CORRELATED DATA FOR STACKED RING SLOT G3

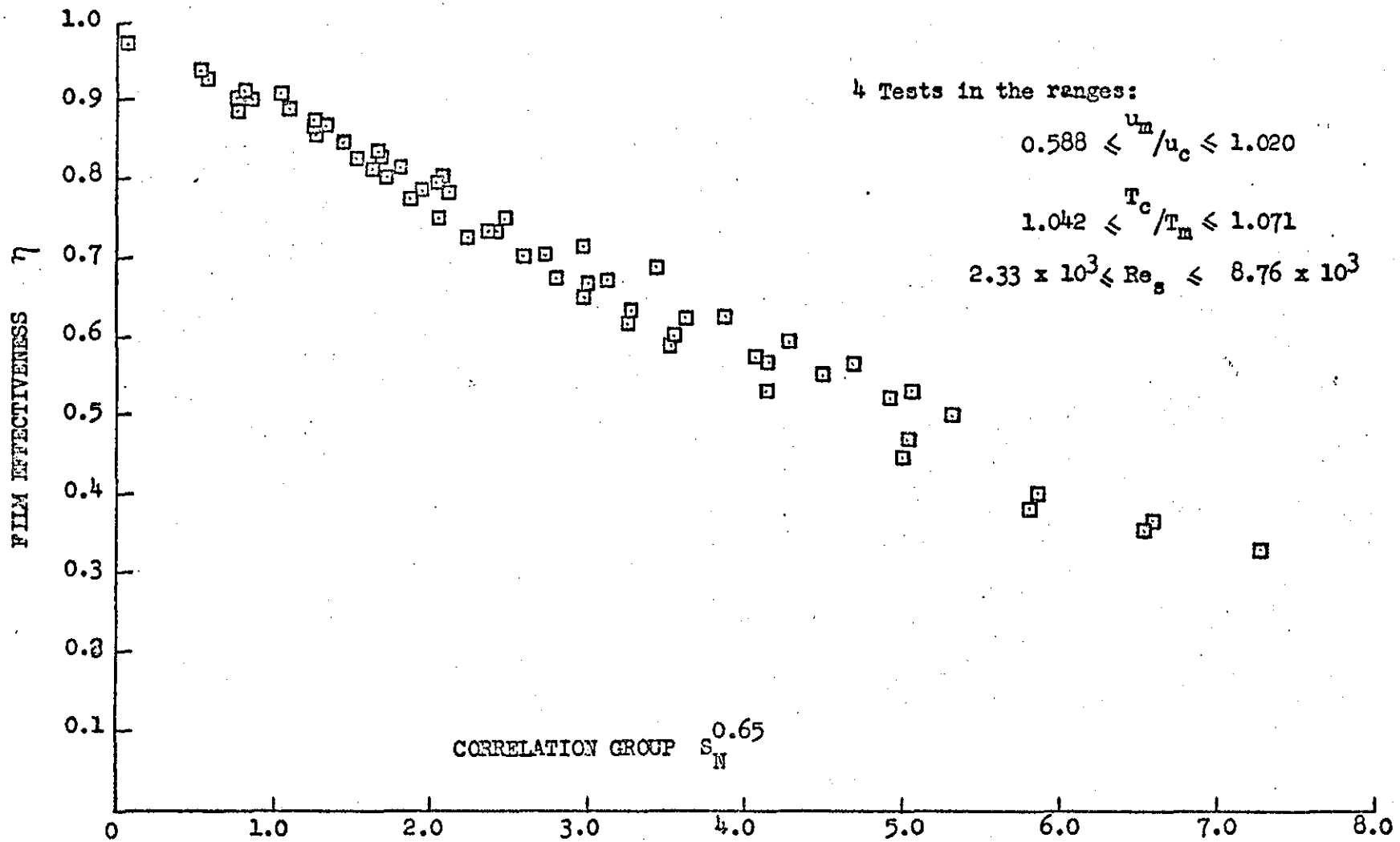

FIG. 4.8: SLOPES OF ALL STACKED RING DATA LINEARIZED BY THE S_{N2} CORRELATION GROUP

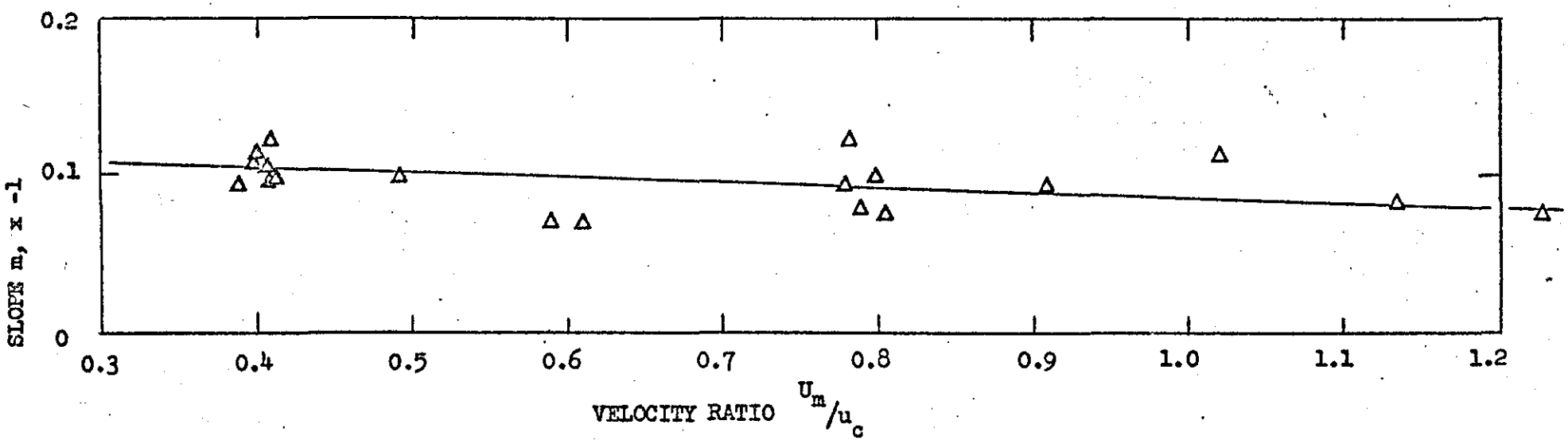

FIG. 4.9: CORRELATION OF CLEAN SLOT DATA USING THE S_N CORRELATION GROUP

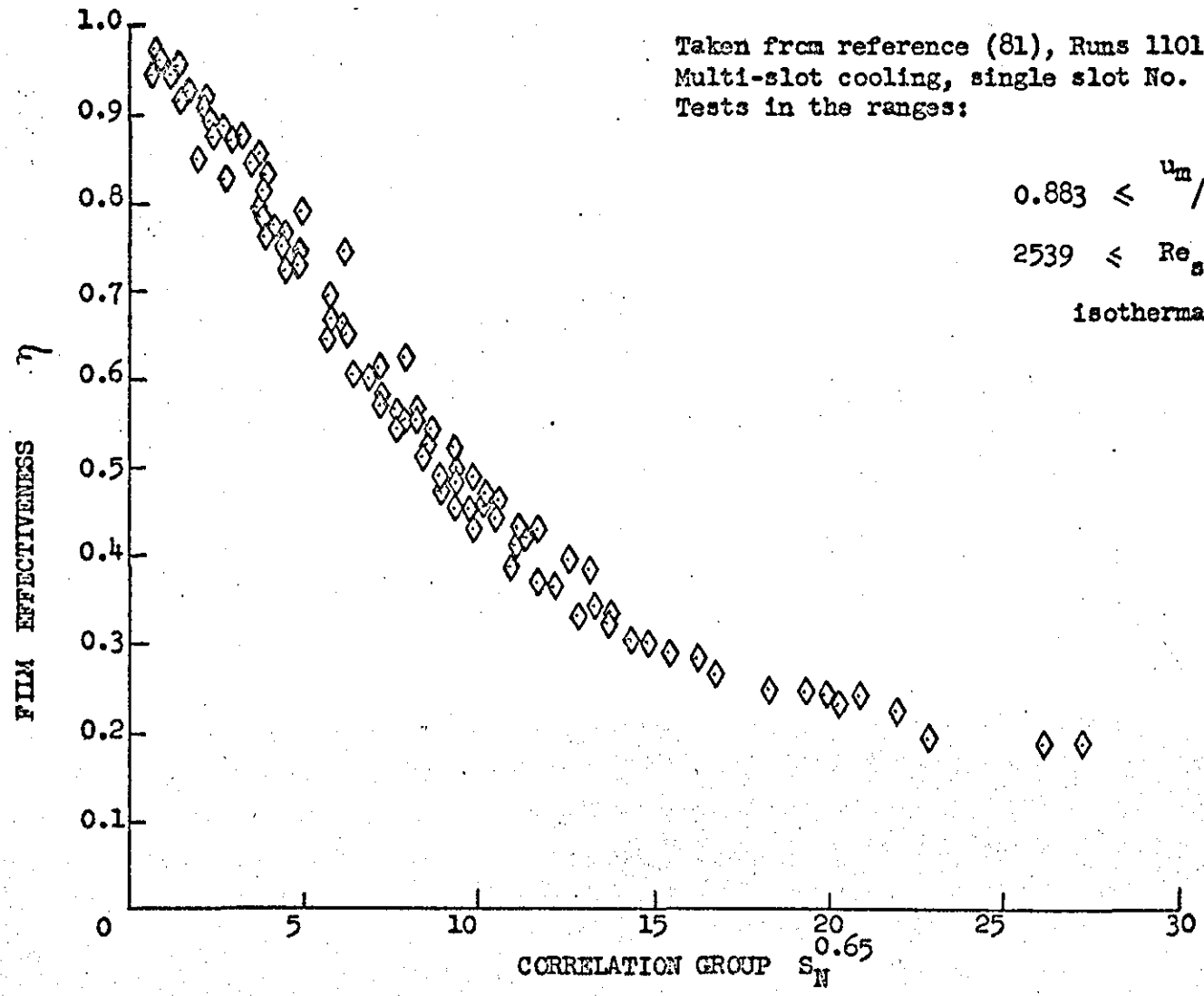

FIG. 4.10: UNIVERSAL CORRELATION OF ALL MACHINED CONSTRUCTION SLOT GEOMETRIES

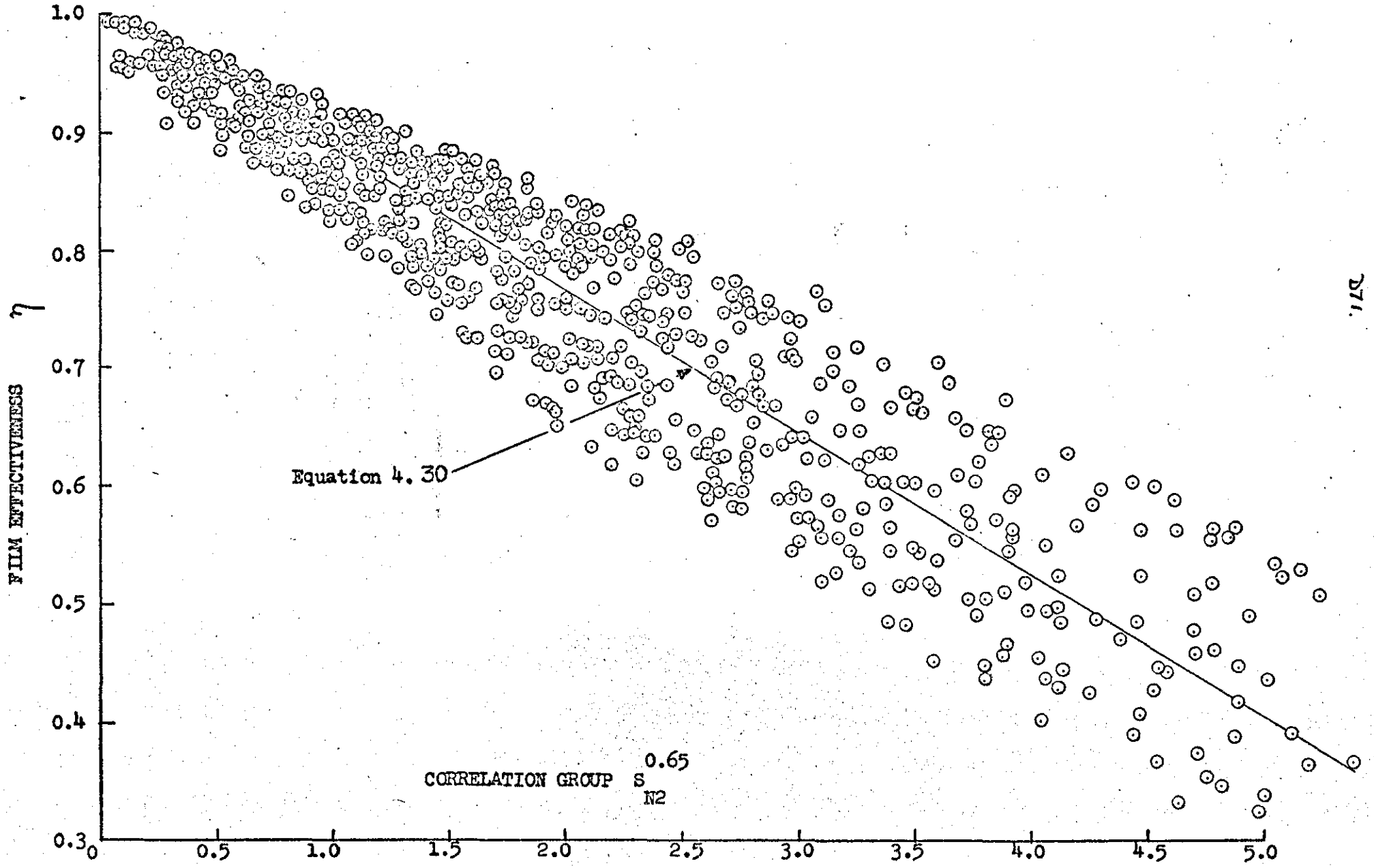

FIG. 4.11: UNIVERSAL CORRELATION OF ALL STACKED RING GEOMETRY SLOTS

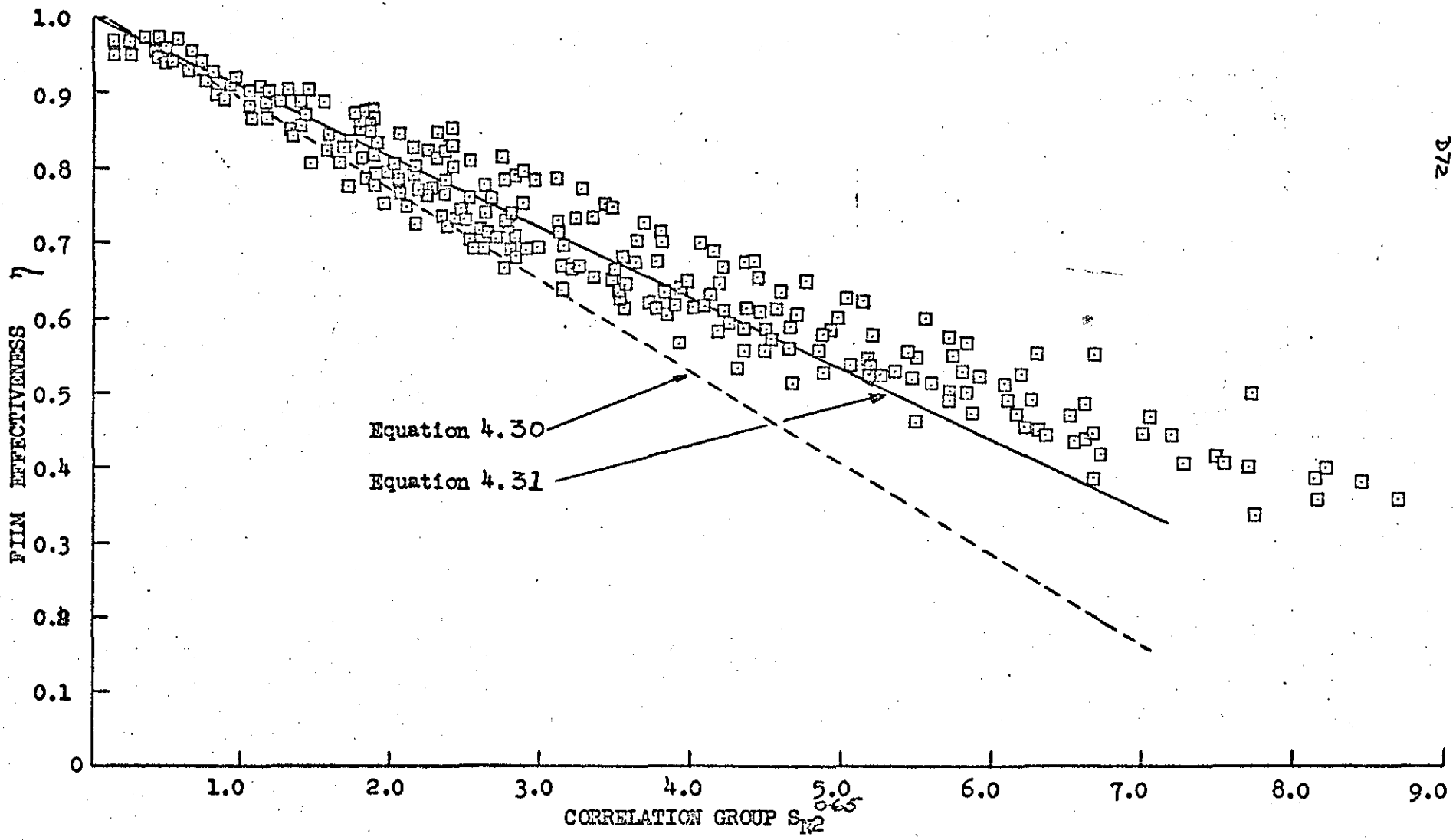

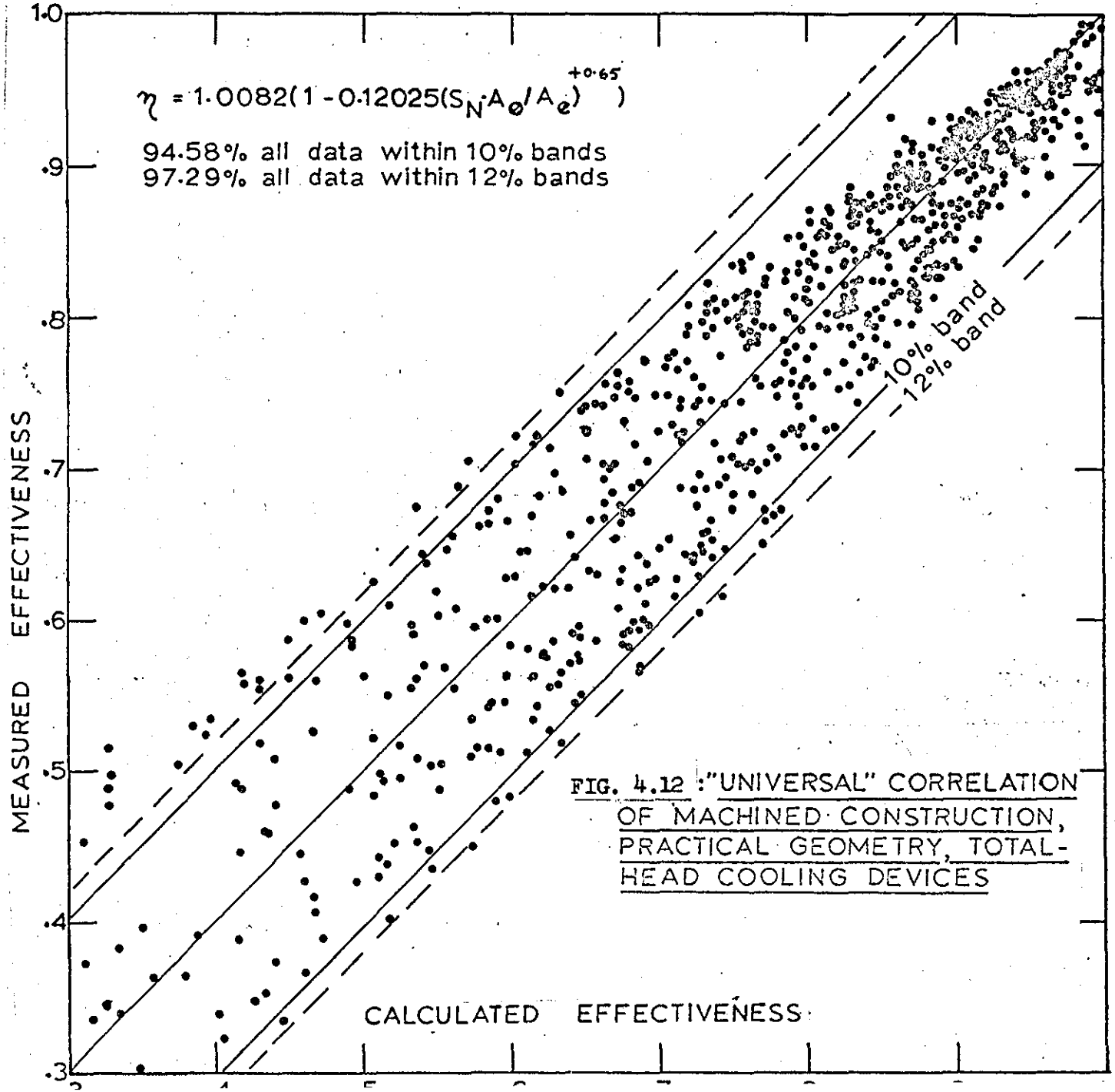

FIG. 4.12 :"UNIVERSAL" CORRELATION OF MACHINED CONSTRUCTION, PRACTICAL GEOMETRY, TOTAL-HEAD COOLING DEVICES

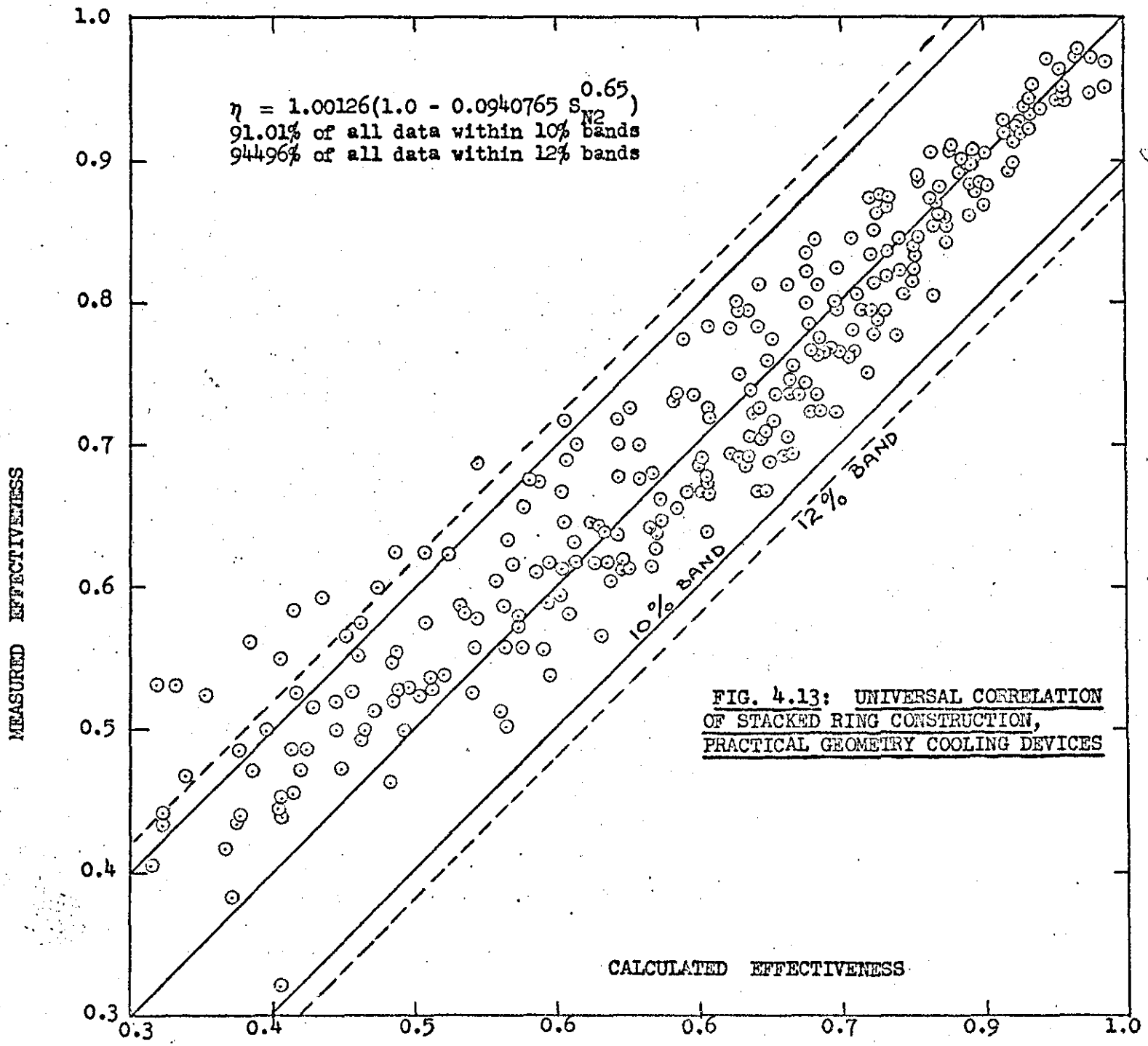

FIG. 4.13: UNIVERSAL CORRELATION OF STACKED RING CONSTRUCTION, PRACTICAL GEOMETRY COOLING DEVICES

FIG. 5.1: COMBUSTOR SCALE EFFECT ON FILM DEVELOPMENT

For two chambers, the second being slightly smaller than the first but having the same cooling design. Expected film effectivenesses for second chamber based on experience with the first.

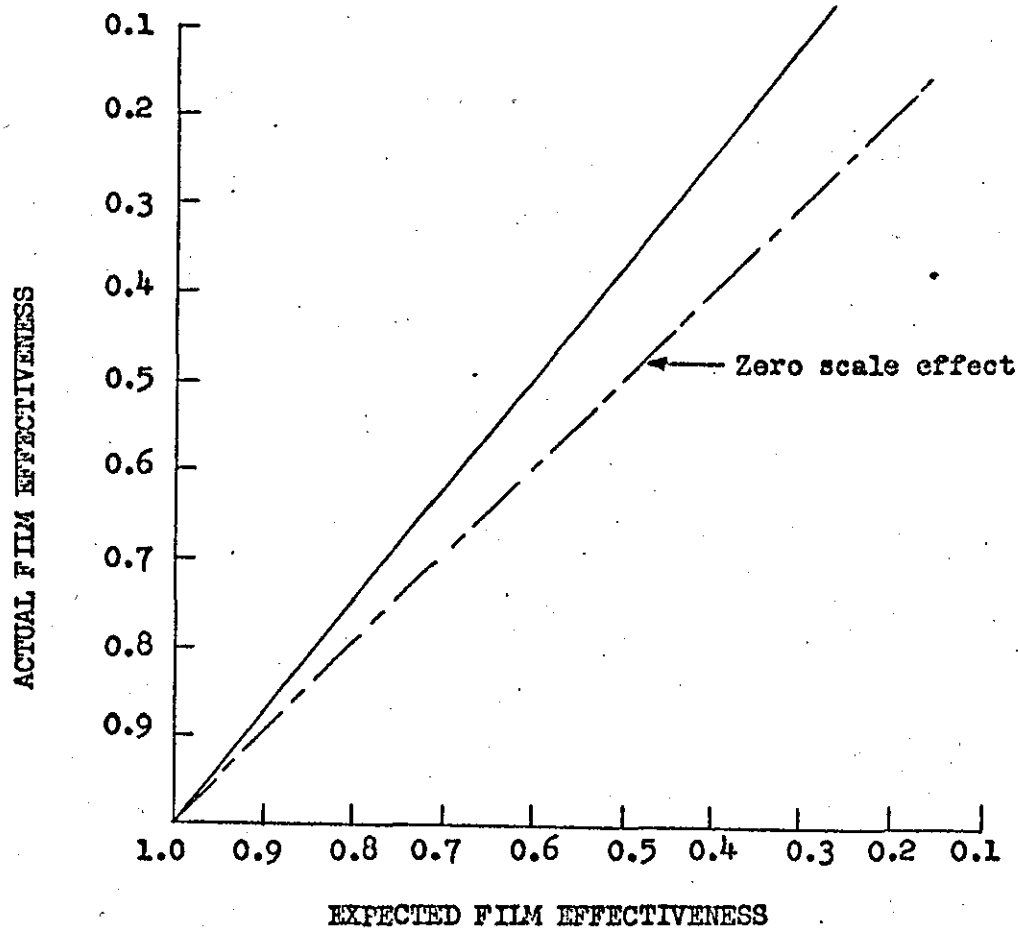

FIG. 5.2: COMBUSTOR SCALE EFFECT ON PRIMARY ZONE WALL TEMPERATURES

For two chambers, the second being slightly smaller than the first but having the same cooling design. Expected wall temperatures for second chamber based on experience obtained with first.

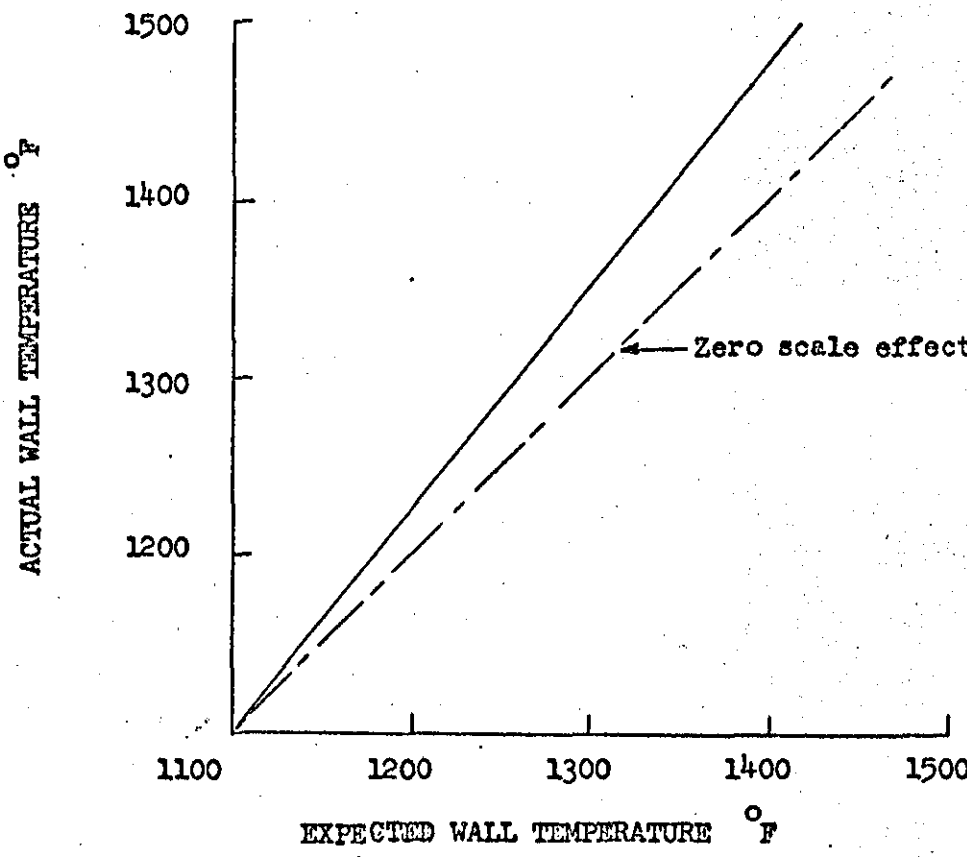

FIG. 5.3: COMBUSTOR SCALE EFFECT ON DILUTION ZONE WALL TEMPERATURES

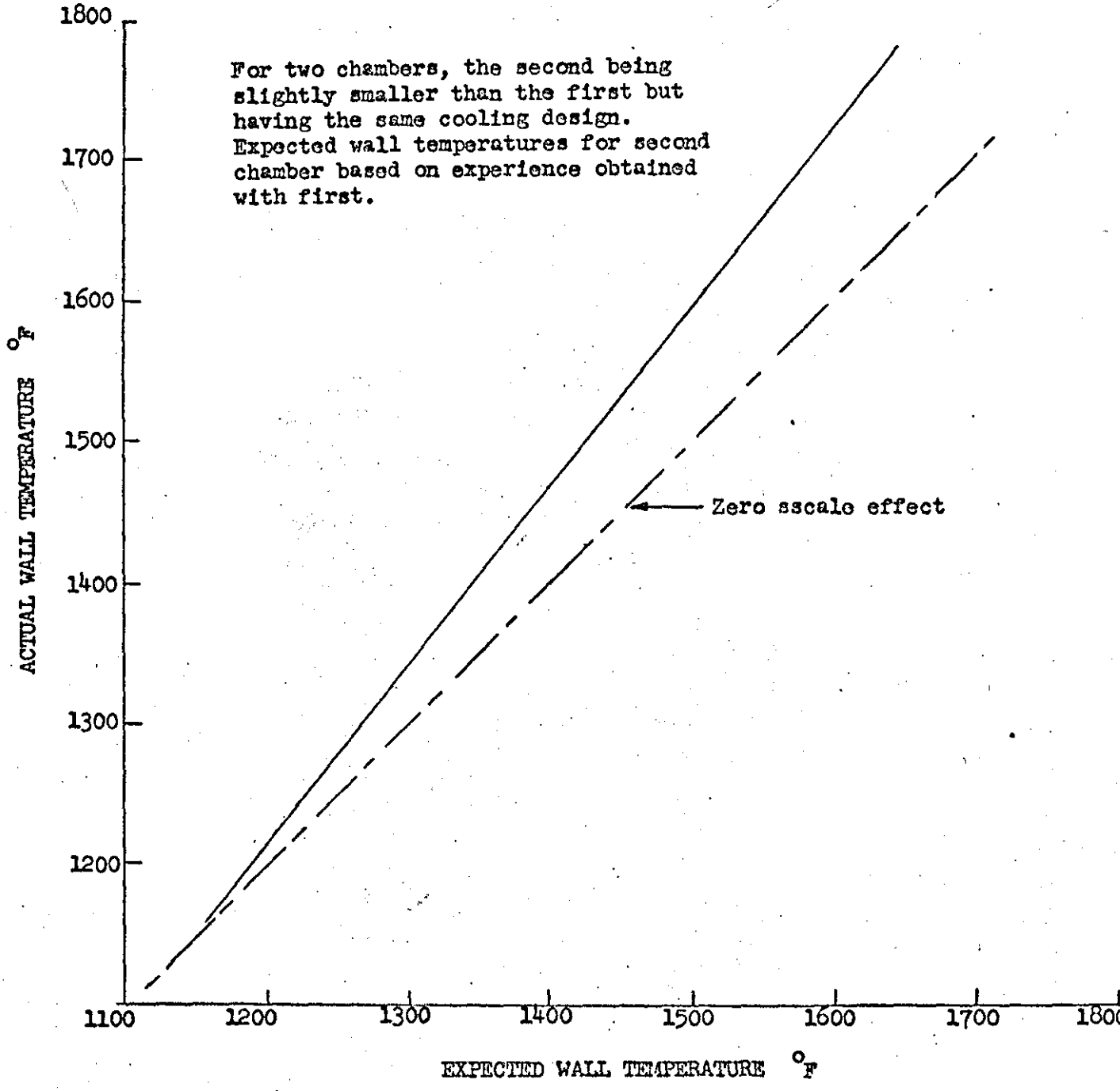

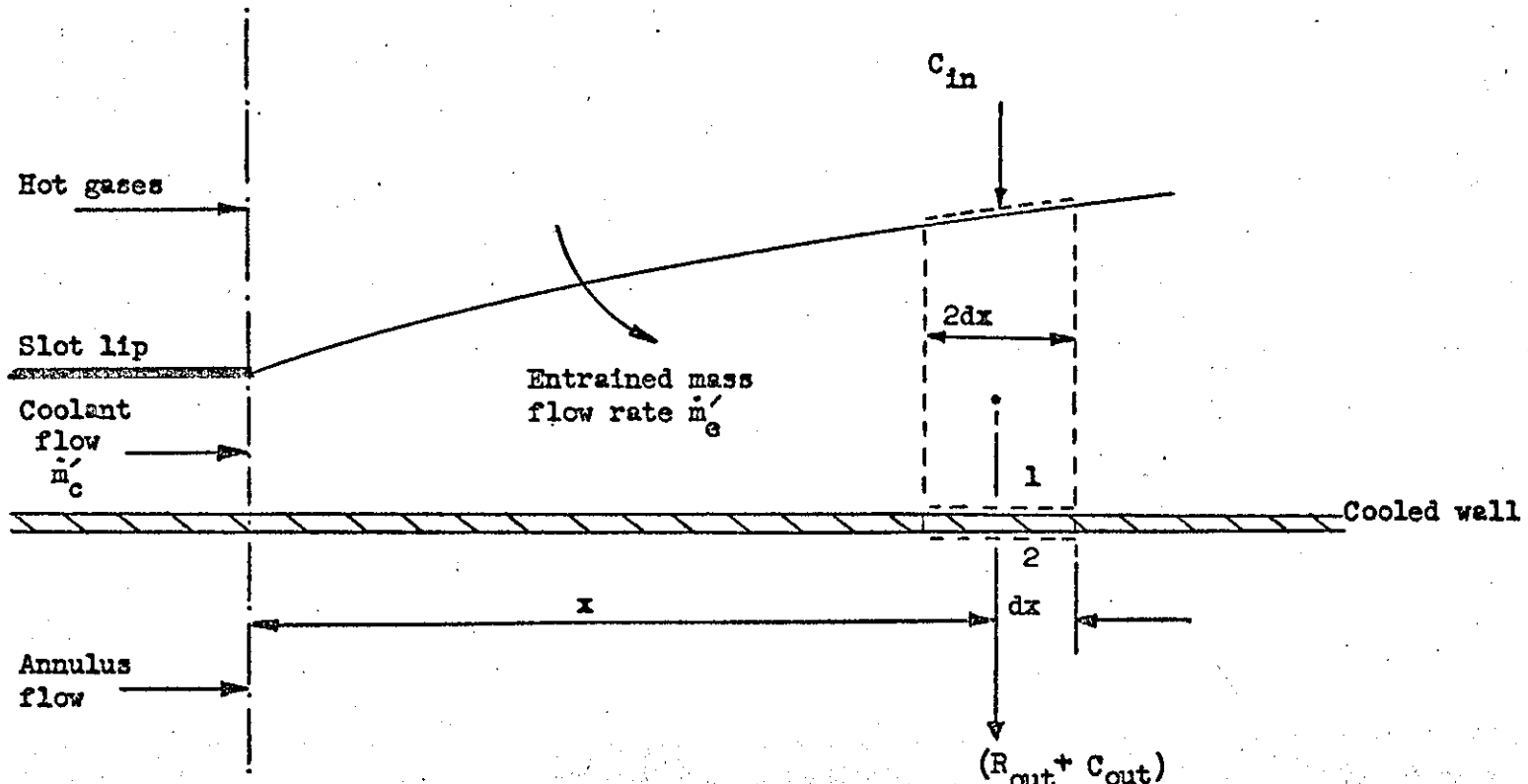

FIG. 6.1: FILM HEAT TRANSFER MODEL

FIG.6.2: EFFECT OF ACTUAL CHAMBER CONDITIONS ON REQUIRED EFFECTIVENESS THROUGH COLE'S ENTRAINMENT LAWS: DILUTION ZONE, EFFECT OF CONSTANT B FOR LOW VALUES OF CONSTANT A

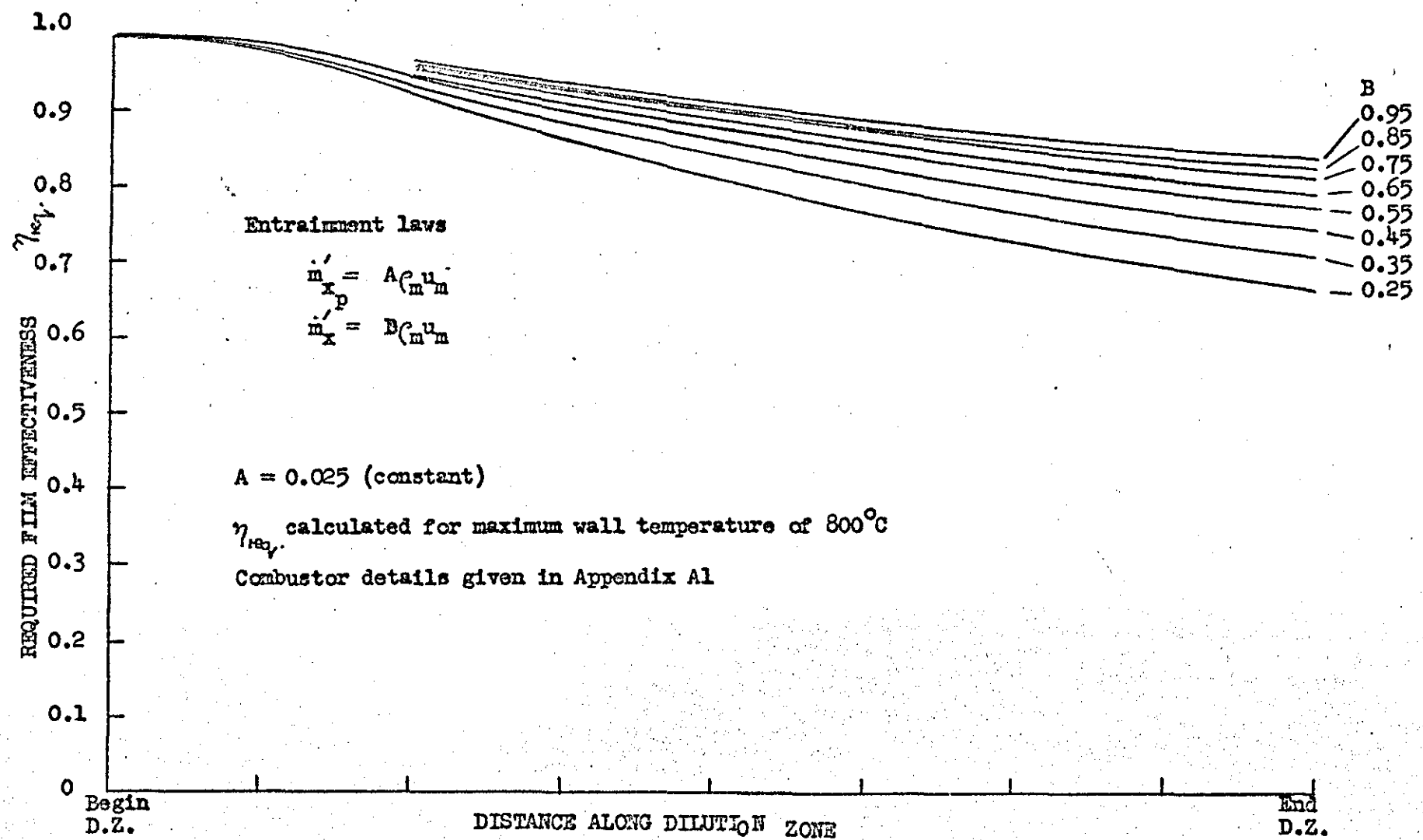

FIG. 6.3: EFFECT OF ACTUAL CHAMBER CONDITIONS ON REQUIRED EFFECTIVENESS THROUGH COLE'S ENTRAINMENT LAWS: DILUTION ZONE, EFFECT OF CONSTANT B FOR HIGH VALUES OF CONSTANT A

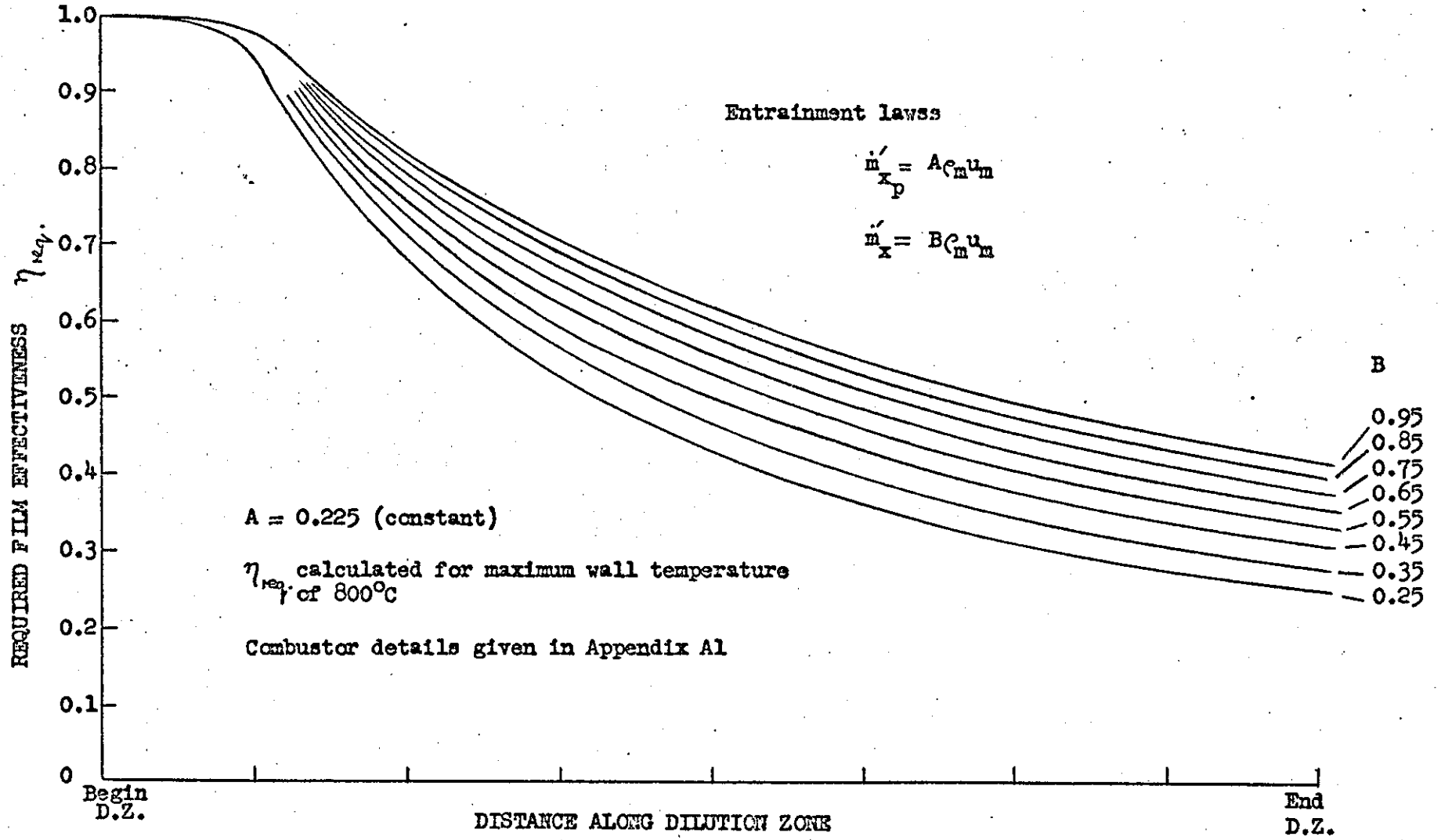

FIG. 6.4: EFFECT OF ACTUAL CHAMBER CONDITIONS ON REQUIRED EFFECTIVENESS THROUGH COLE'S ENTRAINMENT LAWS: DILUTION ZONE, EFFECT OF CONSTANT A FOR LOW VALUES OF CONSTANT B

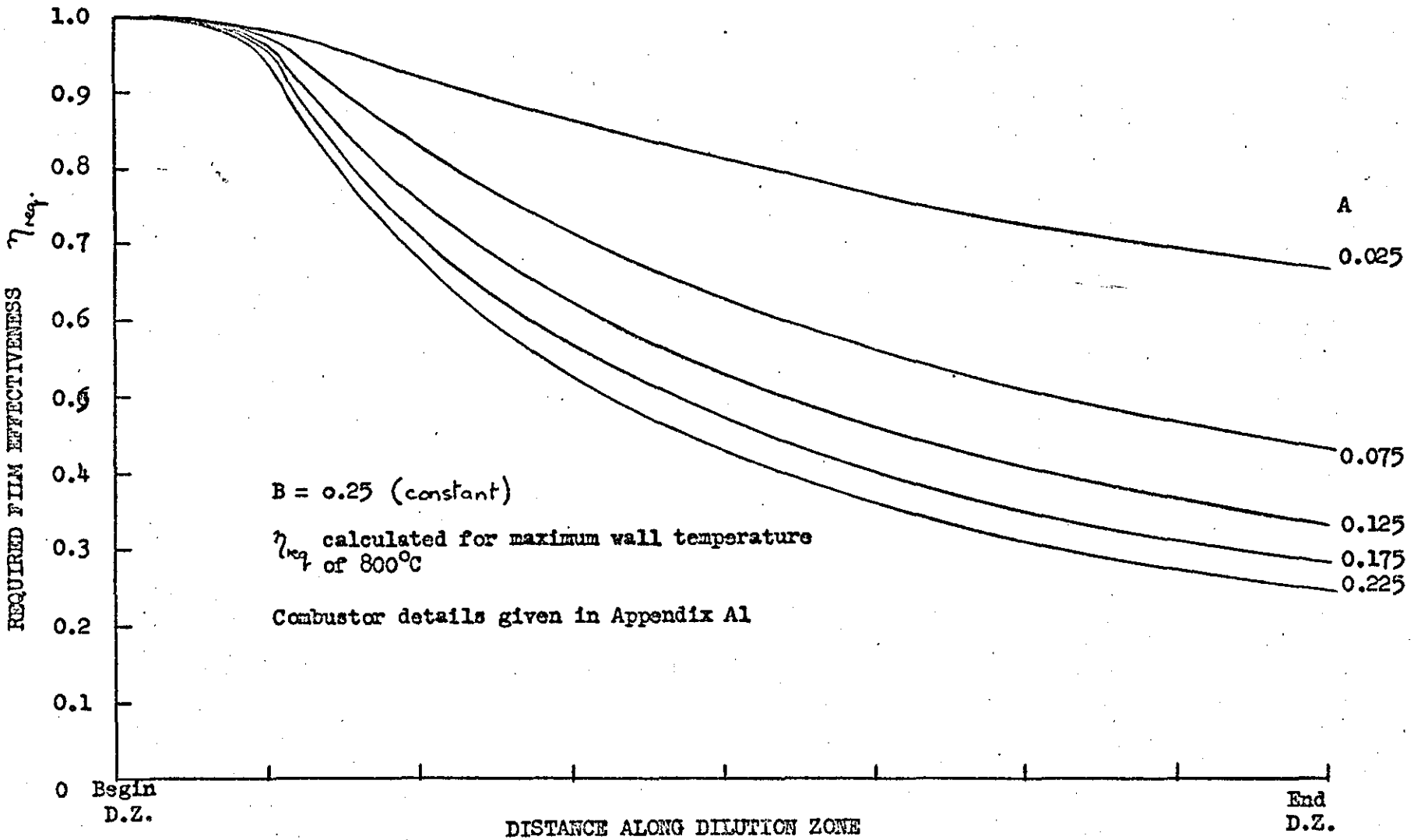

FIG. 6.5: EFFECT OF ACTUAL CHAMBER CONDITIONS ON REQUIRED EFFECTIVENESS THROUGH COLE'S ENTRAINMENT LAWS: DILUTION ZONE, EFFECT OF CONSTANT A FOR HIGH VALUES OF CONSTANT B

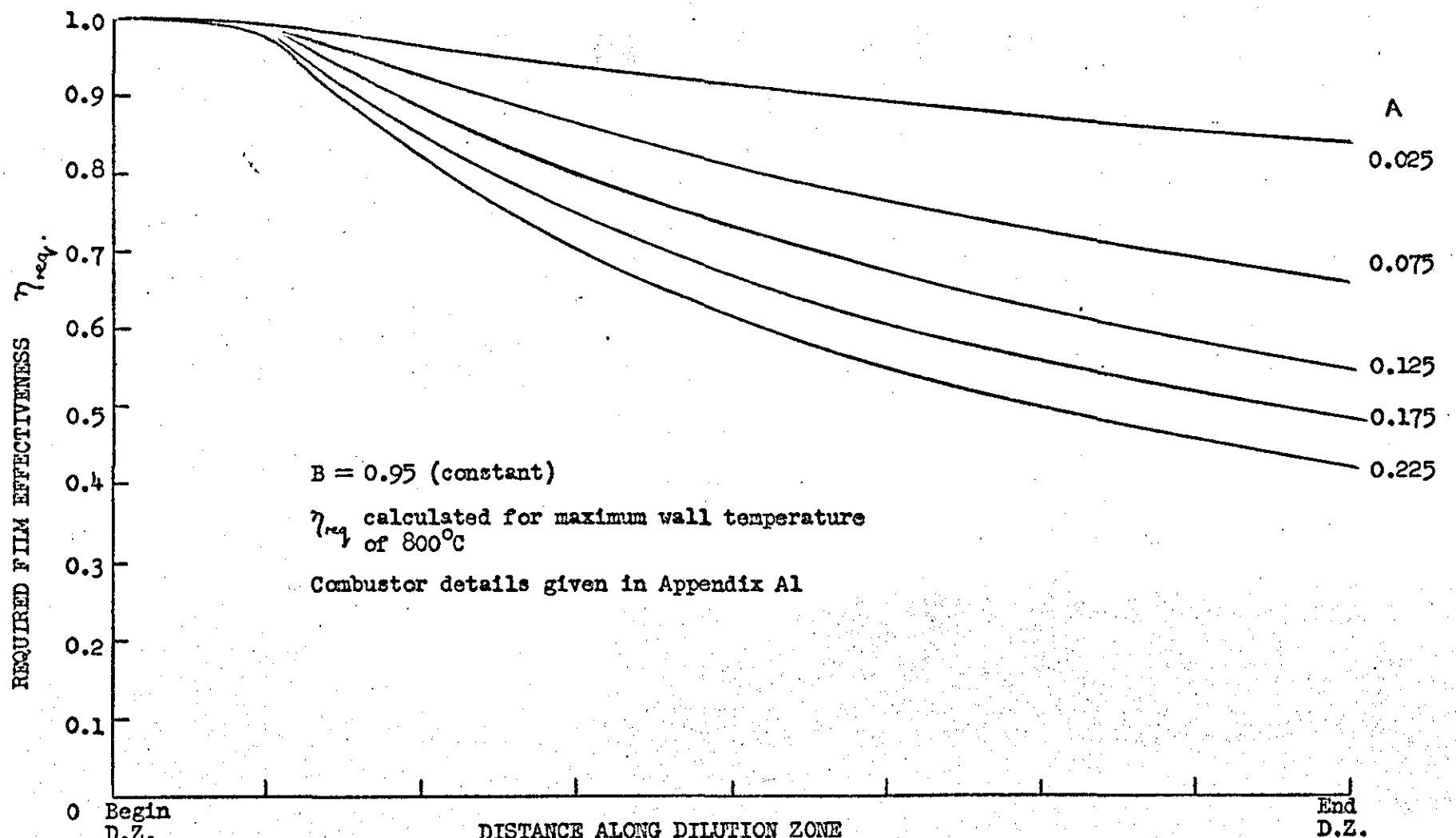

384

Combustor details given in Appendix A1.

Cooling system designed for maximum wall temperature of 800°C (1475°F), in each case.

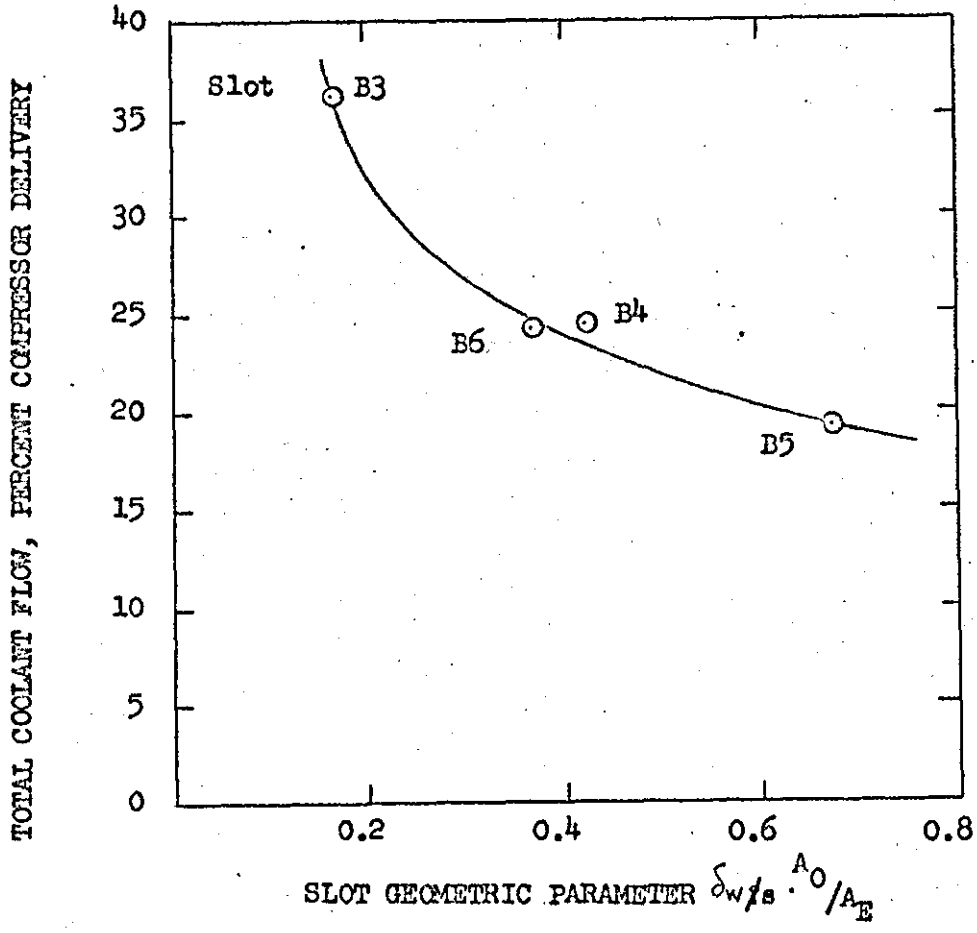

FIG. 6.6: FILM COOLING OF A LARGE ANNULAR COMBUSTOR FOR SUSTAINED FLIGHT AT SUPERSONIC SPEEDS: EFFECT OF SLOT GEOMETRY ON COOLANT REQUIREMENTS.

FIG. 6.7: ILLUSTRATION OF CONSTANCY OF DISTORTION INDEX IN TRANSITION REGION

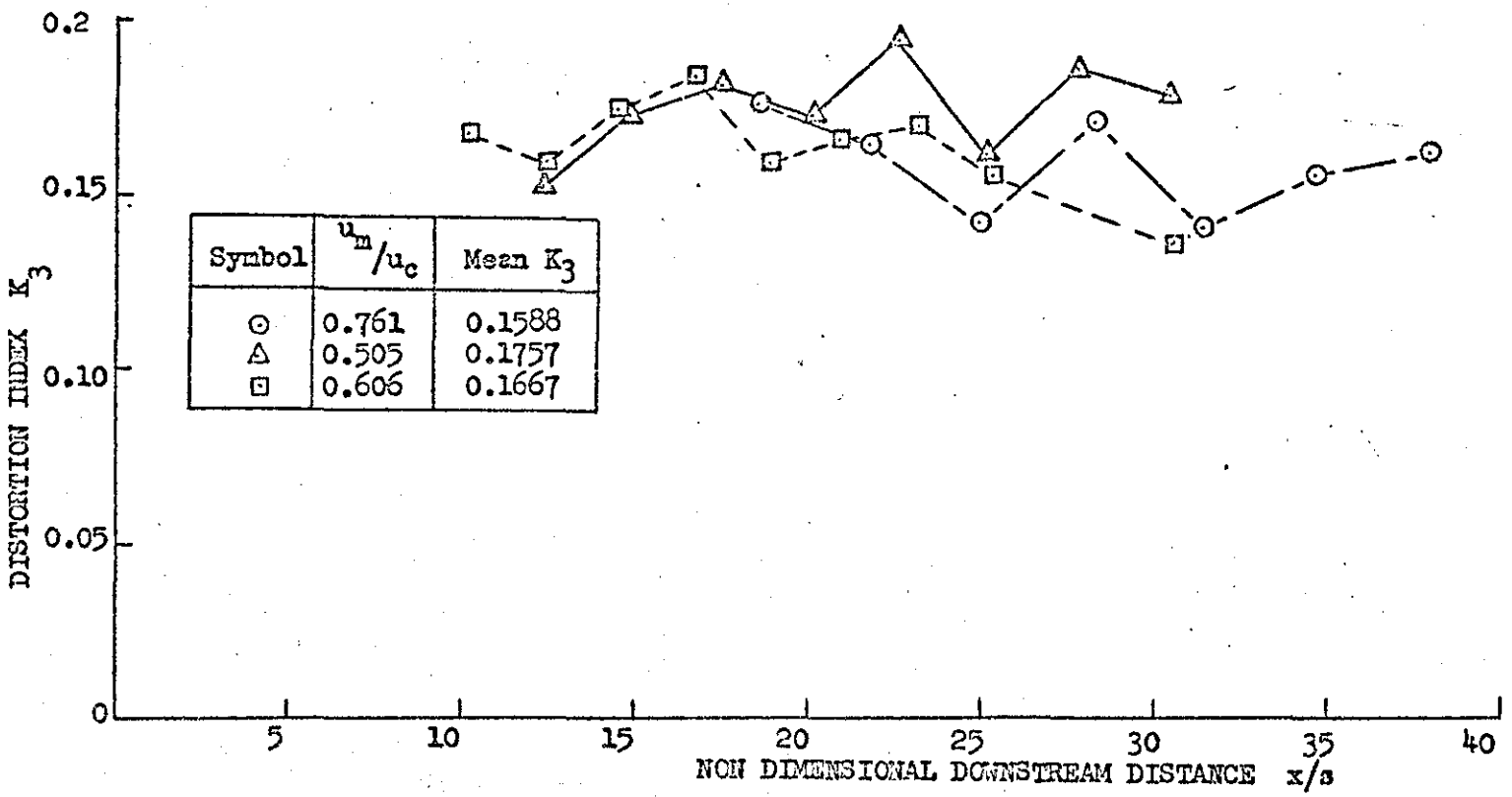

FIG. 6.8: DISTORTION INDEX FOR FILM ENTRAINMENT FOR STACKED RING SLOTS

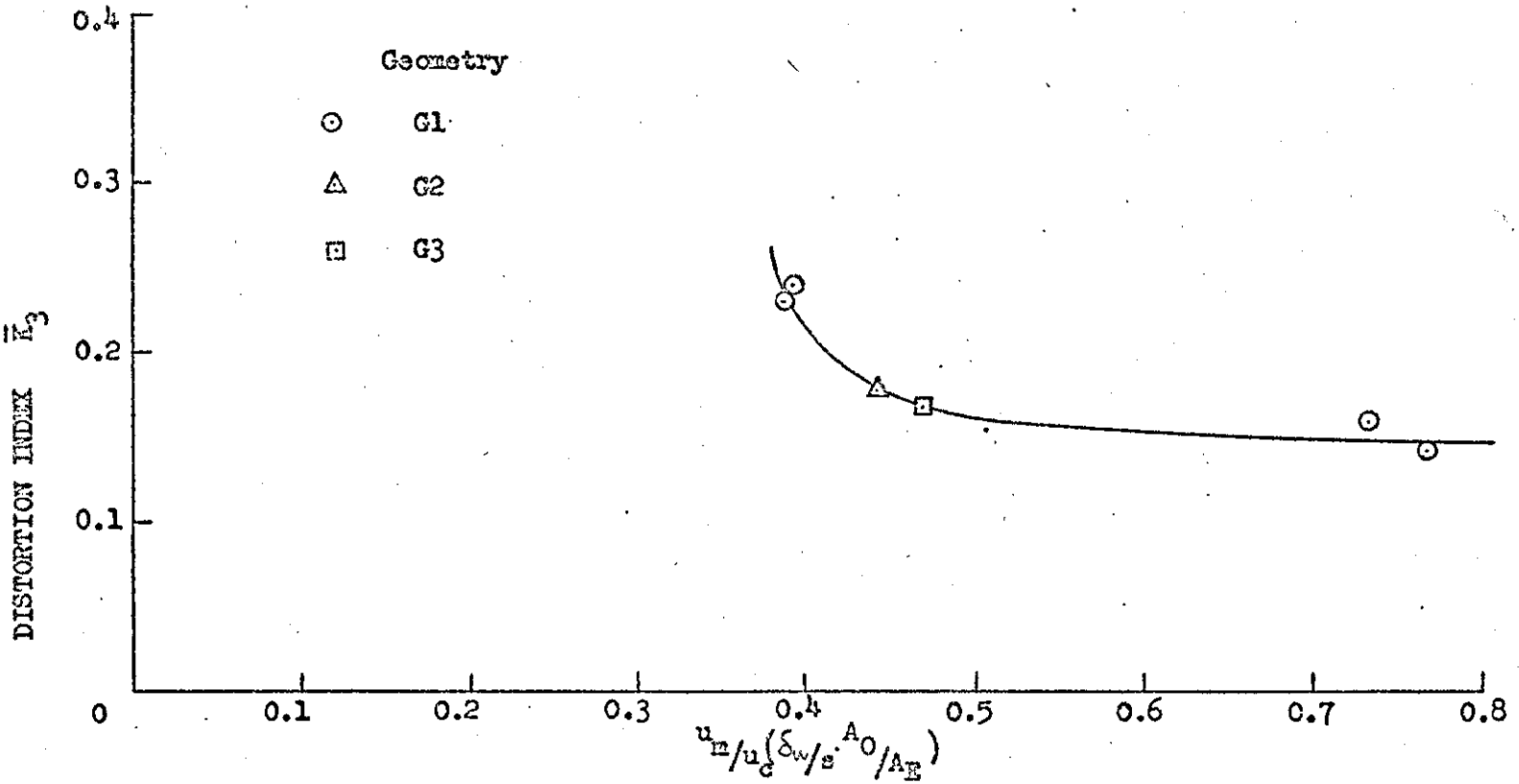

FIG. 6.9: COMPARISON OF MEASURED FILM HEAT TRANSFER COEFFICIENT DATA FROM STACKED RING GEOMETRY G1 WITH PREDICTIONS FROM EQUATION 6.30 AND OTHER POSSIBLE EQUATIONS

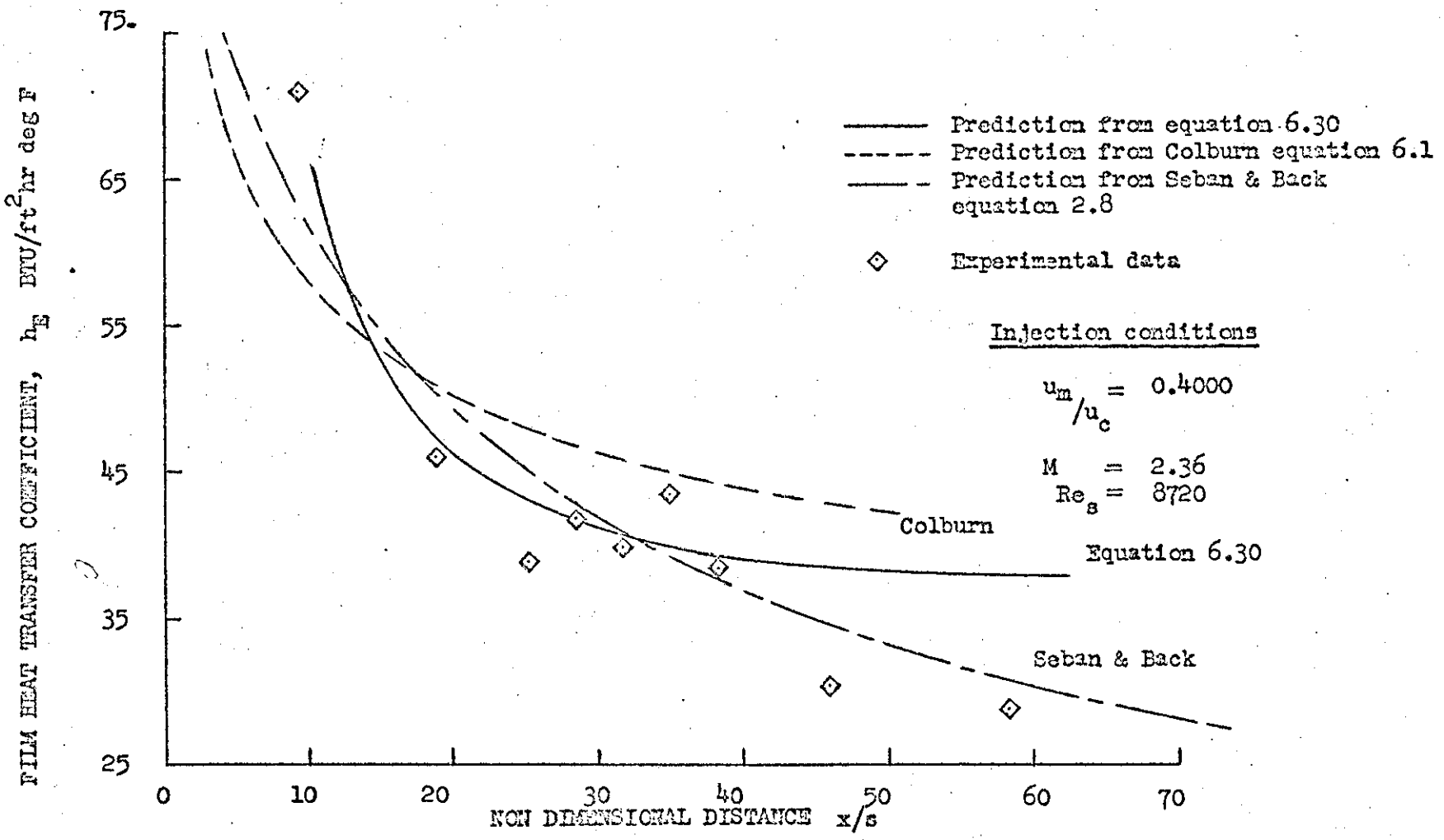

FIG. 6.10: COMPARISON OF MEASURED FILM HEAT TRANSFER COEFFICIENT DATA FROM STACKED RING GEOMETRY G1 WITH PREDICTIONS FROM EQUATION 6.30 AND OTHER POSSIBLE EQUATIONS

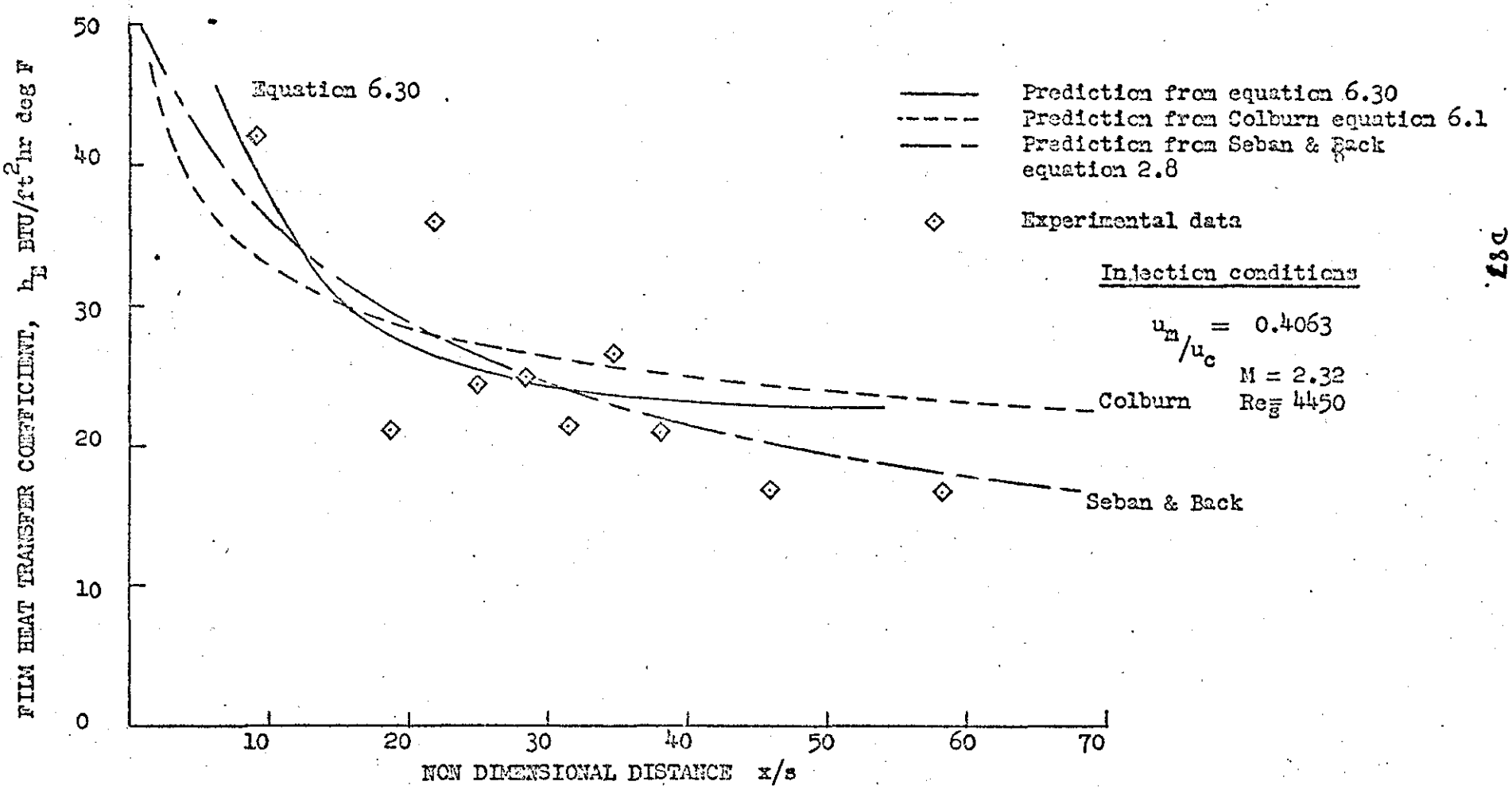

FIG. 6.11: COMPARISON OF MEASURED FILM HEAT TRANSFER COEFFICIENT DATA FROM STACKED RING GEOMETRY G1 WITH PREDICTIONS FROM EQUATION 6.30 AND OTHER POSSIBLE EQUATIONS

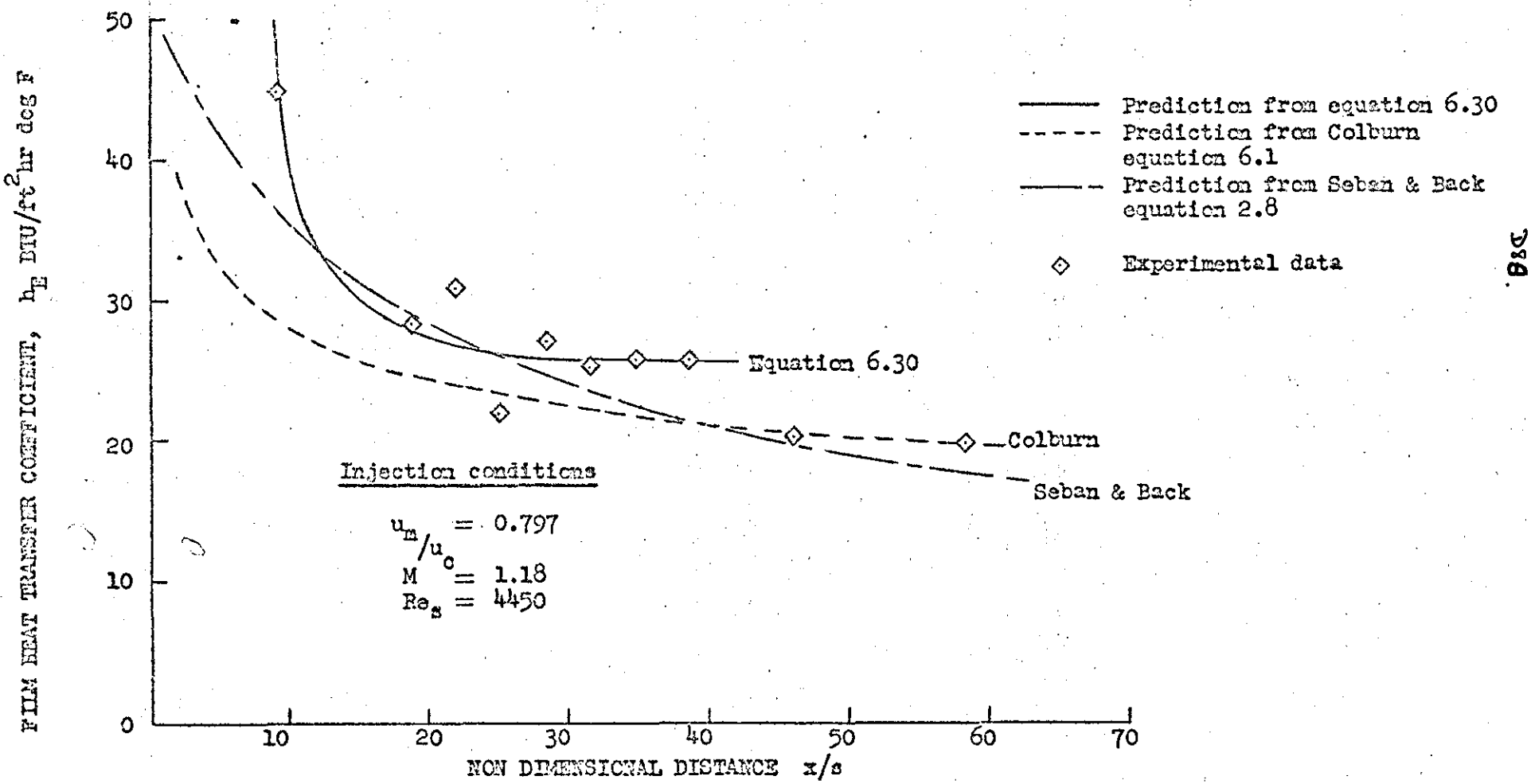

FIG. 6.12: COMPARISON OF MEASURED FILM HEAT TRANSFER COEFFICIENT DATA FROM STACKED RING GEOMETRY G1 WITH PREDICTIONS FROM EQUATION 6.30 AND OTHER POSSIBLE EQUATIONS

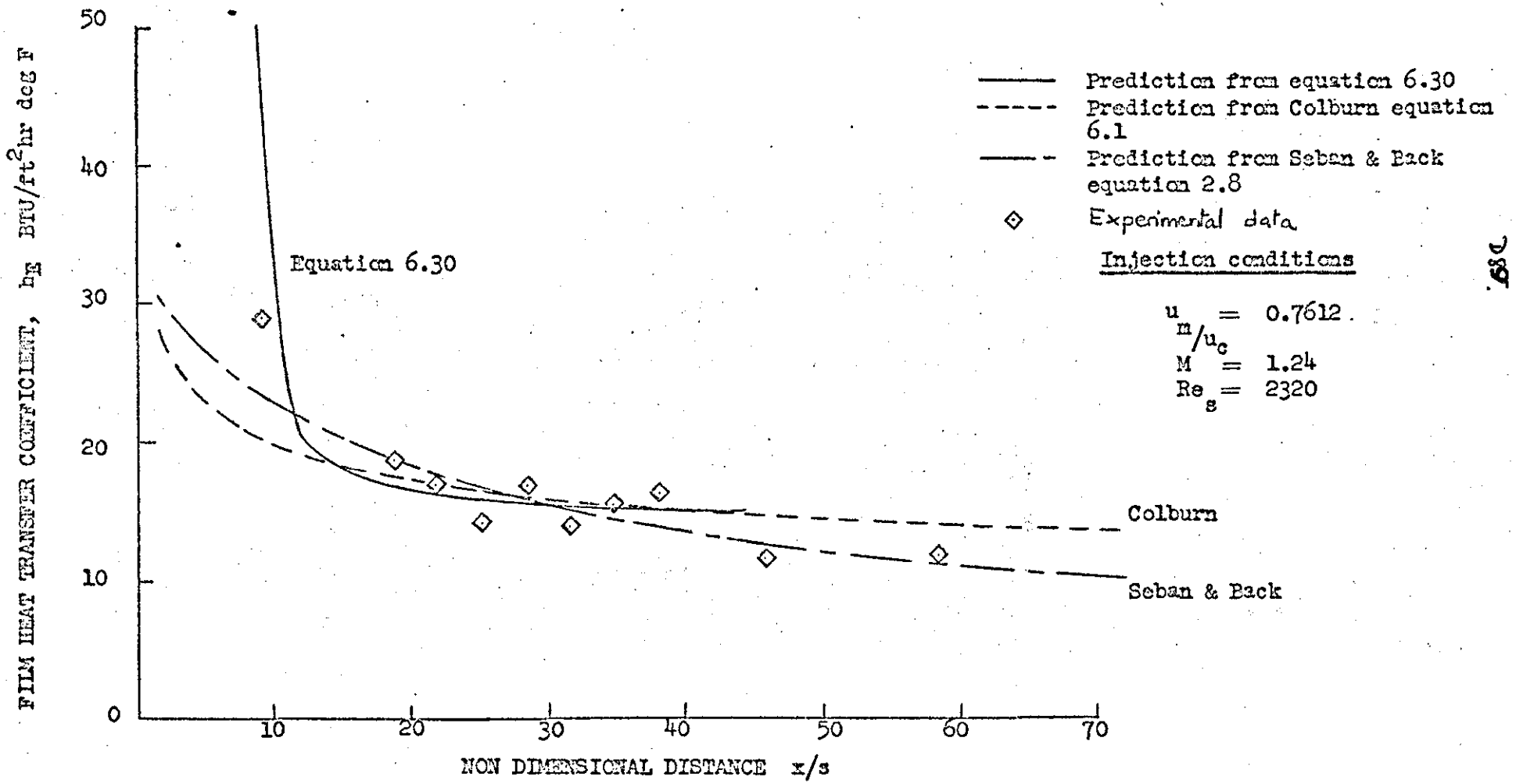

FIG. 6.13: COMPARISON OF MEASURED FILM HEAT TRANSFER COEFFICIENT DATA FROM STACKED RING GEOMETRY G2 WITH PREDICTIONS FROM EQUATION 6.30 AND OTHER POSSIBLE EQUATIONS

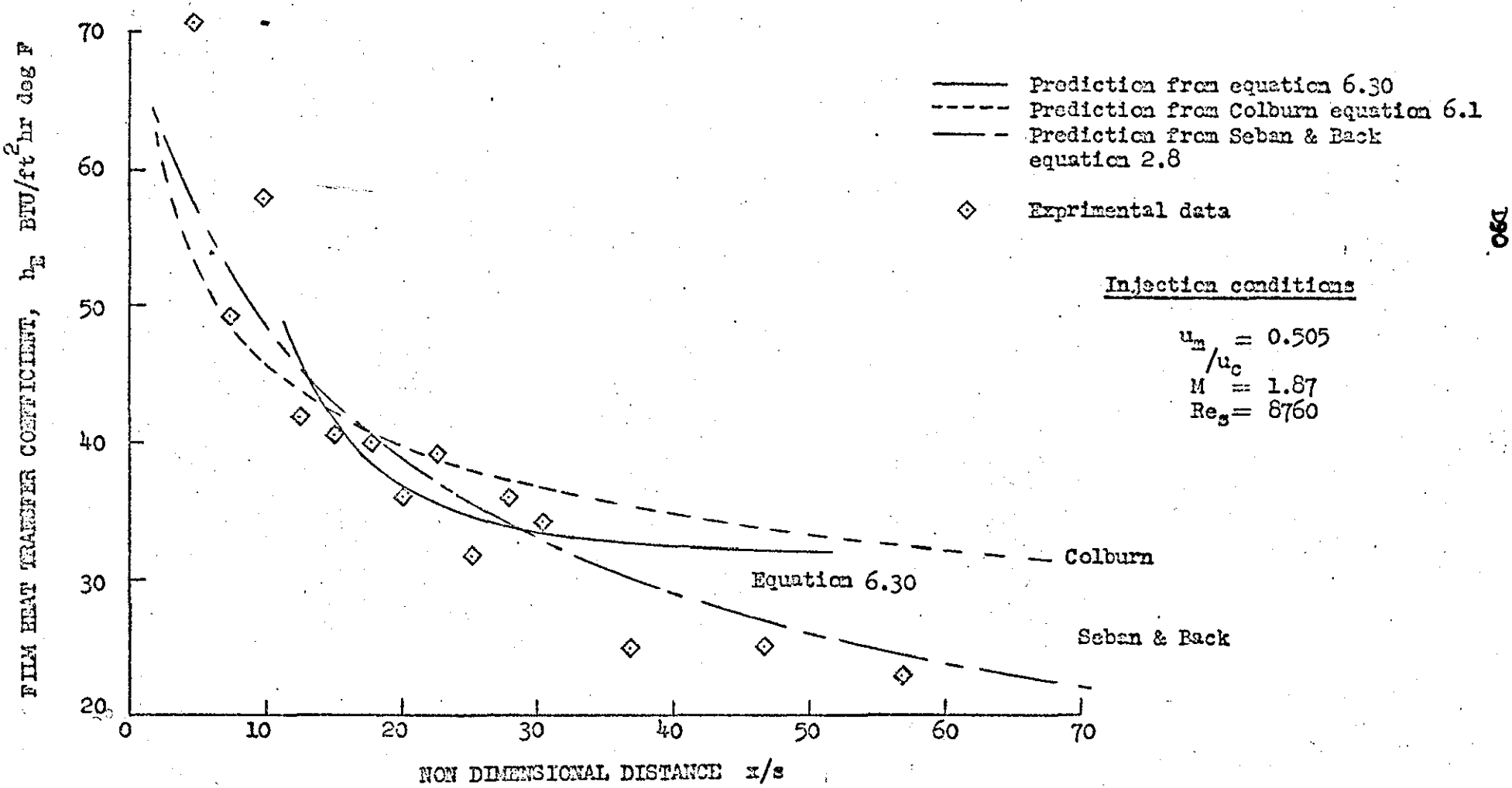

FIG. 6.14: COMPARISON OF MEASURED FILM HEAT TRANSFER COEFFICIENT DATA FROM STACKED RING GEOMETRY G3 WITH PREDICTIONS FROM EQUATION 6.30 AND OTHER POSSIBLE EQUATIONS

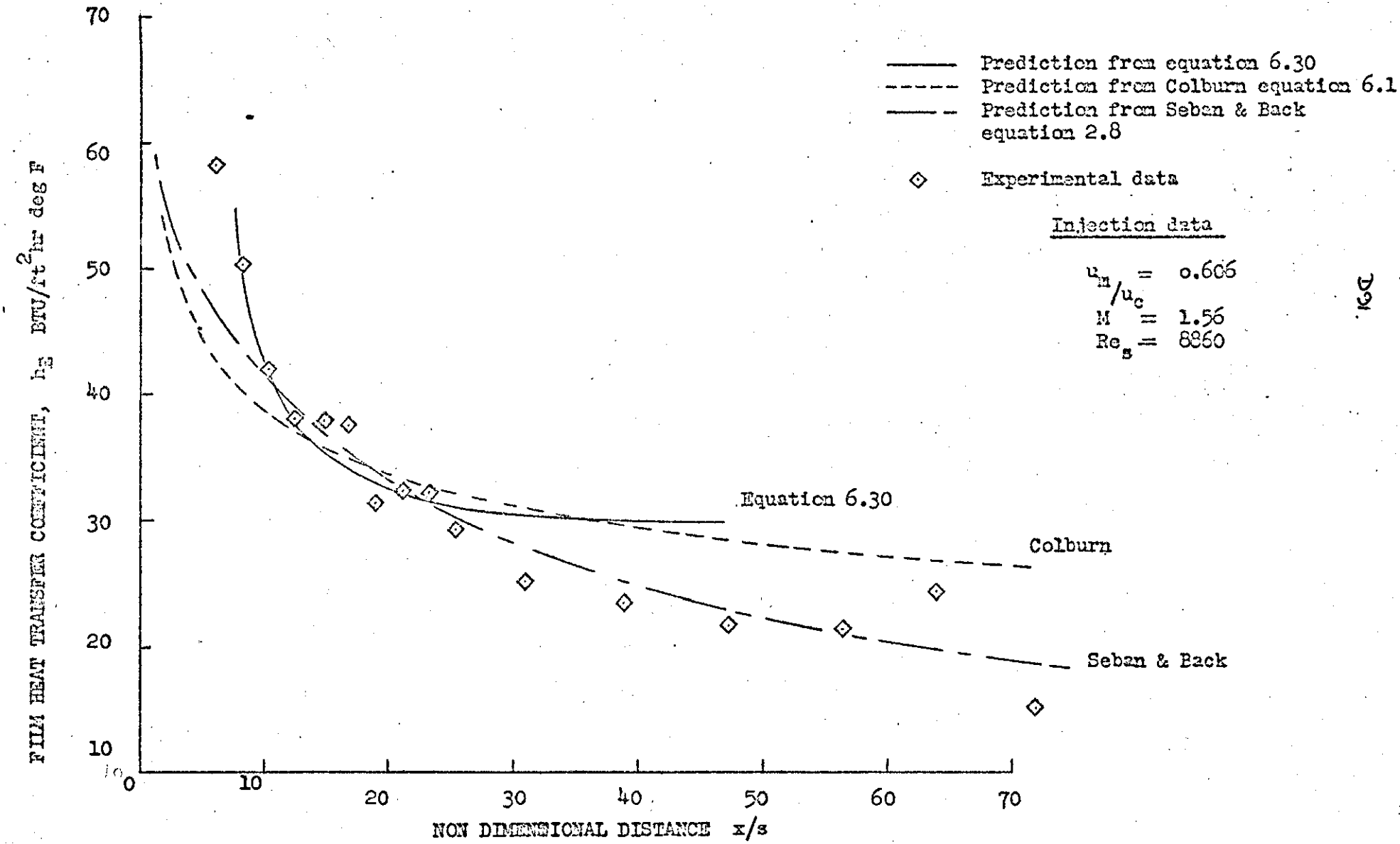

FIG. 7.1a): MODE OF ATTACK

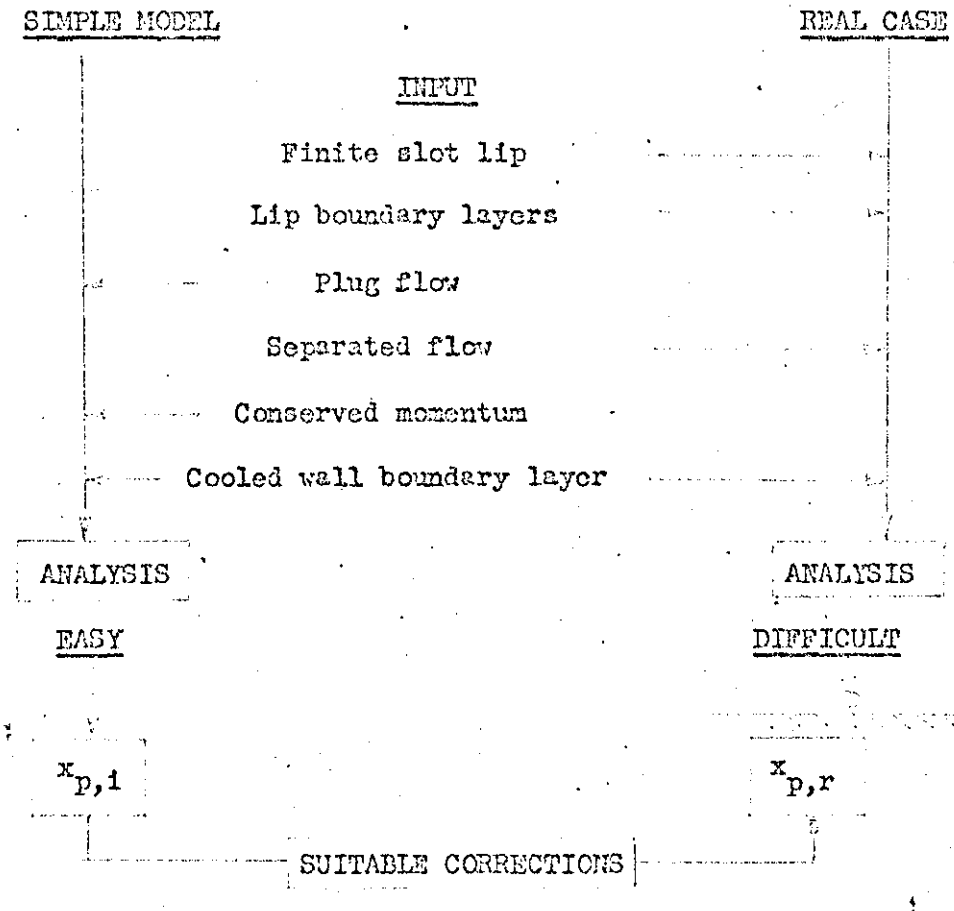

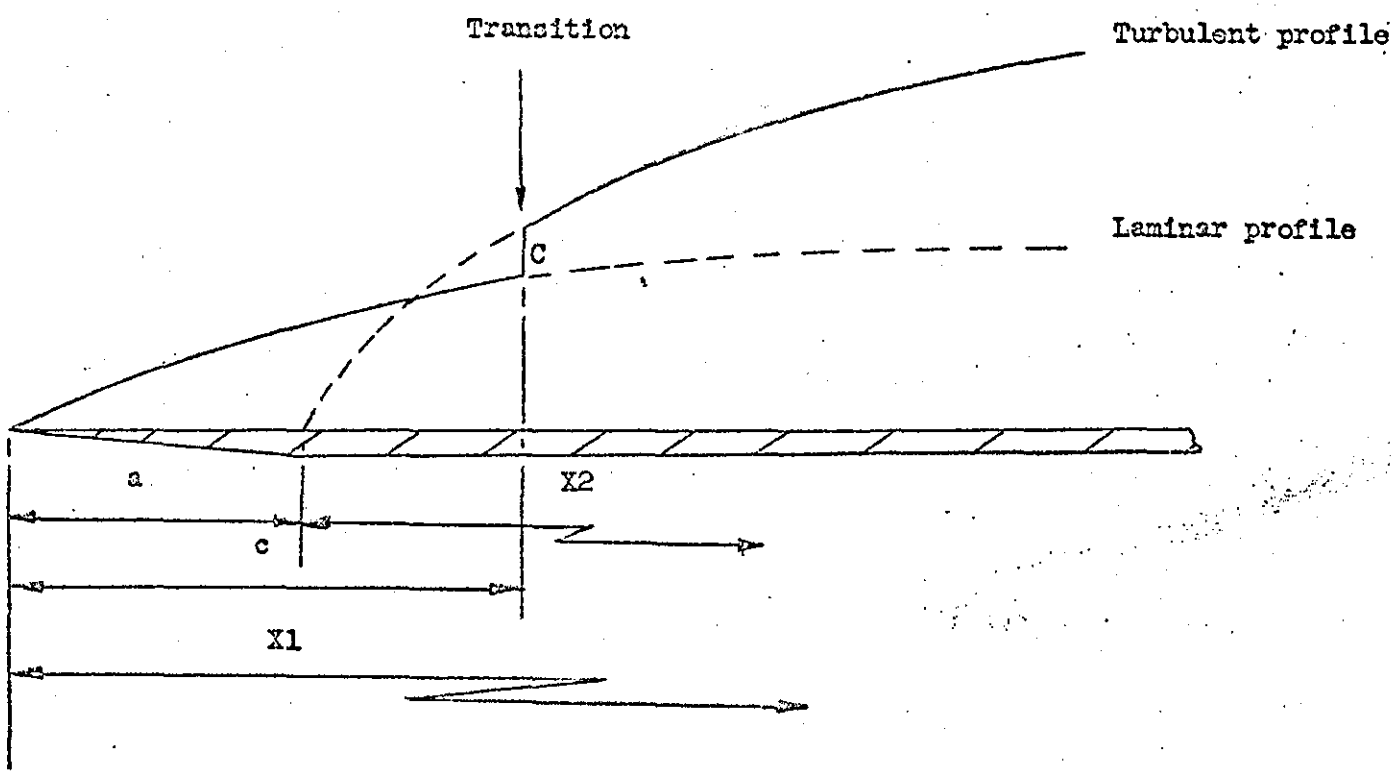

FIG. 7.1: BOUNDARY LAYER GROWTH ALONG A FLAT PLATE

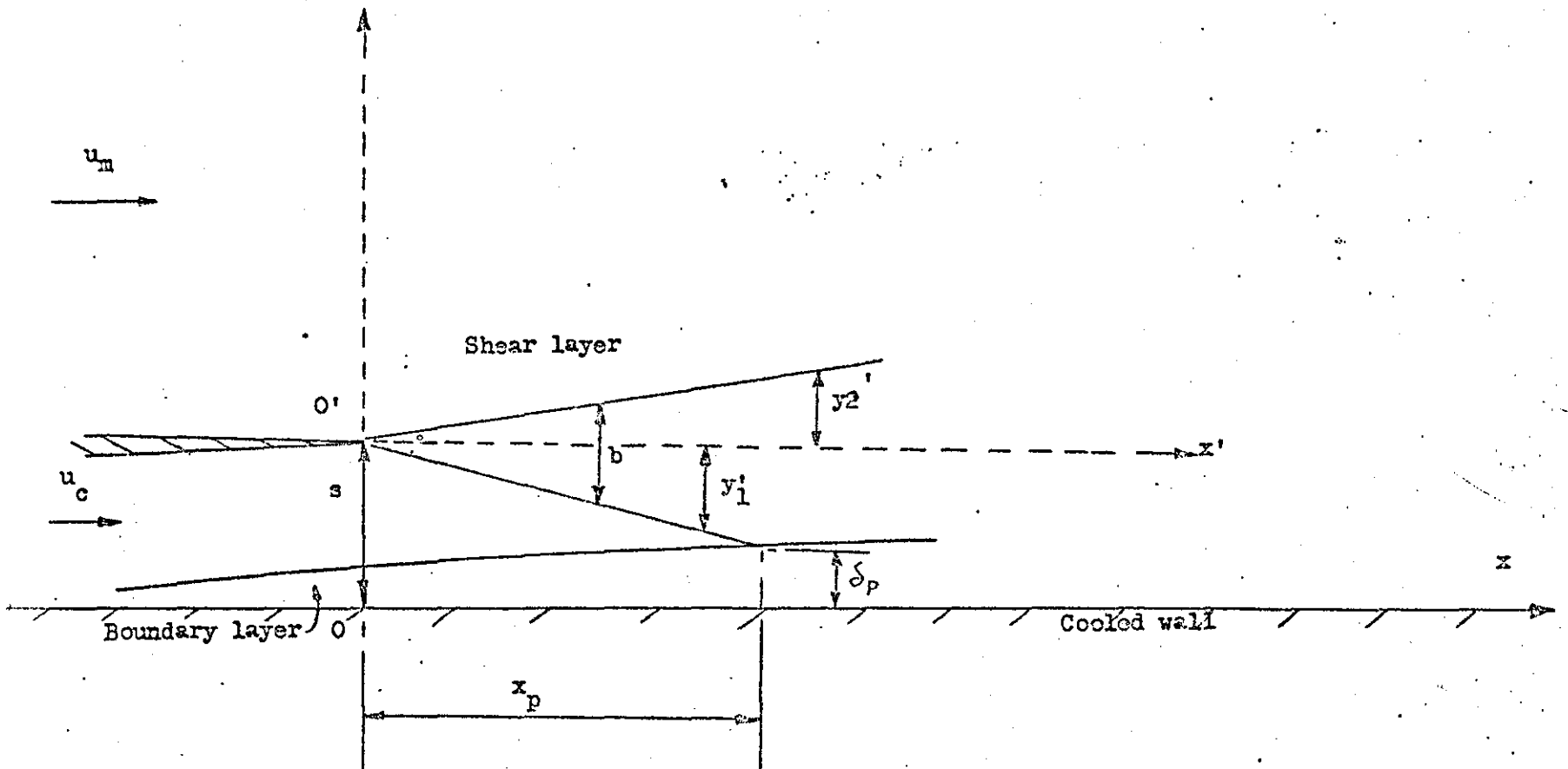

FIG. 7.2: DEFINITIONS IN INITIAL REGION OF FILM - SHEAR LAYER MIXING

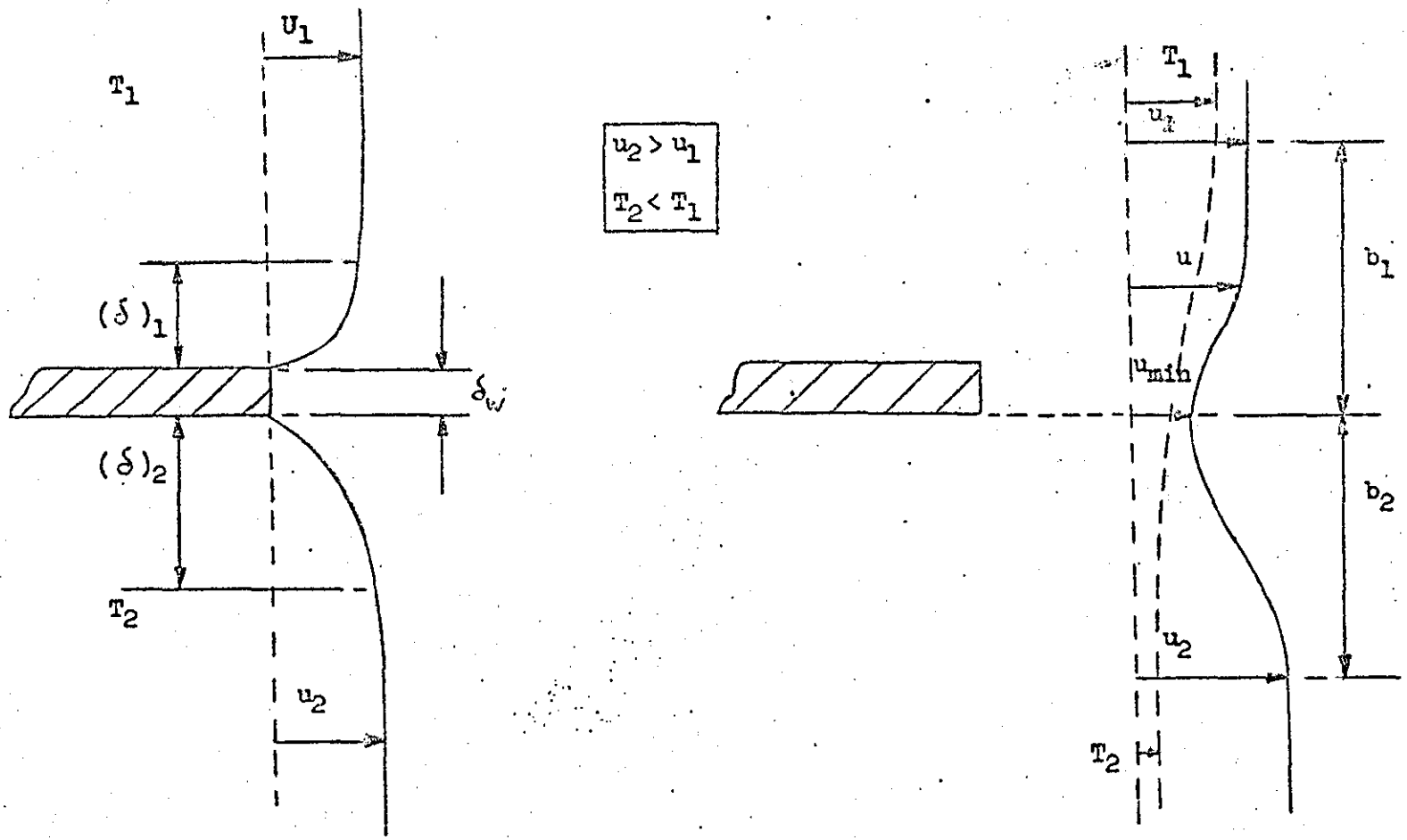

FIG. 7.3: NON ISOTHERMAL WAKE FORMATION

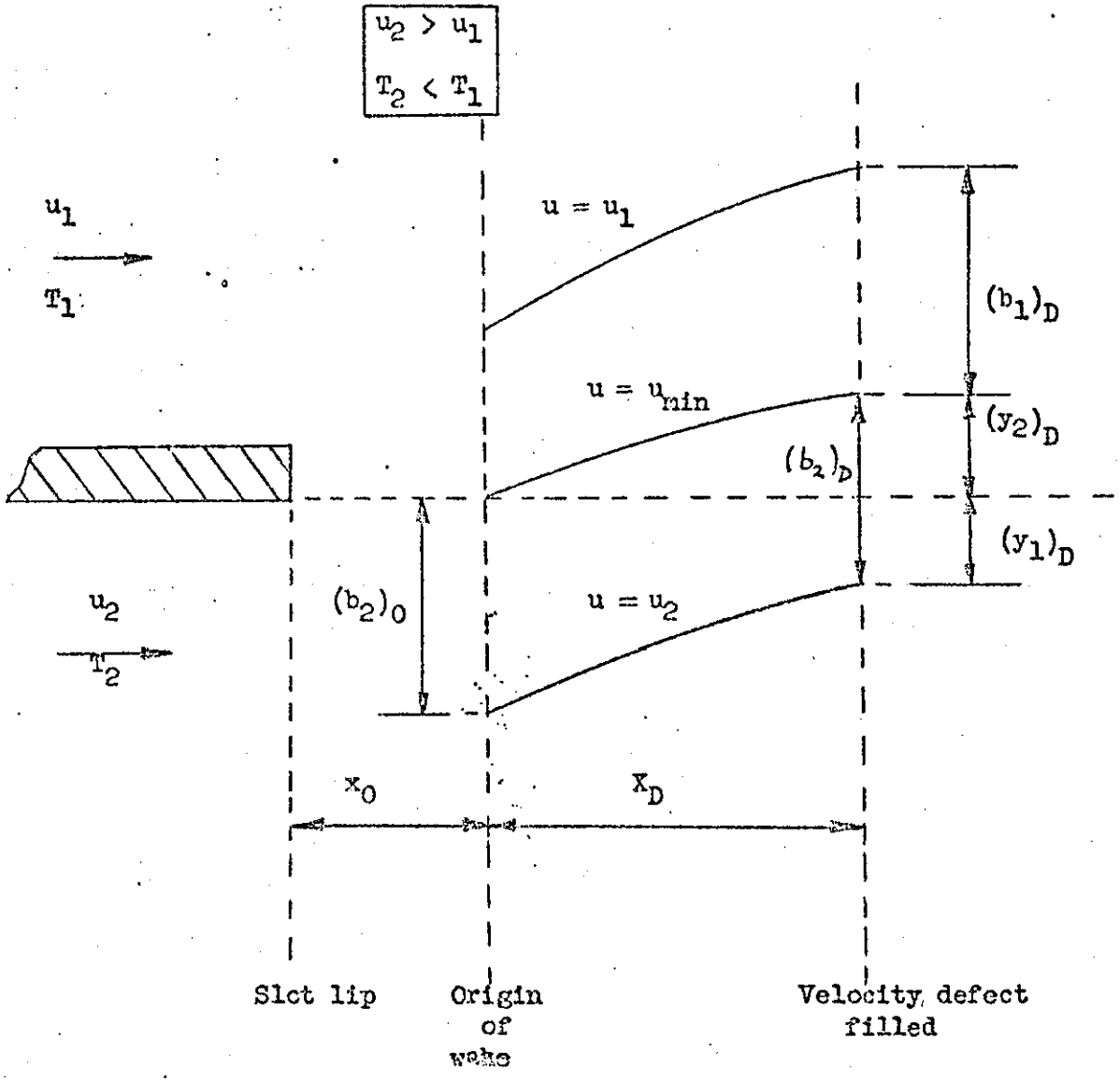

FIG. 7.4: FILLING OF VELOCITY DEFECT

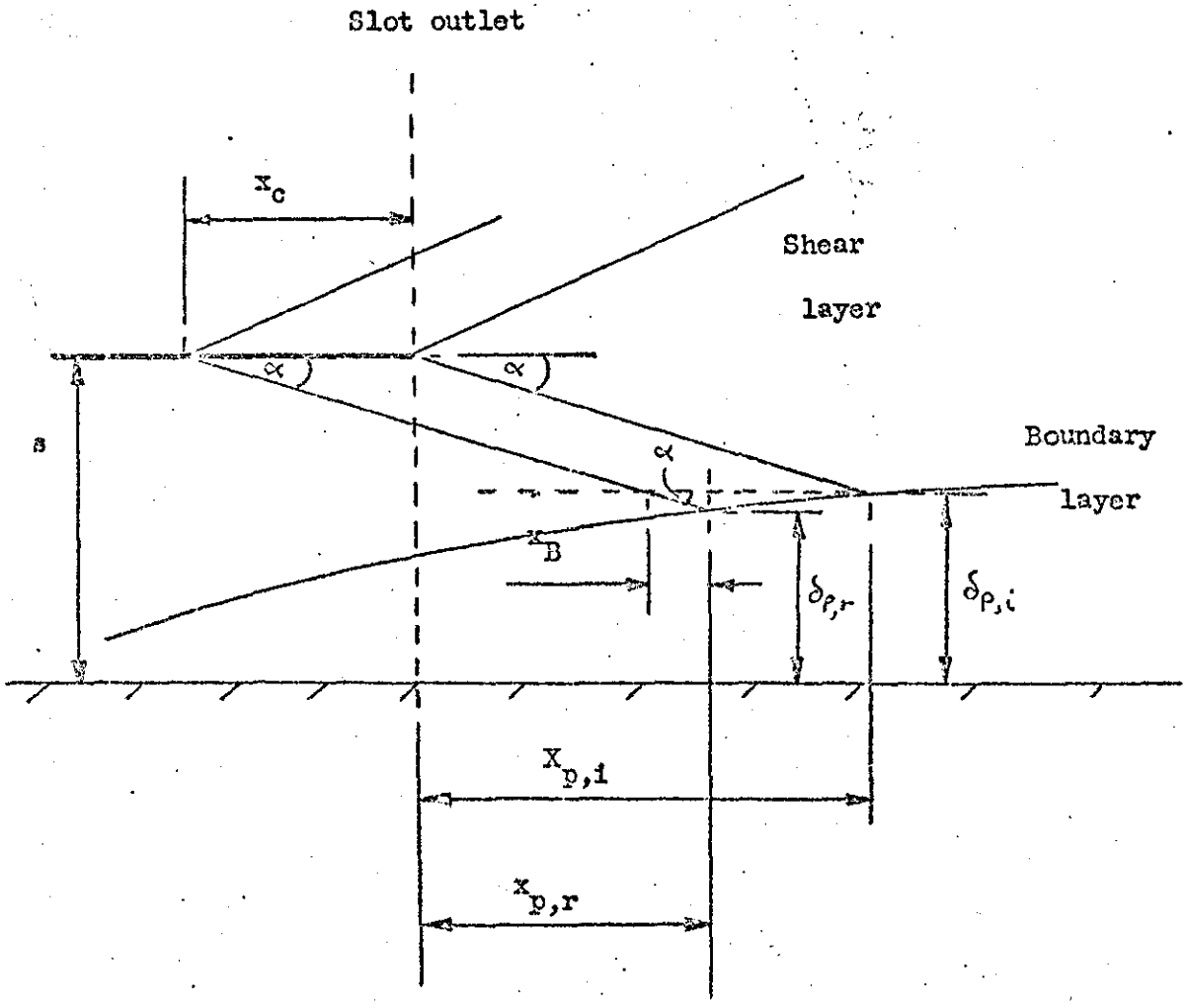

FIG. 7.5: SHIFT OF ORIGIN FOR SHEAR LAYER

FIG. 8.1: TEST FACILITY LAYOUT

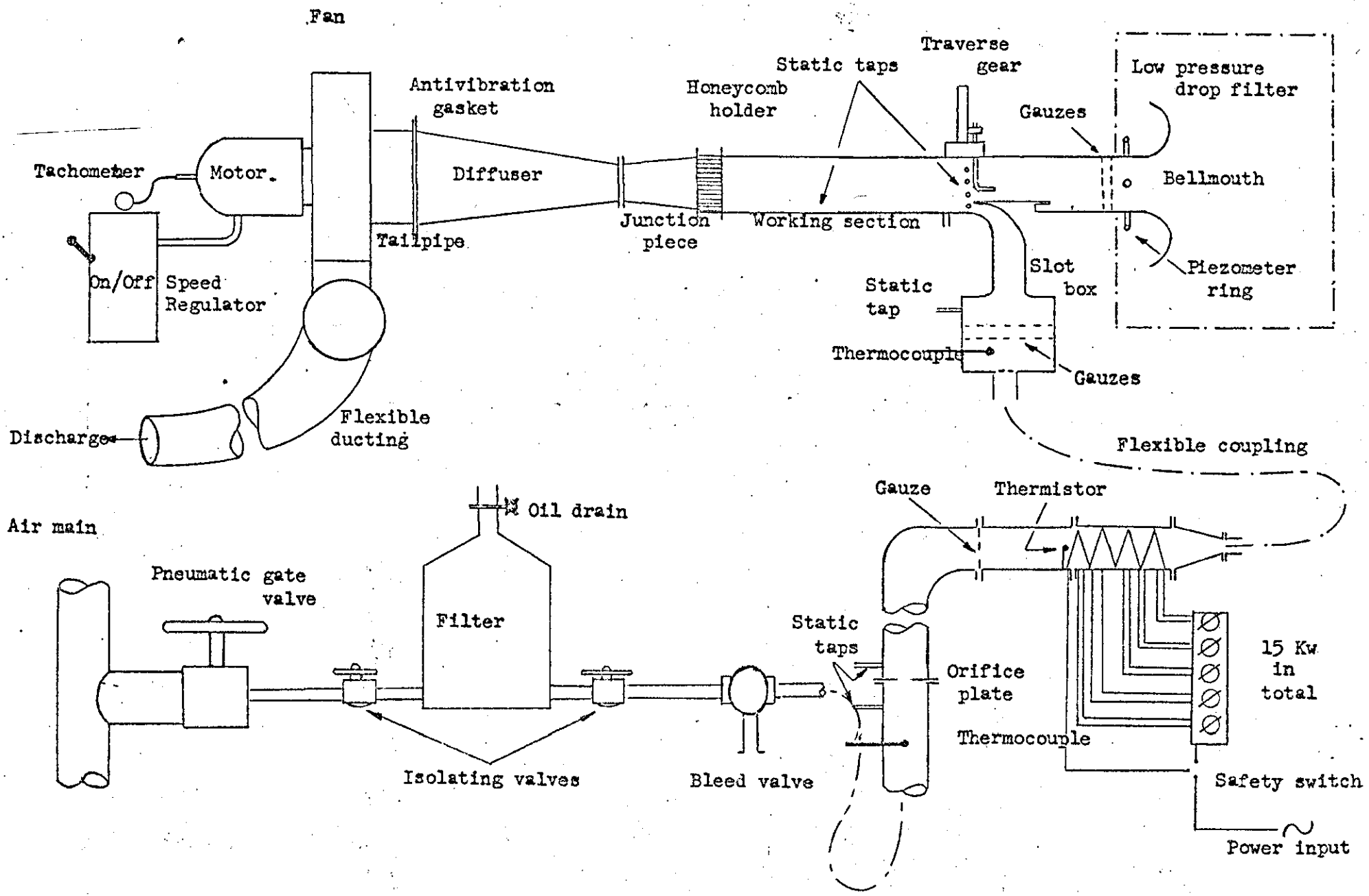

FIG. 8.2: FLOW AREAS NORMAL TO WALL FOR SLOT CONVERGENCES

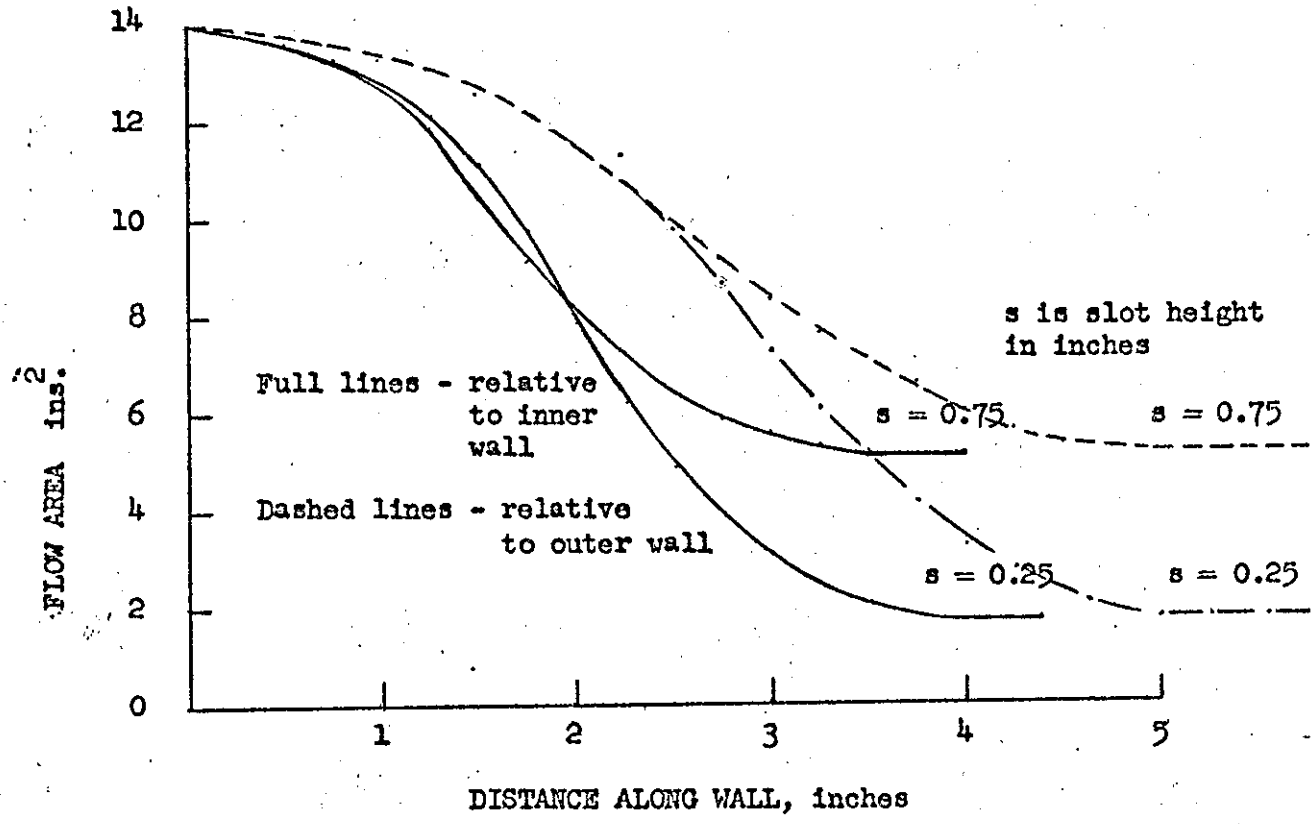

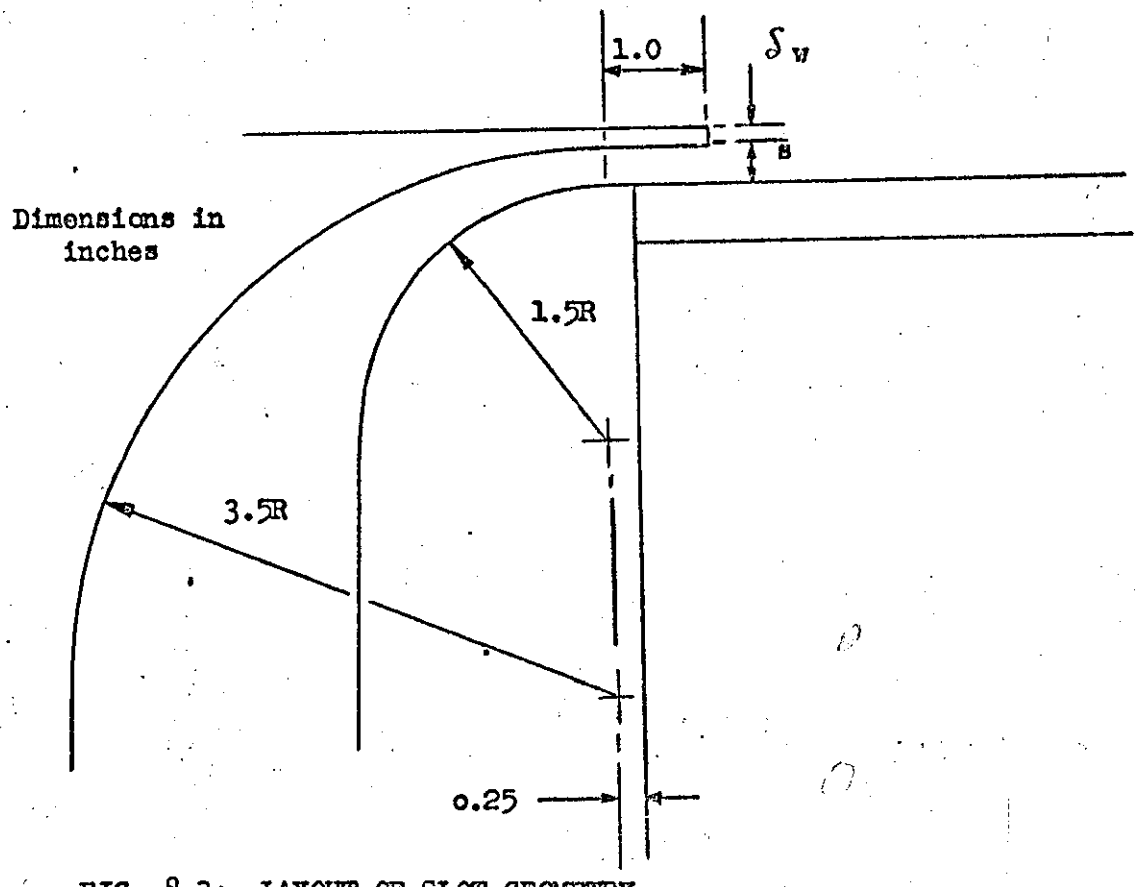

FIG. 8.3: LAYOUT OF SLOT GEOMETRY

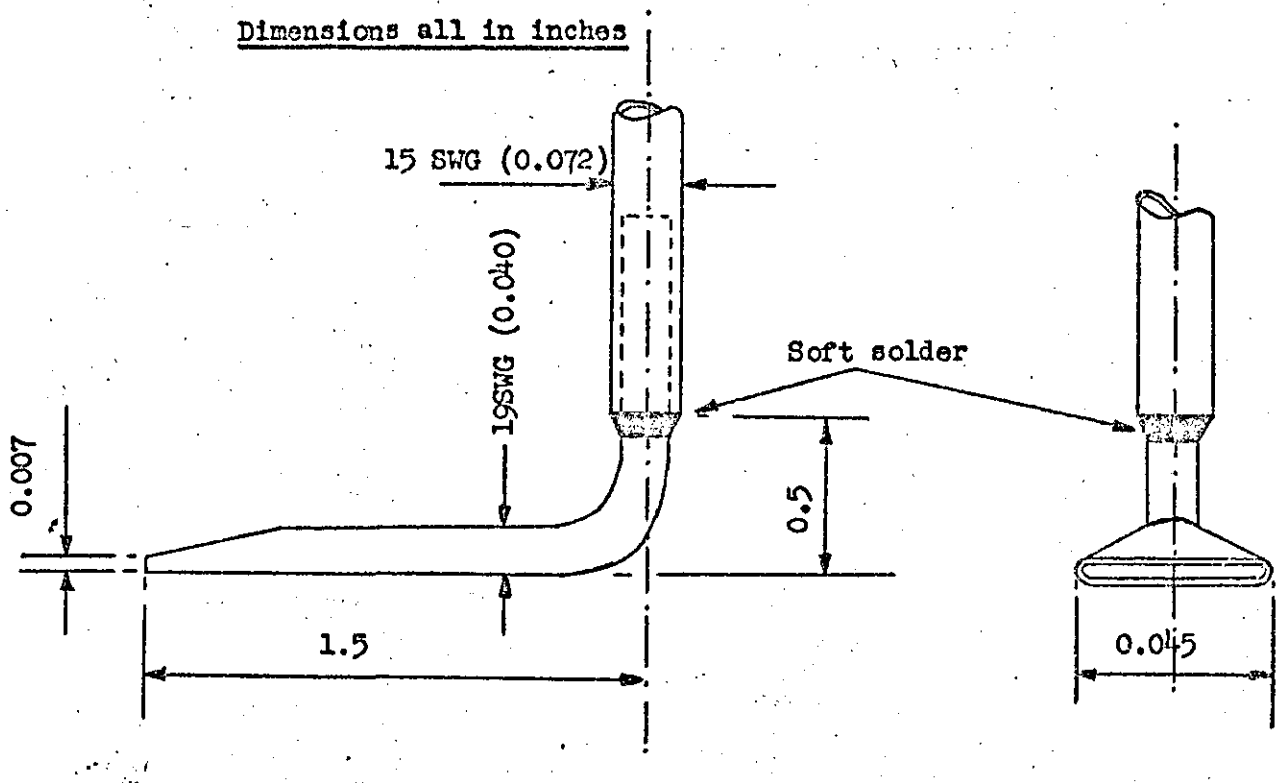

FIG. 8.5: BOUNDARY LAYER PITOT TUBE

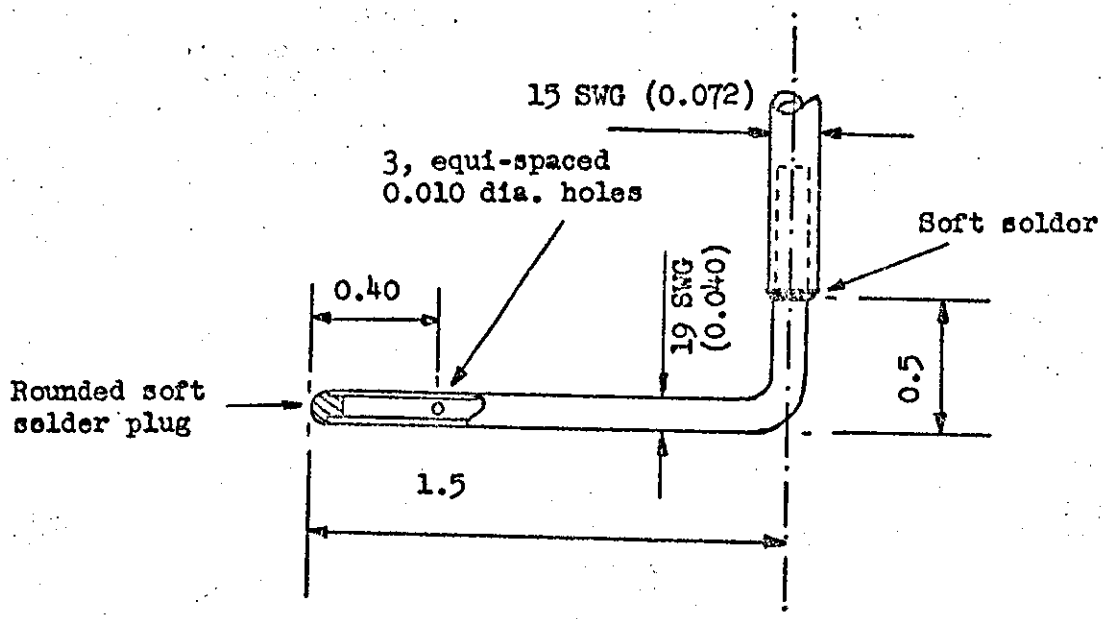

FIG. 8.4: BOUNDARY LAYER STATIC TUBE

All dimensions in inches

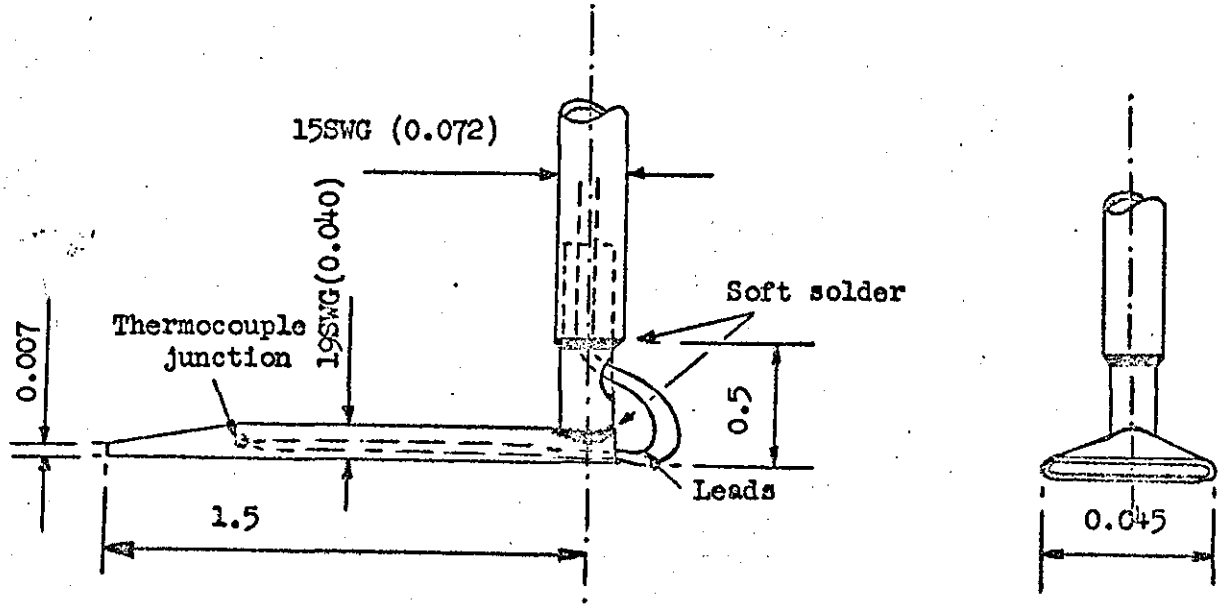

FIG. 8.5b): BOUNDARY LAYER PYROMETER

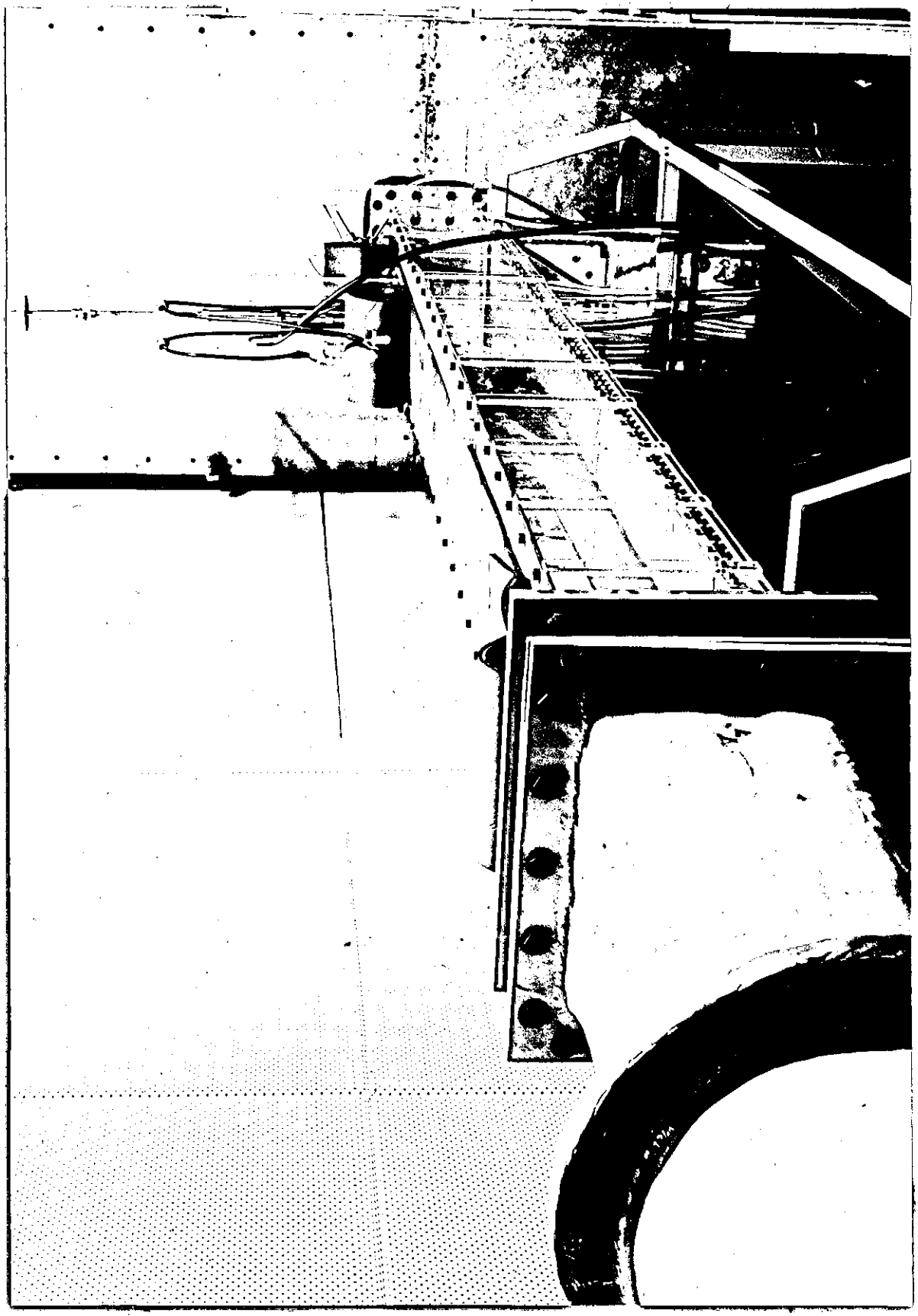

FIG. 8.6: VIEW OF TEST FACILITY FROM REAR

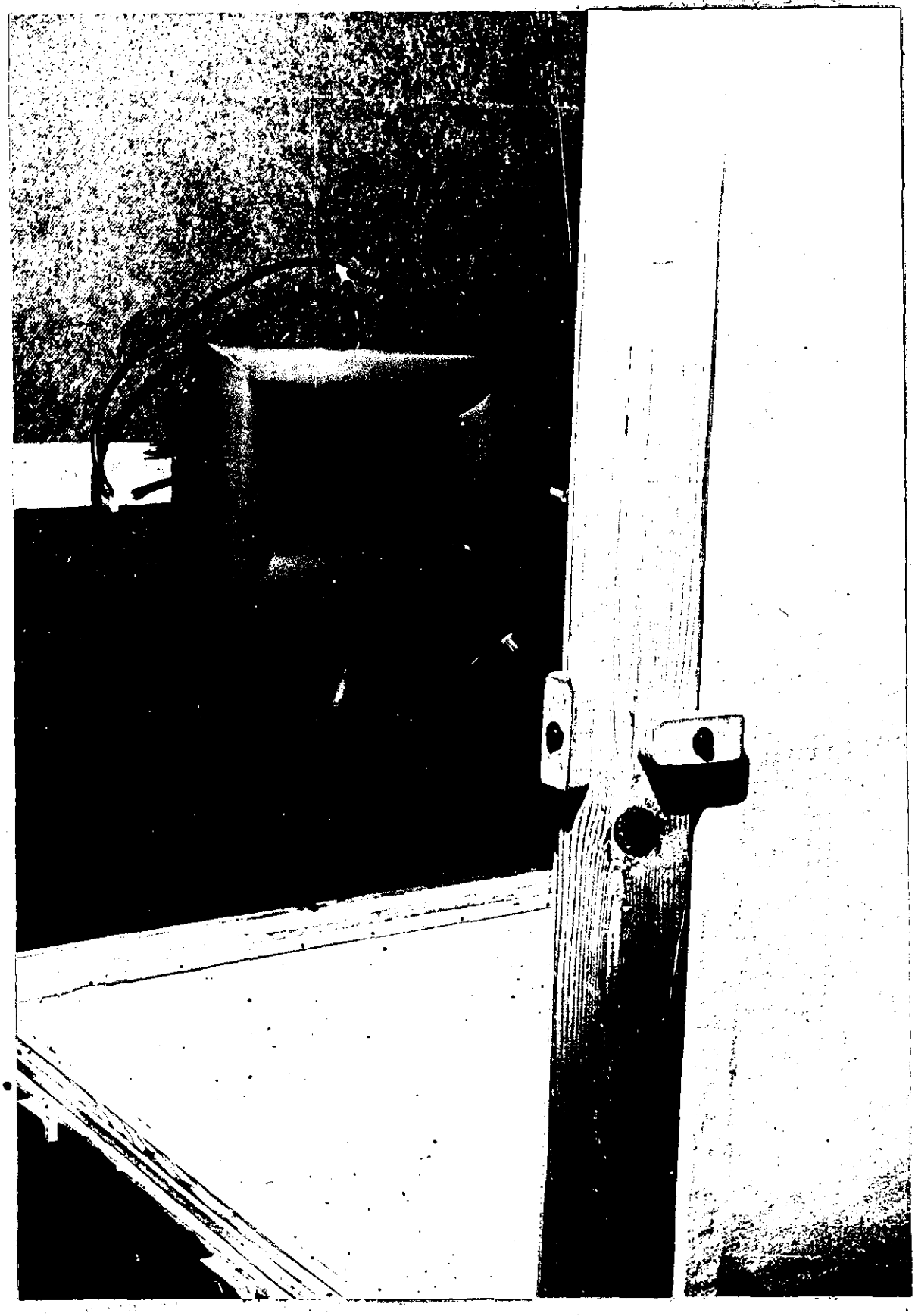

FIG. 8.7: BELLMOUTH INTAKE WITH PIEZOMETER RING FROM INSIDE L.P. FILTER

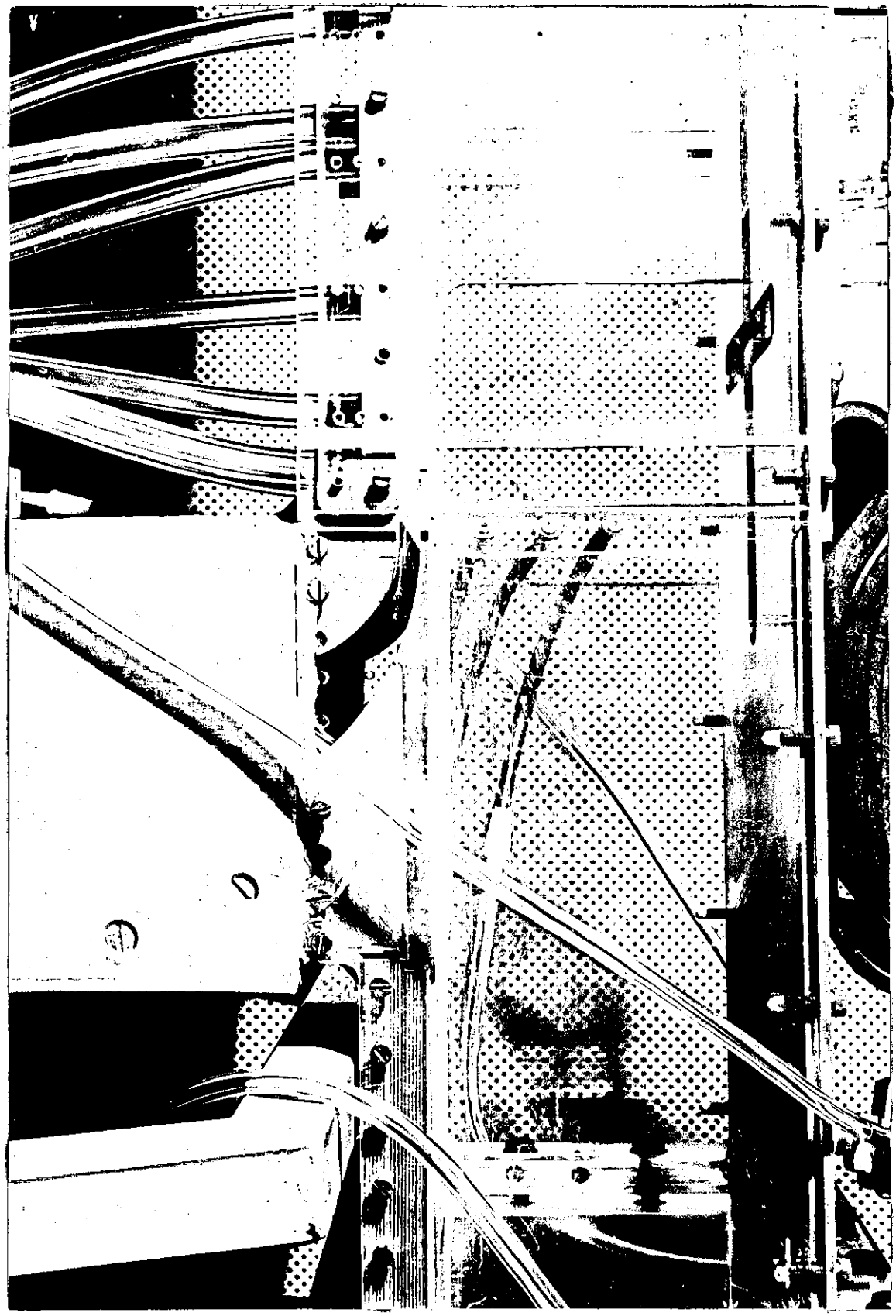

FIG. 8.8: CLOSEUP OF WORKING SECTION SHOWING SLOT CONTRACTION AND LIP

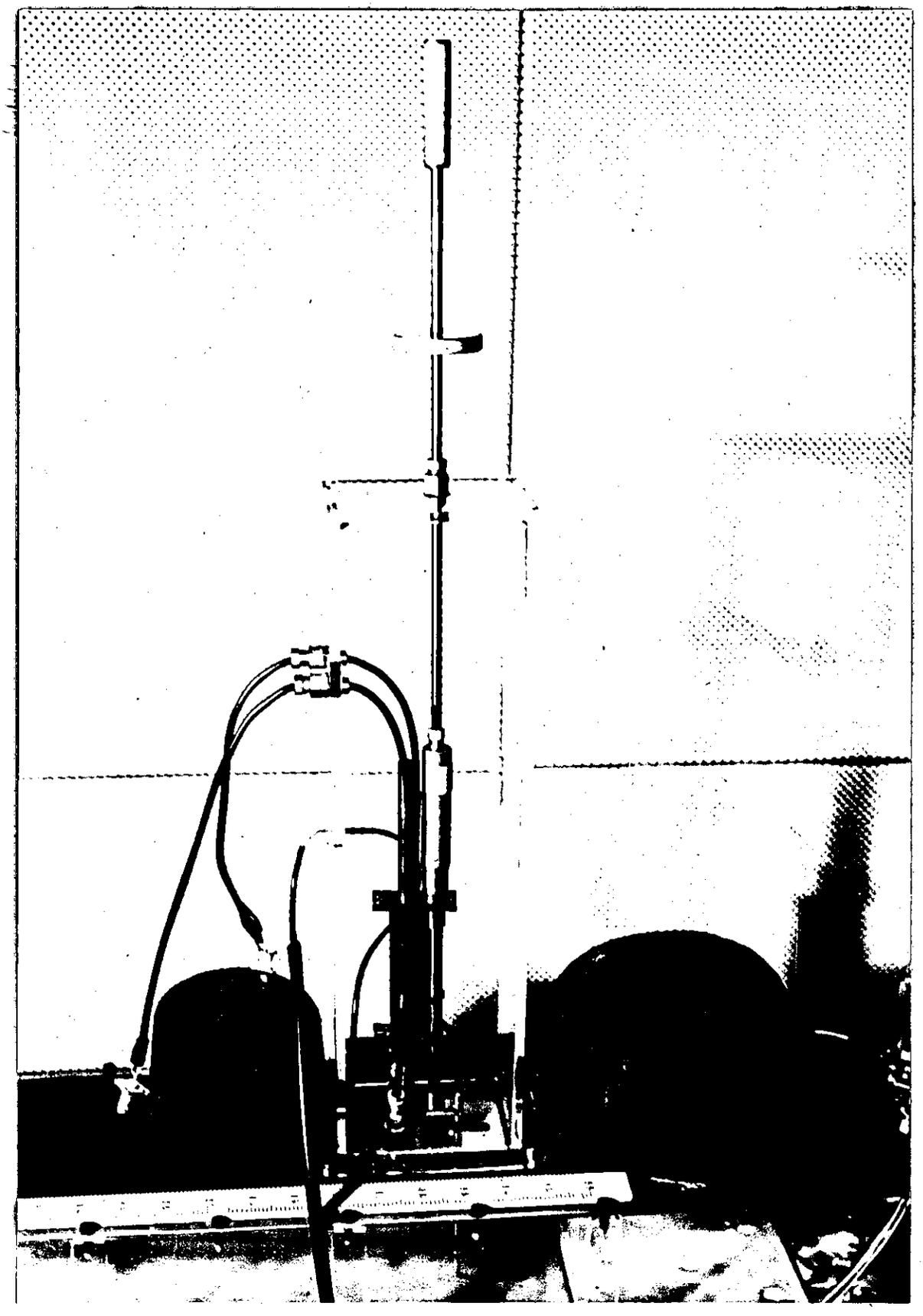

FIG. 8.9: VIEW FROM ABOVE OF TRAVERSE GEAR MOUNTED ON TUNNEL ROOF

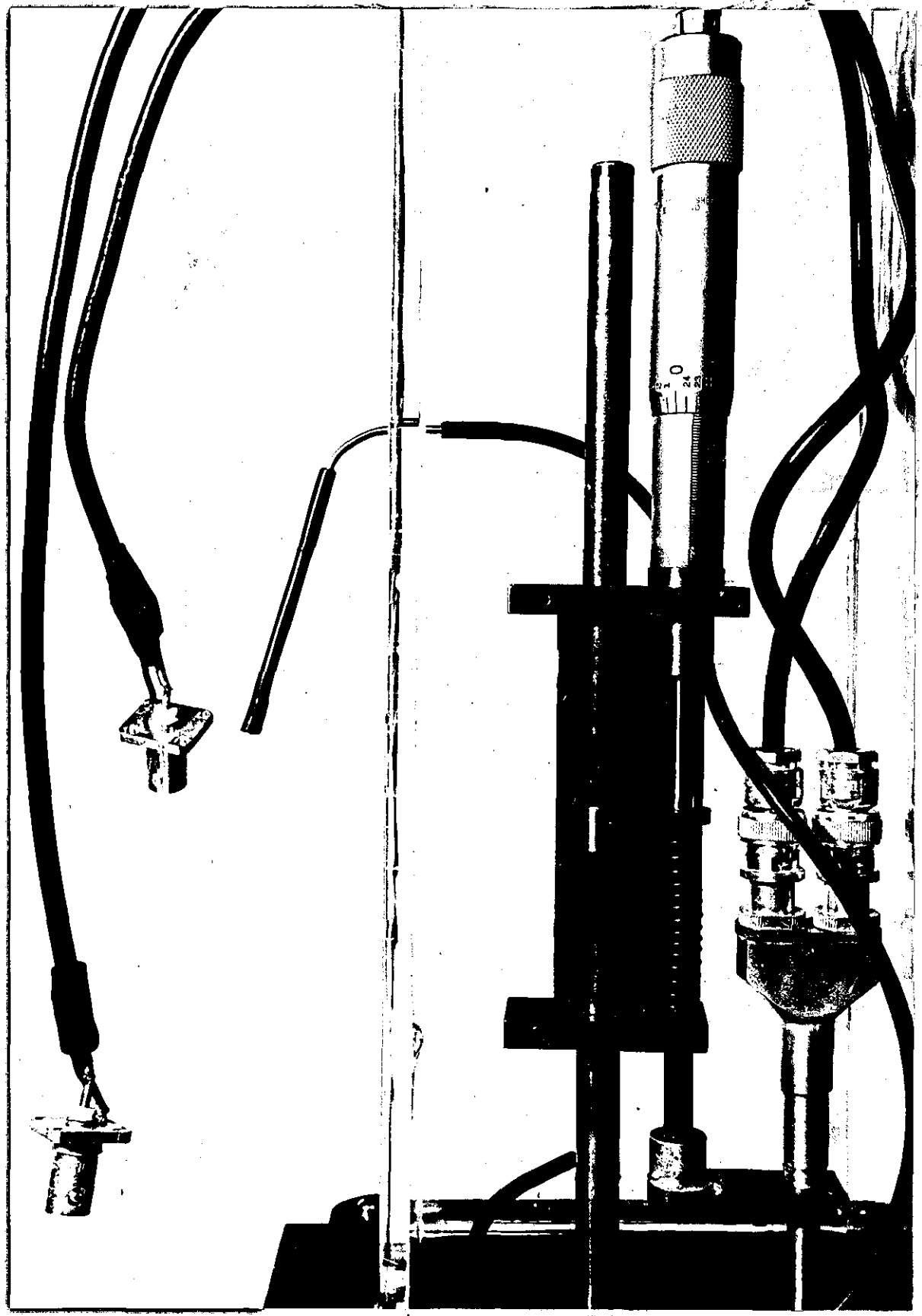

FIG. 8.10: CLOSEUP OF TRAVERSE GEAR INSIDE PRESSURE CASING

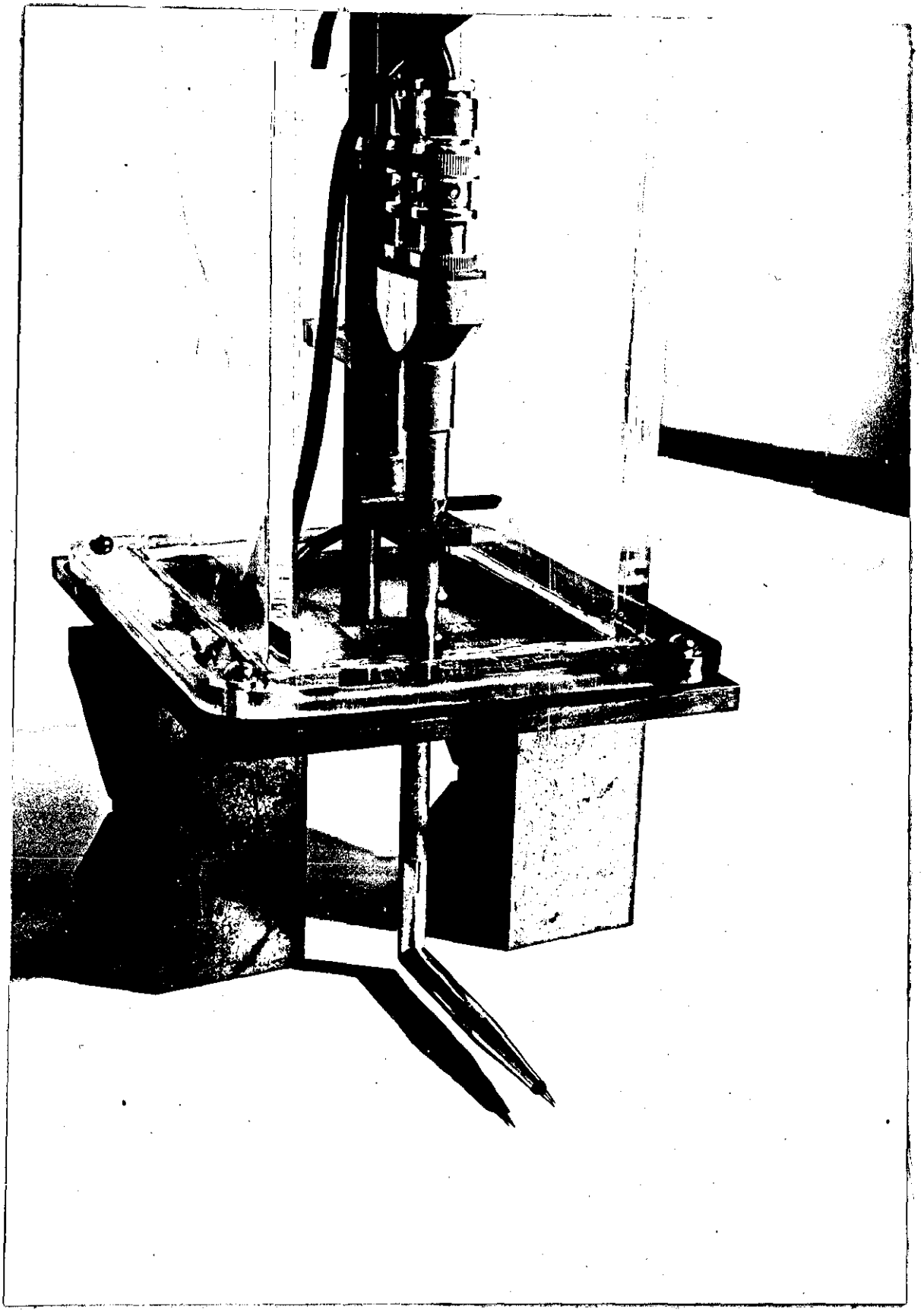

FIG. 8.11: FOREWARD VIEW OF TRAVERSE GEAR SHOWING X-PROBE HOT WIRE MOUNTED

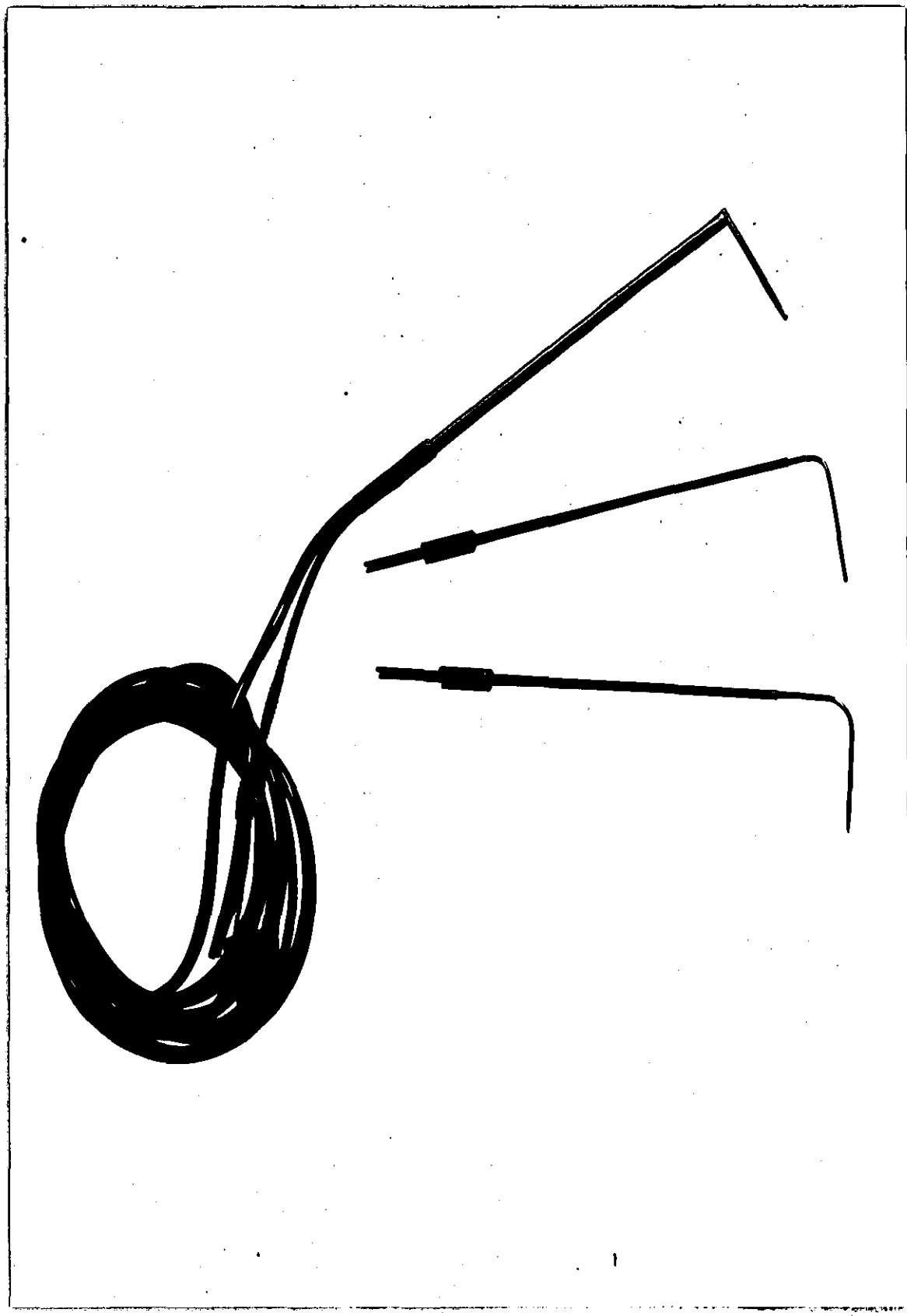

FIG. 8.12: INSTRUMENTATION, L. TO R:
TOTAL PROBE, STATIC PROBE, PYROMETER

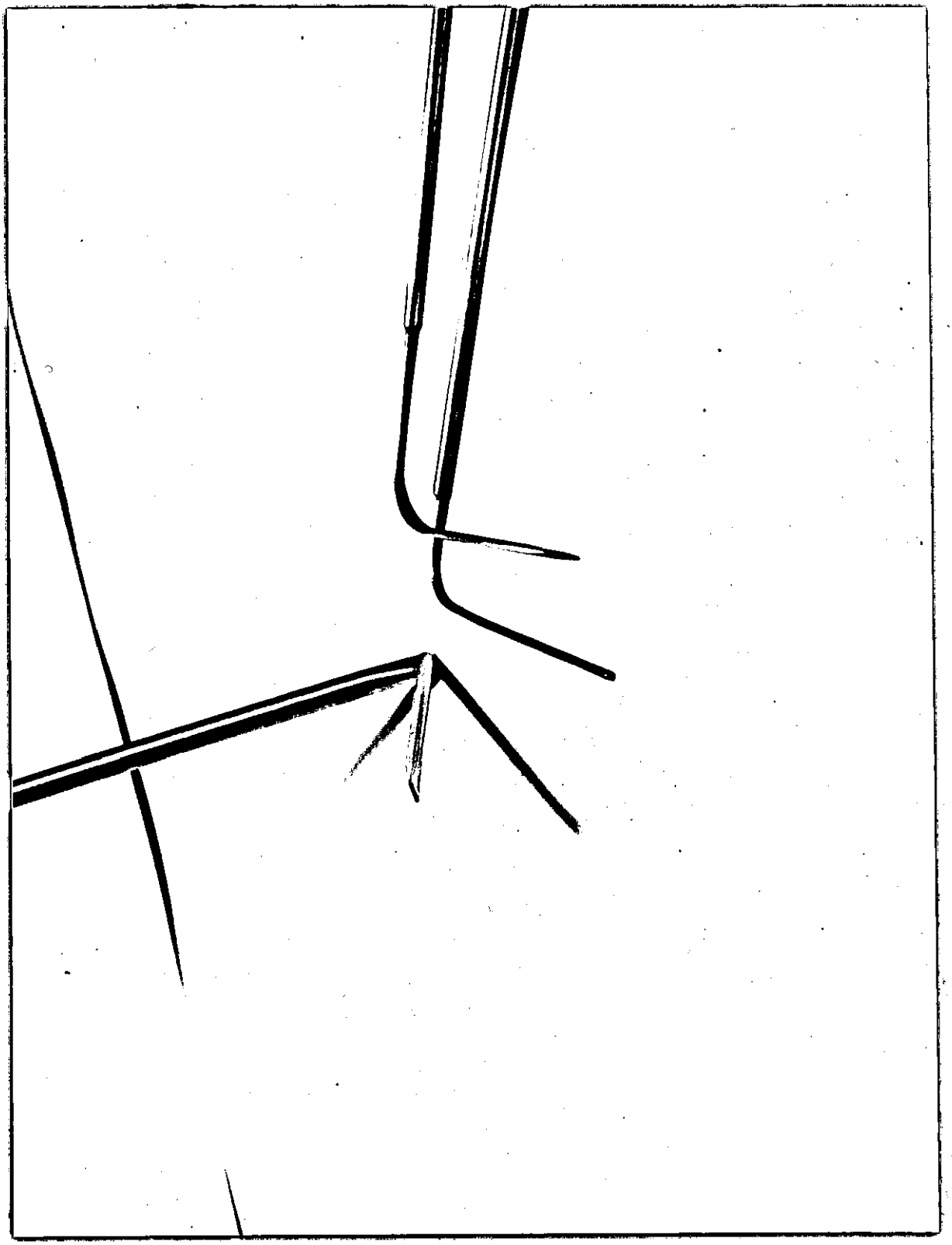

FIG. 8.13: INSTRUMENT SENSING HEADS: PYROMETER, STATIC PROBE, TOTAL PROBE

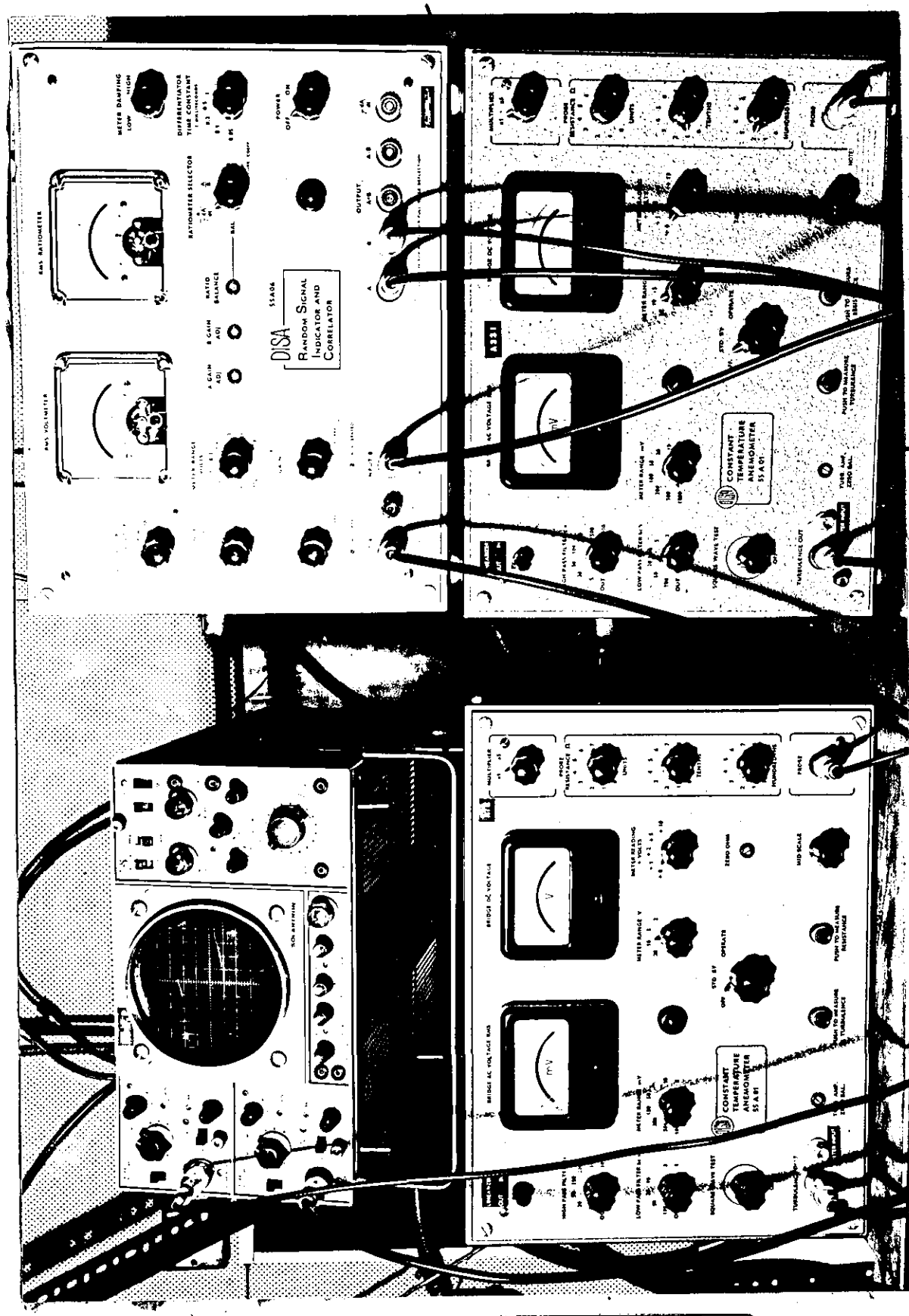

FIG. 8.14: HOT-WIRE ELECTRONICS, SET FOR X-PROBE TRANSDUCER

FIG. 9.1: CALIBRATION OF SLOT-LINE ORIFICE PLATE

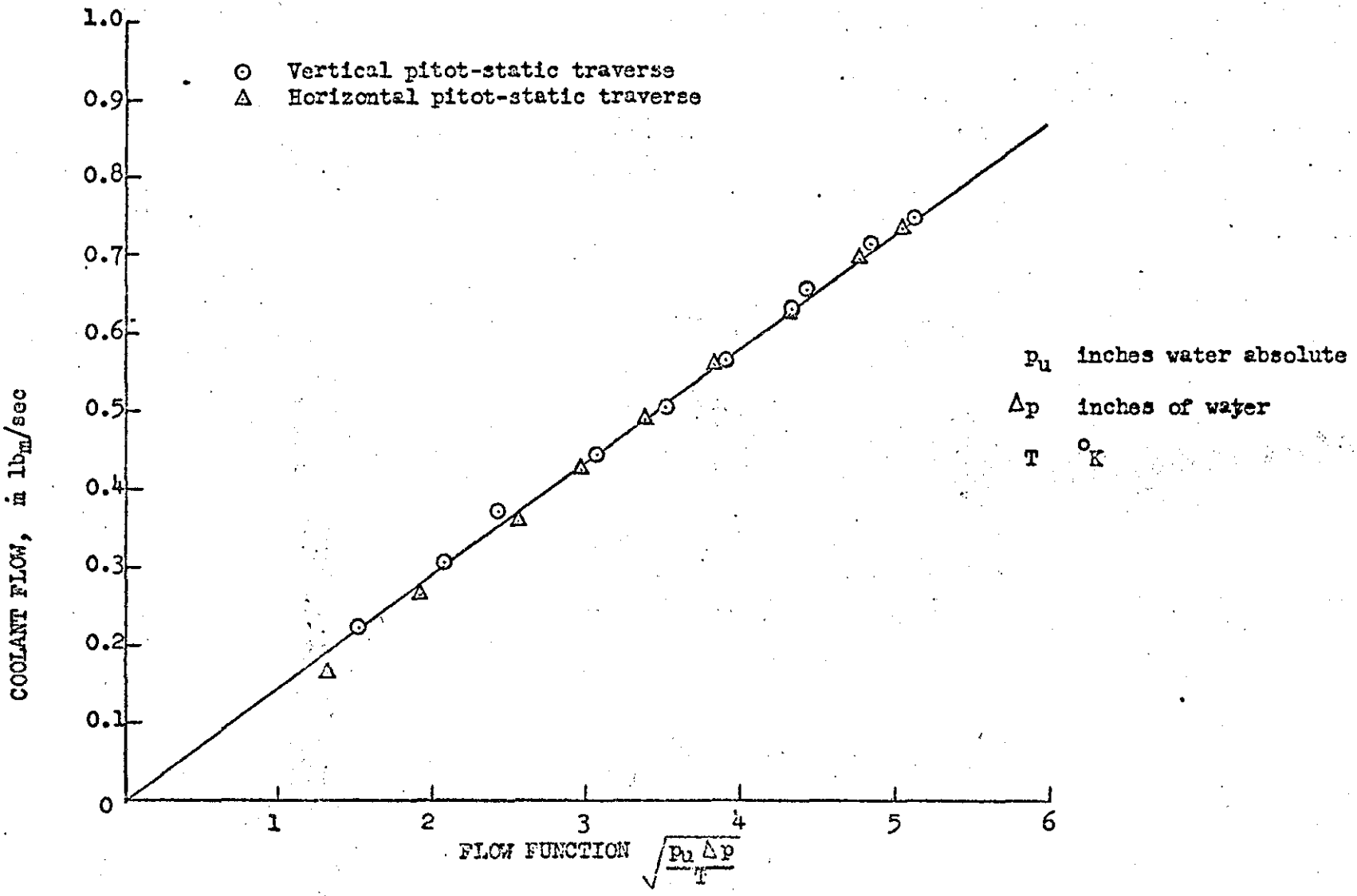

FIG. 9.2: ORIFICE SECTION THERMOCOUPLE WATER-BATH CALIBRATION

Date: 17.5.68.

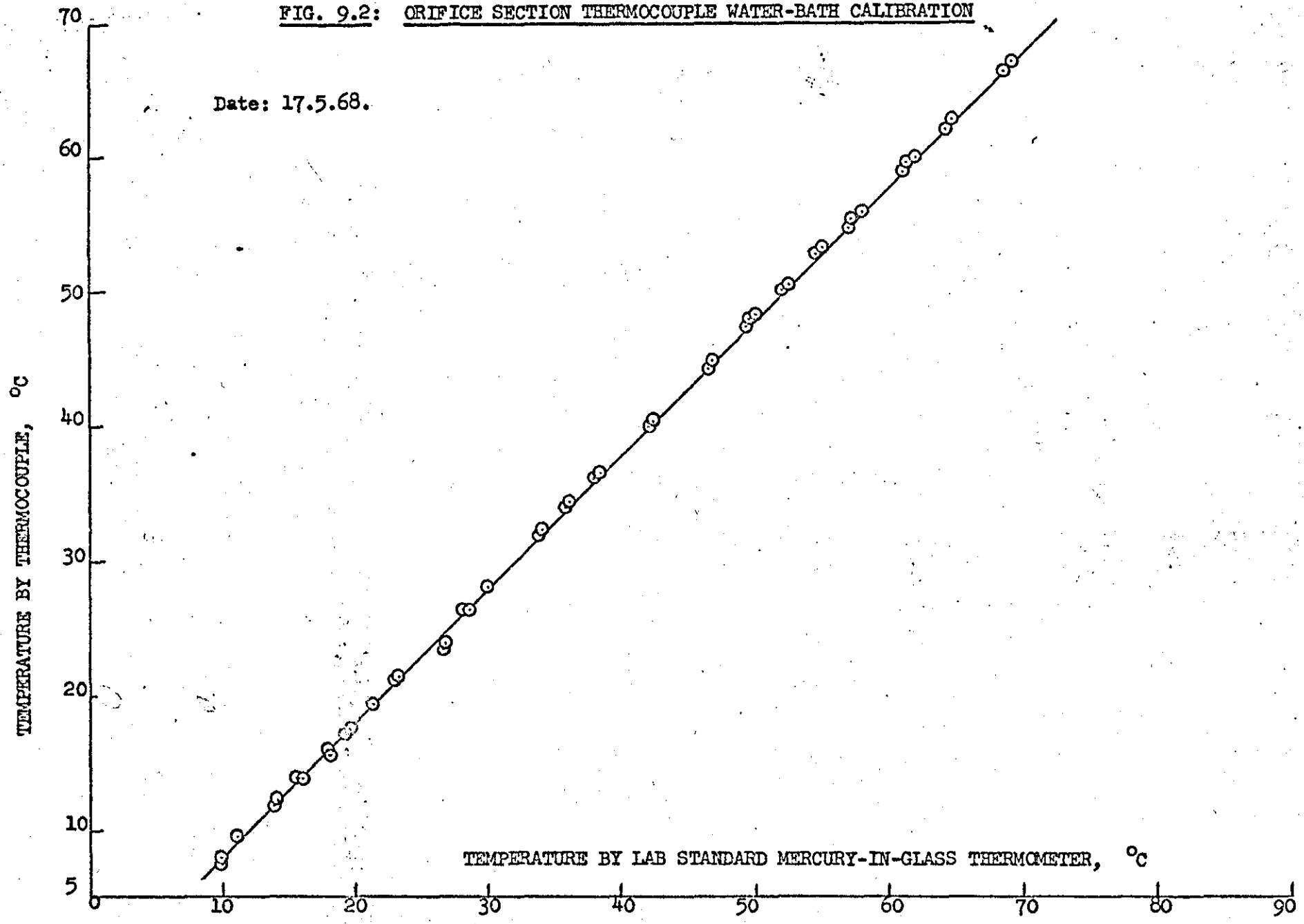

FIG. 9.3: CALIBRATION OF TUNNEL INTAKE

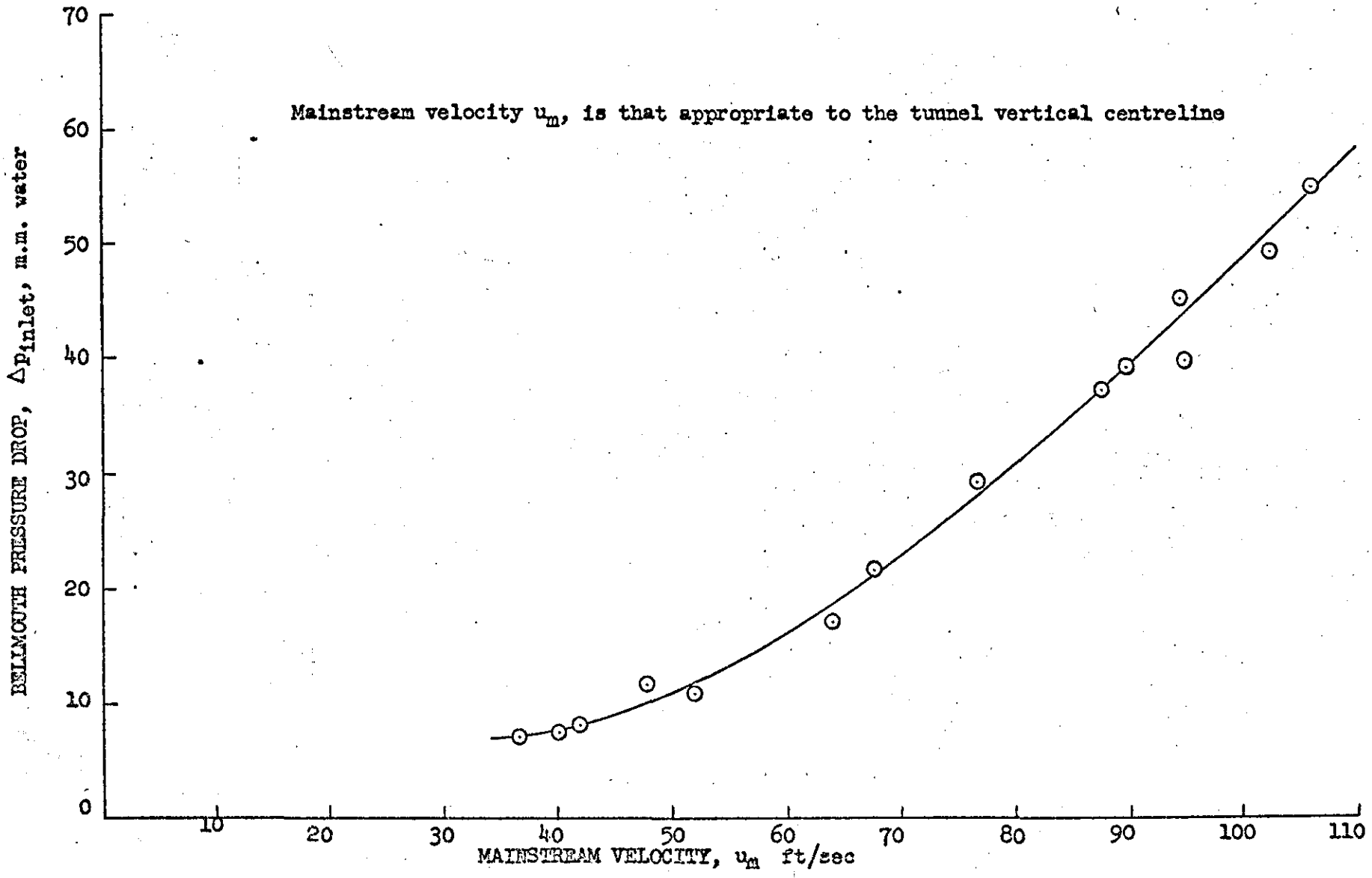

FIG. 9.4: TUNNEL STATIC PRESSURE GRADIENT ALONG FLOOR CENTRELINE

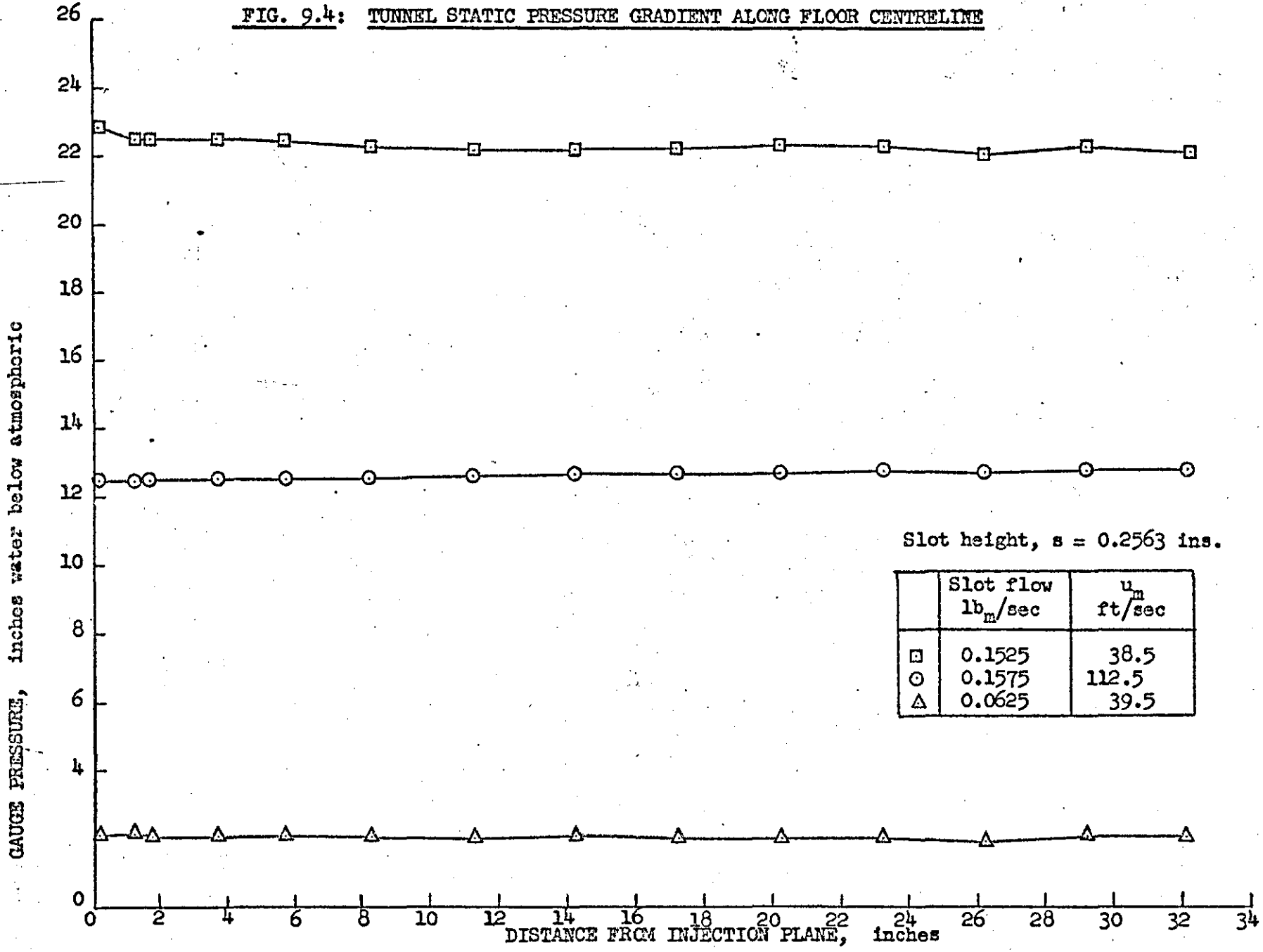

Slot height, s = 0.2563 ins.

	Slot flow lb_m/sec	u_m ft/sec
□	0.1525	38.5
○	0.1575	112.5
△	0.0625	39.5

FIG. 9.5: TRANSVERSE STATIC PRESSURE GRADIENT IN SLOT

Slot height = 0.2563 ins.

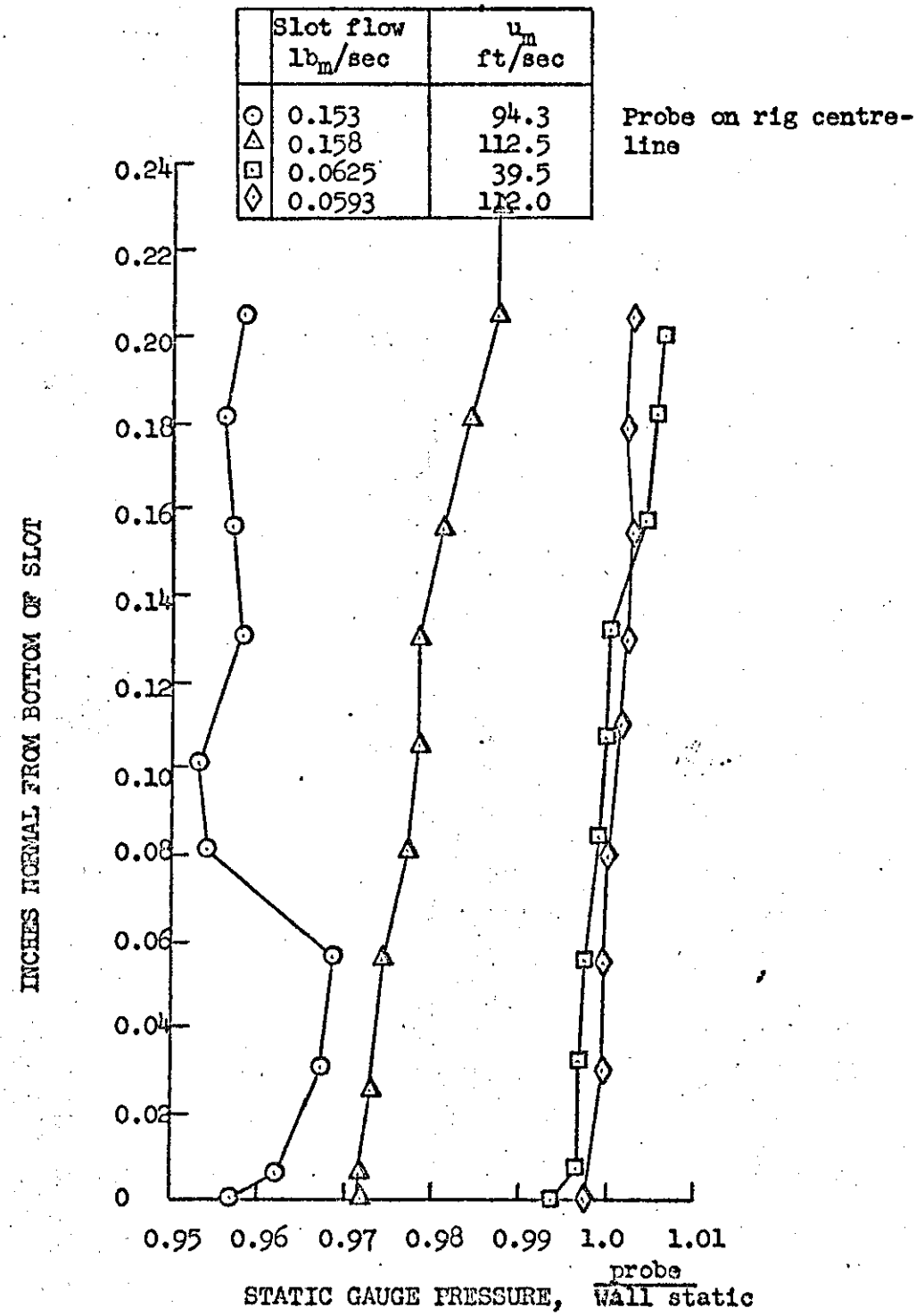

FIG. 9.6: TRANSVERSE STATIC PRESSURE GRADIENT ON SLOT LIP

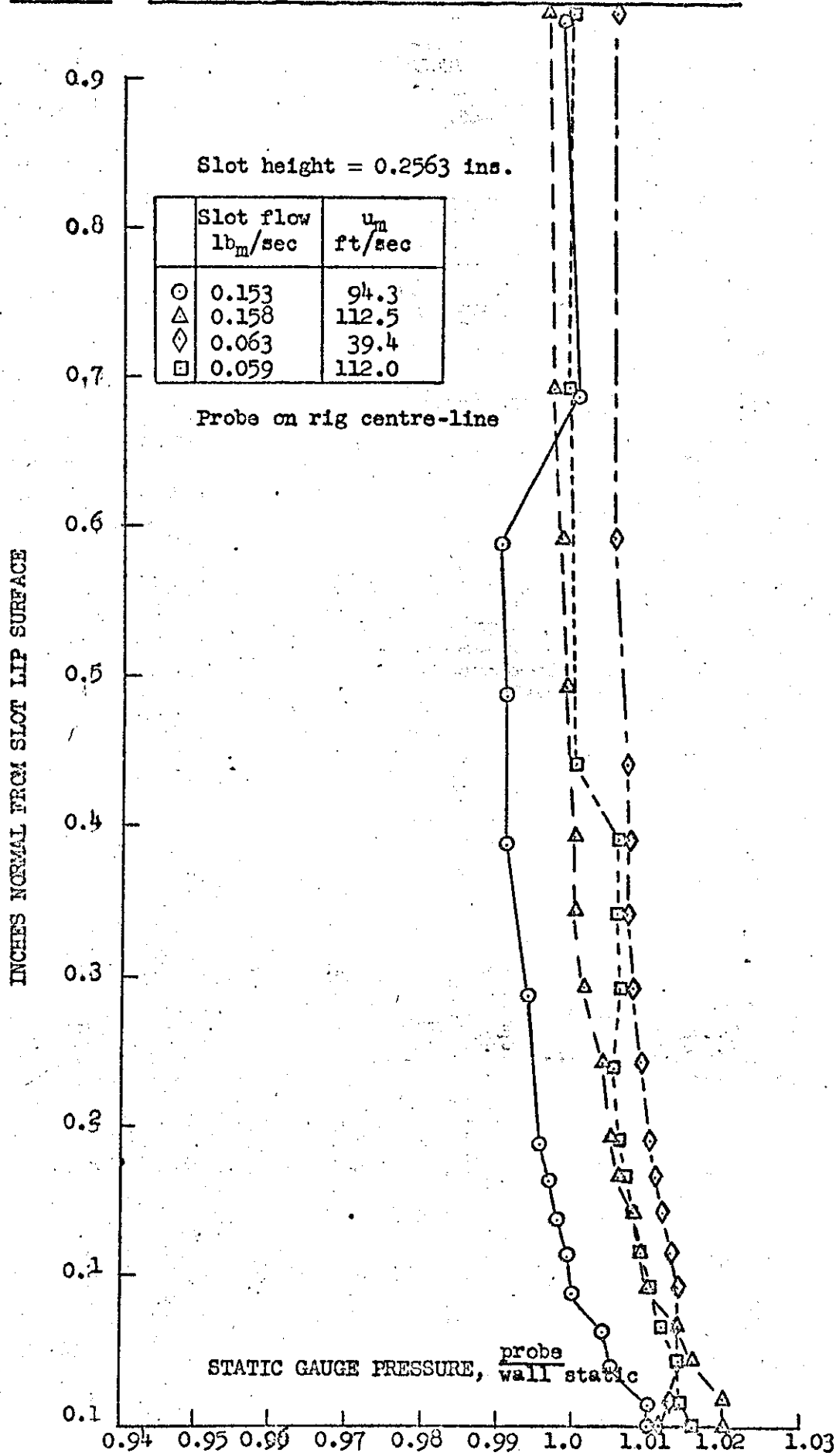

FIG. 9.7: NORMAL STATIC PRESSURE GRADIENTS AT DOWNSTREAM LOCATIONS

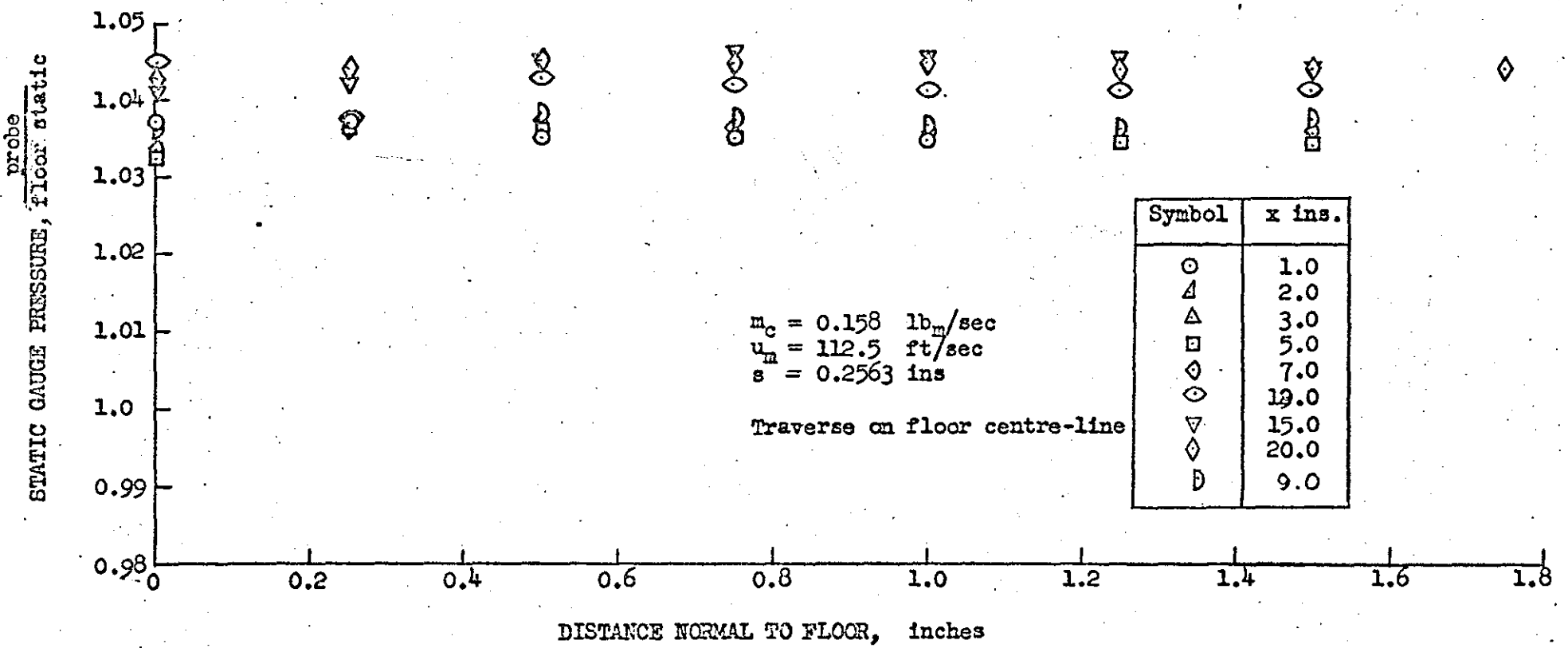

D117

FIG. 9.8: NORMAL STATIC PRESSURE GRADIENTS AT DOWNSTREAM LOCATIONS

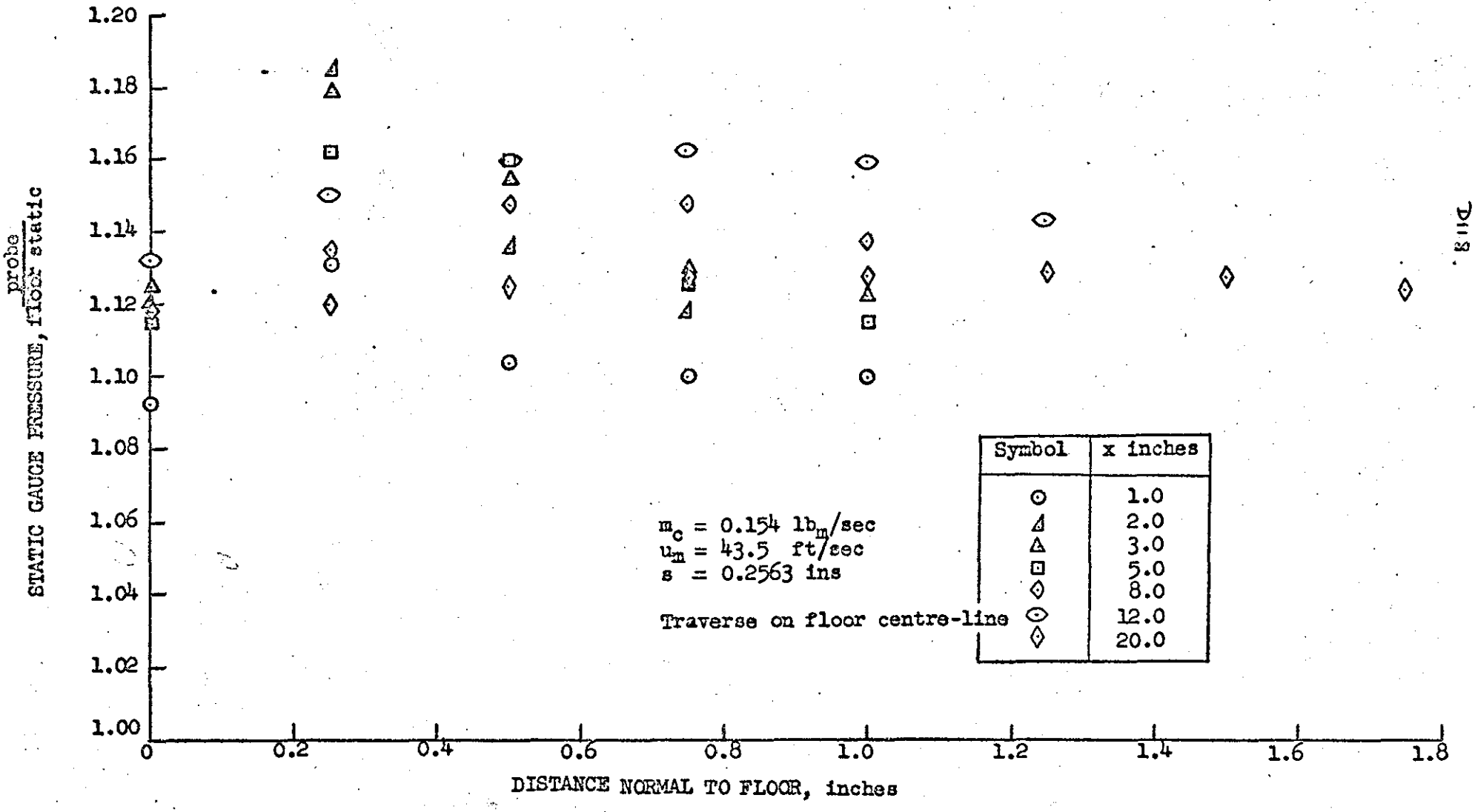

FIG. 9.9: NORMAL STATIC PRESSURE GRADIENTS AT DOWNSTREAM LOCATIONS

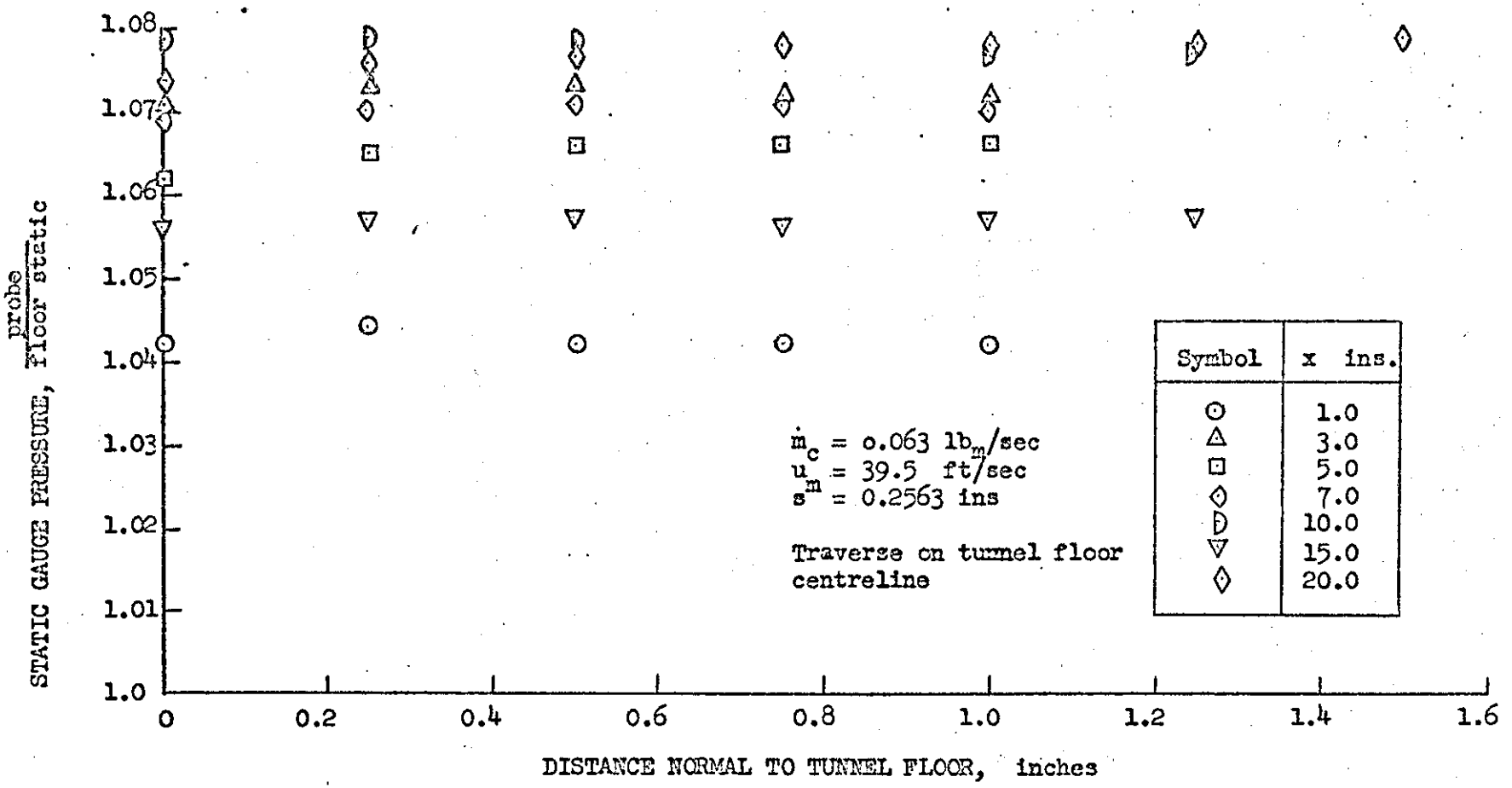

FIG. 9.10: NORMAL STATIC PRESSURE GRADIENTS AT DOWNSTREAM LOCATIONS

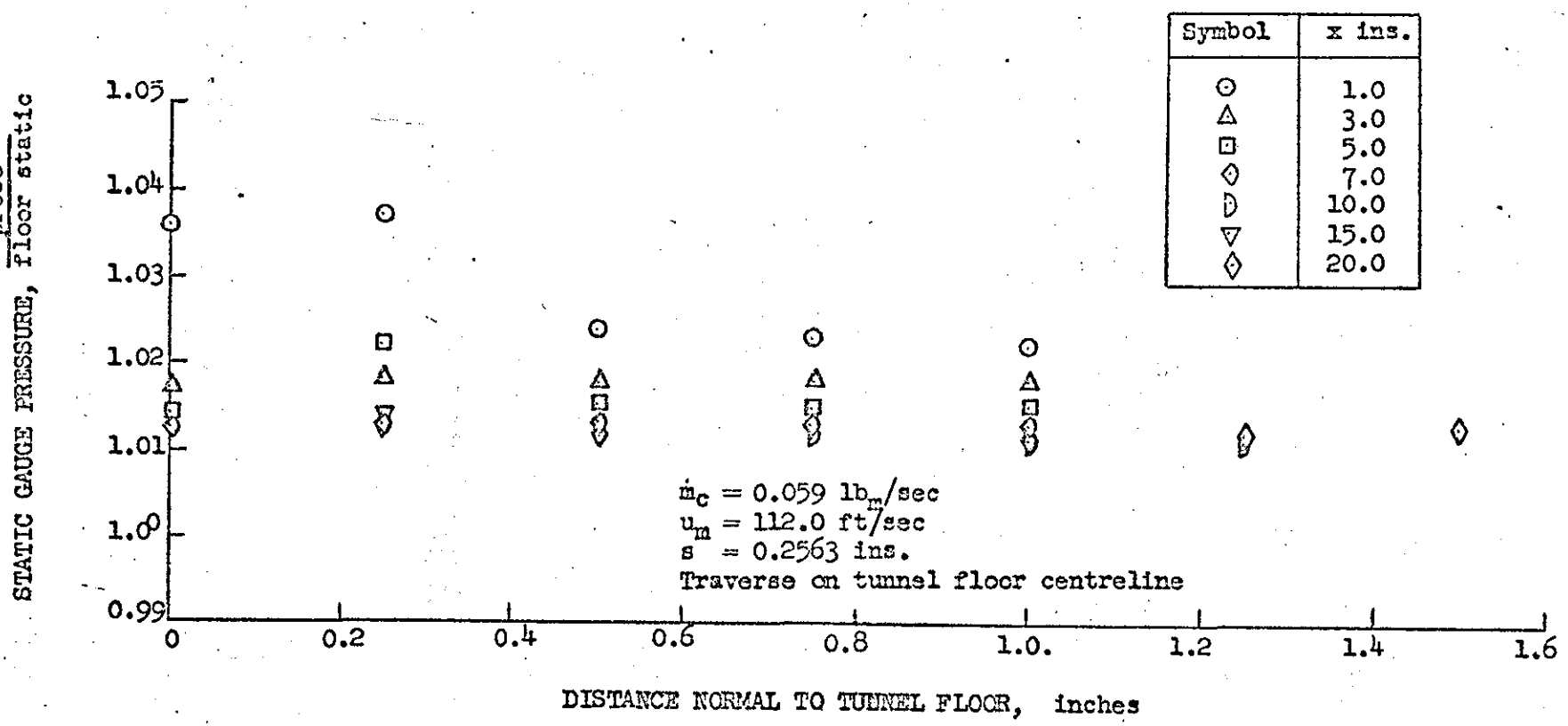

FIG. 9.11: FIEM TRANSVERSE STATIC PRESSURE GRADIENTS IN NEIGHBOURHOOD OF SLOT LIP

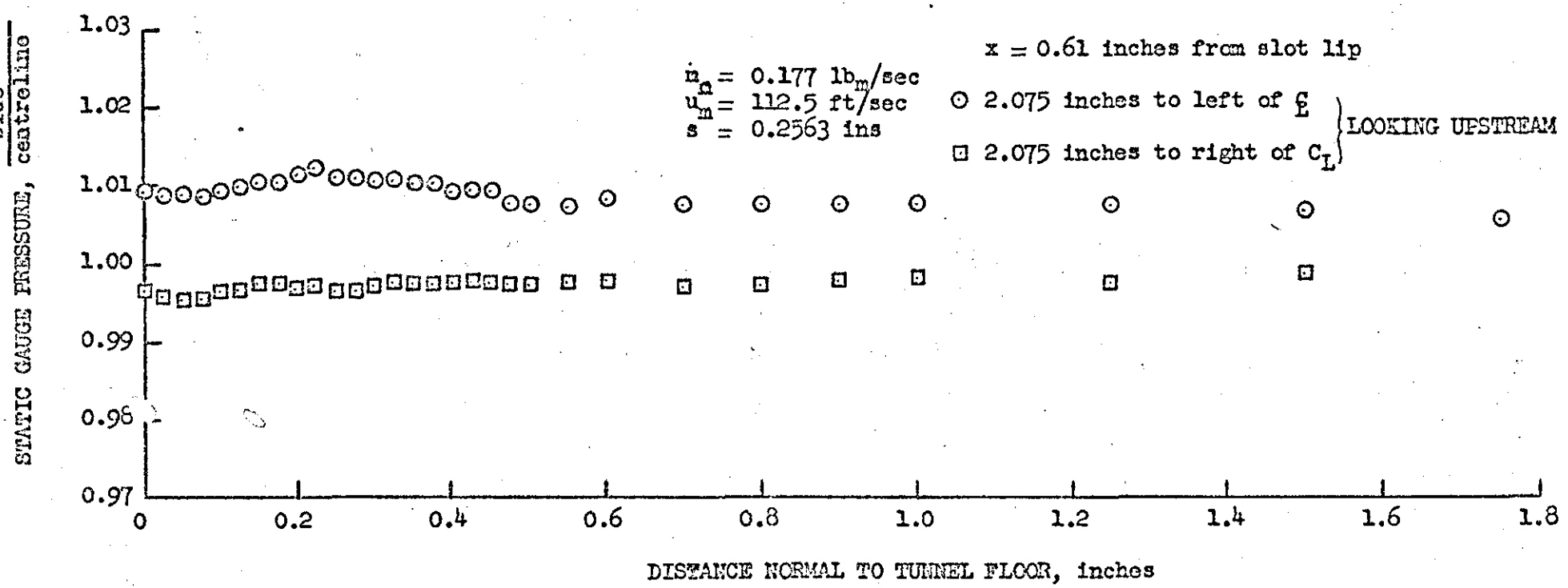

FIG. 9.12: TRANSVERSE STATIC PRESSURE GRADIENTS IN NEIGHBOURHOOD OF SLOT LIP

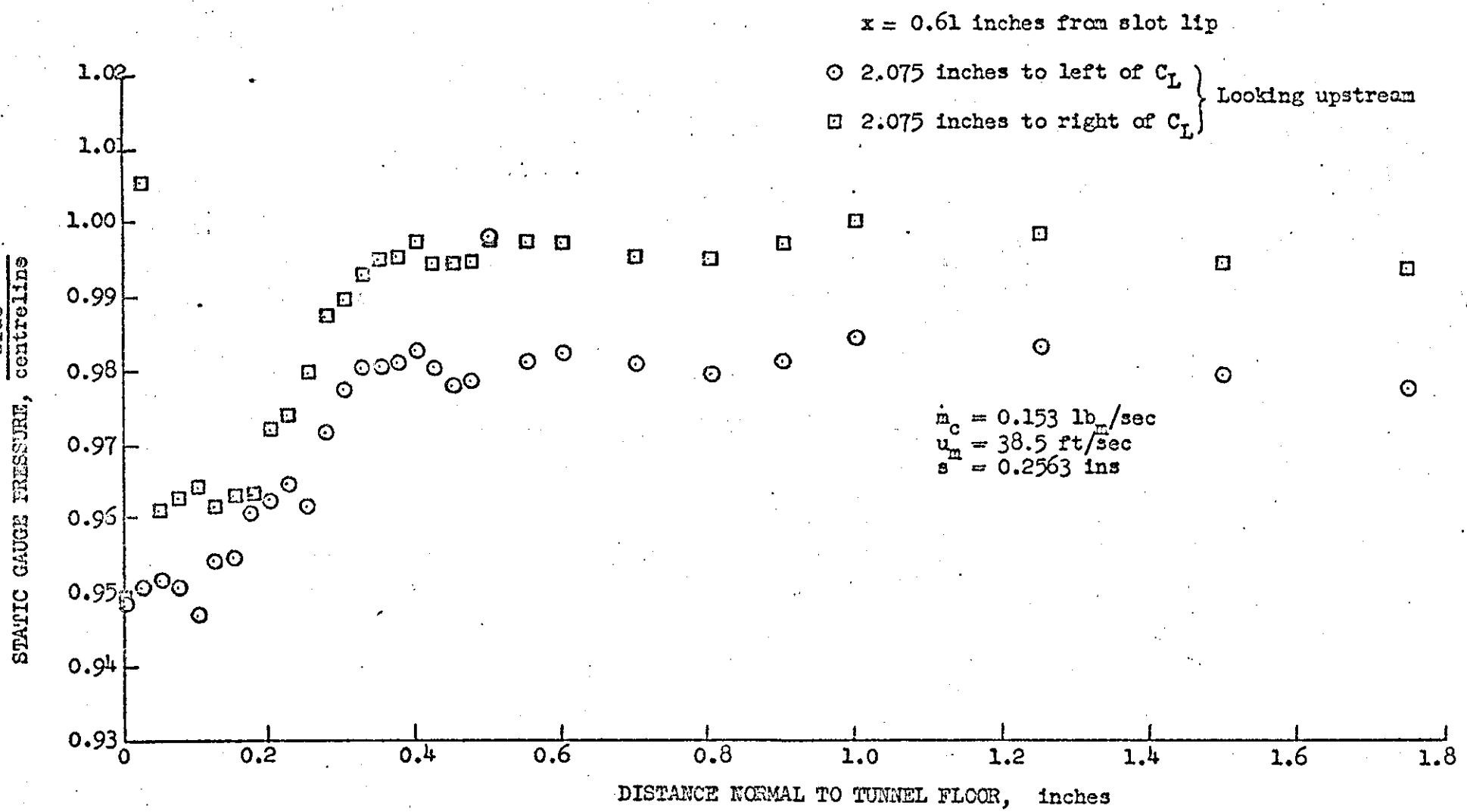

D12.

FIG. 9.13: FILM TRANSVERSE STATIC PRESSURE GRADIENTS IN NEIGHBOURHOOD OF SLOT LIP

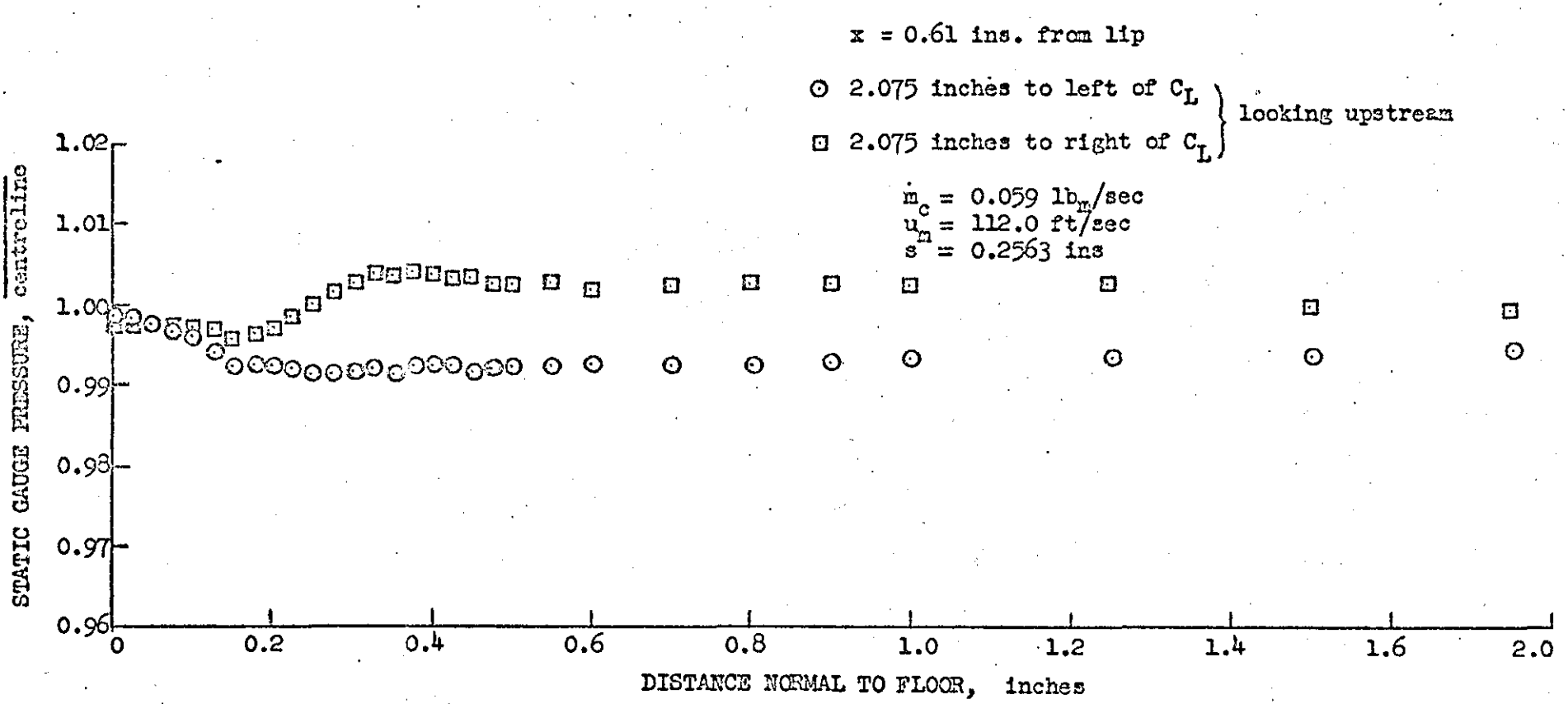

FIG. 9.14: TWO-DIMENSIONALITY OF VELOCITY PROFILES IN THE NEIGHBOURHOOD OF INJECTION

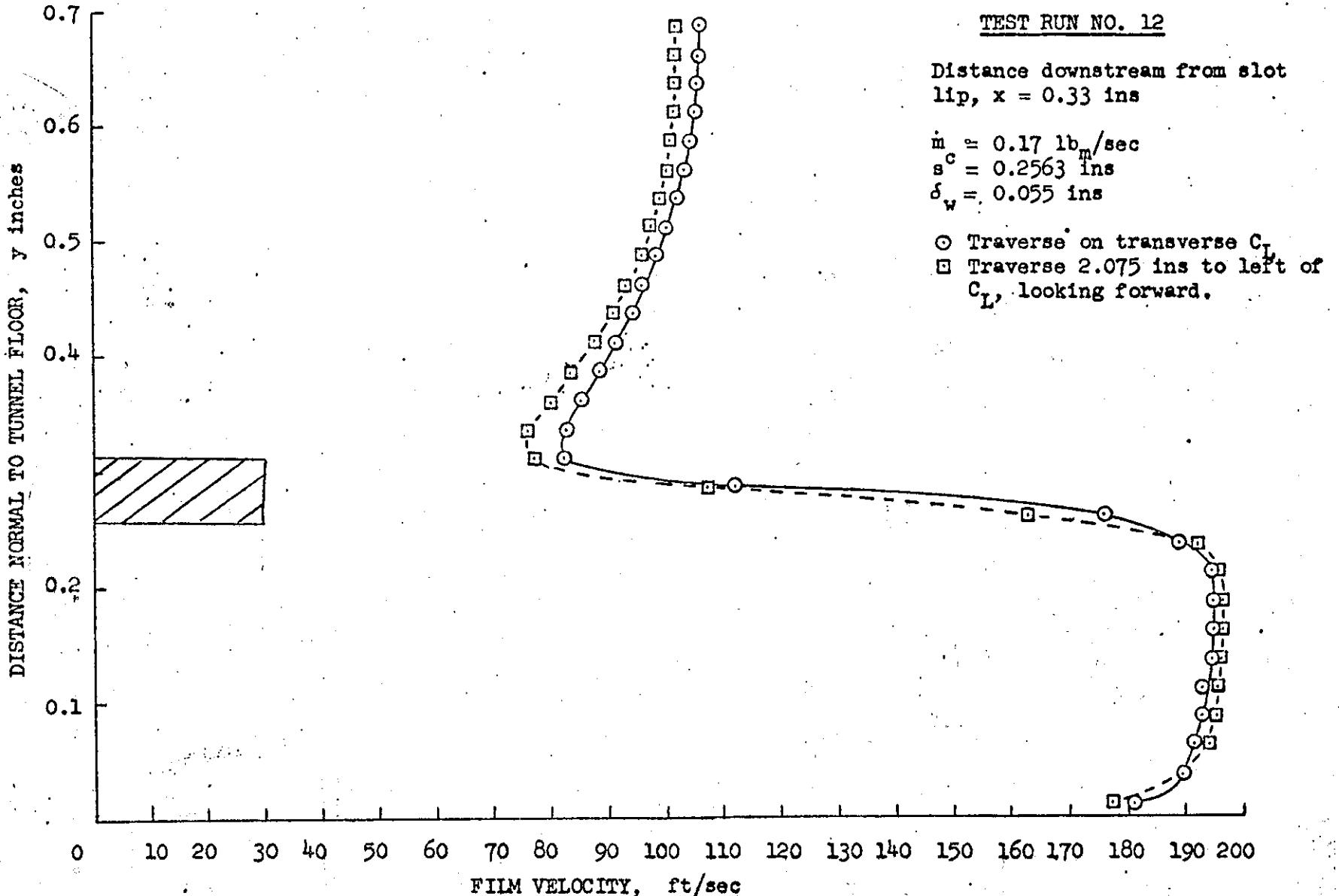

FIG. 9.15: TWO-DIMENSIONALITY OF VELOCITY PROFILES IN THE NEIGHBOURHOOD OF INJECTION

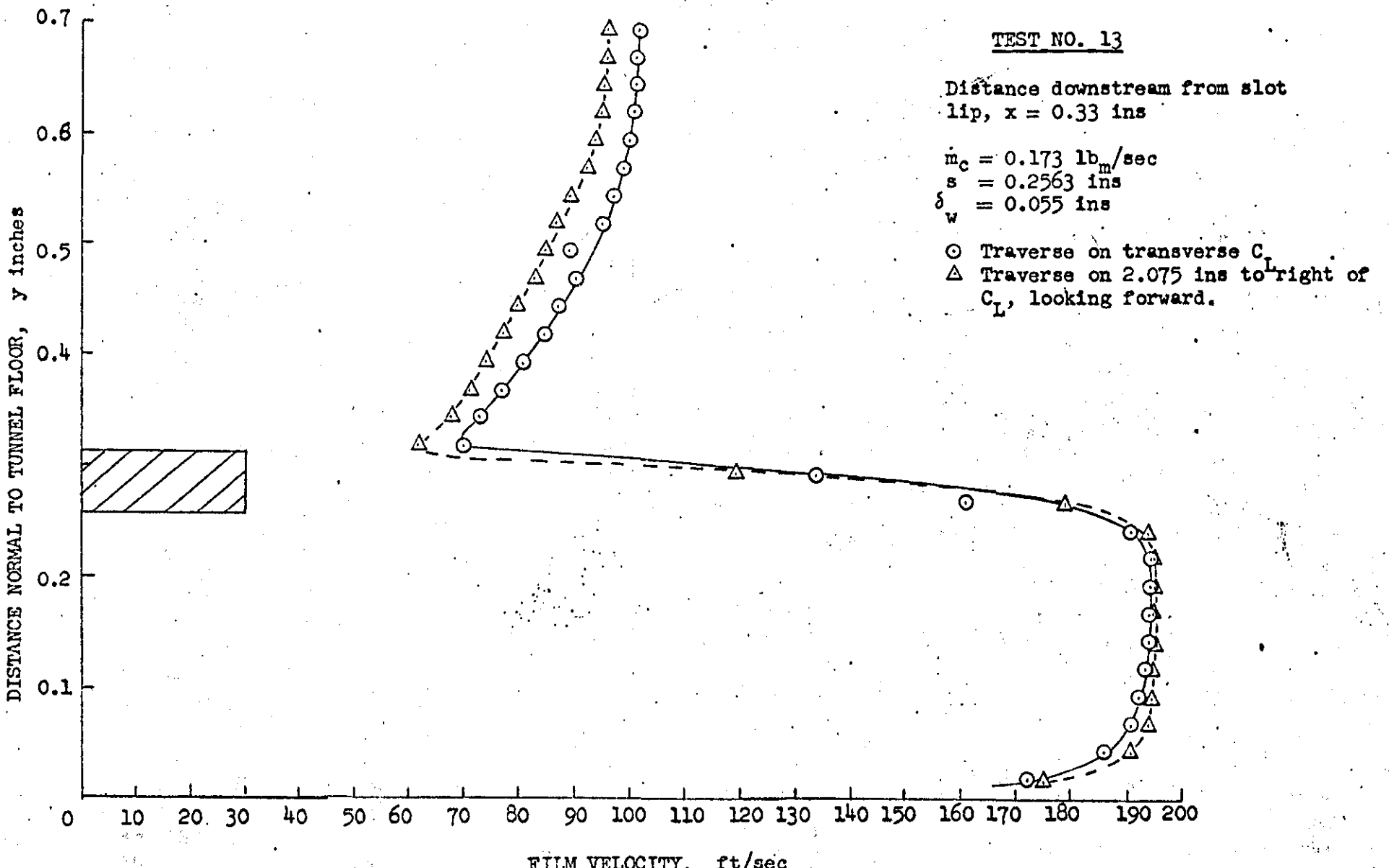

D125

FIG. 9.16: TWO-DIMENSIONALITY OF VELOCITY PROFILES IN THE NEIGHBOURHOOD OF INJECTION

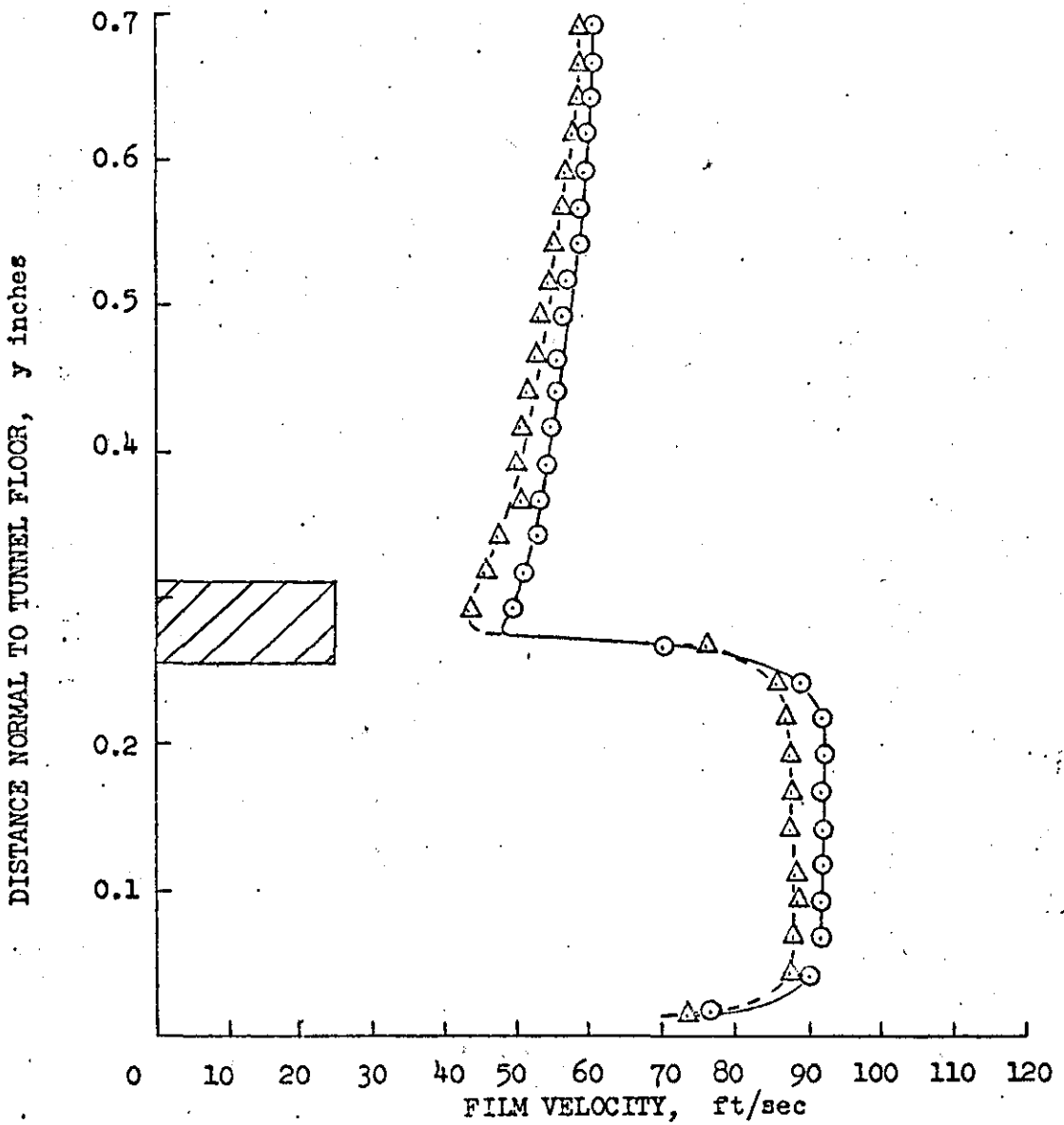

TEST RUN NO. 14

Distance downstream from slot lip, x = 0.33 ins

$\dot{m}_c$ = 0.059 lb_m/sec
s = 0.2563 ins
δ_w = 0.055 ins

⊙ Traverse on transverse C_L
△ Traverse 2.075 ins to right of C_L, looking forward.

FIG. 9.17: TWO-DIMENSIONALITY OF VELOCITY PROFILES IN THE NEIGHBOURHOOD OF INJECTION

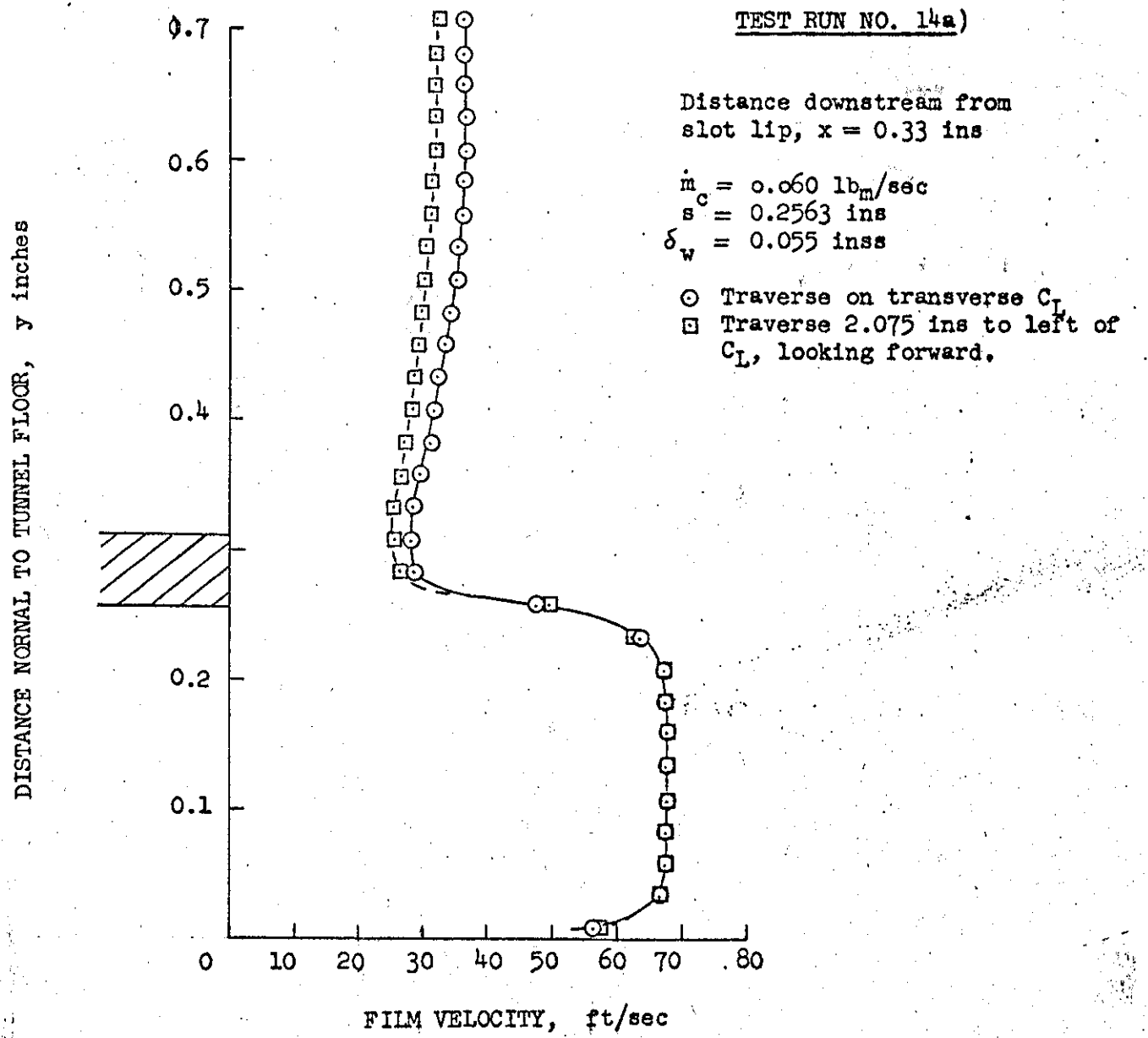

FIG. 9.18: CLAUSER PLOT FOR DATA OF TEST RUN NUMBER 33

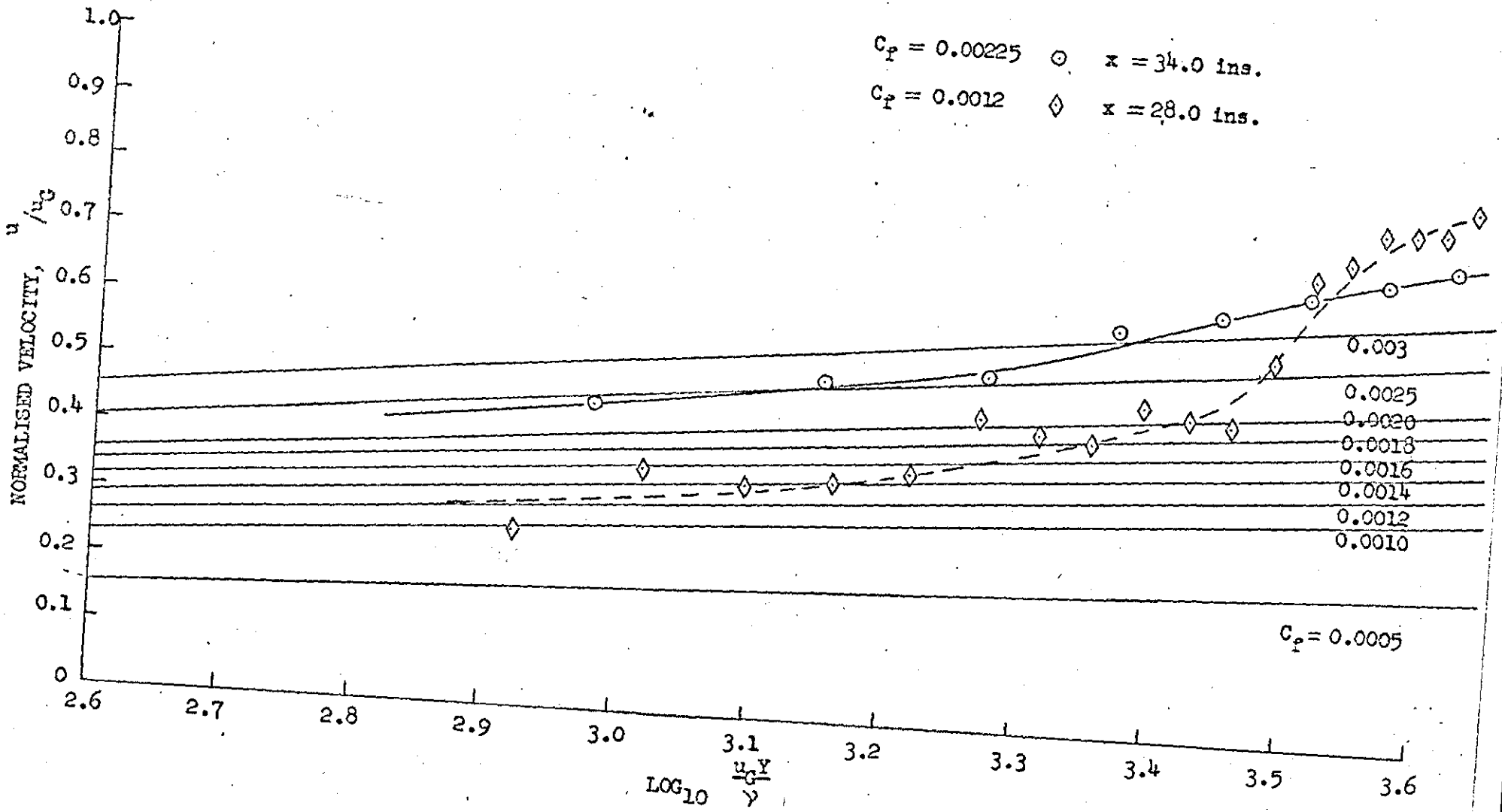

FIG. 9.19: COMPARISON OF MEASURED VELOCITY PROFILES IN TUNNEL WITH UNIVERSAL PROFILE FOR INNER REGIONS

(ZERO BLOWING)

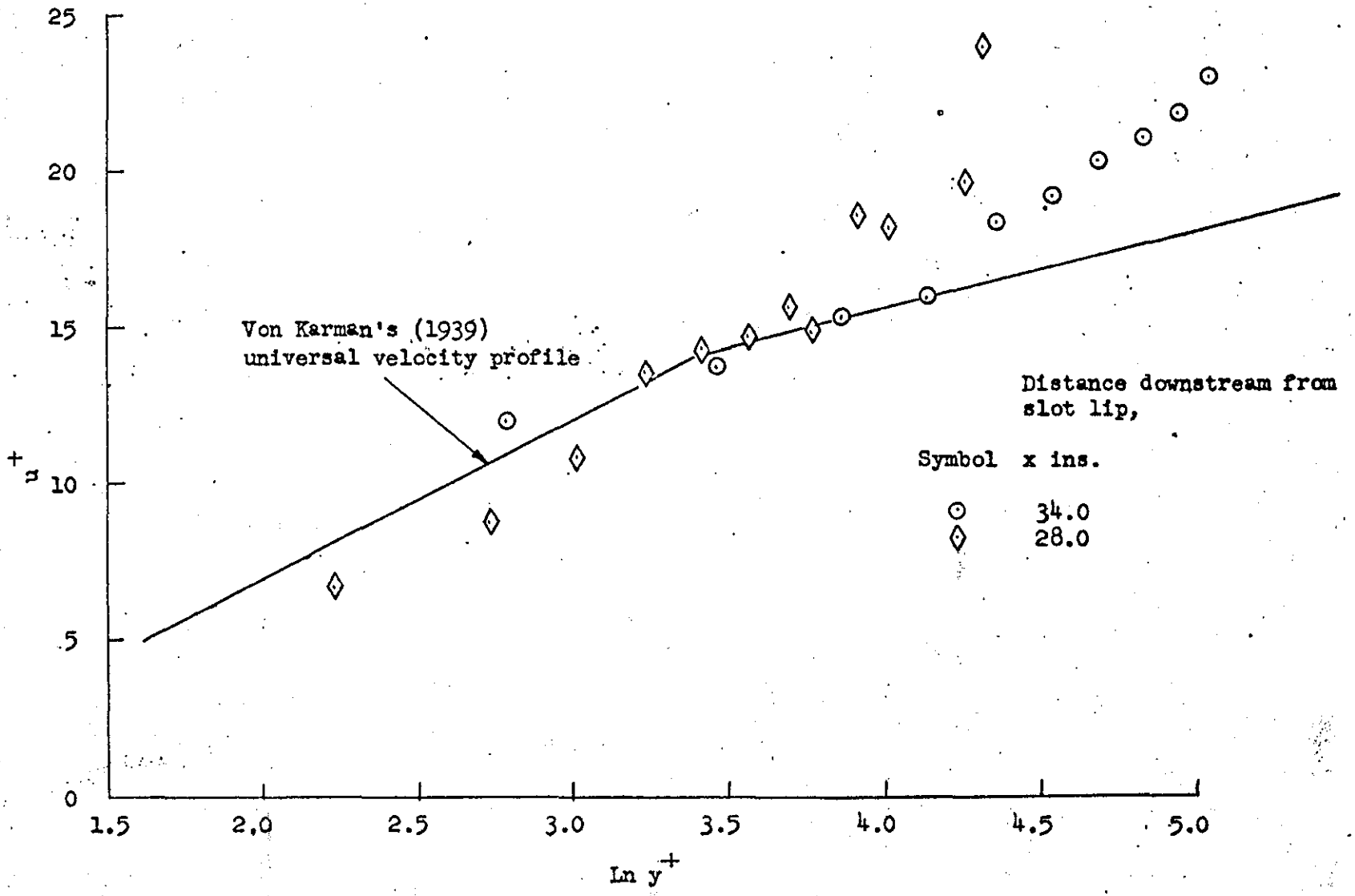

FIG. 10.1: VELOCITY PROFILE DEVELOPMENT FOR THIN-LIPPED SLOT - a) JET-LIKE FLOW

Test Run No. 15

Distance downstream from injection:

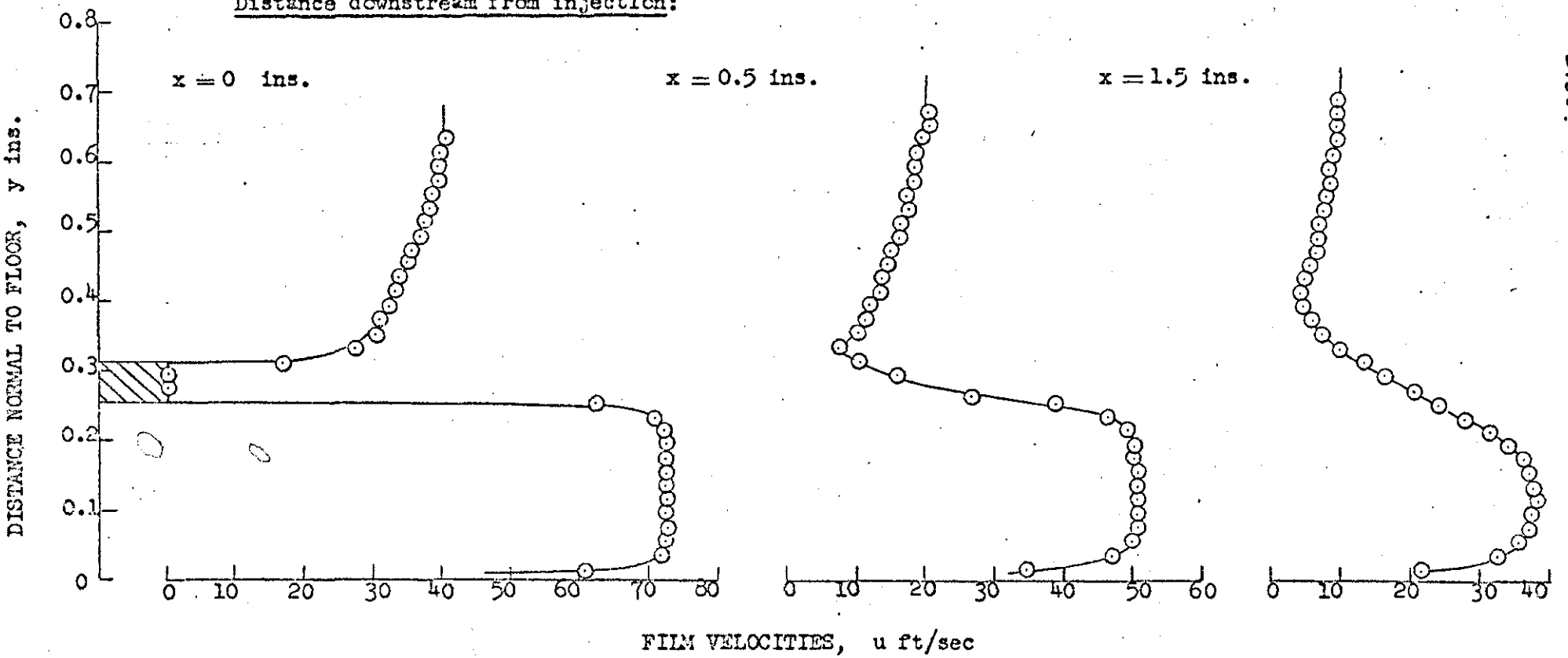

FIG. 10.1 a) CONTINUED

Test Run No. 15

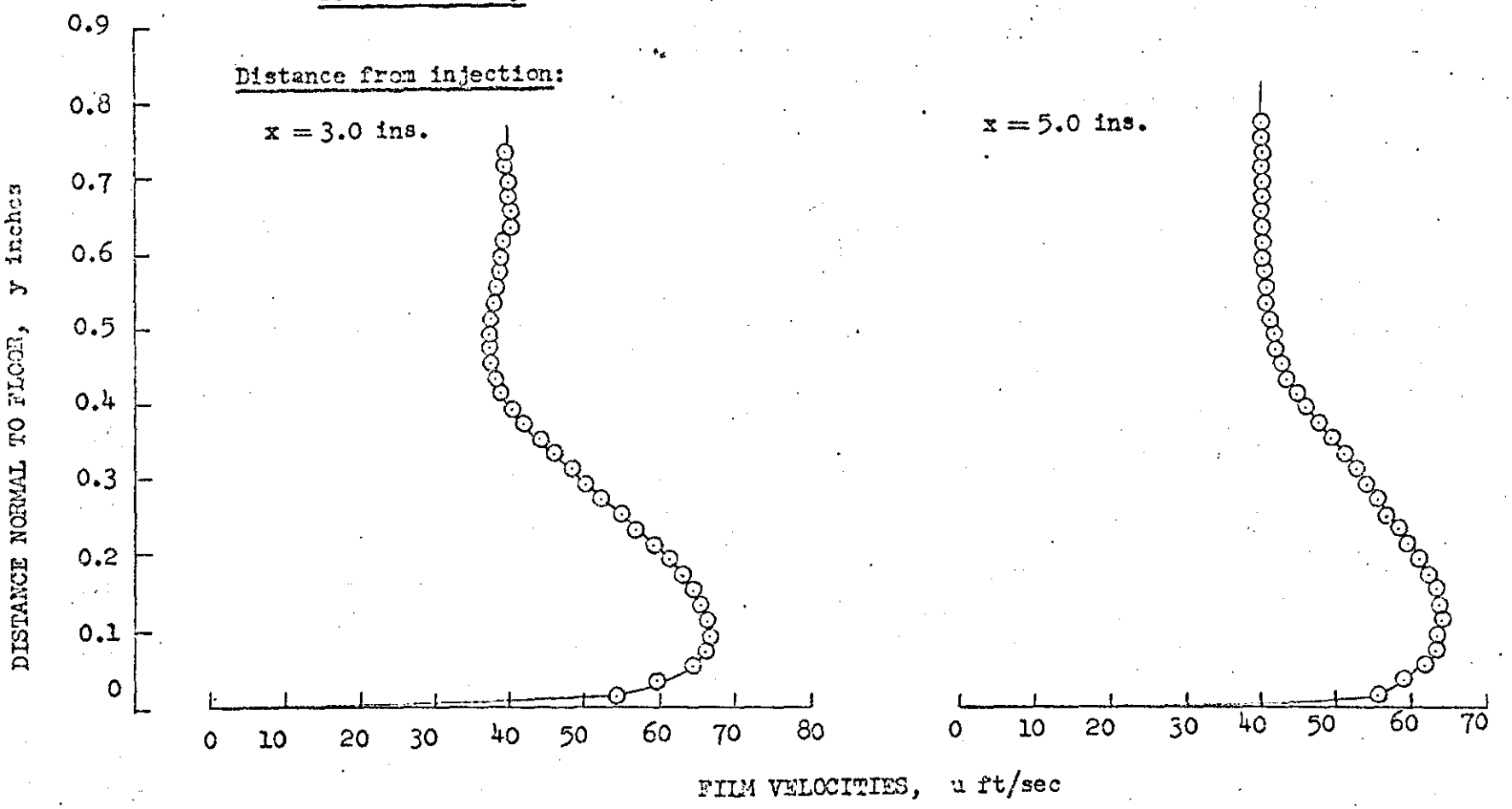

FIG. 10.1: VELOCITY PROFILE DEVELOPMENT FOR THIN-LIPPED SLOT, b) WAKE-LIKE FLOW

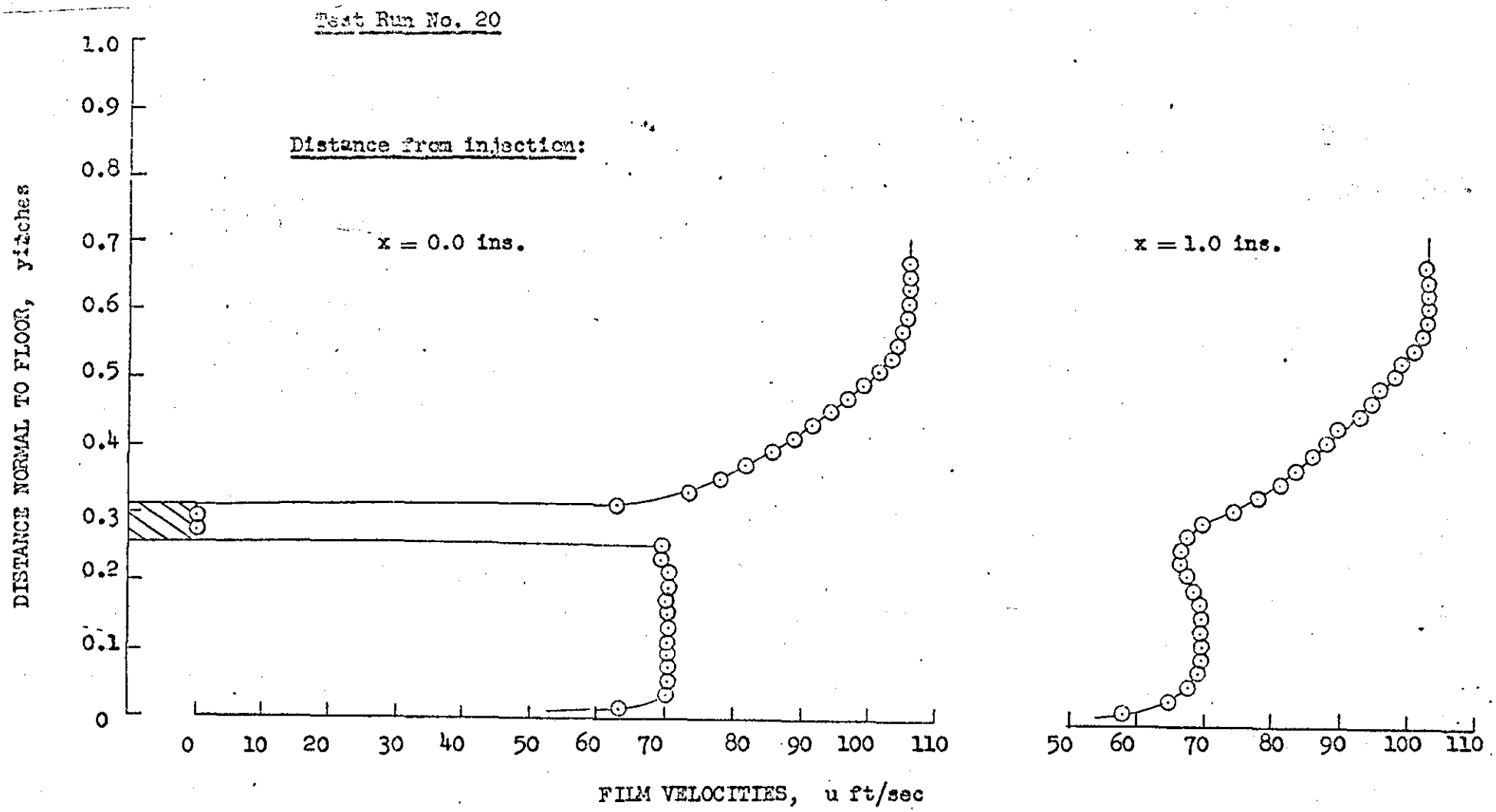

FIG. 10.1 b) CONTINUED

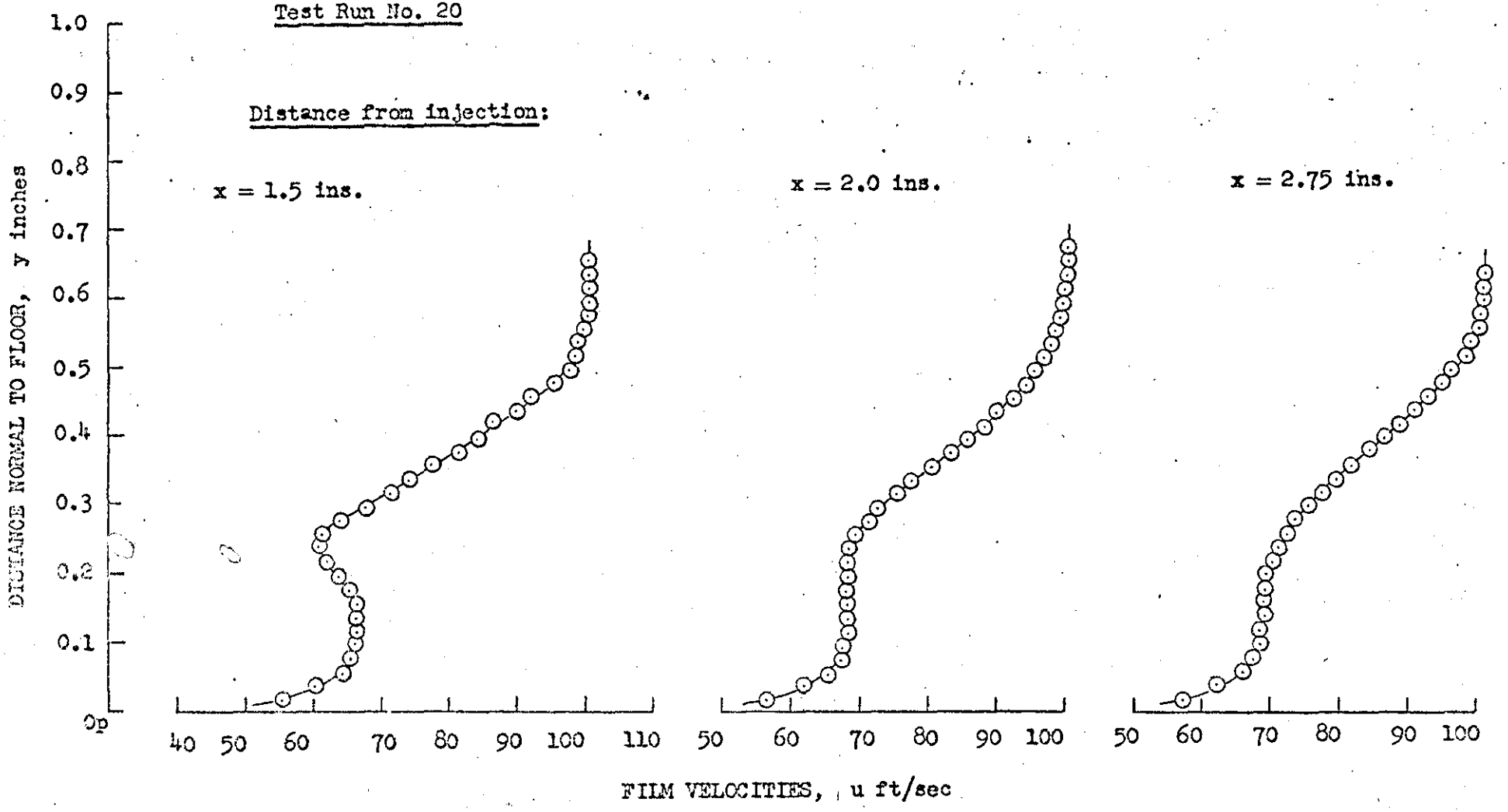

FIG. 10.2: VELOCITY PROFILE DEVELOPMENT FOR INTERMEDIATE - LIPPED SLOTS, a) JET-LIKE FLOW

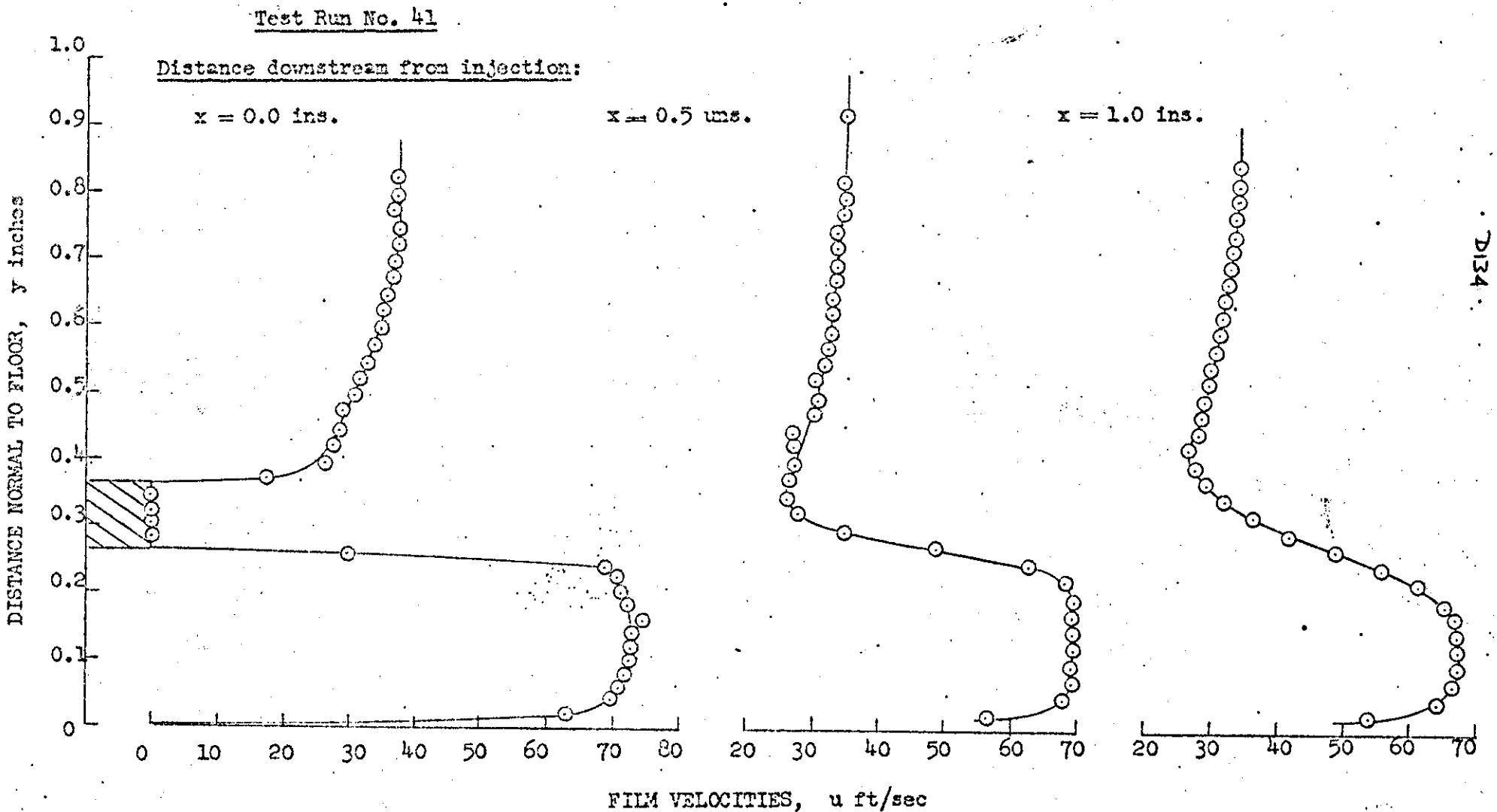

D134

FIG. 10.2 a): CONTINUED

Test Run No. 41

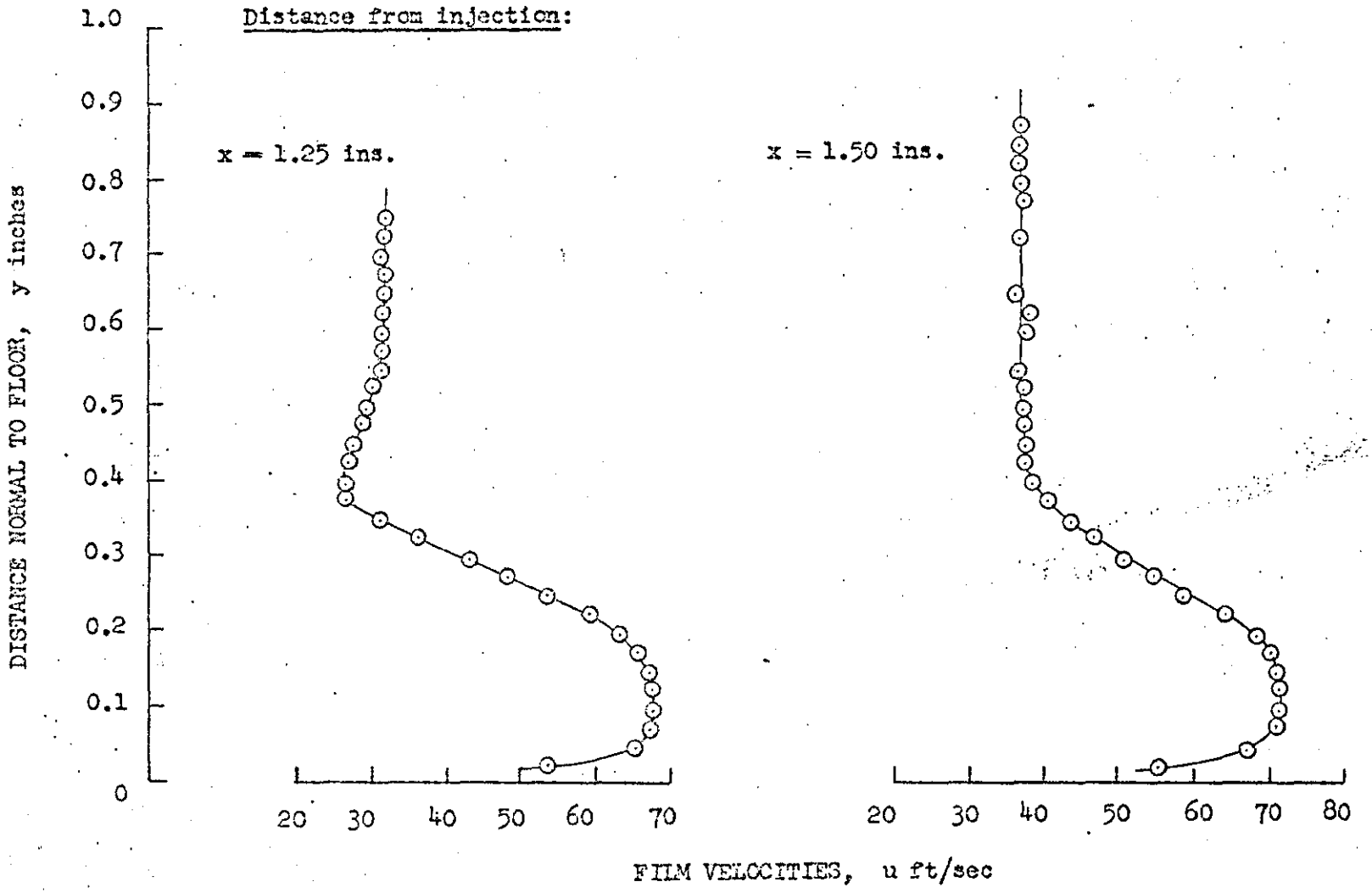

FIG. 10.2: VELOCITY PROFILE DEVELOPMENT FOR INTERMEDIATE - LIPPED SLOTS: b) WAKE-LIKE FLOW

Test Run No. 34

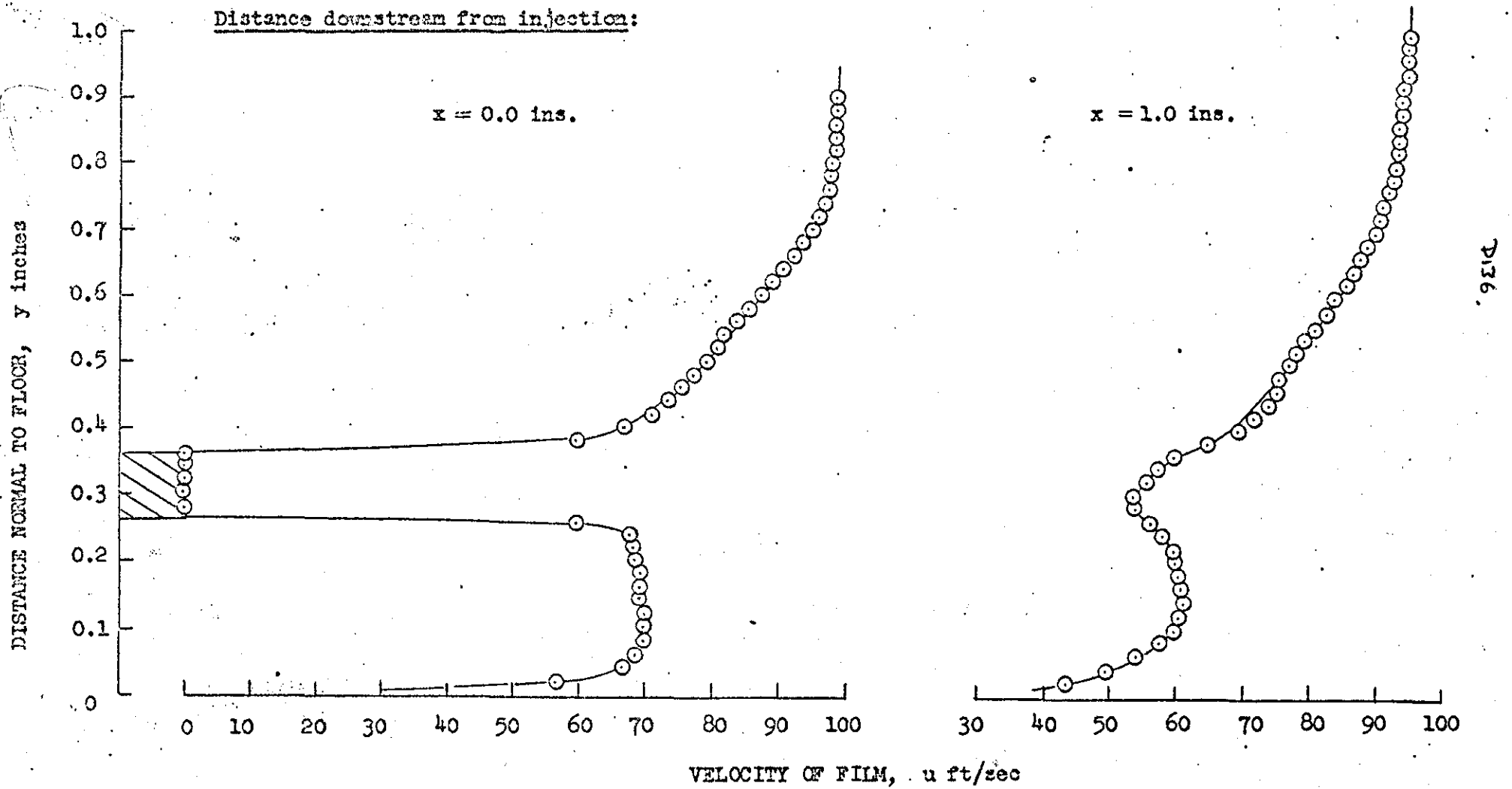

FIG. 10.2 b): CONTINUED

Test Run No. 34

Distance downstream from injection:

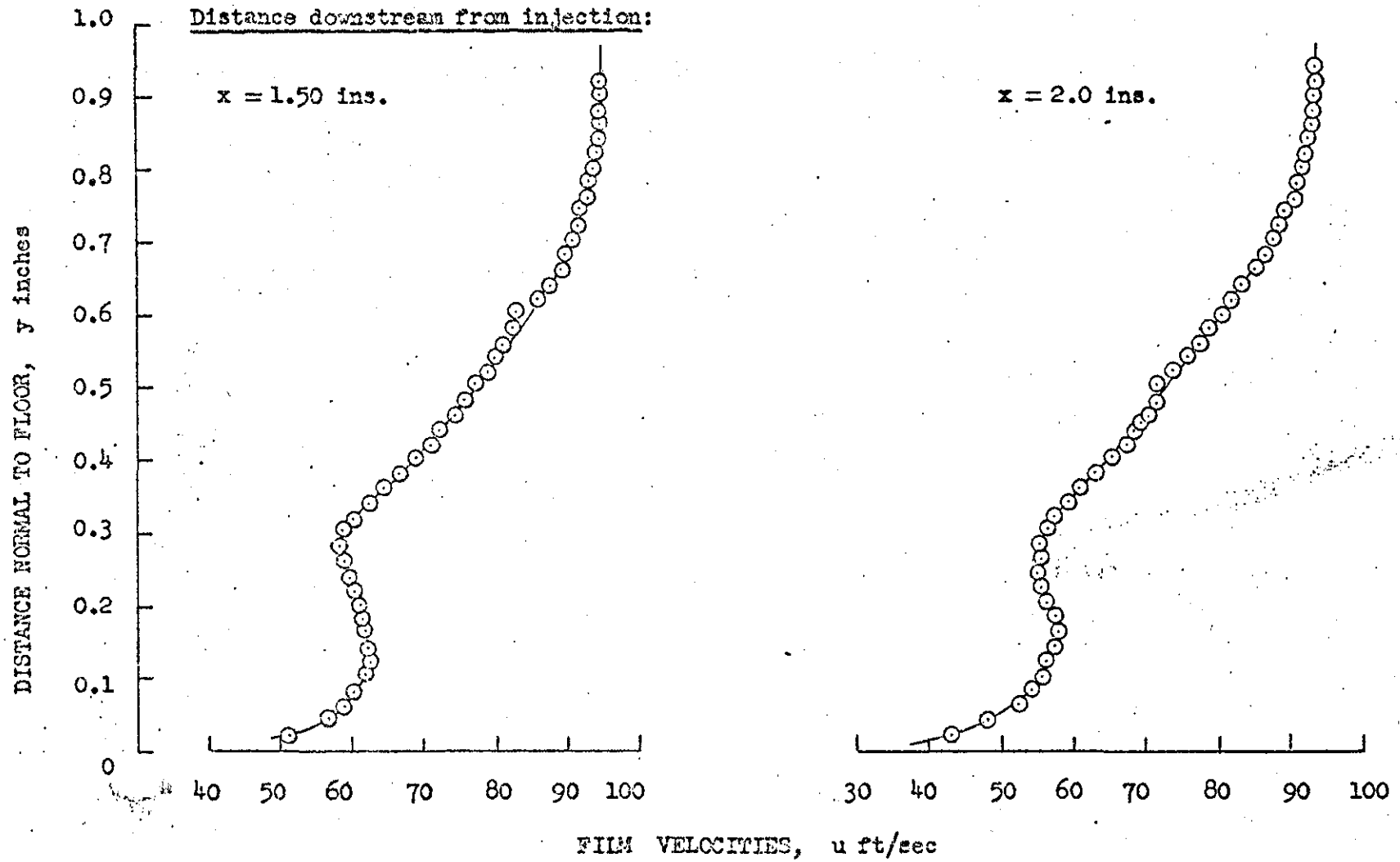

FIG. 10.3: VELOCITY PROFILE DEVELOPMENT FOR THICK - LIPPED SLOT: a) JET - LIKE FLOW

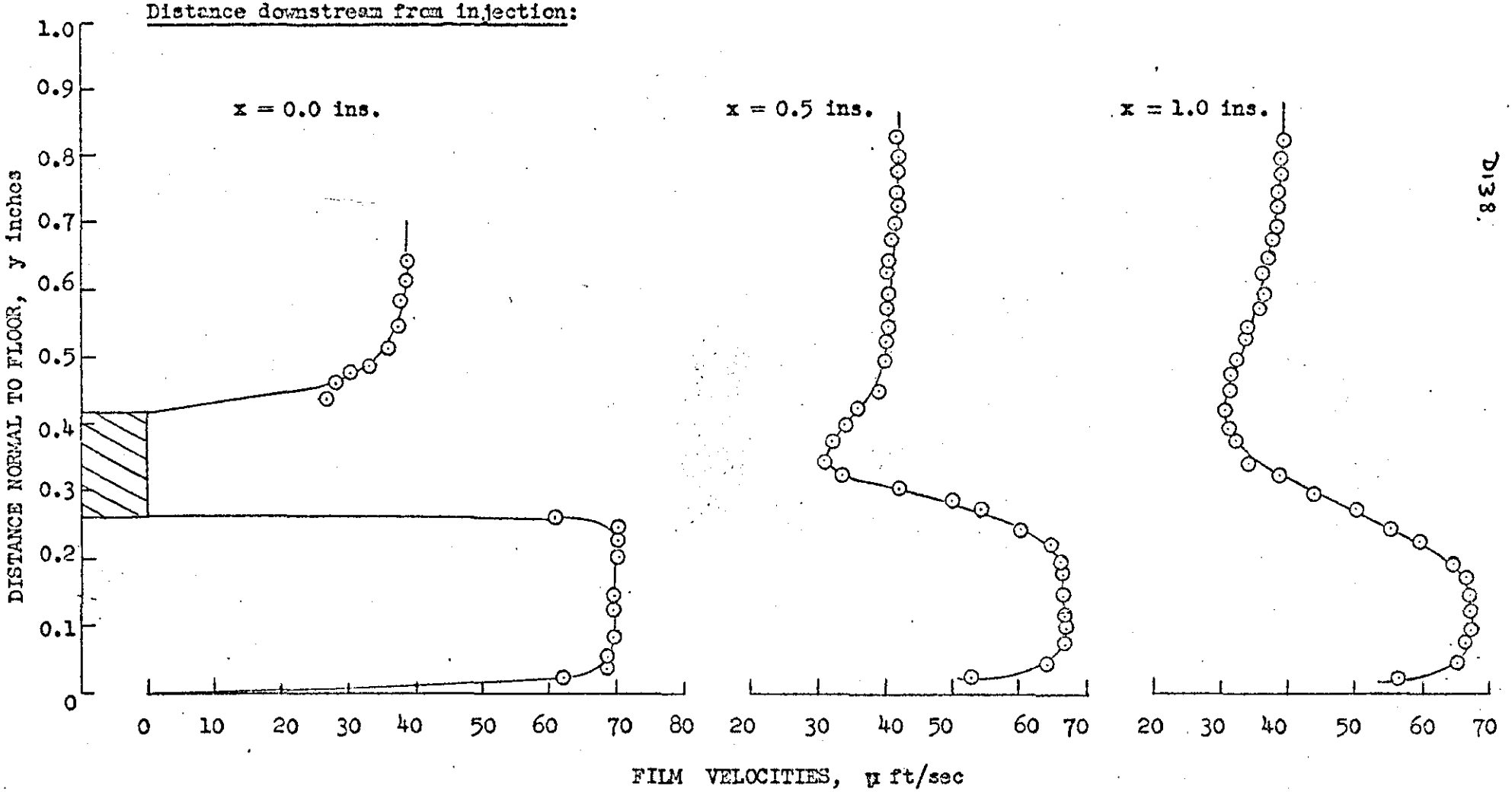

D138.

FIG. 10.4: NEAR UNITY VELOCITY RATIO INJECTION FOR THIN - LIPPED SLOT

Test Run No. 17

Distance downstream from injection:

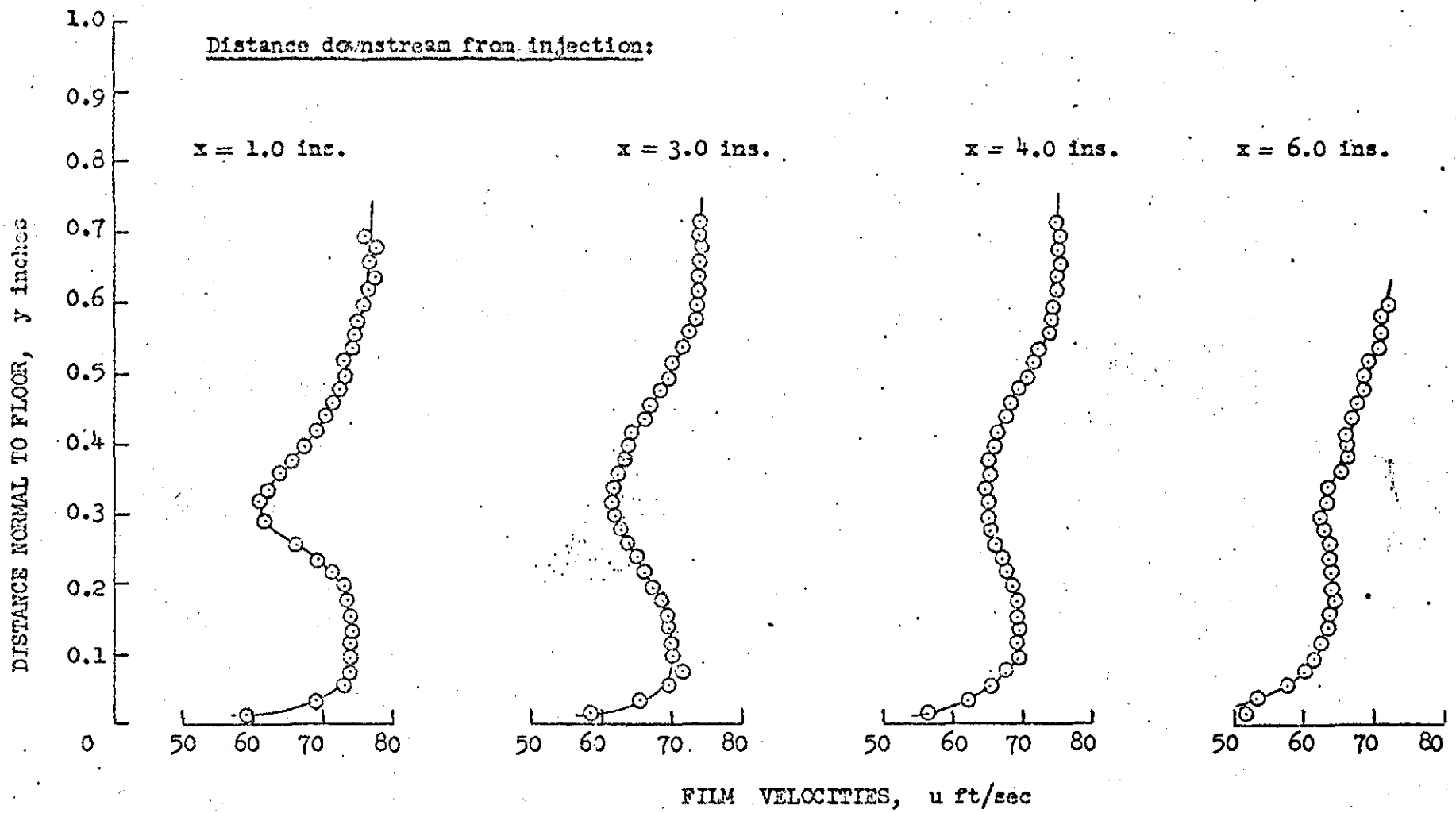

FIG. 10.5: MEASUREMENT OF HYDRODYNAMIC POTENTIAL CORE LENGTH FROM TEST DATA

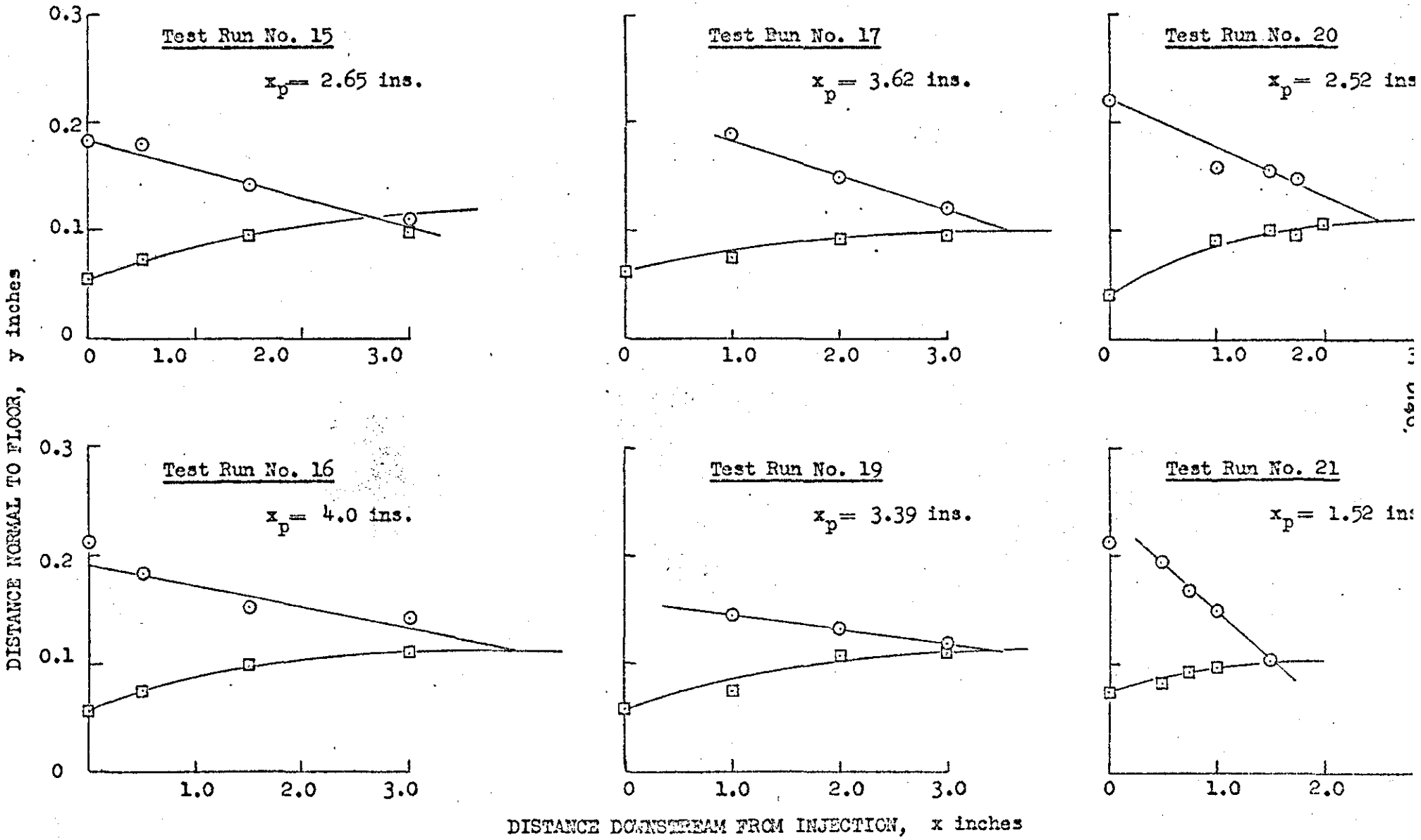

FIG. 10.5: CONTINUED (i)

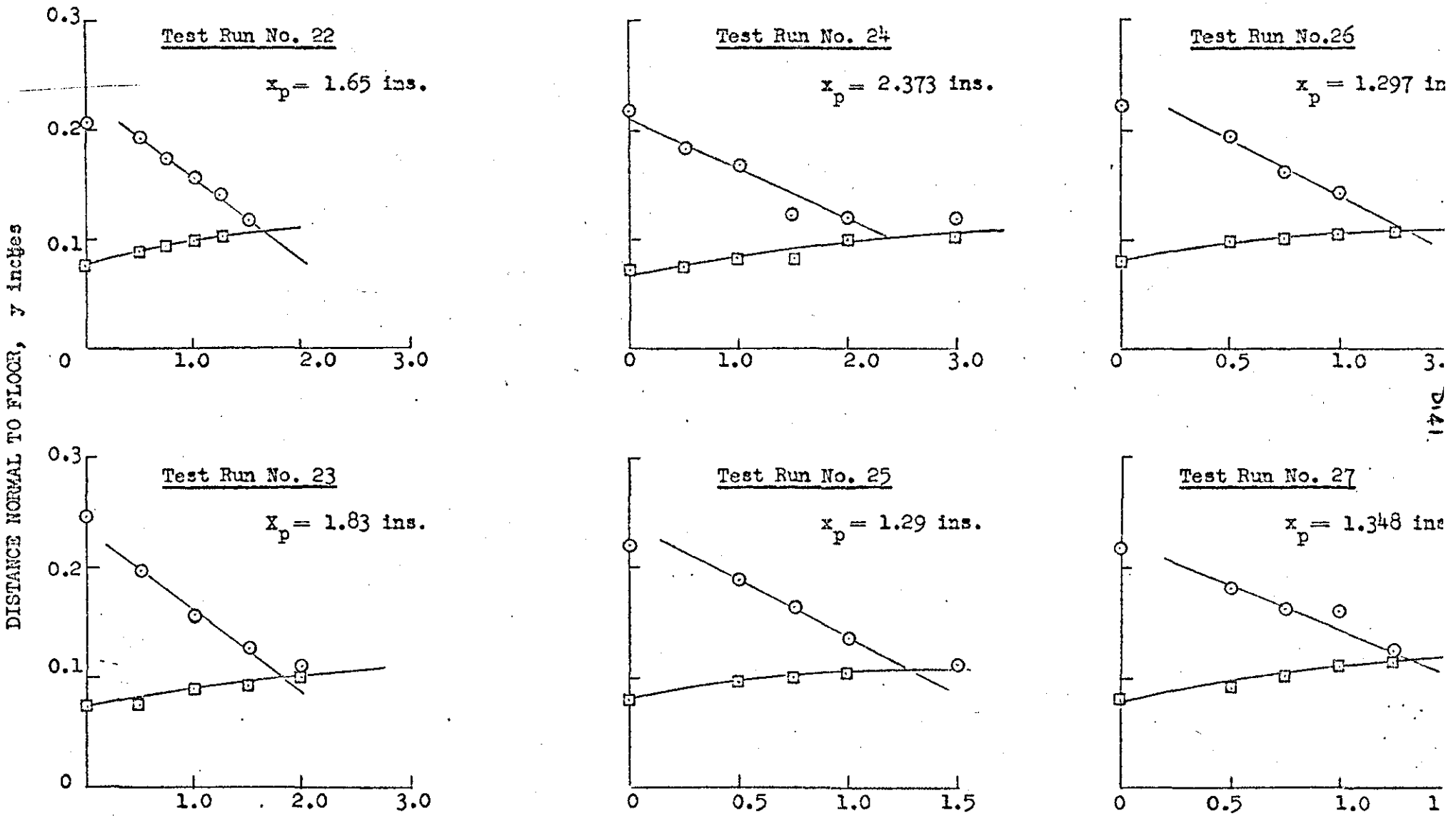

FIG. 10.5: CONTINUED (ii)

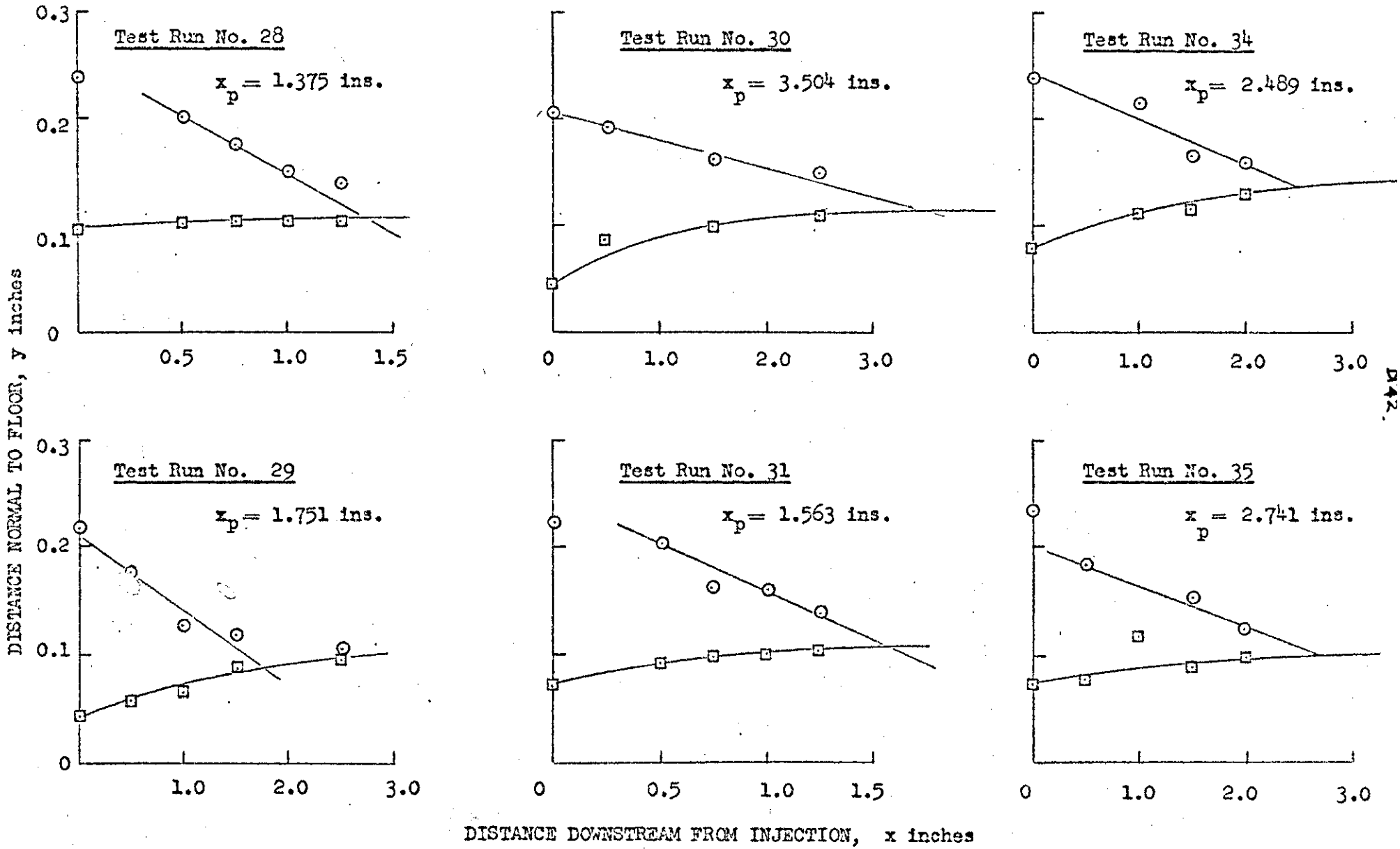

FIG. 10.5: CONTINUED (iii)

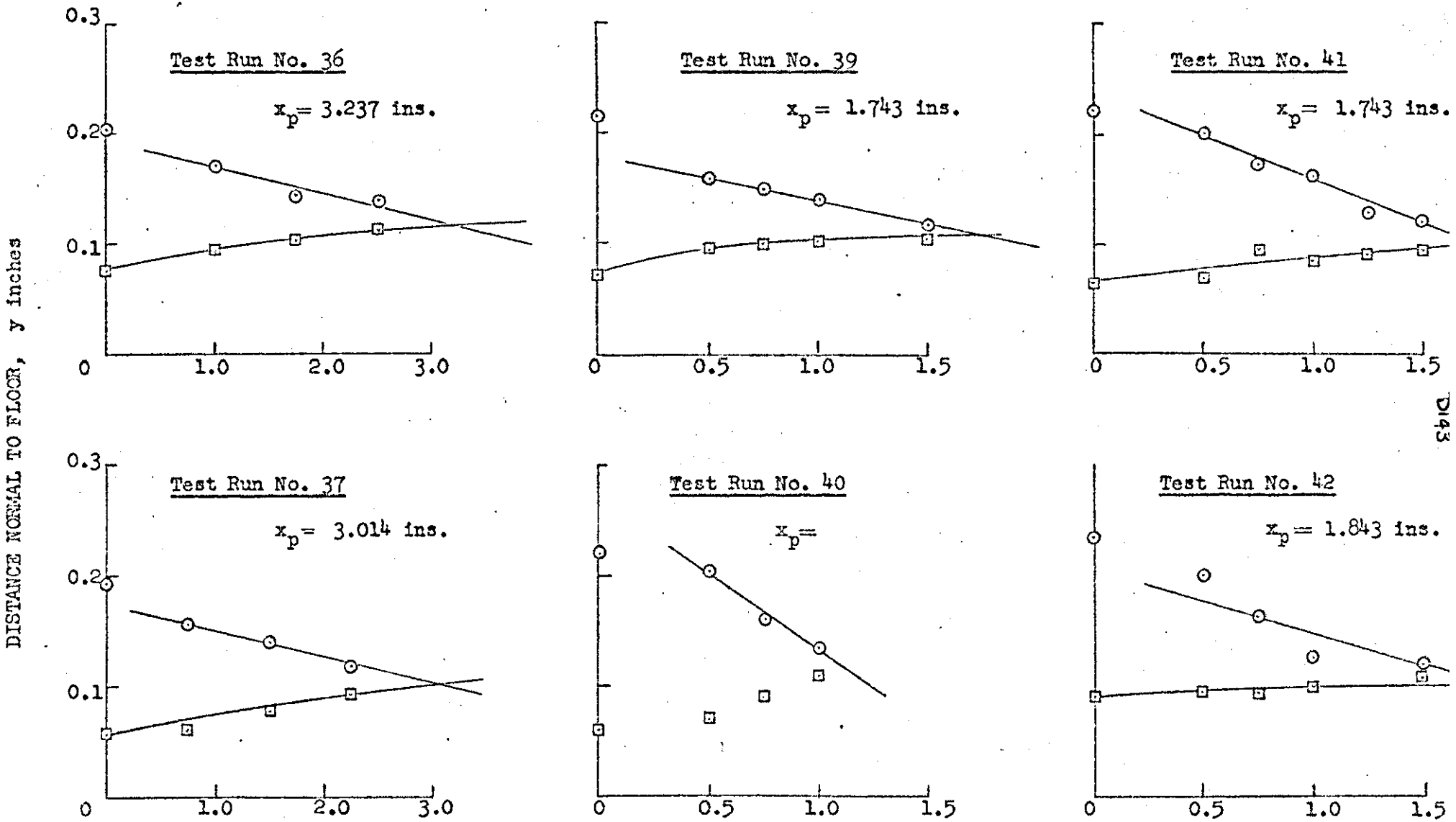

FIG. 10.5: CONTINUED (iv)

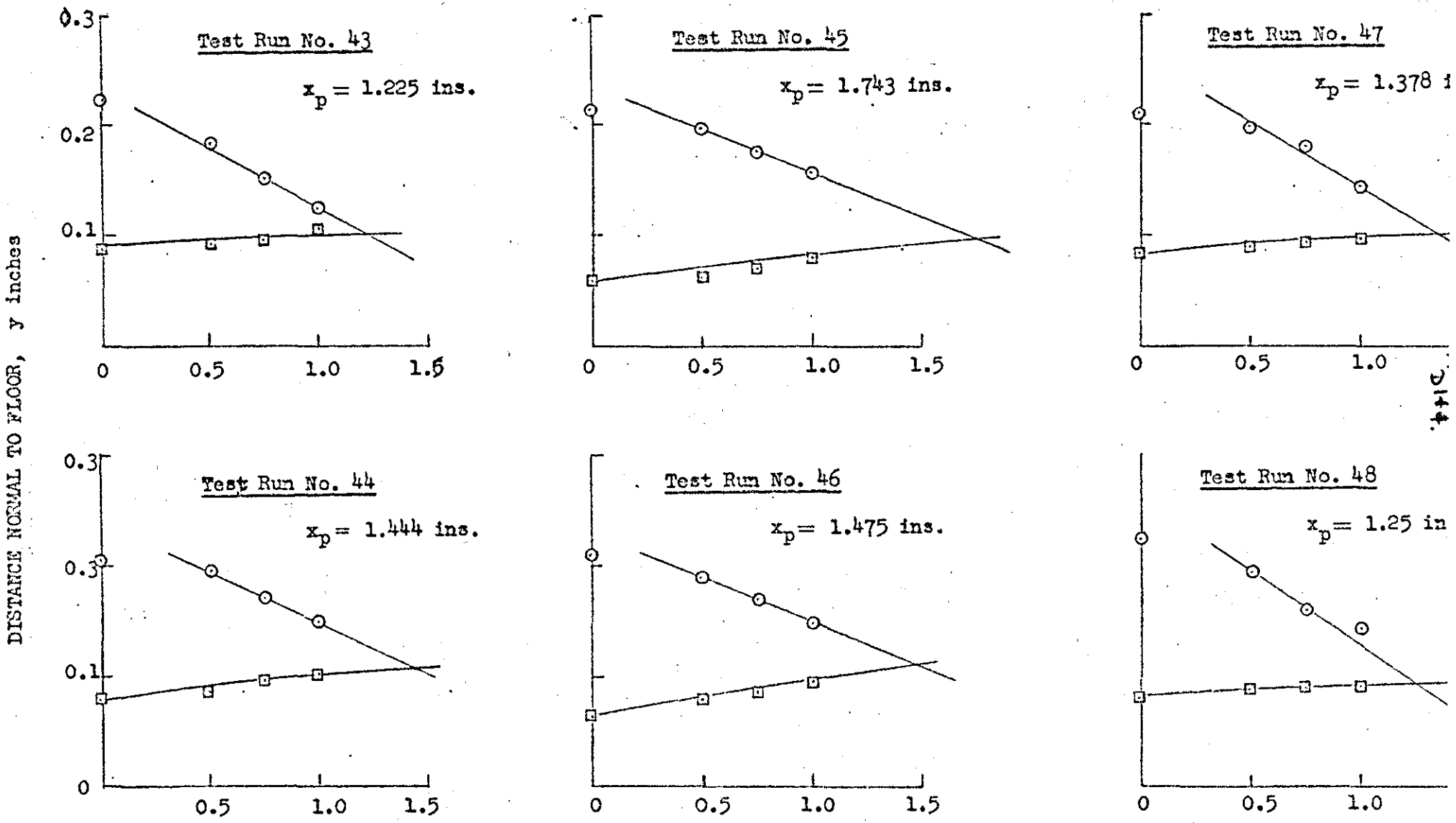

FIG. 10.5: CONTINUED (v)

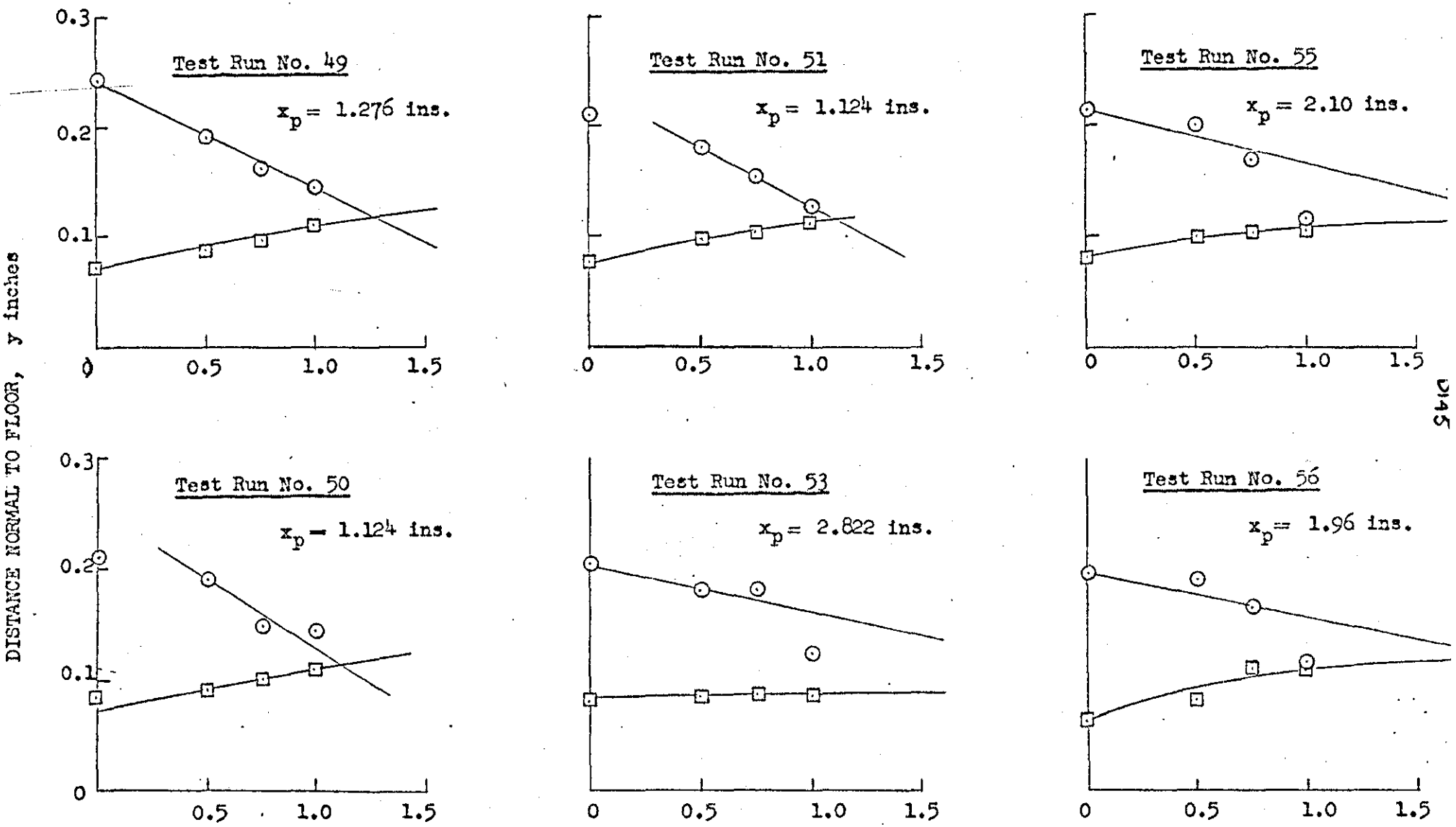

FIG. 10.5: CONTINUED (vi)

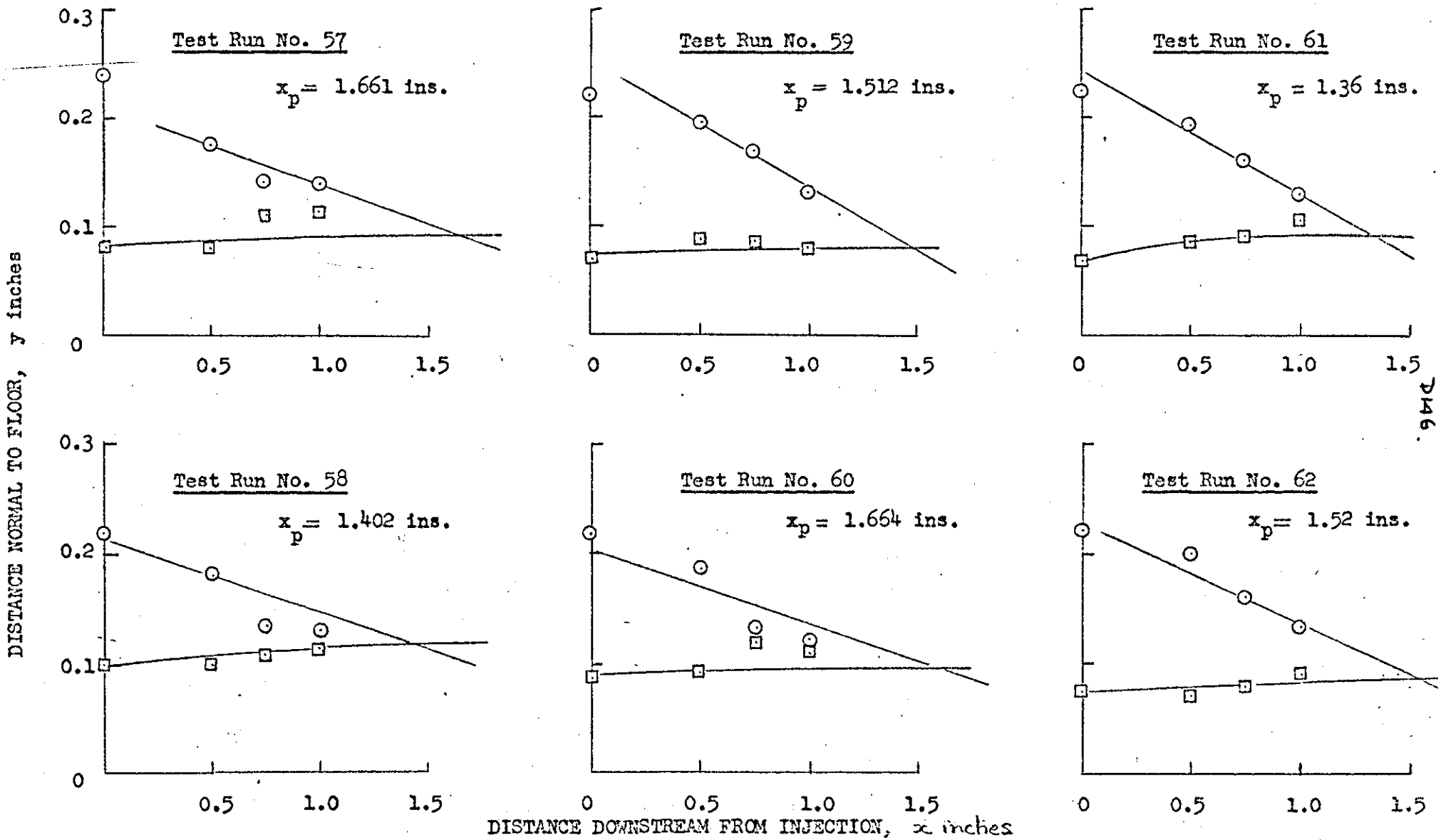

FIG. 10.5: CONTINUED (vii)

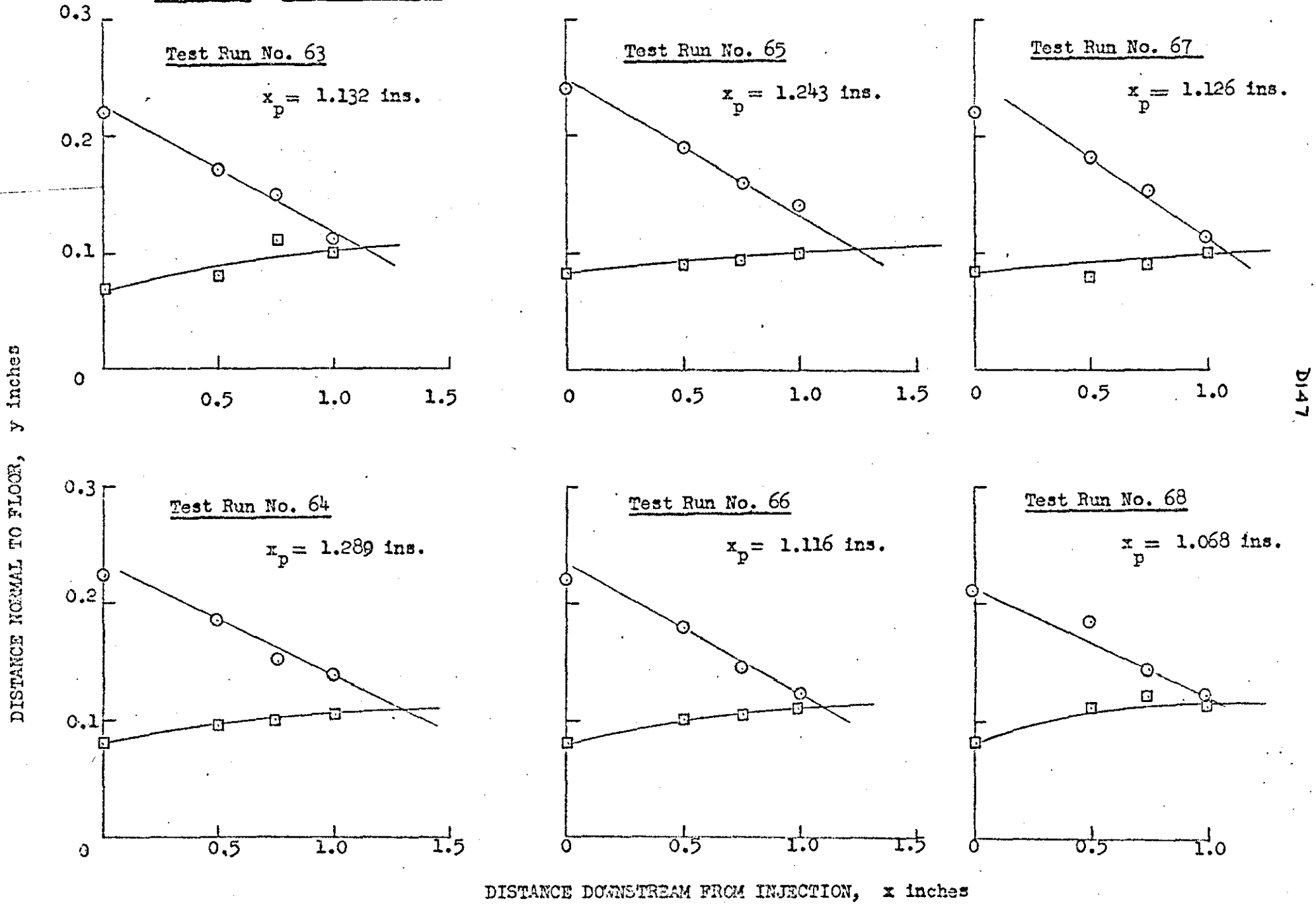

FIG. 10.5: CONTINUED (viii)

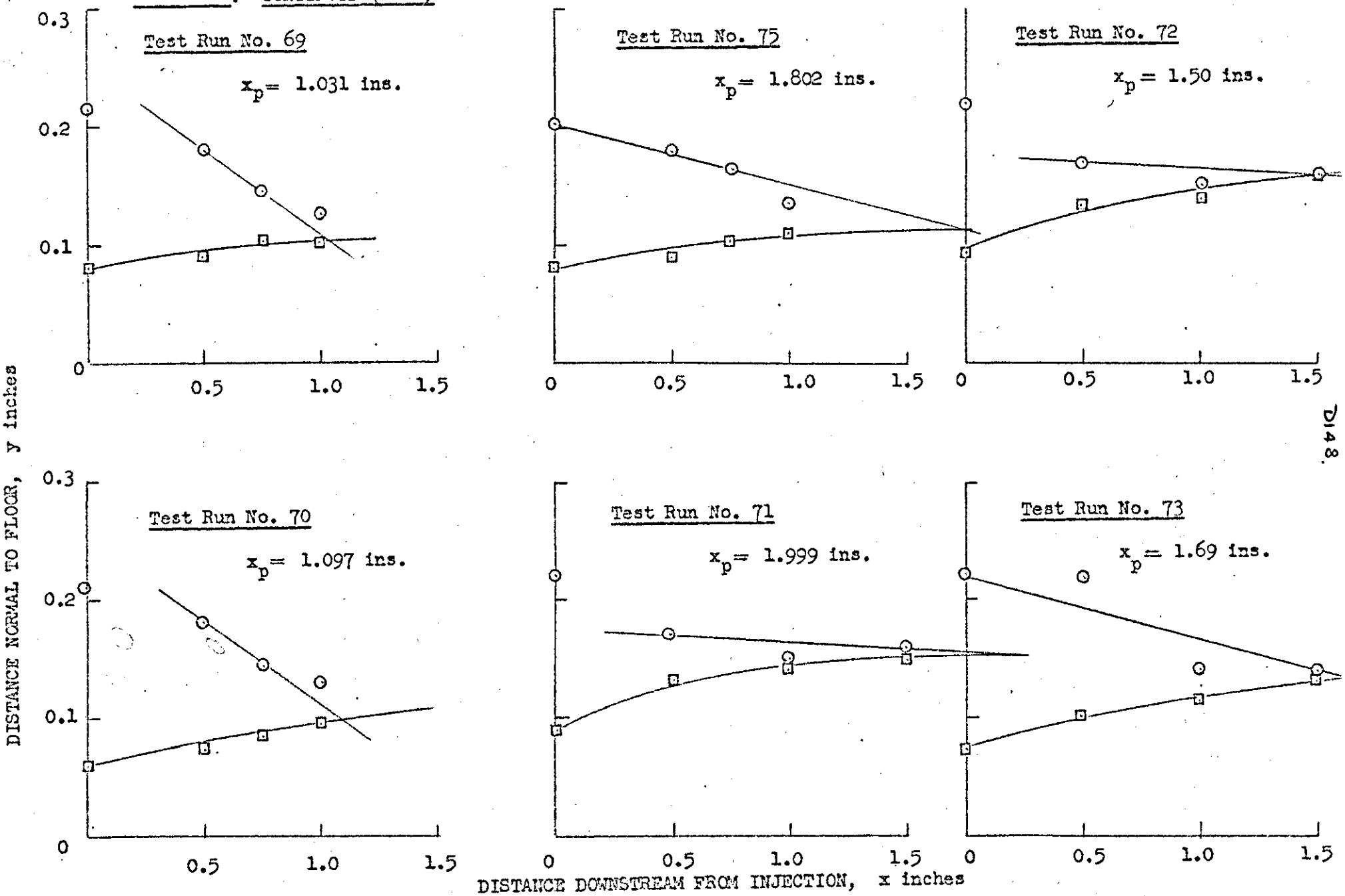

FIG. 10.5: CONTINUED (ix)

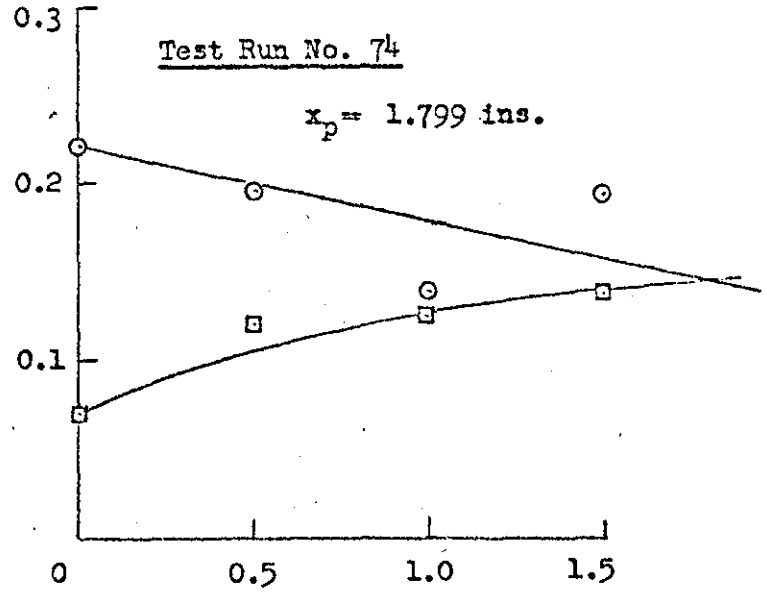

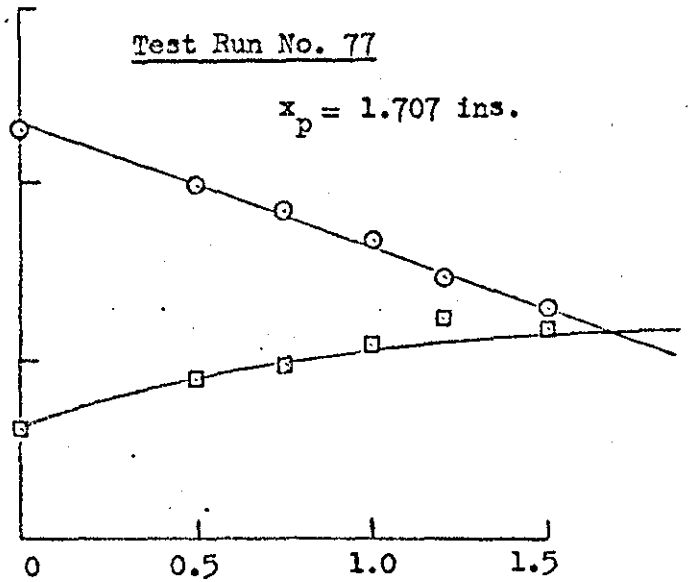

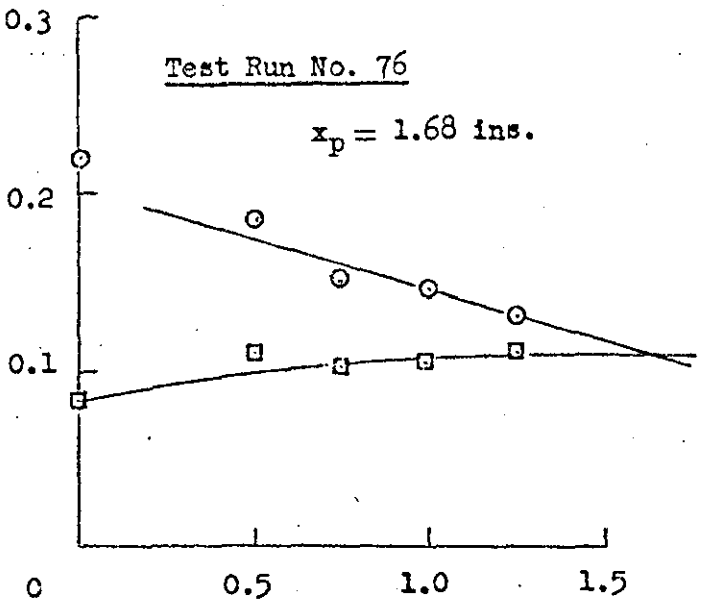

DISTANCE NORMAL TO FLOOR, y inches

DISTANCE DOWNSTREAM FROM INJECTION, x inches

DM 9.

FIG. 10.6: TURBULENCE INTENSITY PROFILES FOR THIN - LIPPED SLOT, $u_m < u_c$

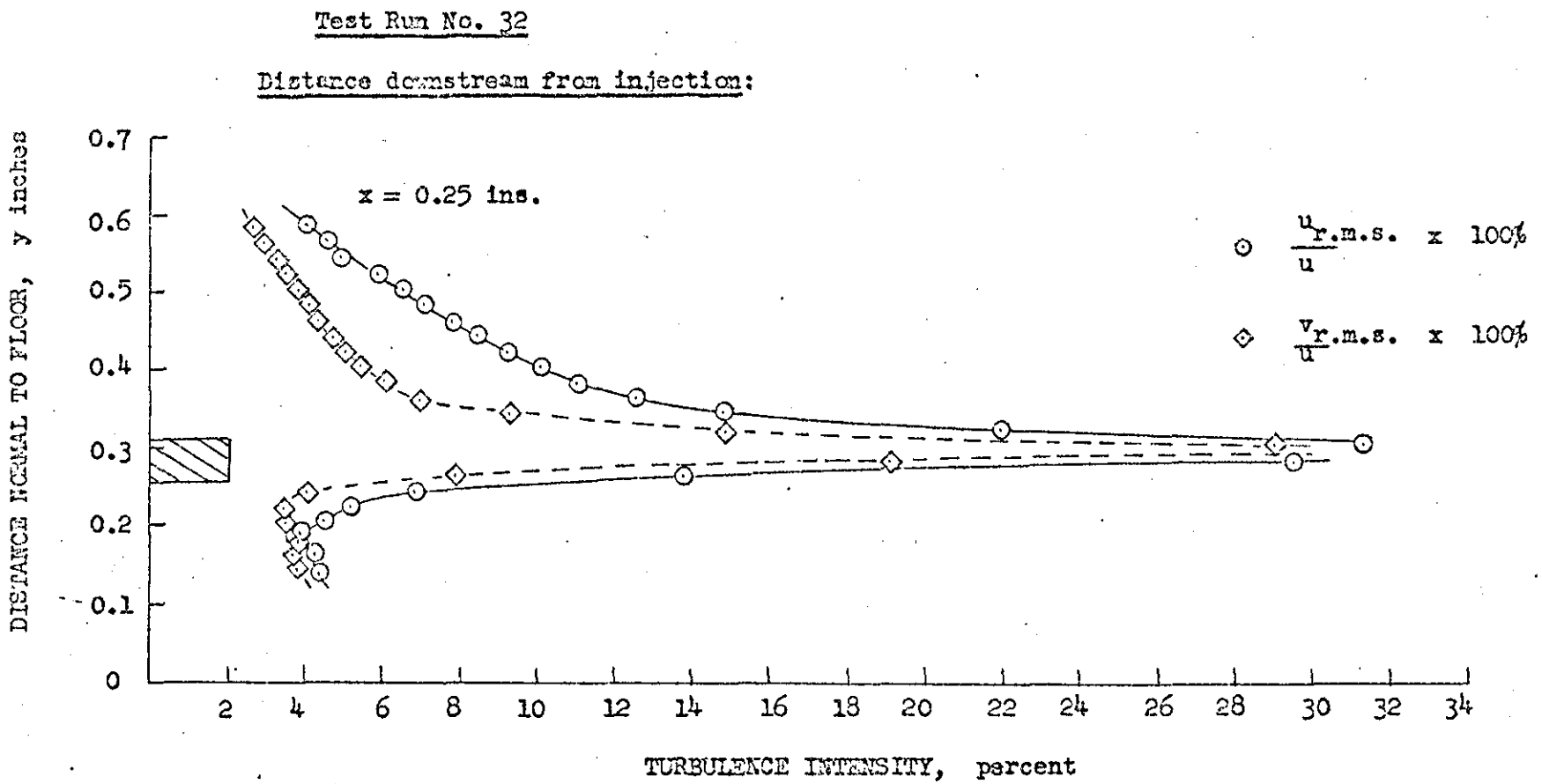

P150.

FIG. 10.6: CONTINUED (i)

Distance downstream from injection:

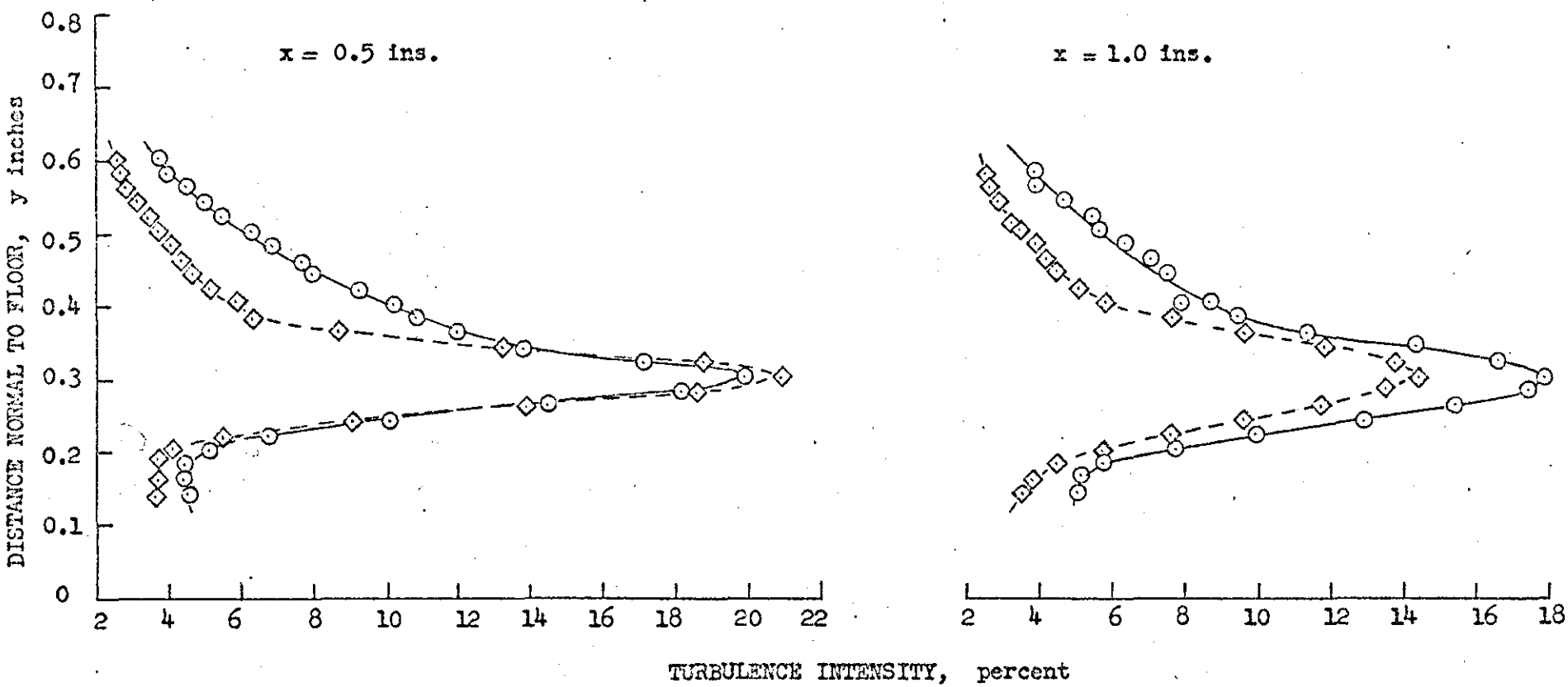

FIG. 10.6: CONTINUED (ii)

Distance downstream from injection:

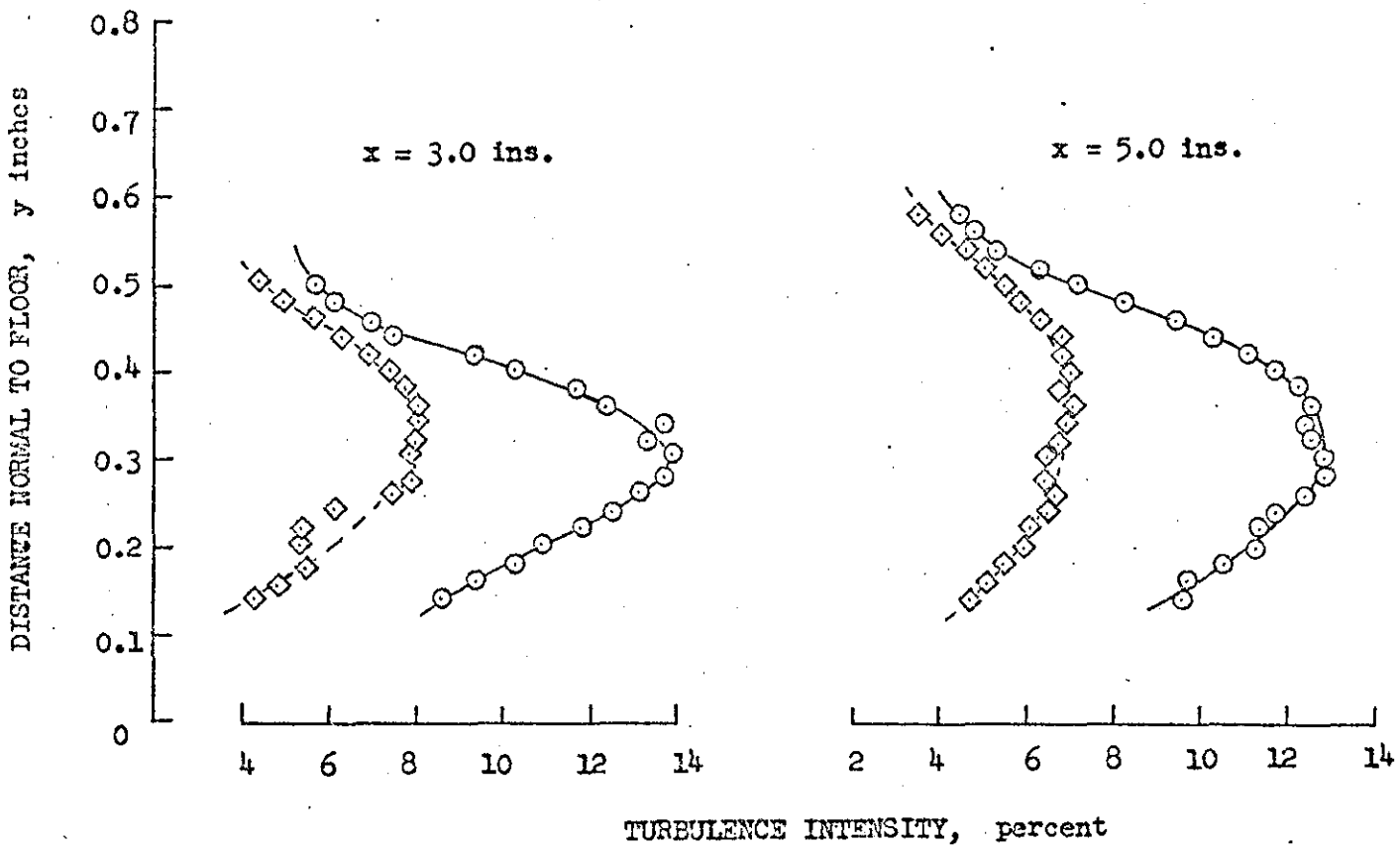

FIG. 10.7: TURBULENCE INTENSITY PROFILES FOR INTERMEDIATE - LIPPED SLOT, $u_m \triangleq u_o$

Test Run No. 38

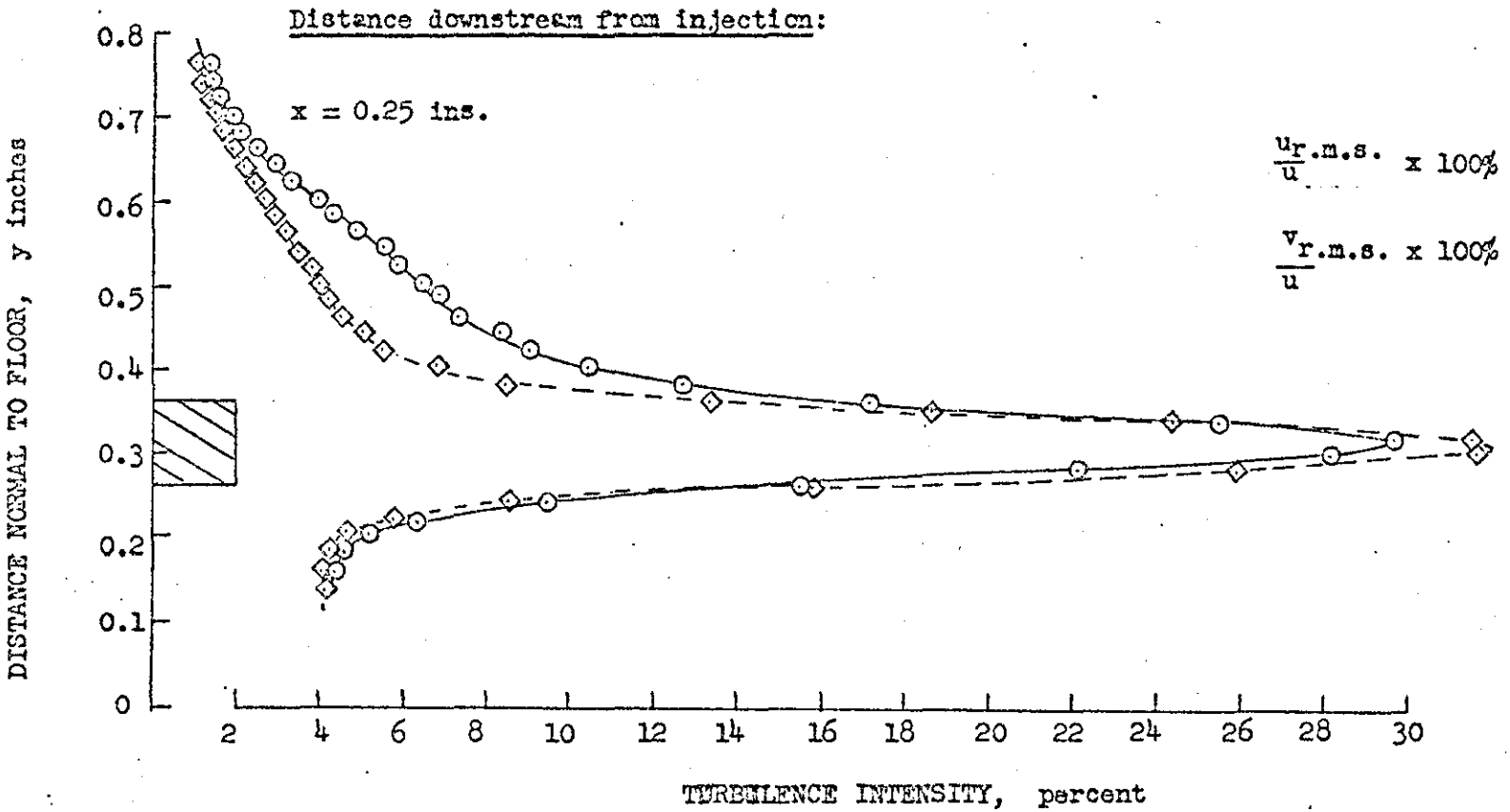

FIG. 10.7: CONTINUED (i)

Distance downstream from injection:

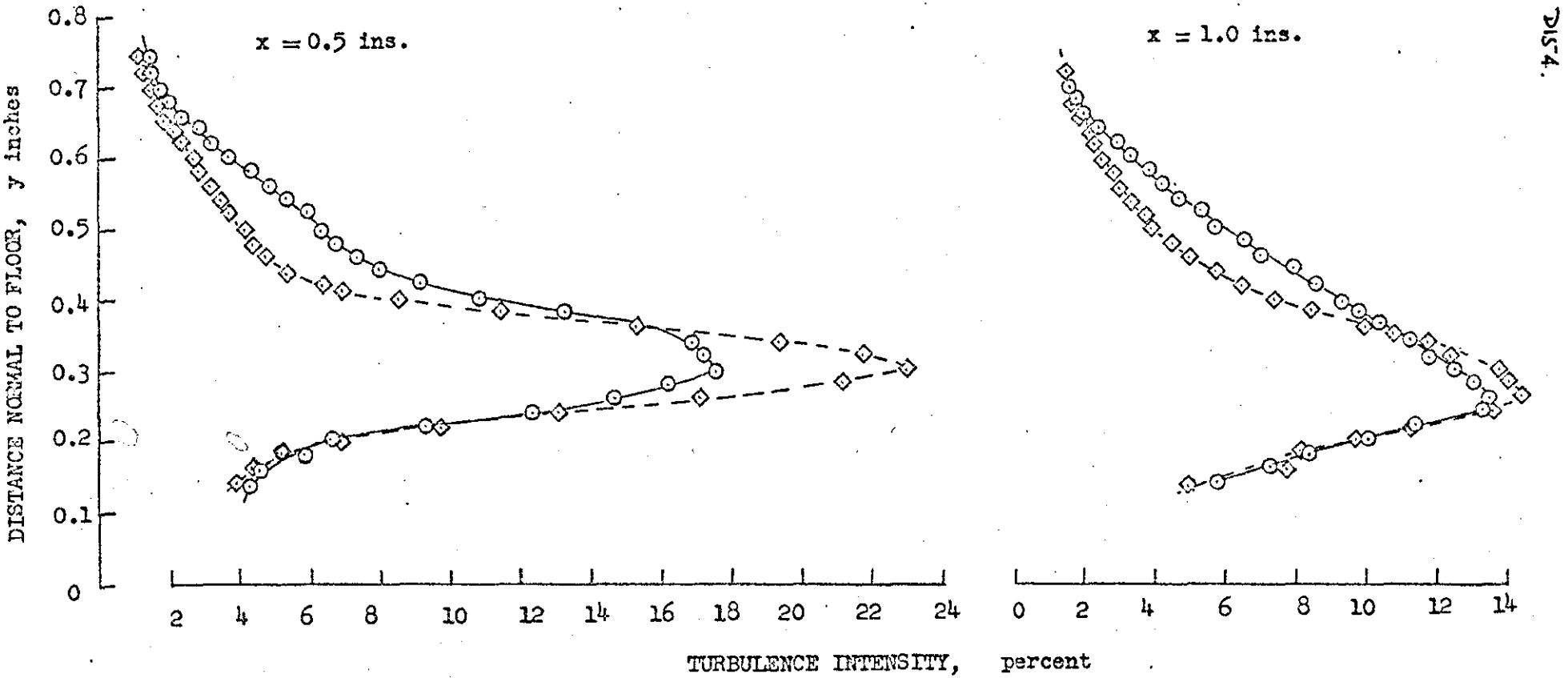

FIG. 10.7: CONTINUED (ii)

Distance downstream from injection:

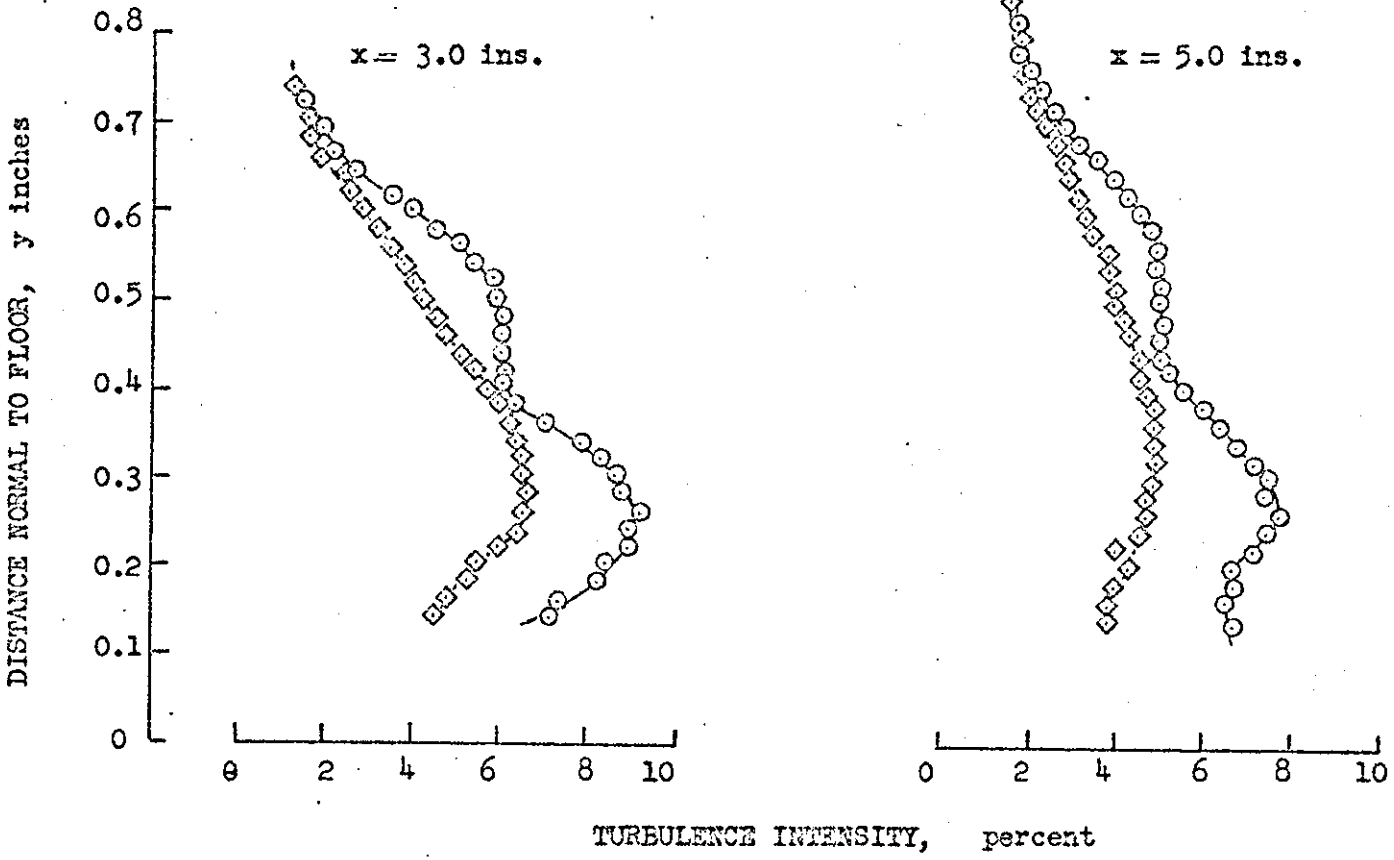

FIG. 11.1: DECAY OF COOLANT POTENTIAL VELOCITY, THIN - LIPPED SLOT

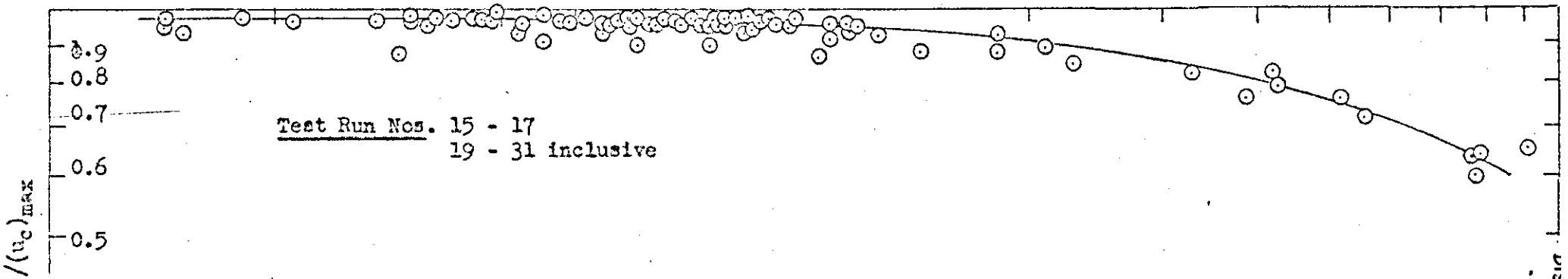

FIG. 11.2: DECAY OF COOLANT POTENTIAL VELOCITY, INTERMEDIATE - LIPPED SLOT

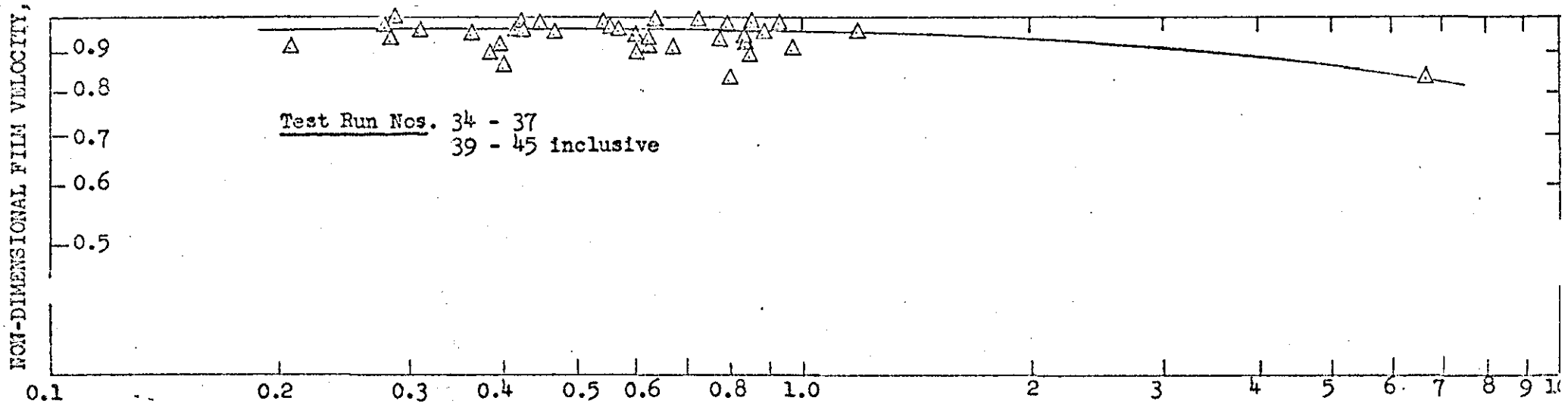

NON-DIMENSIONAL DISTANCE DOWNSTREAM FROM INJECTION, RELATIVE TO POTENTIAL CORE, x/x_p

FIG. 11.3: DECAY OF COOLANT POTENTIAL VELOCITY, THICK - LIPPED SLOT

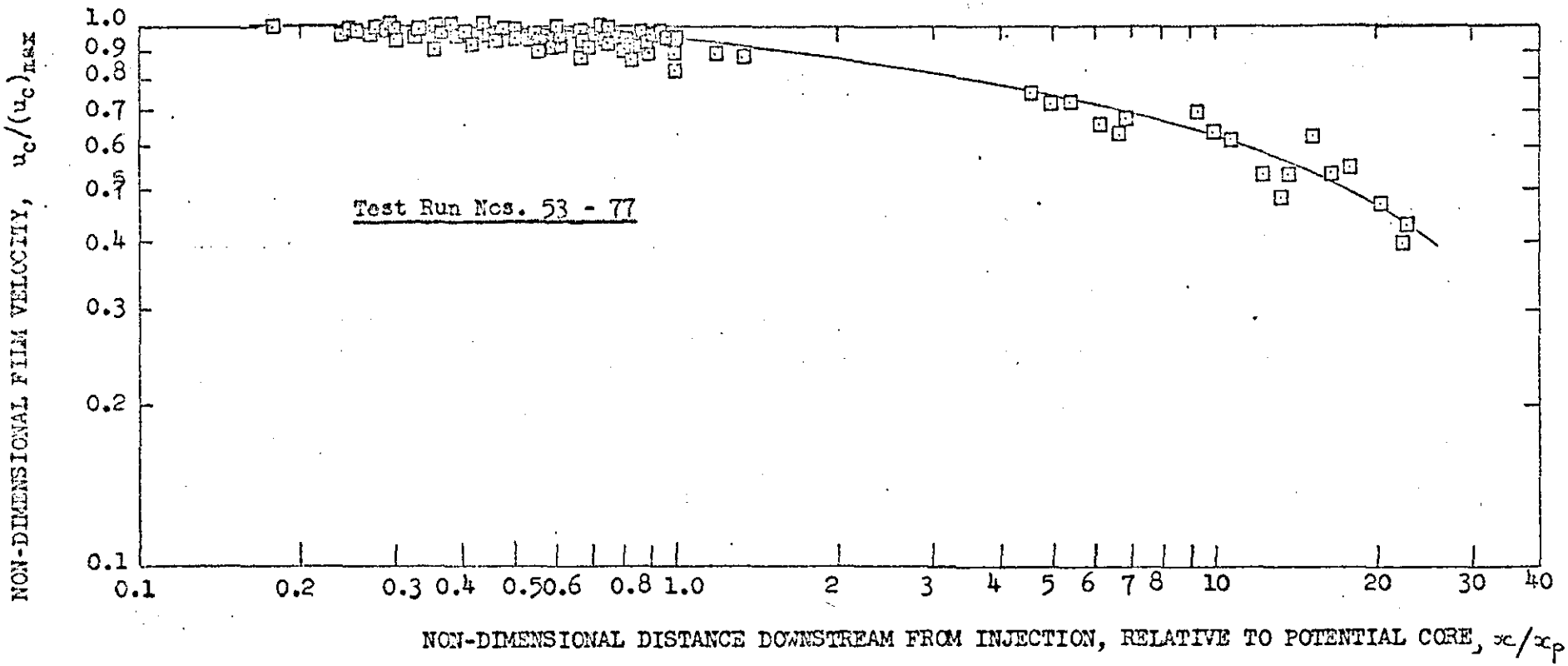

FIG. 11.4: SIMILARITY OF MIXING LAYER VELOCITY PROFILES - SHEAR FLOW REGION

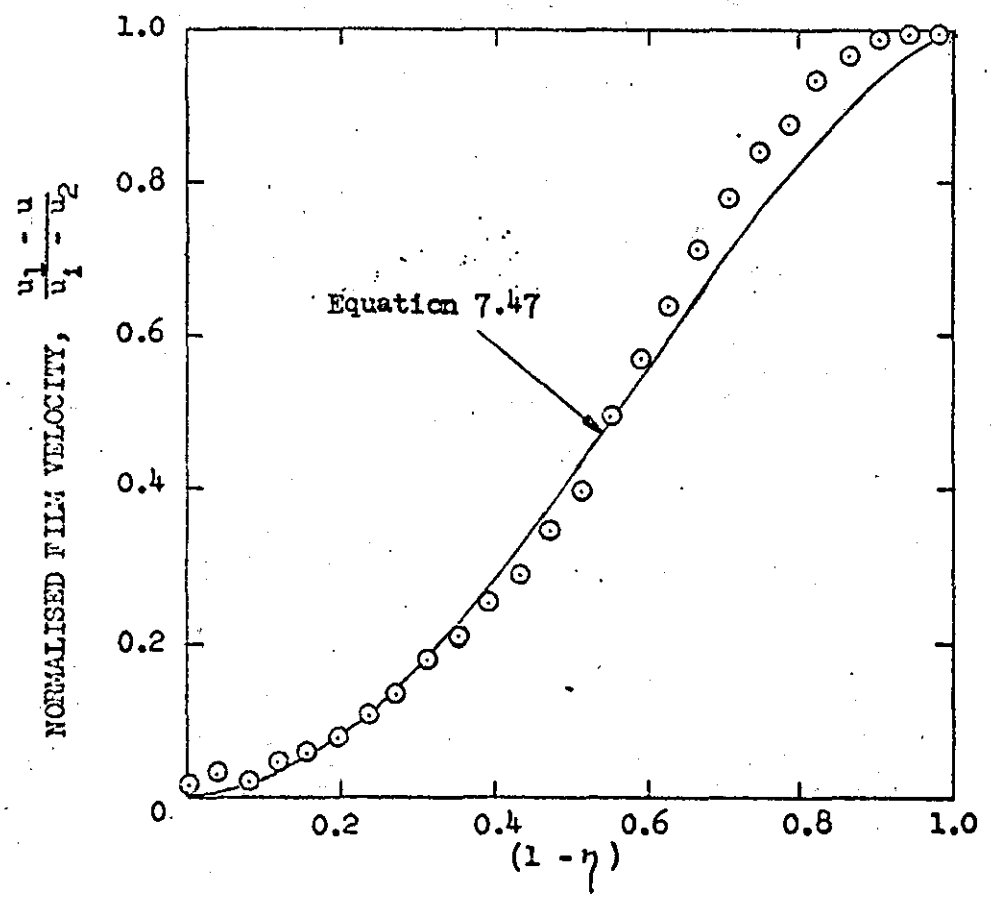

Symbol	Run No.	x ins.
⊙	19	3.0

FIG. 11.4: CONTINUED

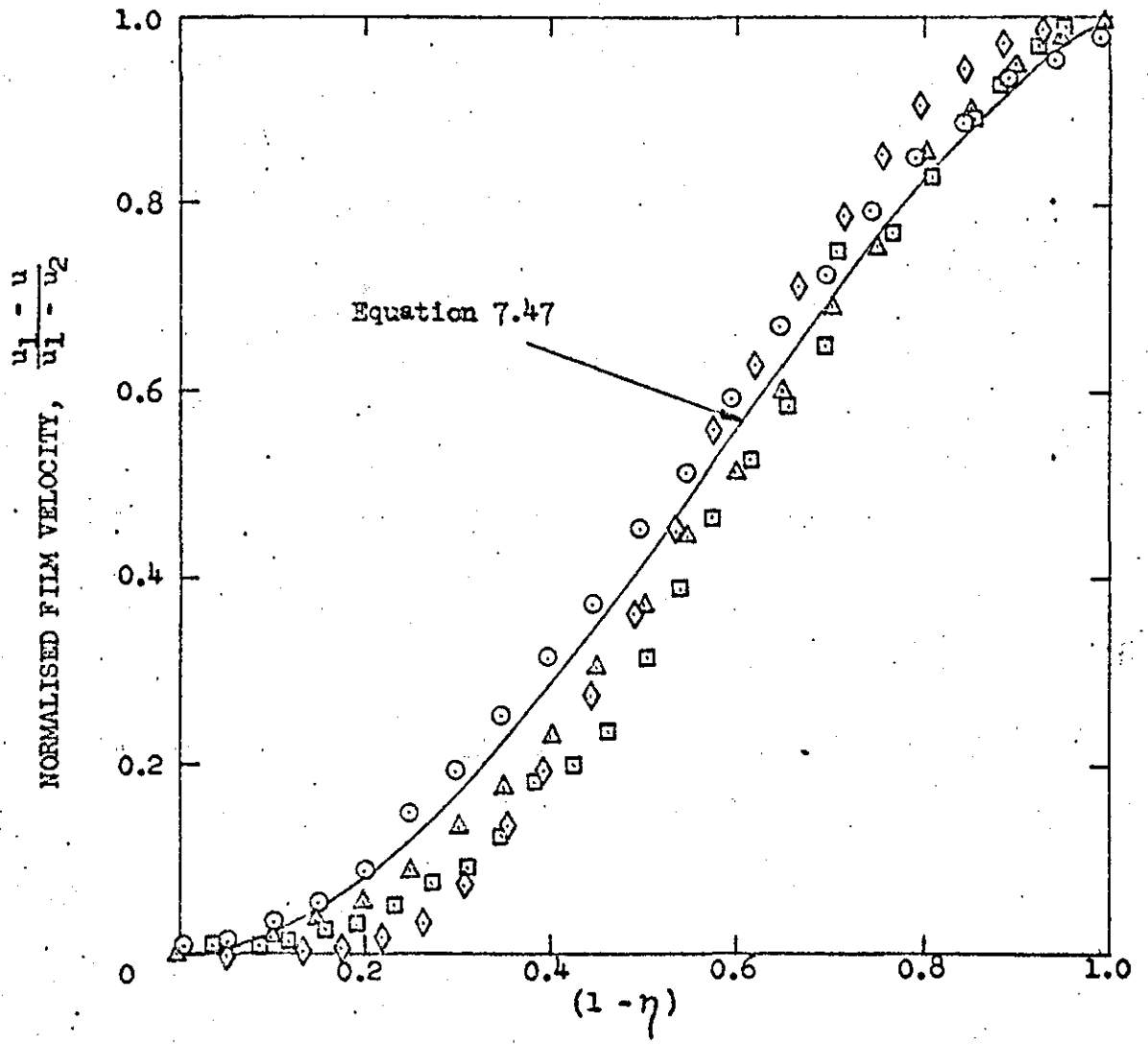

Symbol	Run No.	x ins.
⊡	15	5.0
△	20	2.0
⊙		2.75
◇	25	1.5

DIS9.

FIG. 11.5: SIMILARITY OF MIXING LAYER VELOCITY PROFILES - WAKE FLOW REGION

Symbol	Run No.	x ins.
⊙	19	1.0
△		2.0
⊡	20	1.0
◇		1.5

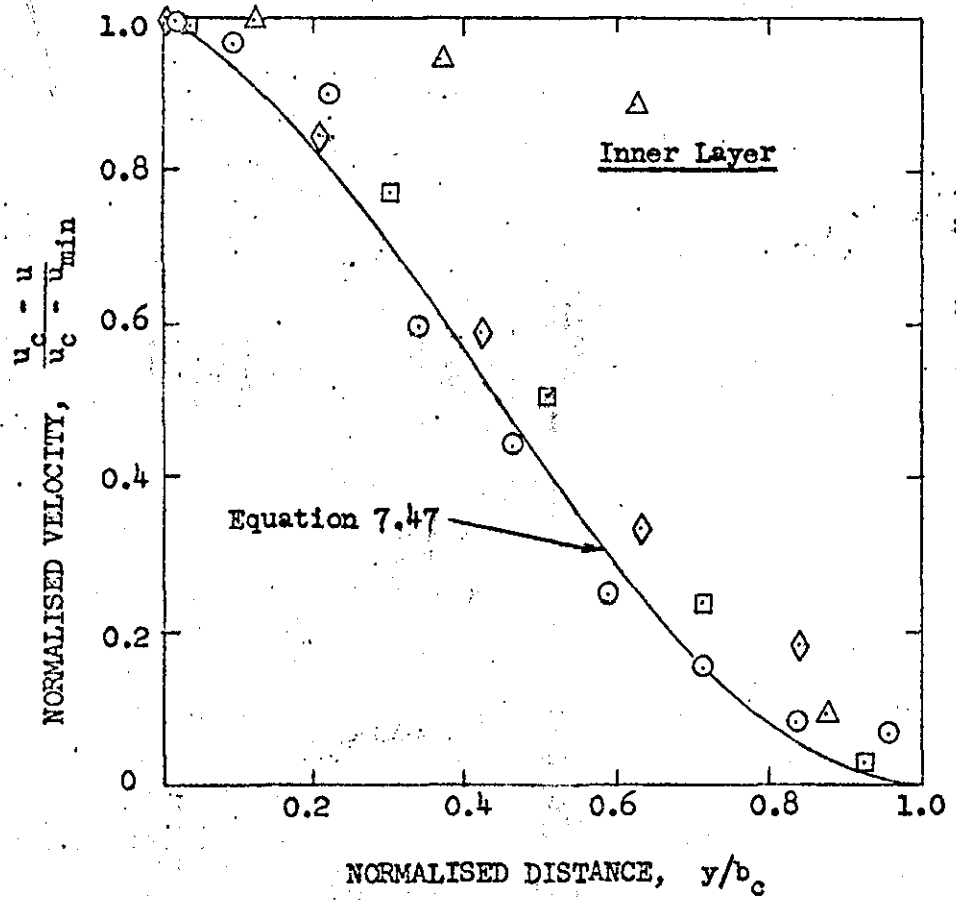

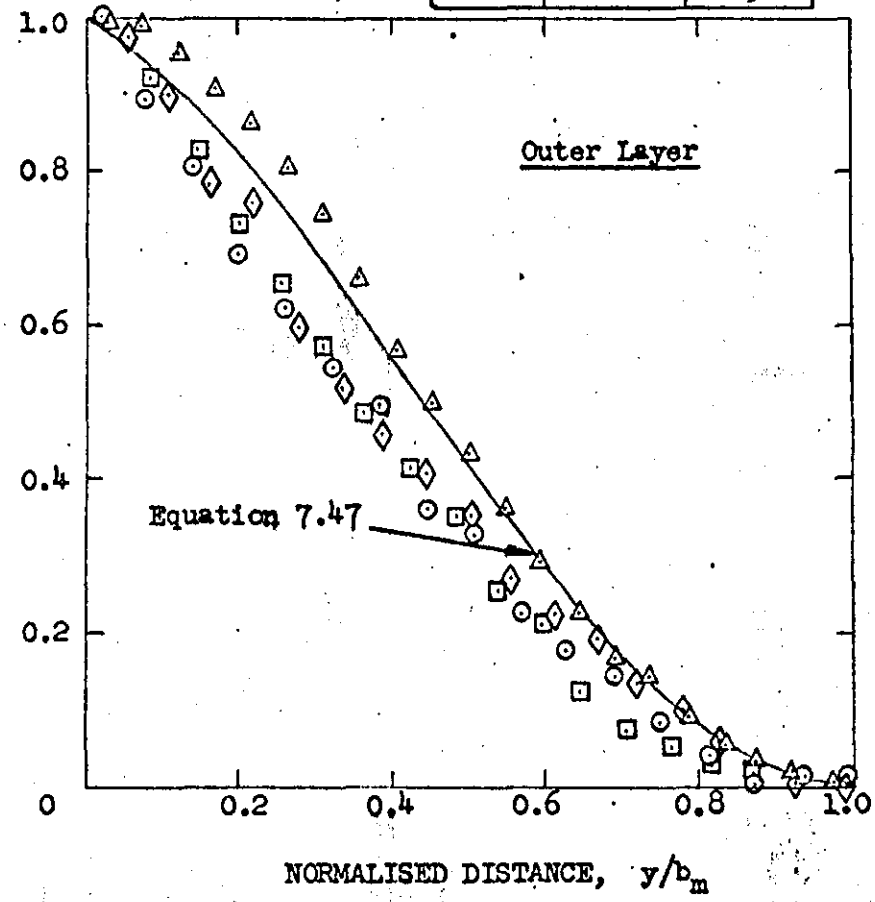

FIG. 11.5: CONTINUED

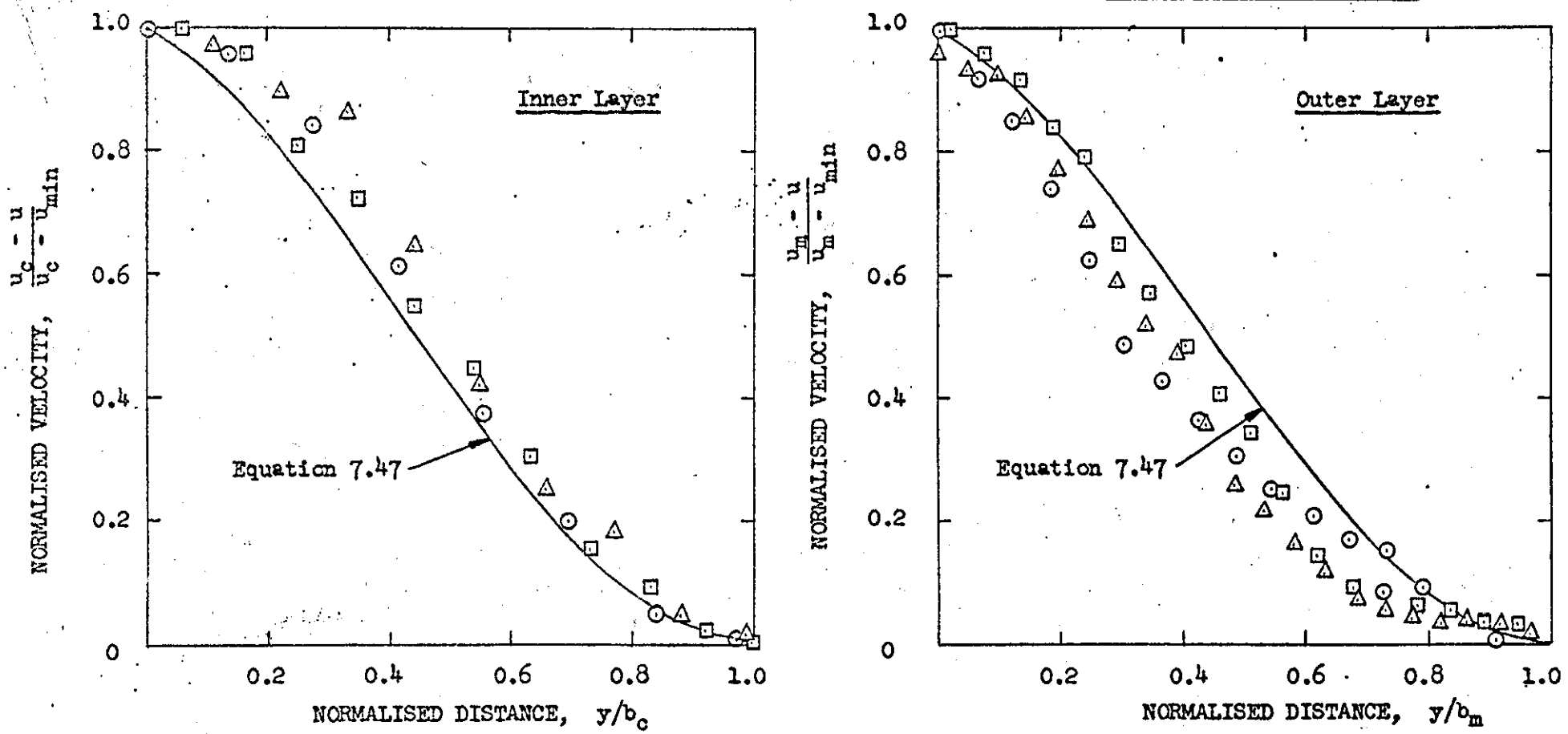

FIG. 11.6: SIMILARITY OF MIXING LAYER VELOCITY PROFILES - WAKE FLOW REGION

Symbol	Run No.	x ins.
⊙	21	0.50
△		0.75
⊡	22	0.50
◇		1.00
◈		1.50

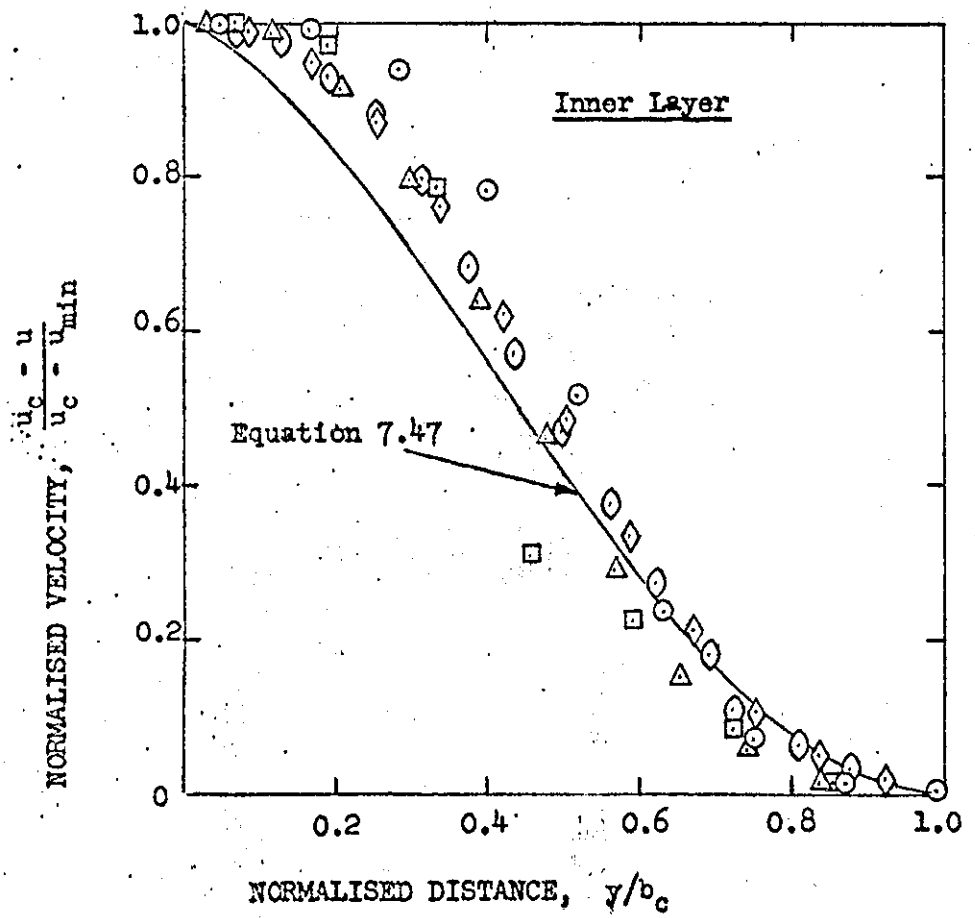

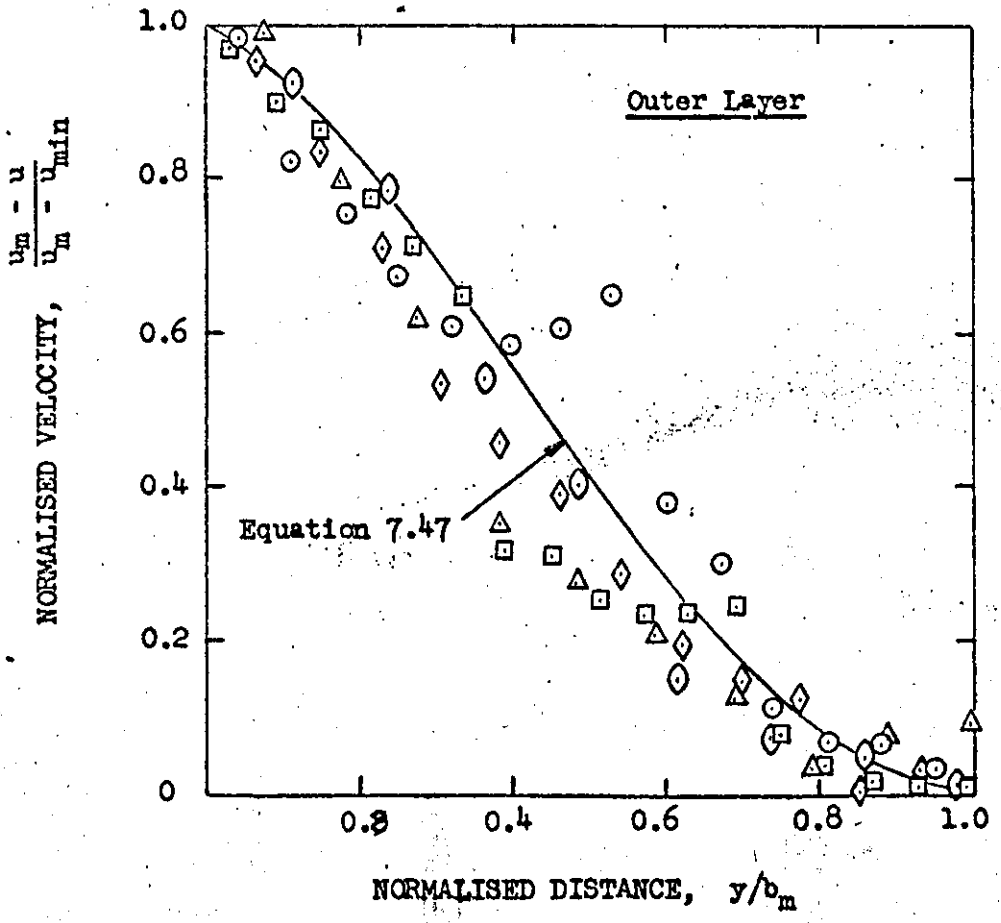

D162.

FIG. 11.6: CONTINUED

Symbol	Run No.	x ins.
▽	23	1.0
◇		2.0
◈		2.5
⊙	24	1.0
△		3.0
⊡		5.0
◎	25	1.0

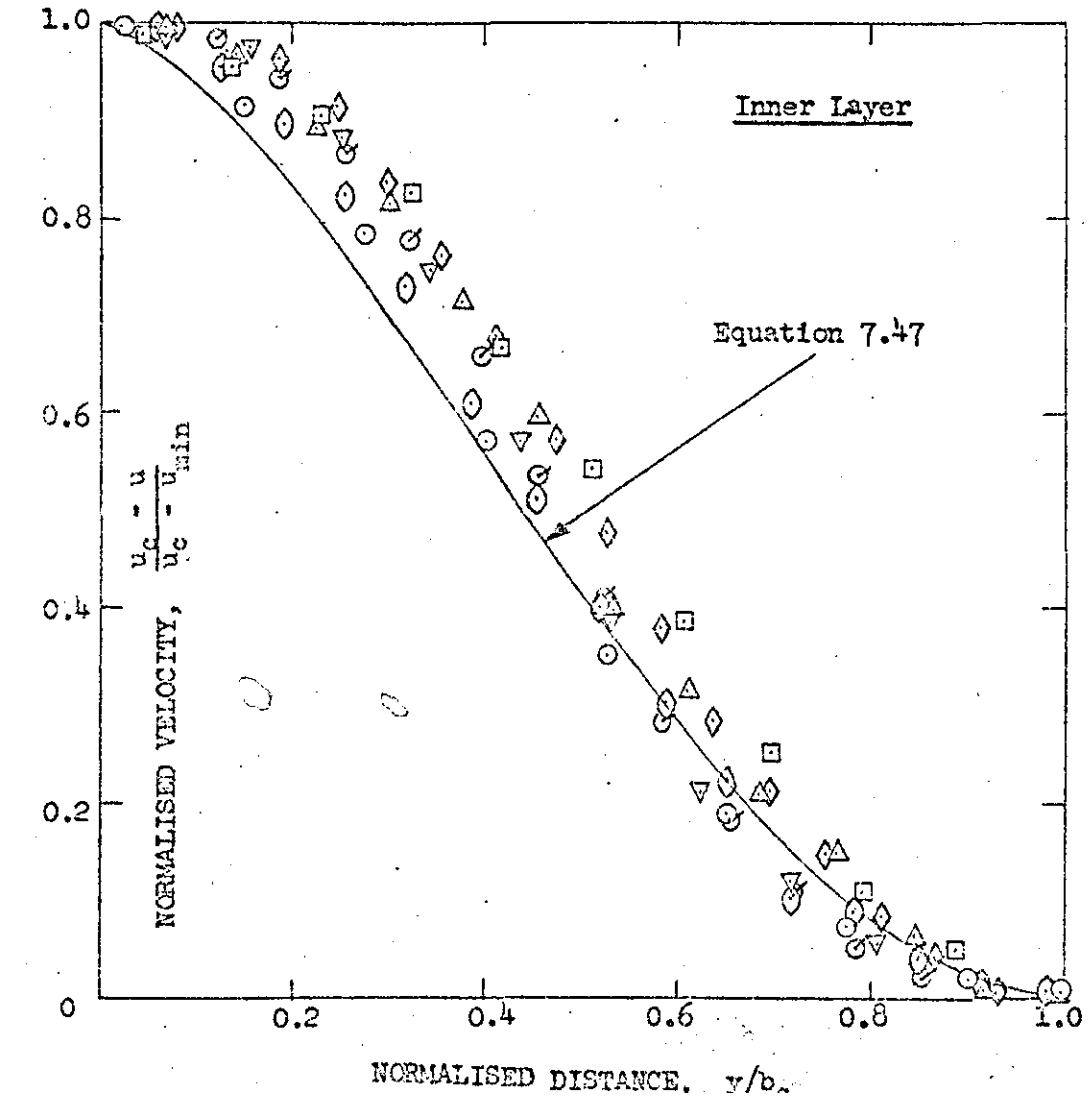

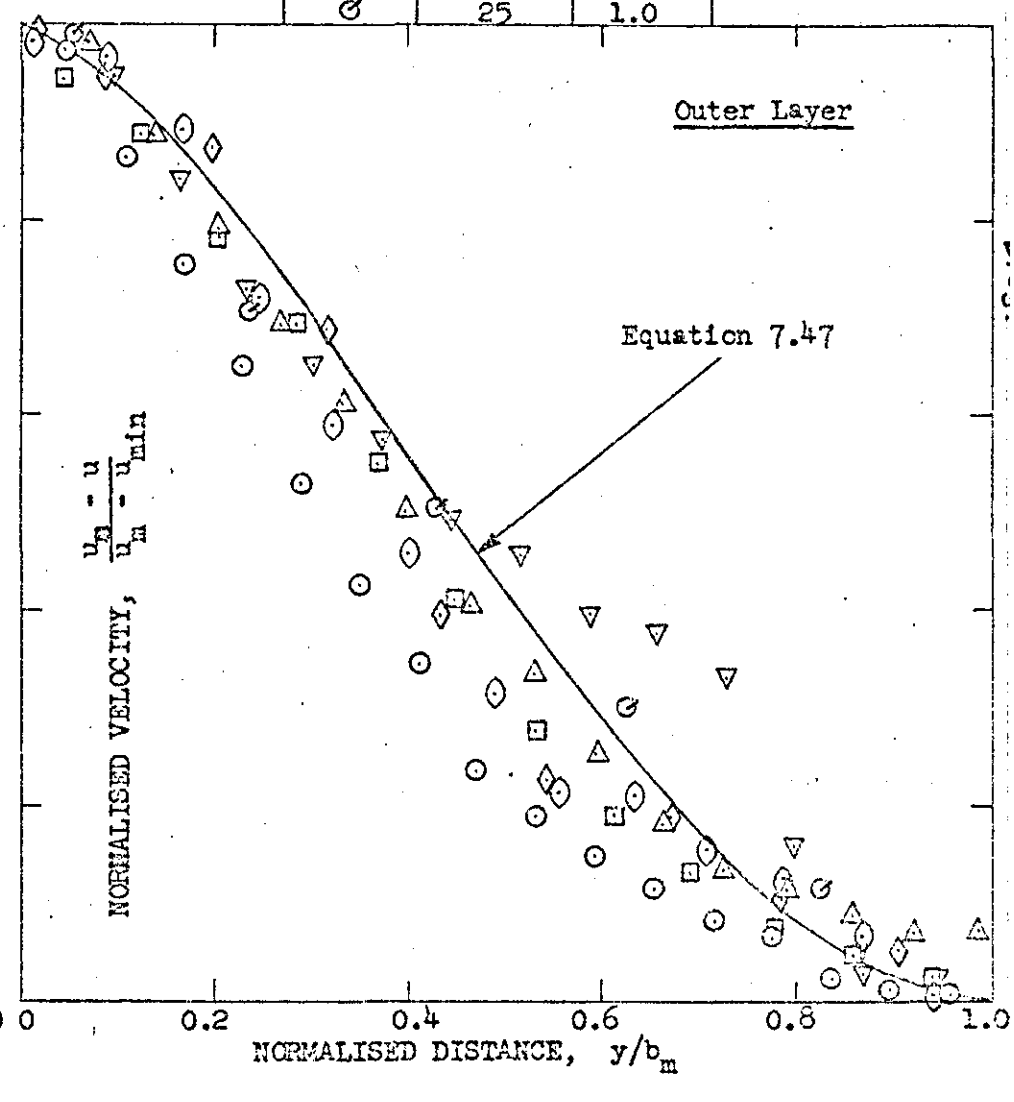

FIG. 11.8: SIMILARITY OF WAKE PROFILES FOR INTERMEDIATE - LIPPED SLOT

Symbol	Test Run No.	x ins.
⊙	41	0.50
△		0.75
◇		1.00
◇		1.50
⊡		1.25

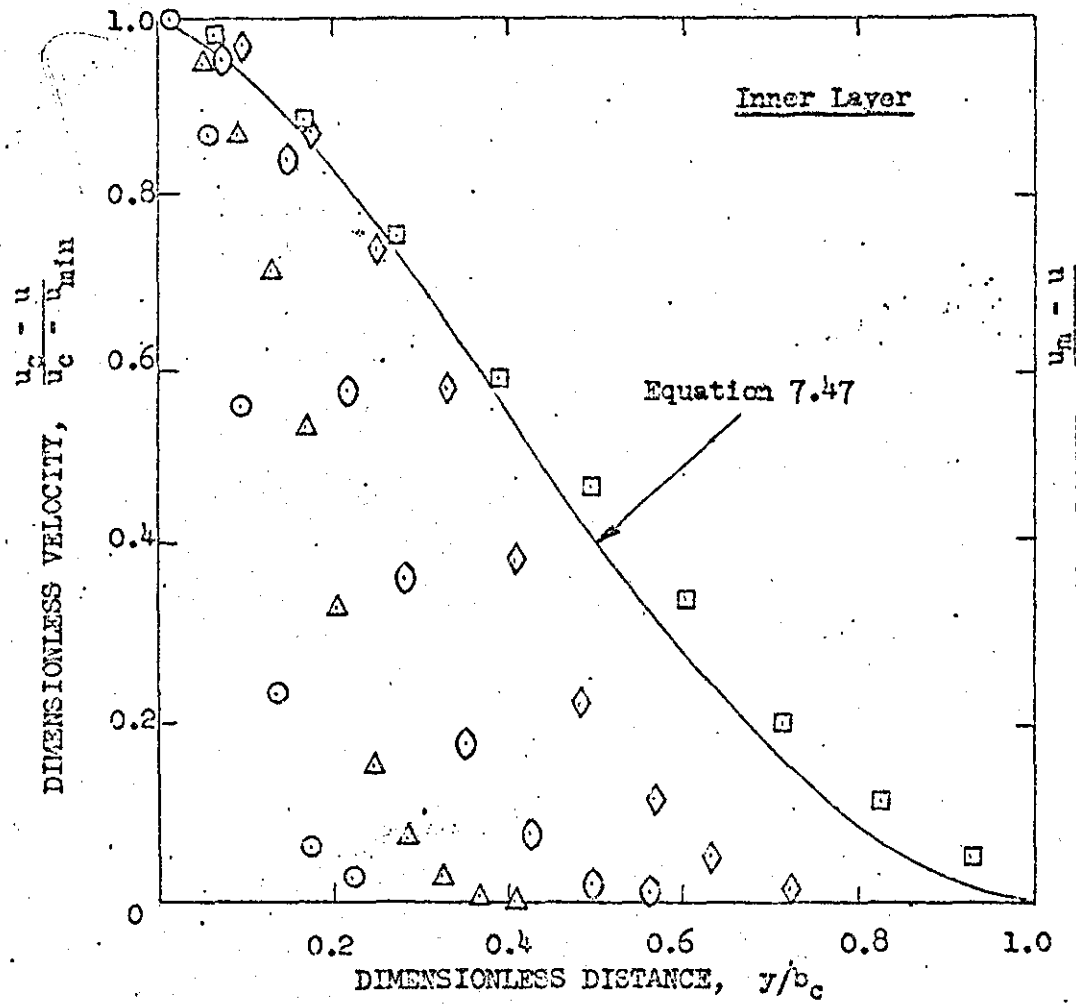

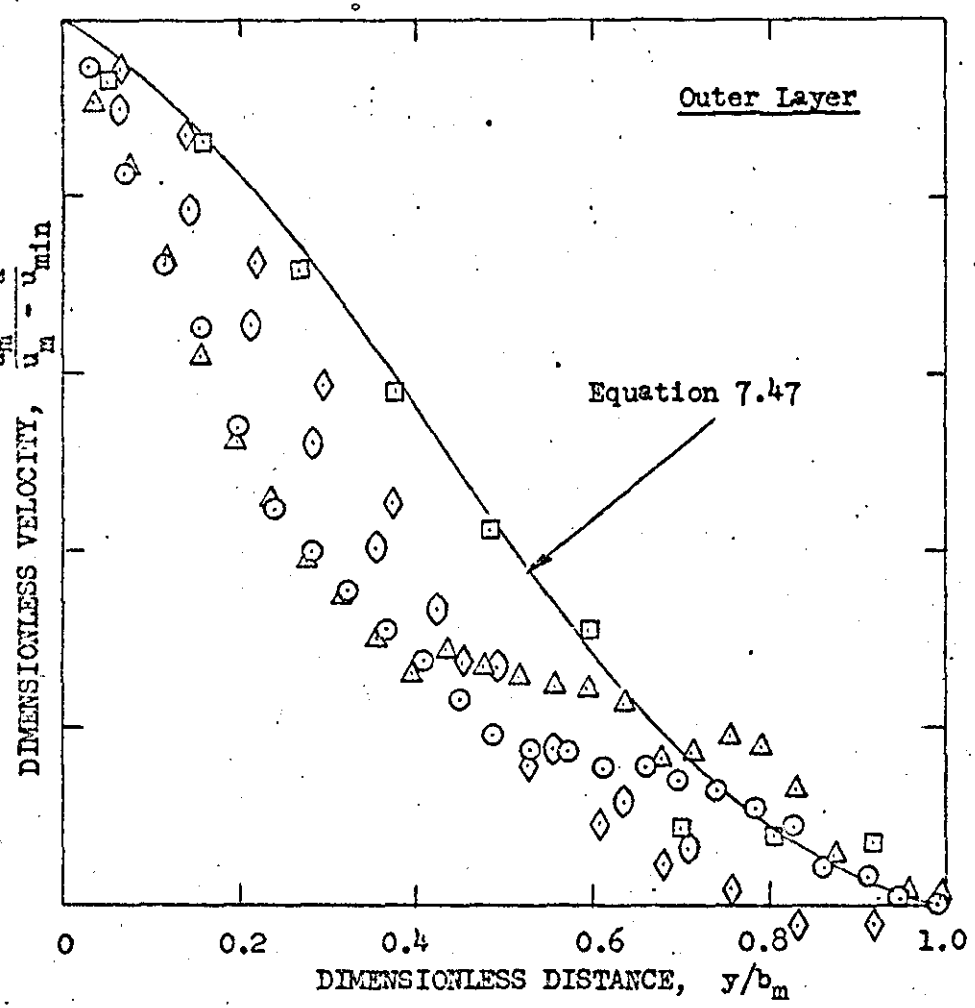

FIG. 11.9: SIMILARITY OF WAKE VELOCITY PROFILES FOR INTERMEDIATE - LIPPED SLOT

Symbol	Test Run No.	x ins.
⊙	37	0.75
◇		1.50
△		2.25

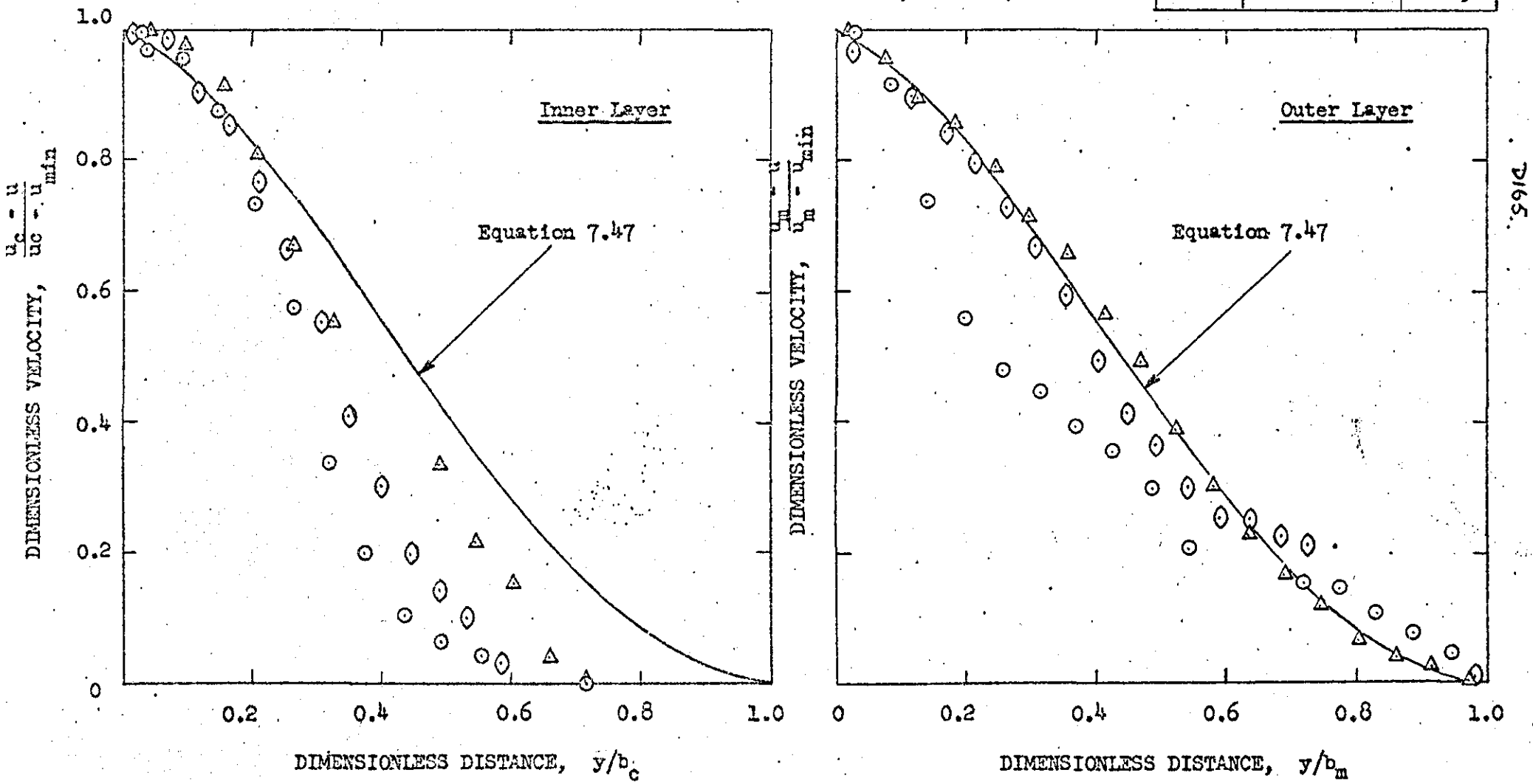

FIG. 11.10: SIMILARITY OF WAKE VELOCITY PROFILES FOR INTERMEDIATE - LIPPED SLOT

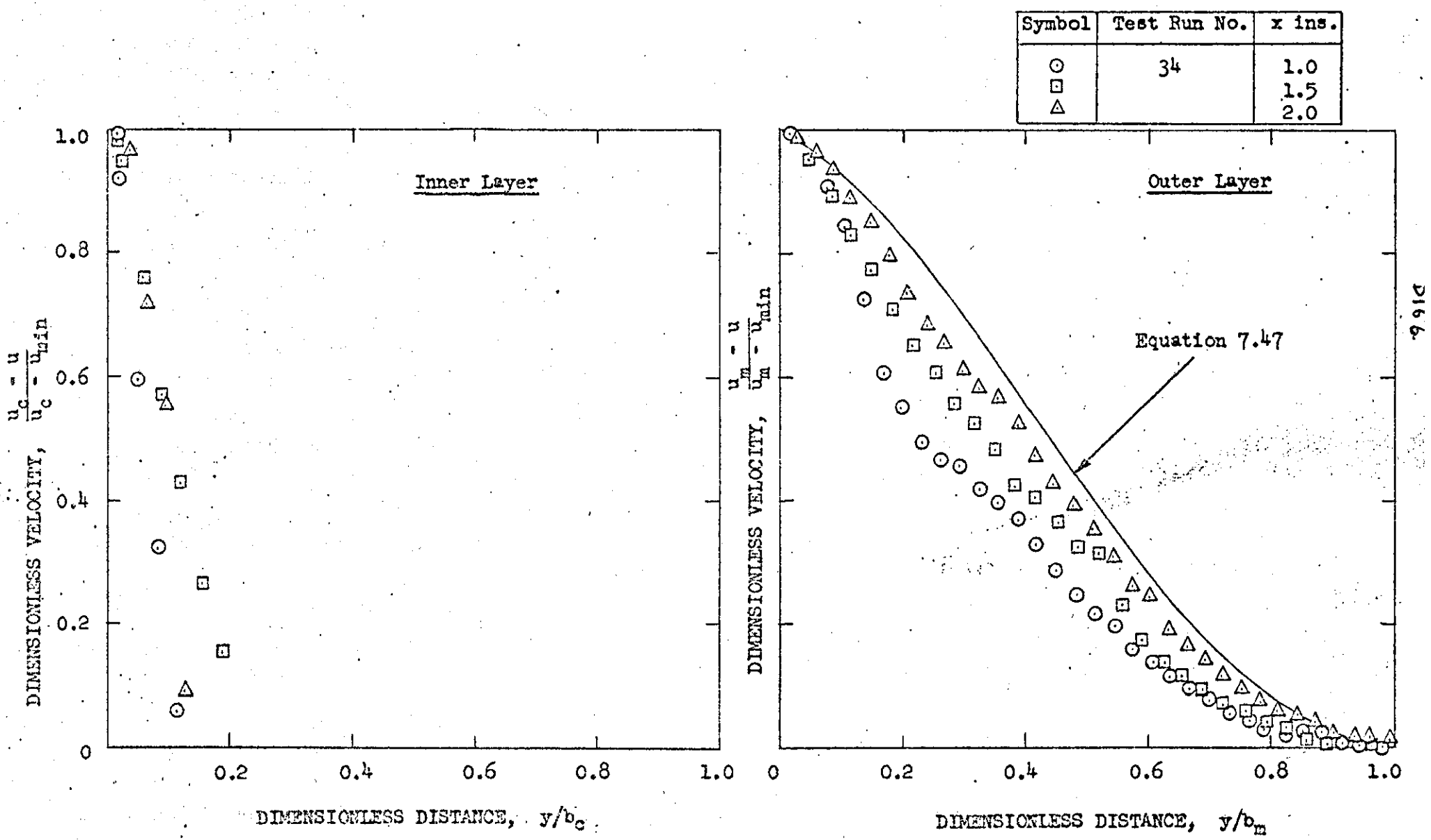

FIG. 11.11: SIMILARITY OF WAKE VELOCITY PROFILES FOR INTERMEDIATE - LIPPED SLOT

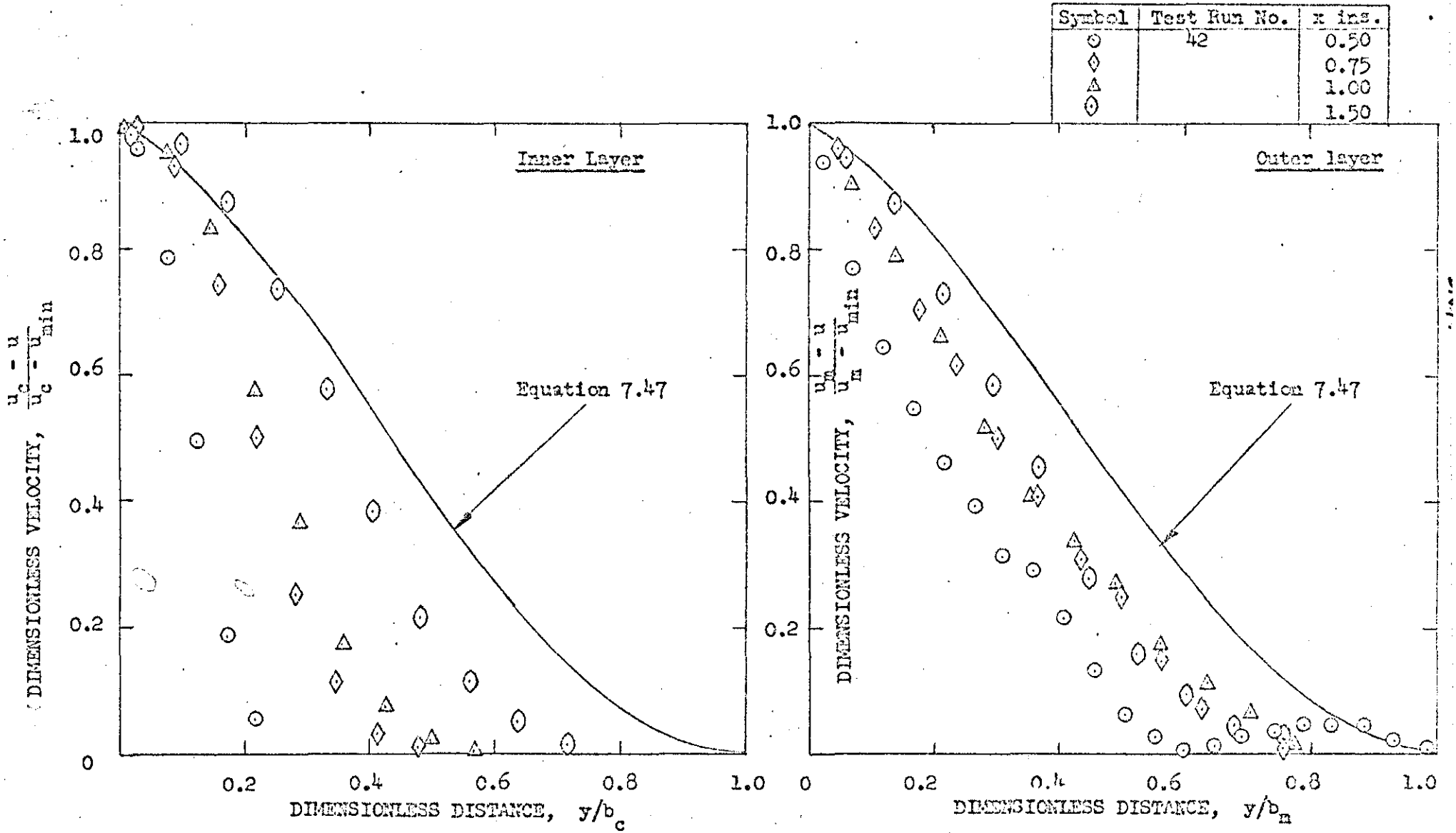

FIG. 11.12: SIMILARITY OF SHEAR FLOW VELOCITY PROFILES FOR THICK - LIPPED SLOT

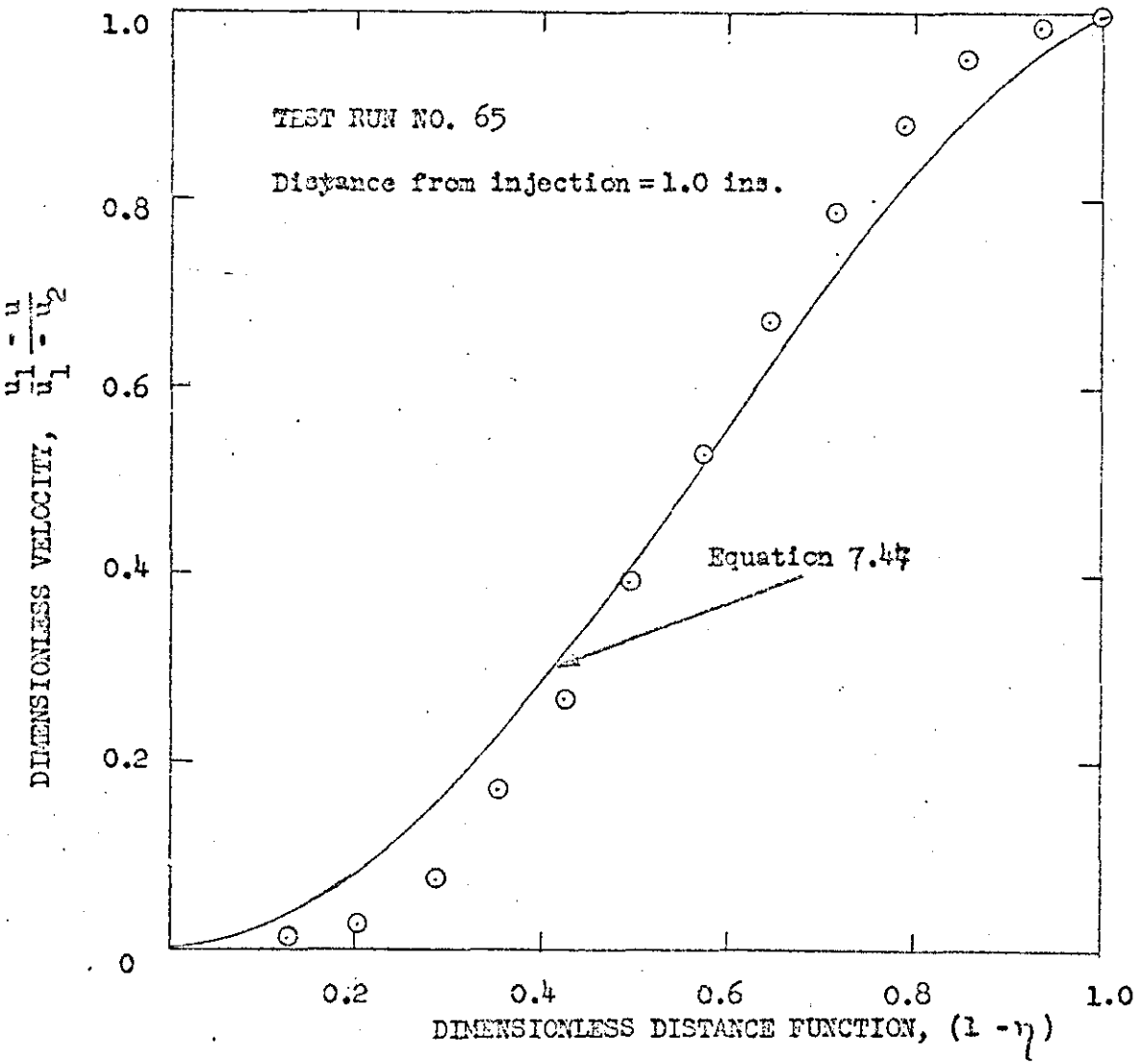

FIG. 11.13: SIMILARITY OF WAKE VELOCITY PROFILES FOR THICK - LIPPED SLOT

Symbol	Test Run No.	x ins.
⊙	53	0.50
△		0.75
□		1.00

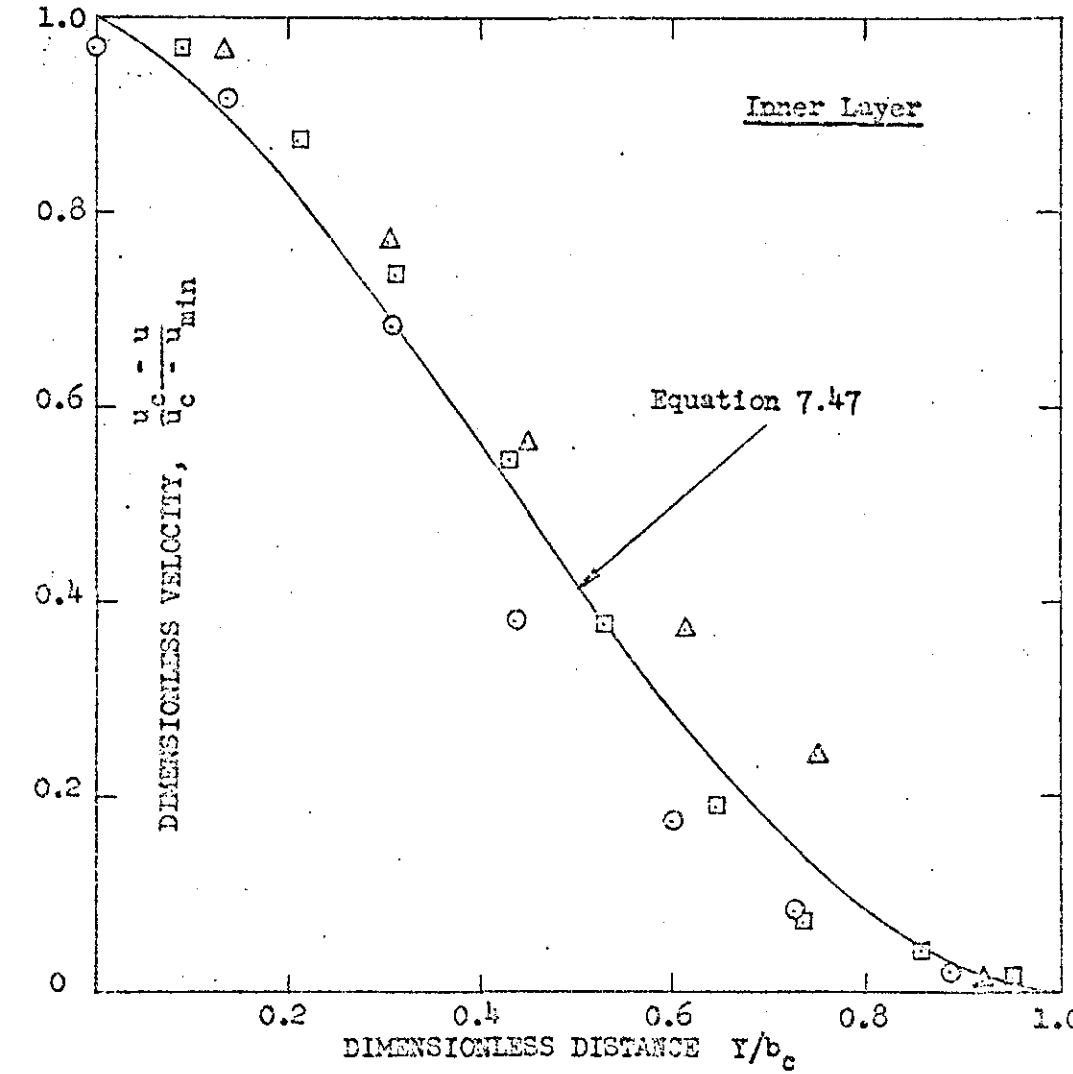

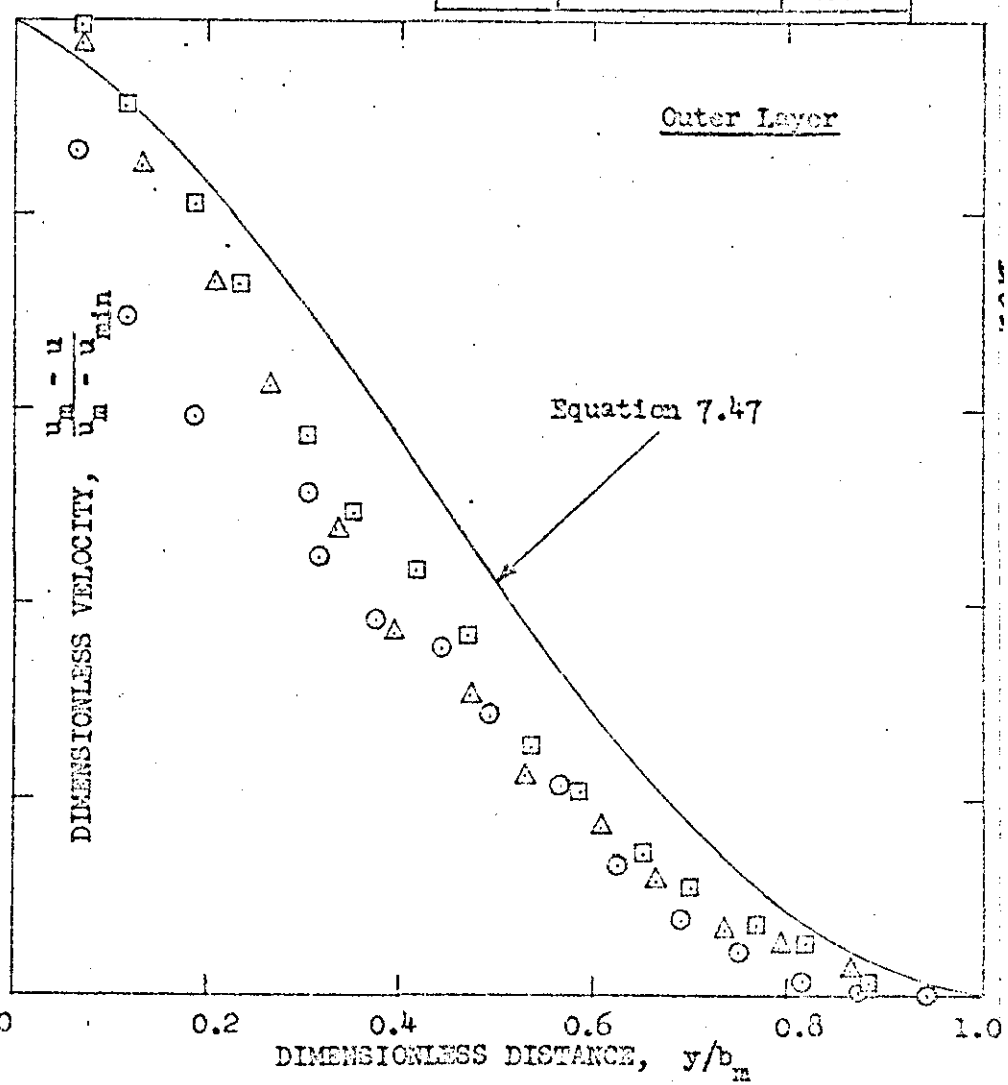

FIG. 11.14: SIMILARITY OF WAKE PROFILES FOR THICK - LIPPED SLOT

Symbol	Run No.	x ins.
⊙	62	0.5
△		1.0

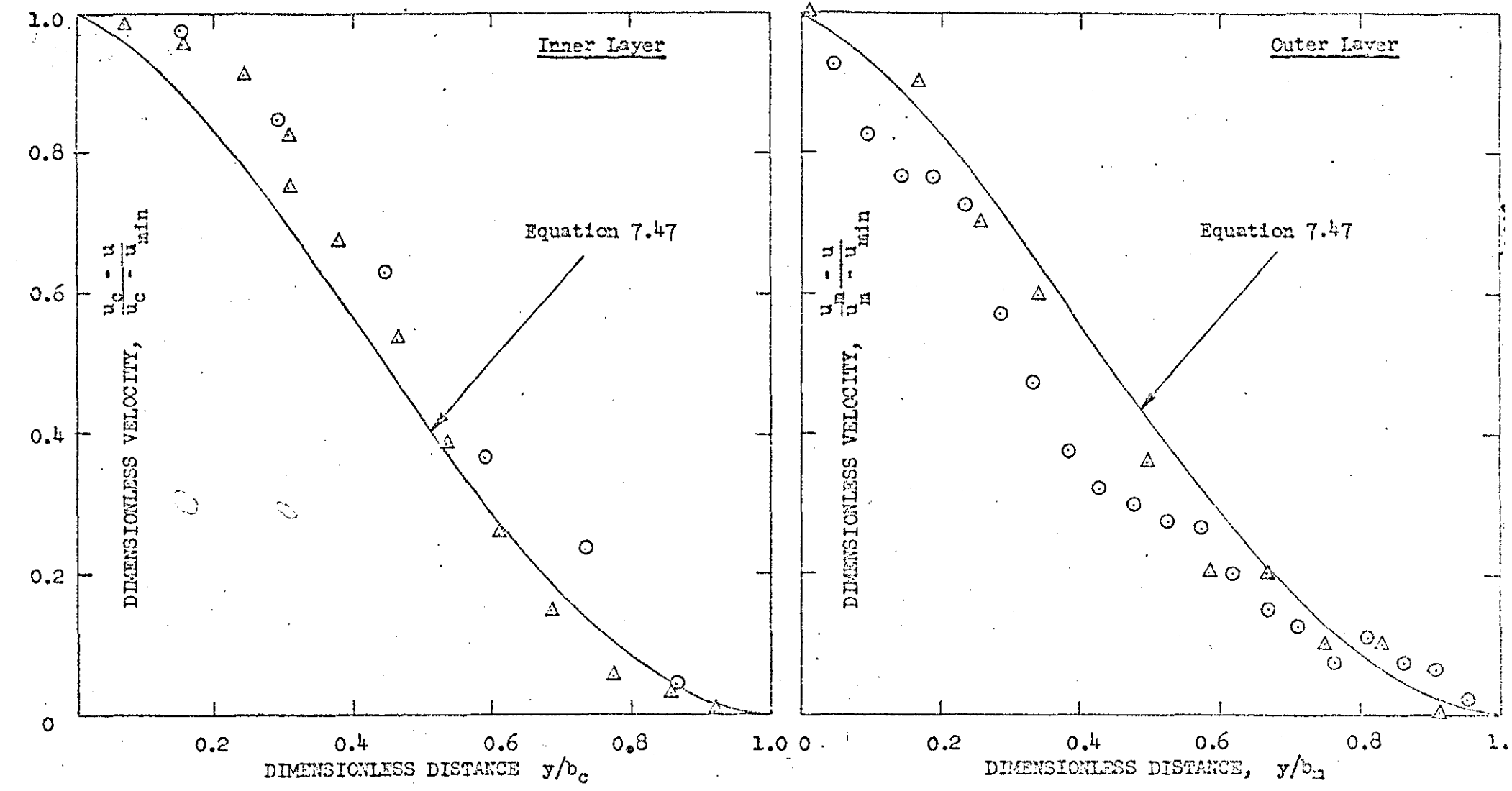

FIG. 11.15: SIMILARITY OF WAKE VELOCITY PROFILES FOR THICK SLOT LIP

Symbol	Test Run No.	x ins.
⊙	60	0.50
△		0.75
□		1.00

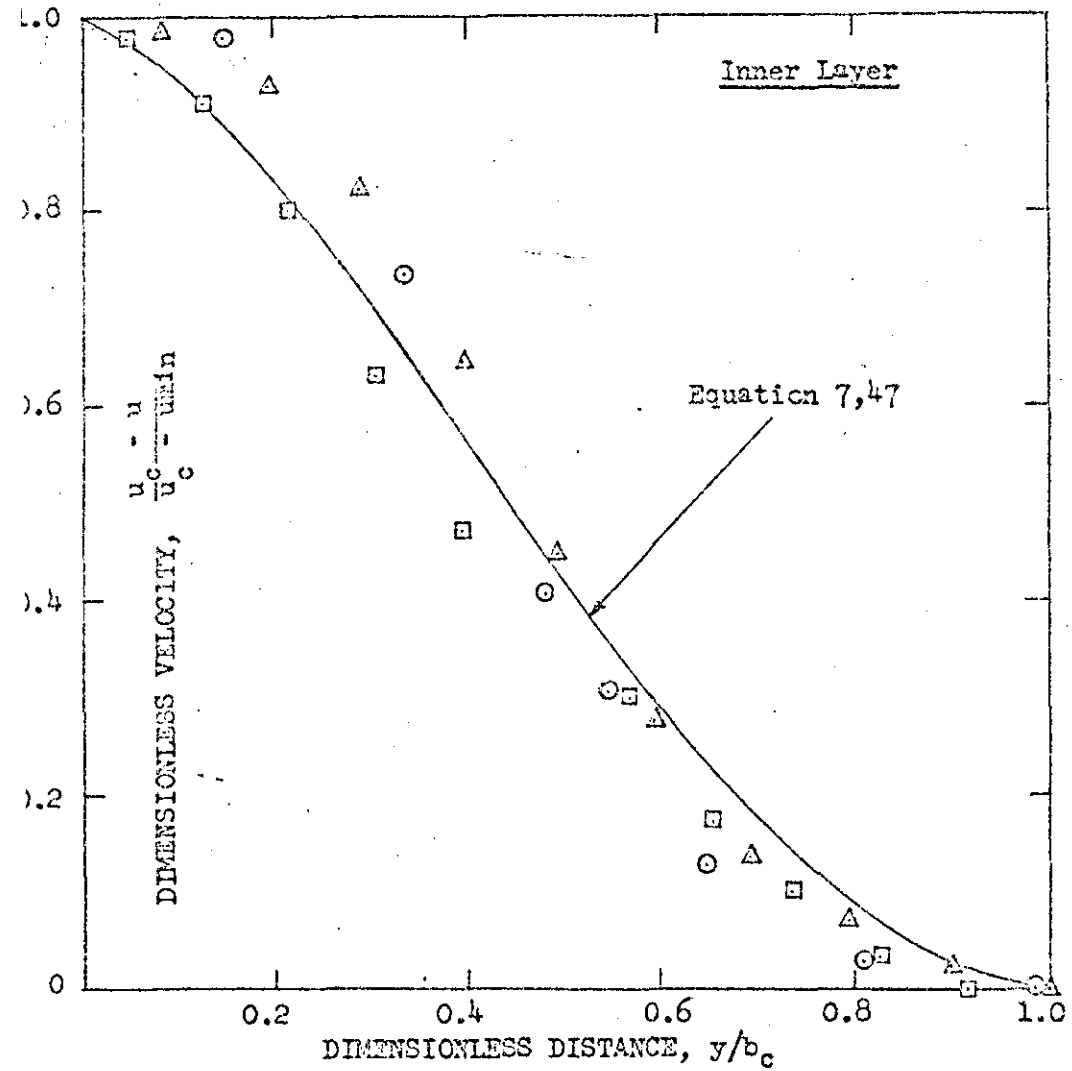

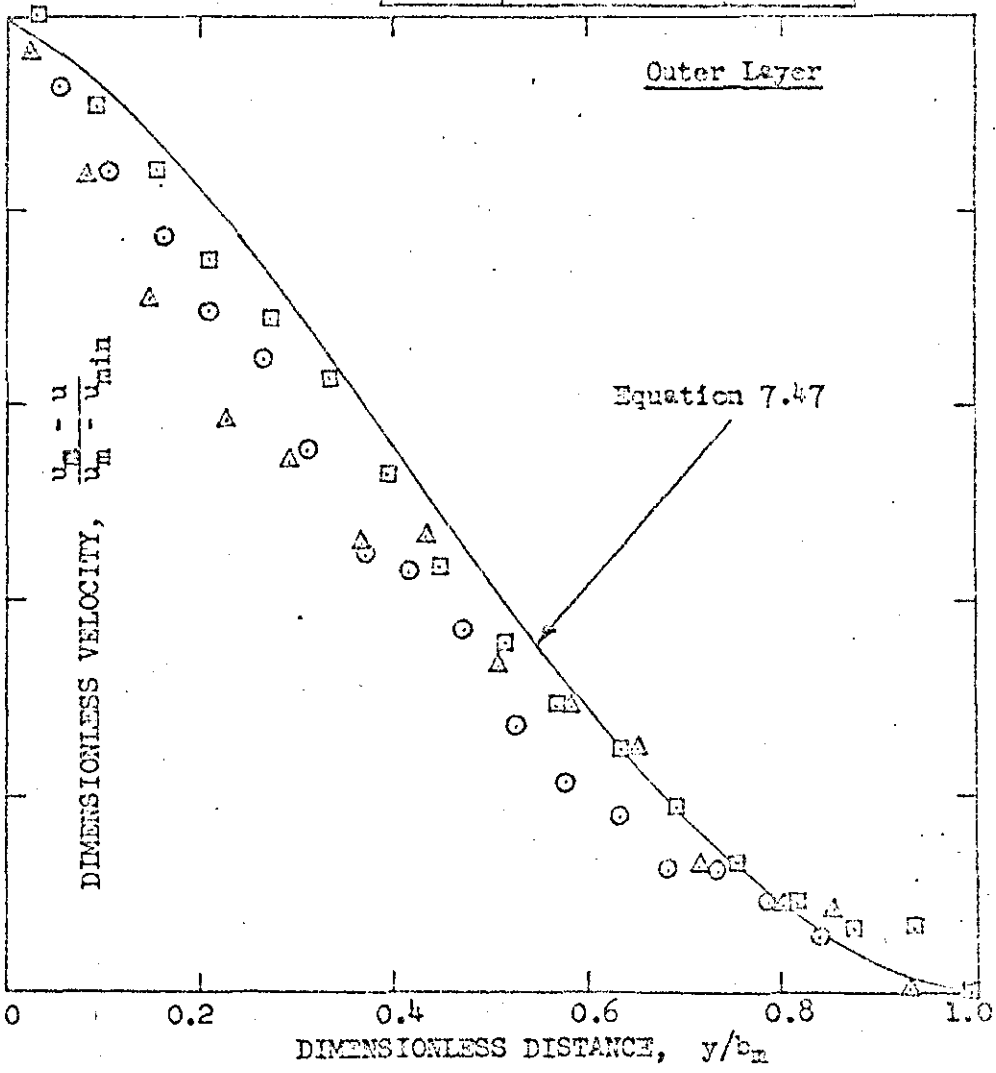

FIG. 11.16: SIMILAR VELOCITY PROFILES FOR MAINSTREAM BOUNDARY LAYER OFF THIN - LIPPED SLOT

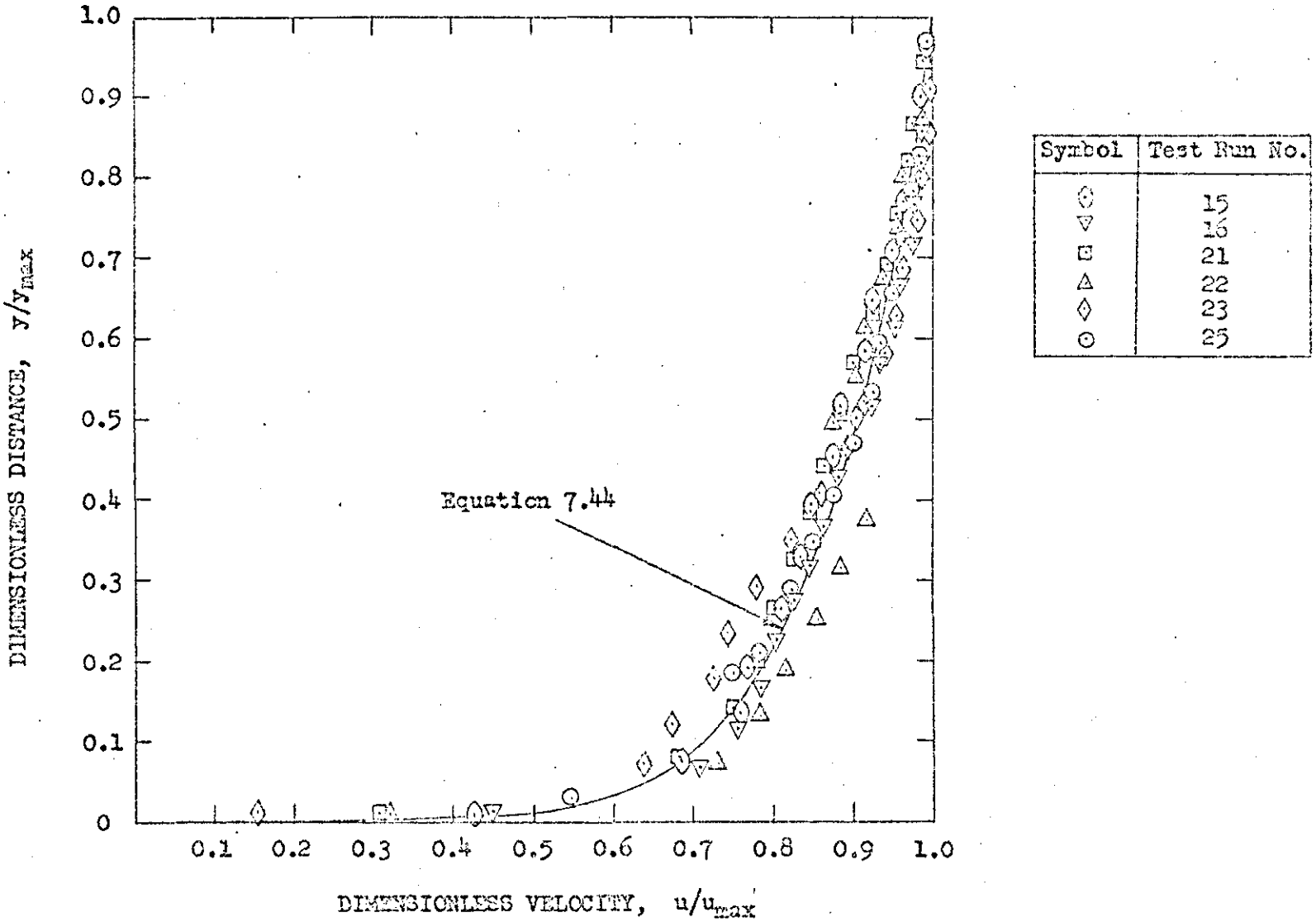

FIG. 11.16: CONTINUED

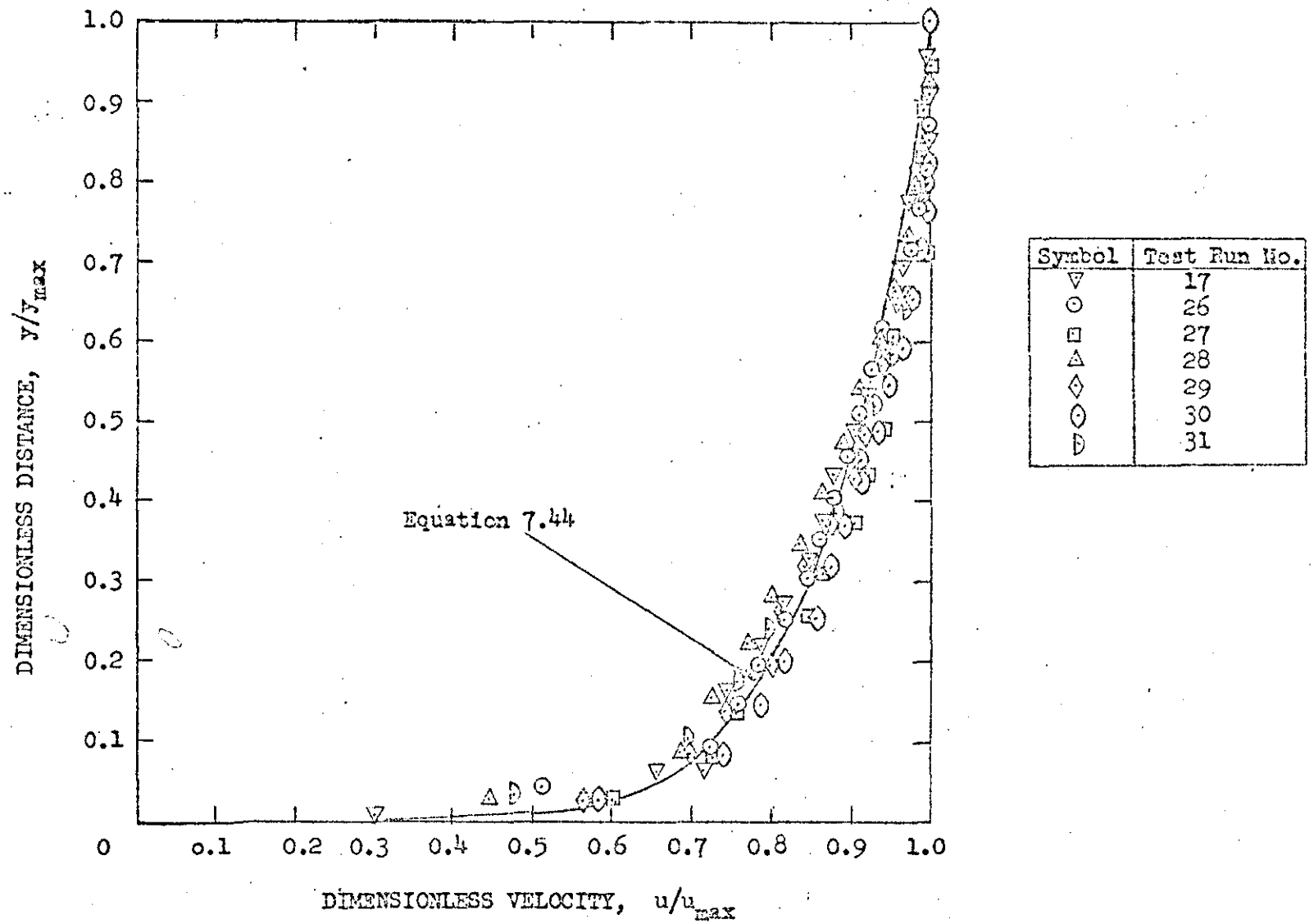

FIG. 11.17: SIMILARITY OF MAINSTREAM BOUNDARY LAYER PROFILES FOR THE INTERMEDIATE - LIPPED SLOT

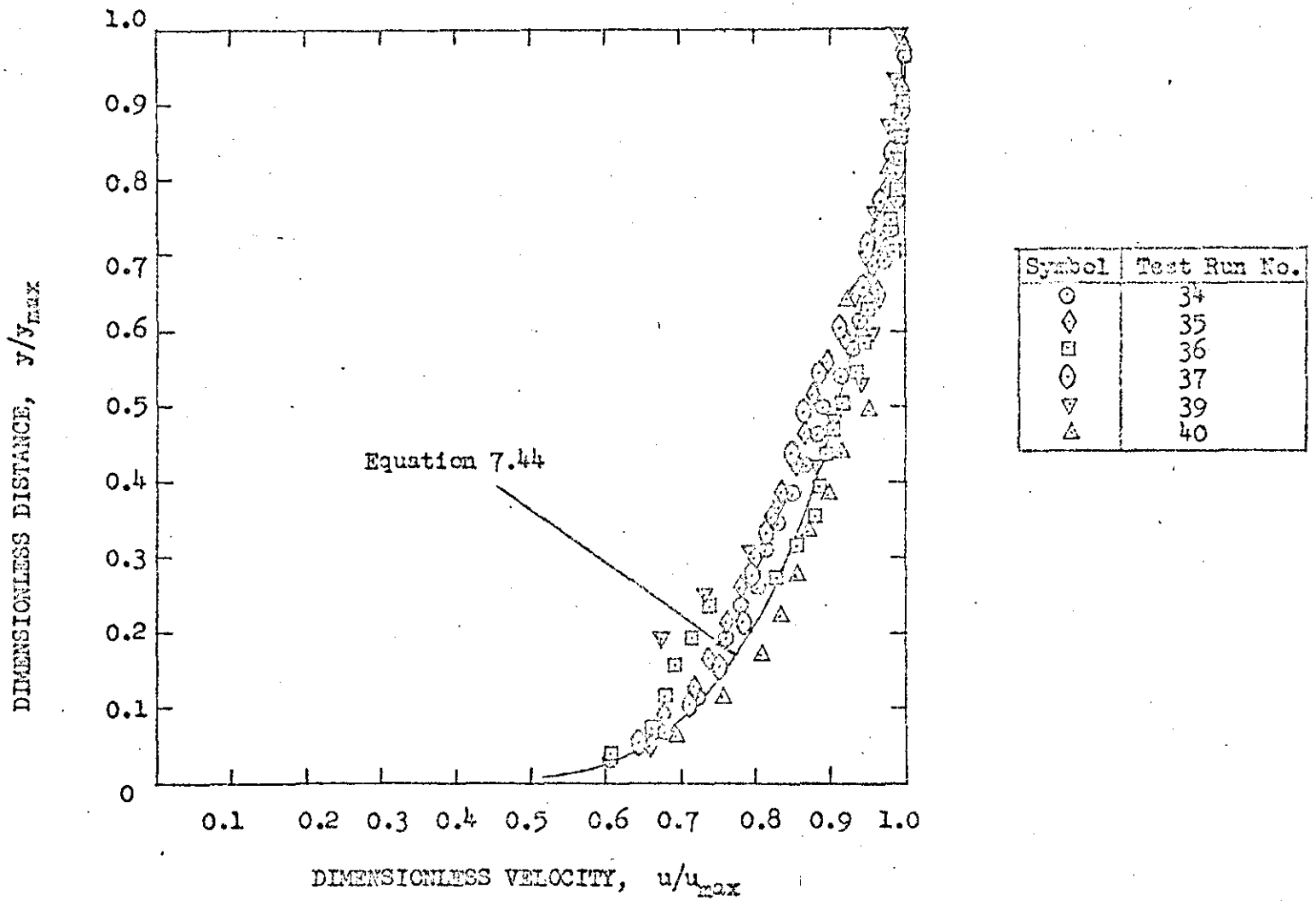

FIG. 11.17: CONTINUED

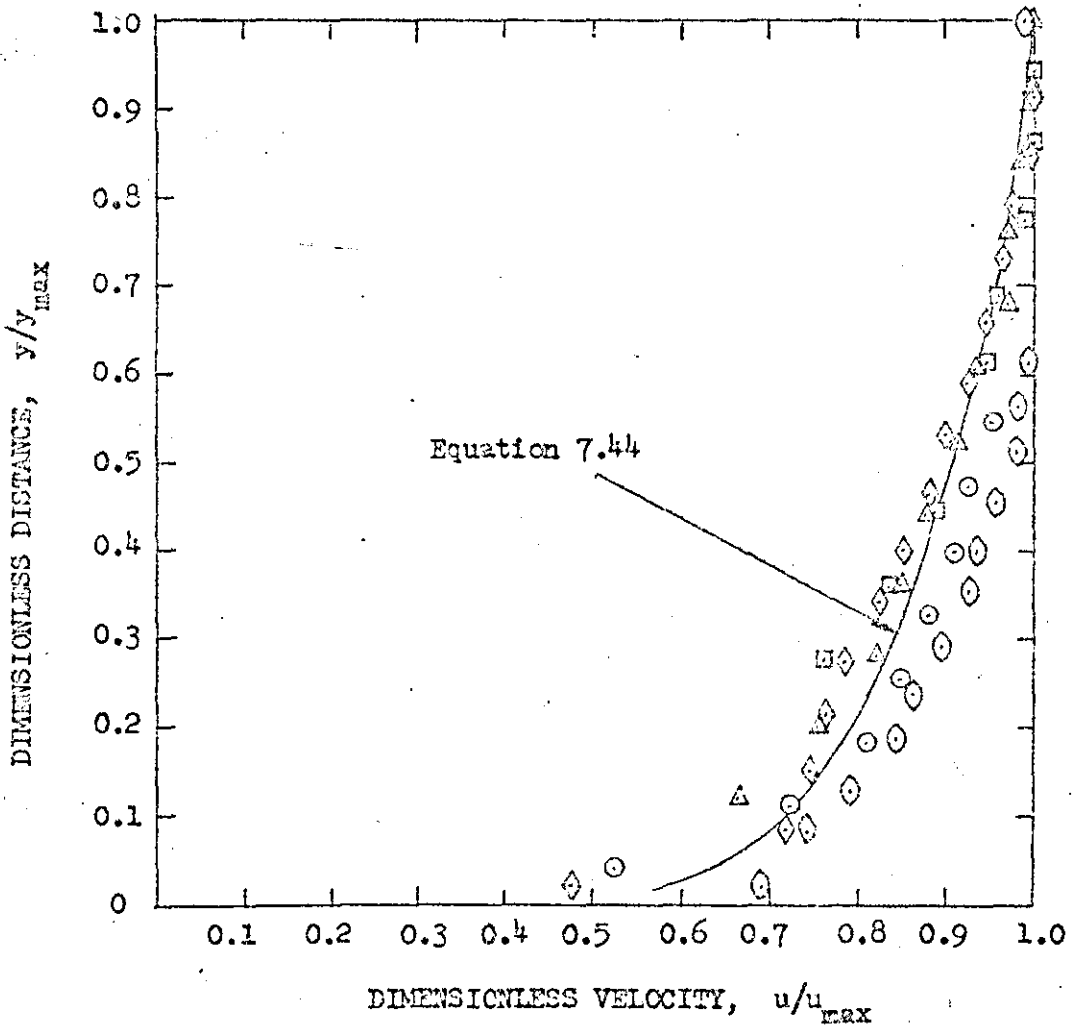

Symbol	Test Run No.
◇	41
◇	42
□	44
○	45
△	46

FIG. 11.18: SIMILAR VELOCITY PROFILES FOR MAINSTREAM BOUNDARY LAYER OF THICK LIP SLOT

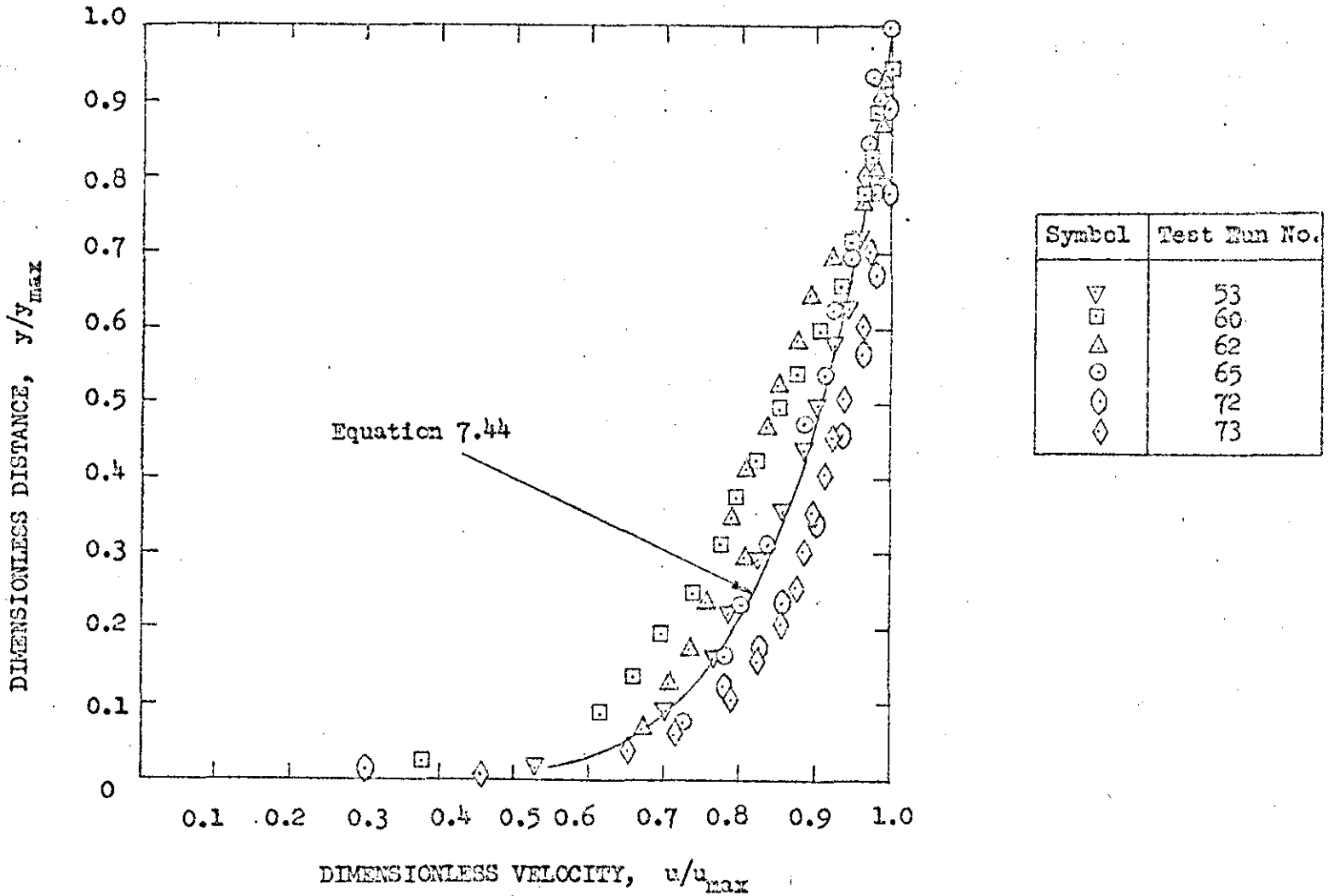

FIG. 11.19: COOLED WALL BOUNDARY LAYER UNIVERSAL VELOCITY PROFILES FOR THIN-LIPPED SLOT

Low Slot Reynolds Numbers

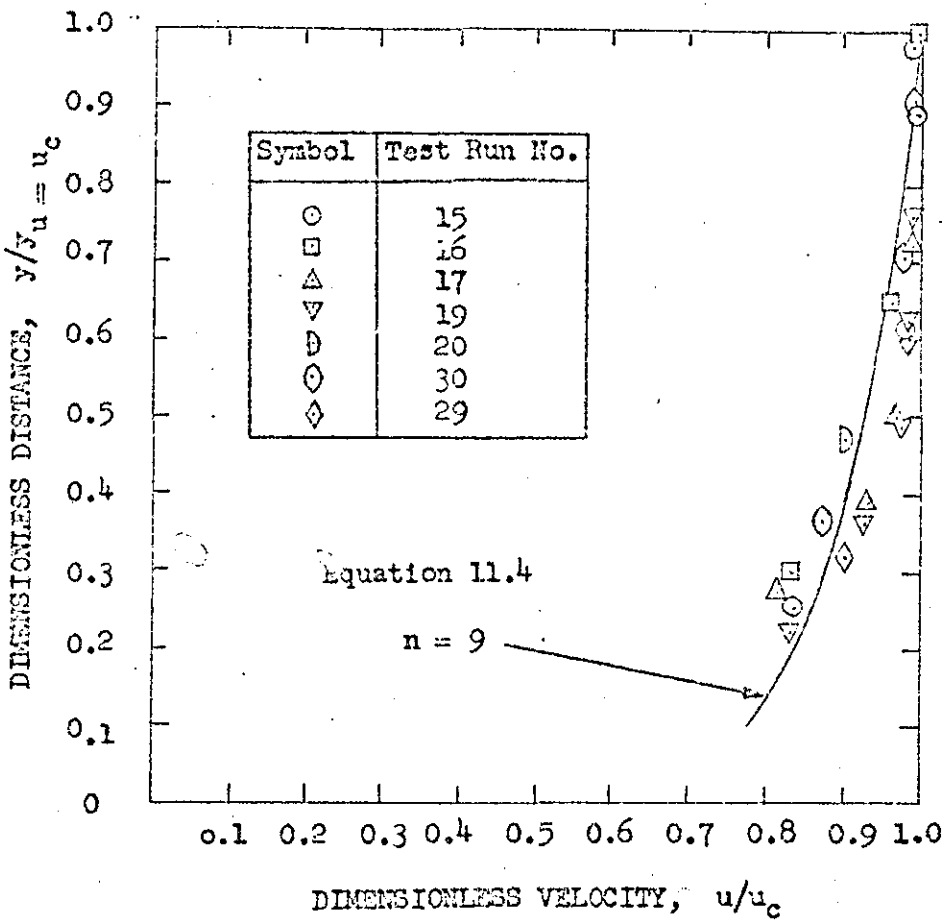

High Slot Reynolds Numbers

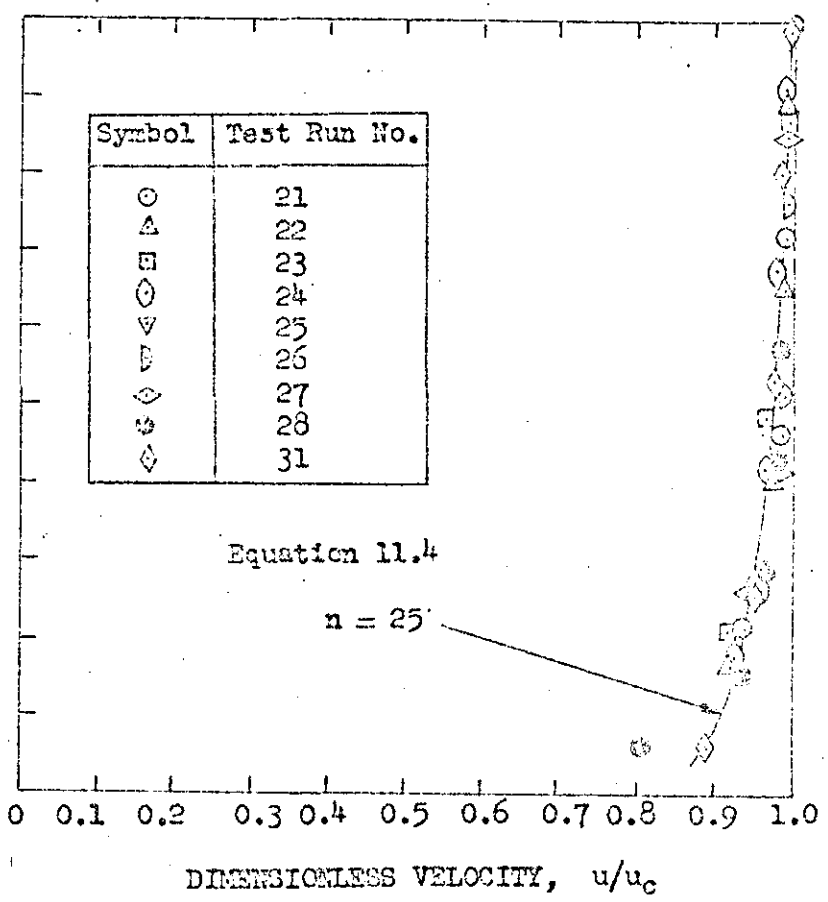

FIG. 11.20: COOLED WALL BOUNDARY LAYER UNIVERSAL VELOCITY PROFILES FOR INTERMEDIATE-LIPPED SLOT

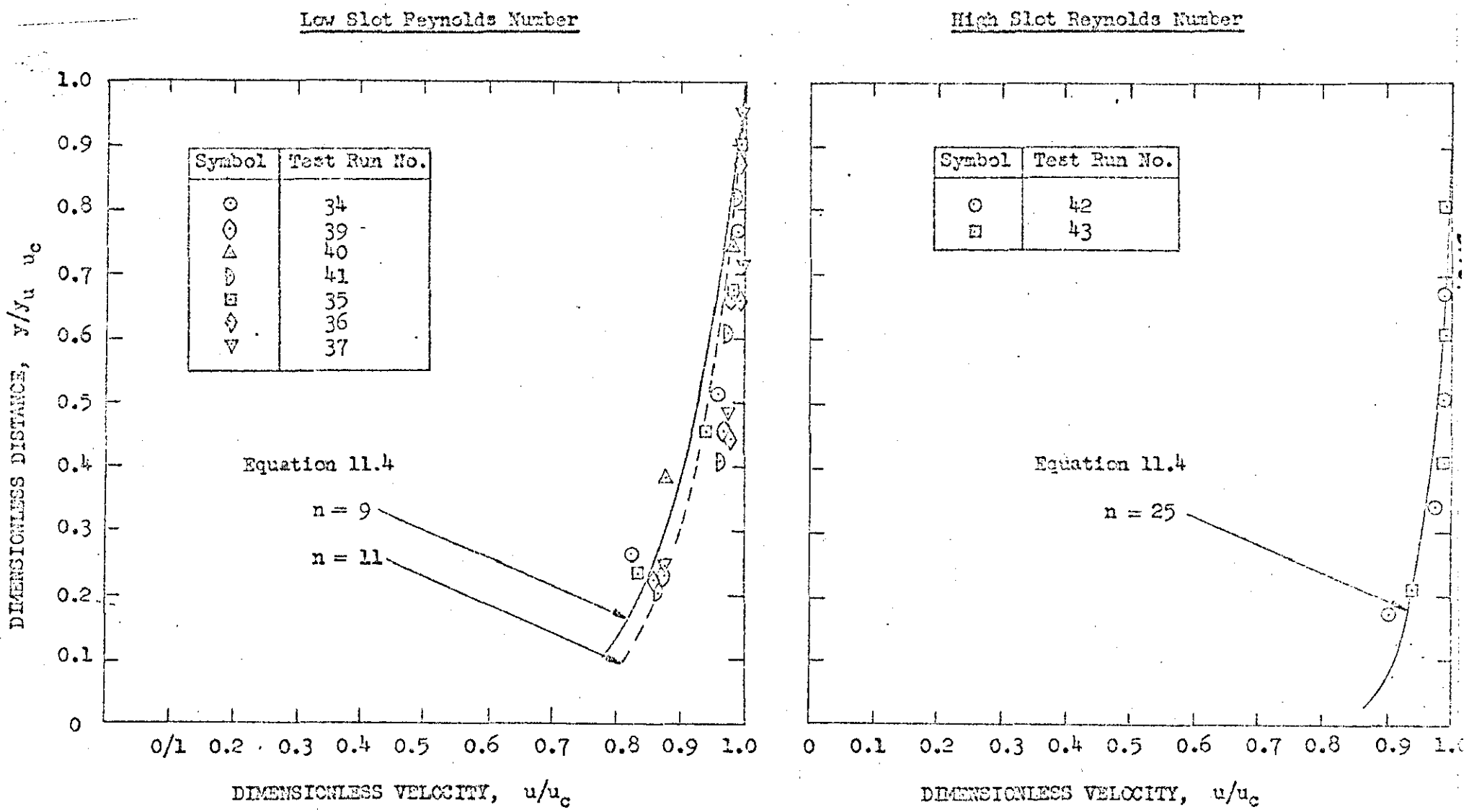

FIG. 11.21: UNIVERSAL VELOCITY PROFILE FOR SLOT LIP INNER BOUNDARY LAYER - THIN LIPPED SLOT

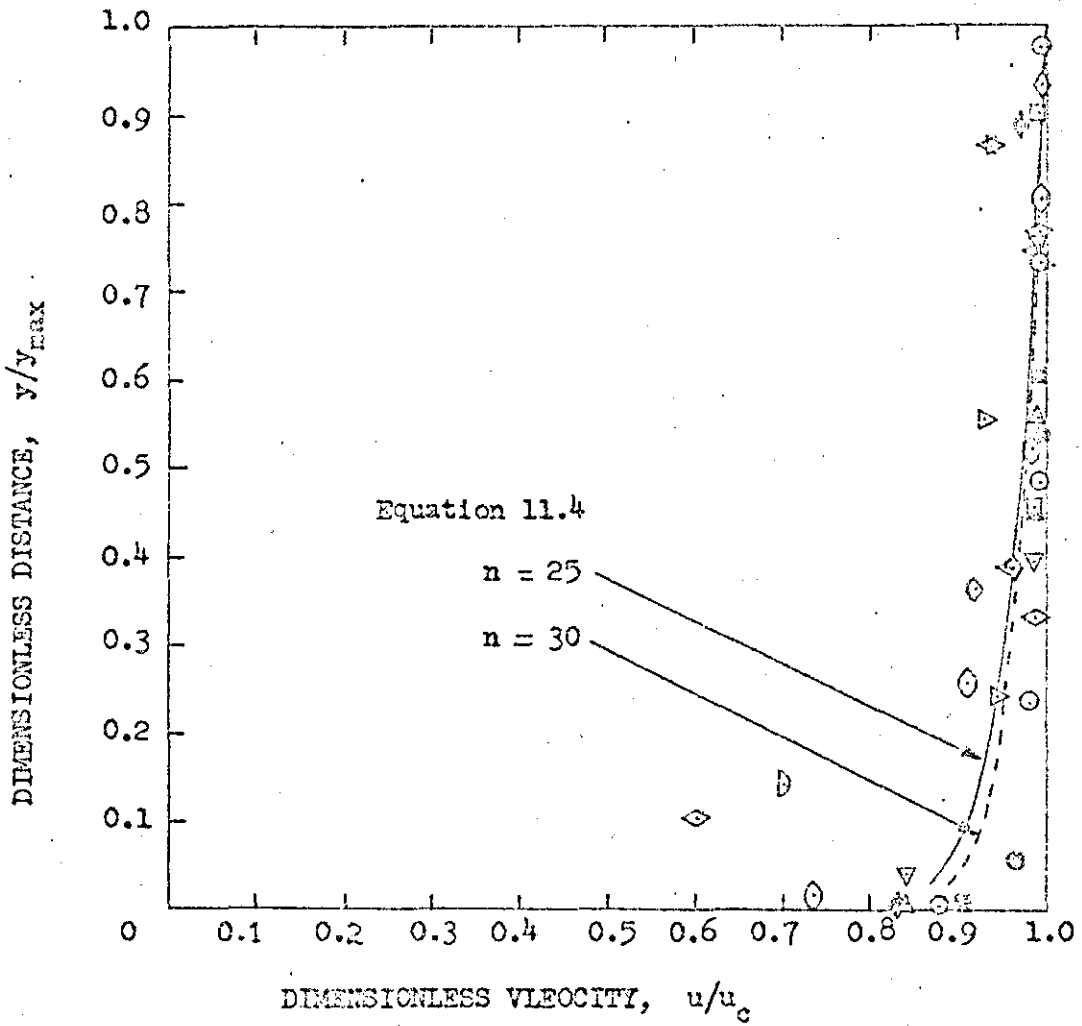

Symbol	Test Run No.
⊙	16
◇	17
⊙	19
△	20
□	21
▽	22
▽	23
⊙	24
◇	25
▷	26
◁	27
◇	28
▷	29
◇	30
◁	31

FIG. 11.22: UNIVERSAL VELOCITY PROFILE FOR LIP BOUNDARY LAYER OF INTERMEDIATE THICKNESS LIP

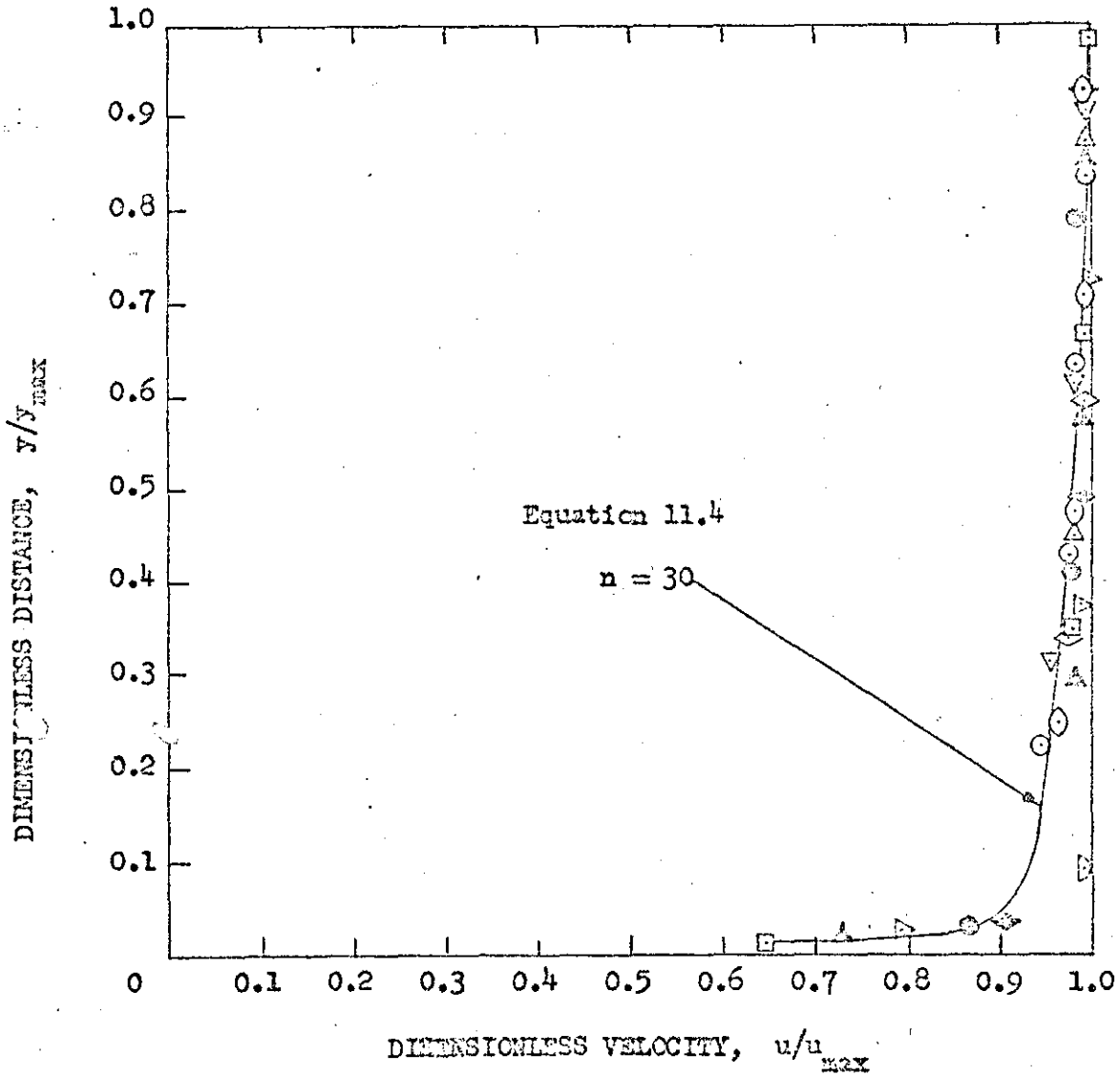

Symbol	Test Run No.
○	34
□	45
◇	37
▽	36
⊙	41
▷	42
△	43
◁	35
▷	44
◇	46
△	39

FIG. 11.23: COOLED WALL BOUNDARY LAYER UNIVERSAL AND SIMILAR VELOCITY PROFILE AT HIGH SLOT REYNOLDS NUMBER

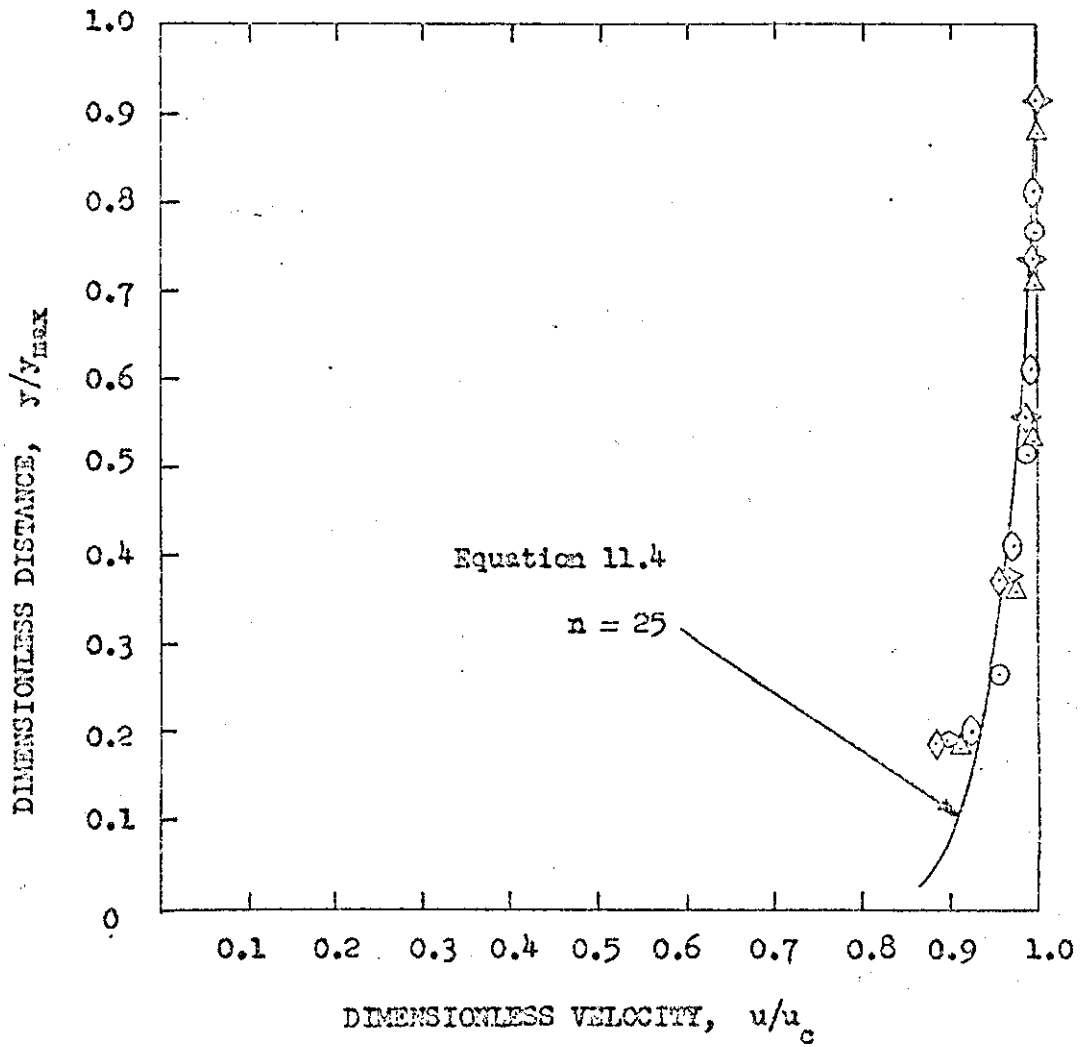

Symbol	Distance from injection, ins.
⊙	0.0
◇	0.25
△	0.75
◈	1.00
◇	1.25

FIG. 11.24: COOLED WALL BOUNDARY LAYER GROWTH

Test Run No. 16

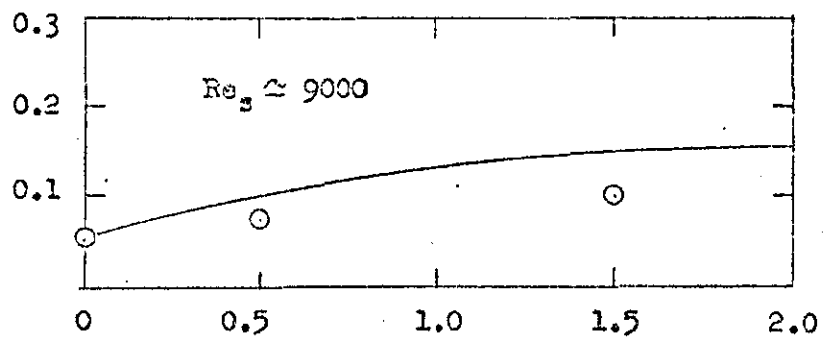

Test Run No.23

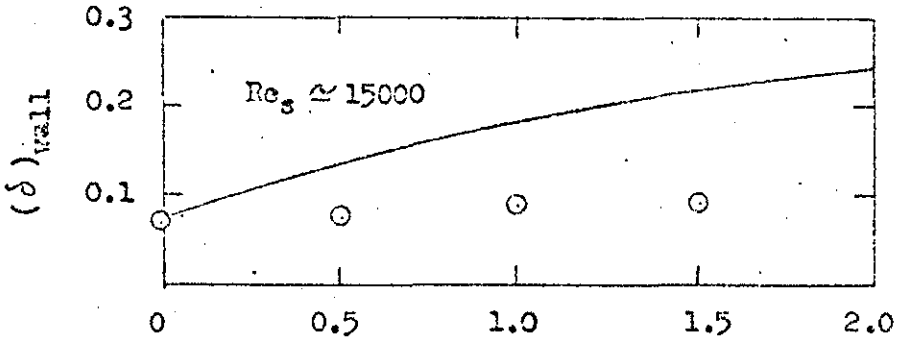

Test Run No. 27

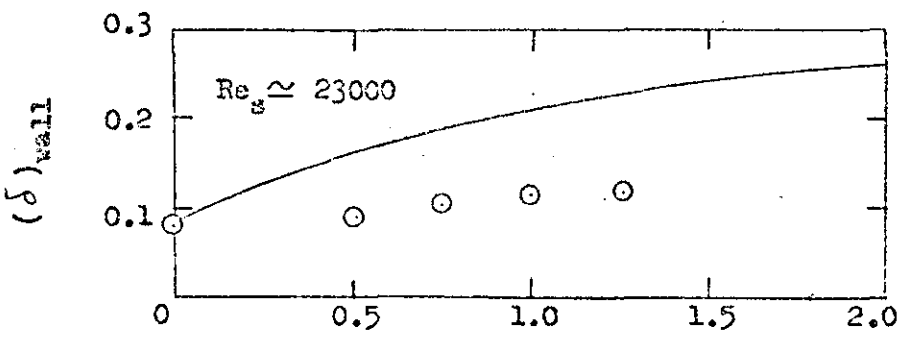

FIG. 11.25: ASSESSMENT OF WAKE EFFECTIVE ORIGIN, x_o

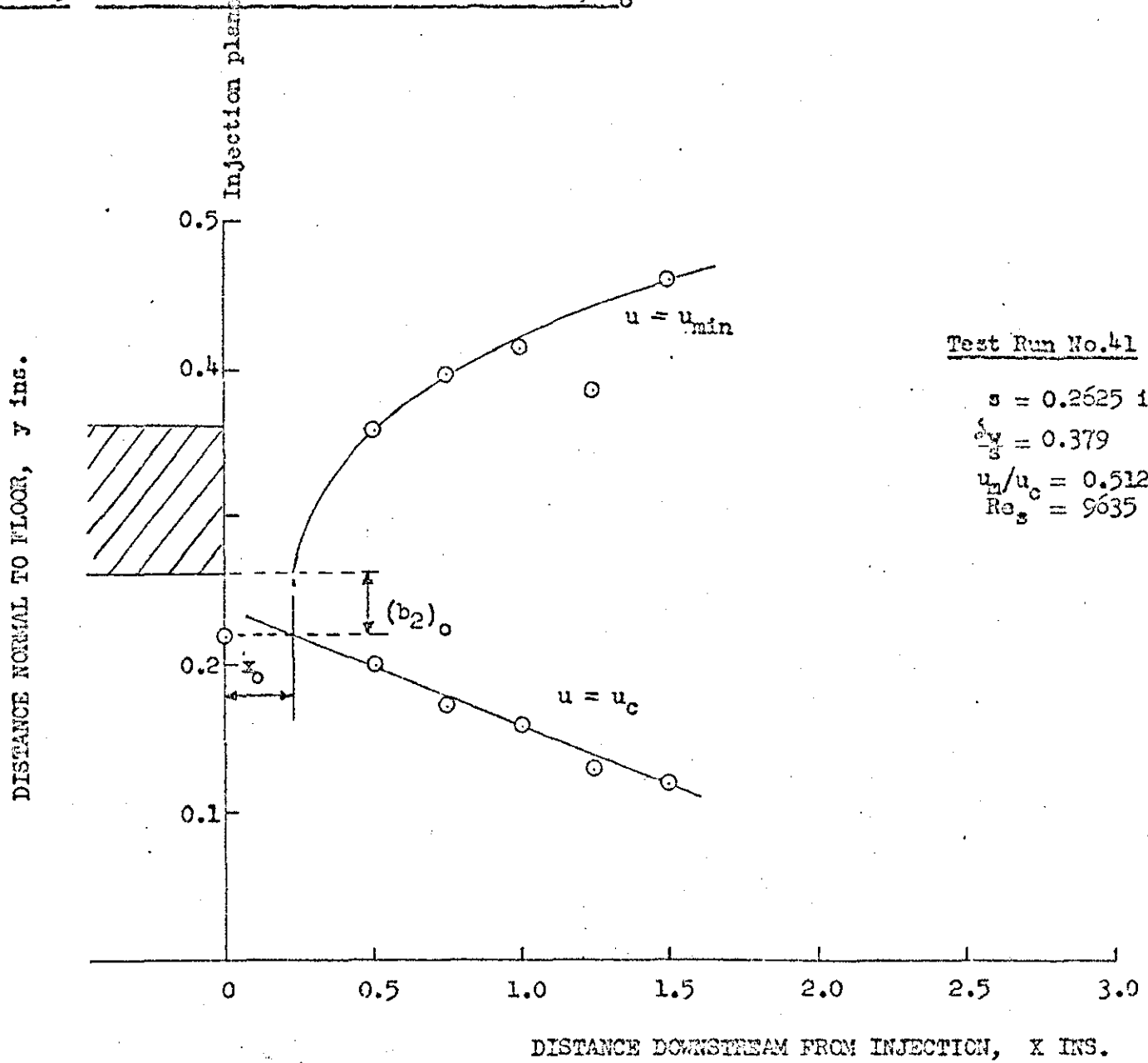

Test Run No.41

$s = 0.2625$ ins.

$\frac{b_2}{s} = 0.379$

$u_m/u_c = 0.512$

$Re_s = 9635$

FIG. 11.26: EFFECTIVE ORIGIN OF LIP WAKE (FOR BOTH JET-LIKE AND WAKE-LIKE FLOWS)

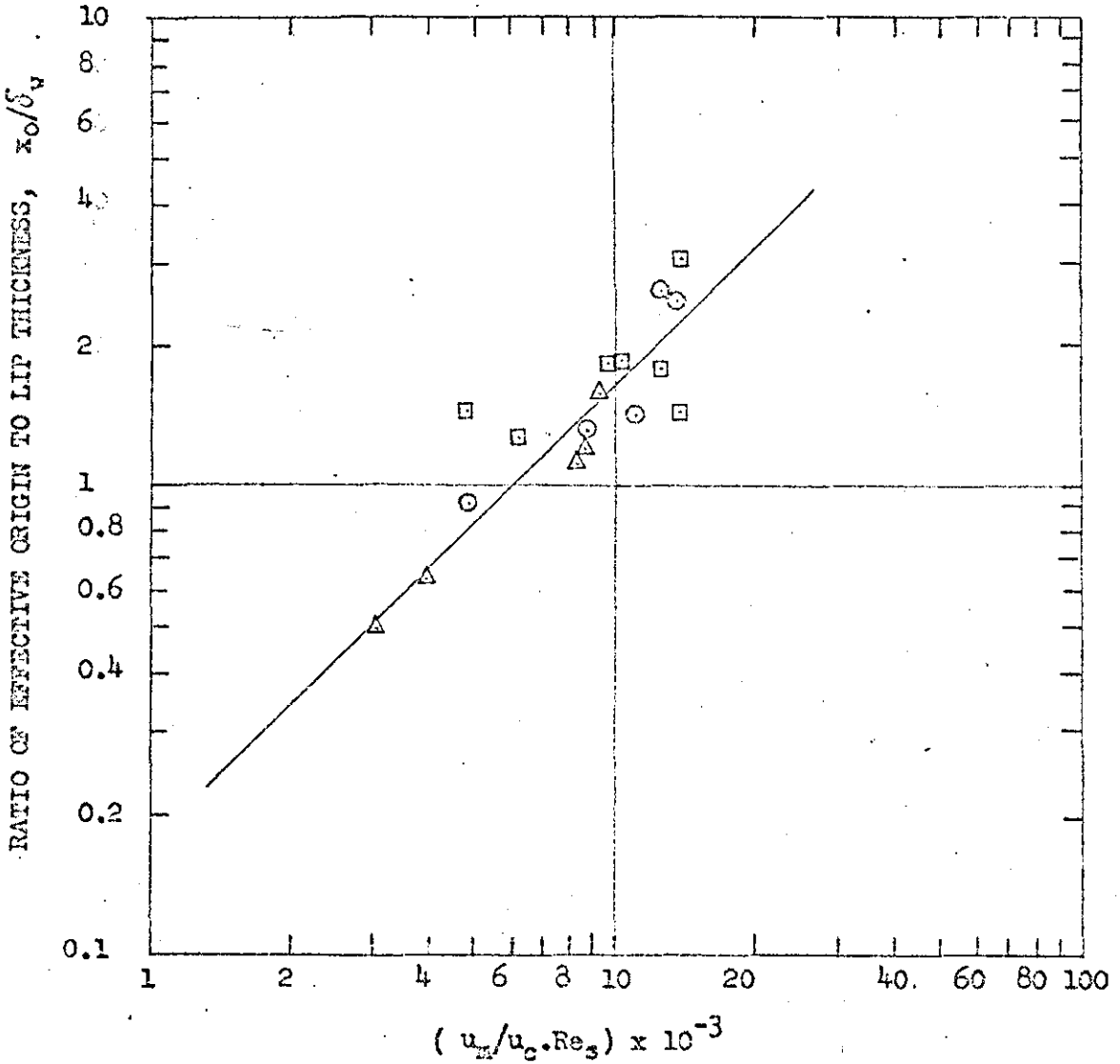

Symbol	Lip Thickness, ins.
⊡	0.055
⊙	0.0995
△	0.1525

D&4.

FIG. 11.27: EMPIRICAL ESTIMATION OF WAKE MIXING FUNCTION

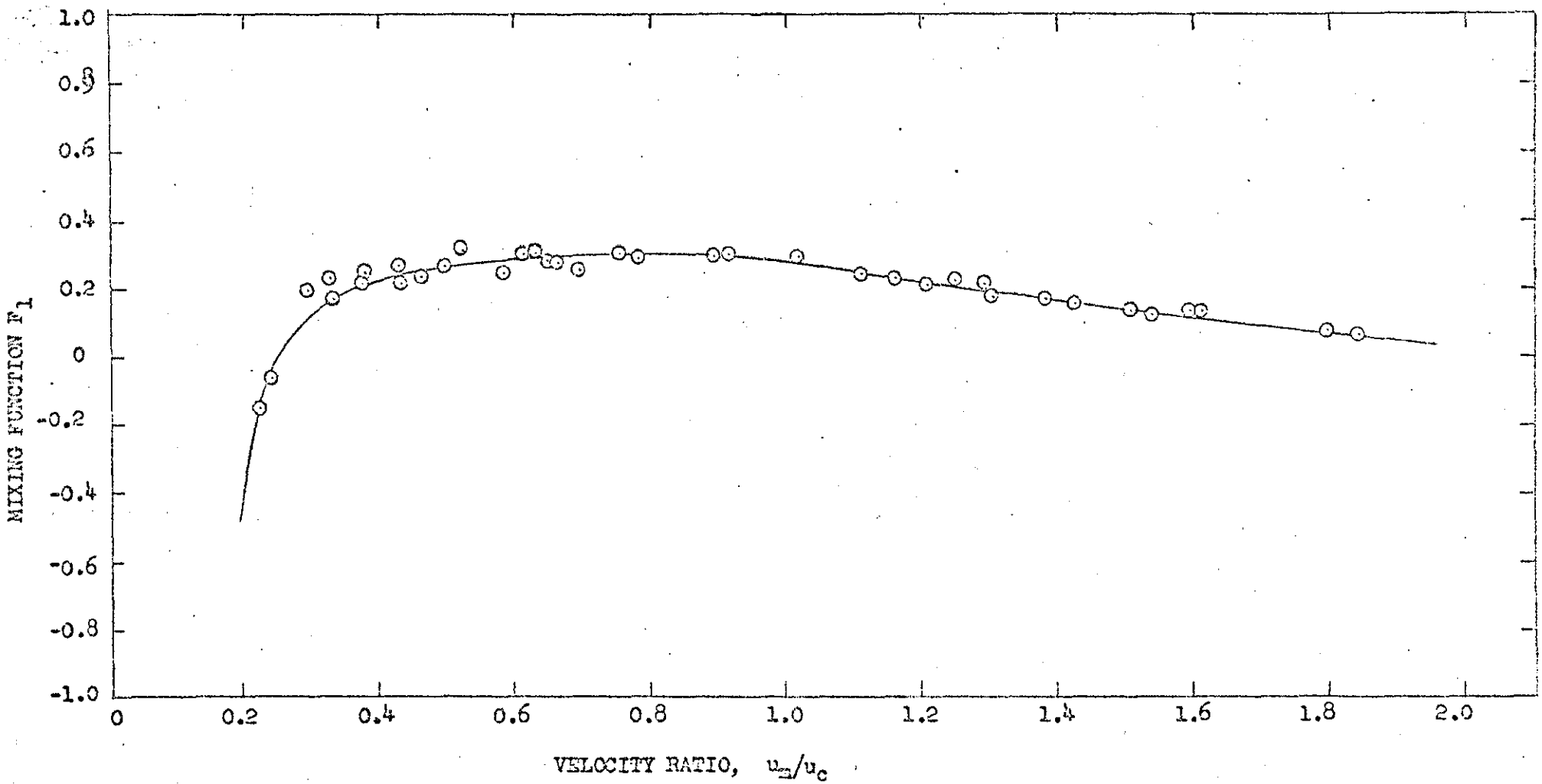

FIG. 11.28: MEASURED EFFECT OF SLOT LIP THICKNESS ON POTENTIAL CORE LENGTH AT LOW SLOT REYNOLDS NUMBERS

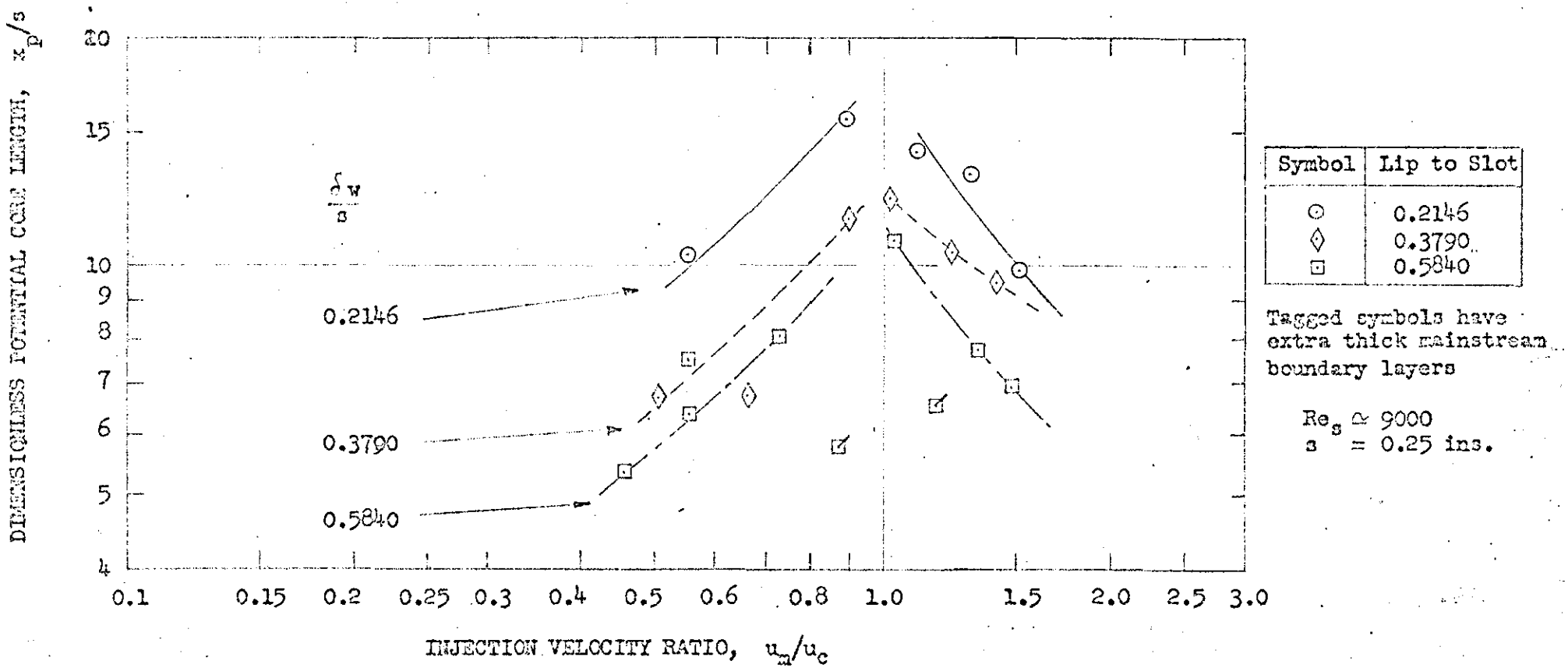

FIG. 11.29: MEASURED EFFECT OF SLOT LIP THICKNESS ON POTENTIAL CORE LENGTH AT INTERMEDIATE SLOT REYNOLDS NUMBERS

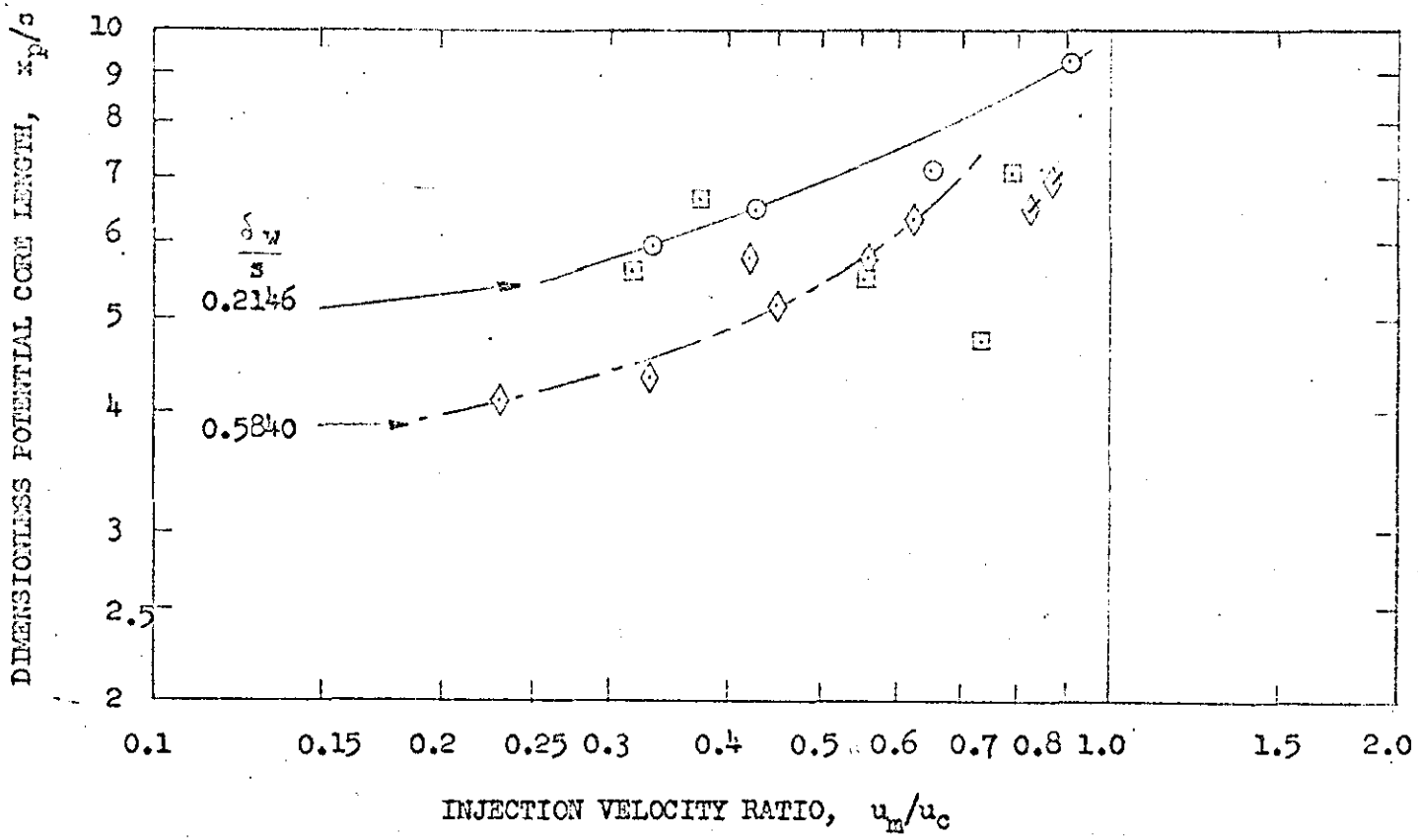

Symbol	Lip to height
⊙	0.2146
⊡	0.3790
◇	0.5840

Tagged symbols have extr
thick mainstream boundar
layers

$Re_s \simeq 14000$
$s = 0.25$ ins.

FIG. 11.30: MEASURED EFFECT OF SLOT LIP THICKNESS ON POTENTIAL CORE AT HIGHER SLOT REYNOLDS NUMBERS

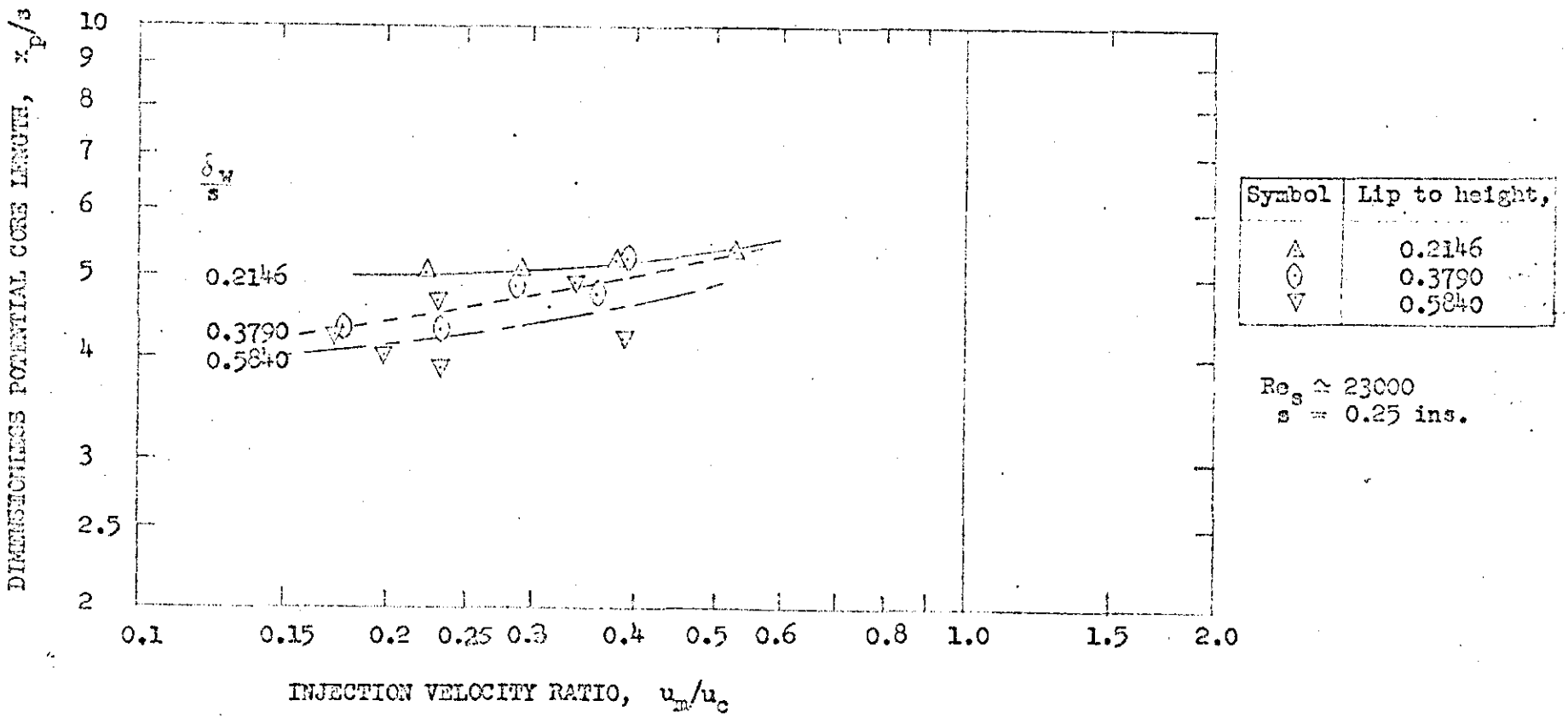

7188

FIG. 11.31: MEASURED EFFECT OF SLOT REYNOLDS NUMBER ON POTENTIAL CORE LENGTH FOR THIN LIP SLOT

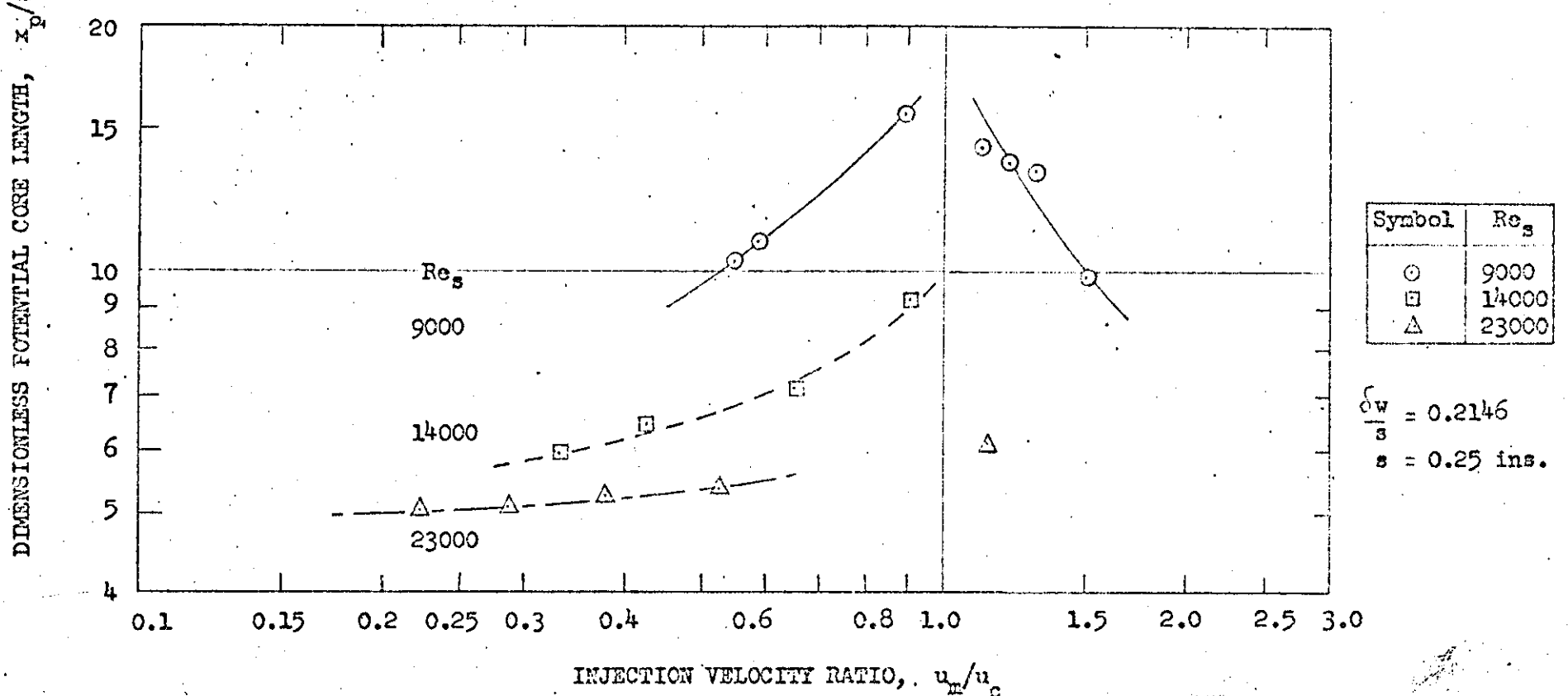

6818

FIG. 11.32: MEASURED EFFECT OF SLOT REYNOLDS NUMBER ON POTENTIAL CORE LENGTH FOR INTERMEDIATE SLOT LIP

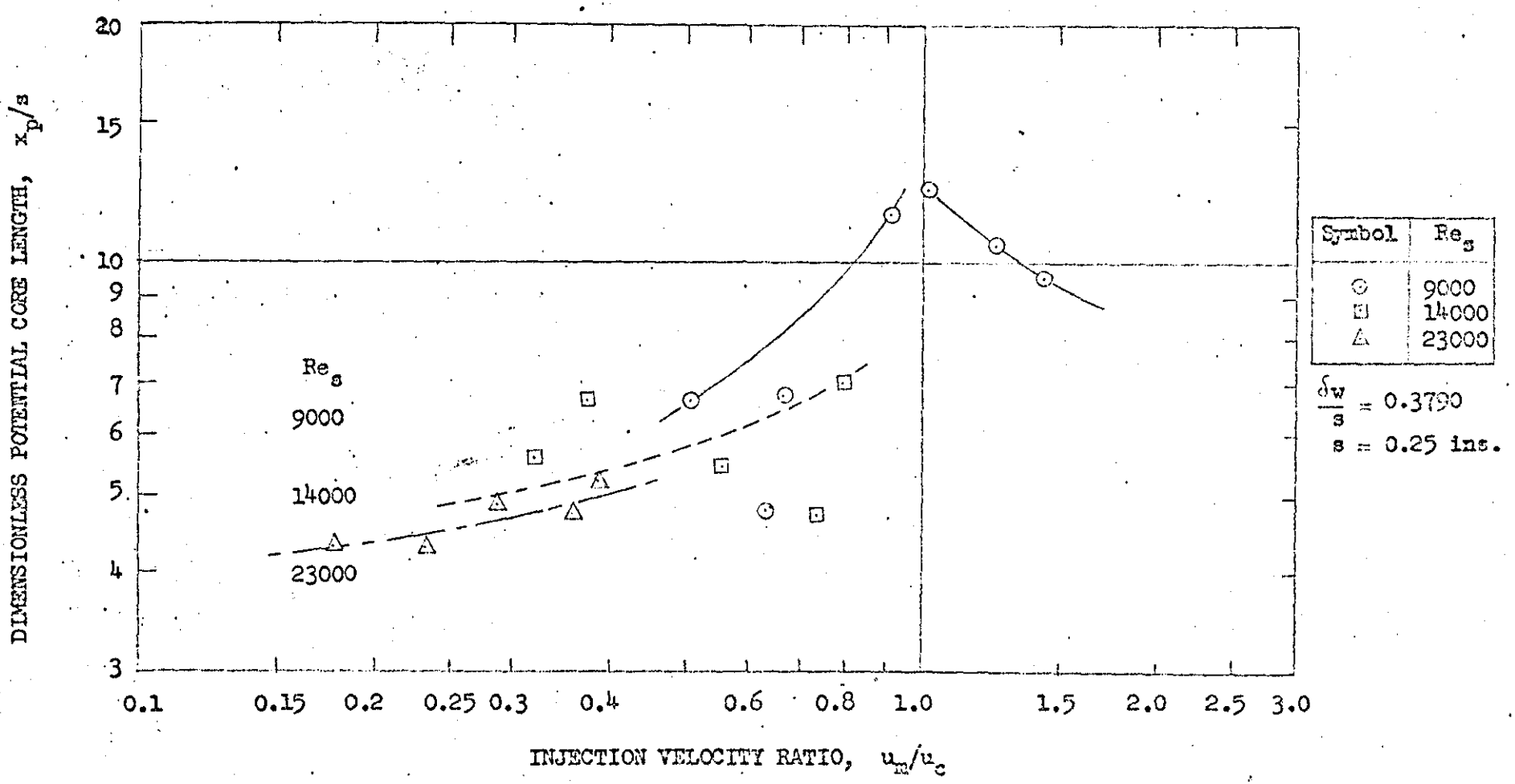

FIG. 11.33: MEASURED EFFECT OF SLOT REYNOLDS NUMBER ON POTENTIAL CORE LENGTH FOR THICK SLOT LIPS

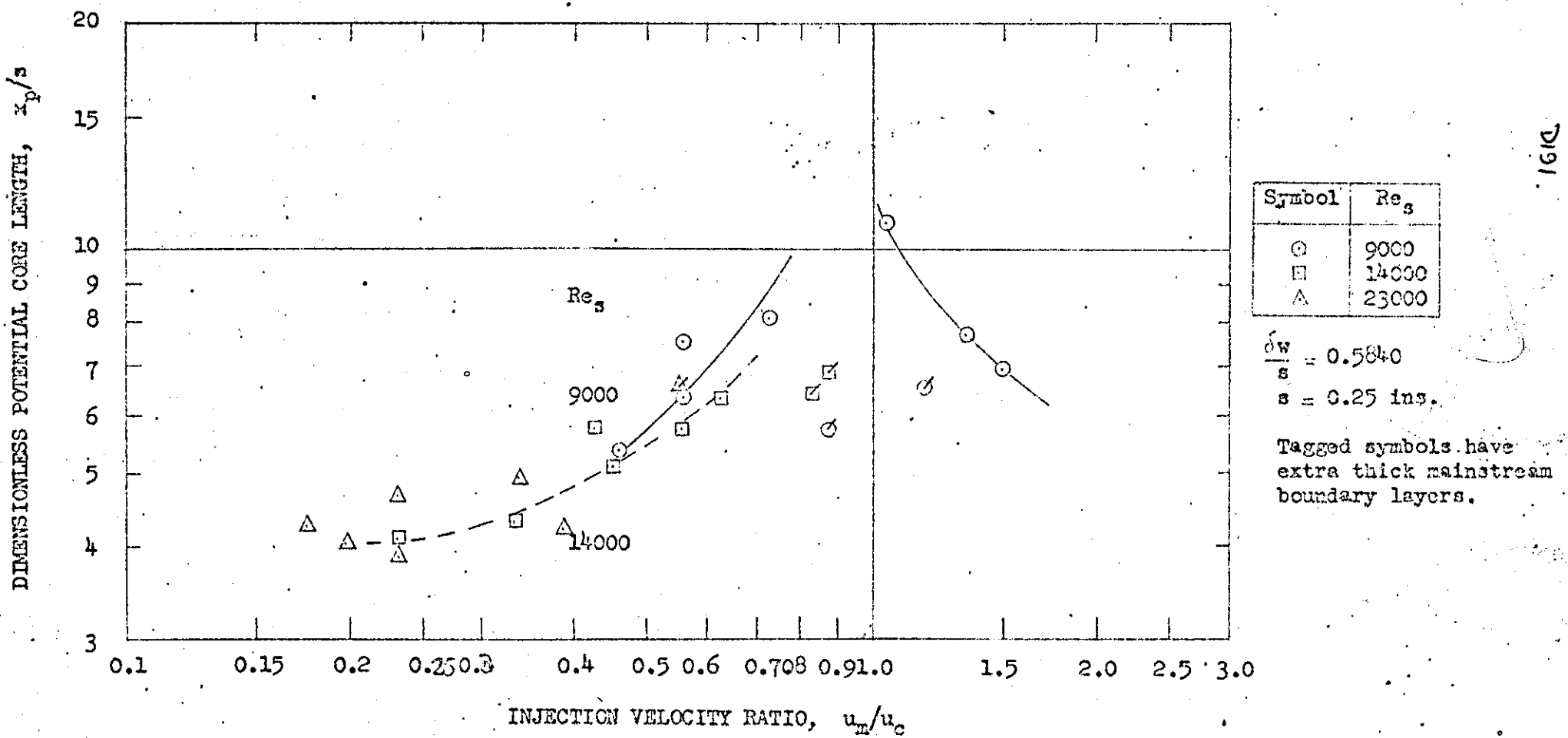

161D

FIG. 11.34: MEASURED EFFECT OF SLOT REYNOLDS NUMBER AT FIXED VELOCITY RATIO ON POTENTIAL CORE LENGTH

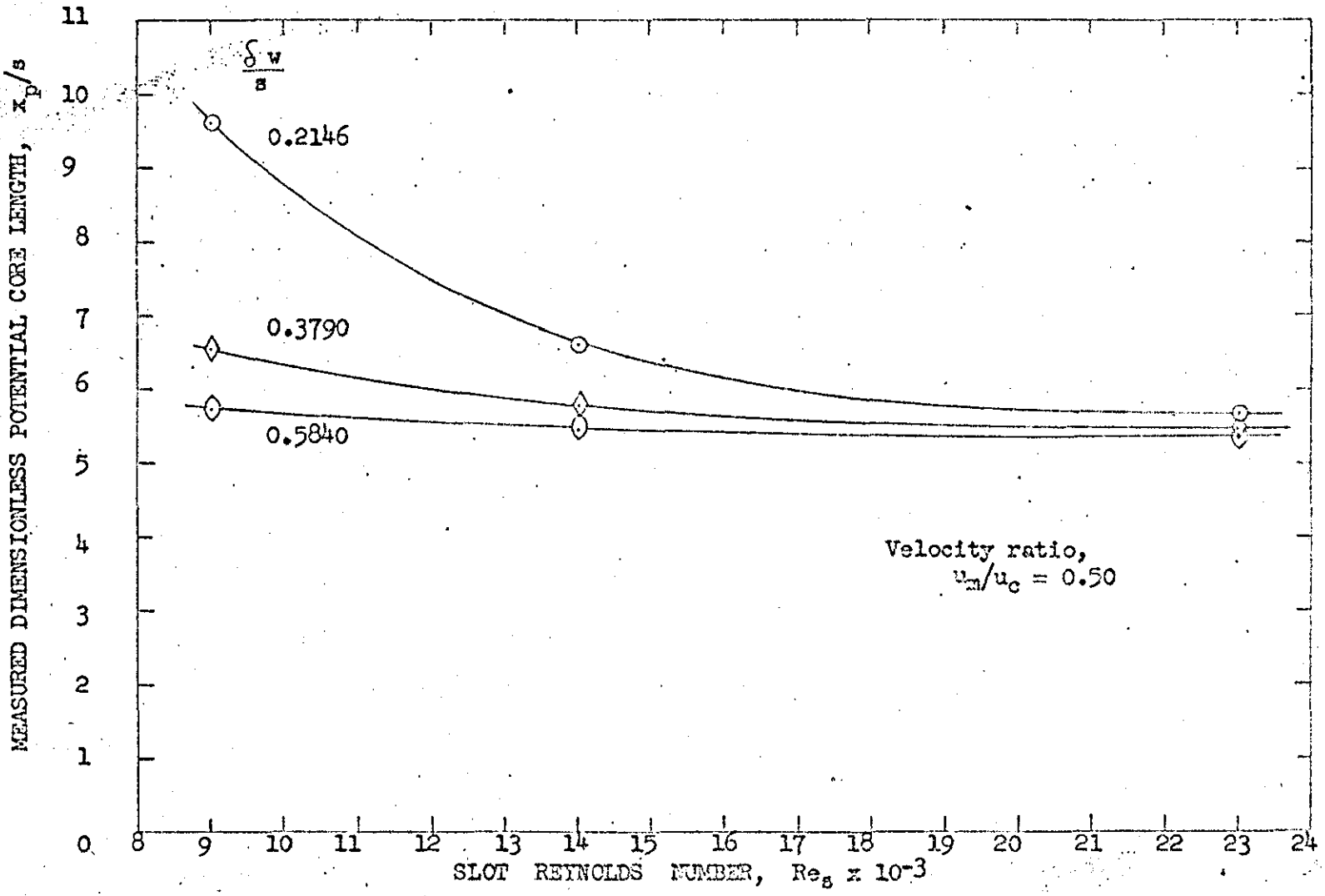

D192

FIG. 11.35: MEASURED EFFECT ON POTENTIAL CORE LENGTH OF SLOT LIP THICKNESS TO HEIGHT RATIO AT FIXED INJECTION VELOCITY RATIO

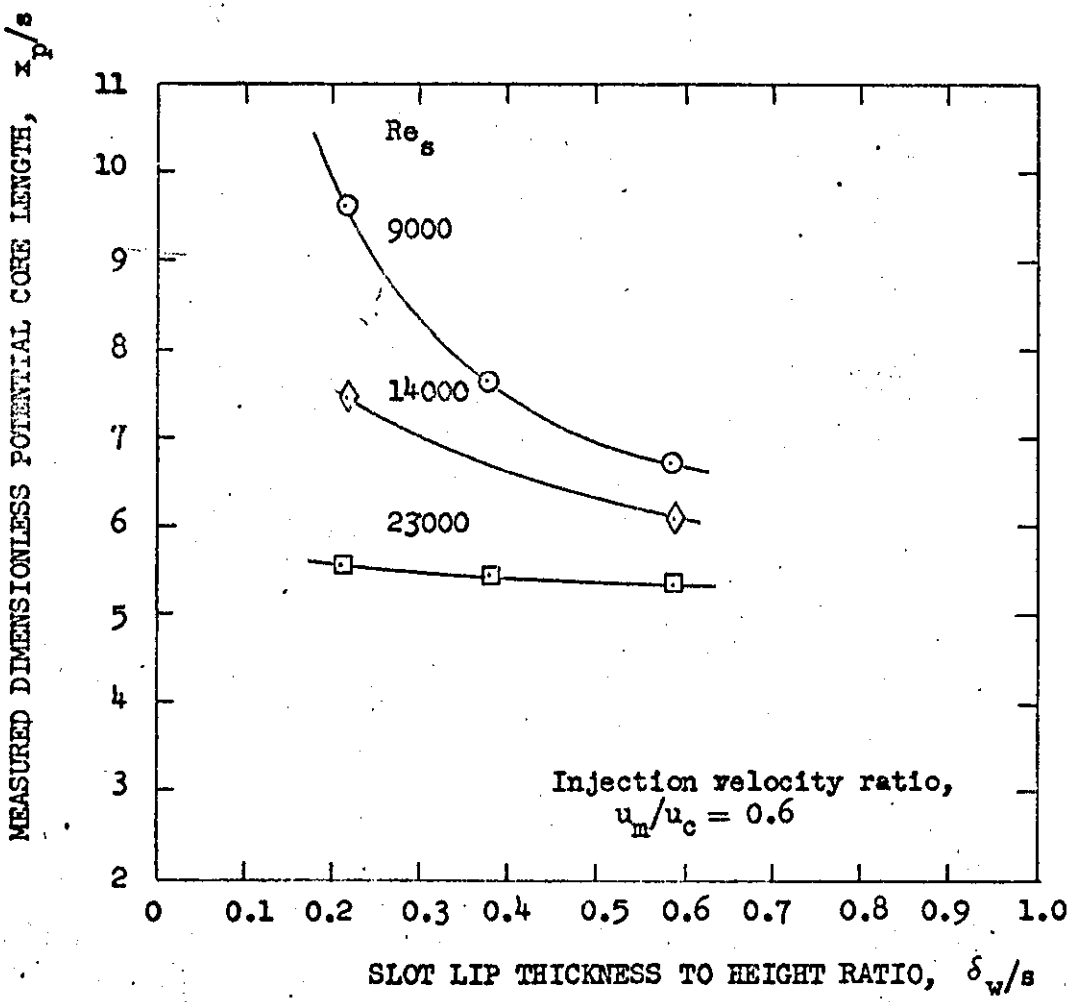

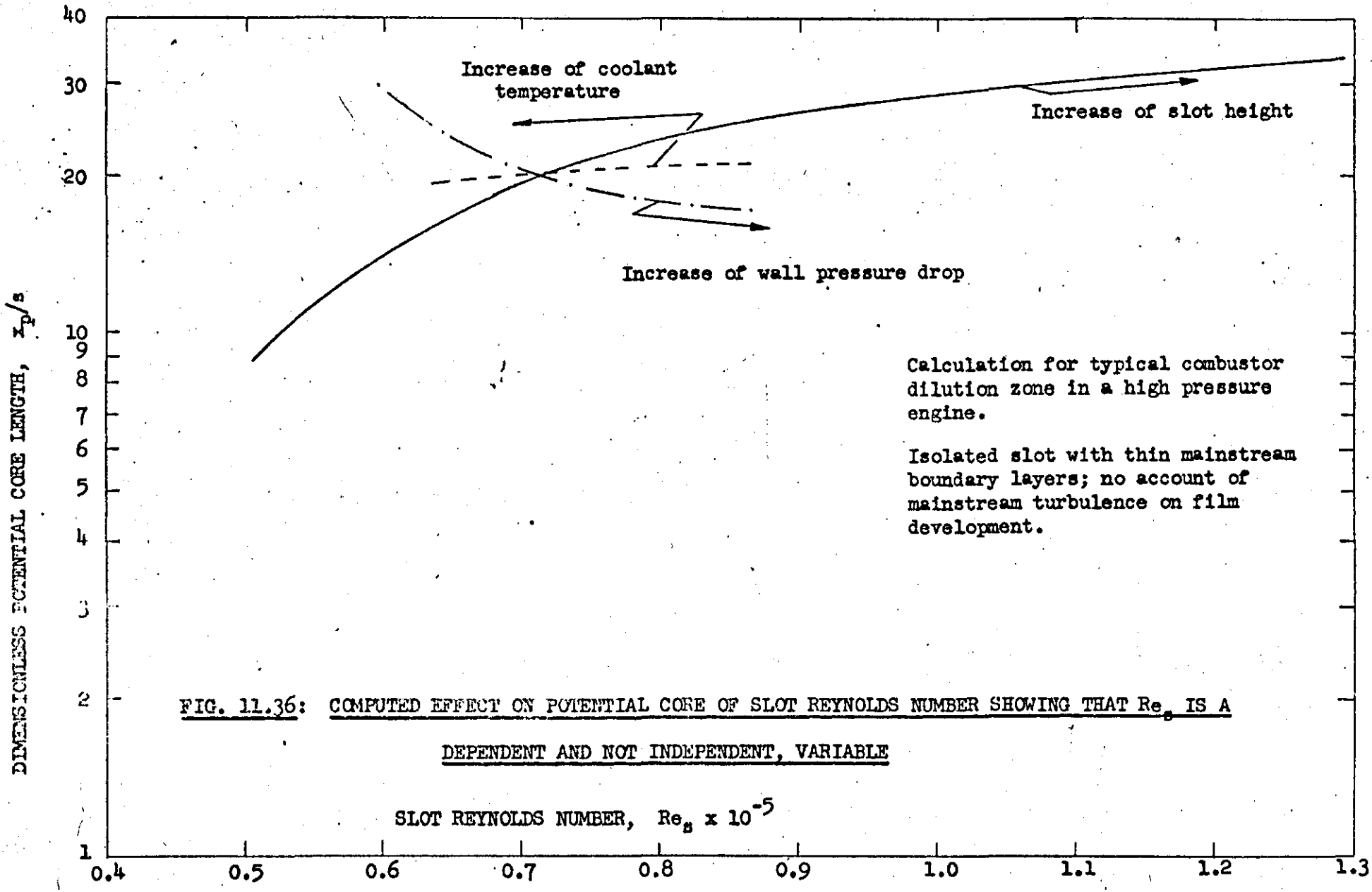

FIG. 11.36: COMPUTED EFFECT ON POTENTIAL CORE OF SLOT REYNOLDS NUMBER SHOWING THAT Re_s IS A DEPENDENT AND NOT INDEPENDENT, VARIABLE

FIG.11.37: COMPARISON OF PREDICTIONS WITH MEASUREMENTS FROM THE DATA OF WHITELAW(63) AND, SIVASEGAREM & WHITELAW(65)

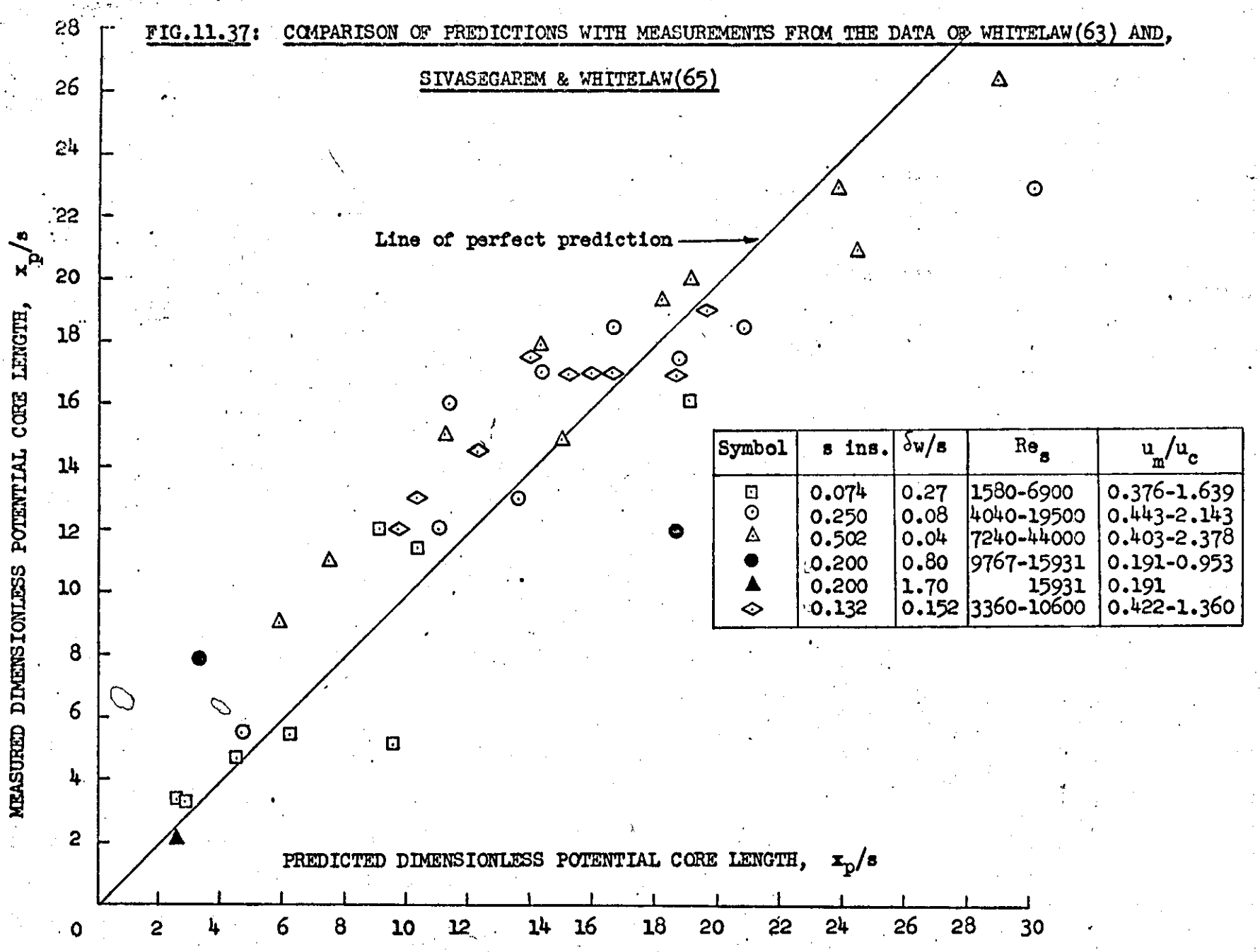

Symbol	s ins.	$\delta w/s$	Re_s	u_m/u_c
⊡	0.074	0.27	1580-6900	0.376-1.639
⊙	0.250	0.08	4040-19500	0.443-2.143
△	0.502	0.04	7240-44000	0.403-2.378
●	0.200	0.80	9767-15931	0.191-0.953
▲	0.200	1.70	15931	0.191
◇	0.132	0.152	3360-10600	0.422-1.360

5912

FIG. 11.38: COMPARISON OF PREDICTIONS WITH MEASUREMENTS FROM THE DATA OF SEBAN(11), SEBAN&BACK(25), GARTSHORE(115) AND, PAPELL & TROUT(34)

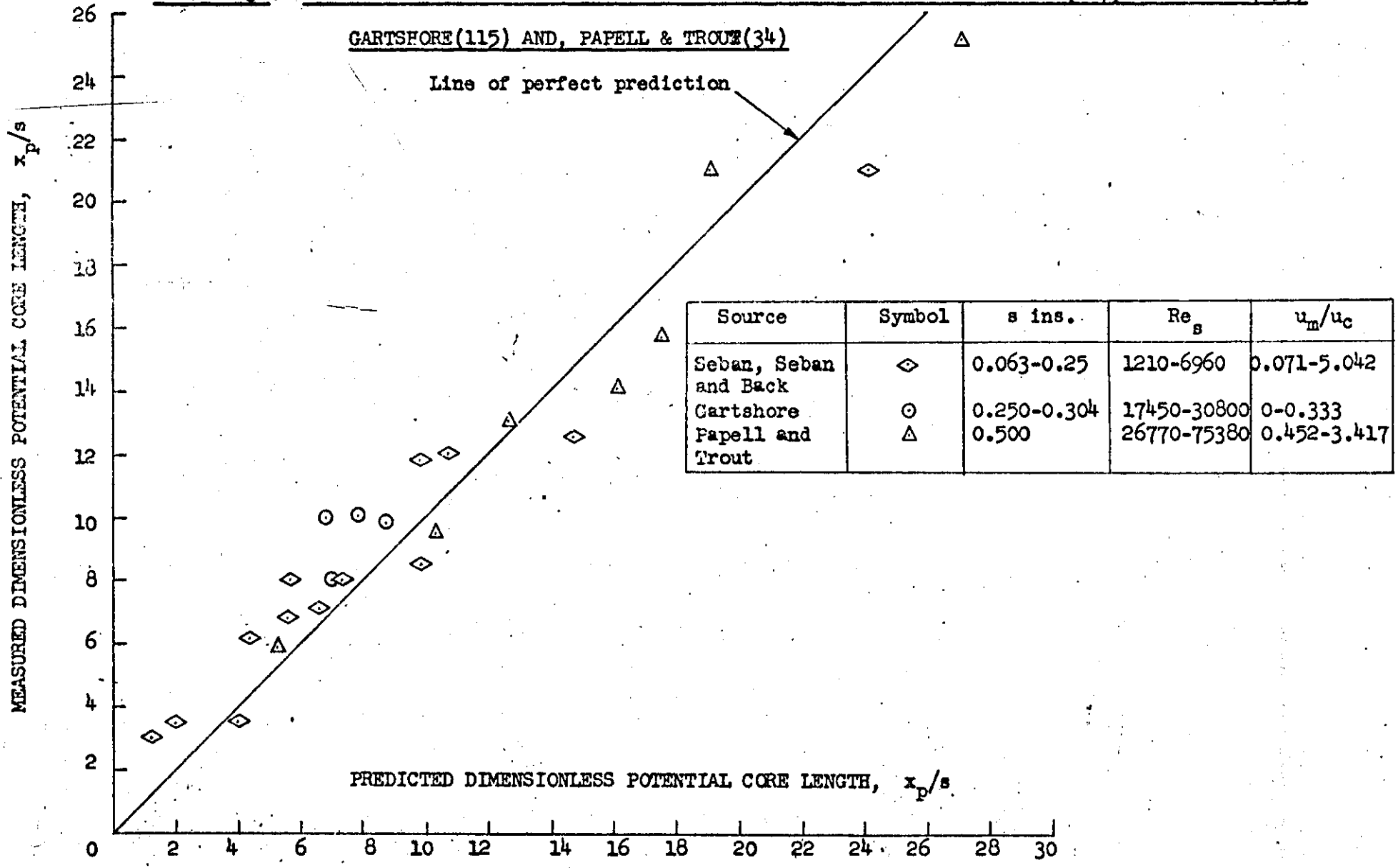

Source	Symbol	s ins.	Re_s	u_m/u_c
Seban, Seban and Back	◇	0.063-0.25	1210-6960	0.071-5.042
Cartshore	⊙	0.250-0.304	17450-30800	0-0.333
Papell and Trout	△	0.500	26770-75380	0.452-3.417

FIG. 11.39: COMPARISON OF PREDICTED HYDRODYNAMIC POTENTIAL CORE LENGTHS WITH MEASURED VALUES

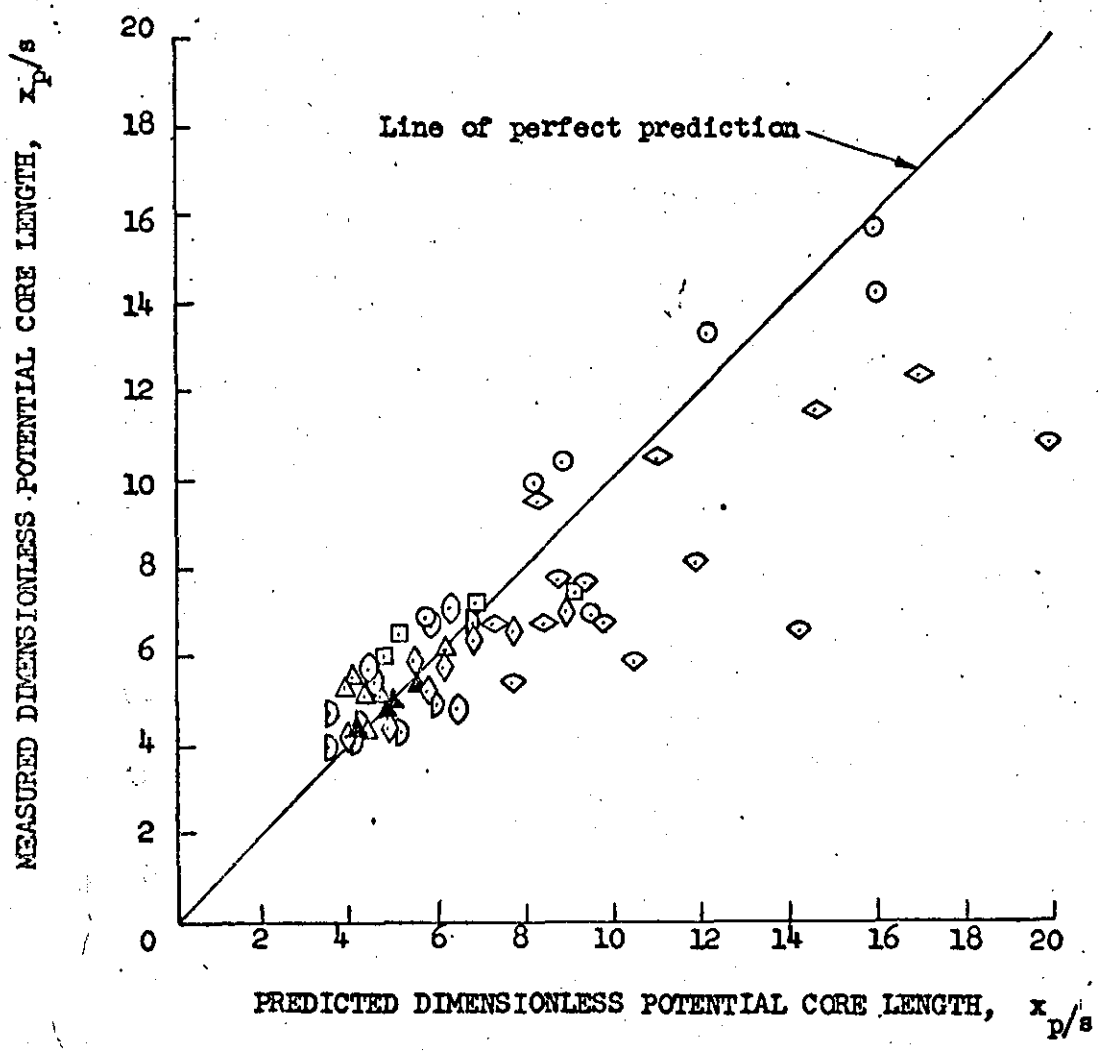

Symbol	$\delta w/s$	u_m/u_c	Re_s
⊙	0.2146	0.585-1.508	9000
⊡	0.2146	0.333-0.910	15000
△	0.2146	0.224-0.527	23000
◇	0.3790	0.510-1.426	9000
◈	0.3790	0.318-0.795	15000
▲	0.3790	0.177-0.387	23000
◇	0.5840	0.457-1.489	9000
◈	0.5840	0.232-0.877	14000
▷	0.5840	0.174-0.550	23000

Re_s values are nominal

FIG. 11.40: ERROR ANALYSIS FOR THIN LIPPED SLOT AS FUNCTION OF VELOCITY RATIO AND SLOT REYNOLDS NUMBER

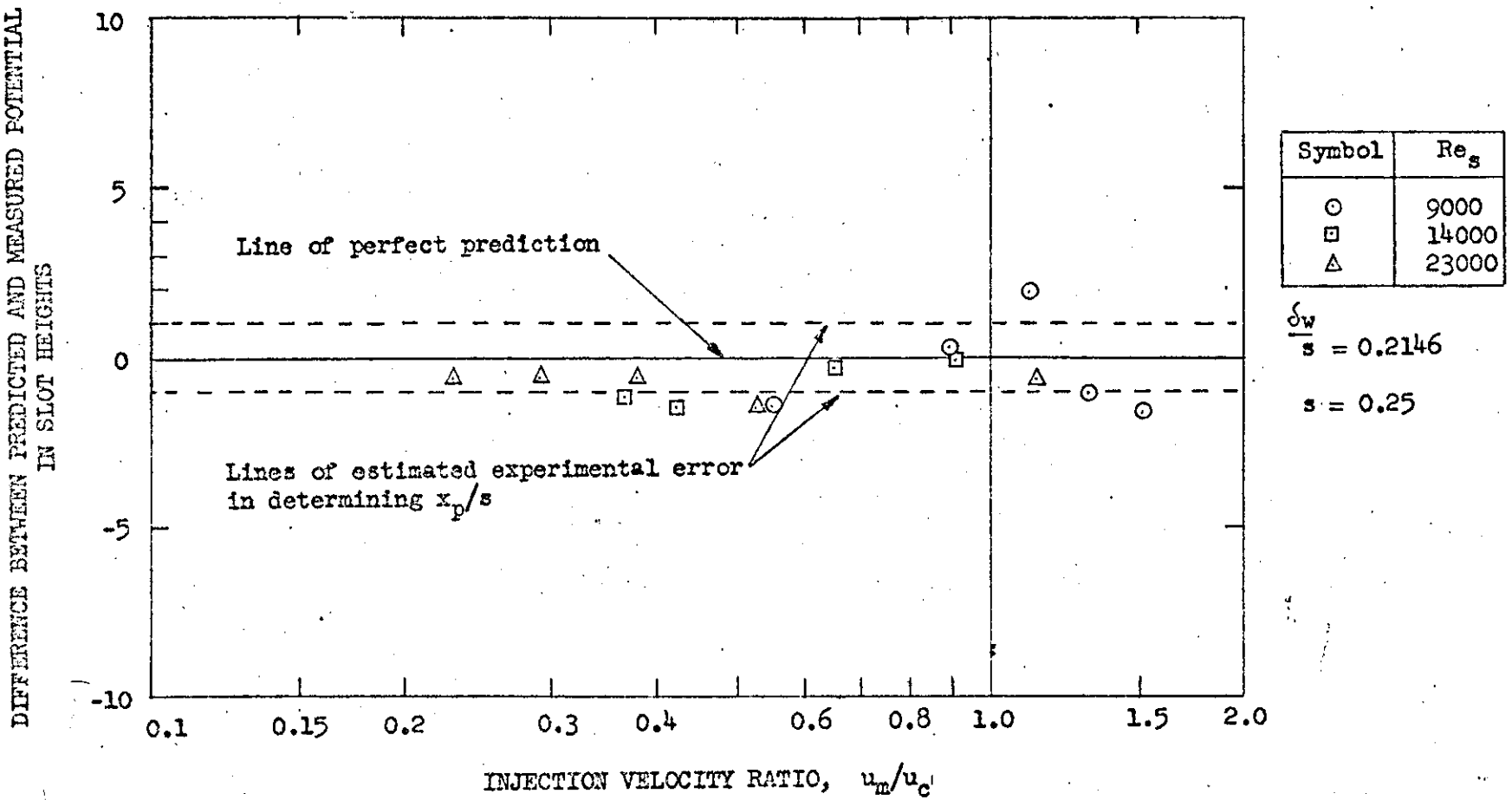

FIG. 11.41: ERROR ANALYSIS FOR INTERMEDIATE LIPPED SLOT AS FUNCTION OF VELOCITY RATIO AND SLOT REYNOLDS NUMBER

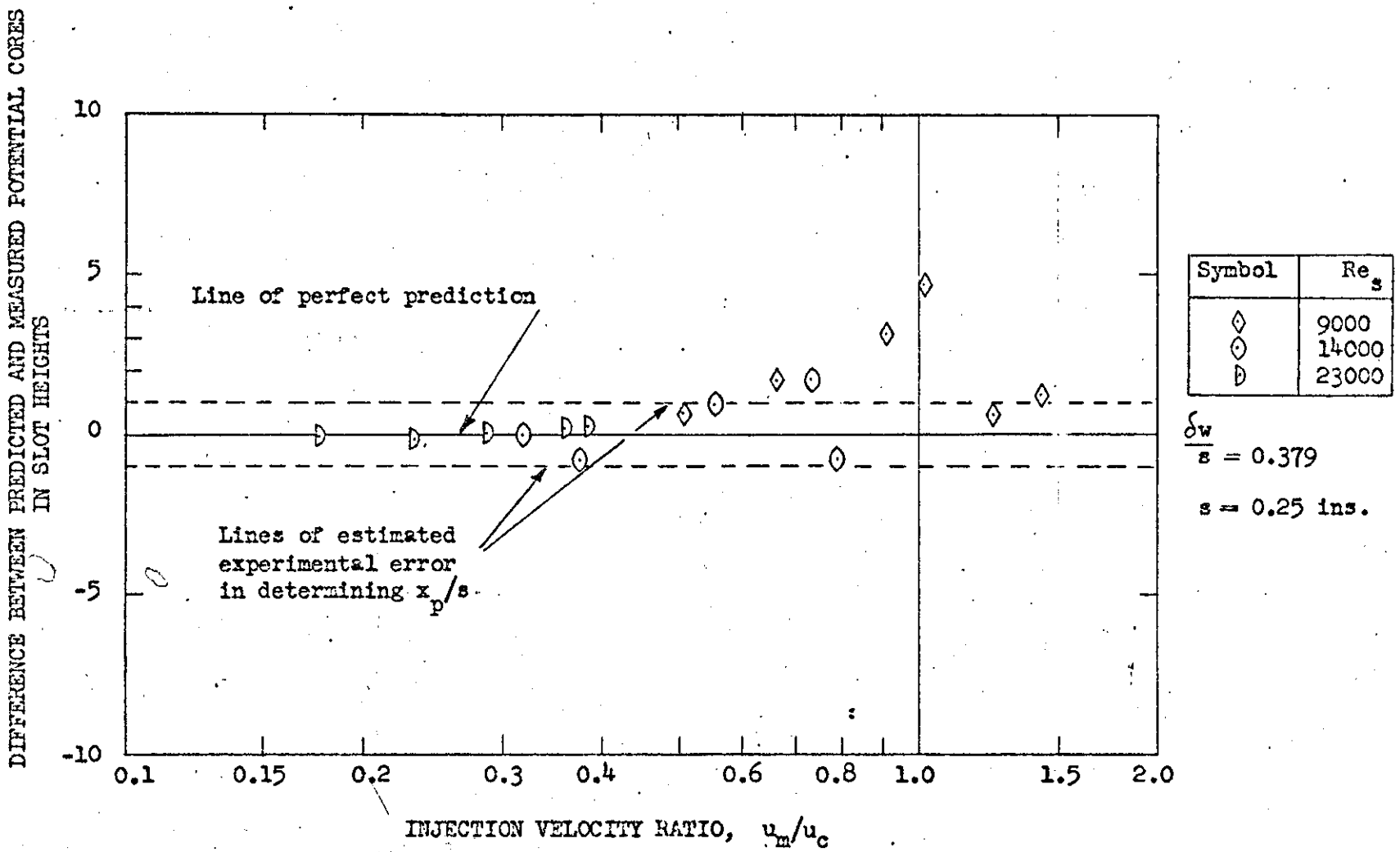

1692

FIG. 11.42: ERROR ANALYSIS FOR THICK LIPPED SLOT AS FUNCTION OF VELOCITY RATIO AND SLOT REYNOLDS NUMBER

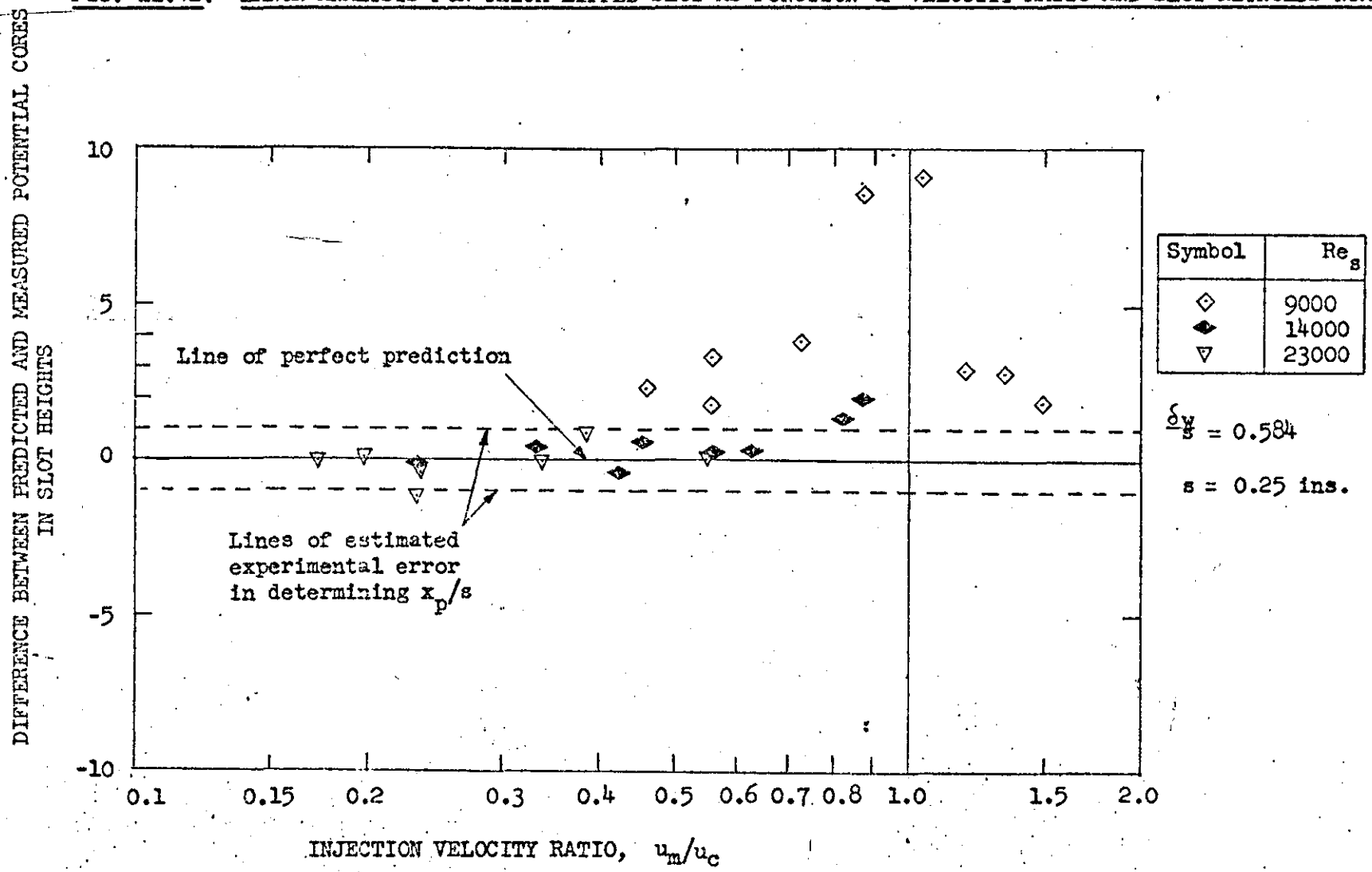

FIG. 11.43: ERROR ANALYSIS FOR LOW SLOT REYNOLDS NUMBER AS FUNCTION OF VELOCITY RATIO AND LIP THICKNESS

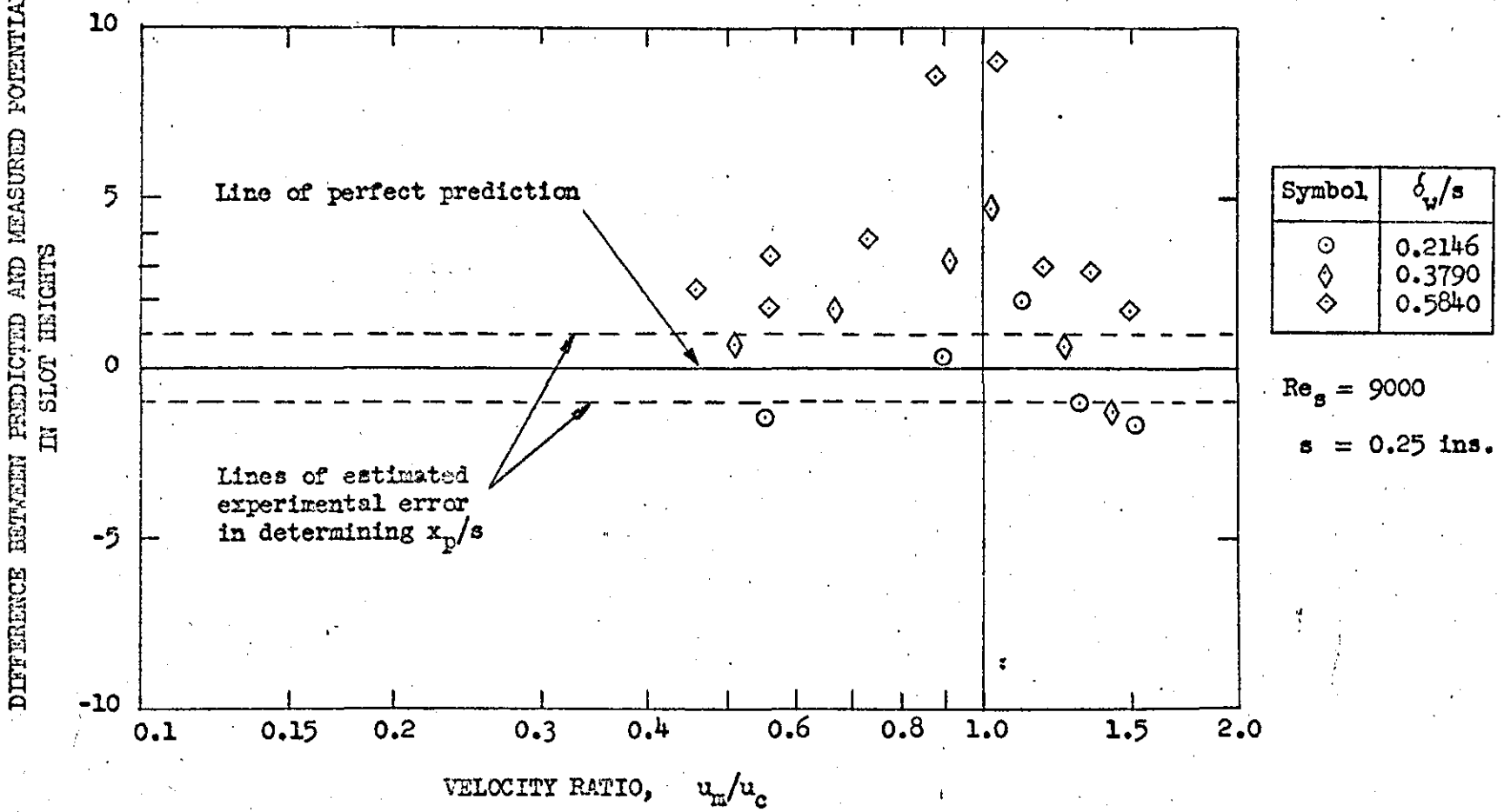

FIG. 11.44: ERROR ANALYSIS FOR INTERMEDIATE SLOT REYNOLDS NUMBER AS FUNCTION OF VELOCITY RATIO AND LIP THICKNESS

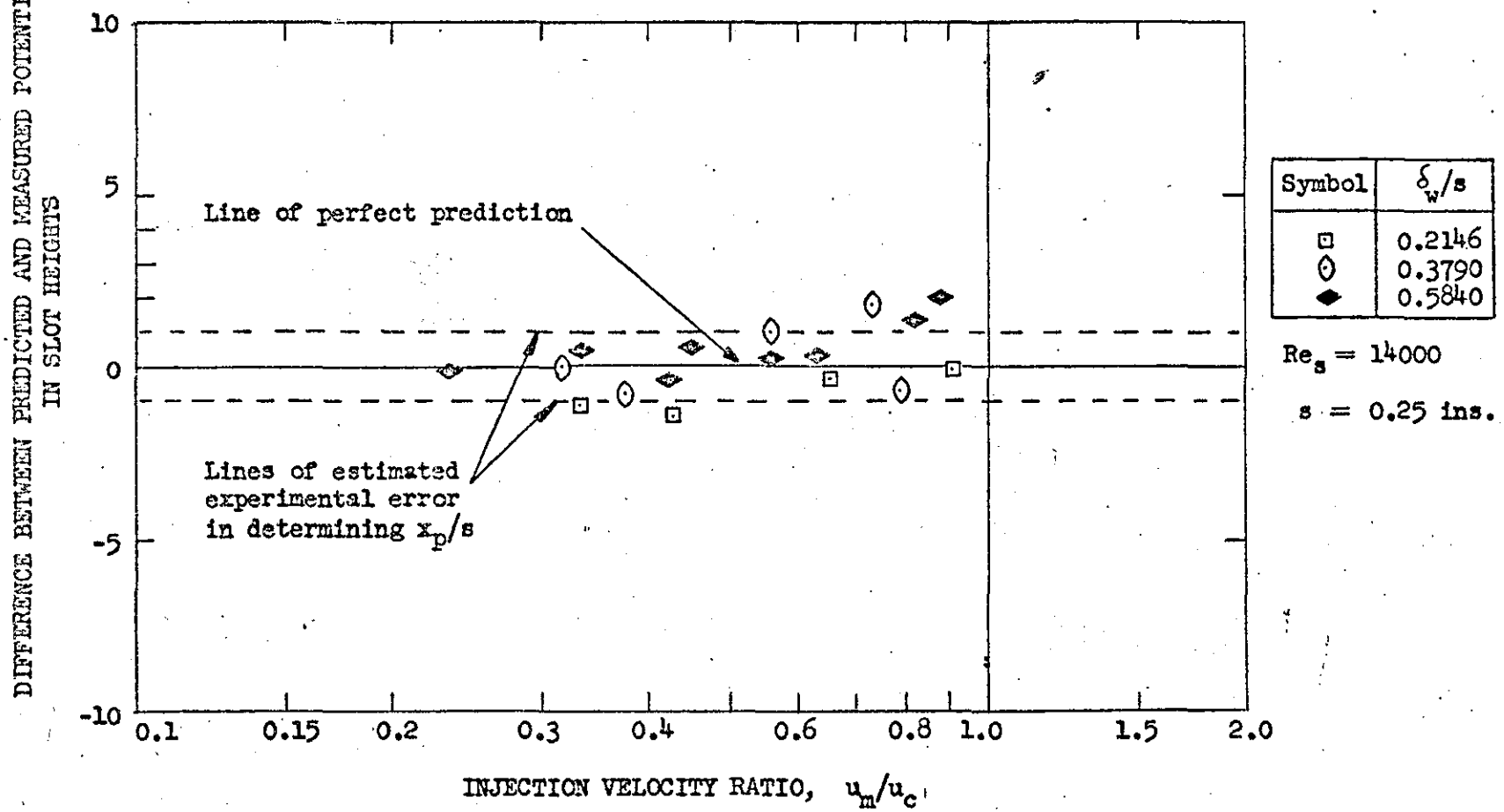

FIG. 11.45: ERROR ANALYSIS FOR HIGH SLOT REYNOLDS NUMBER AS FUNCTION OF VELOCITY RATIO AND LIP THICKNESS

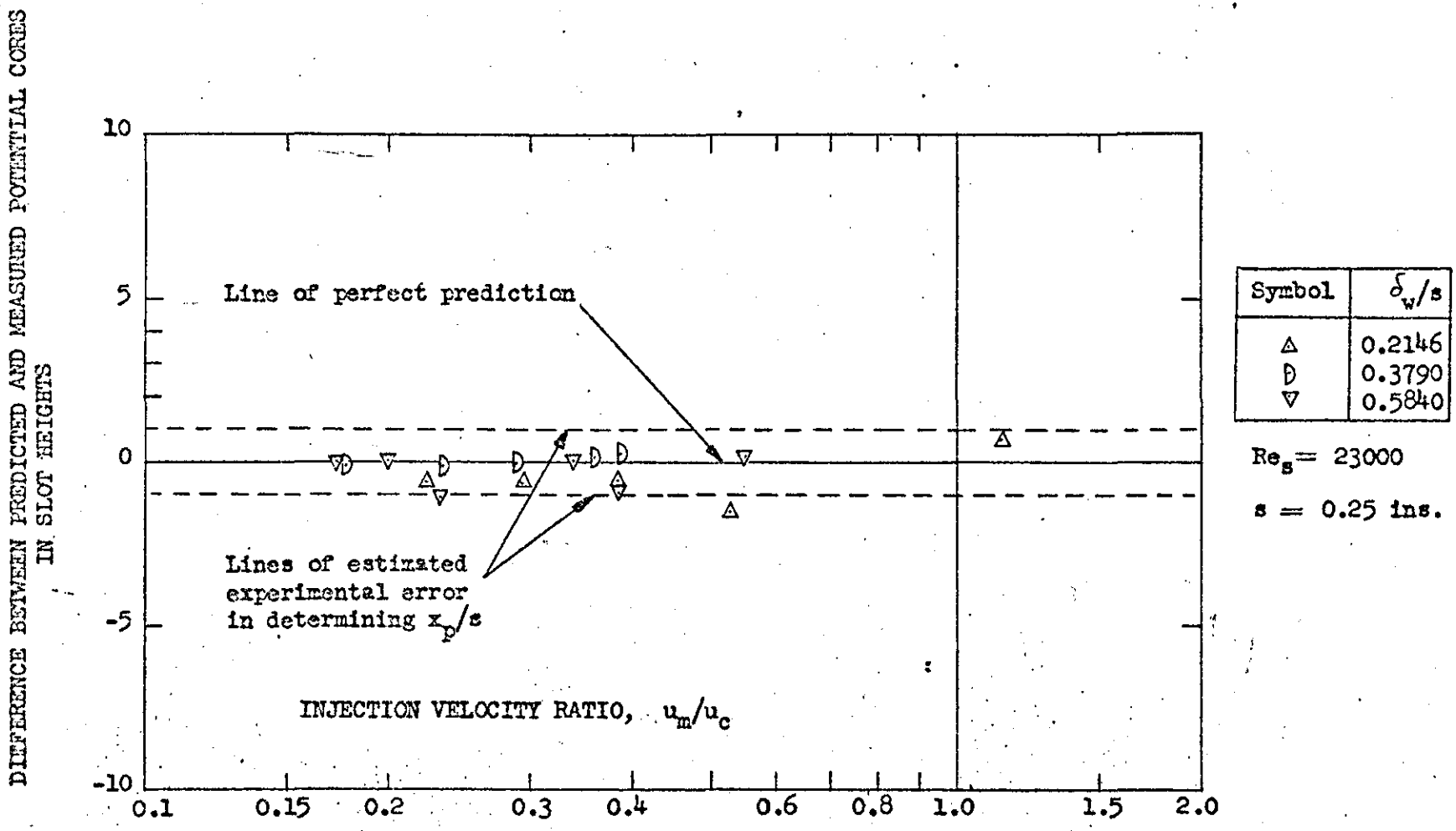

FIG. 11.46: POSITION OF PROFILE MINIMUM VELOCITY

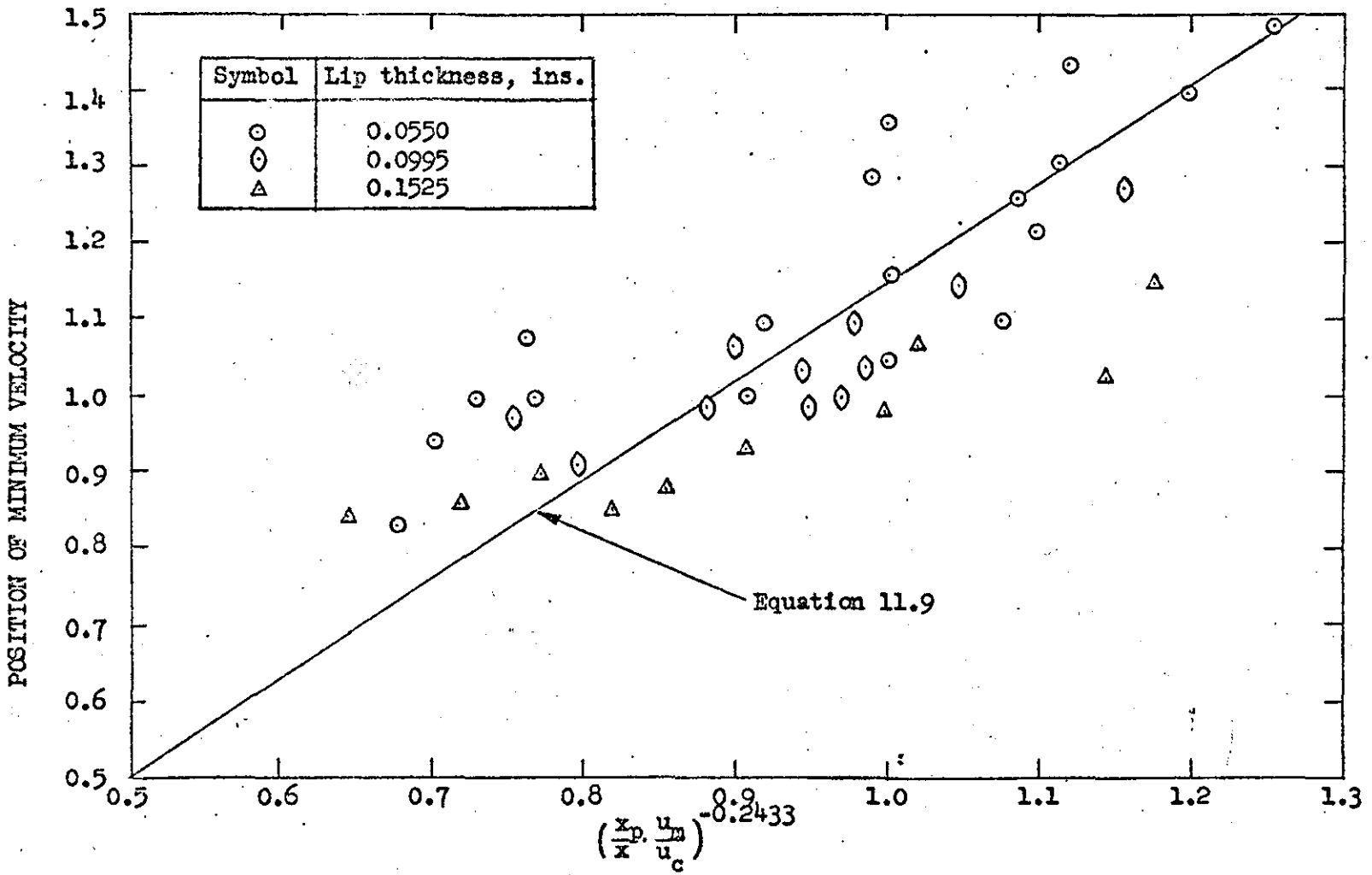

FIG. 11.47: FILLING OF VELOCITY DEFECT IN WAKE

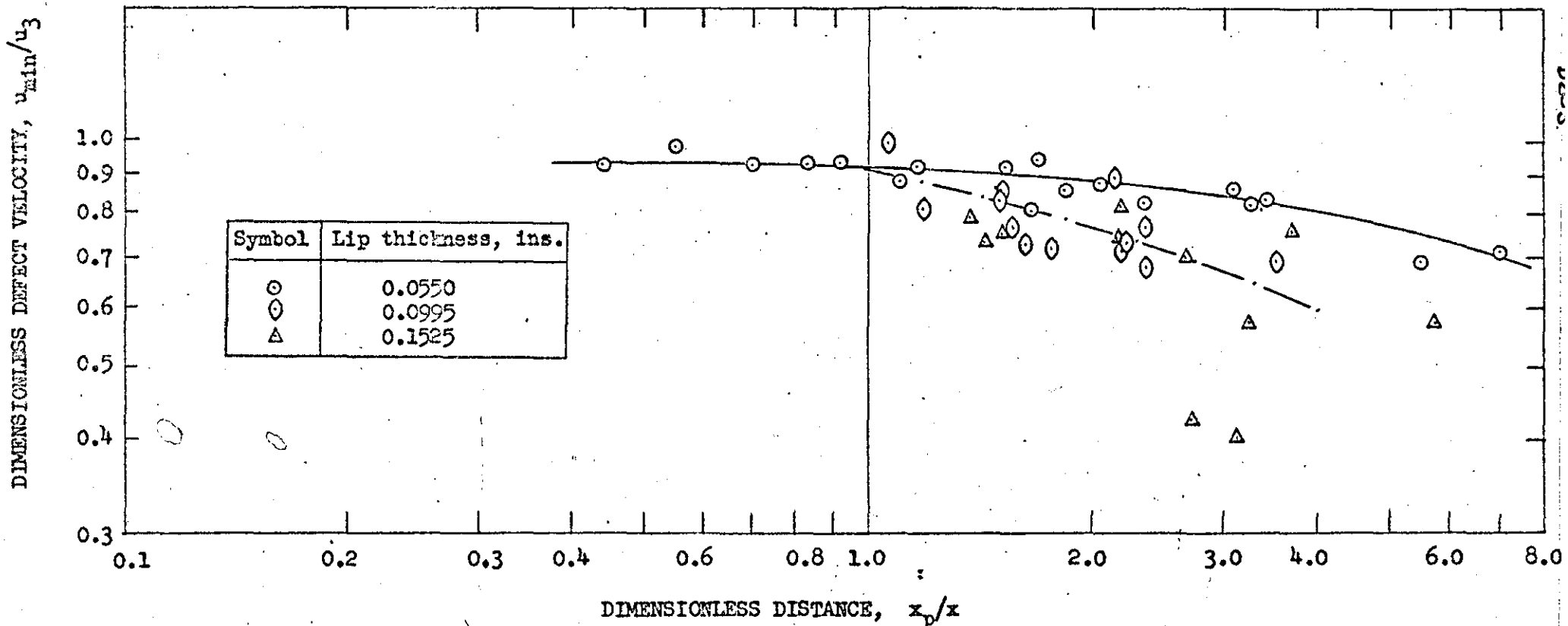

FIG. 11.48: PREDICTION OF FILM DOWNSTREAM DEVELOPMENT BASED ON STURGESS/GARTSHORE METHOD

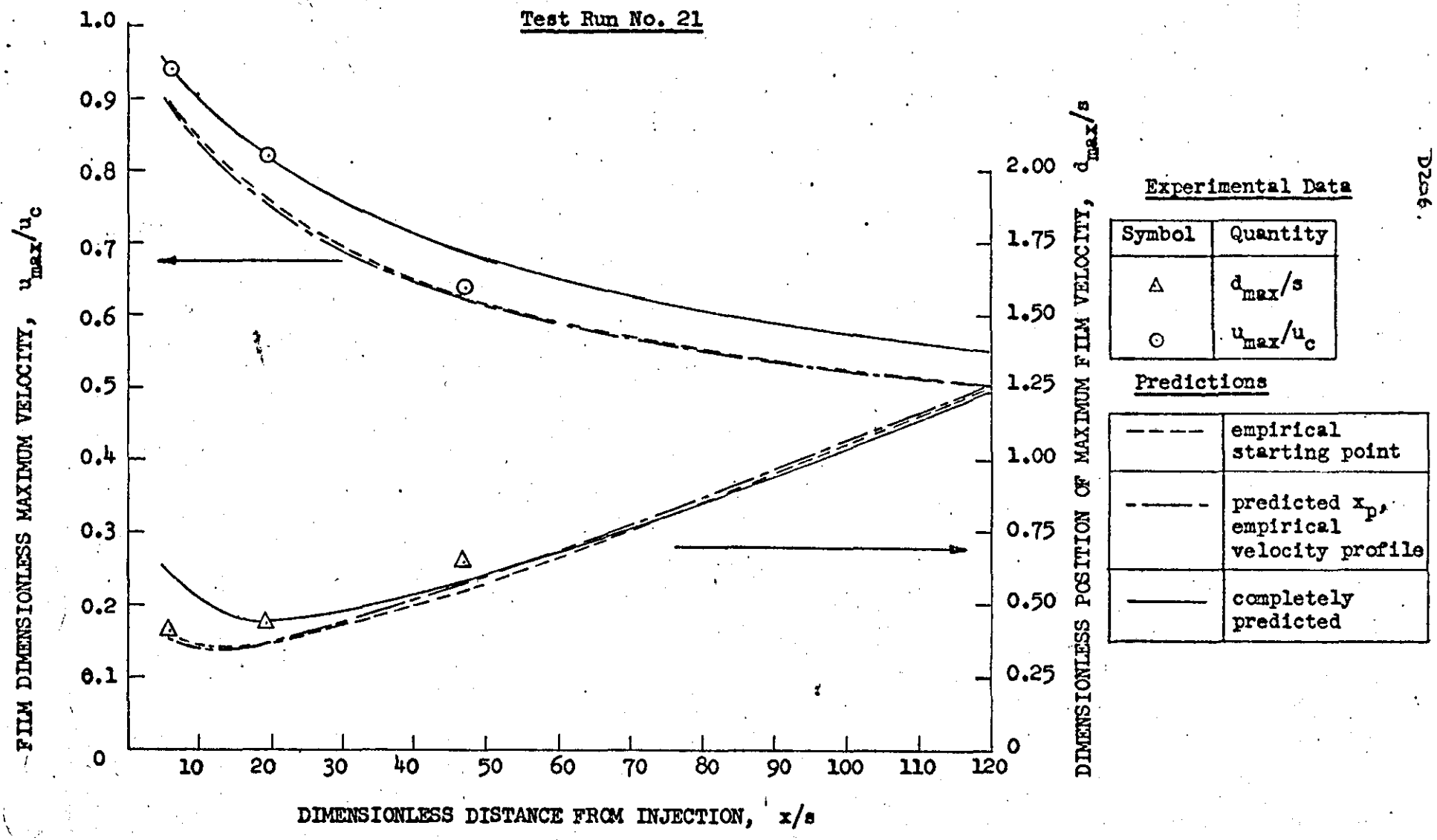

D206.

FIG. 11.49: PREDICTION OF FILM DOWNSTREAM DEVELOPMENT BASED ON STURGESS/GARTSHORE METHOD

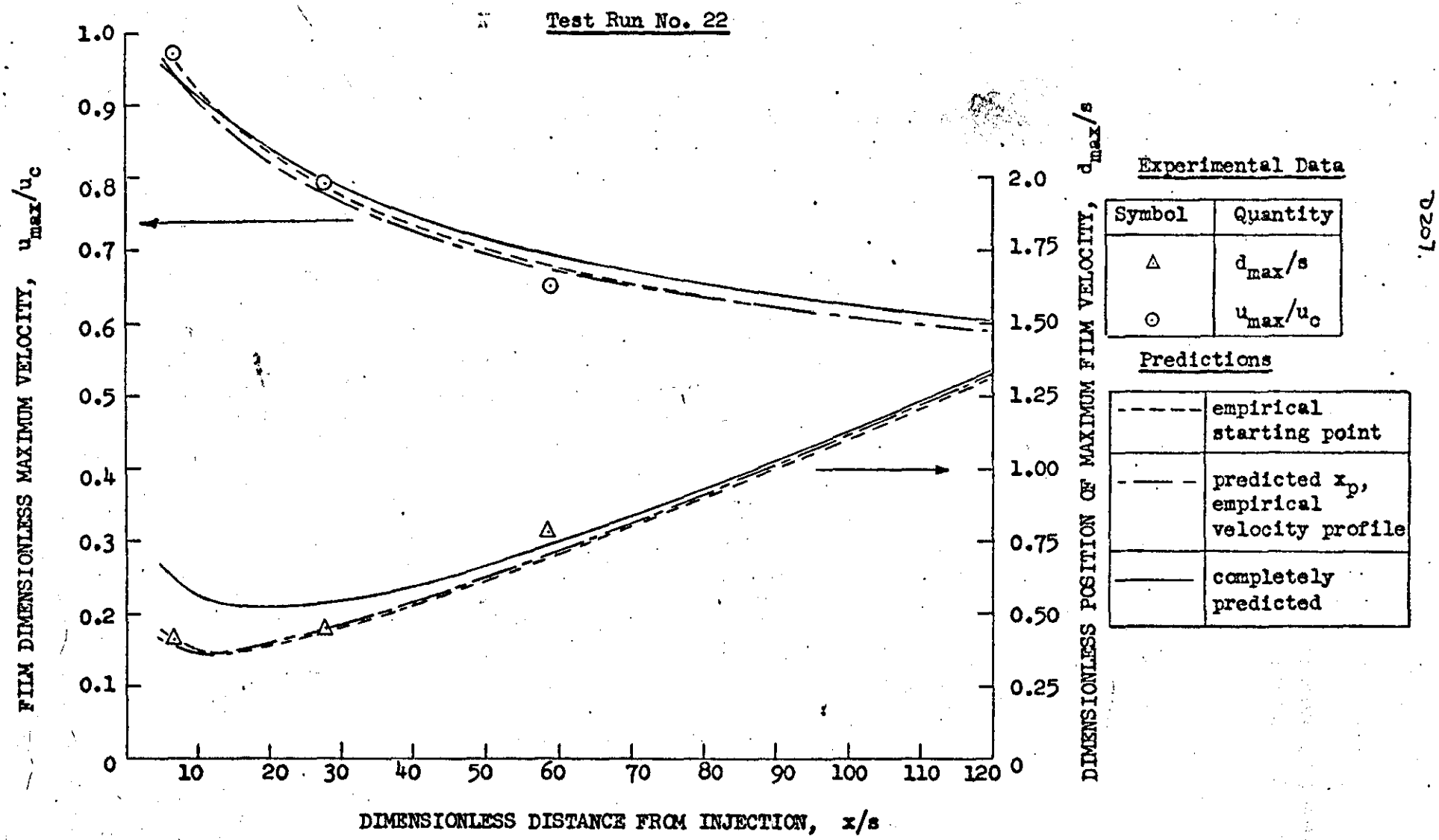

FIG. 11.50: PREDICTION OF FILM DOWNSTREAM DEVELOPMENT BASED ON STURGESS/GARTSHORE METHOD

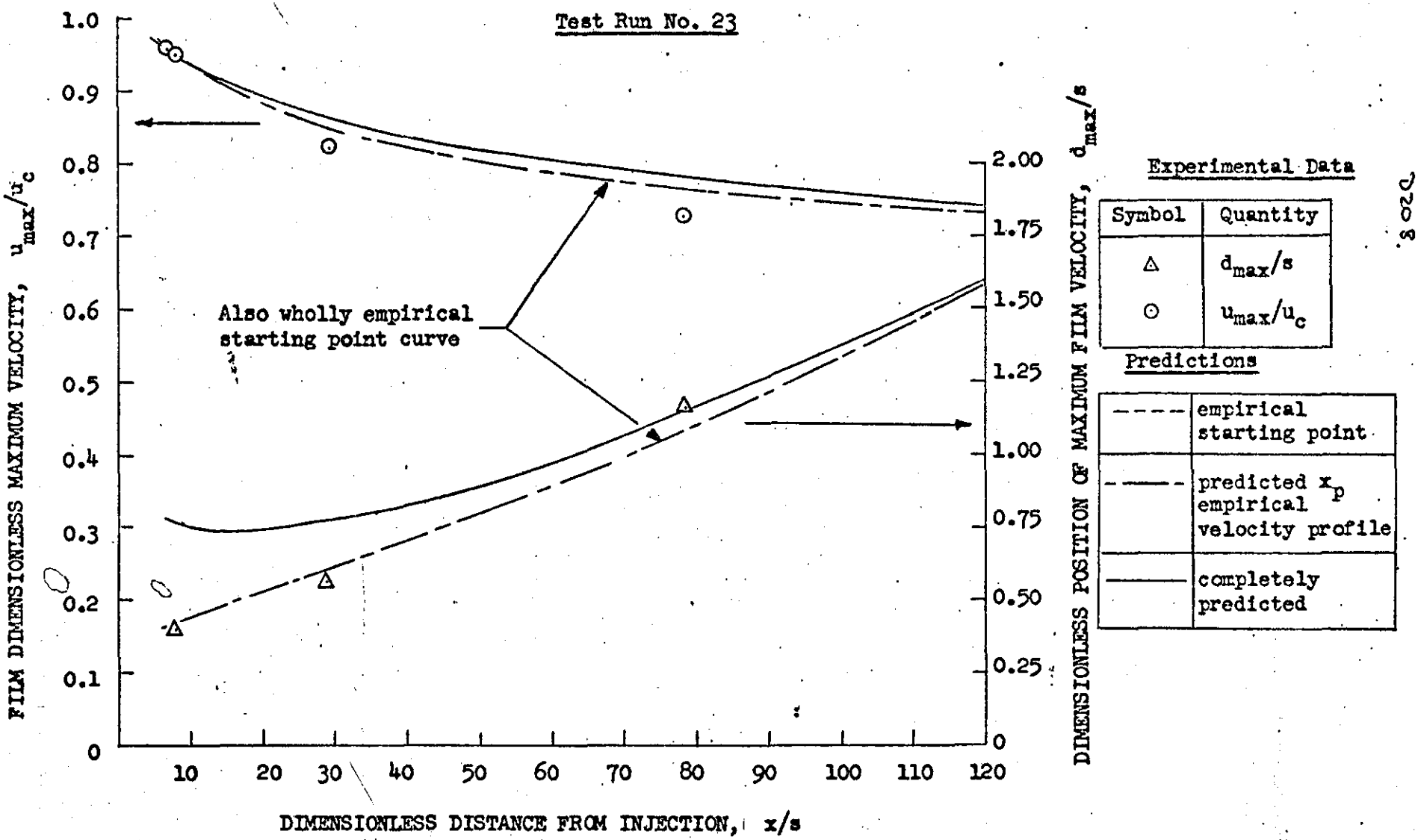

FIG. 11.51: PREDICTION OF FILM DOWNSTREAM DEVELOPMENT BASED ON STURGESS/GARTSHORE METHOD

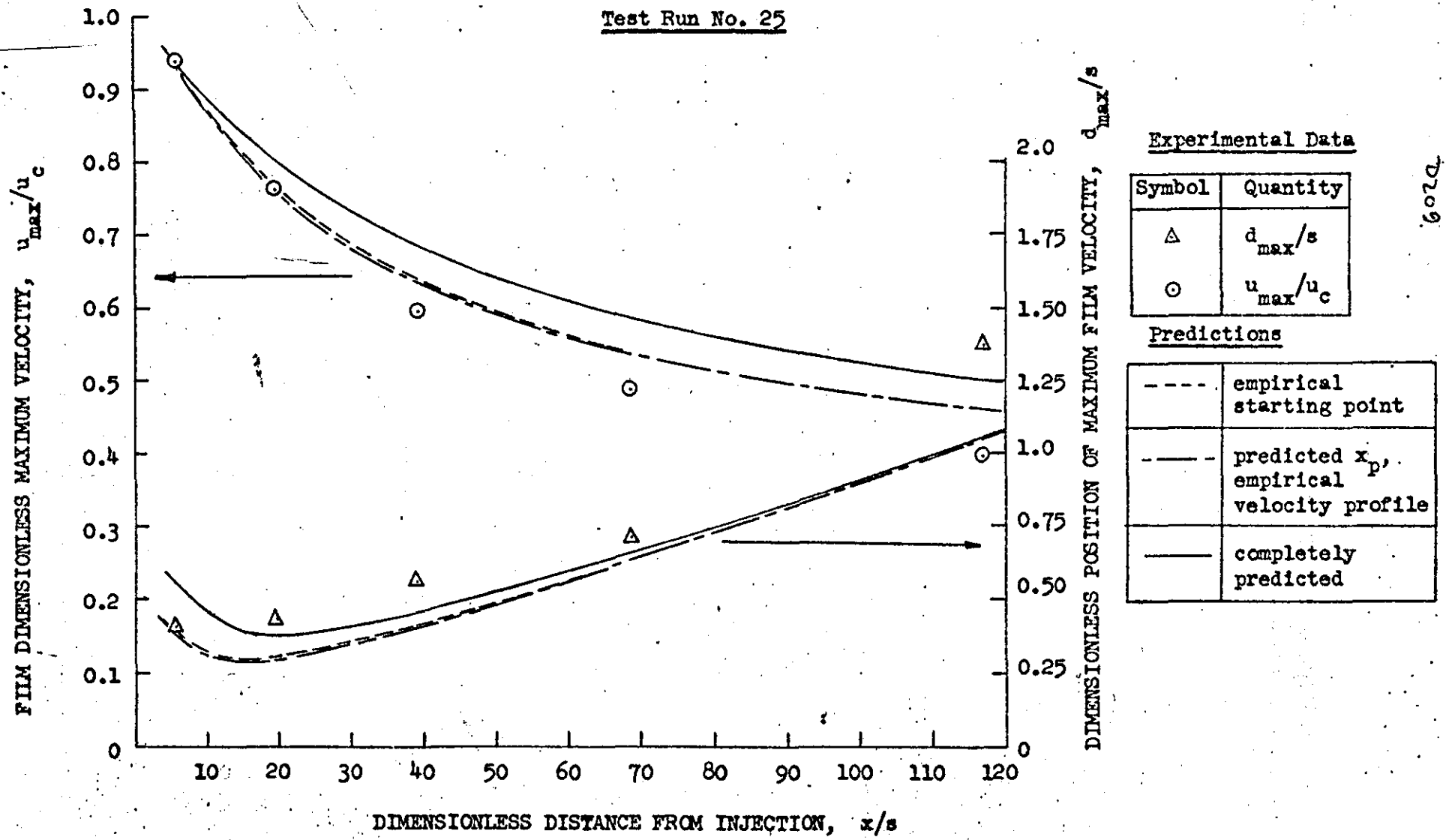

607a

FIG. 11.52: PREDICTION OF FILM DOWNSTREAM DECAY BASED ON STURGESS/GARTSHORE METHOD

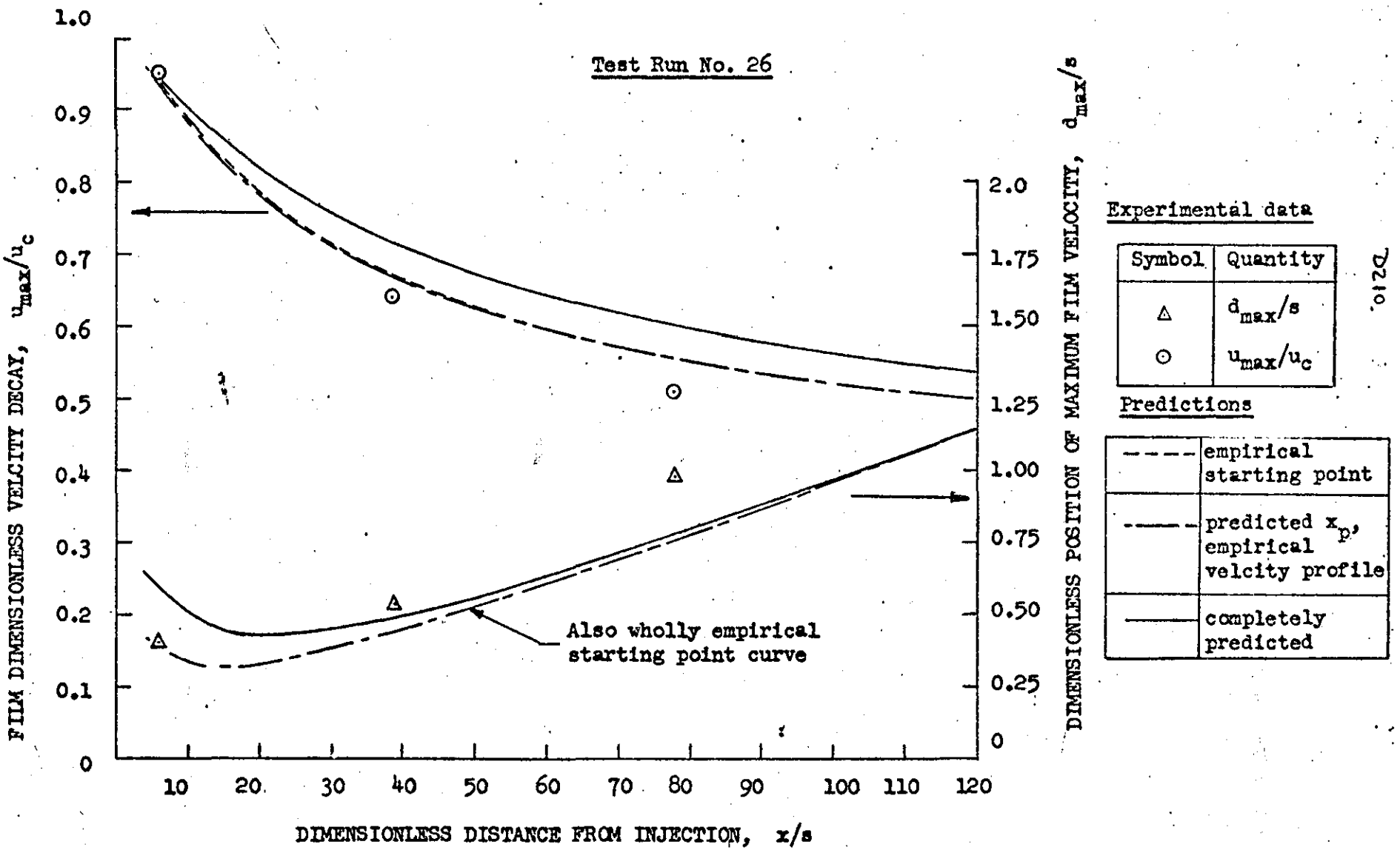

FIG. 11.53: PREDICTION OF FILM DOWNSTREAM DEVELOPMENT BASED ON STURGESS/GARTSHORE METHOD

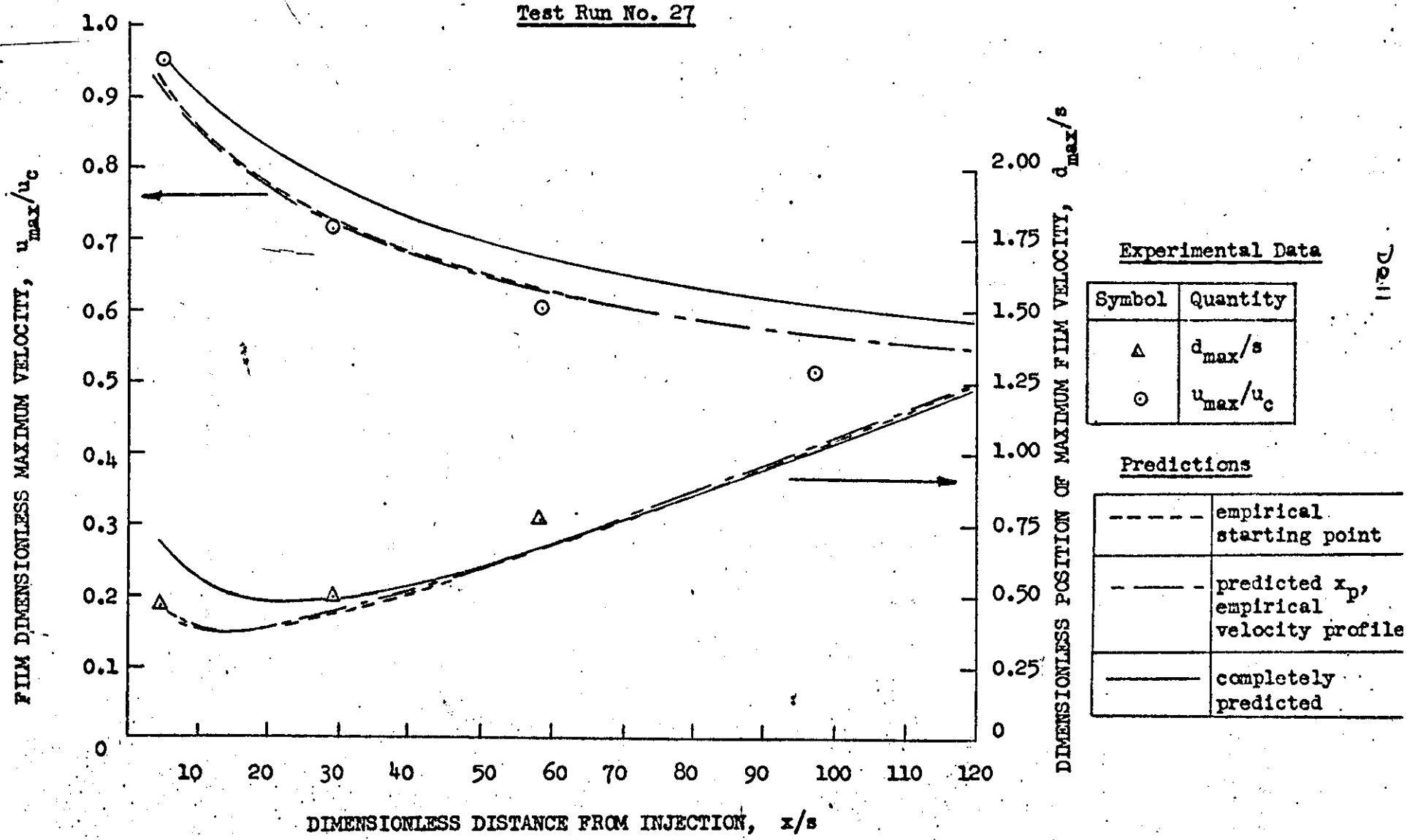

FIG. 11.54: PREDICTION OF FILM DEVELOPMENT DOWNSTREAM BASED ON STURGESS/GARTSHORE

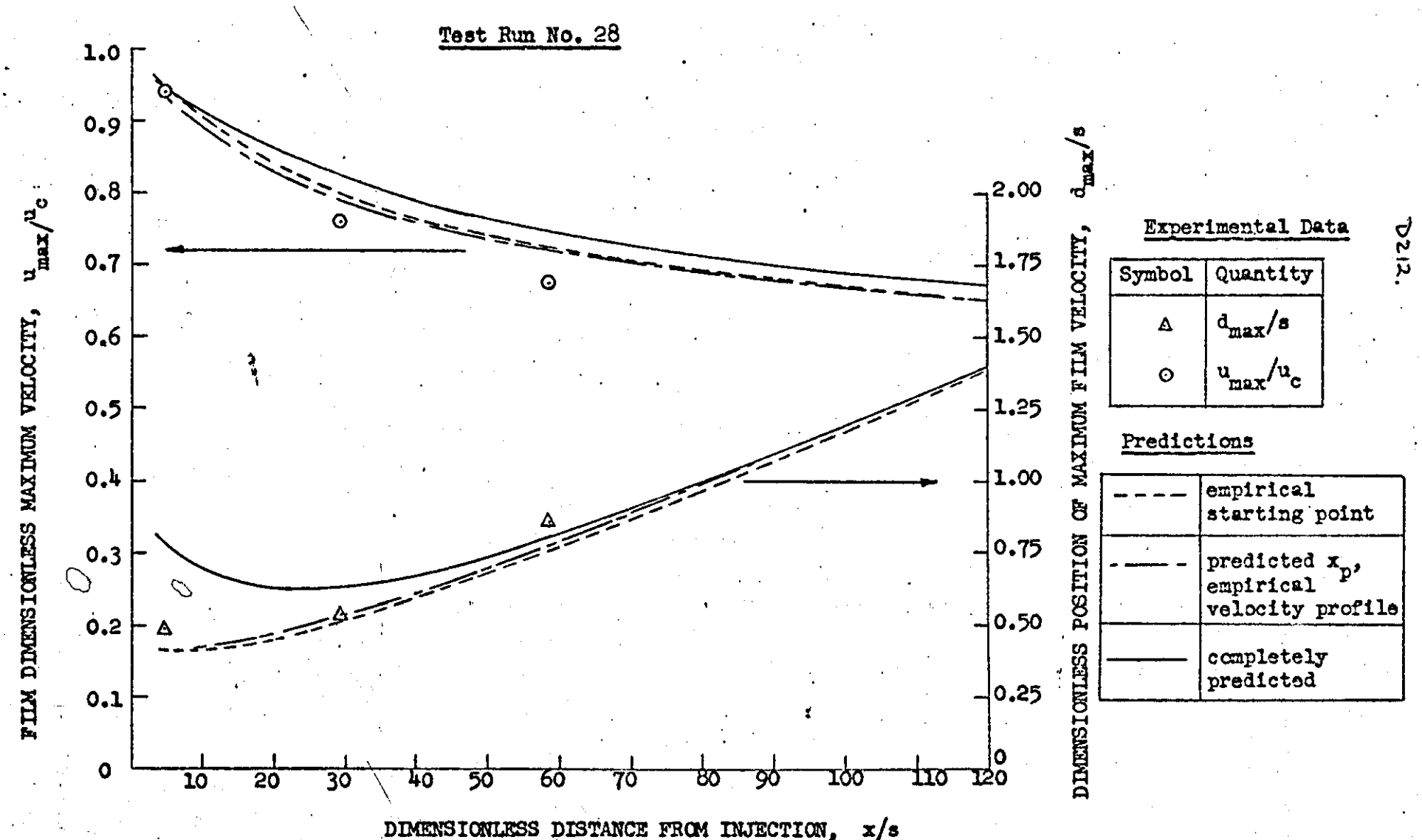

FIG.11.55: PREDICTION OF FILM DOWNSTREAM DEVELOPMENT BASED ON STURGESS/GARTSHORE METHOD

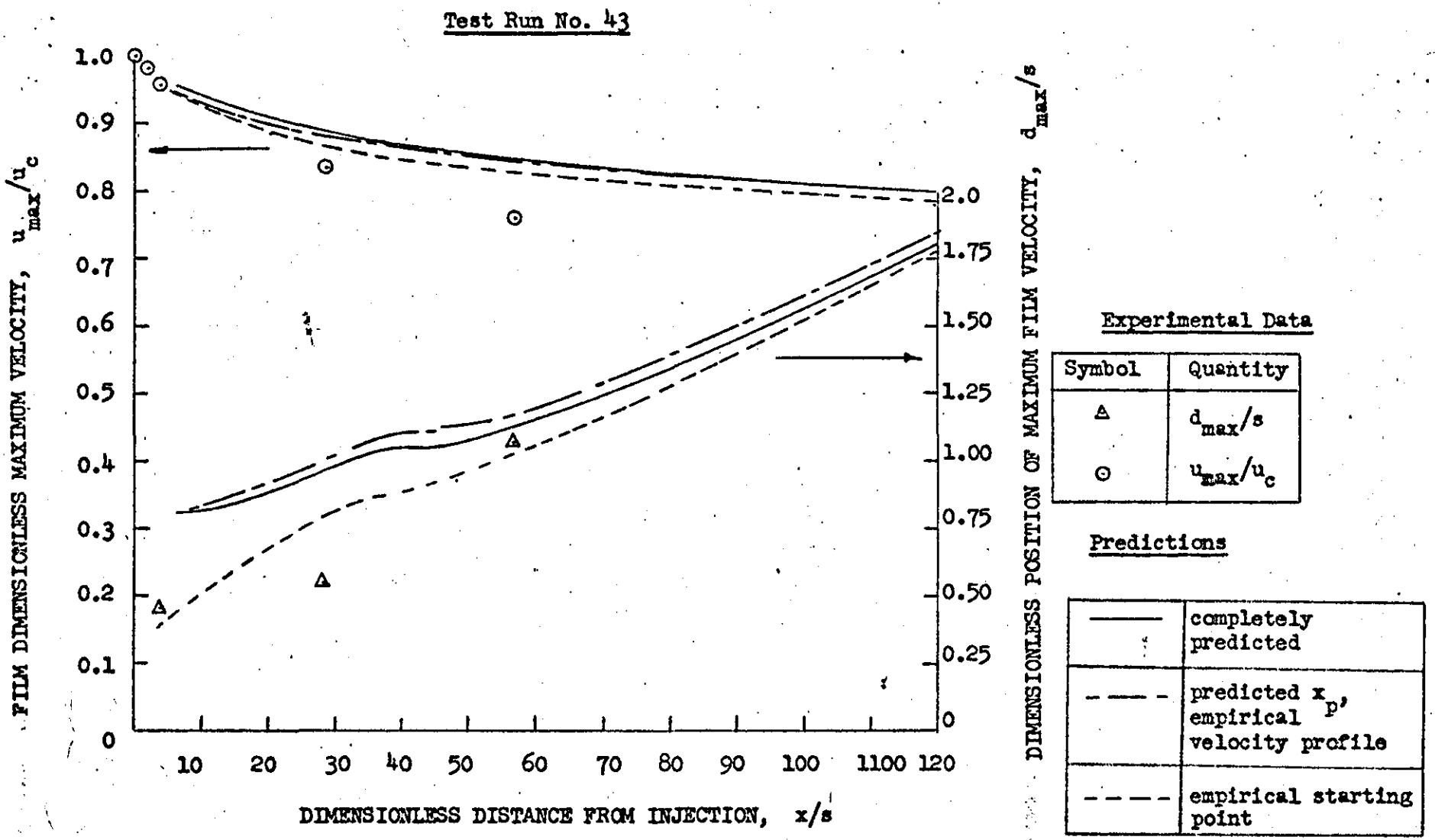

FIG. 11.56: PREDICTION OF FILM DOWNSTREAM DEVELOPMENT BASED ON STURGESS/GARTSHORE METHOD

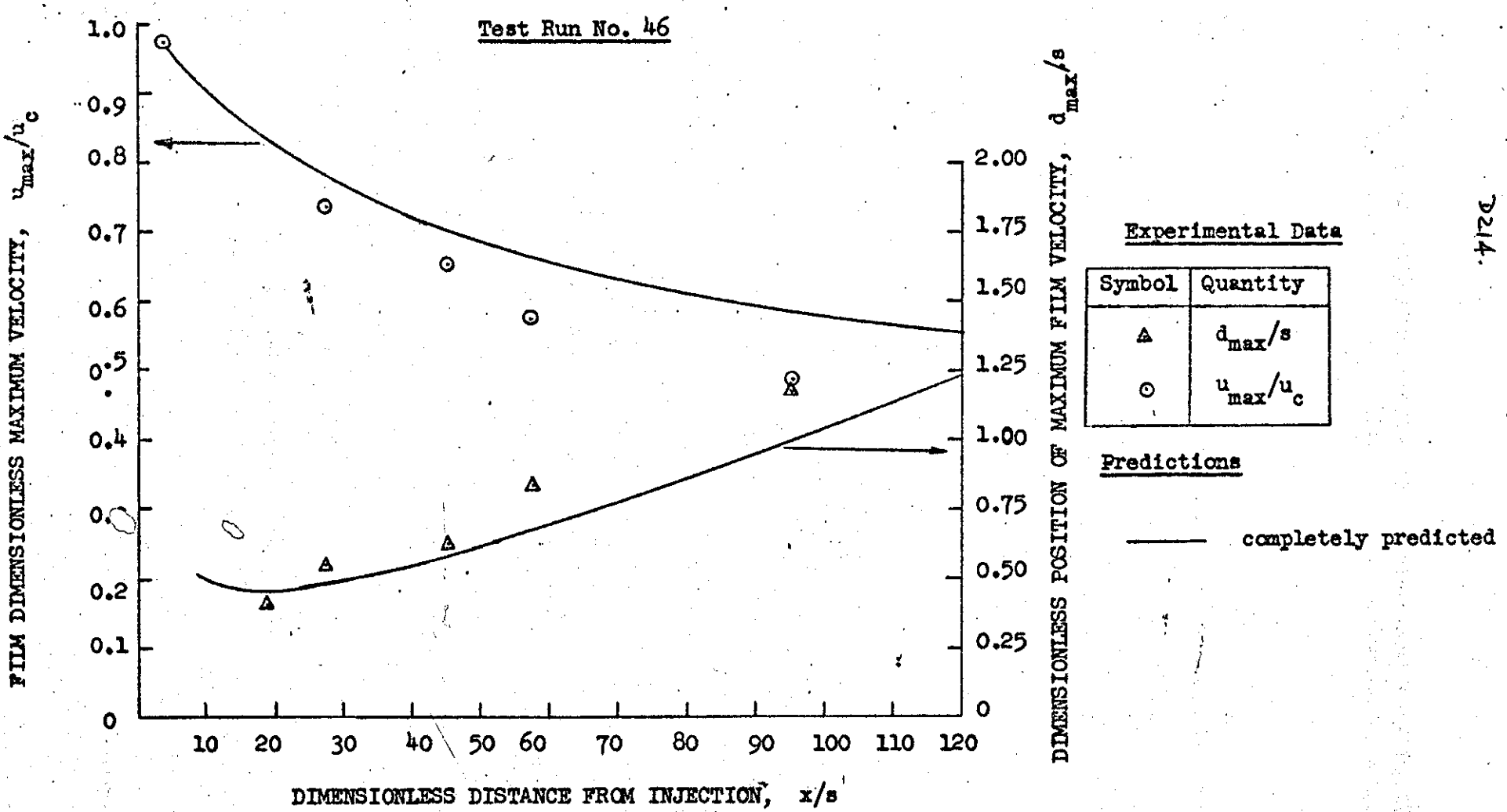

FIG. 11.57: PREDICTION OF FILM DOWNSTREAM DEVELPOMENT BASED ON STURGESS/GARTSHORE METHOD

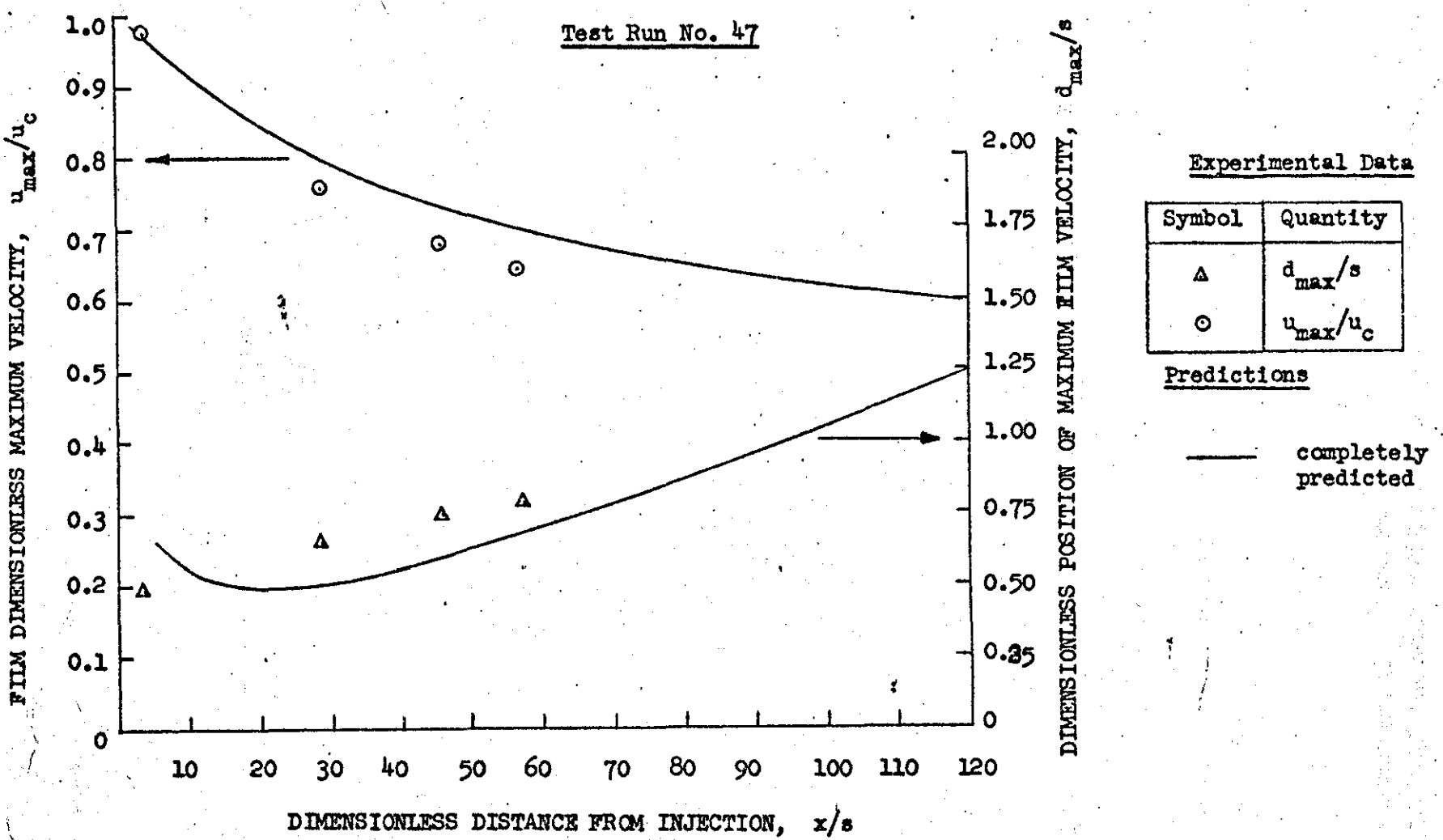

FIG. 12.1: COMPARISON OF EFFECTIVENESS PREDICTIONS WITH MEASURED DATA FOR PRACTICAL GEOMETRY G4

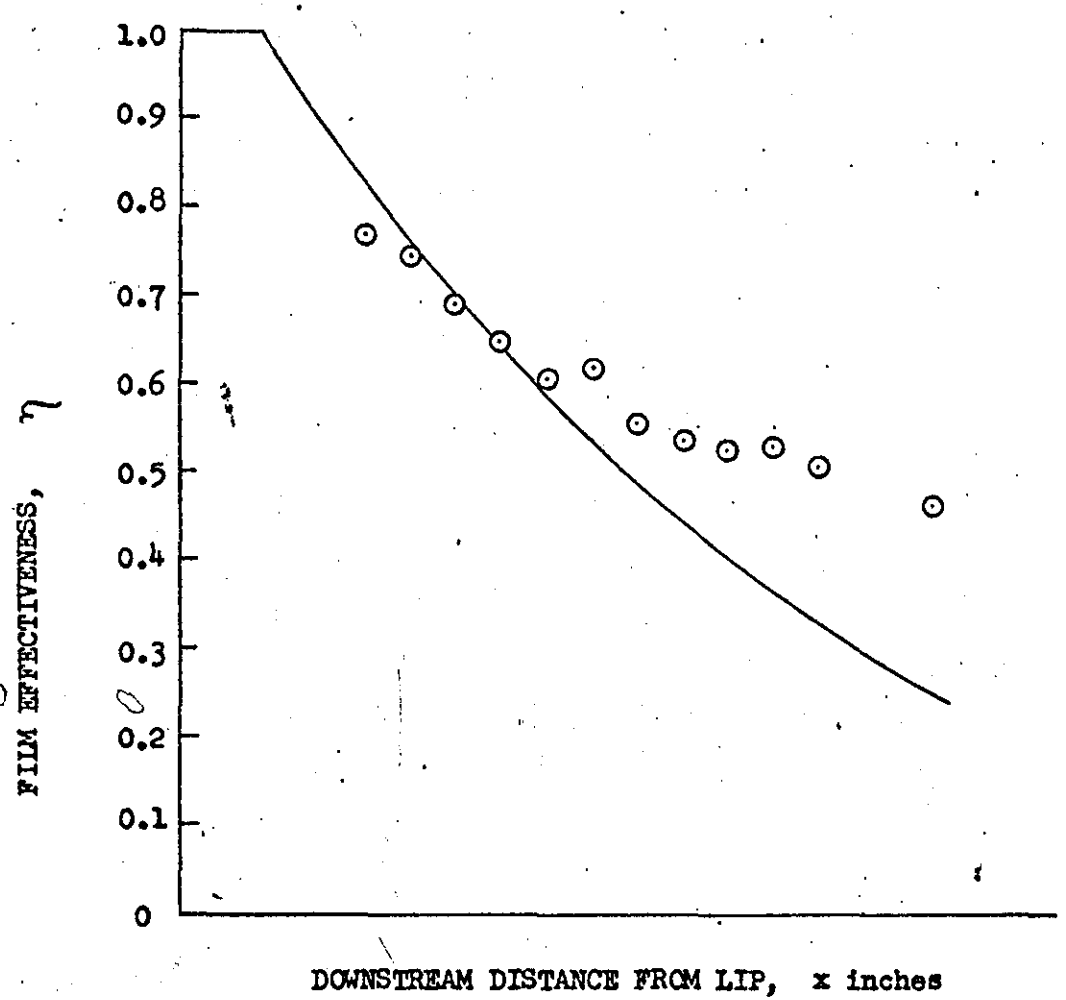

Prediction

⊙ Measured data

Injection Conditions

$M = 1.05$

$u_m/u_c = 0.628$

$Re_s = 6446$

$T_c/T_m = 1.27$

FIG. 12.2: COMPARISON OF EFFECTIVENESS PREDICTIONS WITH MEASURED DATA FOR PRACTICAL GEOMETRY G4

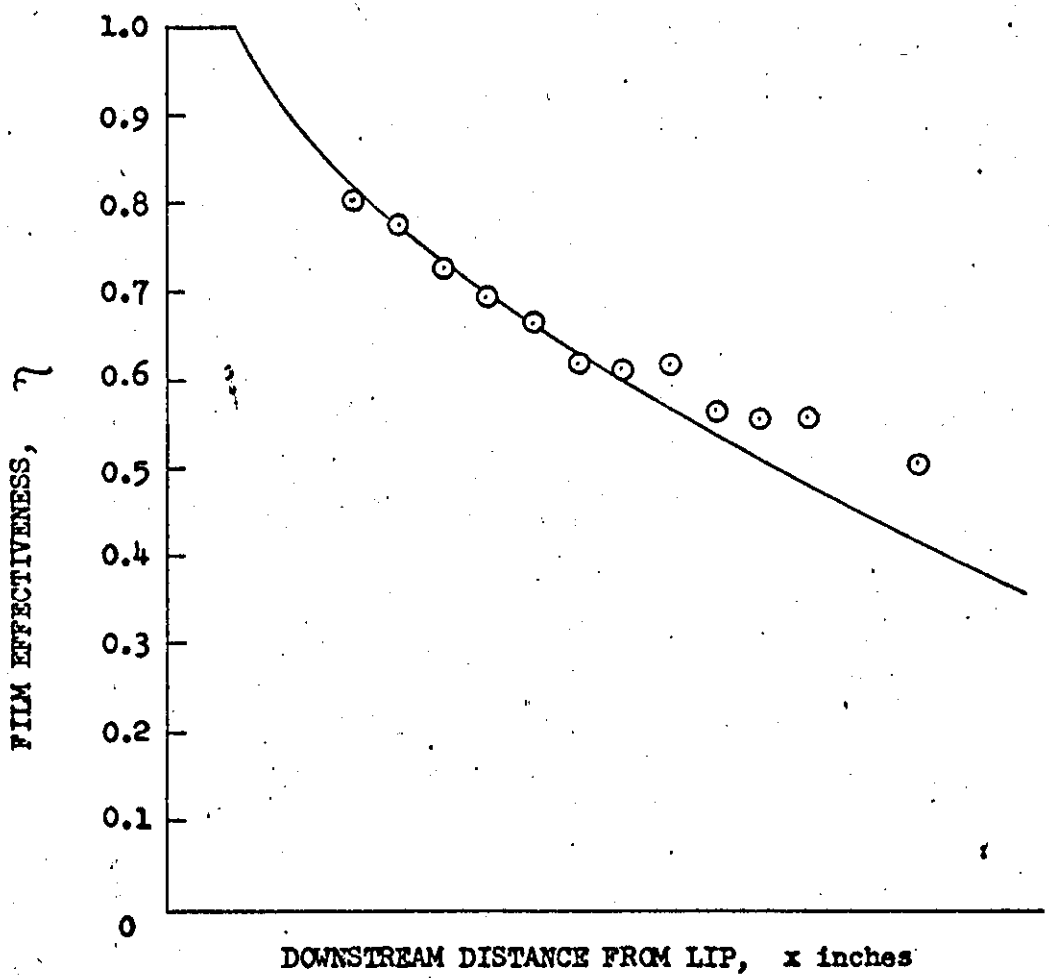

Prediction

⊙ Measured data

Injection Conditions

$M = 1.52$

$u_m/u_c = 0.437$

$Re_s = 9240$

$T_c/T_m = 1.25$

FIG. 12.3: COMPARISON OF EFFECTIVENESS PREDICTIONS WITH MEASURED DATA FOR PRACTICAL GEOMETRY G4

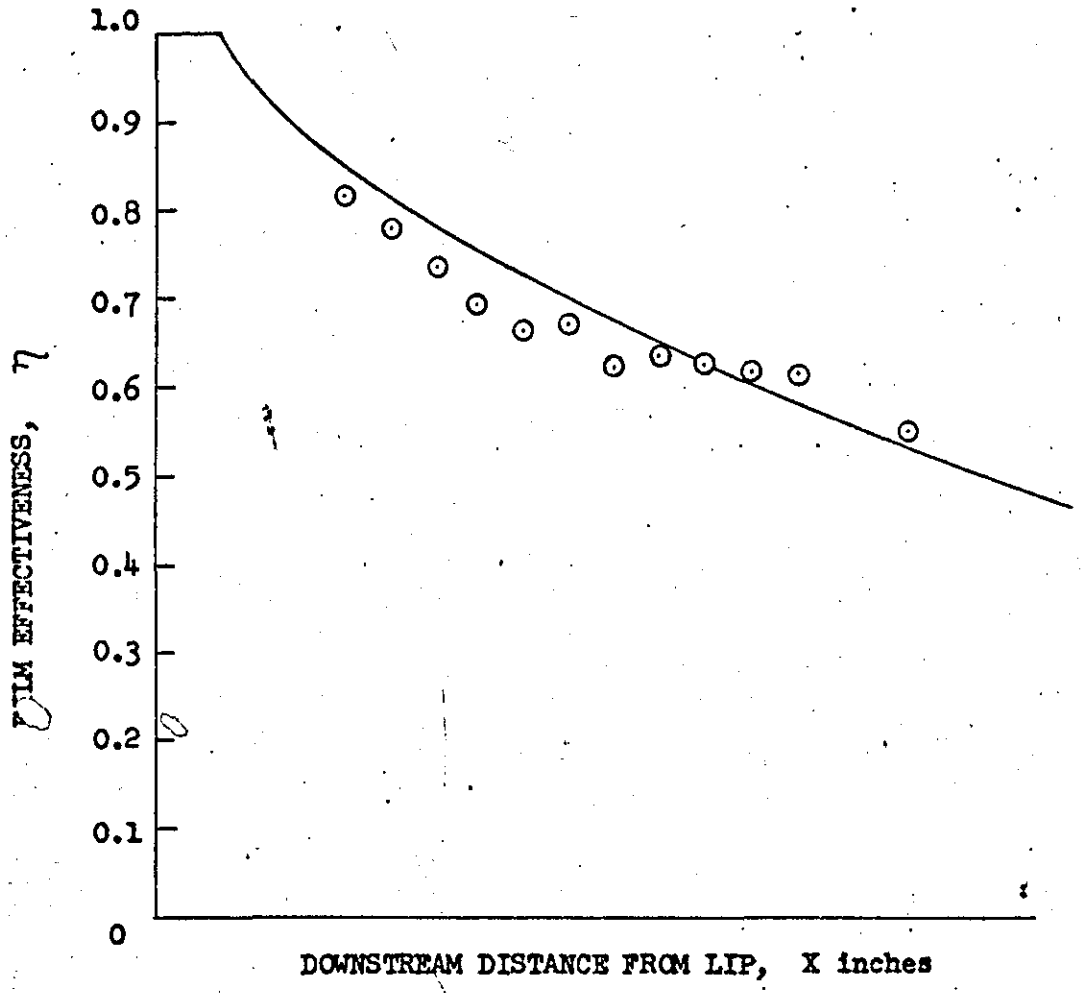

Prediction

⊙ Measured data

Injection Conditions

$M = 2.08$

$u_m/u_c = 0.329$

$Re_s = 12300$

$T_c/T_c = 1.25$

812C

FIG. 12.4: COMPARISON OF EFFECTIVENESS PREDICTIONS WITH MEASIRED DATA FOR PRACTCAL GEOMETRY G5

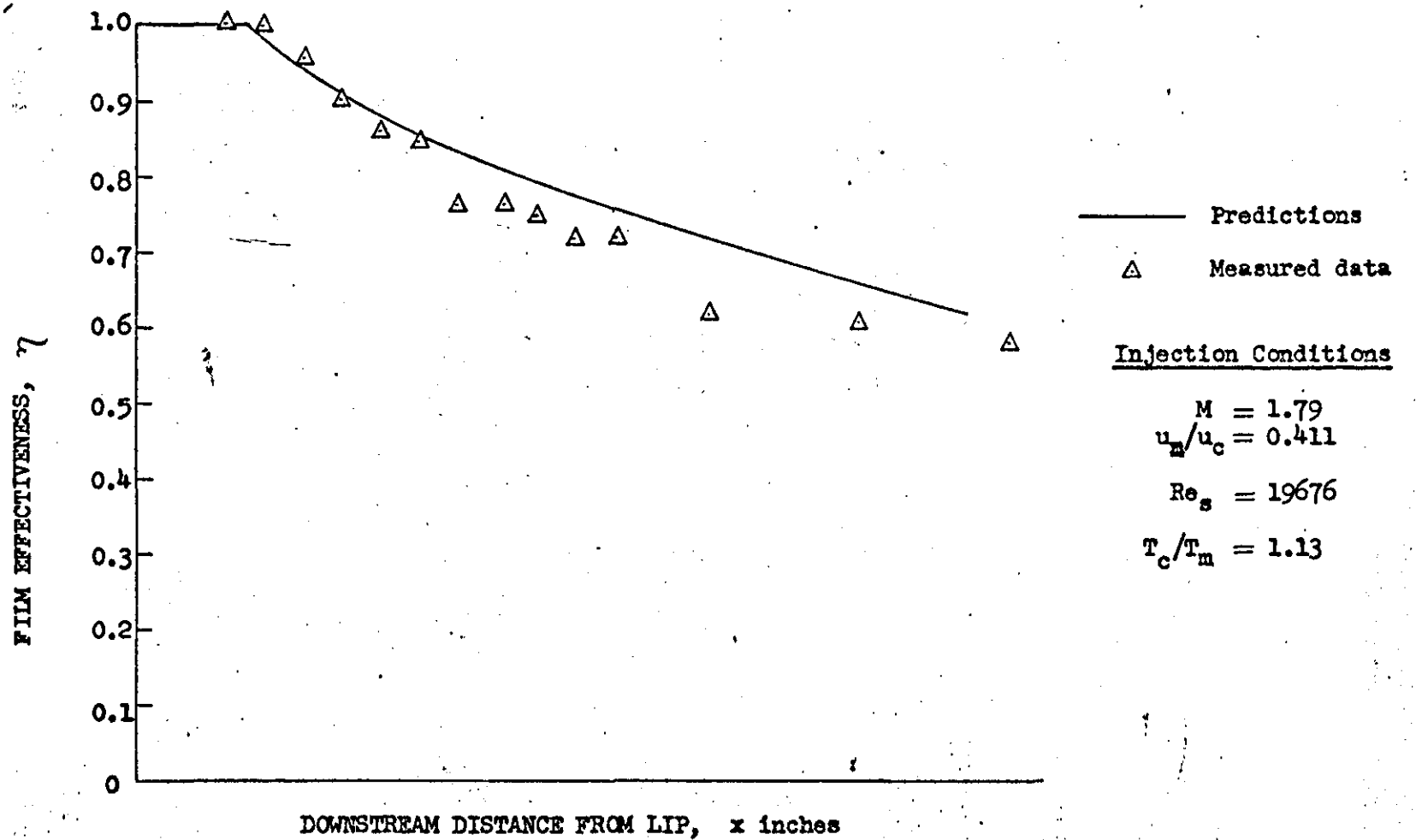

FIG. 12.5: COMPARISON OF EFFECTIVENESS PREDICTIONS WITH MEASURED DATA FOR PRACTICAL GEOMETRY G5

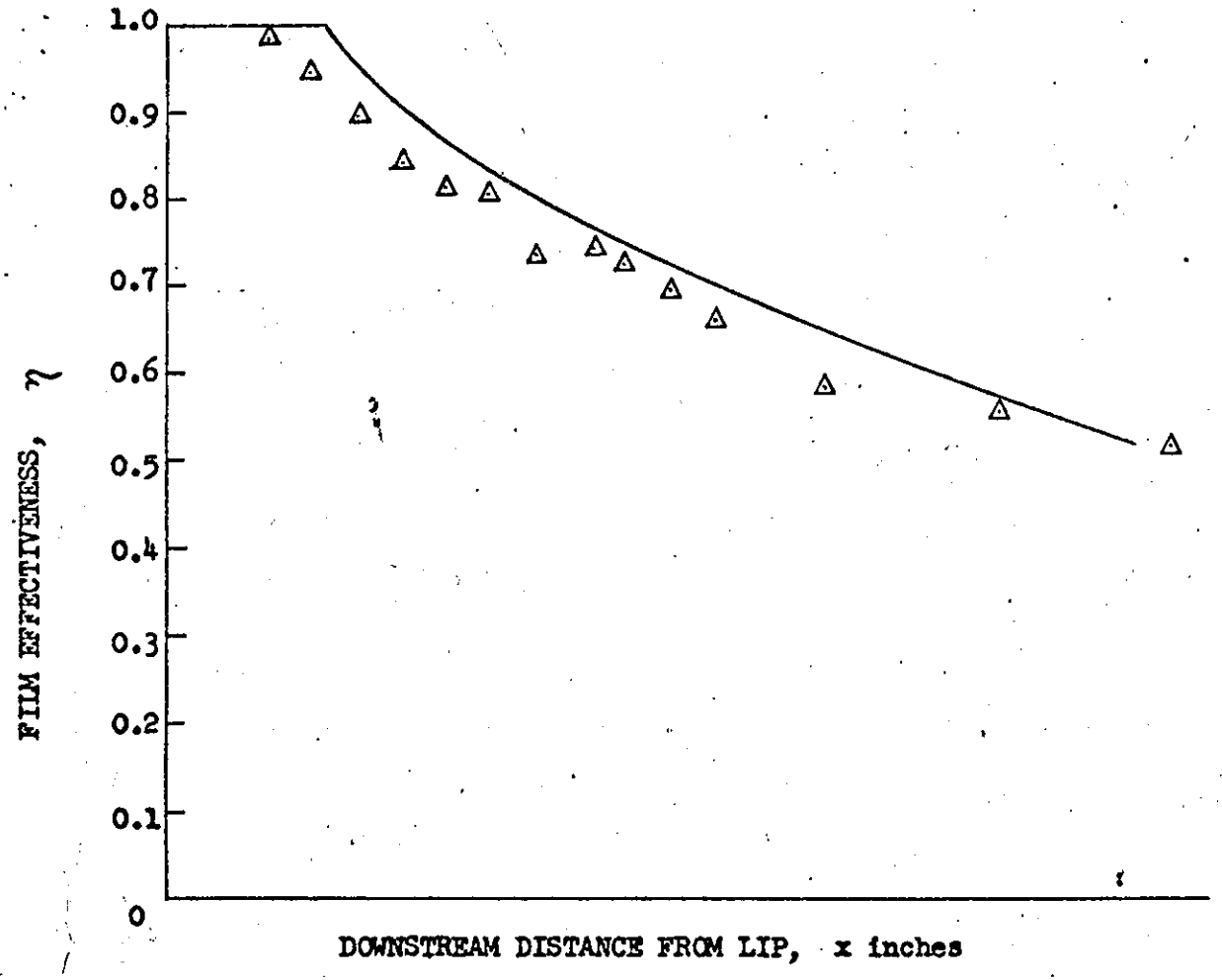

——— Predictions

△ Measured data

Injection Conditions

$M = 1.30$

$u_m/u_c = 0.5317$

$Re_s = 13675$

$T_c/T_m = 1.21$

FIG. 12.6: COMPARISON OF EFFECTIVENESS PREDICTIONS WITH MEASURED DATA FOR PRACTICAL GEOMETRY G5

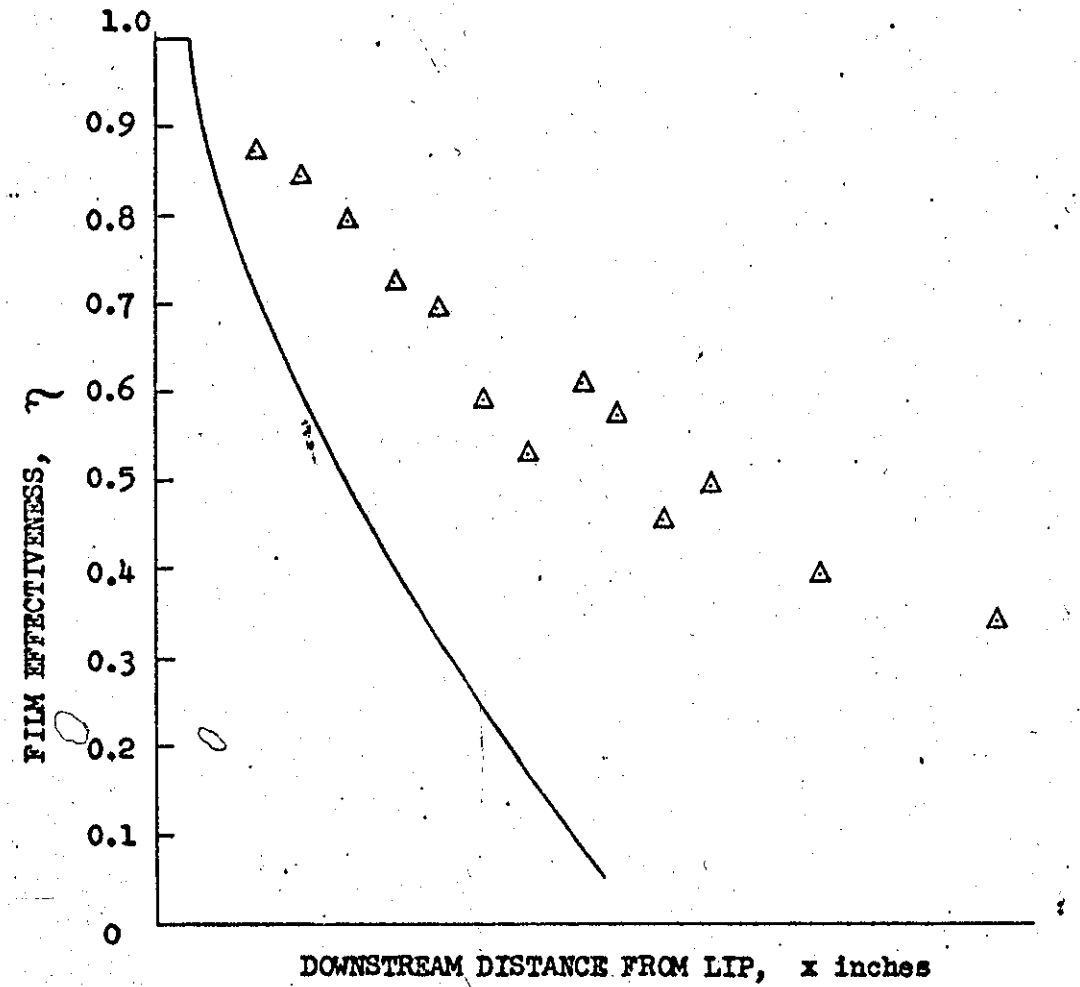

Predictions

△ Measured data

Injection Conditions

$M = 0.295$

$u_m/u_c = 2.2519$

$Re_s = 3685$

$T_c/T_m = 1.25$

FIG. 12.7: COMPARISON OF EFFECTIVENESS PREDICTIONS WITH MEASURED DATA FOR PRACTICAL GEOMETRY G6

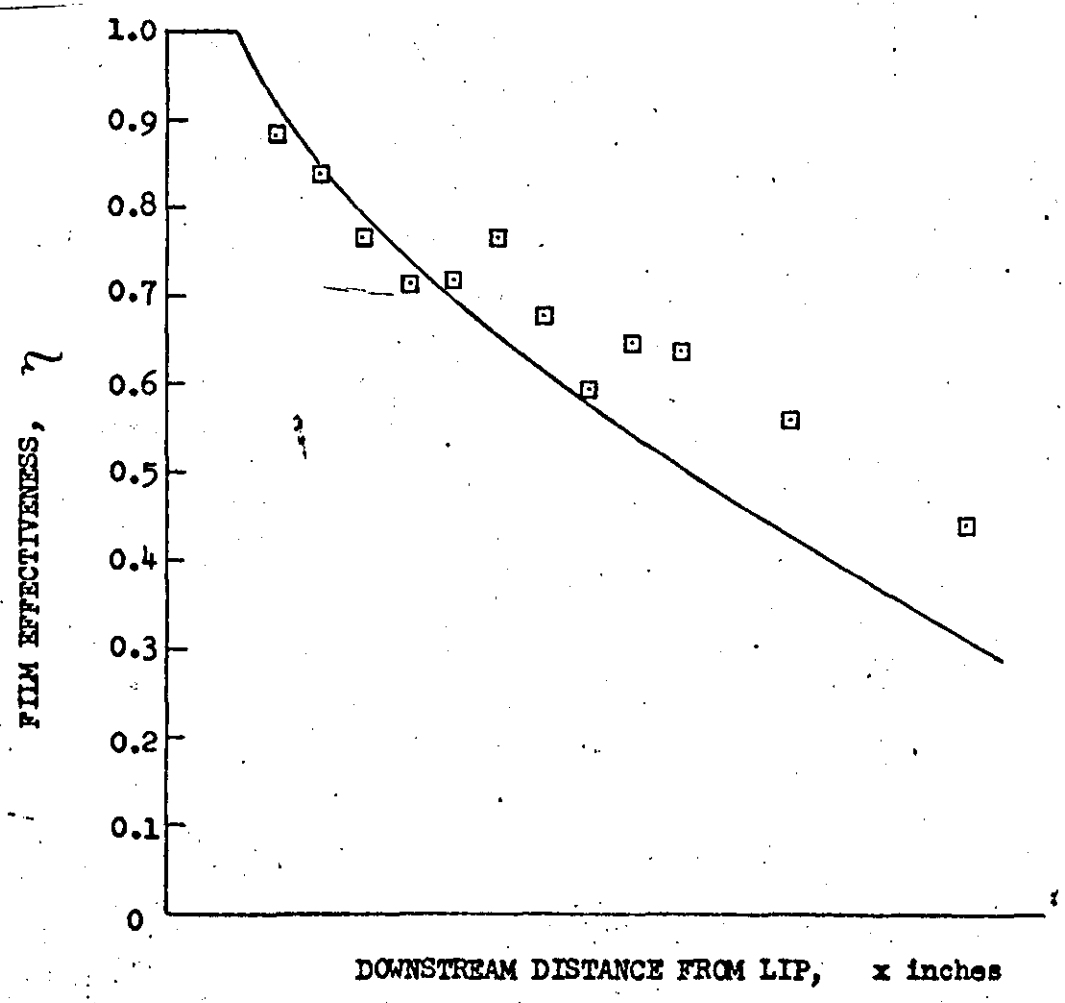

Prediction

Measured data

Injection Conditions

$M = 1.45$

$u_m/u_c = 0.539$

$Re_s = 6360$

$T_c/T_m = 1.285$

FIG. 12.8: COMPARISON OF EFFECTIVENESS PREDICTIONS WITH MEASURED DATA FOR PRACTICAL GEOMETRY G7

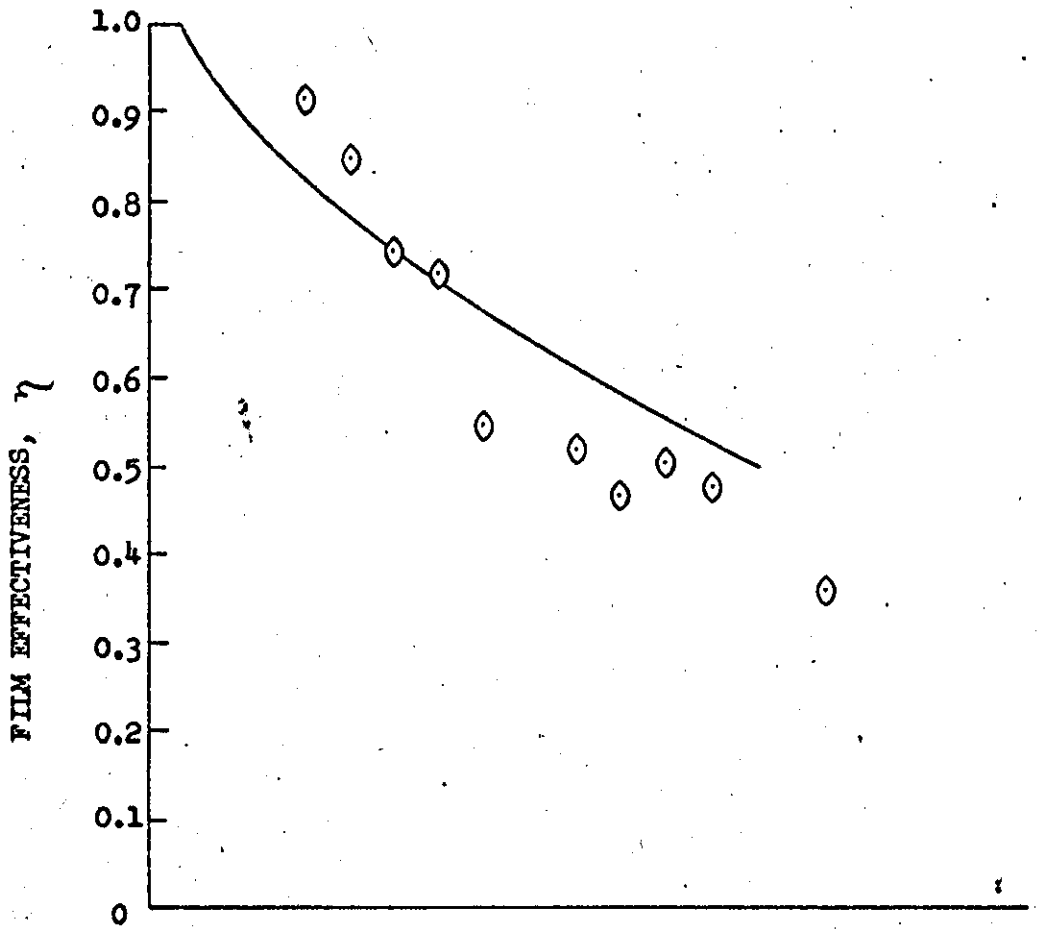

——— Prediction

⊙ Measured data

Injection Conditions

$M = 0.273$

$u_m/u_c = 3.0$

$Re_s = 3991$

$T_c/T_m = 1.282$

FIG. 12.9: COMPARISON OF EFFECTIVENESS PREDICTIONS WITH MEASURED DATA FOR PRACTICAL GEOMETRY G7

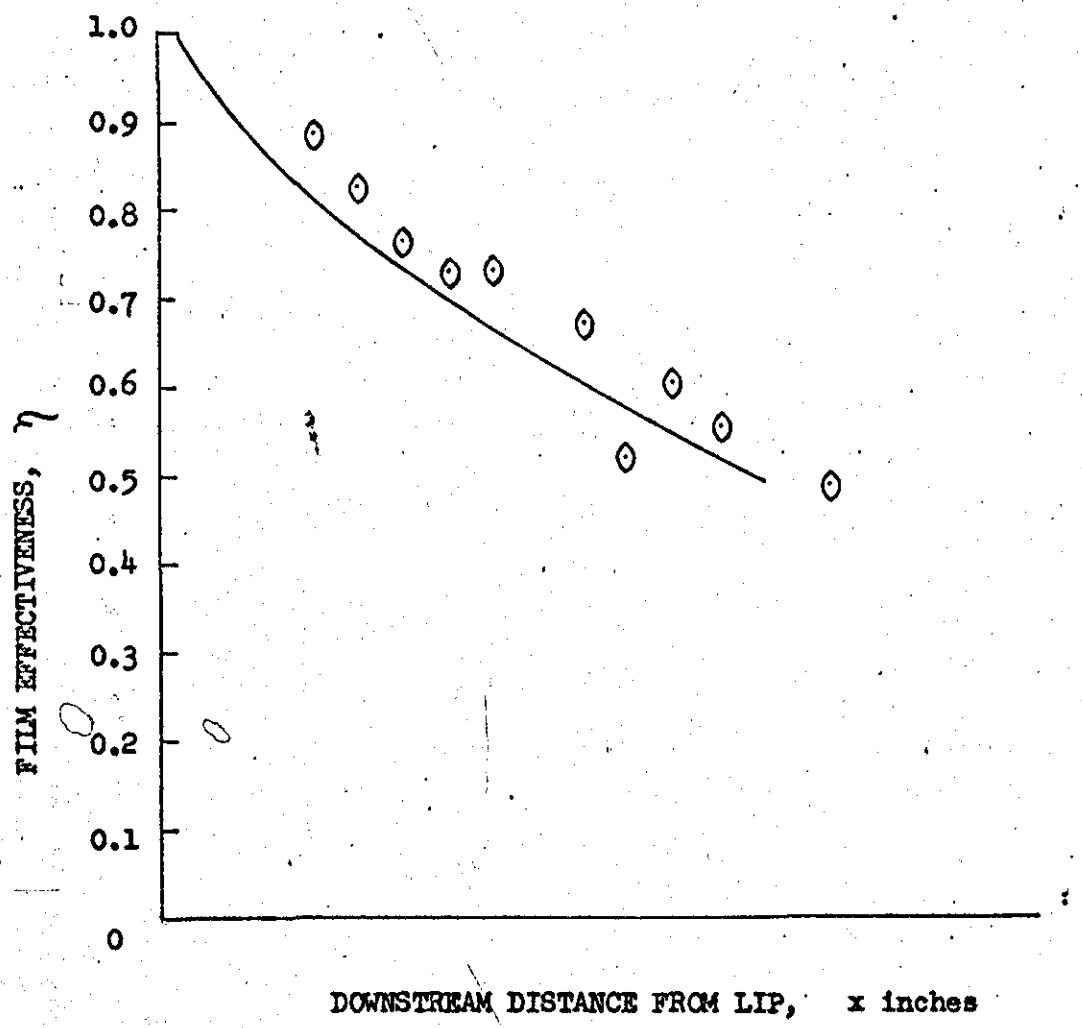

FIG. 12.10: COMPARISON OF EFFECTIVENESS PREDICTIONS WITH MEASURED DATA FROM PRACTICAL SLOT G7

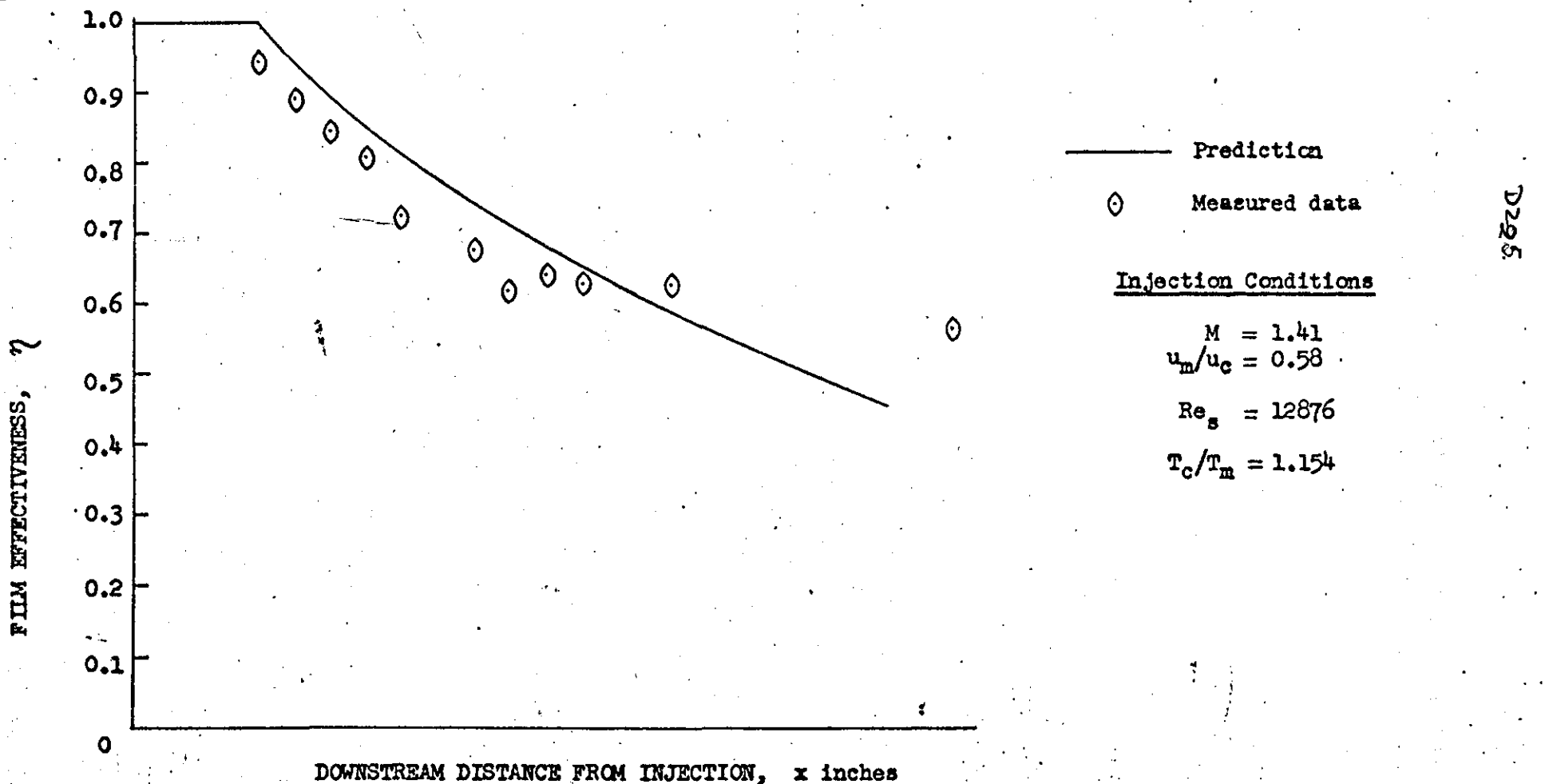

FIG. 12.11: COMPARISON OF EFFECTIVENESS PREDICTIONS WITH MEASURED DATA FOR PRACTICAL GEOMETRY G7

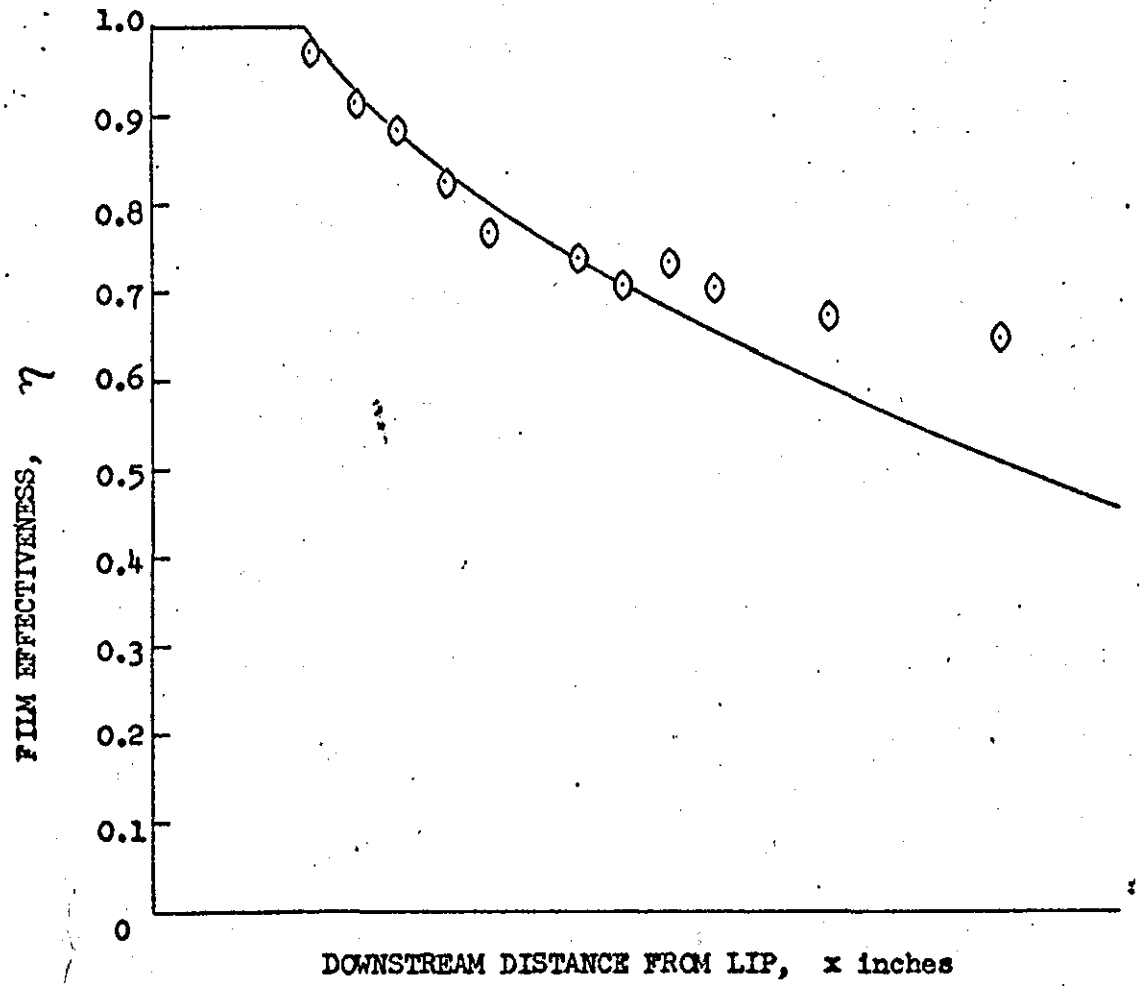

Prediction

Measured data

Injection Conditions

$M = 1.69$

$u_m/u_c = 0.49$

$Re_s = 20331$

$T_c/T_m = 1.063$

FIG. 12.12: COMPARISON OF EFFECTIVENESS PREDICTIONS WITH MEASURED DATA FOR PRACTICAL GEOMETRY G7

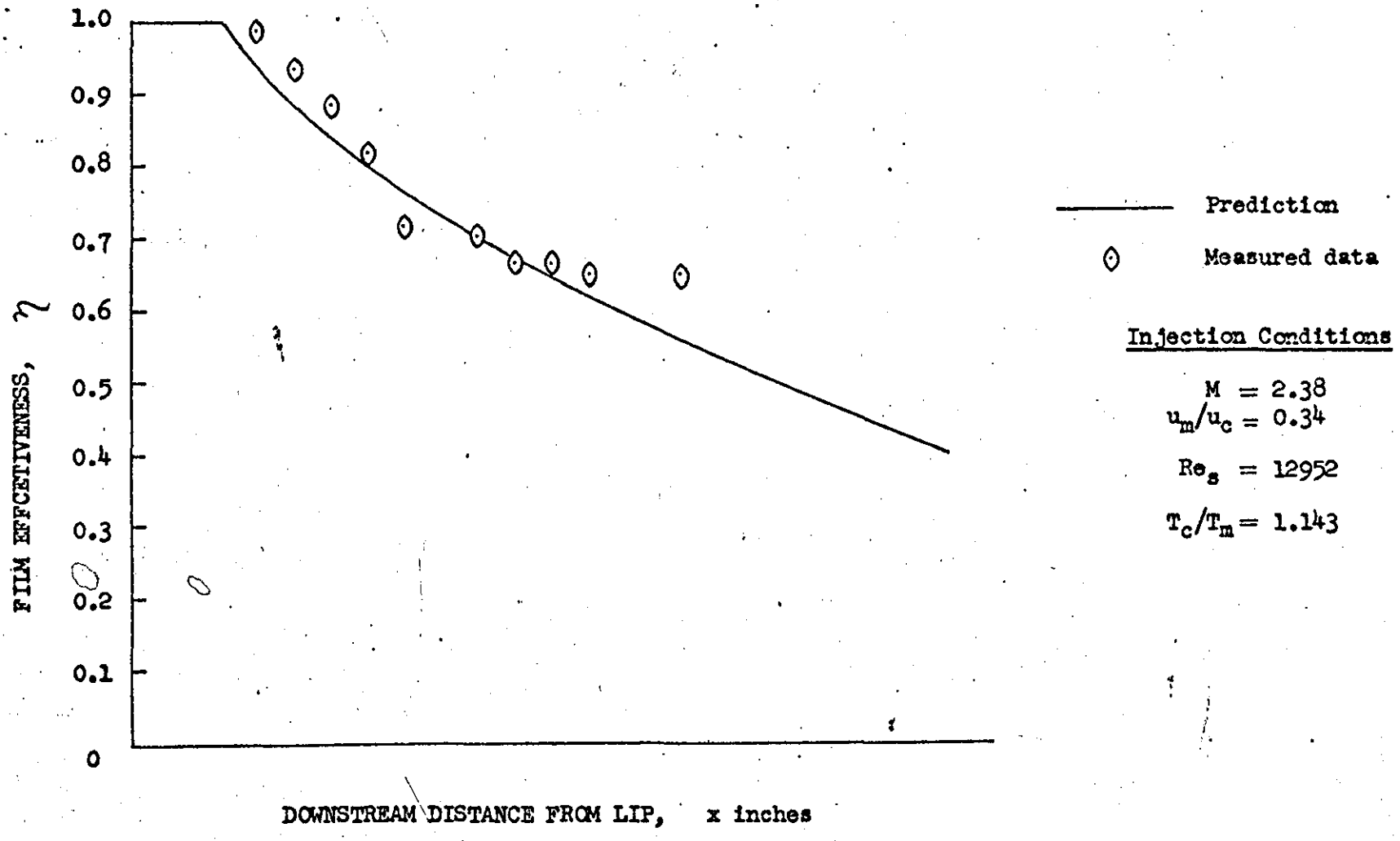

FIG. 12.13: COMPARISON OF EFFECTIVENESS PREDICTIONS WITH MEASURED DATA FOR PRACTICAL GEOMETRY G7

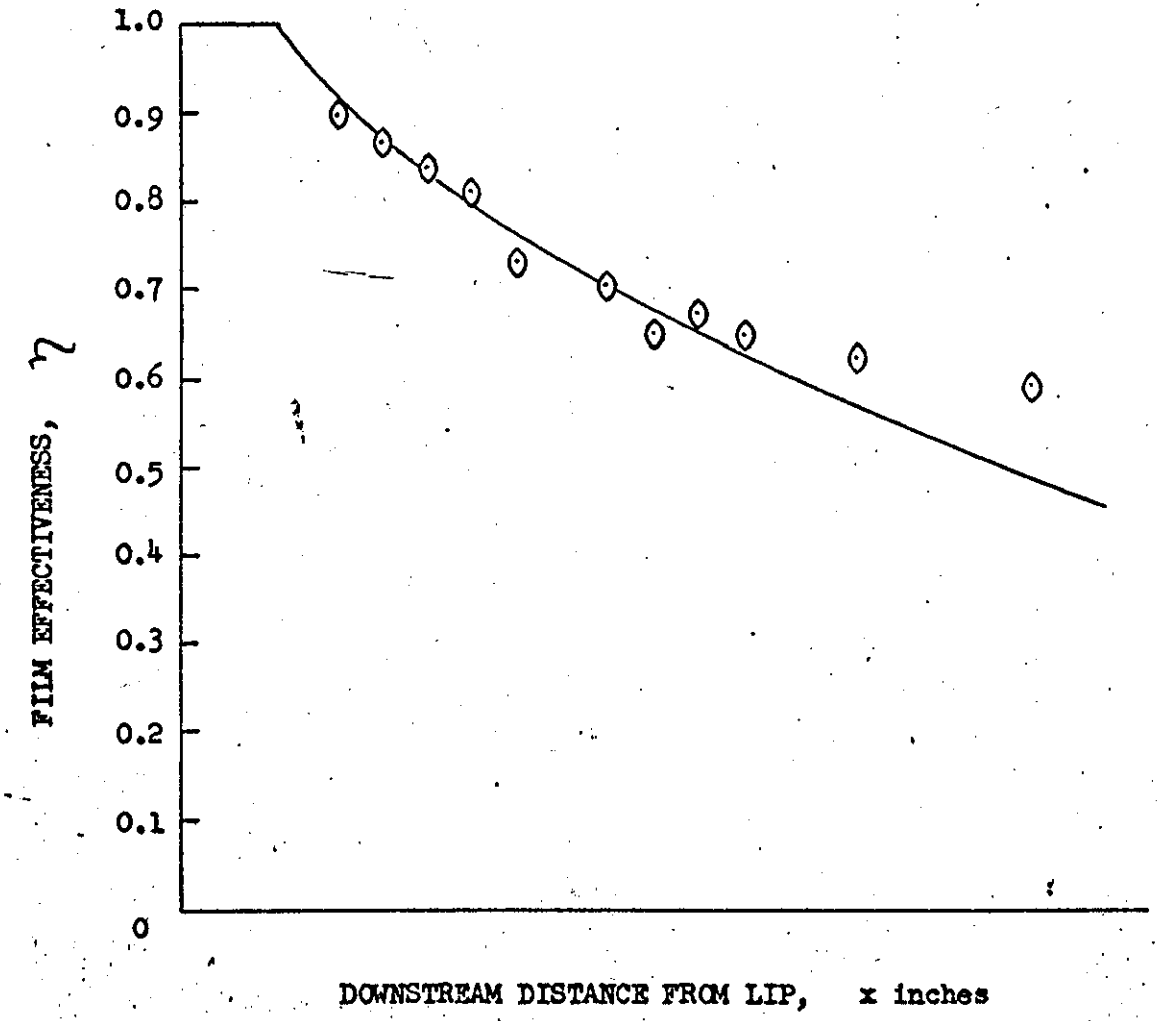

FIG. 12.14: COMPARISON OF EFFECTIVENESS PREDICTIONS WITH MEASURED DATA FOR PRACTICAL GEOMETRY G7